DTU Library

Developing and testing models for rock surface dating using optically stimulated luminescence

Freiesleben, Trine Holm

Publication date:
2021

Document Version
Publisher's PDF, also known as Version of record

[Link back to DTU Orbit](#)

Developing and testing models for rock surface dating using optically stimulated luminescence

Trine Holm Freiesleben

DTU

TECHNICAL UNIVERSITY OF DENMARK

July 2021

Preface

This dissertation is submitted in partial fulfilment of the requirements for the Ph.D. degree in Physics at the Technical University of Denmark (DTU). The Ph.D. project was initiate 15th November 2014 and completed 31st July 2021. The work was carried out at the Luminescence Research Laboratory, Risø, DTU Physics, under the supervision of Senior Scientist Kristina Jørkov Thomsen (main supervisor) and Professor Andrew Sean Murray (co-supervisor, Aarhus University). This project has been funded internally.

The main aim of this work is to i) test rock surface burial and exposure dating methods on controlled experiments, and ii) to use rocks surface burial dating in two archaeological sites of importance for the understanding of Neanderthal living in France.

Abstract

Luminescence dating of rock surfaces is an emerging absolute chronological technique that has the potential to determine how long a rock surface has been exposed to daylight and/or how long it has been buried. The development of this technique into a robust dating method will give the opportunity to determine the ages of previously un-dateable stone structures/formations in both archaeology and geology, including megaliths, chambered burial mounds, cairns, cobble fans, ice-scoured bedrock, and many others. When a rock surface is exposed to light, the latent optically stimulated luminescence (OSL) signal is reset to different degrees depending on the distance from the surface and the duration of daylight exposure. Thus, by measuring the OSL signal as a function of depth into the rock surface, it is possible to determine how long the rock surface has been exposed to daylight, and how long it was subsequently buried, by modelling the measured luminescence-depth profile. The challenges involved in this procedure are addressed here, and in particular, the ability of a rock surface to record multiple sequential burial and exposure events is investigated experimentally. Existing models are examined and new, potentially more appropriate models introduced. These models are tested using both simulated and experimental data. Based on these tests it is concluded that exposure ages are very dependent on the exact model assumptions and that fitting parameters previously assumed to be constant with depth are in fact not.

It is shown that, although correct model assumptions improve the quality of exposure age estimates, a significant discrepancies between observed and expected fitting parameter values remain and these discrepancies leads to inaccurate age estimation. This is particularly the case when post-IR signals from feldspar are used. The spectral dependency of luminescence signals is examined to better understand these problems. The demonstrated depth dependency of fitting parameters previously assumed to be constant with depth, also gives rise to discrepancies in parameter values. The surprising observation that, in rocks, the IR_{50} signal is apparently more easily bleached than the quartz fast-component OSL signal is explained in terms of light attenuation effects other than absorption (e.g. scattering and refraction) increasing the effective path length for shorter wavelengths, and so changing the shape of the light spectrum with penetration depth. This complicates parameter estimates in exposure dating even further.

Alternative approaches (rather than parameter estimation) for estimating how long a rock surface has been exposed to light are considered, based on modelling the shape and position of the measured luminescence-depth profile. It is concluded that the most accurate exposure age is derived by interpolating the depth of an unknown profile onto a curve of profile depths from known age profiles (the Exposure Response Curve, or ERC, approach). Generating ERCs by artificially illuminating surfaces at very high intensities to bracket the unknown profile, may provide calibration profiles of arbitrary 'age', determined by the total number of incident photons. Such an approach is very likely to give more accurate and precise light-exposure ages than using parameters calculated from first principles, or than using a single natural calibration profile (as is current practice).

The model dependency of rock surface burial dating is also investigated, and encouragingly it is concluded that the accuracy of burial dating is not significantly affected by the application of inappropriate models to determine the exposure history of a buried surface (and thus the degree of bleaching before burial).

Dating rock surfaces accurately requires that the environmental dose rate is modelled, because the

dose rate is also depth dependent and influenced by the size of the rock itself. A simple analytical model designed with this is mind is presented and applied.

To investigate the accuracy and precision of rock surface dating, both rock surface and standard OSL dating are applied to two important archaeological sites in Central France. These two different applications determine: 1) the timing of the changeover from Neanderthal to anatomically modern humans, and 2) that Neanderthals were capable of making symbolic engravings on cave walls. In the first case, rock surface dating is successful, but in the other, the signal of interest recorded by the rock surfaces appear to have been erased by a prolonged exposure to daylight prior to sampling, or removed by significant erosion of the surface, and only the sediments retain the chronological information. These two application studies illustrate both the potential and some of the limitations of the method.

Dansk resumé

Luminescensdatering af sten er en absolut kronologisk aldersbestemmelsesmetode, som har potentiale til at kunne bestemme, ikke blot hvor længe en sten har været udsat for dagslys men også længe den har været begravet. Udviklingen af denne teknik til en robust dateringsmetode vil give mulighed for at aldersbestemme tidligere ikke-daterbare stenstrukturer/formationer inden for både arkæologi og geologi, herunder megalitter, gravhøje, varder, og is-skuret grundfjeld.
Når sten udsættes for lys, nulstilles det latente optisk stimulerede luminescenssignal (OSL) forskelligt afhængigt hvor dybt ind i stenen man går samt af varigheden af lyseksponeringen. Ved at måle OSL-signalet som funktion af dybden, er det muligt at anslå, hvor længe stenen har været eksponeret for lys, og hvor længe stenen efterfølgende har været begravet, ved at modellere den målte luminescensprofil.
Der er flere udfordringer med denne lovende metode og her undersøges særligt stens evne til at lagre information om flere sekventielle begravelser og lyseksponerings perioder eksperimentelt. Eksisterende modeller testes og nye, potentielt mere passende modeller introduceres. Disse modeller testes ved hjælp af både simulerede og eksperimentelle data. Baseret på disse forsøg, konkluderes det, at den beregnede lyseksponeringstid i særlig grad afhænger af de nøjagtige modelantagelser, og at flere af modelparametre, som hidtil har været antaget for at være konstante med dybden, rent faktisk ikke er det.

Det viser sig, at selvom korrekte modelantagelser forbedrer kvaliteten af bestemmelsen af lyseksponeringstiden, så er der fortsat betydelige uoverensstemmelser mellem observerede og forventede parametre, og disse uoverensstemmelser fører til unøjagtig aldersbestemmelse. Dette gør sig især gældende, når der bruges post-IR-signaler fra feldspat. Den spektrale afhængighed af luminescenssignaler undersøges for bedre at forstå disse uoverensstemmelser. Den påviste dybdeafhængighed af parametre, der tidligere er antaget at være uafhængig af dybden, giver også anledning til uoverensstemmelser i parameterværdier. Den overraskende observation at IR_{50} signalet i sten tilsyneladende bliver nulstillet hurtigere end signalet fra kvats, tilskrives at have en sammenhæng med andre lysdæmpningseffekter end blot absorption (f.eks. spredning og brydning). Dette kan øger den effektive "path-lengh" for kortere bølgelængder og ændrer således lysspektrets form med indtrængningsdybden. Dette komplicerer parameterestimater i datering af lyseksponeringsperioder i sten.

iv

Der foreslås en alternativ metode bestemmelse af lyseksponeringstider (frem for ved direkte parameterestimering). Denne metode er baseret på positionen af den målte luminescensprofil. Det konkluderes, at den mest nøjagtige eksponeringsalder findes ved at interpolere eksponeringsdybden, fra profilen man ønsker at aldersbestemme, på en kurve af profildybder fra kendte aldersprofiler (eksponerings-respons-kurve eller ERC-metoden). Generering af ERC-kurver kan ske ved kontrolleret laboratorie belysning af sten ved brug af meget høje intensiteter, hvorved man kunstigt kan give disse kalibreringsprofiler en vilkårlig 'alder'. Denne metode vil højest sandsynligt give mere nøjagtige og præcise lyseksponeringsaldre end ved hjælp af parametre bestemt ud fra teoretiske betragtninger, eller ved brug af én enkelt naturlig kalibreringsprofil (som er gældende praksis).

Contents

Chapter 1

Introduction

Rock surface dating using optically stimulated luminescence (OSL) is a novel absolute chronological technique that has significant potential to increase our knowledge of the timescales involved in many important archaeological and geological questions. The technique has the potential to determine how long a rock surface has been both buried and/or exposed to daylight or the rate at which it has been eroded. In archaeological applications, rock surface OSL dating has, for instance, been used to constrain the time of creation of rock art in the Great Gallery in Canyonlands National Park (USA)[1], when a pavement in a "Rodedian" prehistoric cult site in Negev desert (Israel) was constructed[2] and to establish the burial and exposure age of a Danish iron age floor stone previously used as a whetstone[3]. The technique has also been used to e.g. directly date lithic artifacts[4,5], flake scars from lithic quarry sites[6] and Megalithic structures[7–10]. In geological applications, the technique has been used for instance to date raised beach deposits for the purpose of reconstructing past sea levels[11–14], to date glaciofluvial cobbles to understand ice sheet dynamics[15] and paleo-glacier reconstruction[16], and for reconstructing coastal boulder movements for hazard assessment[17]. The technique is also finding increasing use in the evaluation of hard rock surface erosion rates[18–20], which is important for quantification of earth surface processes. The potential of rock surface dating using OSL is just beginning to be tapped, and the potential benefits of improving the accuracy and precision of this technique are considerable.

1.1   Optically Stimulated Luminescence

The evolution of Earth's surface and how it responds to climate change is recorded and preserved in sedimentary archives, but only by establishing an absolute and reliable chronology can we interpret these archives. Optically stimulated luminescence (OSL) dating is a well-established absolute chronological method to determine the the burial age of sedimentary grains. OSL is almost universally applicable to the sedimentary record of the late Quaternary, and the method has, during the past 20 years, evolved to become one of the major chronometric tools used in high-profile late Quaternary research, e.g. study of sea-level changes[21], loess archives[22,23], ice cores[24], continental (de)glaciation histories[25], recurrence frequency of extreme events[26], soil turnover rates[27] and human evolution and migration studies[28–31]. OSL can be applied over a wide age range from ∼10 to ∼500,000 years, depending on the characteristics of the deposit[32].

OSL uses the ability of naturally occurring minerals (particularly quartz and feldspar) to absorb and store energy emitted from the radioactive decay of natural radionuclides, and from cosmic rays. The stored energy is released when the minerals are exposed to daylight (or heated). If a sample is first exposed to daylight (i.e. any latent luminescence signals are bleached, or reset) and subsequently buried, it will store some fraction of the energy absorbed during burial. The longer the burial time, the more energy is stored, until the storage capacity is fully used, and the system saturates. When the energy is released, (e.g. during light stimulation), part of it is converted to visible light (luminescence) and escapes the mineral; if this stimulation occurs in the laboratory, the resulting optically stimulated luminescence (OSL) can be measured. The OSL signal is then calibrated in terms of the amount of energy absorbed (the dose). The rate of energy absorption (the dose rate) can then be derived from a knowledge of the natural radionuclide concentrations in the sediment, determined using, e.g. gamma spectrometry, neutron activation or inductively coupled plasma mass spectrometry (ICP-MS), with corrections for water content effects. A cosmic ray contribution is derived from a knowledge of burial depth, altitude and latitude. Then the burial age (A) is calculated by dividing the dose (D) by the dose rate $(\dot{D})$, i.e. $A = D/\dot{D}$.

One fundamental assumption in standard applications of OSL dating is that the target mineral was sufficiently exposed to light before or during burial to completely reset any latent luminescence signal. If this assumption is not met, the sample is described as poorly bleached or incompletely reset and the resulting OSL age is likely to overestimate the true depositional age. If significant incomplete resetting is expected, single-grain OSL techniques are often applied in combination with statistical "minimum age modelling" [e.g. 33,34] in an attempt to identify the individual grains most likely to have been adequately reset at deposition. However, the success of such an approach when applied to a sample of unknown age hinges on the untestable assumption that a significant number of the sample grains were in fact well-bleached at deposition, otherwise the resulting age is only a minimum estimate [35].

Conventional multi-grain OSL dating may also be inaccurate in environments where significant post-depositional mixing has taken place [e.g. 31,36]. In such situations single-grain techniques are often applied in combination with finite-mixture modelling [37] to identify the grain population most likely to represent the true burial age. This technique is particularly applied in archaeological contexts [e.g. 29,38], because it is widely perceived that post-depositional mixing is commonplace in such contexts. However, the accuracy of this approach has had very limited success against known age samples [39], and it has been pointed out [40] that, amongst other difficulties with the technique, the dose rate to the sediment before mixing is unknown. This is clearly important in cases where it is the older component that is of interest, as is often the case [39].

A second major assumption in routine applications of OSL dating is that the environmental dose rate determined in the laboratory has remained constant throughout the burial period. The presence of water is especially important because water absorbs energy but does not emit energy as it usually does not contain significant amounts of radioactivity. A 1% increase/decrease in water mass fraction typically results in a 1% decrease/increase in the dose rate, and so a 1% increase/decrease the apparent OSL age [41], so knowing the water content history of the sample is very important in deriving accurate OSL age estimates. The determination of the life-time average water content in the sediment matrix is one of the largest sources of uncertainty in standard OSL dating [15].

1.2   Rock surface dating

Rock surface dating using luminescence relies on the same basic principles as OSL dating of sediments. Light falling on a rock surface bleaches superficial grains, and with time, the bleaching front migrates into the rock surface, with the fully bleached portion of the rock increasing with time. During burial, this bleached portion accumulates trapped charge, and the time of burial of these grains can be determined in the the usual manner. Rock surface OSL dating has several potential advantages such as unmixed material, preservation of resetting history, more likely to be bleached in mixed deposits, less likely to be affected by post deposition mixing, more likely to be associated with the burial context, and less uncertainty associated with water content estimation giving more stable dose rates. These advantages are described below.

Whereas unconsolidated sediment grains only record the dose, a rock is consolidated, and so preserves a record of both the burial dose and the extent/degree of resetting of the OSL signal prior to burial (see also section 1.2.3). This record of the light exposure history of a rock is preserved in the form of a profile of latent luminescence as a function of depth into the surface. This record, specific to each surface, or even part of a surface, provides internal evidence for the degree of resetting[42,43] of precisely those grains that are under investigation. Thus, the largely untestable assumption for standard OSL dating is directly testable in rock surface dating. From this, it is clear that rock surface dating has the potential to date difficult geomorphological environments (e.g. high-energy fluvial[44–46], (glacio-)fluvial[15] and colluvial deposits) and even what are regarded as completely unsuitable environments (e.g. moraines[47], rock falls[1,48], talus slopes, landslides, debris flows). In addition, granular convection[49] implies that larger clasts (e.g cobbles) have a better chance of light exposure after deposition than smaller clasts or sand grains, because in any transport/mixing/advection process involving a mixture of grain sizes, the larger clasts will preferentially be found at the surface of the mixture, and so be exposed to daylight. Thus, in a mixed deposit, surfaces of cobbles, for example, are more likely to have received prolonged light exposure than any given sand grain, and are thus more likely to be well-bleached. The interpretation of rock surface ages is also less likely to be complicated by post-depositional mixing (e.g. grain infiltration and/or bioturbation, including human activity). This process is considered important in both the geological and archaeological literature [e.g. 31,36]. Post-depositional mixing does not affect the dating of rock surfaces to the same degree because grains within rocks cannot move with respect to each other in the rock matrix. In addition, in most deposits, rocks are more likely to be correctly associated with their burial context than smaller particles, because they are much less likely to be mobile after deposition compared to sand grains.

A further advantage of rock surface OSL dating compared to standard OSL dating concerns uncertainties in the environmental dose rate. For a rock buried in a sediment matrix, the total dose rate is made up of contributions from both the external sediment matrix and the internal rock matrix. An unweathered rock matrix is mechanically and geochemically stable during burial, and the water content is usually negligible. In most settings, at depths of only 2-3 mm into the rock surface, the contribution from the external sediment matrix is less than 10%[15] and thus any uncertainties concerning e.g. water content history, radon gas escape and other potential disequilibria, are negligible. On the other hand, the problems of calculating the mean effective dose rate giving rise to feldspar signals remain considerable.

Rock surface dating has one major potential disadvantage compared to sediment dating, in that most crystalline rocks can be expected to have greater radionuclide concentrations, and so larger dose rates (typically > 5 Gy.ka^{-1})[18,42], than those in well-sorted sandy sediments (typical dose rates of 2-3 Gy.ka^{-1} [41]). This can reduces the potential age range of the technique, when applied to crystalline rocks. Sedimentary rocks formed from previously weathered and sorted sediments, do not usually suffer from this limitation. Another potential disadvantage is the variable or lack of quartz OSL sensitivity in primary rocks[42]. In standard OSL dating, quartz is usually the preferred dosimeter as it is ubiquitous, easily reset by sunlight exposure[50,51] and the main OSL trap is stable on a time scale of $\sim 10^8$ years[52] at ambient temperatures. However, the variable OSL sensitivity of quartz, which at least partly is determined by lithology[53], can limit its application in rock surface dating. Potassium-rich feldspar is also ubiquitous and has strong luminescence sensitivity even in primary rocks and so is a strong candidate for most rock surface dating applications[42]. However, the luminescence production mechanisms are not as well-understood as those of quartz[54], the luminescence signals are reset orders of magnitude slower[50,55,56], and the signals suffer from significant athermal loss (anomalous fading[57,58]), which requires correction[59]; usually of the order of 30-50%.

1.2.1   Development of rock surface dating

The earliest attempts to date buried rock surfaces made use of the thermoluminescence (TL) signal from calcitic rocks, assuming that the signal was bleached before burial by exposure to daylight[60–63]. This approach was, for instance used to determine the age of construction of a megalithic limestone building[60], the age of the Apollo Temple at Delphi[61], and the age of limestone pyramids in Greece[62]. However, the applicability of this method is limited because a significant residual TL signal remains even after long exposures to sunlight[64], i.e. the residual TL level is significant, and does not appear to continue to decrease with prolonged exposure time. The depth dependency of the TL signal was investigated by Polikreti et al.[65] who first developed a model to describe the dependence of TL intensity on exposure time and depth (see Table 1.1). Their model assumes first order kinetics and no trap filling during exposure/bleaching periods. They furthermore assumed no wavelength dependence on the light attenuation coefficient, the flux and TL cross-section, but proposed a time-depth model using effective values instead. They used a modern known age exposed marble surface to "calibrate" an ancient exposed marble surface.

Luminescence sediment dating was originally also pioneered using TL signals and suffered similarly from large residuals in most geological settings (see e.g. Aitken[66] for references). Huntley et al.[67] were the first to apply OSL to date quartz extracted from sedimentary samples. One of the main advantages of OSL over TL is that the important OSL signal (the 'fast-component') is reset, with negligible residual signal, $\sim 5\%$[50] by just a few seconds of exposure to full sunlight; this is orders of magnitude faster than the bleaching of TL. Thus, by using OSL the problem of large unwanted residuals is significantly reduced in most settings. Since the OSL signal is reset by sunlight faster than the TL signal, it also has the implication that the OSL signal will be bleached to greater depths in rocks. In 1997, Huntley[68] attempted to determine the burial age of quartzite pebbles using OSL. Although they did show that the light penetration was sufficient for OSL dating, their samples were insufficiently sensitive to give reliable ages. Habermann et al.[69] showed that exposure to sunlight for only a few minutes almost completely bleached the infrared stimulated

luminescence signal (IRSL) from feldspar in their granite rock sample to a depth of at least 2 mm. Greilich et al.[70] used the infrared stimulated yellow emission from a stone wall in combination with a high-spatial-resolution detection technique (HR-OSL) based on a CCD camera. Their rock burial ages were in good agreement with the independent archaeological age control for most of their samples. Morgenstein et al.[5] used the IRSL signal from the fine-grained feldspar fraction from lithic artifacts (after scraping off the uppermost part from the bleached surface), but their ages were not in agreement with the available age control. Using the blue stimulated ultraviolet (UV) signal from whole rock slices (i.e. containing both quartz and feldspar), Vafiadou et al.[71] reported complete daylight bleaching up to a depth of 5 mm after 14 days of exposure to sunlight.

1.2.2   Development of models for OSL and IRSL rock surface dating

The depth dependency of bleaching of the IRSL signal was first quantified by Sohbati et al.[42] using the model for TL proposed by Polikreti et al.[65] (see Table 1.1 and Figure 1.1a). The model successfully described the measured luminescence profiles from their naturally exposed samples. Laskaris and Liritzis[72] proposed a new mathematical model describing the attenuation of daylight into rock surfaces, assuming that the depth dependent latent luminescence in rock surfaces has a log-normal distribution (see Table 1.1 and Figure 1.1b). However, it must be noted that this assumption has no physical basis.

With the model proposed by Polikreti et al.[65] rock surface exposure dating (rather than burial dating) also became possible. Sohbati et al.[42] reported credible exposure ages obtained using this method. However, the authors themselves recognised that they were not able to determine physically realistic estimates of various model parameters from first principles; this was particularly true of $\sigma\varphi_0$ (see section 1.2.3). To overcome this problem, Sohbati et al.[1] used a sample of known exposure age (from the same geological setting as the unknown sample) to experimentally determine realistic parameter values with which to calibrate their model, particularly the detrapping rate constant at the surface. It should also be noted that this approach is only appropriate for dating rock surfaces with a relatively short exposure history and a low environmental dose rate, as trap filling during daylight exposure is not included at this point.
Sohbati et al.[73] further developed the OSL surface exposure dating model by including the simultaneous effect of daylight bleaching and environmental dose rate to make the model applicable to date non-terrestrial surfaces, where the environmental dose rates are orders of magnitude greater than on Earth (see Table 1.1 and Figure 1.1c). One of the implications of including the dose rate term is that there will be an upper limit to the measurable exposure age occurring when the bleaching rate equals the filling rate. On the Martian surface, for instance, this upper age limit is reached after exposure times of 10 to 100 ka, whereas it on Earth can be an order of magnitude larger.

One of the advantages of rock surface burial dating is that the rock contains a record of the degree of bleaching before burial. However, in order to determine if the luminescence signal was sufficiently reset, one needs to be able to predict the shape of the pre-burial luminescence profile. As a first attempt to describe a luminescence depth profile measured from a buried rock sample Sohbati et al.[44] further developed their model to include the environmental dose rate (see Table 1.1 and Figure 1.2a). However this model was not robust, because the light level caused by the environmental dose rate simply was added on top of the latent luminescence signal as a constant.

While this was a reasonable approximation for young samples, it was inadequate for modelling older samples, because it failed to represent the upper less bleached part of the luminescence profile, and so could not be used to predict the pre-burial profile accurately. Freiesleben et al. [3] further developed the model of Sohbati et al. [73] to include multiple exposure and burial events (see Table 1.1 and Figure 1.2b-d). They presented a model both with and without trap filling during exposure periods, and successfully used the model to determine the burial age of a granite cobble that was part of the flooring in an iron age hut in Denmark. This sample was exposed to daylight at the time of sampling, but because this was only a short exposure, the previous burial event was still observable in the shape of the luminescence-depth profile measured into the surface of the cobble.

Table 1.1 summarises the various models to describe of luminescence-depth profiles in literature in chronological order. Common to all models is that they assume that first order kinetics apply. In Figure 1.1, the three exposure models are illustrated for seven different exposure times. The exposure times have been selected to correspond to inflection points (the depth at which the normalised luminescence signal is half the saturation value set to unity) ranging between 1 and 13 mm (2 mm increments, see caption for further details). For the model of Polikreti et al. [65] (Figure 1.1a), the shape of the luminescence profiles does not change with depth, whereas the shapes predicted by the models of Laskaris and Liritzis [72] and Sohbati et al. [73] (Figures 1.1b and 1.1c) do change with depth. Furthermore, the model by Sohbati et al. [73] includes trap filling during bleaching (Figure 1.1c), which results in an equilibrium depth, where trap filling and trap depletion occur at same rate (see Sohbati et al. [73]). In the models by Polikreti et al. [65] and Laskaris and Liritzis [72], which do not including trap filling during exposure, the profile continues to migrate into the rock with time.

Figure 1.2 illustrates the burial model of Sohbati et al. [44] (Figure 1.2a), and the multiple event (also incuding a burial model) model by Freiesleben et al. [3] (with and without trap filling, Figure 1.2b-d) for four different burial times. Curves shown in red represent burial models in which the previous exposure period did not include trap filling during light exposure; those in black do include trap filling. All models assume initial saturation at all depths before the first exposure event (i.e. $L_0 = 1$) and the fixed exposure time corresponds to an inflection point $x_p = 7$ mm (i.e. ($L(7) = 0.5$). Thus, $\overline{\sigma\varphi_0}t_e = 760$ with the attenuation factor being $\mu = 1$ mm^{-1}. This gives for instance an exposure time of 0.8 ka if $\overline{\sigma\varphi_0} = 1000$ ka^{-1}. The relative residual luminescence level, r, is set to zero. Different burial times are simulated by choosing four different values of the luminescence at the surface ($x = 0$); i.e. $L_2(0) = 0$, 0.1, 0.3 and 0.5, respectively. These luminescence levels corresponds to the ratio of burial doses and D_c values of $\sim$ 0.10, 0.36, 0.70 giving doses of 20, 70, and 140 Gy, if $D_c = 200$ Gy. Note that the profiles for the model of Sohbati et al. [44] do not saturate to a common level, because the increase in luminescence, K, simply is added as a constant in the model. Figure 1.2b and 1.2c show the burial model by Freiesleben et al. [3] without and with trap filling during exposure, respectively. Figure 1.2d, shows the multiple event model of Freiesleben et al. [3] for a burial giving $L_2(0) = 0.5$ (i.e. corresponding to the longest burial times in Figure 1.2a-c with an subsequently exposure period (time t_{e2}) long enough to reduce the luminescence signal at the surface to zero, i.e. $L_3(0) = r$. Note that the burial event is still visible as a "kink" in the resulting profile. In the models including trap filling during light exposure (black lines in c) and d), the filling rate constant F is set to $F = E(x = 0) \times 10^{-2}$. This corresponds to an unrealistic high environmental dose rate of 200 Gy.ka^{-1} (it is commonly two orders of magnitude

smaller in terrestrial applications) if $\overline{\sigma\varphi_0} = 1000$ ka^{-1} and $D_c = 200$Gy. As the burial dose is set by the lumiescence level at the surface $= 0$ for this illustration, the filling rate constant during burial F_b is $e^{-t_b F_b} = (1 - k)/(1 - L_1(0))$.

Table 1.1: Published models describing luminescence-depth profiles in rock samples. L is the luminescence, t_e the exposure ages and t_b the burial age (see Table footnote). All models assume that first order kinetics apply. Note that the models of Polikreti et al. [65] and Laskaris and Liritzis [72] both include the residual luminescence, r.

First order models*	Assumptions	Comments	Reference
Exposure models			
$L = r + (1 - r)e^{-t_e E}$	No trap filling during bleaching, wavelength independence, no erosion		Polikreti et al., 2002 [65] [TL]
			Sohbati et al., 2011 [42] [OSL]
$L = r + \frac{1-r}{2}erfc\left(\frac{-\ln(x/c)}{d\sqrt{2}}\right)$	Log-normal distribution of residual lum. signal	No physical basis	Laskaris and Liritzis, 2011 [72]
$L' = \frac{[(E+F)L_0 - F]e^{-t_e(E+F)}+F}{E+F}$	Incl. trap filling during bleaching, wavelength independence, no erosion		Sohbati et al., 2012 [73]
Erosion models			
$L(x, \epsilon) = M\left(1, 1 + \frac{F}{\mu\epsilon}, \frac{-E}{\mu\epsilon}\right)$	Incl. trap filling during bleaching, wavelength independence	Erosion rate or exposure time	Sohbati et al., 2018 [18]
Burial models			
$L = e^{-t_e E} + K$	No trap filling during bleaching, wavelength independence, no erosion.	Extends to infinite luminescence levels	Sohbati et al., 2012 [44]
$L_2 = (L_1 - 1)e^{-t_b F} + 1$, $L_1 = L_0 e^{-t_e E}$ or $L_1 = L'$	No trap filling during bleaching, wavelength independence, no erosion.		Freiesleben et al., 2015 [3]
Multiple event models			
$L_{k+2} = L_{k+1}(L_k)e^{-t_e E}$	No trap filling during bleaching, wavelength independence, no erosion.		Freiesleben et al., 2015 [3]
$L'_{k+2} = \frac{[(E+F)L_{k+1}(L'_k) - F]e^{-t_e(E+F)}+F}{E+F}$	Incl. trap filling during bleaching, wavelength independence, no erosion.		Freiesleben et al., 2015 [3]

* L and L^* are the luminescence signals; the prime, $'$, indicates that trap filling during daylight exposure is included.

The saturation level is assumed to be unity (i.e. total number of traps N=1). $E = \overline{\sigma\varphi_0}e^{-\mu x}$. $F = \dot{D}(x)/D_c$,

t_e: exposure time, t_b: burial time, r: residual luminescence level relative to the saturation level.

c: $L(c) = 0.5$, d: dimensionless factor [72], K luminescence acquired during burial [44].

For additional parameter definitions the reader is referred to the original publications.
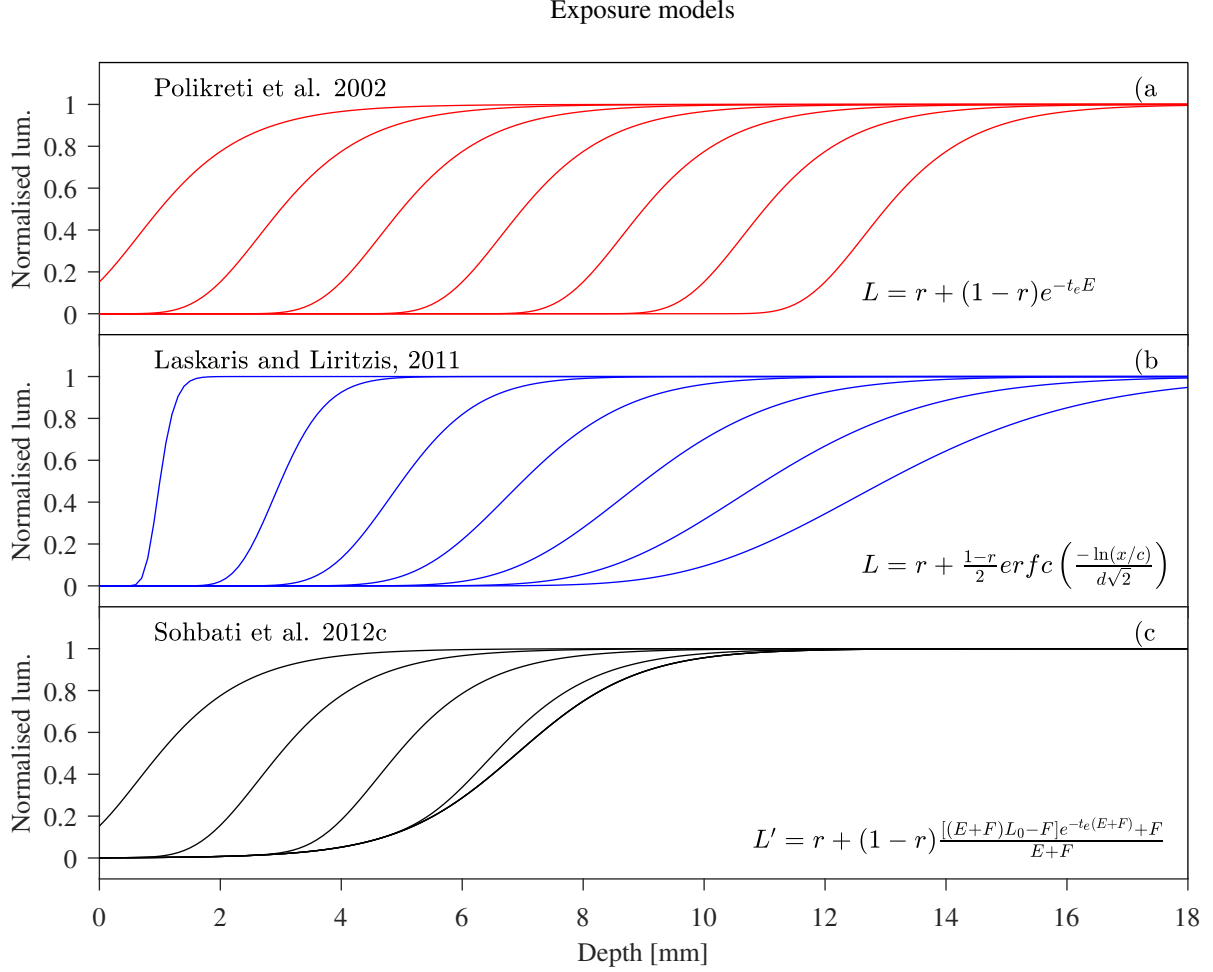
Figure 1.1: Current exposure luminescence-depth models. a) The model by Polikreti et al.,2002 [65], which does not include trap filling during exposure. b) The model by Laskaris and Liritzis, 2011 [72], which does not include trap filling during exposure. The calculation here uses $d = 0.2$. c) The model by Sohbati et al. 2012c [73], which includes trap filling during exposure. The filling rate constant F is here set to $F = E(x = 0) \times 10^{-2}$ corresponding to a environmental dose rate of 200 Gy.ka^{-1}, if $\overline{\sigma\varphi_0} = 1000$ ka^{-1} and $D_c = 200$ Gy. All models assume initial saturation for all depths prior to the first exposure event (i.e. $L_0 = 1$). The seven curves in a) and b) have been calculated using exposure times corresponding to inflection points x_p (i.e. $L(x_p) = 0.5$) ranging from 1 to 13 mm (in steps of 2 mm). In a) the inflections points $x_p = 1, 3, 5, 7, 9, 13$ mm with $\mu = 1$ mm^{-1} give $\overline{\sigma\varphi_0}t_e = \frac{\ln(0.5)}{\exp(-\mu x_p)} \simeq$ 2, 14, 100, 760, $6 \cdot 10^3$, $4 \cdot 10^4$, $3 \cdot 10^5$, respectively (i.e. $\ln(\overline{\sigma\varphi_0}t_e) = 0.6, 2.6, 4.6, 6.6, 8.6, 10.6, 12.6$). In b) the inflections points $x_p = 1, 3, 5, 7, 9, 13$ mm with $d = 0.2$mm^{-1} gives $c = x_p$ as c is defined as $L(c) = 0.5$ in Laskaris and Liritzis [72]. In c) the $\overline{\sigma\varphi_0}t_e$ from a) is used, but generates different inflections points because of the trap filling term. The relative residual luminescence r is set to 0 for simplicity.

Burial models
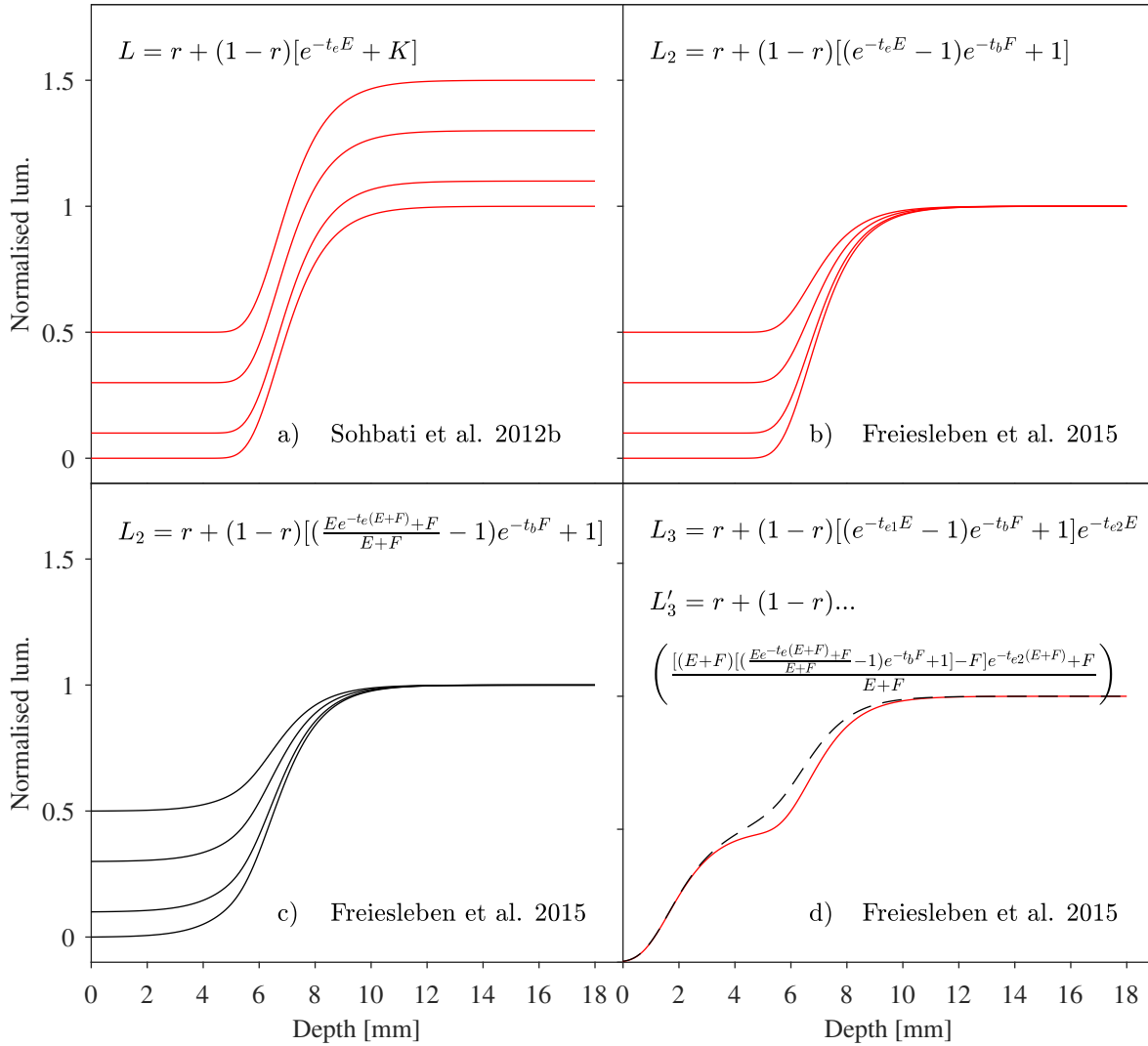
Figure 1.2: Current burial luminescence-depth models not including trap filling during exposure (red curves) and including trap filling during exposure (black curves). All the curves have been calculated assuming complete saturation at all depths prior to the first exposure. The exposure time is set such that the inflection point, x_p, is 7 mm (i.e. $L(7) = 0.5$), thus $\overline{\sigma\varphi_0}t_e = 760$ gives an exposure age of 0.8 ka, when $\overline{\sigma\varphi_0} = 1000$ ka^{-1} and the attenuation factor is $\mu = 1$ mm^{-1}. Relative residual luminescence levels is set to $r = 0$. Profiles are shown for four different burial times t_b, such that $L(0)$ is 0, 0.1, 0.3 and 0.5. These luminescence levels correspond to ratios of burial doses to D_c of $\sim 0.10, 0.36, 0.70$, i.e. doses of 20, 70, and 140 Gy, when $D_c = 200$ Gy. a) Model of Sohbati et al., 2012b [44]. b) Model of Freiesleben et al., 2015 [3] not including filling during exposure. c) Model of Freiesleben et al., 2015 [3] including filling during exposure. d) Model of Freiesleben et al., 2015 [3] for a single burial event giving rise to a luminescence level $L(0) = 0.5$ (corresponding to the longest burial times in a-c), but including a second exposure event occurring after the burial event. The length of the second exposure event t_{e2} reduces the luminescence signal at the surface to zero, i.e. $L(0) = 0$. In the models including trap filling during light exposure (black lines in c) and d), the filling rate constant F is given by $F = E(x = 0) \times 10^{-2}$. This corresponds to a dose rate of 200 Gy.ka^{-1}, when $\overline{\sigma\varphi_0} = 1000$ ka^{-1} and $D_c = 200$ Gy.)

1.2.3   Basic mathematical formulation in rock surface dating

In this section the basic mathematical formulation for rock surface exposure and burial dating is summarised. There are two main assumptions in the mathematical formulation presented here: 1) The luminescence signal, L, is proportional to the trapped electron population, n (cm^{-3}), and thus a change in the trapped electron population is reflected in the measured luminescence signal. 2) first order kinetics is assumed, which means that retrapping is assumed to be negligible.

To describe the electron population (and thus luminescence) with time, mathematically, one needs to know the rate at which the electron population changes with time, i.e. the rate equation for the trapped electron population $\frac{\partial n}{\partial t}$. Solving the rate equation with respect to time and assuming proportionality between the luminescence signal and trapped electron population, i.e. $L \propto n$, gives the luminescence with time.

The trapped electron population in quartz or feldspar crystals can be depleted by detrapping processes or increased by filling processes, i.e. traps can be emptied or filled. The rate at which the electrons population change is $\frac{dn}{dt}$. It is negative when detrapping occurs and positive when trap filling occurs. Both processes can also happens at same time. The rate constants describing the speed of these processes are the detrapping rate constant E, and the filling constant F. Thus, a general description of the change in the trapped electron population (and hence in the luminescence signal) with time is given by including both an emptying term and a filling term and the electron population at time t.

$$\frac{dn(t)}{dt} = -En(t) + F(N - n(t)) \tag{1.1}$$

where N is the total number of traps, which in luminescence terminology corresponds to the luminescence saturation level L_{sat}.

In rock surfaces the detrapping rate constant and the filling constant depend on the depth x, and thus the trapped electron population depends on depth, and Eq.(1.1) is in fact a partial differential equation.

$$\frac{\partial n(x,t)}{\partial t} = -E(x)n(x,t) + F(x)[N(x) - n(x,t)] \tag{1.2}$$

The time of interest in rock surface dating is either a burial age, t_b, or an light exposure age, t_e. Solving Equation 1.2 for either $t = t_b$ or $t = t_e$ gives the fundamental equations used in rock surface dating. However, first of all the filling rate constant, $F(x)$, and the detrapping rate constant, $E(x)$, needs to be derived.

The rate at which traps are filled, $F(x)$, depends on the total dose rate (which comes both from the rock itself as well as the surrounding medium including a usual small contribution from cosmic rays), $\dot{D}(x)$, and a sample-dependent constant D_c that characterises the rate of filling of the electron traps[73], i.e.

$$F(x) = \frac{\dot{D}(x)}{D_c} \tag{1.3}$$

When the sample is exposed to light, the trapped electron population will decrease with time at a rate depending on the probability of eviction of trapped charge from their trapping sites. This probability is the product of the flux of the incident light $\varphi(x, \lambda)$ $(cm^{-1}s^{-1})$ and the photoionisation cross section, $\sigma(\lambda)(cm^2)$ [42]. As described by Lambert-Beer's law the flux decreases with depth because of absorption and scattering processes [e.g. 72]. The flux of the incident light can be described as

$$\varphi(x, \lambda) = \varphi(0, \lambda)^{-\mu(\lambda)x} \tag{1.4}$$

where $\varphi(0, \lambda)$ is the flux of the incident light at zero depth, and μ is the attenuation factor, λ is the wavelength of the incident light and x is the depth into the rock from the surface. Thus multiplying this with the $\sigma(\lambda)$ gives the probability of eviction of trapped charge from their trapping sites for any wavelenght λ at any depth x. Integrating over the wavelength in the daylight spectrum gives an average detrapping rate constant $E(x)$

$$E(x, \varphi, \lambda) = \int_{\lambda_i}^{\lambda_f} \sigma(\lambda)\varphi(0, \lambda)e^{-\mu(\lambda)x}d\lambda \tag{1.5}$$

where λ_f and λ_i describes the effective upper and lower wavelength limits of the solar spectrum. For simplicity, we assume that μ is independent of wavelength. Then the equation reduces to

$$\begin{aligned} E(x) &= e^{-\mu x} \int_{\lambda_i}^{\lambda_f} \sigma(\lambda)\varphi(0, \lambda)d\lambda \\ &= \overline{\sigma\varphi_0}e^{-\mu x} \end{aligned} \tag{1.6}$$

However it has been stated that the assumption of μ being independent of wavelength is problematic (see e.g. Ou et al. [74]).

The solution of Equation 1.2, where t is the exposure or burial time, describes the latent luminescence signal as a function of depth into rock surfaces ($L \propto n$). Solving Equation 1.2 for $t = t_e$ has been done by i) assuming no trap filling during exposure, i.e. $F(x) = 0$ [65], and ii) including trap filling during exposure [73], i.e. $F(x) \neq 0$ to give the luminescence signal with depth and exposure time (t_e). The latter approach allows the processes of trap depletion and trap filling to occur simultaneously. On Earth, the trap filling process comes mainly from the radioactivity contained within the rock matrix itself. At or close to the rock surface (where the light intensity is greatest), the rate of filling is usually much smaller than the rate of emptying. Thus, solving Equation 1.2 with these conditions (and $L \propto n$) gives

$$i) \quad L_1(x) = L_0 e^{-E(x)t_e} \tag{1.7}$$

$$ii) \quad L_1'(x) = \frac{[(E(x) + F(x))L_0 - F(x)L_{\text{sat}}]e^{-t_e(E(x)+F(x))} + F(x)L_{\text{sat}}}{E(x) + F(x)} \tag{1.8}$$

with $F(x)$ and $E(x)$ defined by Equations 1.3 and 1.6, respectively, L_0 being the initial luminescence signal at depth x and L_{sat} the saturation luminescence level. The prime, $'$, in Eq.1.8 indicates that trap filling is included.

If a rock has been buried or in another way shielded from sunlight for an extended period of

time, the trapped electron population will reach "saturation", where the amount of trapped charge will not increase with further exposure to ionising radiation, because all trapping sites are full. The initial luminescence as a function of depth into the rock surface will thus be constant for all depths. (see horizontal blue line in Figure 1.3). Normalising the latent luminescence signal to this saturation level (i.e. $L_0 = L_{\text{sat}} \equiv 1$) simplifies the models. As a consequence of the detrapping rate constant, $E(x)$, decreasing exponentially with depth, the detrapping rate will be the highest at the surface and decrease as a function of depth into the rock surface. This is illustrated by the red line in Figure 1.3. The longer the time the rock is exposed to light, the further the luminescence-depth profile will penetrate into the rock and thus the position of the rising edge of the profile represents how long the rock has been exposed to light, i.e. the exposure age. If trap filling during exposure is ignored (Eq. 1.7), the profile will continue to migrate deeper and deeper into the rock as the exposure time is increased (see Figure 1.1a). If trap filling is included in the mathematical formulation (Eq.1.7), then the migration of the profile eventually reaches a steady-state; as the light intensity is attenuated, the rate of detrapping decreases until it equals the rate of filling (see Figure 1.1c).
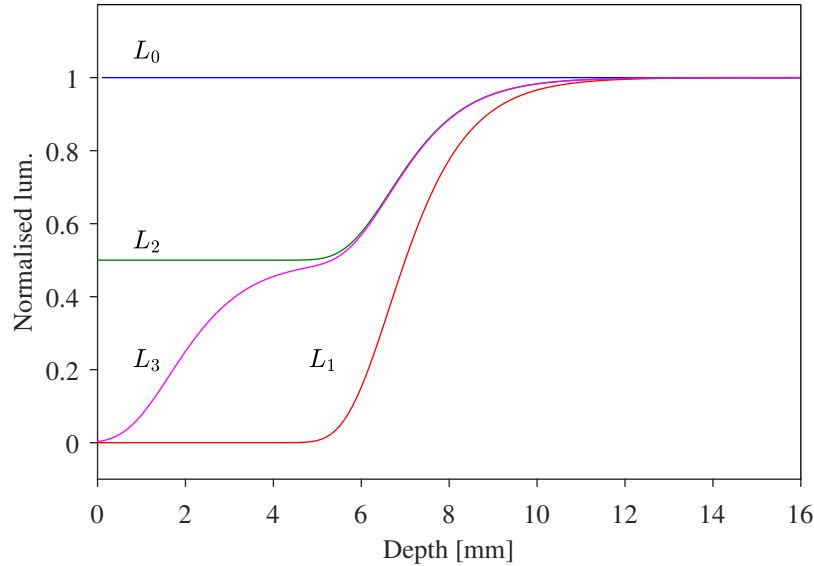
Figure 1.3: Four theoretical luminescence-depth profiles where L_0 (blue curve) is the profile when all traps at all depths are filled (saturation)i.e. with fully saturated traps at all depths, L_1 (red curve) is after a single exposure to light, L_2 (green) is after a subsequent burial, and L_4 (magenta) is after an additional exposure event. The effect of trap filling during exposure has not been included here.

If the rock is subsequently shielded from light (perhaps by burial) refilling of the depleted traps will occur and the luminescence signal will increase (where possible, i.e. where there are empty traps) as illustrated by the green line in Figure 1.3. This is the solution to Equation 1.2 when $t = t_b$ and $E(x)=0$, i.e. only trap filling occurs. This solution rely on the assumption that burial and exposure events take place independently of each other and in order to model the burial luminescence-depth profile, the final exposure profile (L_1) is used as the initial condition for the burial profile (L_2) in the model. If trap filling during light exposure is included then L_2' is given as[3].

$$L_2' = (L_1' - L_{\text{sat}})e^{-t_b F_b(x)} + L_{\text{sat}} \tag{1.9}$$

where L'_1 is given by Eq.(1.8) and $F_b(x)$ is the dose rate during burial (i.e. $F_b(x) = \dot{D}_b(x)/D_c$). Note that $\dot{D}_b(x)$ usually is different from the dose rate during exposure, $\dot{D}(x)$ (see Eq.1.3), where the rock is not surrounded on all sides by a burial matrix. If trap filling is ignored during exposure, then $L'_1 = L_1$ given by Eq.(1.7).

Thus, by fitting a measured luminescence-depth profile with the equations given above, it is not only possible to derive exposure ages, t_e, and burial ages, t_b, but it is also possible to determine to what extent and depth the exposure event bleached the latent luminescence signal during the previous exposure. The latter is particularly important as it enables an assessment of whether the estimated burial age is likely to overestimate the true burial age due to insufficient bleaching of the latent luminescence signal. Thus by knowing the preburial profile i.e. the exposure profile L_1 the rock burial age can be determined by measuring the dose recorded by the initial part of the luminescence profile evaluated to be well bleached from the predicted preburial profile.

Using the mathematical formulation above, it is possible to include an arbitrary number of sequential burial and exposure events. This is illustrated in Figure 1.3, where the pink line shows a luminescence-depth profile after the rock has been exposed to light for a second time, i.e. t_{e2}. This process can be repeated infinitely, and in theory the models could capture all events. Of course if any one exposure is longer than a previous exposure, any record of earlier exposure and burial events will be erased. For each event added to the model, the initial condition is given by the previous event. Freiesleben et al.[3] proposed the following equation for multiple sequential burial and exposure events (see also Table 1.1, L_{sat} is set to 1).

$$L'_{k+2} = \frac{[(E+F)L'_{k+1}(L'_k) - F]e^{-t_e(E+F)} + F}{E+F} \tag{1.10}$$

$$L_{k+2} = L_{k+1}(L_k)e^{-t_e E} \tag{1.11}$$

with $'$ denoting that trap filling during exposure is included and k is an uneven integral number > 0. Thus $L'_1, L'_3, L'_5, ...$ (and $L_1, L_3, L_5, ...$) describe exposure periods (Eq. 1.8 or 1.7), while $L'_2, L'_4, L'_6, ...$ ($L_2, L_4, L_6, ...$) describe burial periods (Eq. 1.9). The depth dependency of F and E are still valid in these equations as $E(x)$ and $F(x)$.

1.2.4 Challenges

There are a number of challenges in both burial and exposure dating of rock surfaces. First of all, a small uncertainty in the measured depth can result in a significantly different exposure time. Thus, estimated exposure ages from model fitting is highly sensitive to the depth used. Improvements in sample processing has begun in the fields of rock surface dating, e.g. using a wire saw rather than a saw blade, and leaving a depth record that can be remeasured. IRPL[75] measurements of rock slices has also opened new possibilities in terms of depth resolution.

Inhomogenity in the composition of the rock also complicates the luminescence depth profiles, and Meyer et al.[76] has reported a relationship between mineralogical composition and variations in luminescence depth profiles. Orientation of the surface with respect to the horizon has also been shown to have a significant influence on the profile shape[76].

In standard model fitting, attenuation is assumed independent of depth and wavelength. These assumptions are most likely not valid; the attenuation coefficient defines the slope of the profile,

and it has been observed that, for a given sample, the slope decreases with depth in profiles with different exposure times, and thus different depths e.g. Polikreti et al.[65]. On the other hand, Ou et al.[74] used modelling to estimate μ from luminescence profiles with measured attenuation coefficients and observed a correlation. The photoionisation cross section, which describes the efficiency with which a photon can eject an electron from a trap, and so bleach the latent luminescence, has been estimated for room temperature IR signals[58], but no such data exist for post IR signals. Only a few studies have used calibration profiles for rock surface exposure dating, but without investigating the degree to which the results rely on model assumptions, or on the time difference between known and unknown luminescence profiles.

Including this information complicate age estimations, but it may be unavoidable if accurate ages are to be achieved. All existing rock surface luminescence depth models assumes first order kinetics, which is probably applicable to quartz signals, but almost certainly not to feldspar signals. The luminescence from feldspar is known not to follow first order kinetics [e.g. 77,78].

1.3   Objectives of this research

The objectives of this study are to 1) develop models for exposure dating using feldspar and investigating the spectral dependency of fitting parameters. 2) demonstrate that rock surface burial and exposure dating is accurate using controlled experiments. 3) develop simple methods for correcting for in-homogenity in field dose rates. 4) test rock surface dating in real applications at two archaeological sites.

The models used in rock surface luminescence exposure and burial dating are largely physically based, but there has been little testing of exposure models using controlled experiments, and none of the burial models. The first objective of this thesis is to investigate whether these models are valid. Previous controlled experiments using exposure models [e.g. 6,74,76] show that some of the physical assumptions made in the model may not be reliable, in particular the attenuation coefficient seems to change with depth/wavelength, and the detrapping rate constant at the surface $\overline{\sigma\varphi_0}$ shows unexpectedly large variability. As exposure dating relies on estimating the values of these parameters from fitting, it is very important to determine to what degree the chosen model influences parameter estimation. All previous luminescence depth models rely on the assumptions of first order kinetics, which may be appropriate for quartz, but most likely not for feldspar. A further objective of this work is to determine the degree to which choice of model affects the accuracy of exposure ages.

Rock surface burial dating would appear to be independent of model fitting (and so choice of model) if the burial age is estimated using the standard SAR protocol on grains/slices from known well-bleached depths. Unfortunately, this depth is itself determined by modelling. This thesis sets out to determine the degree to which the burial depth is model dependent, and to what extent the choice of model affects the derived burial dose.

In most sites where rock surface dating is likely to be applicable, one can expect inhomogenity in dose rates to be an issue, because solid rocks rarely have the same radionuclide concentrations as the surrounding burial matrix. Accordingly, a further objective of this work was to develop a simple analytical model for deriving spatial variations in dose rate in three dimensions.

The final objective of this research is to test the application of the new models and the understanding developed through addressing the earlier objectives, by using this new knowledge to develop a chronology for two sites of archaeological importance in Central France, one recording the change over from Neanderthal to anatomically modern humans, and one which has the potential to demonstrate the ability of Neanderthals to create symbolic engravings.

1.4 Thesis outline

This thesis contains 7 chapters, where chapters 2-4 will be submitted as individual research articles at a later stage and chapter 6 is currently submitted as part of Marquet et al.[79]. Note that some of the rock measurements presented in chapter 3 were made during the candidate's MSc studies[80]. Here additional rock sample measurements have been made, the method of analysis changed and the dose rate calculations refined. In addition, new multi-grain quartz OSL sediment measurements have been included.

The thesis outline is as follows:

Chapter2: Rock surface burial dating at Les Roche D'Abilly

In this chapter, the accuracy of rock surface burial dating is investigated using four rock samples and 15 sediment samples from the Bordes-Fitte rockshelter (Roches d'Abilly site, Central France) at which a succession of Middle and Early Upper Palaeolithic occupations is preserved. This site is archaeologically important because it contains artefacts recording the changeover from Neanderthal to anatomically modern humans (AMH) in the region, and because these artefacts have been sealed in situ by the collapse of the shelter roof. The site was chosen for this research because it has good independent ^{14}C age control[81] and the quartz characteristics of the sediments are known to be suitable for OSL dating[39].

This chapter will be submitted as Freiesleben et al.[82].

Chapter 3: Do luminescence exposure chronologies depend on the chosen kinetic model of electron detrapping?

Rock surface dating using OSL relies on fitting measured luminescence-depth profiles. Such profiles are generally described assuming first-order kinetics for electron detrapping[42]; an assumption which is perhaps reasonable for quartz, but probably not for feldspar which generally follow non-first-order kinetics. Thus, particularly for feldspar, it is important to develop more suitable models describing the development of bleaching profiles. In this chapter, a general-order kinetic model[83] and a localised recombination model[54] are used to develop new analytical expressions for luminescence-depth profiles in rocks. Using simulated data, the sensitivity of various parameters (e.g. the light attenuation coefficient) to the choice of kinetic model is investigated and the degree to which incorrect model assumptions affect estimates of exposure age/erosion rate, and to what extent, is explored. Experimental data from several granite samples exposed to either daylight or to artificial broad-spectrum or monochromatic light sources for known periods of time are also presented.

This chapter will be submitted as Freiesleben et al.[84].

Chapter 4: Controlled exposure and burial experiment

This Chapter investigates the development of luminescence profiles with time in preconditioned granite and sandstone samples. These profiles were developed by exposing the rock samples to natural daylight and artificial broad-band and narrow-band illumination for various prolonged periods. The profiles are then used to test the models developed in Chapter 3. The narrow-band illumination used three laser light sources (405, 532 and 885 nm) and enables investigation of wavelength dependency of the luminescence depth profiles.

The multiple event model Freiesleben et al.[3] is tested here using the results from two controlled burial experiments using beta and gamma irradiation, respectively, to simulate various burial events of different duration (i.e. different doses were added). Model dependency of burial dating is also investigated.

This chapter will be submitted as part of Freiesleben et al.[85].

Chapter 5: Rock surface dating at La Roche Cotard

La Roche Cotard is an archaeological site located in the Loire Valley (France) and consist of a small cave blocked by sediment until 1846, and two nearby shelters. This site is of archaeological interest since, in addition to Mousterian lithic artefacts associated with Neanderthal and a composite object known as the "Mask of La Roche-Cotard", a large area of its cave walls contain spatially structured engravings made by fingertips or tools. Here we set out to use OSL to determine exactly when the cave entrance was blocked and so the last time humans were able to access the cave before excavation after the mid 19th century, i.e. we test the hypothesis that the main cave and the shelters were accessible for some time after the arrival of *Homo sapiens* in the area, around 37,000 years ago[86]. In this chapter, the ultimately unsuccessful results from rock surface burial dating of the cave walls are presented.

Chapter 6: Sediment burial dating at La Roche Cotard

In this chapter, OSL dating is used to determine the time of deposition of the sediments in and around the cave entrance at Le Roche Cotard (LRC) to obtain information on when the cave entrance was last blocked by sediments. OSL ages for 48 sediment samples are presented. Both multi-grain and single quartz measurements as well as multi-grain K-feldspar measurements are reported.

This chapter has been submitted mainly as the supplementary information to Marquet et al.[79].

Chapter 7: Summary and conclusions

Chapter 2

Rock surface and sediment quartz dating using optically stimulated luminescence at the Bordes-Fitte rock shelter, Les Roches D'Abilly, France

2.1 Introduction

The archaeological site of Les Roches d'Abilly is a complex of loci located in the Creuse Valley at the southern limit of Touraine, in Central France. The site includes a rock shelter, Bordes-Fitte (LRA-BF), that preserves stone tool technology and faunal remains from both the last Middle Palaeolithic and first Upper Palaeolithic occupations. When the roof of the rock shelter collapsed, it preserved seven geoarchaeological units (GFU) containing items attributed to the Mousterian, and the Archeulean and Solutrean traditions. These artefacts are related to the changeover period from a Neanderthal to an Anatomically Modern human population [81,87].

Optically stimulated luminescence (OSL) dating is a well-established absolute chronological method that determines the time since sedimentary grains were last exposed to daylight (i.e. the burial age) [32]. One of the main assumptions in OSL dating is that the sediment was sufficiently exposed to daylight to have any prior luminescence signal completely reset at burial. This assumption can be tested by comparison of ages derived from signals with different bleaching rates (e.g quartz OSL with K-rich feldspar IRSL ages [88]) or in some cases by single-grain quartz OSL dating [34,89]. More recently, OSL has also been applied to the dating of rock surfaces [90,91]. One considerable advantage of rock-surface dating compared to the dating of buried sediments is that rock surfaces preserve both qualitative and potentially quantitative information about the duration of past daylight exposure and burial events and thus provide an internal check on the degree of resetting [e.g. 1,42,44].

Two key units (GFU F and D2) from Bordes-Fitte have previously been dated using both ^{14}C AMS and OSL signals from multi-grain aliquots of quartz and K-rich feldspar as well as from single grains of quartz [39,81,87]. The K-rich feldspar and single-grain quartz measurements were in

good agreement with the multi-grain quartz measurements and this shows that at least these units were well-bleached at burial.

The average multi-grain quartz OSL ages of GFU D2 was 44±2 ka (n=2)[39]. The average uncalibrated ^{14}C age for GFU D2 was 39,900±700 (n=5)[81], giving a calibrated age of 49,036-43,161 using OxCal v.4.2 and IntCal 13[92]. Using OxCal v.4.4 and IntCal20[93] the revised calibrated ^{14}C age is 46,470-40,725 at 95%, or an average age of 41.5±0.9 ka (at 68%; assuming a normal distribution), consistent with the OSL age from the same GFU D2. For GFU D1, a single uncalibrated ^{14}C age of 41,900±1,500 years has been obtained[81]. Using OxCal 4.4 and IntCal20[93], the calibrated ^{14}C age for this unit is 46,470-40,725 years at 95%, i.e. 43.6±2.9 (at 68%; assuming a normal distribution).

The main purpose of this study is to establish a multi-grain quartz OSL chronology for GFU layers B, C, D1 and D3 as well as to use rock surface dating on one cobble extracted from unit D1 and three from D2. A mathematical model developed for quantifying multiple bleaching events[3] is used to describe and quantify the burial events for the four cobbles.

2.2   Stratigraphy and sampling

The Bordes-Fitte rock shelter 2,5-metre-thick sequence of deposits under the Turonian bedrock, revealed by excavation between 2007 and 2014 is composed of 9 lithostratigraphic unit (GFU) interpreted in terms of sedimentary dynamics of near-surface sedimentary facies with vertical and lateral variations within a context dominated by run-off and gravitational processes of sediment slope-wash, alluvial and lacustrine deposits[81].

Lithic remains recovered in the GFU A and B have yielded small lithic assemblage of flakes obtained from large recurrent centripetal or preferential Levallois cores. The lithic assemblage from GFU C has been produced through a recurrent uni- and bi-directional convergent or centripetal recurrent Levallois method. The GFU D1 lithic assemblage has been obtained by Levallois recurrent and lineal methods (GFU D1), Discoidal reduction scheme and Chatelperronian blade for backed point have been recovered in the GFU D2, Early Upper Palaeolithic Aurignacian blade and bladelet production characterised the GFU E, Solutrean bifacial thinning flakes, bifacial preforms and several fragments of laurel-leaves and Badegoulian in the GFU F. Technology, refitting studies and taphonomy of lithic artifacts recovered in the GFU D1 yielding Levallois reduction sequence and GFU D2 characterized by Discoidal and Châtelperronian blade result from successive occupations, separated by wall and roof collapse events, and affected by successive natural post-depositional displacement processes. Study has shown that lithic artifacts recovered in the GFU D2, corresponding to blade production, overlie those that relate to Discoidal flake production.

Considering, the technological variability of the lithic assemblage (Discoidal and Blade production) recovered in the GFU D2 and implications in the timing of Middle to Upper Palaeolithic lithic technological transition, age control is crucial.

In 2013, 15 sediment samples and four cobbles were sampled from the Bordes-Fitte rock shelter. Sediment samples (TA2247-61) were taken by inserting steel tubes (ø=5 cm, length=20 cm) into cleaned sections. The sediment samples were taken as follows: one from GFU-B (TA2247), four from GFU-C (TA2248-51), one from the border between GFU-C and D1 (TA2252), 4 from GFU-

D1 (TA2253-56), one from GFU-D2 (TA2257) and three from GFU-D3 (TA2258-61). Eight of the samples were positioned less than 15 cm away from bedrock/rock fall and so a piece of bedrock (TA2262) was sampled to allow us to correct for the any non-uniformity in the gamma field.

The cobbles (TA2266-68) were dug out of the cleaned sections and immediately placed in light tight bags after marking the orientation of the cobbles in the section, i.e. top, bottom, out and in. Three of the cobbles (TA2265-67) were partly (on one side) exposed to daylight for about a month after excavation but prior to sampling (see Figure 2.1). This recently light-exposed part (facing outwards) was clearly marked and not used in the measurements reported here. Three cobbles (TA2266-68) were taken from GFU D2 and one from GFU D1 (TA2265). The dimensions of the cobbles were $\sim 10 \times 10 \times 4$ cm^3 and they are either bio-calcirudite, calcarenite or harder silicified limestone[87].

Table 2.1: Sediment sample locations relative to bedrock. The distances have been used as input to the dose rate modelling (see section 2.4.2). "Depth" is the burial depth, "H" is the horizontal distance to bedrock, "V$_{above}$" and "V$_{below}$" are the vertical distances to bedrock/shelter roof lying above and below the sample, respectively.

Sample	Depth [cm]	H [cm]	V$_{above}$ [cm]	V$_{below}$ [cm]
TA2247	221	12	>30	8
TA2248	205	9	>30	24
TA2249	213	>30	12	>30
TA2250	197	>30	12	>30
TA2251	181	16	90	11
TA2252	168	23	74	12
TA2253	160	48	66	19
TA2254	154	42	60	25
TA2255	159	29	65	11
TA2256	153	54	14	63
TA2257	138	54	21	56
TA2258	127	54	28	48
TA2259	122	54	33	43
TA2260	115	21	44	30
TA2261	108	23	59	17

2.3 Experimental details

2.3.1 Sample preparation

The sediment samples were prepared under subdued red-orange light following standard procedures, i.e. 5 cm of the ends of each sample was removed for radionuclide concentration and water content measurements, quartz from the inner part of each sample tube was extracted from the sediment by sieving (180-250 µm), acid cleaning using HCl, H$_2$O$_2$, heavy liquid preparation (2.58 g.cm^{-3}) and etching in 40% HF[66]. The purified quartz extracts were tested for the presence of

Figure 2.1: Cross-section of part of the Bordes-Fitte rock shelter from where the OSL (Sediment: TA2247-61 and rock: TA2265-67) samples were taken. Also shown as insets are sampling photographs. Here the sample number is indicated by square brackets followed by the burial age in ka. Note that rock sample [68] is not directly visible in the Figure as it was buried behind rock [67]. For the rock samples the ages given are derived for profiles determined to be well-bleached (see section 2.5.3.2 and Table 2.5). Sediment sample locations are shown with white circles and rock samples are shown with dark blue contours. Rock ages are given both for top (e.g. $[66_t]$) and bottom (e.g. $[66_b]$), except for rock sample $[67_t]$ for which the top side was not considered to have been well-bleached at burial.

feldspar using IR stimulation[94] and no significant depletion of the blue stimulated OSL signal was observed.

The cobbles were also prepared under subdued red-orange light. Cores ~10 mm in diameter and ~40 mm long, were drilled into the cobbles using a water-cooled diamond-tipped core drill. The cores were then cut into ~1.2 mm thick slices with a 0.3 mm thick water-cooled diamond wafer saw, to give a known net slice spacing of ~1.5 mm. The cobbles studied here were quartz-rich carbonate-cemented sandstone. In order to avoid any effect of crushing on the luminescence signal and to produce and preserve the in-situ grain size information[91], we first etched the slices in 10% HCl for one hour to remove calcium carbonate. At the end of this stage, the slices were still mostly intact, presumably due to binding by amorphous silica resistant to HCl. We then placed the slices in concentrated HF for one hour to further disaggregate the slices and dissolve any feldspar grains. Any residual fluoride contamination from the HF treatment was removed using a 10% HCl solution for 40 min. The washed and dried grains were sieved to the size range 63-300 μm.

2.3.2 Measurement facilities

All luminescence measurements were made using Risø TL/OSL readers equipped with blue-light stimulation (λ=470 nm, ~80 mW.cm^{-2}) and infrared (IR, λ=870±40 nm, ~130 mW.cm^{-2}). Photon detection used EMI 9635QA photomultipliers through 7.5 mm U-340 Hoya glass filter. Beta irradiation used calibrated ^{90}Sr/^{90}Y sources mounted on the readers[95,96].

Bulk radionuclide concentrations were measured using high-resolution gamma spectrometry[97,98]. The measured concentrations were converted to infinite matrix dose rates using the conversion factors of Guérin et al.[99]. The cobble and sediment samples were dried to 50 °C, then pulverised and homogenised. The sediment samples were heated to 450 °C for 24 h to remove any organic matter. To prevent radon loss and to provide a reproducible counting geometry the materials were cast in wax. The cast samples were stored for at least three weeks to allow ^{222}Rn to reach equilibrium with its parent ^{226}Ra before measurement[97]. An internal quartz alpha dose rate of 0.020 ± 0.010 Gy.ka^{-1} was assumed[100]. Cosmic ray dose rates were calculated following Prescott and Hutton[101] and current burial depths; an uncertainty of 5% was assumed. The long term water content was taken to be 5% and 0% for the sediments and cobbles, respectively.

2.3.3 OSL measurements

All OSL measurements presented here were made using the single-aliquot regenerative-dose (SAR) procedure[51] with blue light stimulation for 100 s at 125°.

Sediment OSL measurements

The OSL measurements of the sediments used a double SAR procedure[102] in which an IR stimulation at 50° for 100 s was inserted immediately before the blue light stimulation. Between each SAR cycle a high temperature (280°) blue stimulation for 100 s was inserted to minimise potential recuperation effects[103]. Unless otherwise mentioned, the sediments were measured using a preheat of 260° (held for 10 s), a cutheat of 220° and a test dose of 50 Gy. The signal was summed over the initial ~0.3 s of stimulation (the blue light power density varied between the different readers used

and so the duration of the initial signal summation was adjusted to include the initial ∼50% of the signal decay). The background subtracted from the initial signal was based on the subsequent ∼0.3 s of stimulation. Multi-grain aliquots were mounted in stainless steel cups using an ∼5 mm spot of silicone oil; each aliquot contained approximately 800 individual grains[35]. Equivalent dose estimation is based on a minimum of three sensitivity corrected regeneration points (L_x/T_x), a recuperation point and a recycling point. Individual dose response curves have been fitted using a single saturation exponential function passing through the origin (i.e. $y = A \times [1 - \exp(-x/D_c)]$, where y is the sensitivity corrected OSL response, L_x/T_x, A is the saturation value and the constant D_c is a measure of the curvature of the dose response curve) and equivalent doses (D_e) derived by interpolation. Average dose values have been calculated using an unweighted arithmetic mean[104] and the quoted uncertainty is the standard error (at 68% confidence). We use the InterQuartile Rejection (IQR) criterion[105] to identify and reject individual dose values more than 1.5 interquartile ranges above the upper quartile (75 percent), or below the lower quartile (25 percent).

Cobble OSL measurements

The OSL measurements of the quartz extracted from the cobbles made use of a preheat of 190° (held for 10 s), a cutheat of 150° and a test dose of 65 Gy unless otherwise stated. The signal was summed over the initial 0.8 s of stimulation, background corrected using the subsequent 0.8 s of stimulation. Multi-grain aliquots were mounted on stainless steel discs coated with silicone oil (8 mm), i.e. each aliquot contained approximately 1,100 grains each[35].

2.4   Dosimetry

This section describes the measured dose rates and the corrections for heterogeneity in the radiation field for both sediment samples and cobbles. For the sediments, we consider the proximity to bedrock, whereas for the cobbles we only need to consider the surrounding sediment as the nearest bedrock is >30 cm away.

2.4.1   Infinite matrix dose rates

The radionuclide concentration and dry infinite matrix dose rates, assuming a mean grain size of 180 μm and 215 μm for cobbles and sediments, respectively, are summarised in Table 2.2. Total dose rates to the surface slices are shown in Table 2.4 and total dose rate to the depth later argued to be well-bleached are summarised in Table 2.5.

In contrast to ^{226}Ra, concentrations of the series parent ^{238}U are poorly known, but on average, the activity ratio ^{226}Ra/^{238}U in the sediments is 1.36±0.08 (n=15). This suggests there may be a small excess of ^{226}Ra. In such a carbonate-rich environment, this is most likely due to ^{238}U mobilisation, leaving behind ^{230}Th ($\tau_{1/2}$ ∼75,000 ka) and progeny, and so should have a negligible effect on the time-averaged total dose rate. The radionuclide concentrations ratios of the sediment samples are, on average 3.3±0.4 (n=4) times those of the unaltered rock samples, and the activity concentrations in the sediments decrease systematically with decreasing elevation (Figure 2.2). If we assume that the sediments have been derived primarily from the surrounding host rock, and that radionuclides (especially Th) behave conservatively, this increase in radionuclide concentration implies a loss of

Table 2.2: Radionuclide concentrations and infinite matrix dose rates for sediments (TA2247-61) and cobbles (TA2265-68). Sediment samples TA2254 and TA2257 were in close proximity to the cobbles and the dose rate for these sediment samples are used in the cobble dose rate calculations. Sample TA2262 is taken from bedrock. For sediment samples only, a 20±10% escape of ^{222}Rn is assumed.

Sample	Depth	Unit	Radionuclide concentrations (Bq.kg^{-1})				Infinite matrix dry dose rates (Gy.kg^{-1})	
			^{238}U	^{226}Ra	^{232}Th	^{40}K	Gamma	Beta
TA2247	221	B	7±4	7.3±0.4	14.3±0.4	110±6	0.31±0.01	0.45±0.02
TA2249	213	C	16±5	14.3±0.4	29.3±0.5	161±7	0.57±0.01	0.75±0.02
TA2248	205	C	13±4	17.7±0.4	24.1±0.4	146±6	0.52±0.02	0.71±0.02
TA2250	197	C	14±1	19.3±0.2	28.9±0.2	142±2	0.59±0.02	0.75±0.02
TA2251	181	C	10±2	15.8±0.2	24.6±0.2	246±4	0.59±0.01	0.94±0.01
TA2252	168	C/D	19±2	24.6±0.3	30.4±0.3	423±5	0.86±0.02	1.52±0.02
TA2253	160	D1	10±5	21.5±0.8	26.6±0.9	444±14	0.81±0.02	1.52±0.04
TA2255	159	D1	15±4	20.2±0.4	24.4±0.4	469±9	0.80±0.02	1.55±0.03
TA2254	154	D1	25±5	23.0±0.5	27.0±0.5	525±11	0.89±0.02	1.74±0.03
TA2256	153	D1	15±10	22.7±0.8	28.9±0.9	532±15	0.92±0.03	1.77±0.04
TA2257	138	D2	27±2	29.0±0.4	34.5±0.3	508±5	1.01±0.02	1.81±0.03
TA2258	127	D3	17±2	23.0±0.3	25.0±0.2	686±6	1.00±0.02	2.13±0.02
TA2259	122	D3	17±4	26.7±0.4	31.0±0.4	664±10	1.07±0.02	2.15±0.03
TA2260	115	D3	16±6	28.5±0.6	32.9±0.7	567±13	1.03±0.023	1.94±0.04
TA2261	108	D3	18±2	24.0±0.2	27.4±0.2	632±5	0.99±0.02	2.02±0.02
TA2262	-	-	17±17	19.3±1.1	4.9±1.0	30±14	0.22±0.02	0.30±0.04
TA2265	154	D1	-2±4	5.8±1.0	7.2±1.0	60±12	0.172±0.017	0.26±0.03
TA2266	138	D2	17±17	10.3±1.1	4.9±1.0	30±14	0.15±0.02	0.21±0.04
TA2267	138	D2	-2±13	6.2±0.9	8.9±0.9	48±10	0.186±0.016	0.24±0.03
TA2268	138	D2	19±11	15.9±0.8	6.6±0.7	66±9	0.241±0.012	0.37±0.02

some 75% of non-radioactive carbonate by dissolution. If this process happened after deposition, then it must have occurred after sedimentation was complete (because the youngest sediments have been modified most). Alternatively, and in our opinion more likely, this enrichment took place before deposition and the systematic change in concentrations with elevation arise from grain-size selection in the transport/ deposition process changing with elevation. The second assumption is employed in age calculations, i.e. the measured radionuclide concentrations are assumed to have persisted throughout the life of the site. For the sediment samples, the beta dose rates vary between ~ 2 Gy.ka^{-1} and ~ 0.5 Gy.ka^{-1}, and the corresponding dry gamma dose rates vary between ~ 1 Gy.ka^{-1} and ~ 0.3 Gy.ka^{-1} (the total dose rates vary from ~ 3 Gy.ka^{-1} at the top of the sequence, TA2261, to ~ 0.8 Gy.ka^{-1} at the bottom, TA2247; see Table 2.2). The bedrock sample has a dry gamma dose rate of ~ 0.2 Gy.ka^{-1}. Thus, for all samples except the deepest (TA2247) the dry gamma dose rate is more than two times larger for the sediments than for the bedrock sample. As some of the sediment samples are taken within 15 cm of the bedrock, the dose rates to all sediment samples have been modified to take into account the heterogeneity in the gamma field arising due to the proximity to bedrock (see Figure 2.1). This modelling is described in section 2.4.2.1.

The infinite matrix dry dose rates for the four cobbles are similar to each other and to the bedrock sample (TA2262) with an average dose rates of 0.28±0.03 Gy.ka^{-1} and 0.19±0.02 Gy.ka^{-1} for beta and gamma, respectively. However, dose rate modelling for the cobbles is necessary because of the effects at the rock-to-surface interface of the gradient in beta dose rate in particular (see section 2.4.2.2).

2.4.2   Dose rate modelling

Some of the sediment samples were taken relatively close to bedrock or the collapsed shelter roof (see Table 2.1) and given that the gamma dose rate for bedrock is between $\sim$1.5 and 5 times lower than that from sediment, the gamma radiation field in the vicinity of at least these samples must have a steep gradient, and this should be accounted for when calculating total dose rates. For the cobbles, one should also consider the variation of dose rate with depth into the rock material.

We have used the dose rate correction model described in Supplementary I of Marquet et al.[79], which relies on the principle of superposition. For the cobbles, we have further assumed that they can be approximated by cubes with dimensions length=height=width=h (the thickness of the cobble).

The total dose rate at a given position (in the cobble or sediment) is a sum of the alpha, beta and gamma contributions, each of which changes with depth due to attenuation effects. The total of each (alpha, beta or gamma) dose rate can be expressed as the sum of contributions from the external, $\dot{D}_{\text{ext,inf}}$, and internal $\dot{D}_{\text{int,inf}}$, infinite matrix dose rates. Due to attenuation the relative contributions are given by correction factors C_{int} and C_{ext}[79]

$$\dot{D}_{\text{total}} = C_{\text{int}}\dot{D}_{\text{int,inf}} + C_{\text{ext}}\dot{D}_{\text{ext,inf}} \tag{2.1}$$
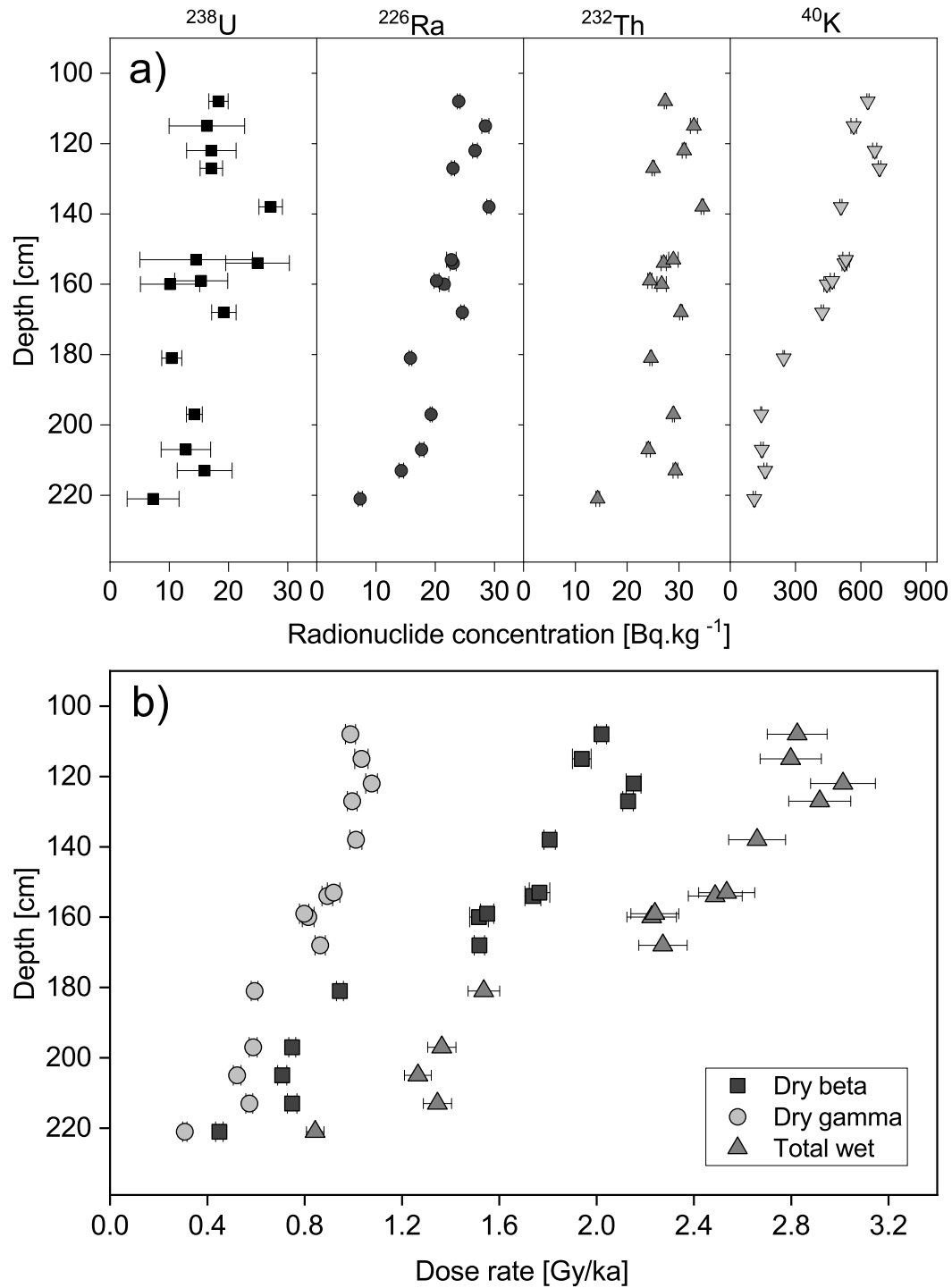
Figure 2.2: Dosimetric data for the sediments as a function of depth. a) Radionuclide concentrations and b) Dry beta, dry gamma and total wet sediment dose rates.

With correction factors defined as

$$C_{\text{int}} = (1 - X_{r,r})(1 - Y_{r,r})(1 - Z_{r,r}) \tag{2.2}$$
$$C_{\text{ext}} = X_{s,r} + (1 - X_{r,r})Y_{s,r} + (1 - X_{r,r})(1 - Y_{r,r})Z_{s,r} \tag{2.3}$$
$$1 - X_{r,r} = 1 - (f_{r1}e^{-\mu_{r1}x_1} + f_{r2}e^{-\mu_{r2}x_2}) \tag{2.4}$$
$$X_{r,s} = f_{s1}e^{-\mu_{r1}x_1} + f_{s2}e^{-\mu_{r2}x_2} \tag{2.5}$$

f_{r1}, f_{r2}, f_{s1} and f_{s2} are the fractional dose rate factors for the active rock material r and the active sediment material, s, respectively. μ_{r1} and μ_{r2} are the linear attenuation coefficients in the rock material r, and x_1 and x_2 are the distances from the point of interest to the boundary of the rock sample in the xth-direction. f_{r1}, f_{r2}, μ_{r1} and μ_{r2} depend on the radiation type, on the type of material and on the distances in the xth-direction (i.e. x_1 and x_2). Similar relationships to that in Equation 2.4 apply to the y- and z-directions i.e. $Y_{r,r}$ and $Z_{r,r}$ (active rock material); for $Y_{r,s}$ and $Z_{r,s}$ (active sediment material) Equation 2.5 applies.

Equation 2.1 describes the variation of alpha, beta or gamma dose rate with depth into a cobble buried in sediment. Infinite matrix dose rates are corrected for water content as appropriate. The total dose rate is then the sum of the alpha, beta, and gamma contributions. For correcting the sediments for nearby rock samples the subscripts s and r are changed in the equations. As f will be the same for sediment and the relevant rock material, only μ need to change to sediment values. i.e. different densities of sediments give different values of μ. As the first 9-10 μm of the grains are etched away due to adding Hydroflouric acid, any contribution due to alpha radiation can be ignored.

Finally, dose rates due to cosmic radiation (not significantly dependent on depth into the rock surface over the scales considered here) and internal depth-independent uranium, thorium inclusions are added and modifications for the effect of grain attenuation are taken into account. The dose rate in a given depth interval x_i to x_f, was estimated from numerical integration of the depth dependent dose rate over the depth of the slice. The cobble material in this site is limestone and the value of μ for the cobble can be approximated by the values for sediment, corrected for the density difference Riedesel and Autzen[106], i.e. 2 g.cm^{-3}. The values used are summarised in Table 2.3. When correcting for the heterogeneity of the sediment samples, the values will change by about 10% using a more appropriate density of 1.8 g.cm^{-3} for sediments.

Figure 2.3 shows the variation of the beta, gamma and total dose rate in the cobble.

Table 2.3: Beta and gamma attenuation factors (μ) and the fractional dose factor (f) for different distances (d) in limestone with a density of 2 g.cm^{-3}, to the boundary of the active material. Adapted from Riedesel and Autzen [106] after density correction.

Bedrock	Beta			Gamma		
Decay chain	μ [mm^{-1}]	f	d [mm]	μ [mm^{-1}]	f	d [mm]
^{40}K	2.81	0.50	all	0.0215	0.50	<10
				0.0138	0.45	>10
^{232}Th	4.66	0.50	<0.15	0.020	0.50	<10
	1.84	0.34	>0.15	0.0138	0.42	>10
^{238}U	3.52	0.50	<0.15	0.0277	0.50	<10
	1.5	0.37	>0.15	0.0154	0.45	>10
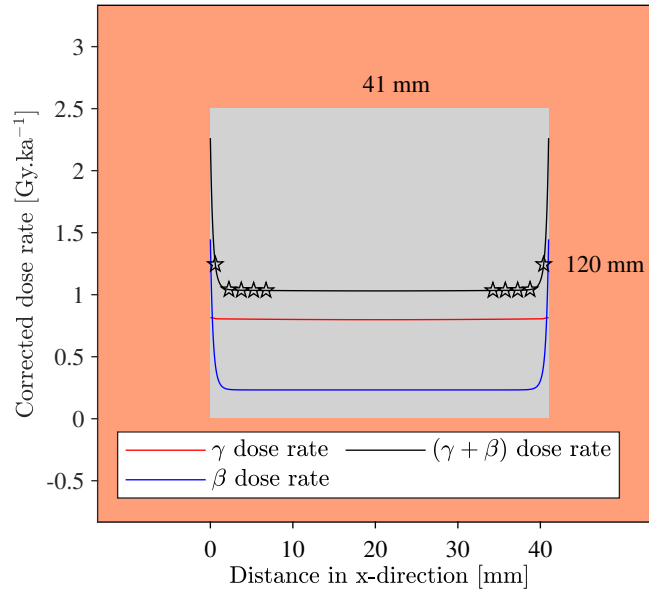
Figure 2.3: Variation of beta (blue), gamma (no cosmic) (red) and the total (black) dose rate with depth in cobble TA2265 (grey area, dimensions 40x40x40 mm) from the cobble itself and from the surrounding sediment (light red), based on the infinite matrix dose rates corrected for water content and beta attenuation. The stars indicate the depths of the first 5 slices.
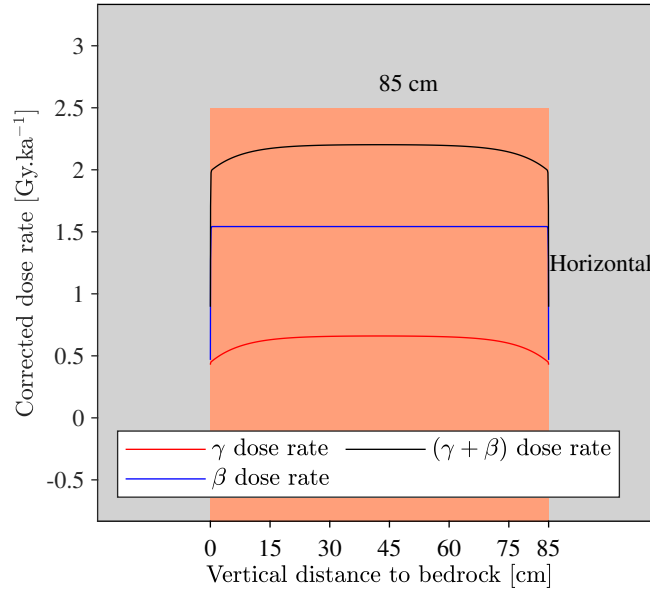
Figure 2.4: Variation of beta (blue), gamma (red, without cosmic) and the total (black) dose rate in sediment (light red), with vertical distance from nearby bed rock (grey) between 0 and 85 cm. A horizontal distance to a nearby bed rock to one side is assumed to 50 cm for this illustration. The distance to nearby bed rock in the last direction (i.e. the z-direction is assumed to infinite). Infinite matrix dose rates corrected for water content and beta attenuation for sample TA2254 are used.

2.4.2.1   Effects of dose rate modelling for the sediments

The average correction to the gamma dose rate for the sediment samples is 0.954±0.007 (n=15) leading to a small correction to the total dose rate of 0.983±0.003 on average, with the largest correction (0.967±0.06) occurring for sample TA2251. The dose rates used for age calculation are given in Table 2.4 as "$\dot{D}_{tot}$". These are based on beta and modelled gamma dose rates, both adjusted for water content and grain size attenuation, and include internal dose rates and a cosmic ray contribution.

2.4.2.2   Cobble dose rate modelling

The dose rate depth dependence in the cobble is only significant in the very first slice. The dose rate in the first slice differs from that in the centre by 20% whereas the second slice only differs by 1% from the centre. Note that dose rate decreases with depth near the surface as a result of the low internal dose rate compared to the external dose rate.

2.5   OSL Results

2.5.1   Luminescence characteristics

Sediment quartz luminescence characteristics

Previous multi-grain measurements on sediment samples from Borde Fitte showed that the quartz OSL signal is fast-component dominated, the natural dose is insensitive to the choice of preheat

temperature in the range 230 to 280°, and the chosen SAR protocol (using a preheat of 260°) were able to accurately recover laboratory given doses in the range from ~5 to 120 Gy[39]. Figure 2.5a shows a representative dose response curve (DRC) from sample TA2253. As with the previous samples from this site, we are able to accurately recover a given regeneration dose (the recycling point, open symbol), the build-up of signal between SAR cycles (recuperation) is negligible and the laboratory DRC is well-represented by a saturating exponential function. The average D_c value for DRCs measured with a test dose of 50 Gy and a largest regeneration dose of 300 Gy is 122±3 Gy (n=302). The inset to Figure 2.5a shows that the OSL stimulation curve is similar to that derived from Risø calibration quartz, which is known to be fast-component dominated[96].

For these samples, a series of additional dose recovery experiments were undertaken as the burial dose was expected to increase for samples from the deeper layers (e.g. GFU D1, C and B) not previously investigated. In these experiments, the individual aliquots were first bleached twice for 100 s (with an intervening pause of 10,000 s) using the blue LEDs at room temperature, before a laboratory dose ranging between 25 and 600 Gy was given to individual aliquots. The SAR protocol was then used to measure these laboratory given doses. Dose recovery ratios (measured dose divided by given dose) are shown as a function of given dose in Figure 2.5b (squares), where each point is an average of doses determined for at least 6 individual aliquots. All dose recovery ratios up to a given dose of 260 Gy (corresponding to ~$2.1D_c$) are considered to be satisfactory (i.e. within ±10% of unity), but for larger given doses the dose recovery ratio decreases with given dose. For a given dose of 600 Gy (and a test dose of 50 Gy), all L_n/T_n values lay significantly above the saturation value, A, of the DRCs. The inset to Figure 2.5b shows how the dose recovery ratio varies as a function of the relative number of individual dose estimates which interpolate above $2D_c$ on the DRC (or do not interpolate on the DRC at all, i.e. no bounded dose estimate could be derived). When the number of individual aliquots with $D_e > 2D_c$ is $\gtrsim$40 % the dose recovery ratio becomes unacceptable. Thus, our ability to recover a laboratory dose decreases as the number of aliquots interpolating above $2D_c$ increases. However, as pointed out by Murray et al.[41], the sensitivity-corrected luminescence (L/T) is the measured quantity, not the dose. In the saturating part of the DRC even small uncertainties in this L/T ratio will be greatly enhanced on the dose axis and can thus lead to unbounded estimates of dose. Thus, in order to determine whether the protocol is applicable it is better to calculate the light recovery ratio, i.e. the ratio of the sensitivity corrected signal from a regenerated dose (L_x/T_x, equal to the given dose) to the signal from the given dose (L_n/T_n). This ratio of the sensitivity corrected light levels is also shown in Figure 2.5b, and indeed the value is acceptable for all given doses, except at 600 Gy, when the ratio is 0.5.

Cobble quartz luminescence characteristics

Figure 2.6 shows the DRC from a surface slice from cobble 68, and the inset shows representative natural OSL decay curves (grey). A significant difference in decay shapes is observed with variable amounts of medium component. For comparison a calibration quartz decay curve (red) is also shown. Nonetheless, the natural OSL signal is mainly dominated by the fast-component, and in addition early background subtraction was used to maximise the fast component contribution to the signal summation[41]. A single-aliquot regenerative (SAR) protocol[107] was adopted for equivalent-dose measurements (see section 2.3.3).
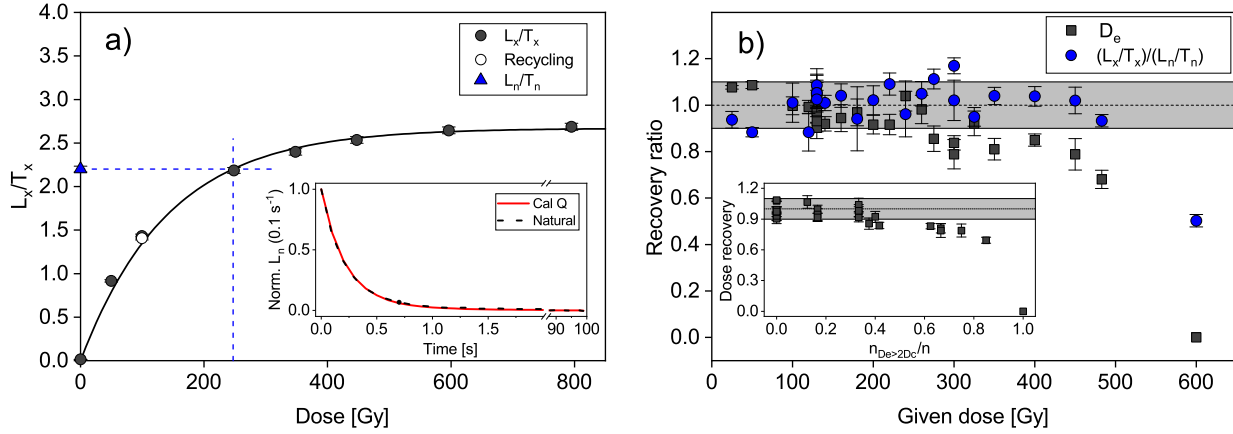
Figure 2.5: Sediment luminescence characteristics. a) Dose response curve (DRC) from sediment sample TA2253. Filled circles: regenerated points. Open circle: recycling point. Triangle: natural sensitivity corrected signal. The data is taken from a dose recovery experiment with a given dose of 350 Gy. The data have been fitted using a saturating exponential function ($y = A \times [1 - exp(-x/D_c)]$).The inset shows the normalised OSL stimulation curve of the natural signal and that from calibration quartz[96], which is known to be fast-component dominated. b) Dose recovery result for given doses ranging between 25 and 600 Gy using a test dose of 50 Gy. Squares indicate dose recovery ratios calculated by taking the arithmetic mean of the individual measured doses. Circles indicate light recovery ratios, i.e. the ratio of the sensitivity corrected signal from a regenerated dose (L_x/T_x, equal to the given dose) to that from the given dose (L_n/T_n). The inset shows the dependence of the dose recovery ratio on the relative number of aliquots with dose estimates larger than $2D_c$. Note that no dose estimates could be derived for a given dose of 600 Gy as the L_n/T_n ratio lay significantly above the saturation value of the DRCs, A.
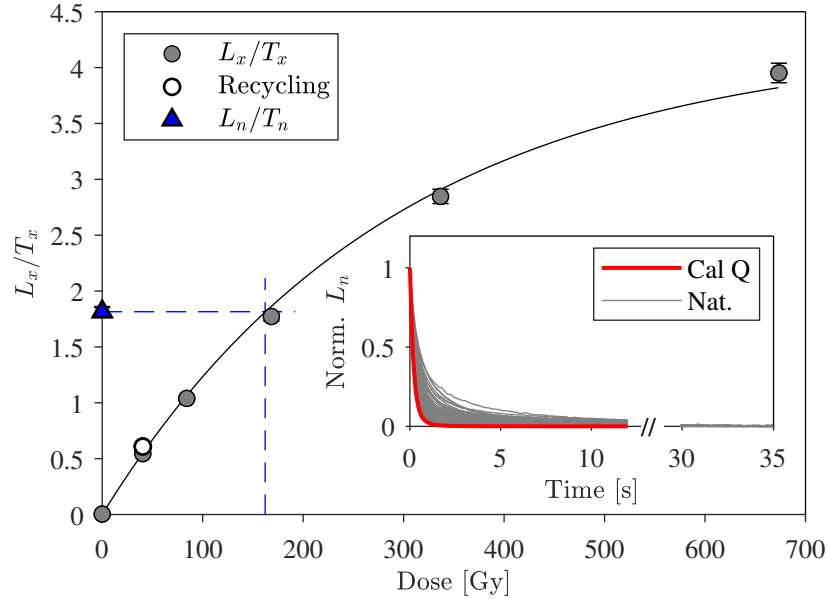
Figure 2.6: Dose response curve from a surface slice from cobble 68. Circles: sensitivity corrected regenerated OSL signals. Triangle: natural sensitivity corrected OSL signal (L_n/T_n). Open square: recycling point. The inset shows the OSL stimulation curve of the natural signal. For comparison, the natural stimulation curve measured from an aliquot of calibration quartz is also shown.

In order to determine the appropriate measurement conditions, natural and dose recovery preheat tests were carried out using grains extracted from the surface slices from cobble sample 68 (see Figure 2.7a). The preheat temperature was varied between 160 and 280°, and the cutheat temperature was 40° less than the preheat temperature.

First, the amount of thermal transfer at each temperature was measured by bleaching the aliquots (three at each preheat temperature) for 100 s at room temperature using the blue LEDs, with a pause of 10,000 s in between. The thermally transferred dose was subsequently measured using the SAR protocol and the results are shown in the inset in Figure 2.7b. In Figure 2.7a we observe estimated natural doses from measurements with preheat temperatures ranging from 160° to 320°. For the natural pretheat test, a plateau in the measured equivalent doses is observed in the preheat temperature range from 160°C to 240°C. The average recycling ratio for this temperature range was 0.965±0.011 (n=15). At temperatures >240°C the doses increase significantly with preheat temperature.

In the dose recovery preheat test, the aliquots were first bleached as in the thermal transfer experiment and subsequently given a known laboratory dose of ∼67 Gy, close to the average equivalent dose measured for the surface grains (see Figure 2.7b). The measured-to-given dose ratios (after subtraction of the appropriate thermal transfer doses) do not vary significantly over the temperature range from 160°C to 200°C, where the average dose recovery ratio is 1.01±0.02 (n=9). This shows that our protocol can accurately measure a known laboratory dose in this temperature range.

Based on these results, a preheat temperature of 190°C was chosen for further measurements; at this temperature the recuperation signal is small (∼0.2 % of the natural signal) and the thermal transfer doses are also negligible compared to the surface equivalent doses (∼1% on average).
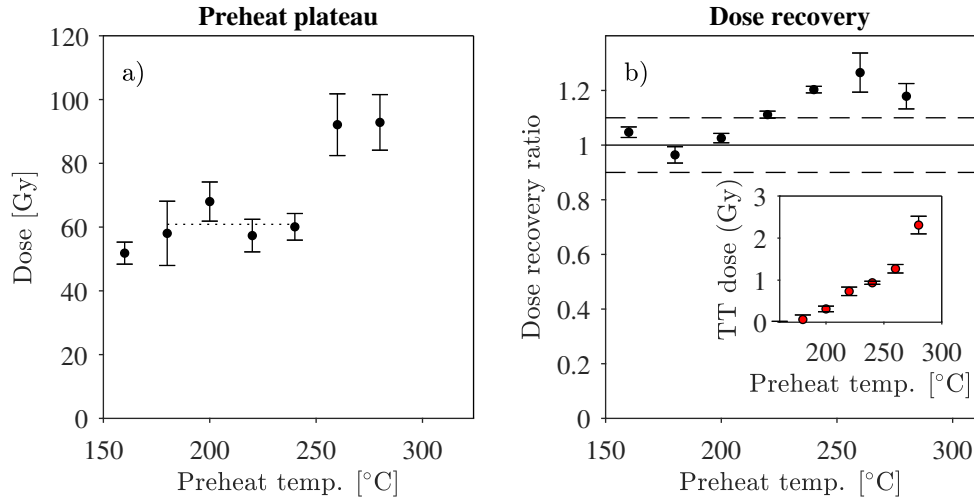
Figure 2.7: Equivalent dose dependence on preheat temperature using three aliquots for each preheat temperature for surface slices from cobble 68. a) Surface natural doses. Dashed horizontal line indicate the thermally stable plateau. b) The ratio of the measured doses (after correction for thermal transfer) to the known given dose of 65 Gy (dose recovery ratio), insert in b) Thermal transfer doses.

2.5.2   Sediment burial ages

The measured multi-grain quartz dose distributions for all samples (except TA2247 for which only 9 aliquots gave bounded dose estimates, see below) are shown as simple dose histograms in Figure 2.8. Dose estimates rejected by the objective IQR criterion are shown in blue. The effect of applying the IQR criterion is predominantly to reject high dose outliers but in some cases also low dose outliers. The average ratio between the arithmetic averages with and without the application of the IQR criterion is 0.97 ± 0.01 (n=15). The main effect of the IQR criterion is to reduce the average equivalent dose uncertainty by $\sim 25\%$.

Table 2.4 summarises the equivalent dose, total dose rate (including the model corrections for hetereogeneity in the gamma field, see section 2.4.2) and OSL burial age determined for each sample as well as the number of accepted and rejected aliquots. The average equivalent dose for GFU D is ~ 120 Gy (n=10), for GFU C ~ 150 Gy (n=4) and for GFU B ~ 300 Gy (n=1). However, it is worth noting that of the 23 aliquots measured for sample TA2247 (GFU B) only 9 bonded dose estimates could be derived, i.e. $\sim 60\%$ of the aliquots were discarded because of saturation effects. Thus, we consider it highly unlikely that the equivalent dose (and hence burial age) determined for this sample is accurate. It can only be regarded as a minimum age, i.e. the burial age of GFU B is > 375 ka. The remaining samples all have equivalent doses less than 260 Gy where the dose recovery ratios begins to underestimate the given dose. Thus, we regard these OSL ages as reliable.

Figure 2.13 shows the resulting multi-grain sediment ages with depth. The sediment burial ages are all in stratigraphic order, although sample TA2251 (107 ± 6 ka) is only just consistent with sample TA2250 (94 ± 6 ka) taken 16 cm below TA2251. The single sample taken from GFU D2 (TA2257) which has C-14 age control of 46.5-40.7 cal BP kyr (at 95%) gives an OSL age of 46 ± 2 ka. Previously measured multi-grain OSL ages[39] from this unit give an average age of 44.3 ± 1.9 ka (n=2) and are also shown. For GFU D1 we obtained four OSL ages, which all are consistent with the average OSL age of 51.5 ± 0.7 ka (n=4). Aubry et al.[81] published a single ^{14}C AMS (Accelerator Mass Spectrometry) age of 46,470-40,725 years (at 95%) for this unit, significantly underestimating the OSL age.

2.5.3   Rock surface burial ages

To derive burial ages from the four cobbles we have used two different approaches: 1) Measuring the burial dose for several surface slices only, and 2) Measuring luminescence depth profiles for the entire length of each cobble and using a mathematical model that quantifies multiple bleaching events[3] to obtain cobble burial estimates.

2.5.3.1   Surface slices

From a single slice (ø 10 mm, thickness ~ 1.2 mm) there is only sufficient material to make ~ 3 multi-grain aliquots, so in this approach $\sim$20 surface slices were taken from both the top and the bottom of the four cobbles. These slices were somewhat irregular in shape but had a mean thickness of 0.70 ± 0.1 mm. From cobble TA2267 only data from the bottom side is available, because this cobble was too fragile to extract slices, and the top surface did not have many suitable sites from which to extract cores. The SAR protocol was applied to measure the equivalent doses (D_e) from
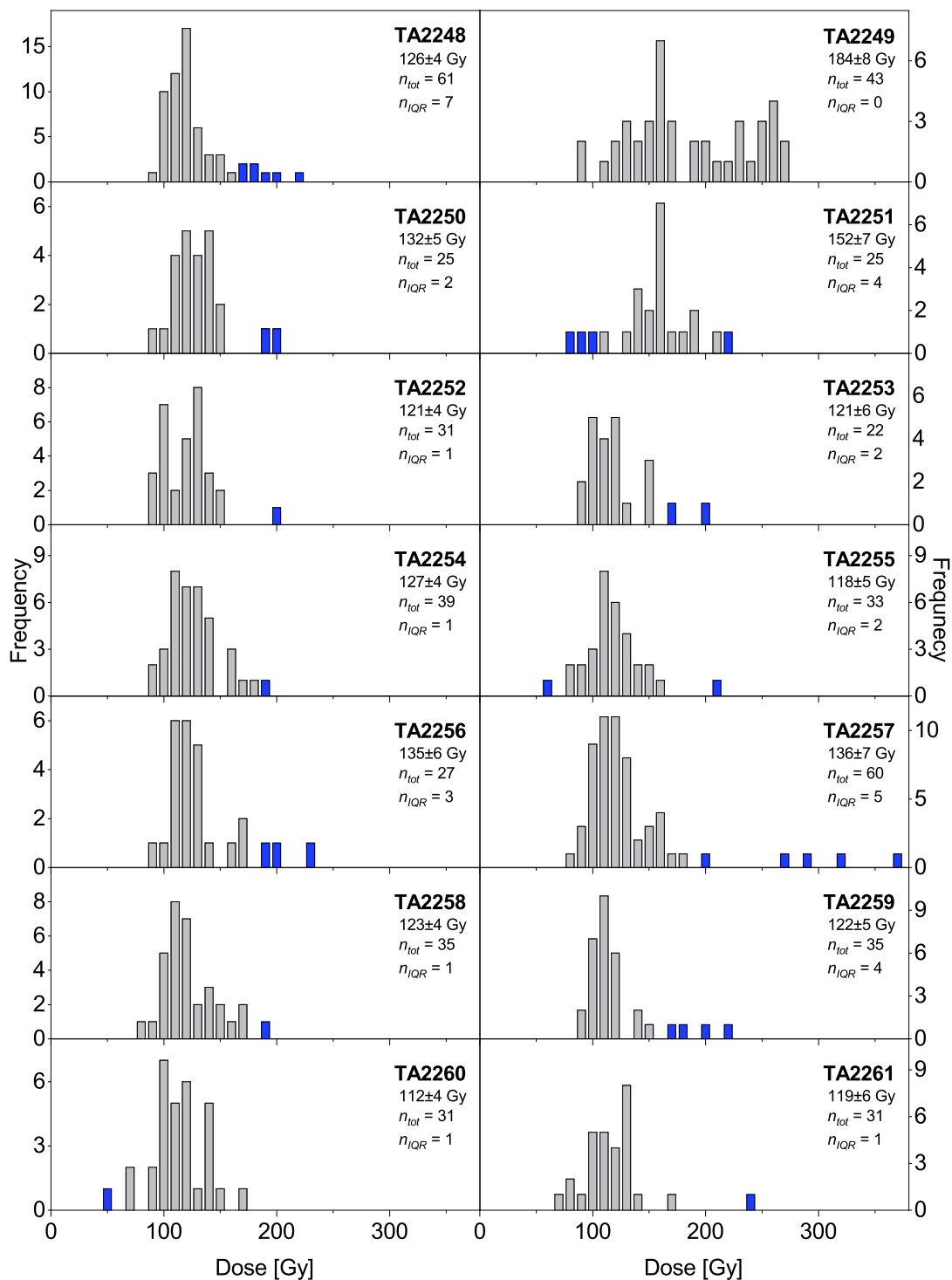
Figure 2.8: Sediment multi-grain dose distributions for all samples, except sample TA2247 for which only 9 aliquots gave bounded dose estimates, i.e. 61% of the measured aliquots could not be interpolated onto the DRC. Doses after application of the IQR criterion are shown as grey bars, whereas dose estimates rejected by the IQR criterion are shown as blue bars. The legend for each sample gives the arithmetic mean dose and its standard error of all measured aliquots giving a bounded dose estimate. Also give is the total number of measured aliquots (n_{tot}) and the number of aliquots rejected by the IQR criterion (n_{IQR})

Table 2.4: Summary of sediment and cobble mixture surface data. TA2247-61 are sediment samples, whereas TA2265-68 are Cobbles. "t" and "b" after the cobble name indicates "top" and "bottom", respectively. The cobble data reported in this table is only from direct measurement of the cobble surfaces. "GFU" is the geoarchaeological unit described in Aubry et al. [81], "D_e" is the arithmetic equivalent dose (after application of the IQR criterion), "n_a" is the number of accepted aliquots, "n_r" is the total number of rejected aliquots, i.e. both unbonded dose estimates and outliers (IQR), "n_{sat}" is the number of aliquots not giving a bonded dose estimate, "Sat" is the relative number of aliquots not giving a bonded dose estimate relative to the total number of measured aliquots, "$\dot{D}_{tot}$" is the total dose rate including correction for gamma heterogeneity, and "OSL age" is $D_e/\dot{D}_{tot}$. The equivalent dose (and thus OSL age) for sample TA2247 is regarded as a minimum age only due to saturation issues.

Sample	GFU	Depth (cm)	D_e (Gy)	n_a	n_r	n_{sat}	sat. (%)	$\dot{D}_{tot}$ (Gy/ka)	OSL age (ka)
TA2247	B	221	310 ± 27	9	14	14	61	0.83 ± 0.04	> 370
TA2249	C	213	184 ± 8	42	1	1	2	1.32 ± 0.06	140 ± 9
TA2248	C	205	118 ± 2	53	8	1	2	1.23 ± 0.05	96 ± 5
TA2250	C	197	126 ± 4	22	3	1	4	1.34 ± 0.06	94 ± 5
TA2251	C	181	159 ± 5	19	6	2	8	1.49 ± 0.06	107 ± 6
TA2252	C/D	168	119 ± 3	30	1	0	0	2.21 ± 0.10	54 ± 3
TA2253	D1	160	114 ± 4	20	2	0	0	2.21 ± 0.10	52 ± 3
TA2255	D1	159	117 ± 3	30	3	1	3	2.18 ± 0.10	53 ± 3
TA2254	D1	154	125 ± 3	37	2	1	3	2.48 ± 0.11	51 ± 3
TA2256	D1	153	125 ± 4	23	4	1	4	2.49 ± 0.11	50 ± 3
TA2257	D2	138	121 ± 3	54	6	1	2	2.63 ± 0.12	46 ± 2
TA2258	D3	127	121 ± 4	32	3	2	6	2.91 ± 0.13	41 ± 2
TA2259	D3	122	113 ± 3	28	7	3	9	3.00 ± 0.13	37 ± 2
TA2260	D3	115	115 ± 4	30	1	0	0	2.78 ± 0.12	41 ± 2
TA2261	D3	108	115 ± 4	28	2	2	6	2.78 ± 0.12	41 ± 2
TA2265t	D2	138	104 ± 6	49	0	0	0	1.43 ± 0.04	73 ± 5
TA2265b	D2	138	79 ± 5	54	1	0	0	1.43 ± 0.04	53 ± 3
TA2266t	D2	138	168 ± 24	47	3	0	0	1.64 ± 0.03	81 ± 8
TA2266b	D2	138	83 ± 6	39	1	0	0	1.64 ± 0.03	49 ± 4
TA2267b	D2	138	101 ± 10	29	1	0	0	1.43 ± 0.04	66 ± 5
TA2268t	D1	154	109 ± 14	52	5	0	0	1.43 ± 0.04	59 ± 4
TA2268b	D1	154	98 ± 6	55	1	0	0	1.43 ± 0.04	66 ± 4

the cobble surfaces (top and bottom) and the resulting distributions of equivalent doses are shown in Figure 2.9 with grey bars. Blue bars shows the distribution of dose estimates rejected by the IQR criterion. The dose distributions are generally symmetric around the average dose, except for the top of cobble TA2266, which appears to be significantly positively skewed. This is potentially a concern as it may indicate that this surface either was not bleached uniformly prior to burial or possibly that a part of the cobble had broken off. For the remaining samples the average doses range between ~ 80 and 110 Gy (see Table 2.4).

2.5.3.2 Luminescence-depth profiles

One of the potential major advantages of rock surface OSL dating compared to sediment OSL dating is that rocks record information about past burial and exposure events. Such information can be extracted by applying appropriate mathematical models to measured luminescence-depth profiles, i.e. it is possible to directly assess whether the rock surface was well-bleached at burial. Thus, we have measured luminescence-depth profiles from top to bottom for all cobbles, except for cobble TA2267 where only part of the profile could be obtained. This was done by measuring natural sensitivity corrected OSL signals (L_n/T_n) from quartz grains extracted from individual rock slices obtained from one to three cores drilled all the way through the cobbles (thickness of ~ 4 cm). The resulting profiles are shown in Figure 2.10, where $x = 0$ is the top surface. At each depth, a minimum of three aliquots were measured.

A simple visual inspection of the profiles suggests that both the top and bottom of the cobbles (except two top surfaces: TA2265a and TA2268a (at $x = 0$ mm), have received a significant daylight exposure prior to burial.

Obtaining an analytical description of the luminescence-depth profiles and the variation of total dose rate with depth requires modelling. Sohbati et al.[73] suggested a model which describes the resetting of the OSL signal with depth during a single bleaching event and included trap refilling during this light exposure. Freiesleben et al.[3] expanded this model to include multiple sequential exposure and burial events in a unified equation. This luminescence-depth profile model assumes a first order system in which the luminescence signal, L, is directly proportional to the trapped charge concentration, n, i.e. $L(x) \propto n(x)$.
We further assume that charge trapping during the exposure period is negligible and that the dose rate during discrete burial events does not change significantly. The relevant events in this work are a single exposure event (Equation 2.6) and a subsequent burial event (Equation 2.7).

$$n_1(x, t_e) = n_0 e^{-\overline{\sigma\varphi_0}t_e}e^{-\mu x} \tag{2.6}$$

$$n_2(x, t_e, t_b) = (1 - T)\left((n_1 - 1)e^{\frac{-\dot{D}(x)}{D_c}t_b} + 1\right) + T \tag{2.7}$$

where $\overline{\sigma\varphi_0}$ (ka^{-1}) is the detrapping rate constant at the surface of the cobble averaged over all wavelengths in the light spectrum reaching the sample. σ (cm^2) is the photoionization cross section and φ (cm^{-2}.ka^{-1}) is the incoming photon flux. μ (mm^{-1}) is the inverse of the mean free path of photons in the cobble, assumed to be constant with depth. For the buried surfaces, t_b (ka) is the time elapsed since final burial, whereas t_e is the preburial exposure time (ka), $\dot{D}(x)$ is the dose rate (Gy.ka^{-1}) (Equation 2.1), and D_c characterises the rate of trapping; $\dot{D}(x)/D_c$ is the probability of trap filling per unit time. Note that thermal transfer is included in the model as T.

thp]
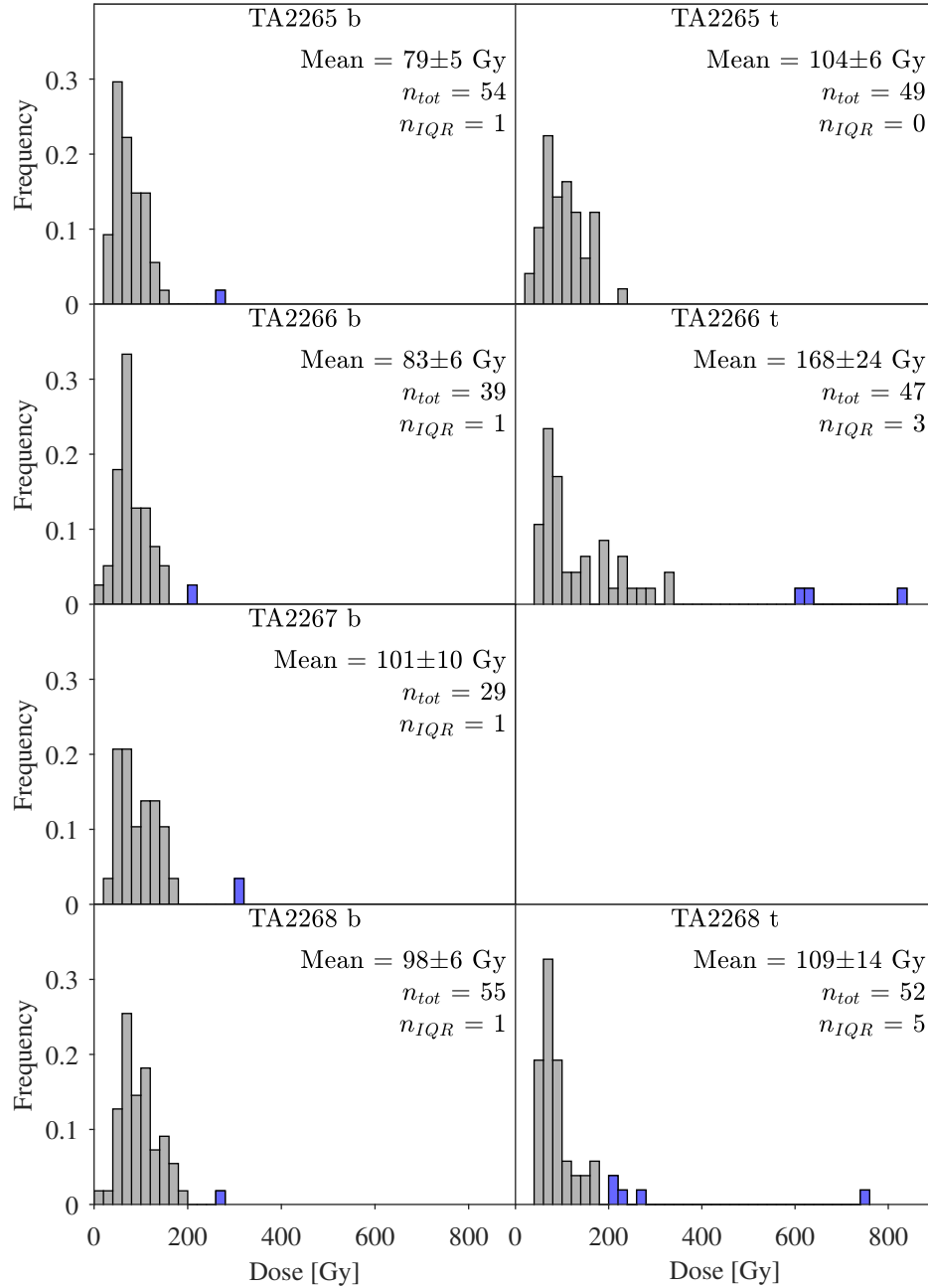
Figure 2.9: Cobble multi-grain quartz normalised dose distributions from both the top and the bottom of the individual cobbles (except sample 67). Doses after application of the IQR criterion are shown as grey bars, whereas dose estimates rejected by the IQR criterion are shown as blue bars. The legend for each sample gives the arithmetic mean dose and the standard error of all measured aliquots giving a bounded dose estimate. The total number of measured aliquots (n_{tot}) and the number of aliquots rejected by the IQR criterion are also given (n_{IQR}).
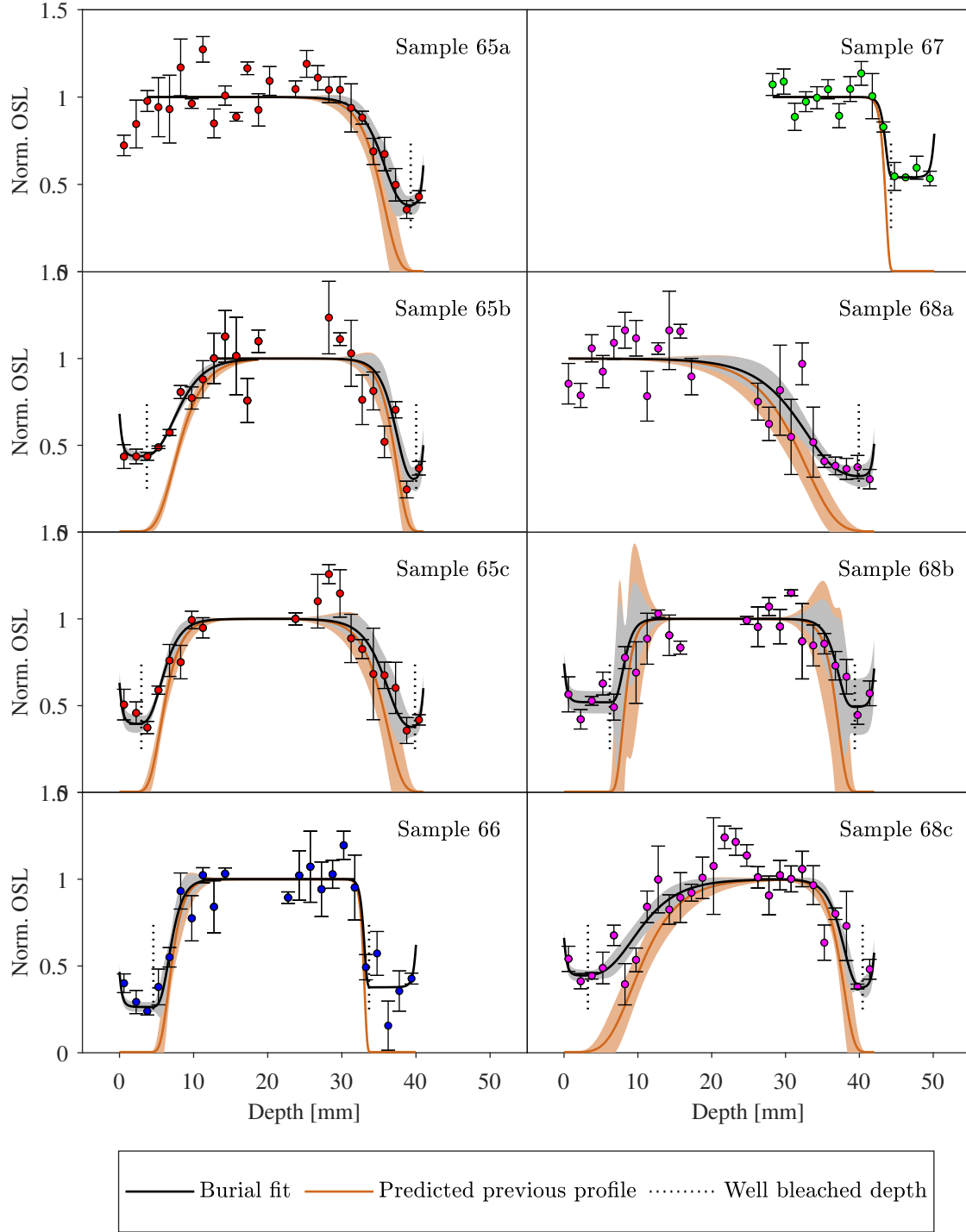
Figure 2.10: Normalised sensitivity-corrected luminescence L_n/T_n profiles from cores drilled from buried surfaces from top ($x = 0$) to the bottom of cobbles TA2265-68 (letters refer to different cores from the same cobble). The data have been normalised to the profile saturation value. Each data point is an average of the results from 3 aliquots. Error bars are one standard error. Fitting these data using the multiple event model [3] with one exposure followed by a single burial (Equation 2.7) results in the full black lines with 68% confidence intervals (grey area). The predicted pre-burial profiles (Equation 2.6) are shown as orange lines and confidence intervals at 68%. Dotted vertical black lines indicate the depths to which the surfaces are predicted to have been well bleached (see text for details).

Equation 2.7 (using the dose rate depth dependence as described in Equation 2.1) is used to fit the profiles. The resulting fits are shown in Figure 2.10 as black lines (the grey uncertainty band is drawn at 68% confidence). Using the parameters μ and $\overline{\sigma\varphi_0}t_e$, Equation 2.6 can be used to determine the pre-burial profile (see orange line in Figure 2.10). Visual inspection of these pre-burial profiles indicate that all surfaces were well-bleached at burial, i.e. these profiles are flat and close to zero near the surfaces. However, the degree of bleaching of the cobble surfaces before burial can be formally estimated using the fitting parameters obtained to predict the shape of the pre-burial luminescence profile. To determine whether a surface is well-bleached we define the following criterion: the rock surfaces were well-bleached to the depth where the value of the predicted pre-burial profile is less than 5% of the light level after burial at same depth. ($n_{n,s} = L_{n,s}/T_{n,s}$) after adding one standard deviation and subtracting the normalised thermal transfer from both profiles, i.e. $n_1(x) + se - T \leq 0.05 \times (n_{n,s}(x) - T)$.

The resulting depths are shown as black dotted vertical lines in Figure 2.10. All aliquots from these depths or shallower are considered to be well-bleached. Doses measured from these aliquots are therefore considered reliable (at least from the point of view of bleaching) and used to determine burial ages.

Burial ages determined from these depths are not significantly different from the burial ages determined from the corresponding surface slice from same core (at 95% confidence), although the ages derived particularly from TA2266b are scattered and poorly known (see Table 2.5). Thus, we conclude that all bottom surfaces were well-bleached to a depth including, at least, the first data point. On the other hand, two of the luminescence profiles from the top surfaces (TA2265a and TA2268a) indicate that at least some parts of these surfaces were either not significantly bleached at burial and/or has suffered from erosion, such that the well-bleached part has been removed. Assuming that all well-bleached ages estimated from the same sample and the same site come from the same distribution we apply the inter quartile rejection criteria to all ages (top and bottom) from each sample. The resulting distributions are seen in Figure 2.11 with grey bars indicating accepted ages and blue bars indicating rejected ages. The arithmetic mean age and its standard error (random) of all measured aliquots are given in the legends.

Multigrain quartz ages from well bleached lum. profiles
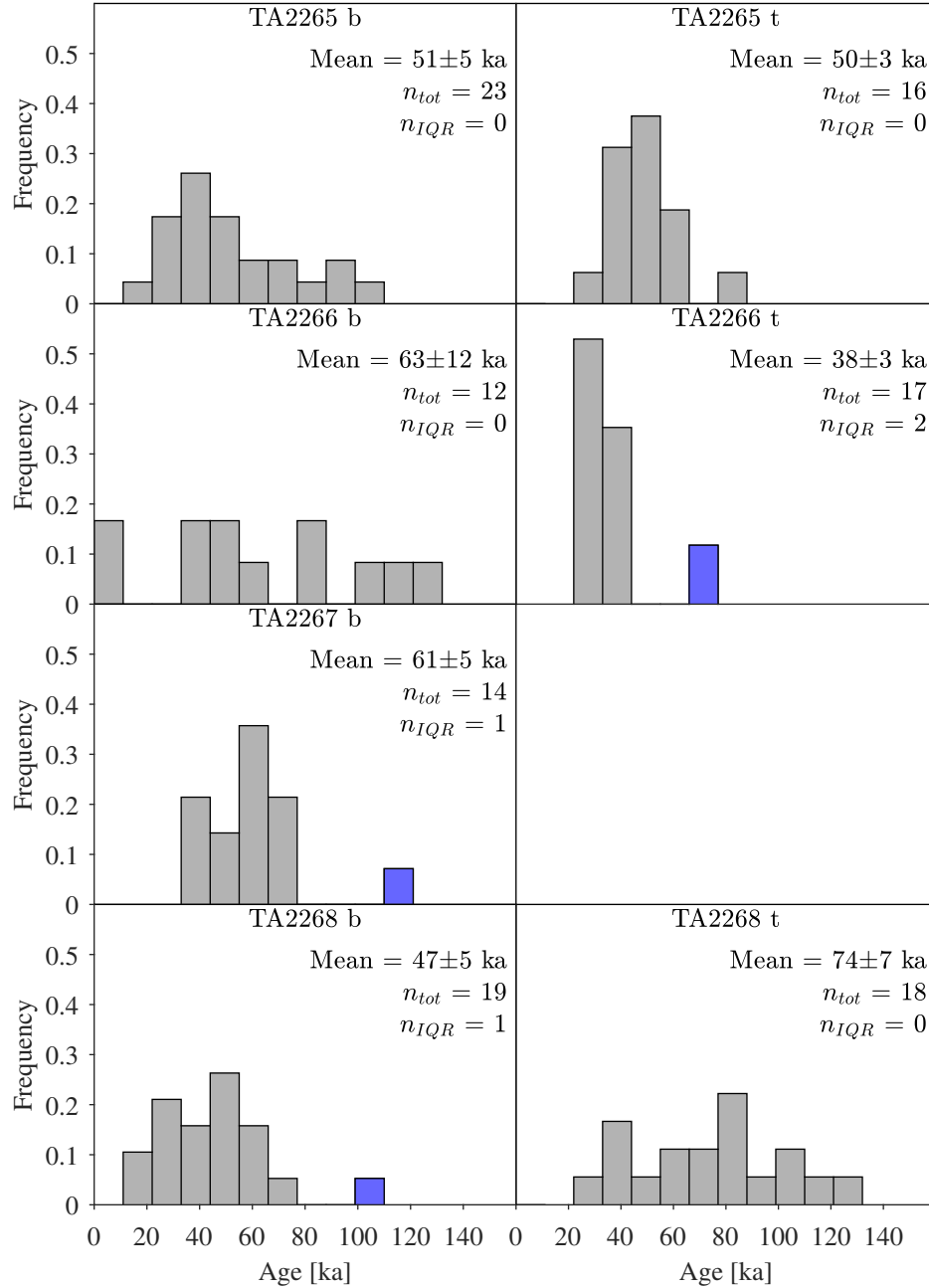
Figure 2.11: Cobble multi-grain quartz normalised age distributions from well-bleached depths, from both the top and the bottom of the individual cobbles (except sample 67). Because the individual aliquots come from different depths with slightly different dose rates (see Table 2.5) it is necessary to average ages rather than equivalent doses. Ages after application of the IQR criterion are shown as grey bars, whereas ages estimates rejected by the IQR criterion are shown as blue bars. The legend for each sample gives the arithmetic mean age and standard error of all measured aliquots giving a bounded dose estimate. The total number of measured aliquots (n_{tot}) and the number of aliquots rejected by the IQR criterion is also shown. (n_{IQR}).

Table 2.5: Summary of cobble results from the individual slices identified to be well-bleached by the pre-burial model. Equivalent doses (D_e), total dose rate ($\dot{D}_{tot}$), and OSL age from the individual slices are given. n is total number of aliquots for each depth. Age_t and Age_b are averaged OSL ages for the top and bottom of the individual cobbles, respectively, after applying the IQR rejection criteria. n_a is the number of accepted aliquots after applying the IQR rejection criterion. Note that no Age_t is given for TA2267 as the cobble was too fragile to obtain a full length core. Age uncertainties include both random and systematic uncertainties.

Sample	Side	Depth [mm]	D_e [Gy]	n	$\dot{D}_{tot}$ [Gy.ka^{-1}]	OSL age [ka]	Age_t [ka]	Age_b [ka]	n_a
TA2265b	Top	0.6	64±6	6	1.43±0.04	45±5	50±4		16
TA2265b	Top	2.25	64±6	3	1.23±0.04	52±5			
TA2265c	Top	0.6	79±12	4	1.43±0.04	55±9			
TA2265c	Top	2.25	67±11	3	1.23±0.04	55±10			
TA2265a	Bottom	40.4	69±10	7	1.43±0.04	48±7		51±5	23
TA2265b	Bottom	40.4	104±21	4	1.43±0.04	72±15			
TA2265c	Bottom	40.4	65±8	12	1.43±0.04	46±6			
TA2266	Top	0.6	55±8	8	1.51±0.04	36±5	33±2		15
TA2266	Top	2.25	54±9	6	1.29±0.04	42±7			
TA2266	Top	3.75	43±3	3	1.29±0.04	33±3			
TA2266	Bottom	34.75	105±34	3	1.29±0.04	82±27		63±12	12
TA2266	Bottom	36.25	26±25	2	1.29±0.04	20±19			
TA2266	Bottom	37.75	48±22	3	1.29±0.04	37±17			
TA2266	Bottom	39.4	135±20	4	1.51±0.04	89±14			
TA2267	Bottom	44.75	84±19	5	1.31±0.04	64±14	-	57±4	13
TA2267	Bottom	46.25	81±3	3	1.31±0.04	62±3			
TA2267	Bottom	47.75	82±8	3	1.31±0.04	63±6			
TA2267	Bottom	49.55	79±10	3	1.53±0.03	51±7			
TA2268b	Top	0.6	138±28	3	1.64±0.03	84±17	74±7		18
TA2268b	Top	2.25	87±12	3	1.44±0.03	60±9			
TA2268b	Top	3.75	111±6	3	1.44±0.03	77±5			
TA2268b	Top	5.25	135±16	3	1.44±0.03	94±12			
TA2268c	Top	0.6	143±44	3	1.64±0.03	87±27			
TA2268c	Top	2.25	63±10	3	1.44±0.03	44±7			
TA2268a	Bottom	41.4	42±7	5	1.64±0.03	26±4		43±4	18
TA2268b	Bottom	39.75	73±11	3	1.44±0.03	51±8			
TA2268b	Bottom	41.4	99±14	8	1.64±0.03	60±9			
TA2268c	Bottom	41.4	71±11	3	1.64±0.03	43±7			

To further support the conclusion that some parts of the top sides were probably not well-bleached, we compare ages from the top and bottom for each cobble (see Figure 2.12a, black points). Only for one cobble (TA2265) is there good agreement between the top and bottom. In Figure 2.12a, we also compare the top and bottom ages for all surface slices (pink symbols, see also Table 2.4) and again observe a relatively poor agreement between top and bottom ages, except for TA2268. In Figure 2.12b, we compare the surface mixture ages with the well-bleached profile ages. For

the bottom sides, there is a good agreement between well- bleached profile ages and the surface mixture ages (blue points). Only, for TA2266 is this agreement poor, i.e. the surface mixture age is 81±8 (n=47) and the profile age is 33±2 ka (n=15). For the top sites then agreement is poorer and this probably indicates that different parts of the cobble surfaces experienced different bleaching histories. Thus, we only use burial ages derived from well-bleached profiles. The ages derived from mixture of the first 1.2 mm we evaluate not to be reliable.
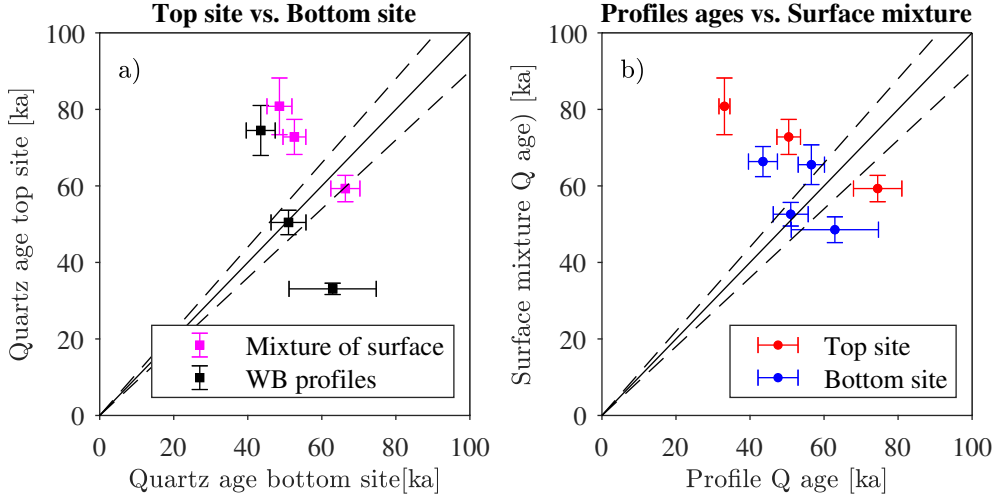
Figure 2.12: a) Comparison between quartz ages derived from the top and bottom sites of the cobble respectively from mixture of surface material (pink symbols), and ages derived from well bleached slices from measured luminescence profiles (black symbols) - see Figure 2.10. b) Comparison between well bleached profile quartz ages and surface mixture quartz ages, respectively from the top sites (red symbols) and the bottom (blue symbols) sites of the cobbles. Only random errors are included in this comparison. The IQR criterion was used on all data sets.

2.6 Burial ages

Figure 2.13 shows the age-depth relationship for both sediment samples (circles) and cobbles (squares). The age for sediment sample TA2247 is not included as it is assumed to be inaccurate due to saturation effects. We have modelled this age-depth relationship for the multi-grain quartz ages using Bayesian statistics with the sediment burial depths as priors (Bacon script[108]). For modelling, only random uncertainties for the individual ages were used, although they are shown with both random and systematic uncertainties in Figure 2.13. The Bayesian model results are shown as a black solid line and the dashed lines around it is the total uncertainty (including both random and systematic uncertainties) at 68% confidence. The sediment ages are all in stratigraphic order, and consistent with the Bayesian model except two samples (TA2249 and TA2251) both from GFU C. The two previously obtained multi-grain quartz sediment ages for GFU D2[39] are also shown as green circles. These two ages of 46±2 and 42±2 are both consistent with both the new burial age determined from this sampling campaign (i.e. TA2257, 46±2 ka) and with the Bayesian modelling results.

In Figure 2.13, we also show the cobble burial ages from profiles determined to have been well-bleached at burial, i.e. from the bottom sides We are presenting the average of individual ages from the cobbles from the same unit, i.e. for GFU D1 (TA2265) an age of 51 ± 3 ka ($n = 39$) and

for GFU D2 (TA2266-68) an age of 54 ± 4 ka ($n = 76$). Both of these ages are consistent with the sediment multi-grain quartz ages i.e. 50.8 ± 0.6 ka (n=4 samples from GFU D1) and 46 ± 2 ka (n=1 sample from GFU D2).
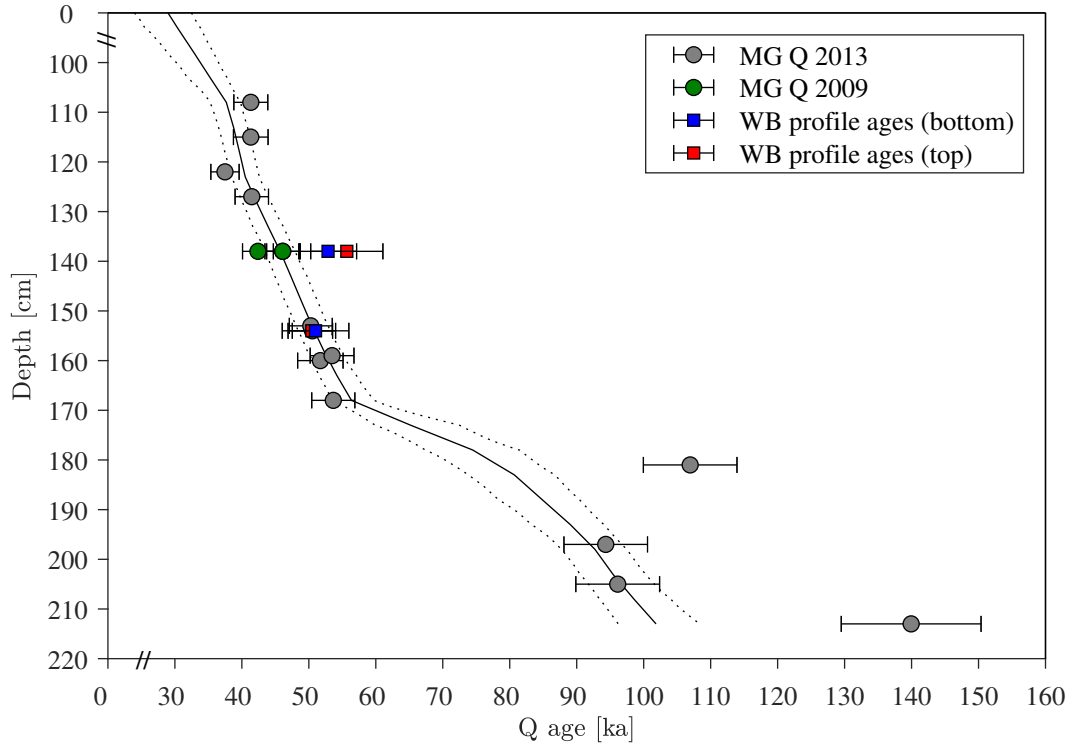
Figure 2.13: Bordes-Fitte quartz luminescence ages vs depth. Sediment (TA2248-61) multi-grain quartz ages are shown as circles. Grey circles show the sediment ages obtained in this work, whereas grey circles are the multi-grain ages from Thomsen et al. [39] from GFU D2. The sediment age for TA2247 is not shown as only a minimum age could be derived due to saturation effects. A Bayesian model (Bacon script [108]) using the depths as priors and only random uncertainties for the individual ages is shown (black line). Dotted black lines show the total uncertainty (including both random and systematic uncertainties) at the 68% confidence interval. Rock surface ages (squares) are derived from slices identified to be well-bleached by the pre-burial profile. Cobbles ages from TA2266-68 (all GFU D2) have been averaged and both top (red squares) and bottom (blue squares) ages are shown. Uncertainties on the all ages include both random and systematic uncertainties.

2.7 Conclusion Les Roches D'Abilly

Considerable qualitative information about the daylight exposure and burial history of the rock samples was obtained measuring optically stimulated luminescence at different depths in rock samples. The underlying luminescence profiles were investigated and well-bleached rock surfaces were identified, and thus dated with confidence. By modelling, insight into the degree of bleaching prior to a burial event were obtained. In this study it has proved possible to recover burial ages rock surface derived from 1 cm diameter cores drilled through the cobbles from top to bottom. Our data and modelling suggest that the bottom sides of the cobbles from Les Roches D'Abilly were all well-bleached before burial. The top sides were in some locations well-bleached and other locations incompletely bleached. Bottom-side burial-ages determined from these well-bleached multi-grain quartz luminescence profiles are in good agreement with multi-grain quartz ages estimated from

mixture of the first 1.2 mm of the cobble bottom surfaces. On the other hand, the multi-grain quartz ages derived from profiles from the top sides are not in good agreement with multi-grain quartz ages from the mixtures of the top surface 1.2 mm slices. This suggest a different bleaching history for some parts of the top surfaces; as a result we only draw conclusions from the known well- bleached profiles, rather than including the mixtures of top surface slices. The value of luminescence-depth profiles in testing the assumption of complete bleaching is demonstrated in this study; such direct information on bleaching history is not available in sand/silt sediment dating. The burial ages obtained from the rock surfaces are in good agreement with the ages obtained by standard OSL dating methods for the sediments.

Well-bleached surfaces give 51 ± 3 ka and 54 ± 4 ka for level D1 and D2, respectively, in agreement with the Bayesian ages based on multi-grain quartz sediment ages of 51.5 ± 0.7 ka (depth 153-160 cm) and 46 ± 2 ka (depth 138 cm) for level D1 and D2 respectively.

Chapter 3

Do luminescence exposure chronologies depend on the chosen kinetic model of electron detrapping?

3.1 Introduction

Rock surface dating using optically stimulated luminescence (OSL) is a relatively new absolute chronological method that in principle can be applied to determine both burial ages [e.g. 42,69,71] as well as exposure ages of solid rocks [e.g. 1,6,16,44], i.e. it can determine how long a rock has been shielded from light and/or how long it has been exposed to light. In particular, rock surface exposure dating relies heavily on modelling, which has been shown to be highly sensitive to the chosen model parameters (e.g. the light attenuation coefficient) and accurate exposure ages have currently only been obtained through the use of calibration samples [e.g. 1,6].

Charge is trapped in rock minerals due to the absorption of energy emitted mainly from naturally occurring radionuclides, primarily from the Thorium and Uranium series and Potassium-40. In a rock sample that has been shielded from sunlight (e.g. has been buried) for a prolonged period of time the trapped electron population in quartz and/or feldspar minerals will usually be in saturation, i.e. further exposure to ionising radiation will not increase the amount of trapped charge. If the sample is then exposed to daylight the trapped electron population will decrease with time. The rate of detrapping will decrease with depth into the rock due to light attenuation following Lambert beers law [e.g. 72], i.e. traps close to the rock surface are more likely to be emptied than traps located deeper into the rock. Trapped charge may be released when the mineral is exposed to light or heat. As a consequence of such exposure, a fraction of the released charge will recombine radiatively which results in the emission of luminescence. Thus, luminescence measurements can be used to assess the trapped charge population into the rock.

Rock surface dating using luminescence relies on fitting measured luminescence-depth profiles into rocks. Such profiles are generally described assuming first-order kinetics for electron detrapping,

i.e. retrapping is assumed to be negligible.[44]. This assumption is perhaps reasonable for quartz, but feldspar is generally understood to follow non-first-order kinetics [e.g. 54,77,109]. Feldspar is often the preferred chronometer in rock surface dating, because quartz extracts often have low luminescence sensitivity in part depending on lithology [e.g. 53]. Thus, in particular for the use of feldspar in rock surface dating, it is important to develop more suitable models. In this study, we use (i) a general-order kinetic model[83] and (ii) a localised recombination model[54] (here referred to as the fading model) to develop new analytical expressions for luminescence-depth profiles in rocks.

Using simulated data, we first investigate how sensitive various parameters (e.g. the light attenuation coefficient) are to the choice of kinetic model. We then explore whether incorrect model assumptions affect estimates of exposure age/erosion rate and to what extent using both simulated and experimental data. The latter were derived from several granite samples exposed to either daylight or to artificial broad-spectrum or monochromatic light sources. Some samples were subsequently irradiated with gamma rays to simulate a burial scenario. We also investigate if the kinetic order determined from IRSL stimulation curves are consistent with those determined from measured luminescence-depth profiles. Erosion of rock surfaces do complicate exposure dating. The effect of erosion on the two new models and on the existing first-order model is investigated analytically.

List of constants and variables

μ	$[\text{mm}^{-1}]$	Light attenuation coefficient
σ	$[\text{cm}^2]$	photoionization cross section
φ	$[\text{cm}^{-2}.\text{ka}^{-1}]$	Incoming photon flux
t	$[\text{ka}]$	Exposure time
t'	$[1]$	Dimensionless exposure time $t' = \overline{\sigma\varphi_0}t$
x	$[\text{mm}]$	Depth
x'	$[1]$	Dimensionless depth $x' = \mu x$
F	$[\text{ka}^{-1}]$	Charge filling rate
n_j	$[\text{m}^{-3}]$	Trapped electron concentration for model j.
n_0	$[\text{m}^{-3}]$	Trapped electron concentration at exposure time $t = 0$.
g	$[1]$	Kinetic order
s	$[\text{s}^{-1}]$	Attempt-to-escape frequency equivalent or the lattice vibration frequency[54]
b	$[\text{s}^{-1}]$	Attempt-to-tunnel frequency[54]
z	$[1]$	Rate of change of lifetime[54]
ρ	$[\text{m}^{-3}]$	Number density of the randomly distributed acceptors.
ρ'	$[1]$	Dimensionless number density of hole sites. $\rho' = 4/3\pi\rho\alpha^{-1}$
α	$[\text{m}^{-1}]$	Tunnelling rate constant[54]
τ_c	$[\text{s}]$	Instantaneous lifetime at the critical tunnelling distance[54]

3.2   State-of-the-art: first-order kinetics

If the minerals in a rock sample are shielded from light for a prolonged period of time, the number of filled traps is constant with depth and in saturation. The trapped charge is then evicted as

a consequence of light exposure. The rate of detrapping, $E(x)$, caused by such light exposure decreases with depth x into the rock because of light attenuation[42] and is here given as

$$E(x) = \overline{\sigma\varphi_0}e^{-\mu x} \tag{3.1}$$

where σ is the photoionization cross section (cm^2) and φ is the incoming photon flux $(cm^{-2}.ka^{-1})$. Both these quantities depend on photon wavelength, but have here been integrated over wavelengths included in the solar spectrum[42] and thus $\overline{\sigma\varphi_0}$ (ka^{-1}) is assumed to be the detrapping rate at the surface. The light attenuation coefficient, μ (mm^{-1}), is defined as the inverse of the mean free path of photons in the rock. The parameters σ, φ and μ all depend on the wavelength of the stimulation light, but here we assume that all wavelengths contribute equally in the trapped charge depletion. Note that σ and φ and time is one combined parameter in the model.

If the rock is exposed to light for a prolonged period of time, usually more than weeks depending on signal bleachability and rock opacity, the trapped charge population will be zeroed at the surface but increase to the saturation value at depth [e.g. 44,65]. This is the experimental relationship observed when measuring luminescence-depth profiles. Thus, in the following, we assume that the trapped charge population $n_j(x,t)$ is proportional to the measured sensitivity corrected OSL signal L_x/T_x.

The currently used equations[1,42] in rock surface luminescence exposure modelling are Eq. (3.2) and Eq. (3.3) given below.

$$n_1(x,t) = n_{0,1}(x)e^{-E(x)te^{-\mu x}} \tag{3.2}$$

$$n_1(x,t) = \frac{-\left(F(x)[N(x) - n_{0,1}(x)] - E(x)n_{0,1}(x)\right)e^{t(E(x)+F(x))} + F(x)}{E(x) + F(x)} \tag{3.3}$$

where $n_{0,1}$ is the trapped charge population at time $t = 0$, $E(x)$ is given by Eq. 3.1, μ is the attenuation coefficient, $F(x)$ is the charge filling rate and $N(x)$ is the total number of traps.

Both these equations assume first-order kinetics. In Eq. (3.2) it is further assumed that the trap filling rate, $F(x)$, is negligible during light exposure, whereas Eq. (3.3) includes the trap filling rate during light exposure. The filling rate is given as $F(x) = \frac{\dot{D}(x)}{D_c}$, where $\dot{D}(x)$ is the dose rate and D_c is a sample-dependent constant characterizing the filling rate of the electron traps[107].

On terrestrial surfaces, the effect of trap filling during daylight exposure is usually negligible (i.e. $F(x) \approx 0$). However, this is not true at depth where the trap emptying rate, $E(x)$, approaches zero. When trap filling during bleaching is included, the profile migration into the rock ceases as the rate of trap filling becomes equal to the rate of trap emptying.

In this study, we derive new analytical solutions for kinetic models assuming either general-order kinetics or localised-recombination. We assume that trap filling during bleaching is negligible, i.e. the profiles will continue to migrate through the rock as a function of time.

3.3 New analytical models for rock surface dating

In this section we present two new models for rock surface dating: i) general-order[83] (G.O.M.) and 2) localised recombination model taking fading into account[54], i.e. here referred to as the

fading model (F.M.). These models have not been applied to rock surface dating before.

In the following, we derive equations describing the trapped charge population as a function of depth, x, and exposure time, t, for the two new models, i.e. $n_m(x,t)$ and $n_f(x,t)$ assuming general order kinetics and localised recombination, respectively.

For the first-order (n_1) and general-order model (n_m), then during light exposure the rate of change of the number density of the trapped charge population is proportional to the number density of filled traps raised to the power of g [110] and the detrapping rate, $E(x)$, i.e.

$$\frac{\partial n_1}{\partial t} = -E(x)n_1 \tag{3.4}$$

$$\frac{\partial n_m}{\partial t} = -\frac{1}{N^{g-1}}E(x)n_m^g \tag{3.5}$$

where n_1 and n_m are for first-order and general-order systems, respectively. $E(x)$ is given by Eq. (3.1), g is the kinetic order and N is the constant total number of traps. Note that when $g = 1$ the general-order model n_m (Eq. 3.5) reduces to the first-order model (Eq. 3.4).

For the fading model we derive the time derivative by combining the expression for the rate of change of trapped electrons and the instantaneous lifetime at the critical tunnelling distance described by Jain et al. [54] (their Equations 8 and 9). In order to investigate the impact of this model on luminescence-depth profiles, we introduce a depth dependency on the excitation probability ($\xi \equiv \ln\left(s/\overline{\sigma\varphi_0}\right)$) as $e^{-\xi(x)} = s^{-1}\overline{\sigma\varphi_0}e^{-\mu x} = s^{-1}E(x)$:

$$\frac{\partial n_f}{\partial t} = -3n_f z\rho'^{1/3}\left(\ln\frac{n_{f,0}}{n_f}\right)^{2/3}e^{-\left(\frac{1}{\rho'}\ln\frac{n_{f,0}}{n_f}\right)^{1/3}}bs^{-1}E(x) \tag{3.6}$$

where z is the lifetime rate of change, ρ' is the dimensionless number density of hole sites given as $\rho' = 4/3\pi\rho\alpha^{-1}$, ρ is the number density of the randomly distributed acceptors, α is the tunnelling rate constant, $n_{f,0}$ is the trapped electron concentration at time t_0 prior to start of stimulation and corresponding to a full nearest neighbour distribution, b [s^{-1}] is the attempt-to-tunnel frequency, and s is the attempt-to-escape frequency equivalent or the lattice vibration frequency [s^{-1}] (see Jain et al. [54] for further details).

Equations (3.4), (3.5), and (3.6) are solved by integration from $t = 0$ to t to give Eq. (3.2), (3.7) and (3.8), respectively. The initial trapped charge population at depth x and time $t = 0$ are $n_{1,0}$, $n_{m,0}$ and $n_{f,0}$, respectively. Note that for the luminescence depth fading model we assume no truncation, i.e. no significant loss of the trapped charge population due to e.g. preheat and $n_{f,i} = n_{f,0}$. This means that no trapped charge was lost before the natural exposure time $t = 0$ ($n_{f,0}$). We further define $\beta = bzs^{-1}$ (z is typically around 1.8 for optical stimulation) for simplification.

$$n_m(x,t) = [(g-1)tE(x) + n_{m,0}^{1-g}]^{\frac{1}{1-g}}, \qquad (g > 1) \tag{3.7}$$

$$n_f(x,t) = n_{f,0}e^{-\rho'(\ln(\beta tE(x)+1))^3} \tag{3.8}$$

In what follows, we have normalised the luminescence profiles to unity at the saturation level, $N = 1$, and we assume full saturation before the onset of bleaching, i.e. $n_{1,0} = n_{m,0} = n_{f,0} = 1$.

Figure 3.1a-c show normalised luminescence profiles described by Eq. (3.2), (3.7), and (3.8), respectively, using the same time intervals ($\overline{\sigma\varphi_0}t = 10^2$ to 10^7), and the same constant $\mu = 1$. For the general-order model we use $g = 2$ as this order is generally observed for IRSL (IR$_{50}$) stimulation curves[77]. In the fading model, we assume the density ρ' to be 0.01 and $\beta = 100$.
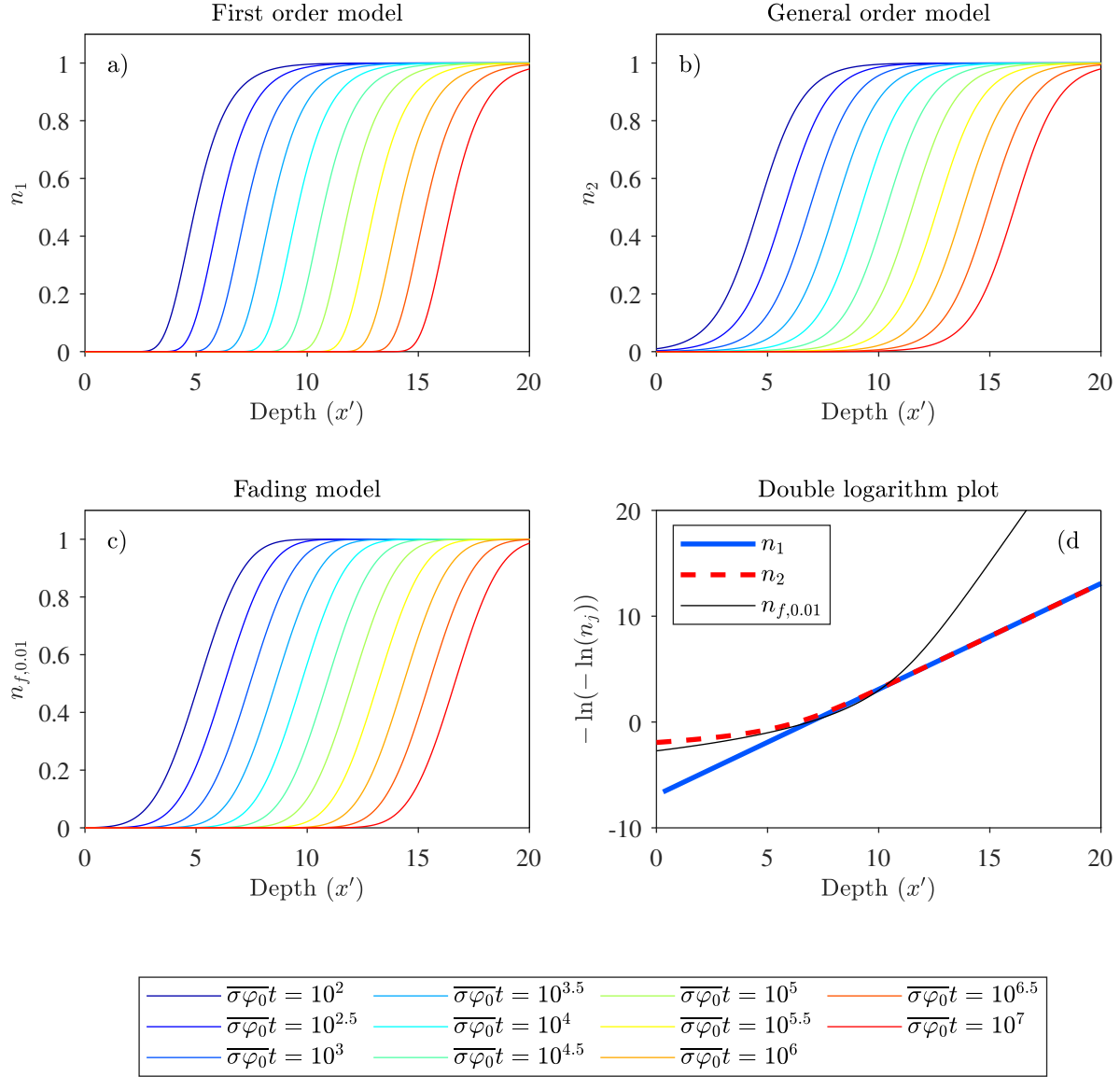
Figure 3.1: a), b), c) Luminescence-depth profiles for values of the dimensionless time variable $t' = \overline{\sigma\varphi_0}t$ ranging from 10^2 to 10^7 in steps of $10^{0.5}$ (colours from blue to red). Depth is set to the dimensionless depth $x' = \mu x$ for the three models described by Eq. (3.2), (3.7), and (3.8), respectively. For the general-order model $g = 2$ and in the fading model the density $\rho' = 0.01$ and $\beta = 100$. d) double logarithmic plot of profiles for $\overline{\sigma\varphi_0}t = 10^3$ and other constants as given in a), b) and c).

For all the models it applies, that the longer the exposure time the further into the rock the OSL signal is bleached. In addition, we observe that the shape of the profiles for a given model does not change with time. The spacing between the shown profiles is model independent and constant for any given luminescence level. This implies that the models have the same *change* in progression

per unit time, i.e. the speed is the same for all models, and it decreases with time, as the spacing between the profiles is $10^{0.5}$. However, for $n_j = 0.2$ and exposure time $\overline{\sigma\varphi_0}t = 10^7$ (red curves), the first order model has evolved to a depth of ~ 16, the second order model to a depth of ~ 15, and the fading model to a depth of ~ 15.2. This does not imply a difference in progression speed for the different models, but rather a difference in shape, i.e. the slope is smaller for higher order and lower density. The change in shape is more clear in logarithmic space. Taking the double logarithm of the first order model gives a linear relationship, but this is not the case for the general order model or the fading model i.e.:

$$-\ln(-\ln n_1) = -\ln(\overline{\sigma\varphi_0}t) + \mu x \tag{3.9}$$

$$-\ln(-\ln n_m) = -\ln\left(\frac{\ln[(g-1)E(x)t+1]}{g-1}\right) \tag{3.10}$$

$$-\ln(-\ln n_f) = -\ln\left(\rho(\ln[\beta E(x)t+1])^3\right) \tag{3.11}$$

In Figure 3.1d the double logarithm of n_j are shown for the third blue curves in Figure 3.1(a-c) (i.e. $\overline{\sigma\varphi_0}t = 10^3$).

In the next section, we derive analytical expressions explaining these observations.

3.4   Evolution of luminescence depth profiles

The profile depth progression with time and the shape of the profiles are the key points when estimating exposure times. In Figure 3.1, we observe that the progression in x of a given luminescence level is model dependent, but also that the speed with which the profile moves into the rock is model independent. This is investigated analytically below.

The profile progression depth is derived by isolating x in Eq. (3.2, 3.7, 3.8), respectively.

$$x(n_1, t) = \frac{\ln t}{\mu} + \frac{\ln \overline{\sigma\phi_0}}{\mu} - \frac{\ln(\ln(n_1^{-1}))}{\mu} \tag{3.12}$$

$$x(n_m, t) = \frac{\ln t}{\mu} + \frac{\ln \overline{\sigma\phi_0}}{\mu} + \frac{\ln \frac{(g-1)}{(n_m^{1-g}-1)}}{\mu} \tag{3.13}$$

$$x(n_f, t) = \frac{\ln t}{\mu} + \frac{\ln \overline{\sigma\phi_0}}{\mu} + \frac{\ln \beta}{\mu} - \frac{\ln\left(e^{\left(\frac{\ln n_f}{-\rho^f}\right)^{1/3}} - 1\right)}{\mu} \tag{3.14}$$

Thus, for any given value of n_j ($j = 1$, m or f) the depth x depends logarithmically on time.

Taking the time derivative of the progression depth given in Eq. (3.12-3.14) gives the speed of progression at any given value of n_j.

$$\frac{dx_{n_1}}{dt} = \frac{dx_{n_m}}{dt} = \frac{dx_{n_f}}{dt} = \frac{1}{\mu t} \tag{3.15}$$

For all models, the speed of progression depends solely on the inverse of μ and t and decreases with time (Eq. 3.15). If we instead differentiate with respect to the logarithm of time, then for all models:

$$\frac{dx_{n_1}}{d\ln t} = \frac{dx_{n_m}}{d\ln t} = \frac{dx_{n_f}}{d\ln t} = \frac{1}{\mu} \tag{3.16}$$

The logarithmic speed ($\frac{dx}{d\ln t}$) is constant with time for all three models and depend only on μ (Eq. 3.16) (see also the constant spacing between profiles in Figure 3.1a-c). In Figure 3.1d, we show a double logarithmic of n_j as a function of depth for a given time ($\overline{\sigma\varphi_0}t = 10^3$). The advantage of using this scale is that the first order model, n_1, becomes a simple straight line with a slope of μ and intercept of $-\ln(\overline{\sigma\varphi_0}t)$ (see Eq. 3.12) and it illustrates that assuming a first order model when fitting a profile with detrapping kinetics different than first order, corresponds to fitting a straight line to a curved line.

The slope at any given value of n_j is determined by taking the derivative with respect to x, i.e. $\frac{\partial n_i}{\partial x}$ of Eq. (3.2), (3.7) and (3.8), respectively, which results in Eq. (3.17-3.19).

$$\frac{\partial n_1}{\partial x} = -\mu n_1 \ln n_1 \tag{3.17}$$

$$\frac{\partial n_m}{\partial x} = \mu \frac{n_m - n_m^g}{g - 1} \tag{3.18}$$

$$\frac{\partial n_f}{\partial x} = \mu 3 n_f \rho \left(\frac{\ln n_f^{-1}}{\rho}\right)^{2/3} \left(1 - \frac{1}{\exp\left([\frac{\ln n_f^{-1}}{\rho}]^{1/3}\right)}\right) \tag{3.19}$$

As expected the slope depends on μ and the kinetic order g or density ρ, but not time, i.e. the shape of the profile remains constant as time increases.

In Figure 3.2a, luminescence profiles with orders ranging from 1 to 2 are shown for constant $\mu =1$ or 0.7 (solid and dashed lines, respectively) and $\overline{\sigma\varphi_0}t = \ln 3$. The horizontal dotted line indicates $n_j = 0.5$. Depth is set to the dimensionless depth $x' = \mu x$. As indicated by the four diamond symbols on profiles with $\mu=1$ the profiles progress to larger depth with decreasing order (for the same μ and $\overline{\sigma\varphi_0}t$). Figure 3.2c, shows depth, $x_{0.5}$ (i.e. the depth at which $n_j = 0.5$) as a function of log time. As expected from Eq. 3.13 the relationship is linear with slope μ. The time it takes for a profile to reach a certain depth decreases with kinetic order, g, for the same n_j. For a lower attenuation μ, the profiles move faster into the rock and the spacing between the profiles with different kinetic orders increases.

Figures 3.2b and 3.2d show the corresponding luminescence profiles obtained using the fading model with densities ranging from 3 to 0.05 (blue, red, green, black lines). The same effects are seen here, i.e. the higher the density the larger the progression for a given exposure time, but the speed of progression is independent of density, and the lower the μ the faster the progression.
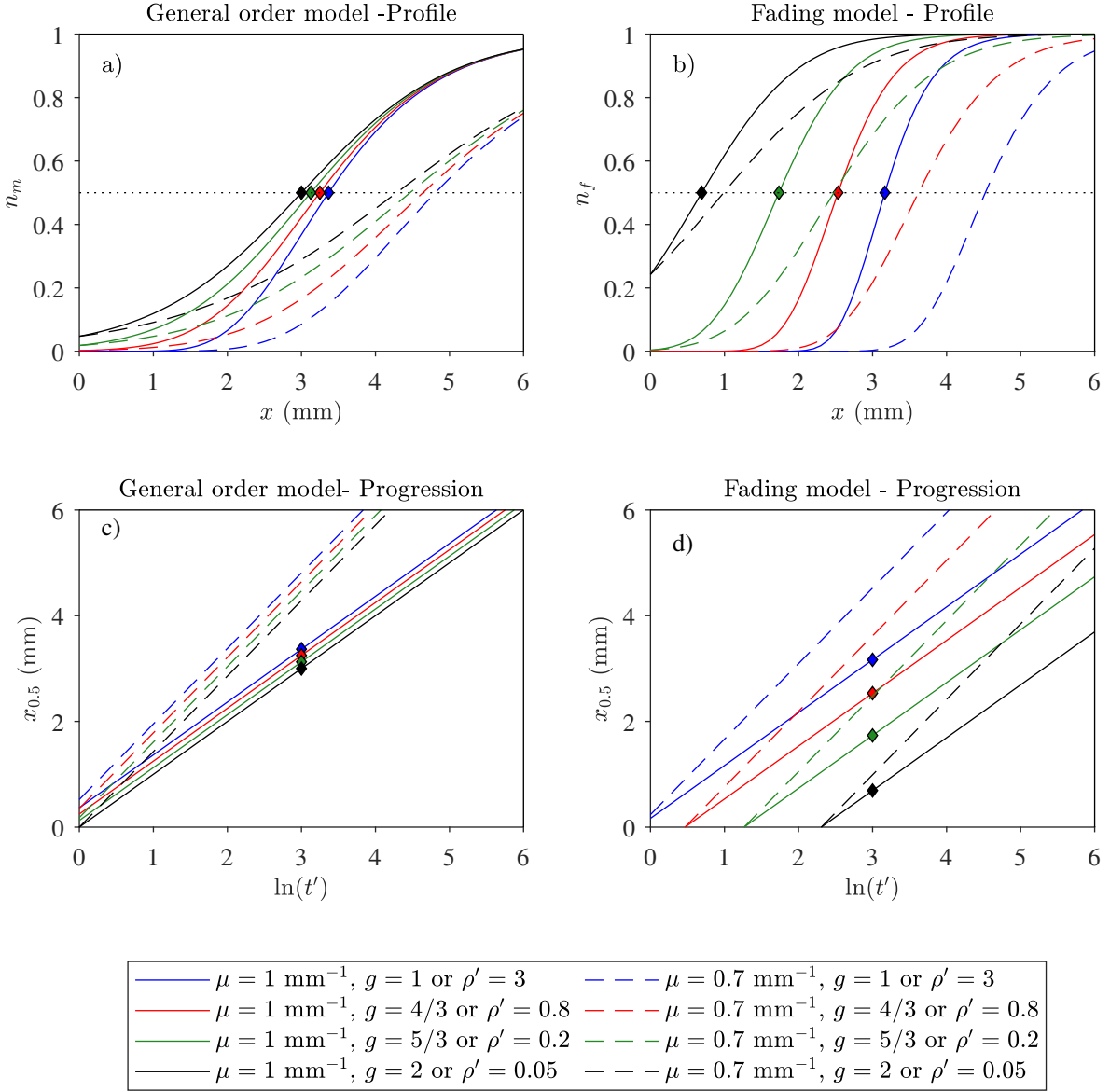
Figure 3.2: Luminescence-depth profiles with $t' = \overline{\sigma \varphi_0} t = \ln 3$, $\mu = 1$mm^{-1} (solid lines) and $\mu = 0.7$mm^{-1} (dashed lines). The four diamond symbols mark where $n_j = 0.5$. a) General order model with $g = 1$, $4/3$, $5/3$, 2 (blue, red, green, black curves), b) Fading model with densities ρ ranging from 3, 0.8, 0.2 0.05 (blue, red, green, black curves). The horizontal dotted line indicates $n_j = 0.5$. c) and d) show how $x_{0.5}$ changes with exposure time ($\ln(t')$).

3.5 Kinetic order determined from stimulation curves

In principle, it is possible to determine the kinetic order directly from the OSL/IRSL stimulation curves and so obtain estimates of the model parameter g and ρ. In this section, we explore how to do this for the three models presented.

Luminescence stimulation curves L_j are measured as a function of measurement time (t_{lab}). The detrapping rate depends on the photon ionization cross section (σ, assumed constant for a given

luminescence signal) and the flux of the laboratory light (φ_{lab}, constant for laboratory measurements) as well as a model specific parameter (p_j, where $j = 1$, m or f) assumed to describe the signal decrease with time (i.e. $p_1 = 1$ in the first-order model, $p_m = g$ in the general-model, and $p_f = \rho$ in the fading model). Note that the model specific parameter $\frac{bz}{s}$ in the fading model is not an independent parameter.

In all cases, the OSL stimulation curve represents the change in the trapped charge population, i.e.

$$L_j(t_{\text{lab}}, \sigma\varphi_{lab}, p_j) = -\frac{dn_j}{d\ t_{\text{lab}}} \tag{3.20}$$

The rate equations for the three models (first-order, general-order ($g \neq 1$) and fading) are thus

$$L_1 = -\frac{dn_1}{dt_{\text{lab}}} = \sigma\phi_{lab}n_1 = \sigma\phi_{lab}n_{1,0}e^{-t_{\text{lab}}\sigma\phi_{lab}} \tag{3.21}$$

$$L_m = -\frac{dn_m}{dt_{\text{lab}}} = \sigma\varphi_{lab}n_m^g = \sigma\varphi_{lab}[(g-1)t_{\text{lab}}\sigma\varphi_{lab} + n_{m,0}^{1-g}]^{\frac{g}{1-g}} \tag{3.22}$$

$$L_f(t) = -\frac{dn_f}{dt} = 3B\rho'n_{f,0}k^2e^{-(\rho'k^3-k)} \tag{3.23}$$

where $k \equiv \ln(Bt + 1)$ with $B \equiv \sigma\varphi_{lab}zbs^{-1}$.

From a laboratory measured stimulation curve, we know the initial value at time zero, $L_{j,0}$, and we know the total area under the curve, $n_{j,0}$. The laboratory parameter $\sigma\varphi_{lab}$ is a constant factor in all three rate equations. Thus, fitting normalised stimulation curves gives the model parameter p_j, which is to be compared to fitting results or used in fitting the luminescence depth profiles $n_1(x,t,p_1)$, $n_m(x,t,p_m)$, and $n_f(x,t,p_f)$. The normalised luminescence stimulation curve for first order kinetics is given by Eq. (3.24). To fit the stimulation curve by assuming first order, the stimulation signal normalised to the signal at $t_{\text{lab}} = 0$ ($L_{1,0} = \sigma\phi_{lab}n_{1,0}$) and fitted to Equation 3.24.

$$\frac{L_1}{L_{1,0}} = e^{-t_{\text{lab}}\sigma\phi_{lab}} \tag{3.24}$$

The normalised general order luminescence stimulation curve (Eq. 3.25) is a function of the area under the stimulation curve ($n_{m,0}$), the initial value of the stimulation curve $L_{m,0}$, the measurement time t_{lab}, and the model specific parameter g (the kinetic order). To fit the stimulation curve by assuming the general order model, the stimulation signal is normalised to the signal at $t_{\text{lab}} = 0$ and fitted to Equation 3.25 including $n_{m,0}$ as the area of the non-normalised stimulation curve.

$$\frac{L_m}{L_{m,0}} = [(g-1)\frac{t_{\text{lab}}L_{m,0}}{n_{m,0}} + 1]^{\frac{g}{1-g}} = L_{m,\ \text{norm}}(t_{\text{lab}}, g, L_{m,0}, n_{m,0}) \tag{3.25}$$

In the fading model, the maximum luminescence does not occur at time zero. At time zero the luminescence begins to build up and peaks at some time $t_{max} > 0$. Thus the stimulation curve

observed is a truncated curve. Thus, in order to normalise to the maximum luminescence value to time zero, we need to use a truncated fading model as shown in Figure 3.3 (See Appendix). Using the truncated fading model with $\hat{k} \equiv \ln(Bt_{\text{lab}} + 1)$ and $t_{\text{lab}} = t + t_{\text{max}}$ the luminescence stimulation curve is described by Eq. (3.26).

$$\hat{L}_f(t_{\text{lab}}) = 3B\rho' n_{f,0} \hat{k}^2 e^{-(\rho'\hat{k}^3 - \hat{k})} \tag{3.26}$$
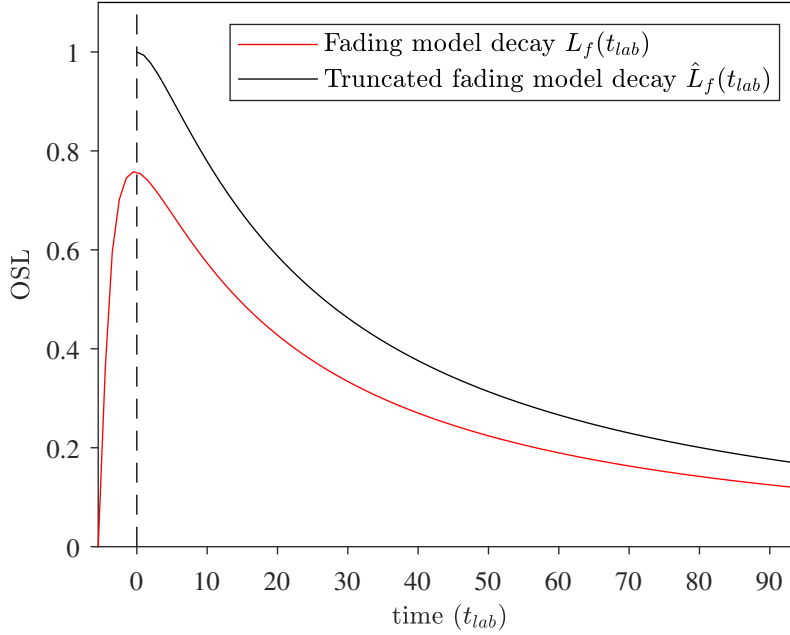
Figure 3.3: OSL stimulation curve for the fading model (red line) and the truncated fading stimulation curve (black) normalised to the maximum of the red line.

Normalising the stimulation curve to the value $\hat{L}_{f,0}$, at laboratory time $t_{\text{lab}} = 0$ gives a function with four parameters: $\rho', \hat{L}_{f,0}$, and $\hat{n}_{f,0}$ (see Eq. 3.27).

$$\frac{\hat{L}_f}{\hat{L}_{f,0}} = \frac{\hat{k}^2 e^{-(\rho\hat{k}^3 + \hat{k})}}{k_{\text{max}}^2 e^{-(\rho k_{\text{max}}^3 + k_{\text{max}})}} = \hat{L}_{f, \text{ norm}}(t_{\text{lab}}, \rho', \hat{L}_{f,0}, \hat{n}_{f,0}) \tag{3.27}$$

To get an expression for $\hat{k}$, we need an expression for B. B is derived from the initial value of the stimulation curve $\hat{L}_{f,0}$, from the area under the stimulation curve $\hat{n}_{f,0}$, and from k_{max}, which is a function of ρ'. Thus the procedure to fit a stimulation curve to the fading model is i) normalise the stimulation curve to the value at $t_{\text{lab}} = 0$ ($\hat{L}_{f,0}$), ii) fit the normalised curve to Eq. (3.27), including the area ($\hat{n}_{f,0}$) under the non-normalised stimulation curve in the expressions for $\hat{k}$, B,

and $k_{\max}$ as

$$B = \frac{\hat{L}_{f,0}}{3\rho' k_{\max}^2 e^{-k_{\max}} \hat{n}_{f,0}} \tag{3.28}$$

$$\hat{k} = \ln(Bt_{\mathrm{lab}} + e^{k_{\max}}) \tag{3.29}$$

$$k_{\max} = q^{\frac{1}{3}} - \frac{1}{9\rho'} q^{-\frac{1}{3}} \tag{3.30}$$

$$q(\rho') = \left(\frac{1}{(3\rho')^2} + \frac{1}{(9\rho')^3} \right)^{\frac{1}{2}} + \frac{1}{3\rho'} \tag{3.31}$$

Combining Eq. (3.28-3.31) gives $\hat{L}_{f,\mathrm{norm}}$ to be used in fitting having only the density (ρ) as a free parameter. Thus, the normalised truncated stimulation curve becomes a function of $\hat{n}_{f,0}$, $\hat{L}_{f,0}$, t_{lab}, and the model specific parameter ρ'.

Equation 3.28 was derived from isolating B in the truncated stimulation curve. (notice that $B \equiv \sigma \varphi_{lab} z b s^{-1}$). For detailed derivations see appendix.

$$\hat{L}_{f,0} = 3Bn_{f,0}\rho k_{\max}^2 e^{-(\rho' k_{\max}^3 + k_{\max})} = 3B\rho' k_{\max}^2 e^{-k_{\max}} \hat{n}_{f,0} \tag{3.32}$$

3.6   Erosion

Erosion of rock surfaces can be a major challenge for accurate rock surface dating using luminescence as a least part of the surface is progressively removed with time. In the following, we assume that erosion is constant with time and given by the constant ϵ, i.e. the removal of the surface is given by

$$\frac{dx}{dt} = -\epsilon \Rightarrow x(t) = x_i - \epsilon t \tag{3.33}$$

where x_i is the initial depth at time $t = 0$. The rate of detrapping by light exposure $E_\epsilon(x,t)$ is then given by

$$E_\epsilon(x,t) = \overline{\sigma \varphi_0} e^{-\mu(x_i - \epsilon t)} \tag{3.34}$$

Erosion can be included in the three luminescence-depth models as

$$\frac{\partial n_{1,\epsilon}}{\partial t} = -E_\epsilon(x,t)n_1 \tag{3.35}$$

$$\frac{\partial n_{m,\epsilon}}{\partial t} = -E_\epsilon(x,t)n_m^g \tag{3.36}$$

$$\frac{\partial n_{f,\epsilon}}{\partial t} = -3n_f \rho^{1/3} \left(\ln \frac{n_{f,0}}{n_f} \right)^{2/3} e^{-\left(\frac{1}{\rho} \ln \frac{n_{f,0}}{n_f} \right)^{1/3}} \beta E_\epsilon(x,t) \tag{3.37}$$

i.e. analogous to Eq. (3.4-3.6), but with $E(x)$ replaced by $E_\epsilon(x,t)$. To solve this, $E_\epsilon(x,t)$, needs to be integrated. Doing so (see the Appendix for details), we can rewrite the equation to be analogous

with the model equations without erosion, replacing t with an apparent erosion time t_ϵ i.e. the exposure time one would get from fitting an eroded luminescence profile without taken erosion into account. The solutions (with $E(x) = \overline{\sigma\varphi_0}e^{-\mu x}$) to these three differential equations are

$$n_{1,\epsilon}(x,t_\epsilon) = n_{1,0}e^{-t_\epsilon E(x)} \tag{3.38}$$

$$n_{m,\epsilon}(x,t_\epsilon) = [(g-1)t_\epsilon E(x) + n_{m,0}^{1-g}]^{\frac{1}{1-g}} \tag{3.39}$$

$$n_{f,\epsilon}(x,t) = n_{f,0}e^{-\rho(\ln(\beta t_\epsilon E(x)+1))^3} \tag{3.40}$$

where the apparent exposure time t_ϵ for all models is given by

$$t_\epsilon = \frac{1}{\mu\epsilon}\left(1 - e^{-\mu\epsilon t}\right) \tag{3.41}$$

Including erosion in the models gives two opposing effects on the luminescence profile. On the one hand, erosion of the surface moves the profile closer to the surface, but as the profile is moved closer to the surface the charge detrapping rate $E(x(t))$ increases and thus the profile is moved further into the rock.

In the following, we investigate how the apparent exposure time t_ϵ is affected by varying erosion rates and how it relates to the true exposure time t. As the effect of erosion depends on μ (Eq. 3.41) we make use of dimensionless variables for time $(t' = \overline{\sigma\varphi_0}t)$, erosion rate $\epsilon' = \mu\epsilon(\overline{\sigma\varphi_0})^{-1}$, and depth $(x' = \mu x)$. By doing so a single graph can be used to illustrate the effect of erosion on the estimated time for any value of μ.

Figure 3.4 shows t'_ϵ/t' plotted versus $\epsilon't'$. (Note $t'_\epsilon/t' = t_\epsilon/t$ and $\epsilon't' = \mu\epsilon t$). The physical meaning of ϵt is the total erosion. The apparent exposure time t'_ϵ is, as expected, smaller than the actual time t' i.e. the erosion of the surface has a larger effect than the increasing of the light emptying rate. The ratio of apparent exposure time to actual exposure time (t'_ϵ/t') is seen to decrease with either higher erosion rates or longer exposure times. The apparent to actual exposure time is for example below 0.9 for values of $\epsilon't' > 0.2$.

The dimensionless variables t', t'_ϵ, and ϵ' converts to the corresponding real variables t, t_ϵ, and ϵ depending on μ and $\overline{\sigma\phi_0}$. For example using $\mu = 1$ mm^{-1} this limit would be valid for exposure times greater than 0.2 ka with erosion rate $\epsilon = 1$ mm/ka or greater than 2 ka with erosion rate $\epsilon = 0.1$ mm/ka.
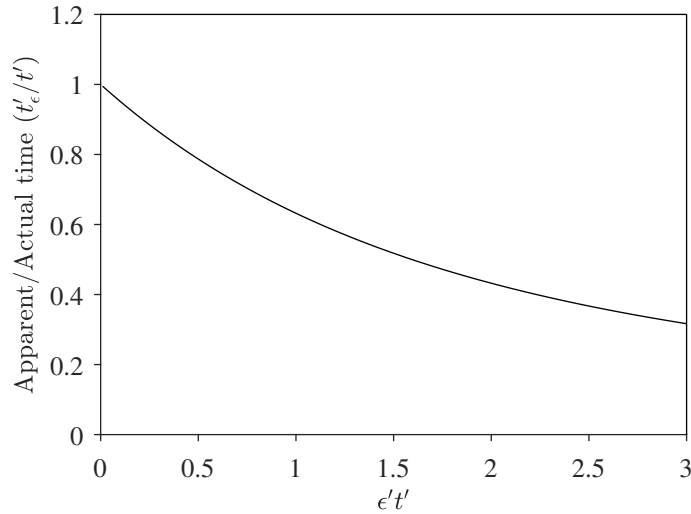
Figure 3.4: Dependency on erosion rate times actual exposure time ($\epsilon' t'$) of apparent to actual exposure time ratio (t'_ϵ/t'), for luminescence profiles of all three models presented in this paper. Notice the variables are dimensionless. Values from μ are needed to get real variables.

3.7 Effect of choice of fitting model on the exposure age

Previous rock surface exposure ages [e.g. 1,6,16,44] have made use of estimates of μ and $\overline{\sigma\varphi_0}$ derived from samples from the same site but with a known exposure age, i.e. so-called calibration samples. In this section, we investigate how sensitive the estimated exposure age for an unknown age sample derived using a calibration sample is to the choice of kinetic model. Fitting a inappropriate kinetic model to the profile will give incorrect in values of μ and $\overline{\sigma\varphi_0}$. The question is whether the incorrect estimates cancel out not to affect the exposure age or erosion rate estimates. In the following, the apparent exposure time is the time derived from fitting an assumed model to a profile of unknown kinetics. Below we investigate how accurate the apparent exposure time is for different fitting models and fitting parameters and how it depends on the exposure age of the calibration profile. We do this using both simulated data (section 3.7.1) and experimental data (section 3.7.2). This is also explored analytically for the 1st order case (section 3.7.1.3).

3.7.1 Simulated data

To investigate the importance of using an appropriate model, we calculated a 2nd order profile with exposure time $t' = \overline{\sigma\varphi_0}t = 10^3$ and $x' = x\mu$. We simulated 6 random numbers from a normal distribution with a relative standard deviation of 10% and an absolute standard deviation of 5% centered on the 2nd-order model value for 20 discrete depths. For each depth, we averaged these 6 values and associated an uncertainty equal to the standard error of the mean. In addition, we assumed a background/thermal transfer level of 2% of the saturation level.
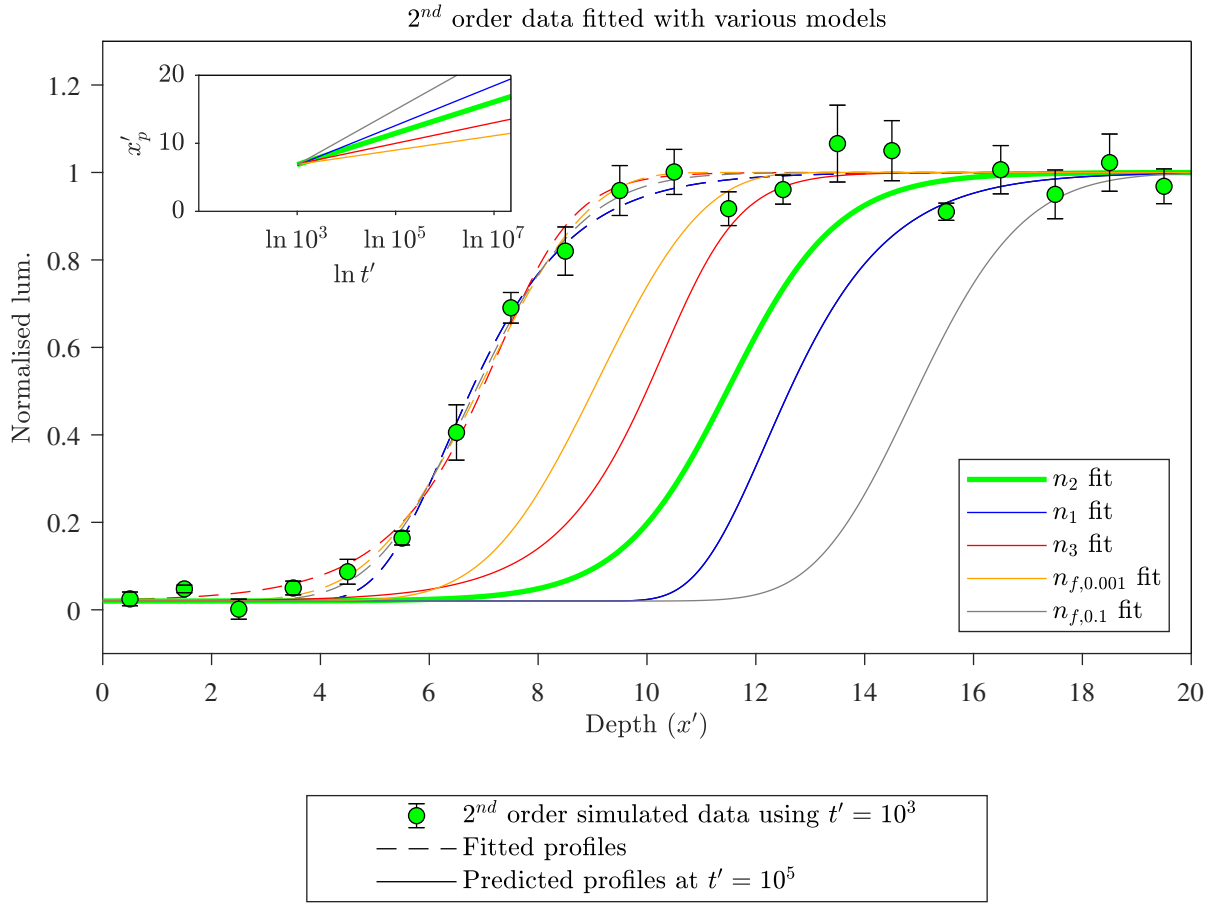
Figure 3.5: Evolution of fitting results 100 times later (solid lines) than the fitted "calibration" profile (dashed lines), using an inappropriate model to fit data (green points). The green data points have been generated from simulation a discrete data set of a 2nd order model with $t' = 10^3$ (see text for details). Note that the x-axis is dimensionless ($x' = \mu x$), where μ is the true value of μ for the simulated data. These data points have subsequently been fitted using 1st order (dashed blue line), 3rd order (dashed red line) models, and the fading model using ρ' of either 0.0001 or 0.1 (dashed orange and grey lines, respectively). The corresponding solid lines show the profiles predicted using the fitting parameters determined for the "calibration" profile but with an exposure time of $t' = 10^5$. The insert shows the progression of $x'_0.5$ (i.e. the depth for which $n_j = 0.5$) as a function of time, $\ln t'$. The slopes of these lines give the progression speed of the individual profiles.

The simulated data points are shown as green circles in Figure 3.5. Note that the x-axis is dimensionless ($x' = \mu x$), where μ is the true value of μ for the simulated data. To make the figure applicable to any given value of μ, the x-axis is multiplied by μ. Also shown in this Figure are various model fits to the simulated data: i) first-order model (dashed blue line), ii) general-order model with $g = 3$ (dashed red line), iii) fading model with $\rho' = 0.001$ (dashed orange line) and iv) fading model with $\rho' = 0.1$ (dashed grey line). Visually, all fits appear acceptable, but the estimates of e.g. the apparent μ vary considerably from the known value of μ, i.e. by i) 78% , ii) 165%, iii) 58% and iv) 223%, respectively. This is problematic when the exposure age of an unknown sample is to be determined. This is illustrated by the solid lines in Figure 3.5. Here the green solid line is the 2nd order profile calculated using $t' = 10^5$ (so 100 times older than the calibration profile). The other solid lines have been calculated using the fitting parameter μ_a determined for the "calibration" profile and 100 times the parameter $\overline{\sigma\varphi_0}$ estimated in the fitting

of the data (green data points). Thus these profiles are the predicted profiles 100 times older than the calibration profile. If the kinetic order used for fitting is less than 2 ($g < 2$, blue line), the profile will progress too fast into the rock and too slow if $g > 2$ (red line). Conversely for the fading model, if ρ' is too high the profile will move too fast and if ρ' is too low then it will move too slowly. This is illustrated more clearly in the inset to Figure 3.5, where the the depth, $x'_{0.5}$ for which the value of the luminescence profile is at 50% of saturation (i.e. $n_j = 0.5$) is shown as a function of the logarithm of t'.

The speed of progression for the individual profiles is given by the slope of these curves, which is equal to the inverse of μ (see Eq. 3.16 and Figure 3.1c,d). Note that the estimate of μ vary significantly between the individual models.

In any real situation one need at least one known profile with exposure time t_1 to estimate the exposure age of one unknown profile with exposure time t_2. One would fit these two measured profiles assuming a given model, and then use the estimated fitting parameter $\overline{\sigma\varphi_0}t_1$ and the known time $t_1 = t_{\mathrm{cal}}$ to estimate $\overline{\sigma\varphi_{\mathrm{cal}}}$ to be used as the fitting parameter $\overline{\sigma\varphi_0}t_2$ when fitting the unkown profile to estimate t_2 Thus if the estimated $\overline{\sigma\varphi_0}t_1$ is incorrect, the estimated unknown time t_2 will be inaccurate. This is illustrated in Figure 3.6. Here we have simulated two 2$^{\mathrm{nd}}$ order profiles with known exposure ages of $t_1 = 10^3$ and $t_2 = 10^5$, where the profile with exposure time t_1 is acting as the known age calibration profile and the profile with t_2 as the profile with unknown exposure age. These data are fitted using three different models: 1$^{\mathrm{st}}$ order, 3$^{\mathrm{rd}}$ order and the fading model using ρ'^{-1} (models 1, 4 and 8 in Table 3.1). From these fit we derive estimates of $\overline{\sigma\varphi_{\mathrm{cal}}}$, which subsequently are to be used to evaluate the apparent exposure time t_a for each model, when fitting profile 2 and thereby determining a fitting parameter $(\overline{\sigma\varphi_0}t)_{\mathrm{unknown}}$ The ratios of t_a to t_2 are: 0.3 ± 0.2, 1.1 ± 0.8, 7 ± 4 and 0.7 ± 0.3, respectively. Thus, the choice of fitting model has a significant impact on the accuracy of the apparent exposure age.

In the following, we first we investigate how much $\overline{\sigma\varphi_0}t$ and μ depend on model used by fitting a series of simulated data sets with different exposure times, orders or densities. Each profile for a given exposure time is used as a calibration profile for the remaining profiles.

We make use of the 8 different models given in Table 3.1.

Model no.	G.O.M. g	Model no.	F.M. ρ'^{-1}
1.	1	5.	20
2.	1.5	6.	40
3.	2	7.	60
4.	3	8.	100

Table 3.1: Parameters for creating simulated data for the general-order model (G.O.M.) and the fading model (F.M.). For each model we use dimensionless depths from 0 to 30, the known dimensionless time $t' = \overline{\sigma\varphi_0}t$ ranging in logarithmic steps from $\ln(t) = 3.1$ to $\ln(t) = 6.4$ in steps of 0.1, giving 34 profiles for each model. (see text for details).

For each model we use dimensionless depths ranging from 0 to 30, the known dimensionless time $t' = \overline{\sigma\varphi_0}t$ ranging from $\ln(t) = 3.1$ to $\ln(t) = 6.4$ in steps of $\Delta \ln(t) = 0.1$, giving 34 profiles for each model, i.e. a total of 272 profiles. The corresponding times depend on $\overline{\sigma\varphi_0}$, e.g. if $\overline{\sigma\varphi_0} = 10$
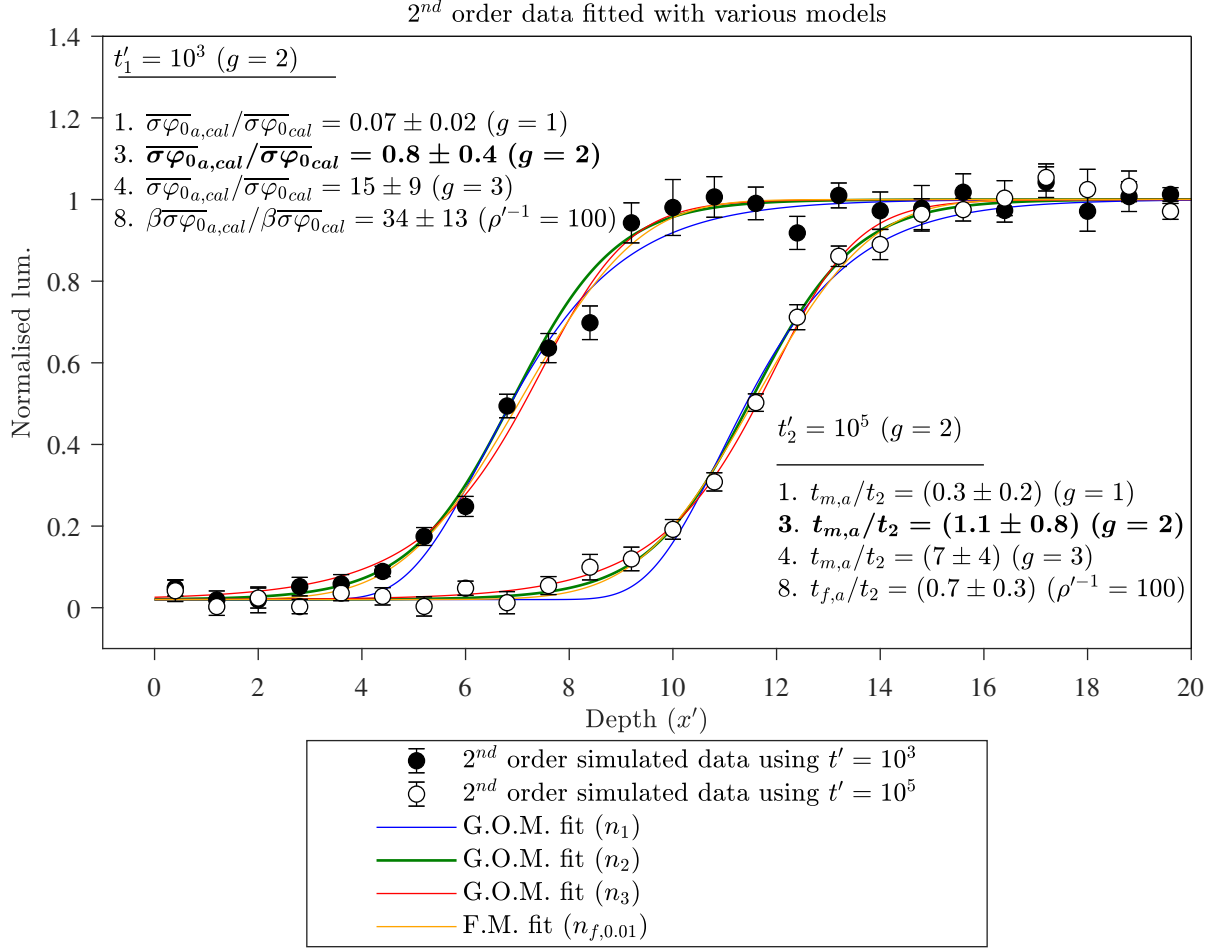
Figure 3.6: Illustration of the calibration procedure to derive apparent exposure times. Two simulated 2nd order data sets for $t'_1 = 10^3$ (closed circles) and $t'_2 = 10^5$ (open circles). The closed circles (representing the known exposure age calibration profile) is fitted with model no. 1. blue lines (1st order), 3. green lines (2nd order), 4. red lines (3rd order) and 8. orange lines (fading model) given in Table 3.1 to derive estimates of $\overline{\sigma\varphi_{cal}}$. e.g. if $\overline{\sigma\varphi_0} = 1000\text{ka}^{-1}$ $t_1 = 1\text{ka}$ and $t_2 = 100\text{ka}$. The estimates of $\overline{\sigma\varphi_{cal}}$ for the various models are subsequently used as fitting constants when fitting the "unknown" age profile ($t' = 10^5$) to derive estimates of the apparent exposure time t_a.

ka^{-1} and $\mu = 1$ mm^{-1} this corresponds to times ranging between 2 and 60 ka and depths from 0 to 30 mm.

To simulate a measured (i.e. discrete) data set we calculated 6 random numbers from a normal distribution around the model value for 30 discrete depths with a relative standard deviation of 1% and an absolute standard deviation of 5%. We averaged these 6 numbers and the uncertainty associated with each such simulated data point was equal to the standard error of the mean. In addition, we assumed a background/thermal transfer level of 2% of saturation level for all models.

Each of the 272 simulated data sets were subsequently fitted using all 8 models given in Table 3.1 to derive estimates of $\overline{\sigma\varphi_{cal}}$ (since the exposure time t_{cal} is known). The parameter $\overline{\sigma\varphi_{cal}}$ is then used when fitting a simulated data set obtained using a different t. The resulting apparent exposure time t_a can then be compared to the known t and so the accuracy assessed.

3.7.1.1 Effect of assuming first-order kinetics on the apparent exposure time t_a

Figure 3.7g and 3.7b show how the ratio between the apparent time t_a and t vary as a function of how close (in terms of exposure time) the calibration data set is to the data set with "unknown" exposure time, i.e. the ratio between t_{cal} and t. In these graphs, the data sets have been simulated using the 8 models given in Table 3.1 but have all been fitted using the first-order model (i.e. $g = 1$). Note, that we take the log of both these ratios because we later describe this relation analytically and see a linear relation). When the data has been generated using the first-order model, then the apparent exposure time t_a is similar to the actual exposure time t regardless of which t_{cal} is used, i.e. the slope of all blue data points in Figure 3.7a is zero. However, using the first-order model to fit data sets generated with the general-order model (with $g > 1$) results in positive slopes. Thus, the higher the kinetic order of the simulated data set, the steeper the slope. If the calibration profile is younger than the unknown profile ($t_{\mathrm{cal}} < t$) then the exposure age will be underestimated ($t_a < t$) and if it is older ($t_{\mathrm{cal}} > t$) then the exposure age will be overestimated ($t_a > t$). Only, when $t_{\mathrm{cal}} = t$ will this approach result in accurate exposure ages. If data has been generated using the fading model but fitting is done using the first-order model then the slopes can be either positive or negative (see Figure 3.7d depending not only on the density ρ but also on the weighting used in the fitting (see next section)

3.7.1.2 Effect on estimated exposure time t_a when the fitting model assumes higher order/density

If the simulated data is of a lower order/density than the order/density used for fitting (i.e. the data has been generated assuming 2nd order but is fitting using a 3rd order model) then the slopes become negative. This is illustrated in Figure 3.7c and 3.7f, where the determined slopes ($d\ln[t_a/t]/d\ln[t_{\mathrm{cal}}]$) are shown as a function of the order or density used in the fitting, i.e. the blue points in Figure 3.7c are derived from a first-order model and fitted with models using values of g ranging between 1 and 6.

A slope different from zero means that the apparent μ, and thus the apparent time, t_a, is different from the actual time t. If the order used for fitting is lower than the real order then the slope is positive and the exposure age is underestimated if $t_{\mathrm{cal}} < t$ or overestimated if $t_{\mathrm{cal}} > t$. If the order used for fitting is higher than the real order then the slope is negative and the exposure age is overestimated if $t_{\mathrm{cal}} < t$ and underestimated if $t_{\mathrm{cal}} > t$. Only if the correct kinetic order is used will the exposure time be accurate.

Open squares show the estimated values of $1 - \mu_{m,a}/\mu$ (G.O.M.) and $1 - \mu_{f,a}/\mu$ (F.M) respectively in c) and d). It is observed that the slope (small points) different from zero indeed reflect an estimated $\mu_{j,a}$ different from the true μ.
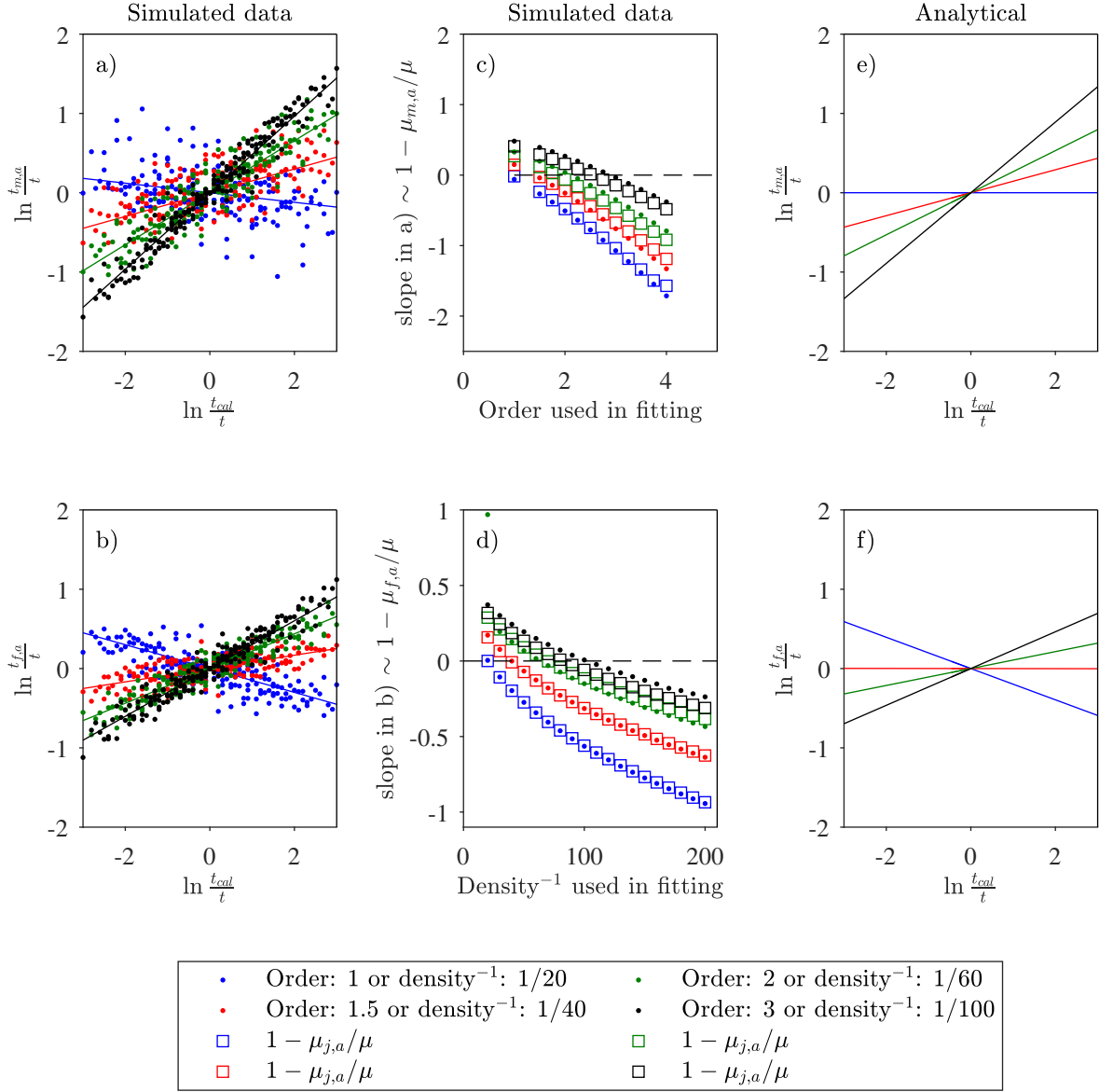
Figure 3.7: Relation in apparent time ratio with calibration time to actual time ratio shown as $\ln\frac{t_a}{t}$ or $\ln\frac{t_{f,a}}{t}$ as a function of $\ln\frac{t_{\text{cal}}}{t}$ when using the first-order model to fit profiles of general orders (a) and profiles described by the fading model (b), respectively. The relations are shown for different values of order and density respectively. c) and d) shows the slope of linear fits to the data points in a) and b) (points), respectively, using the general order model and the fading model with fixed order or density. Squares shows the estimated values of $1 - \mu_{j,a}/\mu$. e) and f) Theoretical plots similar to a) and b), assuming that the first-order fit intercepts the data sets at specific levels (See text for details, $p_1 = 0.2$ and $p_2 = 0.85$.)

3.7.1.3   Theoretical analysis of effect of assuming first order model in fitting

We saw from the simulated data that parameter estimation depends on which model is used. Now we investigate whether the linear relation we observe in Figure 3.7a) and b) can be derived analytically, and thereby obtain information about the dependency on weighting in the fitting. The double logarithm of the first order model is a straight line (Eq. 3.9), but double logarithm of G.O.M and F.M do not give straight lines. (Eq. 3.10 and 3.11) (see Figure 3.1d). Thus assuming

first order model as fitting model to profiles of other kinetics, corresponds to fitting a straight line (the first order model) to the double logarithm of the luminescence data which are not described by a straight line. Thus a first order model will never make a perfect fit, i.e. a straight line will intercept a curved line twice (See Figure 3.8).
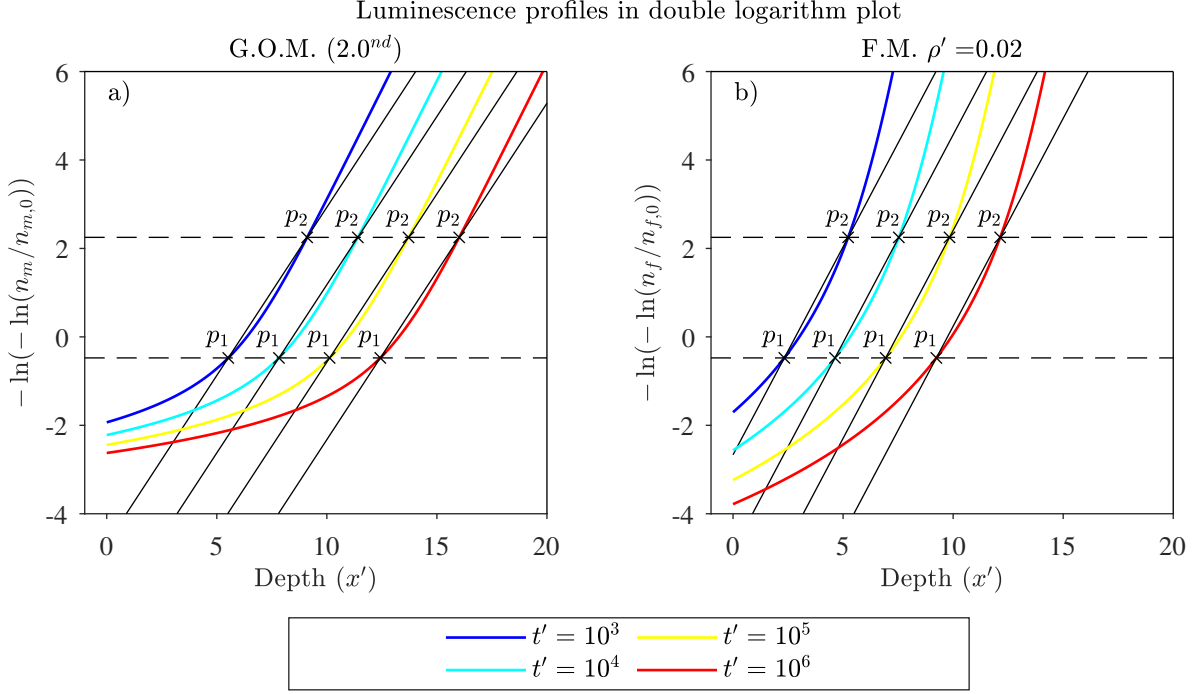
Figure 3.8: Intersection between analytical curves generated from G.O.M. with $g = 2$ and F.M. with $\rho' = 0.02$ using t' ranging from 10^3 to 10^6 (in double logarithm plot) and straight lines intersecting at $p_1 = 0.2$ and $p_2 = 0.9$.

In the limits of infinite depth we see that double logarithm of the general order model approx the first order model (Eq. 3.42), and the fading model approx a straight line with slope 3 times the slope of the first order model (Eq. 3.43).

$$\lim_{x \to \infty} -\ln(-\ln n_m) = -\ln \overline{\sigma \varphi_0} t + \mu x \qquad (3.42)$$

$$\lim_{x \to \infty} -\ln(-\ln n_f) = -\ln \rho (\beta \overline{\sigma \varphi_0} t)^3 + 3\mu x \qquad (3.43)$$

These limits corresponds to the inner part of the profiles. Here G.O.M approx saturation level at the same speed with depth as the first order model. The F.M. does approx saturation at a higher speed, but depending on values of ρ and bzs^{-1}.

We assume that weighting profiles equally when fitting with the first order model corresponds to letting the fit in the double logarithm plot cross the profile twice at the same luminescence values p_1 and p_2 irrespective of how deep the profile is, i.e. this is reasonable since profile shape does not change with time. Thus to estimate analytical dependencies of estimated μ and $\overline{\sigma \varphi_0} t$ on profile order/density and on weighting of fitting, we derive slope and intersection of a straight line crossing the actual profile at two points, p_1 and p_2 with corresponding x-values, $x_{p,1}^m = x_m(p_1)$ and $x_{p,1}^f = x_f(p_1)$, from Equation 3.13 and 3.14, respectively (and likewise with p_2). The slope

give an apparent values of the attenuation coefficient ($\mu_{j,a}$) and the intercept gives an apparent value of $\ln(\overline{\sigma\varphi_0}t)$, namely $\ln(\overline{\sigma\varphi_0}t)_{j,a}$, where j is m or f for G.O.M. and F.M. respectively. Using $y_1 \equiv -\ln(-\ln p_1)$ and $y_2 \equiv -\ln(-\ln p_2)$, and Eq. 3.13 and 3.14, the apparent $\mu_{m,a}$ and $\mu_{f,a}$ are given as the slope of the straight line intersecting the profile at $(x^j_{p,1}; p_1)$ and $(x^j_{p,2}; p_2)$:

$$\mu_{j,a} = \frac{y_2 - y_1}{x^j_{p,2} - x^j_{p,1}} = \mu \frac{\ln \frac{\ln p1}{\ln p2}}{\ln \frac{A_{j,2}}{A_{j,1}}} \tag{3.44}$$

where $A_{j,i}$ ($j = m$ or f and $i = 1$ or 2) are defined for the the two luminescence levels p_1 and p_2 for the two models derived from Eq. 3.13 and 3.14 letting $n_j = p_i$.

$$A_{m,i} \equiv \frac{a - 1}{p_i^{1-a} - 1} \tag{3.45}$$

$$A_{f,i} \equiv \frac{1}{e^{\left(\frac{\ln p_i}{-\rho}\right)^{1/3}} - 1} \tag{3.46}$$

The apparent $\mu_{j,a}$ does not depend on time, but on the real μ, on the weighting (here the specified luminescence levels p_1 and p_2), and on the model parameter order or density in the fading model. Thus $\mu_{m,a} = f(a, p_1, p_2, \mu)$ and $\mu_{f,a} = f(\rho, p_1, p_2, \mu)$, respectively.

In Figure 3.9, $\mu_{m,a}/\mu$ and $\mu_{f,a}/\mu$ are shown as a function of order and of density^{-1} (Figure 3.9a and 3.9b, respectively) for different values of p_1 (p_2 is fixed to 0.85). Here we observe that $\mu_{j,a}$ decreases with higher profile order (or lower density). The decrease with order or density^{-1} is larges for small values of p_1 (with fixed $p_2 = 0.85$. Notice that $\mu_{f,a}$ becomes larger than 1 for values p_1 close to 1 and approx 3μ for $\rho \to \infty$ (i.e. Density$^{-1} \to 0$). These observation fits with the expectations from Equation 3.10 and 3.11 in the limits. For instance if a IR$_{50}$ which often has an order of ~ 2 is fitted with a first order model that intersects the true profile at 0.18 and 0.85, which is realistic, the μ will be 80% of the true μ. Also shown are estimated values of mu_a to actual μ for three simulated data set with $\overline{\sigma\varphi_0}t = 10^2, 10^3, 10^4, \mu = 1$, and orders between 1 and 3 (a) and densities (ρ') between 0.09 and 0.005 ($1/\rho'$ between 11 and 200). Regardless of the time parameter $\overline{\sigma\varphi_0}t$ the fitted attenuation factors follows
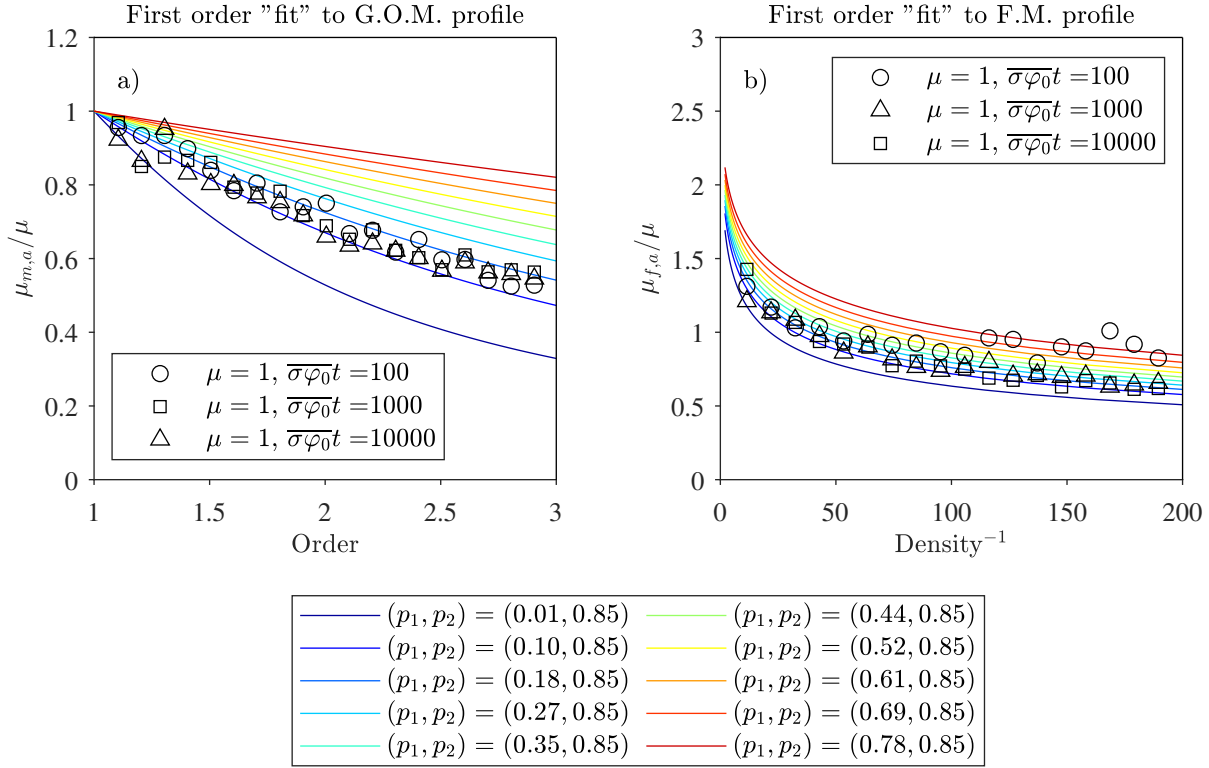
Figure 3.9: Theoretical change in apparent μ with order (a) and density (b) when using first order model to "fit" a profile described by general order model or the fading model with different weighting of fit (i.e. different values of p_1 and p_1). Here we fix p_2 to 0.85 and let p_1 vary from 0.01 to 0.78, imaging the situation were you include less and less from the bottom of the profile. Also shown are estimated values of mu_a to actual μ for three simulated data set with $\overline{\sigma\varphi_0}t = 10^2, 10^3, 10^4, \mu = 1$, and orders between 1 and 3 (a) and densities (ρ') between 0.09 and 0.005 ($1/\rho'$ between 11 and 200).

The apparent values for $\ln(\overline{\sigma\varphi_0}t)_{j,a}$ are given from the negative intersect of the fitted straight line because the first order fit give a straight line with intersect $-\ln(\overline{\sigma\varphi_0}t))$ (See Eq. 3.11).

$$\ln(\overline{\sigma\varphi_0}t)_{j,a} = -\frac{y_1 x_{p,2}^j - y_2 x_{p,1}^j}{x_{p,2}^j - x_{p,1}^j} \tag{3.47}$$

$$= \ln\overline{\sigma\varphi_0}t\beta\frac{\ln\frac{\ln p_1}{\ln p_2}}{\ln\frac{A_{j,2}}{A_{j,1}}} + K_j \tag{3.48}$$

$$= \frac{\mu_{j,a}}{\mu}\ln\overline{\sigma\varphi_0}t\beta + K_j \tag{3.49}$$

where $\beta = 1$ in G.O.M, and K_j are defined for G.O.M and F.M, respectively as K_m and K_f:

$$K_j = \frac{\ln(-\ln p_1))\ln A_{j,2} - \ln(-\ln p_2))\ln A_{j,1}}{\ln(A_{j,2}) - \ln(A_{j,1})} \tag{3.50}$$

Since $\mu_{j,a}/\mu$ is a constant $(\overline{\sigma\varphi_0}t)_{j,a}$ only depend on the real time t, and on the model parameters g (G.O.M), ρ and β (F.M.) and the points of intersection p_1 and p_2. Thus $(\overline{\sigma\varphi_0}t)_{m,a} = f(\overline{\sigma\varphi_0}t, a, p_1, p_2)$ and $(\overline{\sigma\varphi_0}t)_{f,a} = f(\overline{\sigma\varphi_0}t, \beta, \rho, p_1, p_2)$.

When a calibration profiles is used to estimate the exposure time from a profile with unknown exposure time, it is crucial that the $\overline{\sigma\varphi_0}$ remains the same for all times. This is not the case when a inappropriate model is used for fitting as the apparent value for the calibration profile ($\overline{\sigma\varphi_0}_{j,a,\mathrm{cal}}$, $j = m$ or f) depends on the time of the calibration profile (see Equation 3.51, below). We use Equation 3.49 to write the apparent $\overline{\sigma\varphi_0}t$-value for the calibration profile (i.e. $(\overline{\sigma\varphi_0}t)_{j,a,\mathrm{cal}}$) in terms of actual calibration time and apparent to real μ-ratio.

$$\ln(\overline{\sigma\varphi_0})_{j,a,\mathrm{cal}} = \ln\frac{(\overline{\sigma\varphi_0}t)_{j,a,\mathrm{cal}}}{t_{\mathrm{cal}}} = \frac{\mu_{j,a}}{\mu}\ln(\overline{\sigma\varphi_0}t\beta)_{\mathrm{cal}} + K_j - \ln t_{\mathrm{cal}} \tag{3.51}$$

$$\Rightarrow \frac{d\ln(\overline{\sigma\varphi_0})_{j,a,\mathrm{cal}}}{d\ln t_{\mathrm{cal}}} = \frac{\mu_{j,a}}{\mu} - 1 \tag{3.52}$$

with $j = m$ or f for G.O.M. and F.M., respectively ($\beta = 1$ for G.O.M).

As $\mu_{m,a} < \mu$ profile with kinetic order>1 fitted with the first order model $(\overline{\sigma\varphi_0})_{m,a,\mathrm{cal}}$ decreases with calibration time, and the decrease becomes larger for higher order models. For profiles described by the fading model $(\overline{\sigma\varphi_0})_{f,a,\mathrm{cal}}$ decreases with calibration time for low densities. Above a certain density it increases with calibration time. This density depends on the chosen weighting (i.e. on p_1 and p_2).

A consequence of the change in $(\overline{\sigma\varphi_0})_{j,a,\mathrm{cal}}$ with calibration time is, that an exposure time estimated from a known calibration exposure profile of some kinetics order different from first order, fitted with a first order model will be either under- or overestimated (see Equation 3.55). We use Equation 3.49 to write $(\overline{\sigma\varphi_0}t)_{j,a,\mathrm{cal}}$ in terms of actual calibration time and apparent to real μ-ratio. Notice that $\beta\overline{\sigma\varphi_0}$ cancels out.

$$\ln t_{j,a} = \ln\frac{(\overline{\sigma\varphi_0}t)_{j,a}}{(\overline{\sigma\varphi_0})_{j,a,\mathrm{cal}}} = \ln(\overline{\sigma\varphi_0}t)_{j,a} - \ln(\overline{\sigma\varphi_0}t)_{j,a,\mathrm{cal}} + \ln t_{\mathrm{cal}} \tag{3.53}$$

$$= \frac{\mu_{j,a}}{\mu}\ln t + \left(1 - \frac{\mu_{j,a}}{\mu}\right)\ln t_{\mathrm{cal}} \tag{3.54}$$

$$\Rightarrow \ln\frac{t_{j,a}}{t} = \left(1 - \frac{\mu_{j,a}}{\mu}\right)\ln\frac{t_{\mathrm{cal}}}{t} \tag{3.55}$$

The apparent exposure time depends on both the calibration profile time and on its own actual time, the real time, on model parameters order or density, and on the weighting of the fit (i.e. on p_1 and p_2) In Figure 3.7e we set $p_1 = 0.2$ and $p_2 = 0.7$. Slopes>0 means that shallow exposure calibration profiles will underestimate the unknown time, and if the slope<0 shallow calibration profiles will over estimate the time. As expected the slope becomes zero when the profile order is 1.

From Figure 3.7e we observe that fitting with first order to a general order profile overestimates the exposure time when the calibration profile is deeper (i.e. older) than the unknown profile, and it underestimates the age when the calibration profile is younger than the unknown profile exposure age. We also see that the bigger the absolute ratio between the actual time and the calibration time is, the more inaccurate becomes the estimated apparent time.

The same is true for a profile is described by the fading model up to a certain density. Above this density the time is overestimated for small calibration times and underestimated for large calibration times, see Figure 3.7f.

The differential with either calibration time t_{cal} or actual time t is given from Equation 3.56, and shown for a specific weighting ($p_1 = 0.2$ and $p_2 = 0.85$ in Figure 3.7e and f)

$$\frac{d \ln \frac{t_{j,a}}{t}}{d \ln t} = \frac{\mu_{j,a}}{\mu} - 1 \quad \text{and} \quad \frac{d \ln \frac{t_{j,a}}{t}}{d \ln t_{\text{cal}}} = 1 - \frac{\mu_{j,a}}{\mu} \tag{3.56}$$

The degree of this change in apparent time ratio $\ln(t_a/t)$ depends on order (i.e. the slope of the lines in Figure 3.7e and f) increases with higher profile order or lower profile density. But for a certain density (depending on p) the change in apparent time ratio is actually zero implying that using a certain weighting, if a profile described by the fading models is not effected by fitting it to the first order model. However this is only theoretical and not possible to know in advance.
Notice that assuming that fitting results in intersecting the real profile at the same two luminescence levels for all depth make the apparent μ independent on time. This may not be true in real fitting, e.g. fitting shallow profiles and deep profiles may give rise different apparent μ.

Thus as fitting with the first order model to profiles with kinetics different from first order gives apparent values of μ, the speed of progression of the fitted profile will be different from the real profile, thus giving inaccurate exposure time estimates. If $\mu_{j,a} = \mu$ the time estimation will be correct. The different profile shape is most pronounced for small depth fitting only the inner part of the profiles may solve this problem. This corresponds to using p_1 close to p_2. In Figure 3.10 $(1 - \mu_{j,a}/\mu)$ (i.e. same as the slope of figures like 3.7a and b), is shown for different values of p_1 with a fixed value of p_2 using order $g = 2$ (black line) and $\rho^{-1} = 62$ (red line). As the general order profiles differ from first order profile for low luminescence levels, only (near the surface), wee see that as p_1 approx the high value of $p_2 = 0.85$, $\mu_{j,a}$ approx the true value of μ indicating that any calibration profile will give the correct answer. The limits of $(1 - \mu_{j,a}/\mu)$ for p_1 approx 1, are as expected (0 and -2, respectively), as the slope in the double logarithm plots goes towards μ for $x \to \infty$ and to 3μ in G.O.M. and F.M., respectively. Notice that these relations (Equation 3.56) imply that the reason for the change in calibration values with time is a change in μ, when a inappropriate model is assumed.
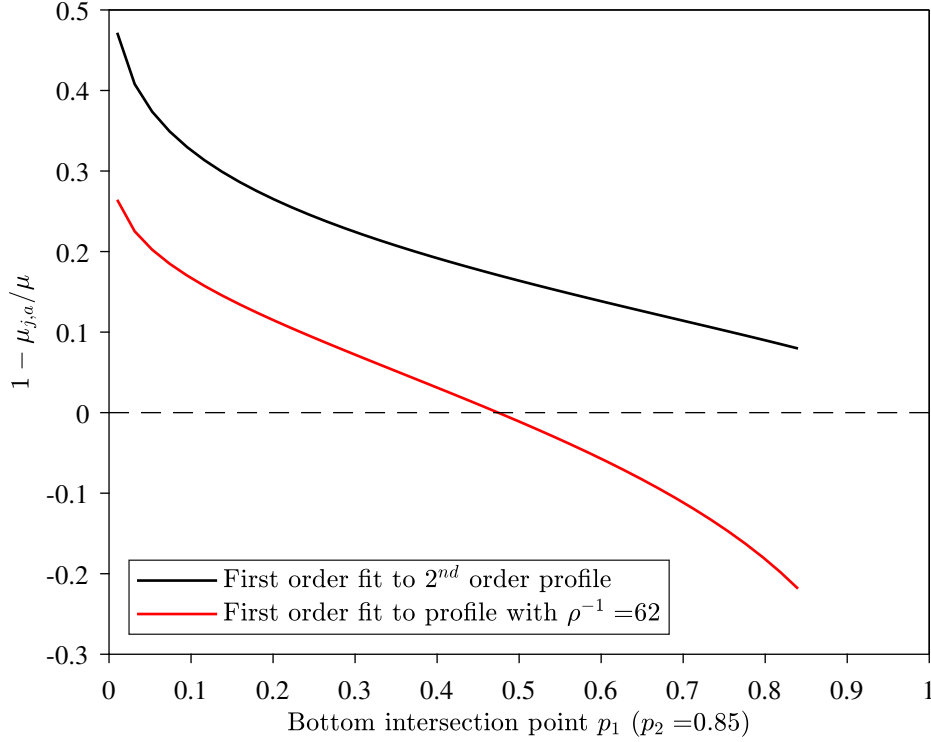
Figure 3.10: Theoretical dependency on $(1 - \mu_{j,a}/\mu)$ on different values of intersection (p_1) (corresponding to weighting), when letting first order model intersect profiles of 2nd orders (black) and profiles described by the fading model with $\rho^{-1} = 200$ (red) at luminescence levels p_1 and $p_2 = 0.85$. This relations is the the slope of the green lines in Figure 3.7e) and f) and for similar lines using different values of p_1 with $p_2 = 0.85$.

Assuming a inappropriate model results in over- or underestimation in estimated unknown exposure times, and it is therefore necessary to fit with the new models presented in this paper and to do it with the correct order/density.

However first we investigate how the parameter values derived from fitting depend on weighting with simulated data as well as this analytical approx. We simulate 2nd order profiles in the same way as mentioned previously, bu increasing the resolution in depth from 1 to 0.1 mm. and fit these with first order model and G.O.M. with $g = 3$. We also simulate a data set using the F.M. with $\rho^{-1} = 36$ and fit these data sets with first order model and with F.M. with $\rho^{-1} = 106$. We included data points within an interval $[k_1; k_2]$, fixing k_2 0.85 of saturation level, and letting k_1 vary from 0.05 to k_2. We see the same relations as in Figure 3.10 implying that, if only data giving high luminescence levels are included, a inappropriate assumed order in fitting does not affect the estimated apparent time if the profile model is best described by the general order model.If the profiles is best described by the fading model, there is one specific cut off value k_1 that would results in no change in calibration values over time when assuming first order model in fitting. but as this level depends on the actual density it is not possible to know the level in advance.
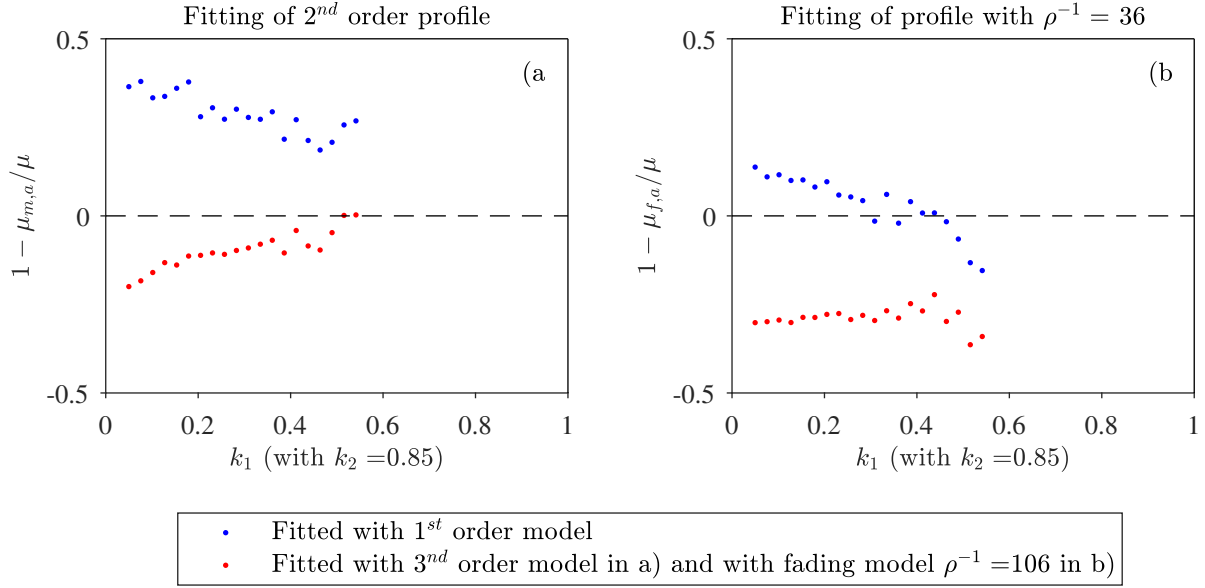
Figure 3.11: Dependency of $(1 - \mu_{j,a}/\mu)$ on lower cut off level, k_1 (with $k_2 = 0.85$) when simulated data of 2nd order profiles (a) are fitted fitted with 1st order model and 3rd order model (blue and red, respectively in a), and when simulated data generated using fading model with $\rho^{-1} = 36$ are fitted with 1st order model and fading model ($\rho^{-1} = 106$ (blue and red, respectively in b)).

Often the resolution of data sets are not good enough to including only part of the data in the fitting, and it is therefore often crucial to know the right model to be used in fitting.

To sum up, assuming first order in fitting a luminescence profiles of higher kinetic order give inaccurate apparent values for μ and $\overline{\sigma\varphi_0}t$.
As the apparent values of $\overline{\sigma\varphi_0}$ depends on exposure time, using a calibration profile and first order fitting will either over- or underestimate the unknown exposure time using large or small calibration profiles, respectively even though the same mistake in chosen model is done on both profiles. If the luminescence is best described by the fading model and fitted with the first order model the same mistake is seen for high densities. For low density profiles the over- and underestimation is opposite.

3.7.2 Experimental data

In this section, we use experimental data to explore if the conclusions reached using simulated data (see section 3.7.1) also applies experimentally. The experimental data was obtained from seven granite rock cylinders all cut from the same rock. These 7 cylinders (ø=80 mm, height=100 mm) were first given a 20 kGy gamma dose with a Co-60 gamma source to ensure saturation of all relevant traps. These irradiated cylinders were then exposed to light from a halogen lamp (here we need the make of the simulator or similar description) for times ranging between 0.1 and 320 days. The cylinders were subsequently cored (ø= 40 mm) to a depth of ∼40 mm and using a water cooled diamond wire saw. The thickness of each slice was ∼ 1.2 mm and ∼ 16 individual slices were obtained from each cylinder. The dried samples easily fall into grains and were subsequently sieved to 90-180 μm. These raw grains were mounted on stainless steel cups and directly measured without chemical treatment. Infrared stimulated luminescence (IRSL) signals

was then measured for individual aliquots (∅=8 mm). A minimum of six aliquots were measured at 50°(IR_{50}) for each slice and subsequently two post IR measurements at 225°and 290°($pIRIR_{225}$ and $pIRIR_{290}$, respectively). The aliquots were sensitivity corrected using a test dose of 150 Gy and preheated to 320°(60 s) prior to IRSL measurement. Here we only present the results from the IR_{50} measurements.

Figure 3.12g shows an average normalised natural IR_{50} stimulation curve from 42 aliquots (grey points). These data were fitted with the 1st order model (blue curve) using Eq.(3.24). As expected the observed decay is not described well by 1st order kinetics. The data were also fitted using the general-order model (Eq. (3.25), green curve) and the fading model (Eq. (3.27), red curve) giving estimates of $g_{stim} = 1.81 \pm 0.03$ and $\rho_{stim} = 0.0121 \pm 0.0003$ ($\rho_{stim}^{-1} = 83 \pm 3$), respectively.

The luminescence-depth profiles were fitted individually using 1st order, general-order and the fading model, respectively (see Figure 3.12b, 3.12c and 3.12d). Visually, all models appear to describe the individual profiles well, although the uncertainties (95% confidence) on the 1st order fits are larger. This is investigated further below. The general-order model was fitted to all seven profiles simultaneously to derive a single shared estimate of the order $g_{share} = 2.54 \pm 0.14$. A similar fitting approach was used for the fading model to obtain a single estimate of $\rho_{share} = 0.0141 \pm 0.0012$ ($\rho_{share}^{-1} = 71 \pm 6$), i.e. when fitting the order/density is shared amongst the seven profiles.i.e. we let order/density be a free fitting parameter, but that have the same value for the shared profiles. The estimates of g derived from the average stimulation curve and from the profiles are significantly different from each other. The estimates of ρ derived from the average stimulation curve and from the profiles are not significantly different from each other and so it would appear that estimates of these parameters derived from stimulation curves are not directly applicable to profiles. This is also explored below.
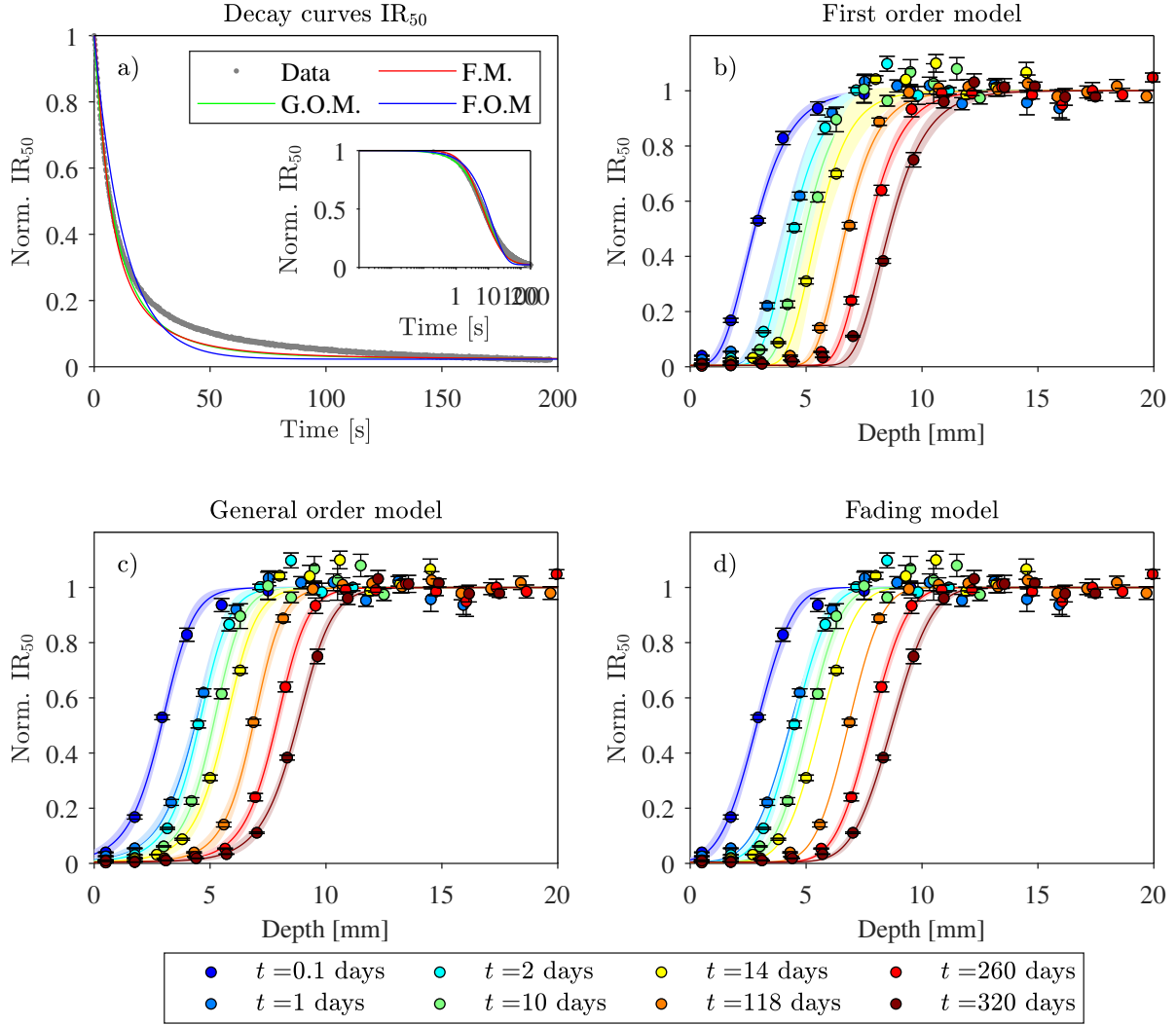
Figure 3.12: a) Average IR$_{50}$ stimulation curve from 42 aliquots (grey circles) fitted using the 1st order model (blue curve), the general-order model (green curve) and the fading model (red curve). b), c), d): IR$_{50}$-depth profiles obtained from seven different granite cores exposed in a halogen lamp using exposure times ranging from 0.1 days to 320 days (blue to red colours) fitted with b) the 1st order model, c) the general-order model and d) the fading model. In c) and d) the order g_{share} and the density ρ_{share} was treated as shared free parameters for all 7 profiles. 95% confidence intervals are shown for each fit as pale areas. Error bars on data points are given at one standard error.

Using each of the fitted profiles as a calibration profile for the other profiles enables the calculation of the apparent exposure time t_a. Figure 3.13 shows the ratio of t_a to the known exposure time t as a function of the ratio of t_{cal} and t for all three models. Note, that we show the logarithm of these ratios and use the dimensionless time exposure estimates (see Table 3.1) for convenience. The data points have been fitted using linear functions (solid lines). Using the 1st order model (blue), we observe a positive slope of 0.355 ± 0.006 indicating that the data do not follow 1st order kinetics (see section 3.7.1.1). Using the general-order model (green) with the order $g_{share} = 2.54 \pm 0.14$ gives a negative slope of -0.073 ± 0.010 (inconsistent with zero) and an intercept on the y-axis of $2 \cdot 10^{-17} \pm 0.04$, indicating that young calibration profiles overestimate unknown older exposure

profiles. Also shown in Figure3.13a are the linear fits obtained using the value of g_{stim} obtained from the stimulation curves (dashed green line). The slope is 0.149 ± 0.009 (and the intercept $-5 \cdot 10^{-17} \pm 0.04$), i.e. the slope is significantly different from zero and positive indicating that if $\sigma\varphi_{\text{cal}}$ is used from a calibration profile with t_{cal} younger than the "unknown" profile, the exposure time will be underestimated (and vice versa).

Also shown in Figure3.13a are the results obtained using the fading model (red). Here the slope is positive (0.245 ± 0.007) indicating that the value of ρ derived for fitting all seven profiles with the same shared (but free) ρ_{share} is, on average, too high (see section 3.7.1.2). If we use ρ_{stim}, then the slope is positive as well (0.204 ± 0.008).
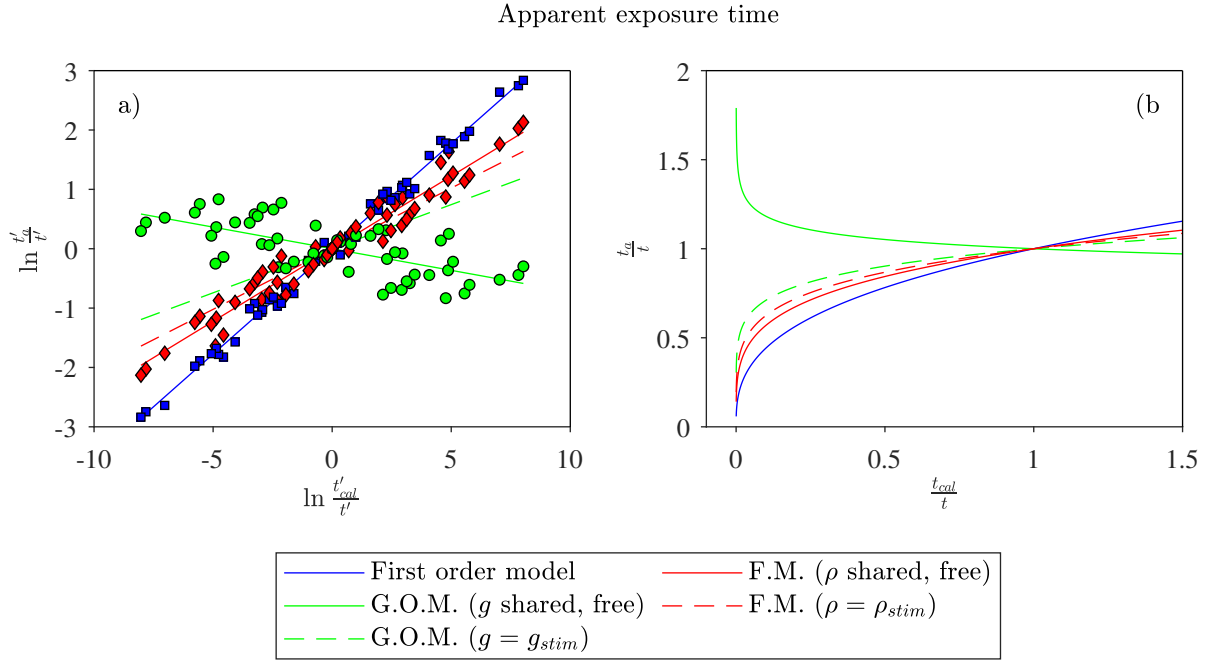
Figure 3.13: a)Logarithm of the apparent exposure time to actual exposure time ($\ln \frac{t'_a}{t'}$) as a function of the logarithm of calibration exposure time to actual exposure time ($\ln \frac{t'_{cal}}{t'}$) for first order fitting (blue), general order fitting with shared free order (green), and fading model fitting with shared free density (red). Solid lines are linear fits to the data. The dashed lines are the linear fits to data obtained using g_{stim} and ρ_{stim} (data points not shown). b) shows the same curves as in a) but in linear scale.

Figure 3.14a shows how the slope ($\left(\frac{d\ln(t'_a/t')}{d\ln(t'_{\text{cal}})}\right)$) vary as a function of the order g used in the fitting. Here the diamond symbol indicates fitting using 1$^{\text{st}}$ order model, the circle and star fitting using the general-order model with g_{stim} and g_{share}, respectively. A slope of zero is obtained when $g = 2.35$, which is indistinguishable from g_{share}. Notice that the estimated $\mu_{m,a}$ i) all reflects the same change with assumed order g (the x-axis) as the slope of the lines in Figure e3.13 and ii) is underestimated by $40.0\pm0.7\%$ (n=8 profiles) (i.e. $\mu_a/\mu = 0.60$) when first order model is assumed in fitting, when the correct value is considered to be one estimated by letting the order be shared.

The tendency is the same for the fading model (b), however μ-points (squares) does not intersect the zero line at same density as the slope points (crosses) act same numbers as the slope. This

implies that sharing the density or using the density from stimulation curves may over or under-estimate the μ and thus the exposure time.

A $\mu_a/\mu = 0.60$ estimated when fitting a IR_{50} with $g_{stim} = 1.81$ or if it is better described by the fading model a $\rho'^{-1} = 83$, assuming first order kinetics does give the expected underestimation of μ from analytical analysis and the simulated data set (see Figure 3.9)a).

In Figure 3.14c, we evaluate if the goodness of the fits can be used to determine the most appropriate kinetic order. Here we show how the average fitting regression standard error (reduced chi-squared) vary as a function of g. Reduced chi-squared is defined as $\chi^2_\nu = \chi^2/\nu$, with $\nu = o - p$ (number of observations minus number of parameters) and $\chi^2_\nu = \sum \frac{n_{\text{data}} - n_{\text{fit}}}{\sigma^2}$ (n_{data} is measured luminescence at x and n_{fit} is fitted value x and). The minimum value of χ^2_ν occurs for $g = 2.5$, which is indistinguishable from g_{share}.

Similar plots are shown for the fading model in Figures 3.14b and 3.14d. The value of ρ^{-1} for which the slope is zero occurs between the values of ρ_{stim} and ρ_{share}. However, when evaluating the goodness of the different fits (Figure 3.14d) then we observe no minimum but rather a broad range of ρ values giving the same χ^2_ν.
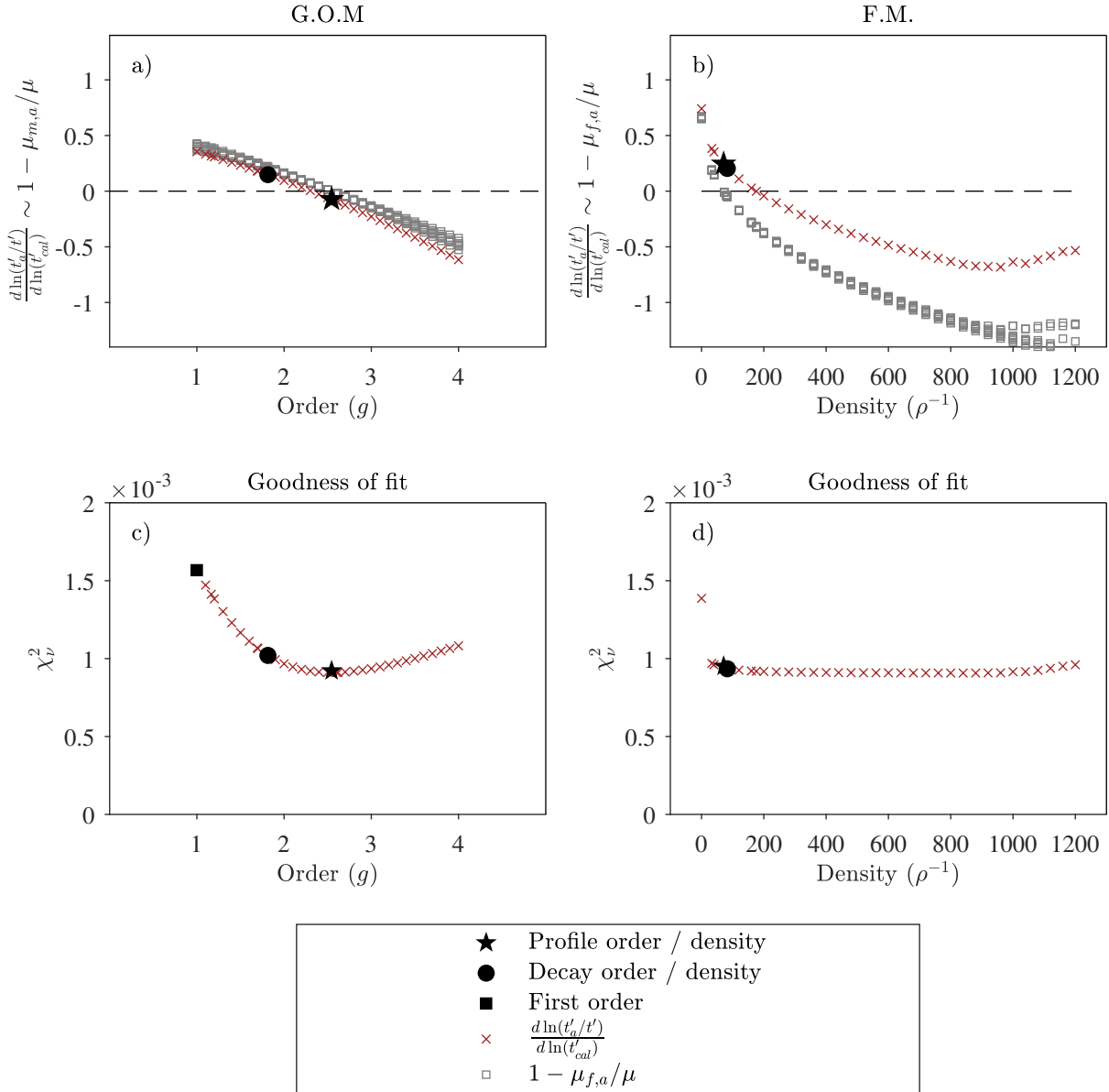
Figure 3.14: Change in the apparent (t_a) to actual time (t) with respect to calibration time (t_{cal}), i.e. $\frac{d\ln(t'_a/t')}{d\ln(t'_{\text{cal}})}$ also shown is $1 - \mu_{j,a}/\mu$ (open grey squares) shown as a function of a) kinetic order (general-order model) and b) inverse density (fading model). The goodness of the fits to the profiles are evaluated using χ^2_ν as a function of a) kinetic order (general-order model) and b) inverse density (fading model). Diamonds indicate 1$^{\text{st}}$ order fitting, circles indicate the order or density derived from stimulation curves (i.e. g_{stim} or ρ_{stim}) and stars indicate the order or density derived from simultaneous and shared fitting (i.e. g_{share} or ρ_{share}).

Accuracy of the apparent exposure time

As stated previously, the accuracy of the apparent exposure time t_a depends on the exposure age of the known age profile (i.e. t_{cal}, the "unknown" exposure time t as well as the model and model specific parameters chosen to fit the profiles, see Figure 3.13). If for instance the unknown exposure age is 3 ka and the calibration exposure age is one year (i.e. $t_{\text{cal}}/t = 1/3000$) then using the 1$^{\text{st}}$ order model, the apparent exposure age, t_a, is 175 years, i.e. the true exposure age is

underestimated by $\sim$94%. If the general-order model with the kinetic order estimated from the stimulation curves (g_{stim}) is used then the underestimate is $\sim$70%, but using the shared order (g_{share}) gives an overestimate of $\sim$80%. The corresponding numbers for the fading model are $\sim$-80% and $\sim$86% (see Figure 3.13b).

Cutting off lower data points results in fitting only taken the higher points into account. In theory one would expect the effect of a wrong assumed order or density to vanish as only the very top data points are included. In this data set we do see this tendency (see Figure 3.15), but as the resolution of the data points are 1 mm this method is not very good. But if the resolution was better as it is in IRPL measurements one could use this method to avoid errors in exposure time estimation.
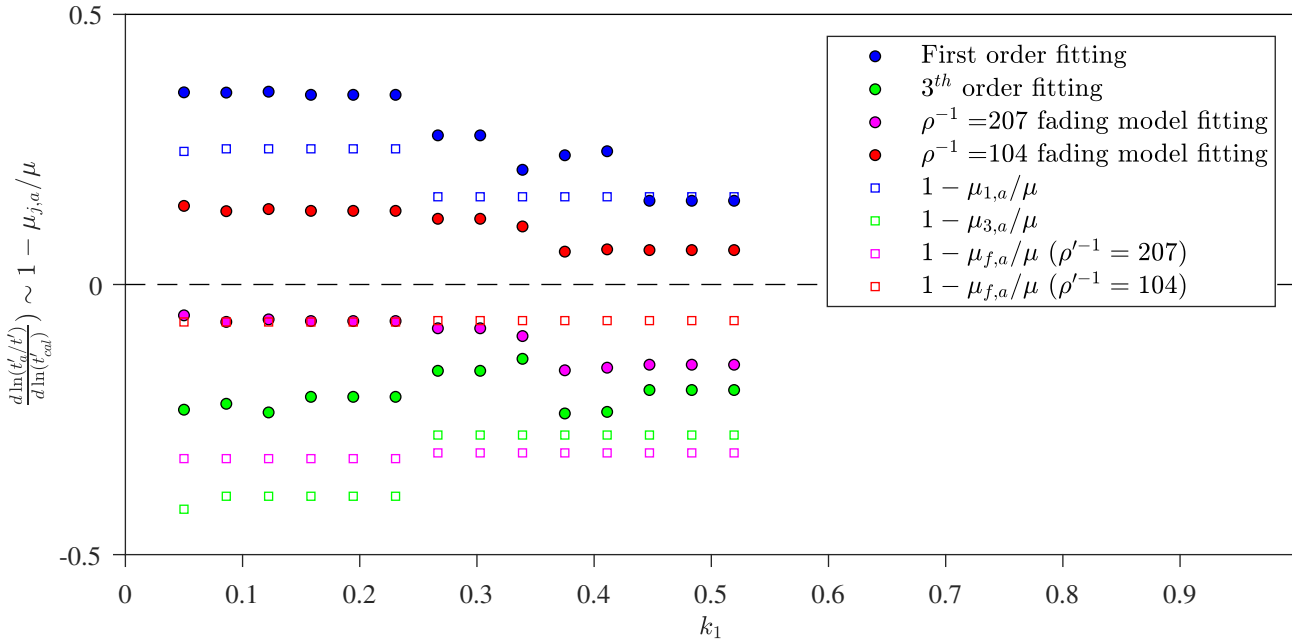
Figure 3.15: Change in apparent time to actual time with calibration time shown as filled circles and $(1 - \mu_{j,a}/\mu)$ as open squares plotted as lower cut off level, k_1 when IR$_{50}$ data are fitted fitted with 1$^{\text{st}}$ order model (blue) and 3$^{\text{rd}}$ order model (green), and using fading model with $\rho^{-1} = 104$ (red) and $\rho^{-1} = 207$ (pink).

3.8 Discussion and conclusion for kinetic models

The progression speed of luminescence profiles depends on the attenuation coefficient μ (and time). When assuming a wrong model an apparent μ will be obtained in fitting because both the attenuation and the kinetics determines the shape of the luminescence depth profile. Thus a different μ will give incorrect estimates of exposure times, as the speed will be incorrect. It is therefore crucial to use the correct model to be able to use a known age profile for calibrating an unknown profile. If possible at least two calibration profiles will give one the possibility to evaluate whether the model chosen is correct and thereby whether the exposure times are reliable.

The order and densities estimated from decay curves are not significantly different from the values estimated from profile fitting letting the order or density being free and shared between all profiles.

Whether these fit then give reliable exposure estimates depend on the model used. Using the fading model in fitting, a good fit is achieved within a large range of densities, but as we need the correct values of density to avoid errors in the estimated exposure time, using the fading model is not as robust as using the general order model. The general order model also need the correct order to give accurate exposure times, but the model is more robust and a good fit is only achieved when the correct order is used.

As the deviation from other kinetic order, happens in the lower luminescence levels, cutting off lower data points could in principle avoid this problem about model dependency, but the resolution of the data set must by very high to do so. In IRPL data sets this could be investigated further.

Chapter 4

Controlled rock surface exposure and burial experiment

4.1 Introduction

This Chapter investigates the development of luminescence profiles with time in preconditioned granite and sandstone samples. These profiles were developed by exposing the rock samples to natural daylight and artificial broad-band and narrow-band illumination for various prolonged periods. The profiles are then used to test the models developed in Chapter 3.

It was concluded in Section 3 that it is not always appropriate to use a first order model when fitting luminescence depth profiles. In particular, the general order model (G.O.M., Eq. 4.4) seems to perform better at returning reliable exposure times when using IR signals. This was deduced from simulated data and from an IR_{50} experimental data set after exposure of a sample to a broad-band artificial light source (halogen lamp). Here, the issues of model dependency are considered further investigated. We first investigate model performance using post IR signals from the same aliquots, and the blue signal measured from quartz grains extracted from the same depths, and compare these analyses with those from similar experiments using daylight exposure. Samples are also exposed to three different wavelengths of monochromatic light to investigate the wavelength dependency of the luminescence depth profiles.

The multiple event model Freiesleben et al.[3] has never been tested in a controlled experiment. Here the results from two controlled burial experiments are also analysed. In the first, aliquots from a light-exposed granite sample were irradiated, to simulate various burial events of different duration (i.e. different doses were added). We test whether the multiple event model can be used to predict the known pre-burial profile. In the second experiment, three light-exposed granite samples were measured after giving a ^{60}Co gamma dose 200 and 500 Gy. Finally, the model dependency of burial dating is also investigated.

4.2 Luminescence exposure models

In this section we study the migration of the luminescence profile for different exposure times. As feldspar IRSL is known to be non-first order, the usefulness of the general-order model (G.O.M.) for luminescence depth profiles (n_m) is investigated, and compared with the well-known first order model (n_1). The general order model assumes that during light exposure the rate of change of the number density of the trapped charge population is proportional to the number density of filled traps raised to the power of $g^{(110)}$ and the detrapping rate constant, $E(x) = \overline{\sigma\varphi_0}e^{-\mu x}$, i.e. for first order

$$\frac{\partial n_1}{\partial t} = -E(x)n_1 \tag{4.1}$$

and for general order

$$\frac{\partial n_m}{\partial t} = -\frac{1}{N^{g-1}}E(x)n_m^g \tag{4.2}$$

where g is the kinetic order and N is the constant total number of traps. Note that when $g = 1$ the general-order model n_m (Eq.4.2) reduces to the first-order model (Eq.4.1). The solutions for these differential equations describe the luminescence with depth and time. We normalise all profiles to the saturation level $N = 1$.

$$n_1(x,t) = n_{1,0}e^{-\overline{\sigma\varphi_0}te^{-\mu x}} \tag{4.3}$$

$$n_m(x,t) = [(g-1)\overline{\sigma\varphi_0}te^{-\mu x} + n_{m,0}^{1-g}]^{\frac{1}{1-g}}, \qquad (g > 1) \tag{4.4}$$

where t is exposure time (ka), and $\overline{\sigma\varphi_0}$ (ka^{-1}) is the detrapping rate constant at the surface of the rock averaged over all wavelengths in the light spectrum reaching the sample. σ is the photoionisation cross-section (cm^2), φ is the incoming photon flux (cm^{-2} ka^{-1}). μ (mm^{-1}) is the inverse of the mean free path of photons in the rock. We set the initial electron population, and thus luminescence to be saturated for all depth, so that $n_0 = N = 1$. For $g = 1$, we use Eq.(4.3), and the first order model has two fitting parameters, μ and $\overline{\sigma\varphi_0}t$. The general order model (Eq.4.4) has an additional parameter, the order g.

The slope at any given value of $n_j(x)$, i.e. the luminescence depth profile, is determined by taking the derivative with respect to x, i.e. $\frac{\partial n_i}{\partial x}$ of Eq. (4.3) and Eq.(4.4):

$$\frac{\partial n_1}{\partial x} = -\mu n_1 \ln n_1 \tag{4.5}$$

$$\frac{\partial n_m}{\partial x} = \mu\frac{n_m - n_m^g}{g - 1} \tag{4.6}$$

Thus the slope depends only on μ and the kinetic order g, and the shape of the profile remains constant as time increases (see also Chapter 3). In these models trap filling due to irradiation is assumed to be negligible compared to detrapping.

4.2.1 Parameter estimation by other methods than luminescence

In rock surface exposure and burial dating models, the detrapping rate constant $\overline{\sigma\varphi_0}t$ at the surface is assumed to be constant with time, and is thus an integral of the product of flux φ [cm^{-2}ka^{-1}]
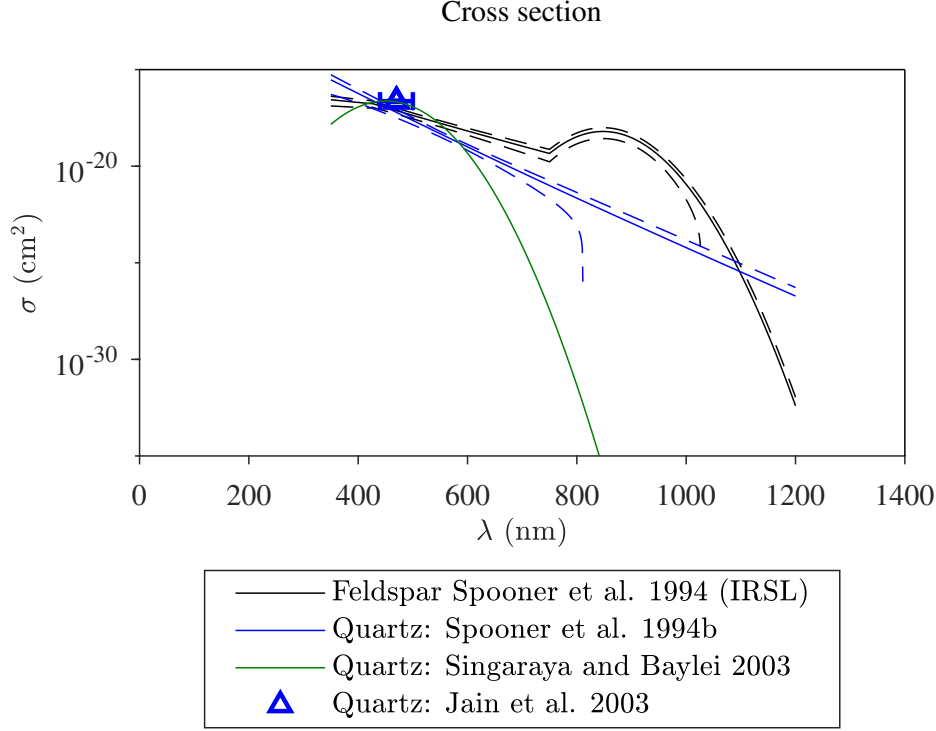
Cross section

Figure 4.1: Photoionisation cross-sections $\sigma(\lambda)$ for feldspar and quartz as a function of wavelength. The data for feldspar (black lines) have been derived from Spooner,1994 [58] for the depletion of the IRSL signal measured at room temperature for microline by 10, 50 and 90%, respectively. Also shown are similar data from quartz (blue lines) obtained from Spooner,1994b [111] for the depletion of the OSL signal to 5, 50 and 95%, respectively. For quartz, we also show the data of Singarayer and Bailey,2003 [112] (green curve) and the single point (blue triangle) at 470 nm from Jain et al.,2003 [113].

and photoionisation cross section σ [cm^2], over the daylight spectrum. This physical parameter is measurable by other methods, which enables comparison with the estimates derived from profile fitting. However the daylight spectrum and daylight time/intensity vary through the year, thus we first estimate expected values for cross section and flux.

4.2.1.1 Photoionisation cross section

We estimate $\sigma(\lambda)$ for feldspar and from quartz from the data published by Spooner [58] and Spooner [111], respectively, where the bleaching energy required at various wavelength to reduce luminescence signal to a fraction $(\frac{I}{I_0})$ of initial level is given. Given that the bleaching energy is given as flux and time (φt) (J.m^{-2}) the wavelength dependency on the photoionisation cross-section $\sigma(\lambda)$ (m^2) is

$$I = I_0 e^{-\sigma(\lambda)\varphi(\lambda)t} \Rightarrow \sigma(\lambda) = \frac{\ln\left(\frac{I_0}{I}\right)}{\varphi(\lambda)t}\frac{\lambda}{hc} \tag{4.7}$$

with Planck's constant: $h = 6.63 \cdot 10^{-34}$J.s, speed of light: $c = 3 \cdot 10^8$m.s^{-1}. The photoionisation cross-section for feldspar and quartz is shown in Figure 4.1, together with other published values for quartz from Singarayer and Bailey [112] and Jain et al. [113].
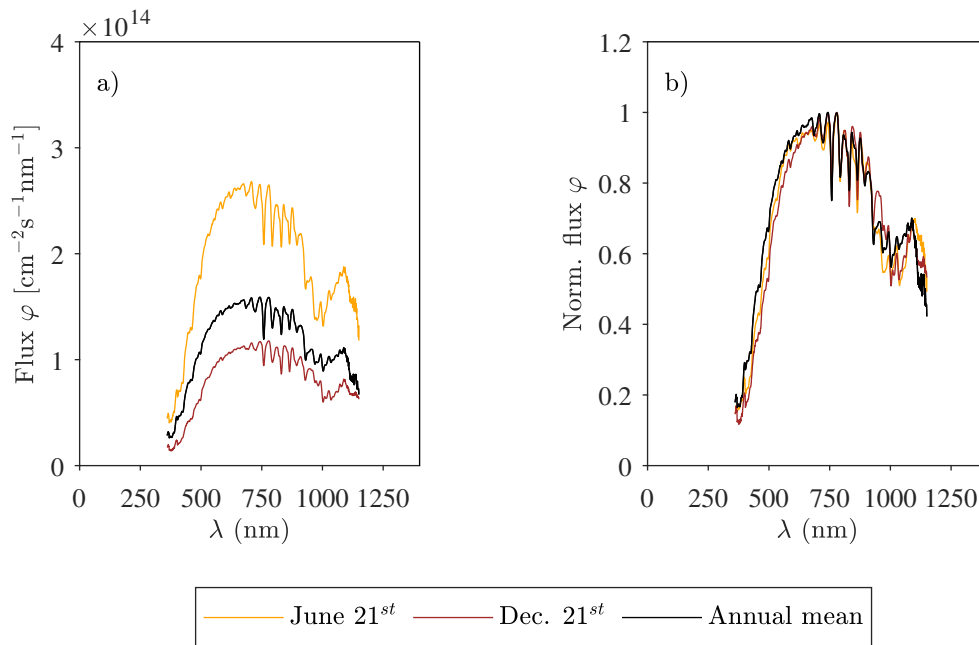
Figure 4.2: Daily mean of solar flux, $\varphi(\lambda)$ [m^{-2}s^{-1}] from two specific days, i.e. 21st of June (orange) and 21st of December (brown) shown in a). All spectra are normalised horizontally to the O_2 absorption peak at 759 nm. In b) the flux spectra are normalised to maximum intensity.

4.2.1.2   Photon flux from daylight

The solar irradiance (J.s^{-1}m^{-2}nm^{-1}) has been measured every 5 minutes from sunrise to sunset at Risø, Denmark throughout 2020[114]. These data were used in this study to calculate the flux $\varphi(\lambda)$ to be used to evaluate fitting parameters in the daylight exposure experiments presented below. From the solar irradiance, the flux of photons [m^{-2}s^{-1}] as a function of wavelength were estimated as a daily mean. To illustrate these data, the flux from June 21st and Dec. 21st are shown in Figure 4.2a) (orange and brown lines, respectively). All spectra are normalised horizontally to the O_2 absorption peak at 759 nm. Also shown is a yearly mean (black line). The result of normalising these spectra with respect to flux is shown in (b), and it is seen that the main effect of seasonal change is in the intensity of the incident light; there is no significantly change in the shape of the spectrum during the year. This means that samples exposed for several years at a given location will most likely experience the same average light exposure for each year (assuming no significantly change from one year to another), however samples exposed for only part of a year may experience different intensities.

The spectrum from the halogen lamp used in some of the exposure experiments was measured using a Power meter (PM16-401, 190 nm-20 μm, with a thermal sensor) and an Ocean Optics QE 6500 CCD spectrometer. The resulting spectrum is shown as the black line in Figure 4.3b (left axis).

4.2.1.3   Effective photon flux

The effective flux that detraps electrons is the detrapping rate constant, derived from the product of the flux φ and the photoioisation cross section σ integrated over the full spectrum. This is

done for every daily average of φ and then multiplied with the time S, from sun rise to sun set that specific day. From this a daily mean for each day in the year is derived. In the experiment with the halogen lamp the time S is 24 hour. In Figure 4.3 the effective photon flux $\sigma(\lambda)\varphi(\lambda)$ is shown with wavelength (right axis) for feldspar (red) and quartz (blue) using the cross section data provided by Spooner[58] and[111], respectively. Also shown are the yearly mean of the flux, and the single spectrum from the halogen lamp (black lines, left axis). Based on the photoionisation cross-sections from Spooner[58] for feldspar, it is mainly the high energy (low λ) and photons with wavelengths from $\sim 750 - 900$nm that are effective at bleaching the feldspar IR_{50} signals (red lines) in both the daylight spectrum and halogen lamp spectrum. For quartz it is manly the high energy photons[111] (blue lines).

The integral of the daily effective photons as a function of wavelength is taken to estimate the total daily mean. Then to estimate the total number of effective photon for each individually exposed sample a sum over the days corresponding to the actual days of exposure t in 2018, 2019, and 2020, assuming no change in the three years, i.e.

$$\overline{\sigma\varphi_0}t = \sum_t \int_{\lambda_i}^{\lambda_f} \sigma(\lambda)\varphi(\lambda)d\lambda \tag{4.8}$$

where λ_i and λ_f are the initial and final wavelength in the integration interval.
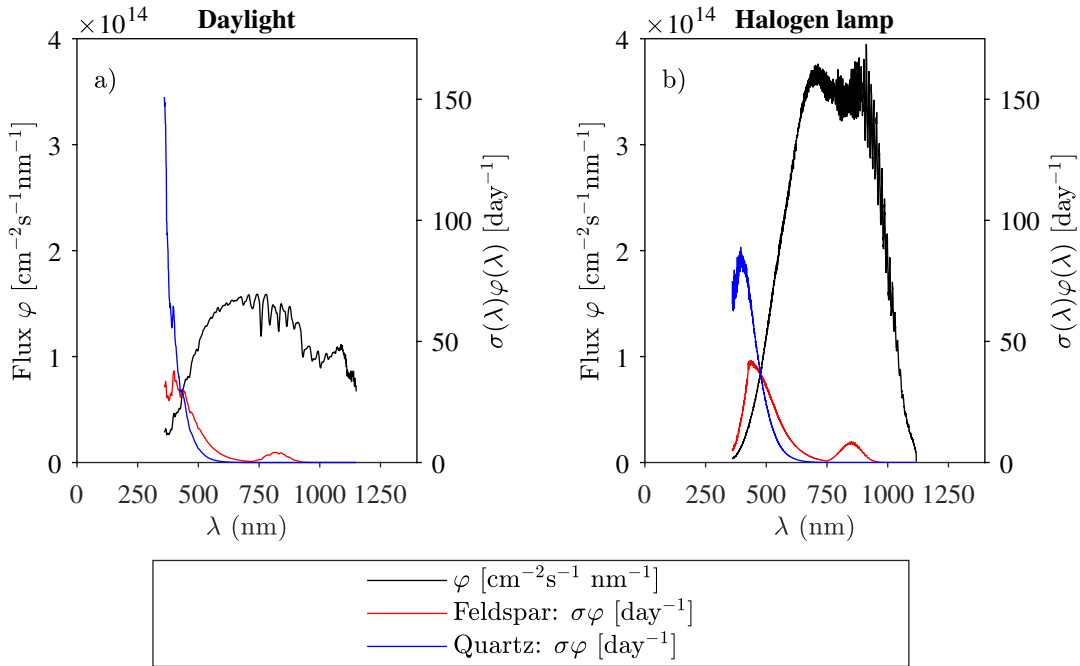
Figure 4.3: Flux $\varphi(\lambda)$ from daylight (black line in a) and from the halogen lamp (black line in b). Also shown are the corresponding effective photon counts, $\sigma(\lambda)\varphi(\lambda)$, [day^{-1}] using cross section derived by Spooner[58] for feldspar (red line) and for quartz Spooner[111] (blue).

4.2.2 Light attenuation

When describing the progression of a luminescence depth profile, the change in light intensity with depth must be incorporated. Lambert-Beers law describes the transmittance with depth, i.e. the

change in intensity with depth ($I/I_0 = e^{-\mu x}$), with the attenuation coefficient μ (mm^{-1}) being the inverse of the mean free path. The parameter μ includes absorption effects (i.e. creation of electron-hole pairs), but the transmittance includes scattering as well. However, in luminescence-depth profile models the effective attenuation is regarded simply as attenuation, regardless of the underlying mechanisms for this attenuation. Measuring the transmittance, i.e. the change in intensity when passing through the material, gives information on the net effect of both attenuation and scatter. In existing luminescence models, μ is assumed to be independent of depth, although estimates of μ from luminescence-depth profiles have been reported to be depth-dependent [65,76]. Others have reported a decrease in slope of the luminescence profiles Ou et al. [74], and using direct attenuation measurements on varying thickness (from ∼0.4 to 2.4 mm) of rock material (sandstone, granite and quartzite), however they have showed that attenuation (absorbance) increases linearly with thickness, thus that μ does not change with depth. The transmittance part of Lambert-Beers law states that with the same concentration (in our case homogeneous material) and the same path length through the material, the transmittance per depth remains constant. However, this may not be true for a variety of reasons, e.g. interactions between particles and scattering effects, and so the transmittance, and hence μ, may change with depth. Furthermore, the refractive index decreases with wavelength [115] for the wavelengths of interest in luminescence, letting fewer high energy photons reach large depths. This could result in an apparent decrease in attenuation with depth for signals most sensitive to shorter wavelengths.

To obtain direct estimates of the light attenuation coefficient in the wavelength range from 300 - 900 nm, we measured the absorbance in a 40 x 25 x 1.74 mm slice of one of the granite samples (see section 4.3.1) using a Shimadzu UV-2700 spectrophotometer. The measured absorbance was divided by the slice thickness, and this estimate of μ is plotted as a function of wavelength in Figure 4.4. As expected, the attenuation coefficient decreases with wavelength implying that long wavelengths penetrate to greater depths than the shorter wavelengths. Similar measurements were done for the sandstone sample (see section 4.3.1), but no light was transmitted through the sample in the investigated wavelength range implying a very high attenuation coefficient for this sample. However, a small transmittance was measured at 1400 nm (data not shown) giving a μ at that particular wavelength of ∼2 mm^{-1}.
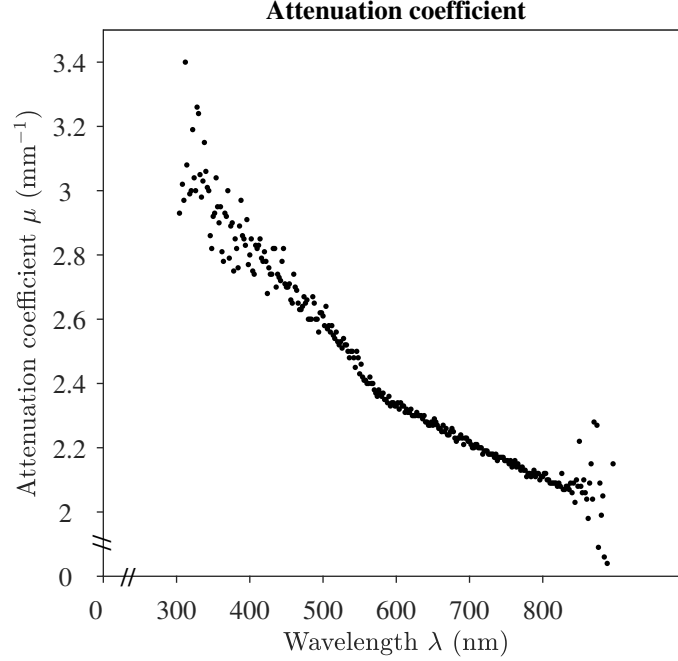
Figure 4.4: Spectrophotometer measurements of the light attenuation coefficient μ for wavelengths ranging from 300 to 900 nm. See text for details.

4.2.3 Well bleached depth in rock surface burial profiles

Information about the duration of a burial period following a period of light exposure is recorded in the luminescence depth profile. A mathematical model describing a burial luminescence profile $n_{m,2}$ $(L \propto n)^{(3)}$ is given in Equation 4.9 with D'_e as the dimensionless burial dose $(D'_e = \frac{D_e}{D_c})$. In this study the pre-burial profile $n_{m,1}(x,t)$ can either be first order $(m = 1)$ or general order for a single exposure event with t being the exposure time of the previous exposure period (see Chapter 3). Here we assume that the trap filling process is first order. Normalised to the saturation level we have

$$n_{m,2}(x) = (n_{m,1}(x,t) - 1) \, e^{-D'_e} + 1 \qquad (4.9)$$

However when rock surfaces are used to date an unknown burial event the unknown dose in Eq. 4.9 is given from the unknown burial time t_b, the dose rate $\dot{D}(x)$ and sample dependent parameter D_c as $(D'_e = t_b \dot{D}(x)/D_c)$ (see Section 1.2.3 for details).

In order for the estimated burial dose to be accurate, it requires that only the depths for which the luminescence signal was adequately reset prior to burial are included in the evaluation. The depth to which the signal was sufficiently reset is defined as the well-bleached depth, x_{WB}. At this depth the residual luminescence signal before burial is less than some arbitrarily chosen fraction (e.g. 5%) of the luminescence signal after burial at the same depth[116], i.e. $n_{m,1}(x_{\mathrm{WB}}, t) \leq 0.05 \cdot n_{m,2}(x_{\mathrm{WB}}, t)$. (Using the luminescence signal for the criterion is more restrictive than a residual dose criterion because the growth curve is sub-linear.)

Let B_{lum} define this luminescence criterion, then the well-bleached depth will depend on the ex-

posure model and the burial dose:

$$B_{\text{lum}} \geq \frac{n_{m,1}(x_{\text{WB}})}{n_{m,2}(x_{\text{WB}})} = \frac{n_{m,1}(x_{\text{WB}})}{(n_{m,1}(x_{\text{WB}}) - 1)e^{-D'_e} + 1} \tag{4.10}$$

As the reconstructed pre-burial profile depends on the exposure model, the well-bleached depth also depends on the exposure model. The first order model $n_{1,1}(x)$ and the G.O.M. $n_{m,1}(x)$ for the pre-burial profile are

$$n_{1,1}(x) = e^{-t_e e^{-\mu x}} \tag{4.11}$$

$$n_{m,1}(x) = ((g-1)\overline{\sigma \varphi_0} t_e e^{-\mu x} + 1)^{1/(1-g)} \tag{4.12}$$

To compare the well-bleached depth from the two models, x_{WB} needs to be solved in these model equations and expressed in terms of B_{lum}. Using dimensionless variables $x' = \mu x$, $t' = \overline{\sigma \varphi_0} t$ for depth and exposure time we avoid dealing with values of μ and $\overline{\sigma \varphi_0}$. Solving for x gives

$$x'_{\text{WB},1} = \ln t' - \ln\left(-\ln(n_{1,1}(x_{\text{WB}}))\right) \tag{4.13}$$

$$x'_{\text{WB},m} = \ln t' + \ln \frac{(g-1)}{(n_{m,1}(x_{\text{WB}})^{1-g} - 1)} \tag{4.14}$$

The term $n_{m,1}(x_{\text{WB}})$, the luminescence level in the reconstructed pre-burial profile at the well-bleached depth, is given by solving for $n_{1,m}(x_{\text{WB}})$ in Equation 4.10

$$n_{m,1}(x_{\text{WB}}) = \frac{B_{\text{lum}}(1 - e^{-D'_e})}{1 - B_{\text{lum}} e^{-D'_e}} \tag{4.15}$$

Including this in Equation 4.13 and 4.14 gives functions of the well-bleached depth dependence on model and model order (g), and on (D_e/D_c), μ, and $\overline{\sigma \varphi_0} t$. Using an inappropriate model, e.g. a first order model to fit feldspar profiles, will predict the well-bleached depth to be either too deep within the rock or too close to the surface. The latter is not a major concern as it will mainly influence the precision of the result, but if the well-bleached burial depth is predicted to be larger than it was, it may result in an overestimate of the burial dose. The question is how important is this effect? How wrong will the well-bleached depth be if an inappropriate model is used, and will it affect the burial age estimation? This is investigated by i) simulated data and ii) experimental data with known given doses.

4.3   Experimental details

4.3.1   Samples

Two lithologies were investigated in this study: granite and sandstone. Rock slabs were collected commercially from an unknown location in China, In total, 95 cores, each 10 x 8 cm in size were collected and shipped to Denmark. The selection, drilling and shipping were supervised by Dr Jinfeng Liu of the Institute of Geology, Chinese Academy of Sciences, Beijing.

The granite shows a fine-medium crystalline (<2 mm) saccharoidal texture with 40% quartz and 50% feldspar as groundmass components (Figure 4.5a). The minor constituents (∼10%) are predominantly elongate amphibole hornblende and oxidised biotite. This rock is determined to be

Table 4.1: Concentrations of radioactive isotopes, beta and gamma dry infinite matrix dose rates and total dose rate for quartz (Q) and K-rich feldspar (KF) for the granite samples.

Sample	Radionuclide concentrations Bq/ka					Dose rate Gy/ka			
	^{238}U	^{232}Th	^{40}K	^{226}Ra	^{210}Pb	Beta	Gamma	Total Q	Total KF
Granite	4.7 ± 0.5	6.8 ± 0.2	974 ± 8	5.9 ± 0.2	7 ± 2	2.6 ± 0.4	0.89 ± 0.13	3.6 ± 0.4	4.5 ± 0.4

aplite, formed from relatively rapid crystallisation of the later-stages of granitic fractionation, and throughout this study, samples from this source will be termed as granite (Warren Thompson, personal communication, 2021).

Figure 4.5b shows a μXRF map of Si (quartz), Na, K and Ca distribution (representative of feldspar) in the granite. There is an abundance of K-feldspar, with some Na-rich feldspars. The calcium distribution is thought to be from the presence of mica. X-ray fluorescence (XRF) measurements of the raw granite (unseparated mineral constituents) using the Risø reader XRF attachment show that the bulk feldspar components are indeed alkali in composition (red circle in Figure 4.5c), with both Na- and K-dominated feldspars, and minimal plagioclase. Bulk XRF analysis of the density separated K-feldspar fraction (KF feldspar, pink triangle in Figure 4.5c) shows that the K-feldspar grains contain up to 12.25% potassium and are thus classified as orthoclase.

The dose rate in the granite was determined using high resolution gamma spectrometry[97,98], where concentrations (Bq/kg) of the main radioactive elements (U,Th, K, Ra, Pb) were measured. The beta and gamma dose rate contributions and total dose rate were then derived (see Table 4.1), assuming 0% water content and grain sizes between 90-180 μm. Accounting for the size of the samples as described in section 6.3 using a height and diameter of 10 cm, the beta dose rate at the surface is 50% of the infinite matrix dose rate and gamma is 10%. At a depth of 3 mm, the beta dose rate is 100% of the infinite matrix. The gamma dose rate at the centre (5 cm from the surface) is 11% of that of the infinite matrix. The beta dose rate in particular may contribute to trap filling during bleaching experiments, however given the maximum time of exposure (i.e. 730 days) this would contribute only ~0.006 Gy at the centre, which is significantly lower than that measured from thermal transfer. In other words, trap filling during exposure is not of importance in this study.

The sandstone is fresh (no signs of weathering), fine grained (<250 µm), with a pinkish-red colour considered to be from oxidised Fe^{3+} coating the individual grains, possibly as a cement. The grains are rounded, well sorted, structure-less and well consolidated (see Figure 4.5d, Warren Thompson, personal communication, 2021). Figures 4.5d and 4.5e show a photograph and a µ-XRF map of the sandstone, respectively. As the sample is fine grained, it is hard to distinguish individual mineral compositions from the 2D image of the different elemental distributions. To determine the compositions of the feldspar constituents in the sandstone, XRF measurements were performed using the Risø XRF attachment on the bulk unseparated sandstone grains (raw sandstone) as well as the K-feldspar fraction after density separation. The results from the raw sandstone do not provide a composition for the feldspar (dark blue diamond in Figure 4.5c), likely due to the presence of Ca- and Na-bearing minerals other than feldspar. From the separated K-feldspar fraction we see that the composition is close to orthoclase (blue square in Figure 4.5c).
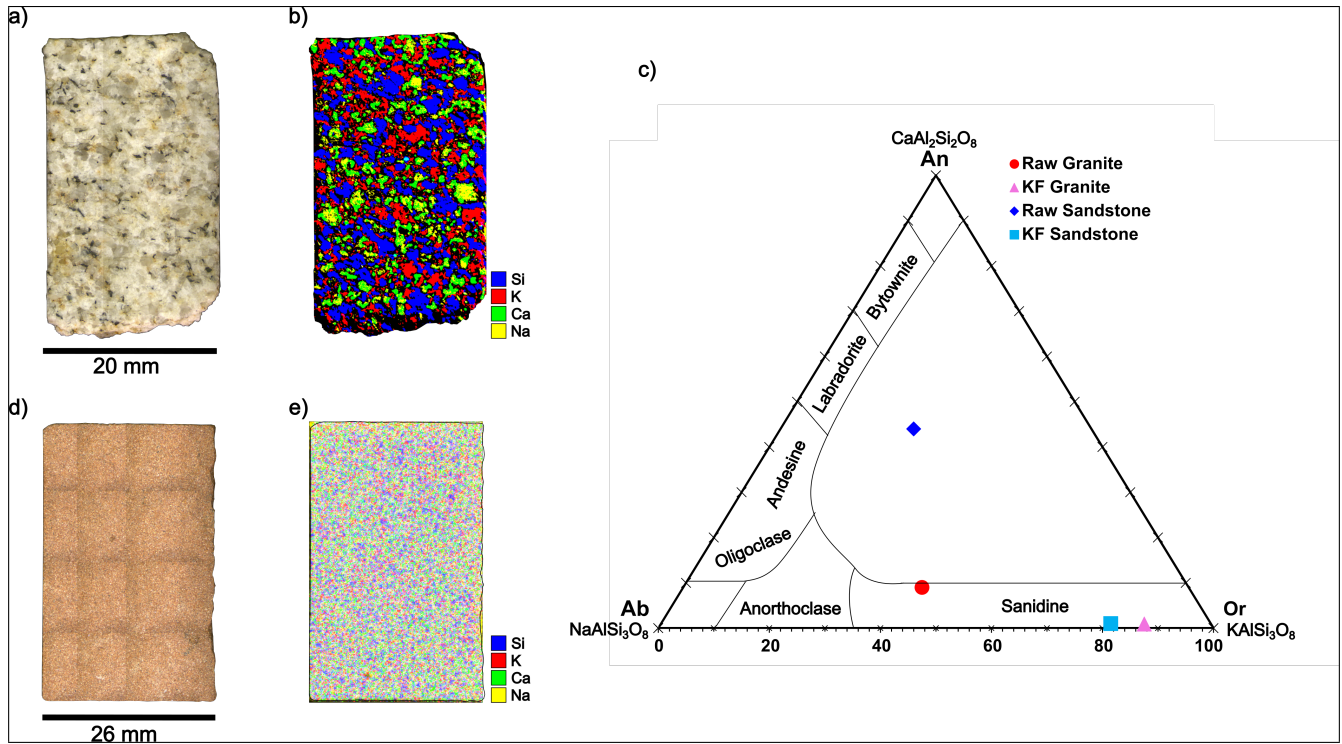
Figure 4.5: a) Photograph of one of the granite samples. b) μXRF elemental map of the granite sample showing Ca, Na, K and Si content of the granite. c) Ternary diagram showing bulk XRF results of feldspar compositions for the granite and sandstone (separated grains and raw grains). d) Photograph of of one of the sandstone samples. e) μXRF elemental map showing Ca, Na, K and Si content of the sandstone

4.3.2 Experimental Setup

The sandstone and granite cores were heated to 700°C for 24 hours to sensitise quartz grains. The samples were then given a ^{60}Co gamma dose of 20 kGy to saturate all luminescence traps. This preconditioning process was decided on after showing that satisfactory dose recovery data could be obtained on loose quartz and feldspar grains from this material using standard blue SAR (quartz extracts) sand pIRIR SAR sequences (K-rich feldspar extracts and untreated samples, see Tables 4.3-4.6). The cylindrical samples were wrapped in black plastic, and light-proof tape used on all sides except the top surface, to make sure light only fell on this one face (see Figure 4.6). 14 granite samples and 14 sandstone samples were placed outside at a location not experiencing shadow at any time during daylight hours. A further eight granite samples were placed on a rotating wheel under 4 halogen lamps inside an otherwise dark room, in a configuration designed to ensure that all samples received the same flux of photons. Finally an additional three granite samples were exposed to monochromatic laser light. The details of these exposures are given below.

Five controlled experiments were undertaken using these preconditioned samples:

1) Monochromatic light exposure
Three granite samples were exposed to monochromatic light sources, one each to infra-red (885 nm), green (532 nm), and violet (405 nm) laser light. The power distribution of the light sources at the sample position were measured using a calibrated Ophir Starlight power meter photodiode. The exposure times were then chosen so that each sample received $1.3 \cdot 10^{22}$ cm^{-2} photons per unit area, independent of the light source.

2) Halogen lamp exposure
Eight granite samples were exposed to broad-band halogen lamps fitted with H7 24V/70W automotive bulbs (102 mW.cm^{-2} at the sample surface), one each for 2.5 hour, 1, 2, 10, 14, 118, 260, and 320 days (see Table 4.2).

3) Daylight exposure
Eight granite and eight sandstone samples were exposed to daylight in Denmark for 1, 2, 21, 31, 68, 118, 566, and 730 days (see Table 4.2). The solar irradiance spectrum was recorded every 5 min during 2020 (see section 4.2.1).

4) Simulated burial using individual aliquots
One granite sample was exposed to artificial broad-band light for 730 days before coring, slicing and chemically processing to recover quartz and feldspar grains. Sieved grains from each depth were then given seven different doses ranging from 35 to 2381 Gy, before measuring the IR$_{50}$, pIRIR$_{225}$, and pIRIR$_{290}$ signals.

5) Simulated burial using a rock sample
One granite sample was exposed to a halogen lamp for 320 days. Subsequently i) one part of the sample was prepared for direct measurement (see section 4.3.3), ii) one part was given a gamma dose of 200 Gy, and iii) a third part was given a gamma dose of 500 Gy. IR$_{50}$, pIRIR$_{225}$, and pIRIR$_{290}$ signals were then measured from all three profiles.
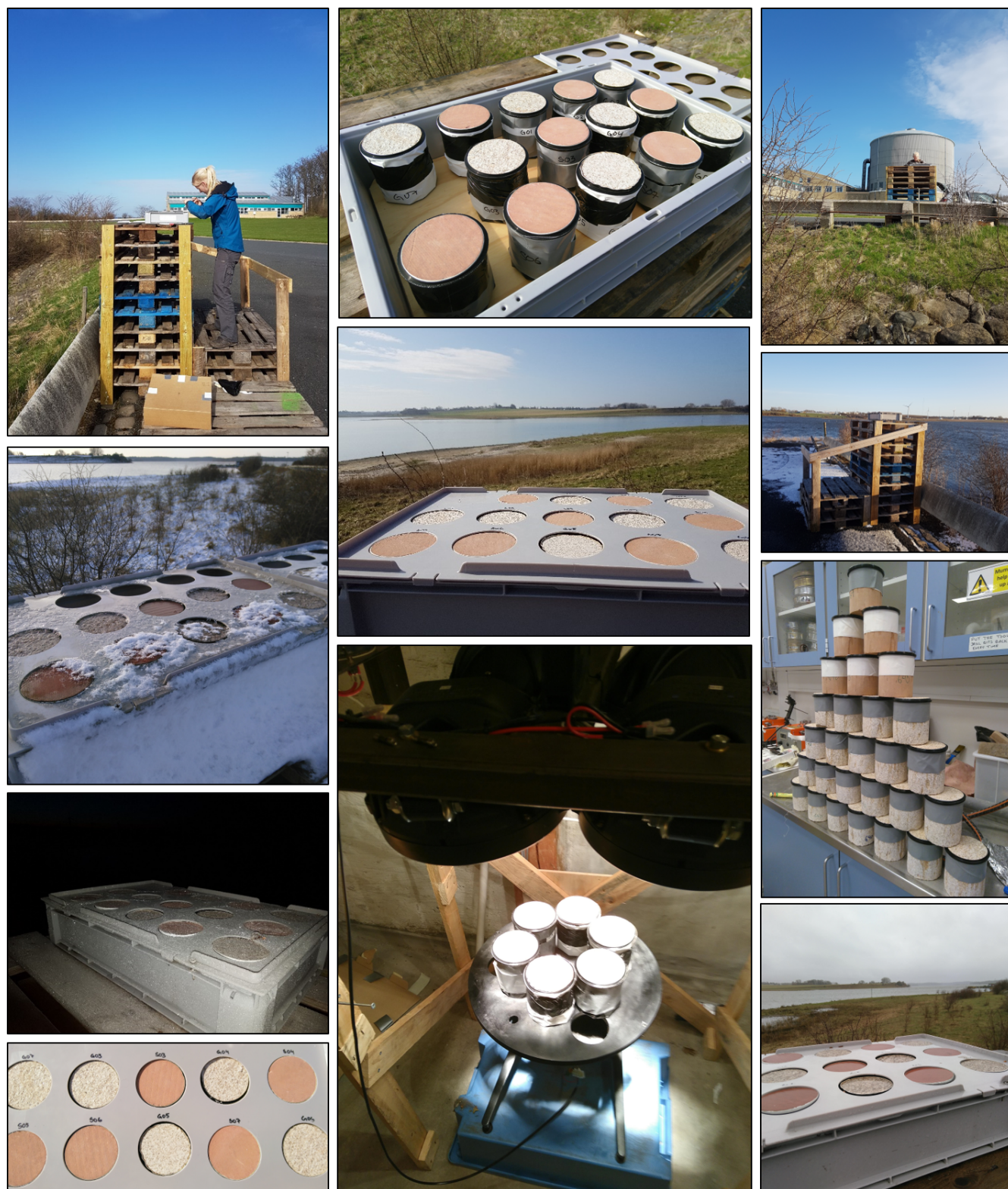
Figure 4.6: Pictures of the experimental setup for daylight bleaching and halogen lamp exposure.

Table 4.2: Overview of the duration of exposure (both halogen and daylight) and periods of daylight exposure. The starting month is give as MM and the year as *YY*, i.e. for Exposure no. 8 the daylight exposure began in April 2018 and ended in April 2020.

Exposure no.	1	2	3	4	5	6	7	8
Halogen t_e (days)	0.1	1	2	10	14	118	260	320
Daylight t_e (days)	1	2	21	31	68	118	566	730
Daylight Period (MM*YY*)	03*20*	03*20*	03*20*	11-12*19*	03-05*20*	03-06*20*	04*18*-11*19*	04*18*-04*20*
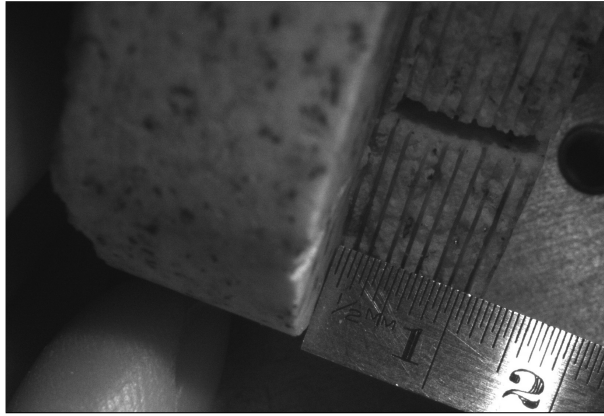
Figure 4.7: Picture showing the remaining core after slicing, with a ruler for scale.

4.3.3 Sample preparation

Under subdued red-orange light the rock samples were drilled with a 4.5 cm diameter diamond-tipped coring drill to a depth of ∼4 cm and sliced in 1.2 mm increments with a water-cooled wire saw, wire thickness 0.35 mm. The slices were cut until almost detached, but remained in place until all cuts had been made. They were then broken off, in such a way as to leave a small part of the core recording the exact location of each slice. Slice depth was then measured on this remaining part.

Because of the prior heating, the slices were fragile and disaggregated easily. Grains were sieved to 90-180 μm and for the majority of samples the IRSL signals were measured without further treatment. The IR$_{50}$, pIRIR$_{225}$, and pIRIR$_{290}$ signals were measured in the same sequence using a preheat of 320 °C (see section 4.3.5). The sieved grains for each depth were also taken through seven standard chemical treatment steps to separate a clean quartz fraction and for one sample a K-rich feldspar (KF fraction). The latter fraction was used to test whether the untreated grains gave the same results as the treated grains. To extract the KF grains in these tests samples 10% HCl solution for one hour was used to remove to remove any acid-soluble component (e.g. carbonate). After rinsing with water three times the samples were placed in 10% HF for 20 minutes to clean the grains, and to remove the outer alpha irradiated layer from the feldspar. Any residual fluoride contamination from the HF treatment was then removed using a 10% HCl solution for 40 min. Quartz and potassium-rich feldspar grains were separated using an aqueous heavy liquid (FastFloat) with a density of 2.58 g.cm^{-3}.

For the samples where only quartz grains was required (since IR stimulations were mainly per-

formed using untreated grains), sieved raw grains were placed in 10% HCl for one hour, rinsed with water three times, and placed directly in 40% HF for 20 min to remove feldspar, and the outer 10 μm affected by alpha radiation. Any residual fluoride contamination from the HF treatment was removed using a 10% HCl solution for 40 min. The luminescence purity of the resulting quartz extracts was examined by testing for IRSL sensitivity. The washed and dried grains were mounted on either stainless steel discs or cups using silicon oil as an adhesive to give an aliquot size of 8 mm diameter for quartz and 2 mm for feldspar.

4.3.4   Instrumentation

Luminescence measurements were made using Risø TL/OSL readers[95] equipped with infrared (IR) LEDs ($\lambda = 870 \pm 30$ nm, $\sim$150 mW.cm^{-2}) and blue LEDs ($\lambda = 470 \pm 20$ nm, $\sim$80 mW.cm^{-2}). Photon detection made use of a UV/Blue sensitive photomultiplier tube (ET PDM9107Q-AP-TTL-03) which has a spectral range of 160–630 nm with maximum detection efficiency between 200 and 400 nm. IR stimulation of untreated grains and K-rich feldspar extracts used photon detection through a Schott BG39/Corning 7-59 filter combination (2 and 4 mm, respectively). Blue LED stimulation was used for quartz extracts with photon detection through 7.5 mm of Hoya U-340 glass filter. Beta irradiation used a calibrated ^{90}Sr/^{90}Y source mounted on the reader[118].

Major element concentrations were determined using a μXRF instrument (Brüker M4 Tornado μXRF) with a spatial resolution of $\sim$20 μm. Initially, the entire surface of the sample was scanned to obtain a qualitative elemental map to identify regions of the main feldspar and quartz elements. These feldspar and quartz components were quantified by measuring a least three randomly placed spots with acquisition times of 45 s using a single Rh target X-ray tube (600 μA, 50 kV) focused to a spot size of $\sim 25 \mu$m by polycapillary lens optics[119].

Bulk K-contents, relative to the sum of K+Na+Ca, was measured using an XRF attachment to the Risø reader[120,121].

Radionuclide concentrations were determined using a low-resolution gamma spectrometry system[122] based on 3"×3" NaI(Tl) crystal. The concentrations were converted to infinite matrix dose rates using the conversion factors of Guérin and Mercier[123].

In the monochromatic light exposure experiment three cylinders (ø10 cm) from the same granite slab were exposed to three monochromatic light sources (one sample, one light source). The IR light source was a 500 mW diode laser centred at 885 nm (Changchun New Industries Optoelectronics Tech co. Ltd) with a power density of 64 mW.cm^{-2} at the sample surface. The green light source (centred at 532 nm) was a 300 mW Nd:YVO$_4$ diode-pumped solid-state laser[118] with a power density of 15.3 mW.cm^{-2} at the sample surface. The violet light source (405 nm) was the 100 mW laser module also used in VSL applications[124] with a power density of 18.2 mW.cm^{-2} at the sample surface.

In the halogen lamp exposure experiment four broad-band (400 to 1100 nm) halogen lamps fitted with H7 24V/70W automotive bulbs (102 mW.cm^{-2} at the sample surface) were used. To achieve a uniform illumination, the samples were placed on a slowly rotating turntable at a distance of approximately 70 cm from the four lamps (see experimental setup in Figure 4.6). The lamp spectrum was measured using a Ocean Optics QE6500 CCD calibrated spectrometer and is shown

in Figure 4.3.

4.3.5   Measurement protocols

Quartz grains were measured using a standard SAR protocol using blue LED stimulation for 40 s at 125 °C with a preheat of 260 °C for 10 s, a cut heat of 220 °C and a test dose of 150 Gy. Quartz signal analysis relied on early background subtraction, i.e. the initial 0.48 was summed for the signal and the subsequent 0.48 s was subtracted as background. Infrared stimulated luminescence (IRSL) signals were measured for both K-rich feldspar extracts and untreated grains using a multiple post-IR[125,126] SAR protocol (i.e. pIRIR(50,225,290)), a preheat of 320°C (60 s) prior to each IRSL measurement of 200 s and sensitivity correction using a test dose of 150 Gy. The first IR stimulation was measured at 50°C (IR_{50}) and subsequently two post IR measurements at 225°C and 290°C (here referred to as $pIRIR_{225}$ and $pIRIR_{290}$), respectively). IR signal analysis relied on late background subtraction, i.e. the initial 2.8 s was summed for the signal and the final 10 s was subtracted as background.

4.4   OSL characteristics

Dose recovery, recuperation, thermal transfer, and IR depletion ratio (only relevant for quartz) are summarised in Table 4.3 and 4.4 for the granite sample. Both raw (untreated) grains and K-rich feldspar (KF) grains were tested using different SAR protocols (see Table 4.3). With the exceptions of the $pIRIR_{180}$ and $pIRIR_{290}$ signal in the multiple post-IR protocol (i.e. pIRIR(50,225,290) for the raw grains, none of the dose recovery ratios are within 10% of unity, but otherwise, we do not observe any major differences in the OSL characteristics for untreated (raw) and treated (separated) KF grains. As a result, further work made use of raw grains; this had the advantage of improving sample size and significantly reducing sample preparation time. A similar conclusion has been reported by Meyer et al.[76], who also reported that measured IRSL luminescence-depth profiles were not affected by the sample preparation method. Table 4.4 summarises dose recovery results as a function of preheat temperature (210-280 °C) for quartz extracted from the granite samples. The quartz dose recovery ratio is acceptable for all preheats, i.e. within ±10% of unity at 68% confidence. Recuperation is less than 4% of the given dose and the IR depletion ratio satisfactory (except for a preheat of 260°C).

Tables 4.5 and 4.6 summarise the same OSL characteristics for the sandstone sample. Again, we do not observe any major differences in the characteristics of KF and raw grains, but for the sandstone an acceptable dose recovery ratio (i.e. within ± 10% of unity at 68% confidence), is only obtained for $pIRIR_{180}$ signal. The higher temperature post-IR signals overestimate the given dose significantly. For the quartz extracted from the sandstone, the dose recovery is only acceptable at a preheat temperature of 240 °C, but the recuperation is below 0.4% and the IR depletion ratio acceptable (i.e. the sample is not contaminated by feldspar grains or inclusions).

In what follows, the raw grains are measured using the pIRIR(50,225,290) protocol for both granite and sandstone, although the dose recovery is poor for the sandstone sample. Quartz grains are measured using a preheat temperature of 240 °C.

Table 4.3: Dose recovery ratio (corrected for thermal transfer), Recuperation (%) and Thermal transfer doses for K-feldspar grains ($90 - 180\mu$m) and for raw (untreated) grains ($90 - 180\mu$m) extracted from the granite sample, measured with four different SAR-protocols. In the dose recovery and thermal transfer experiments, the aliquots were bleached in a solar simulator (Hönle SOL2) for 48 h. A dose of 50 Gy was then given before SAR measurement. All entries are the arithmetic average of at least 3 aliquots.

Material	Preheat (°C)	SAR protocol	Dose Recovery ratio			
			IR_{50}	$pIRIR_{180}$	$pIRIR_{225}$	$pIRIR_{290}$
K-Feldspar	225	pIRIR(50,180)	0.821±0.003	0.879±0.018	-	-
	320	pIRIR(50,290)	0.812±0.021	-	-	0.872±0.010
Raw grains	225	pIRIR(50,180)	0.769±0.010	0.910±0.007	-	-
	250	pIRIR(50,225)	0.787±0.014	-	0.851±0.006	-
	320	pIRIR(50,290)	0.804±0.012	-	-	0.816±0.014
	320	pIRIR(50,225,290)	0.803±0.017	-	0.812±0.015	1.088±0.044

Material	Preheat (°C)	SAR protocol	Recuperation (%)			
			IR_{50}	$pIRIR_{180}$	$pIRIR_{225}$	$pIRIR_{290}$
K-Feldspar	225	pIRIR(50,180)	1.06±0.05	2.42±0.07	-	-
	320	pIRIR(50,290)	0.47±0.68	-	-	1.91±0.16
Raw grains	225	pIRIR(50,180)	0.58±0.06	2.04±0.13	-	-
	250	pIRIR(50,225)	0.33±0.02	-	1.17±0.05	-
	320	pIRIR(50,290)	0.99±0.09	-	-	1.47±0.08
	320	pIRIR(50,225,290)	0.70±0.05	-	0.71±0.03	2.63±0.12

Material	Preheat (°C)	SAR protocol	Thermal transfer (Gy)			
			IR_{50}	$pIRIR_{180}$	$pIRIR_{225}$	$pIRIR_{290}$
K-Feldspar	225	pIRIR(50,180)	0.69±0.06	3.9±0.2	-	-
	320	pIRIR(50,290)	1.6±0.6	-	-	11.9±0.4
Raw grains	225	pIRIR(50,180)	0.91±0.07	3.68±0.16	-	-
	250	pIRIR(50,225)	1.74±0.05	-	6.0±0.2	-
	320	pIRIR(50,290)	1.49±0.04	-	-	9.1±0.5
	320	pIRIR(50,225,290)	1.91±0.05	-	6.29±0.19	17.6±0.4

Table 4.4: Dose recovery ratio, Recuperation (%) for quartz grains extracted from the granite sample and treated with HCl and HF and sieved to $90 - 180\mu$m measured at seven different temperatures. In the dose recovery experiment, the aliquots were bleached twice with the blue LEDs for 100 s with an intervening pause of 10 ks. A dose of 50 Gy was then given before SAR measurement.

Material	Preheat (C°)	n	Dose Recovery ratio	Recuperation (%)	IR depletion ratio
	210	6	1.05±0.05	3.68±0.13	1.00±0.02
	220	6	0.96±0.05	3.6±0.5	0.89±0.02
	230	6	0.95±0.05	3.1±0.4	0.91±0.02
Quartz	240	6	0.94±0.02	0.31±0.05	0.941±0.013
	250	6	0.89±0.02	0.257±0.015	0.921±0.007
	260	6	0.93±0.02	2.5±0.2	0.81±0.02
	280	6	1.07±0.05	1.8±0.3	0.96±0.02

Table 4.5: Dose recovery ratio (corrected for thermal transfer), Recuperation (%) and Thermal transfer doses for K-feldspar extracted grains ($90 - 180\mu$m) and for raw (untreated) grains ($90 - 180\mu$m) from the sandstone sample, measured with four different SAR-protocols. In the dose recovery and thermal transfer experiments, the aliquots were bleached in a solar simulator (Hönle SOL2) for 48 h. A dose of 50 Gy was then given before SAR measurement. All entries are the arithmetic average of at least 3 aliquots.

Material	Preheat (°C)	SAR protocol	Dose Recovery ratio			
			IR_{50}	$pIRIR_{180}$	$pIRIR_{225}$	$pIRIR_{290}$
K-Feldspar	225	pIRIR(50,180)	0.79±0.02	0.99±0.03	-	-
	320	pIRIR(50,290)	0.76±0.08	-	-	1.76±0.10
Raw grains	225	pIRIR(50,180)	0.862±0.016	1.06±0.06	-	-
	250	pIRIR(50,225)	0.81±0.04	-	1.25±0.09	-
	320	pIRIR(50,290)	0.69±0.04	-	-	1.23±0.08
	320	pIRIR(50,225,290)	0.69±0.03	-	1.35±0.09	1.68±0.11

Material	Preheat (°C)	SAR protocol	Recuperation (%)			
			IR_{50}	$pIRIR_{180}$	$pIRIR_{225}$	$pIRIR_{290}$
K-Feldspar	225	pIRIR(50,180)	1.41±0.05	2.78±0.09	-	-
	320	pIRIR(50,290)	1.9±0.3	-	-	2.47±0.05
Raw grains	225	pIRIR(50,180)	0.52±0.14	3.5±0.3	-	-
	250	pIRIR(50,225)	0.85±0.10	-	2.0±0.2	-
	320	pIRIR(50,290)	0.6±0.3	-	-	2.13±0.13
	320	pIRIR(50,225,290)	0.96±0.11	-	1.3±0.2	3.0±0.2

Material	Preheat (°C)	SAR protocol	Thermal transfer (Gy)			
			IR_{50}	$pIRIR_{180}$	$pIRIR_{225}$	$pIRIR_{290}$
K-Feldspar	225	pIRIR(50,180)	6.7±0.5	20.0±0.9	-	-
	320	pIRIR(50,290)	9.8±1.2	-	-	24.7±0.4
Raw grains	225	pIRIR(50,180)	7.9±0.6	19.9±1.2	-	-
	250	pIRIR(50,225)	9.9±0.9	-	17.0±1.6	-
	320	pIRIR(50,290)	12.9±1.4	-	-	41±3
	320	pIRIR(50,225,290)	10.3±0.4	-	6.0±0.3	40±2

Table 4.6: Dose recovery ratio, Recuperation (%) for Q grains extracted from the sandstone sample and treated with HCl and HF and sieved to $90 - 180\mu$m, measured with seven different temperatures. In the dose recovery experiment, the aliquots were bleached twice with the blue LEDs for 100 s with an intervening pause of 10 ks. A dose of 50 Gy was then given before SAR measurement.

Material	Preheat (°C)	n	Dose Recovery ratio	Recuperation (%)	IR depletion ratio
Quartz	220	6	1.16±0.03	0.02±0.002	0.984±0.004
	240	6	0.959±0.013	0.023±0.002	0.987±0.003
	260	6	0.80±0.03	0.033±0.002	0.985±0.006
	280	6	0.73±0.02	0.062±0.002	0.960±0.006

In Figure 4.8, stimulation curves are shown for the blue stimulated quartz grains (blue data), IR stimulated raw grains at 50 °C (black data), 225 °C (green data), and 290 °C (red data) from the granite and the sandstone samples. Also shown is a stimulation curve for calibration quartz (pink), which is known to be fast-component dominated[96]. In b) and d) the same data are shown on a logarithmic time scale. Model fits to the data are also shown, using the general order model (G.O.M) for the IR stimulated signals, and the sum of three first order exponential functions to the quartz data (only one exponential was required for the calibration quartz data). It is clear that the quartz grains from both these samples contains more than a single component. Based on these fits, the fast component in the sandstone aliquot makes up 94% of the signal in the summation intervals used (i.e. initial 0.48 s as signal and the immediately following 0.48 s for background - early background subtraction), whereas in the granite sample the fast component contributes only 63% of the total signal (had we used late background subtraction these numbers would be 77 and 28%, respectively). Interestingly, it is the sandstone, with a 93% contribution of fast component in the summed signal, that does not have consistently satisfactory dose recovery across all preheat temperatures (acceptable only for the chosen preheat of 240 °C).
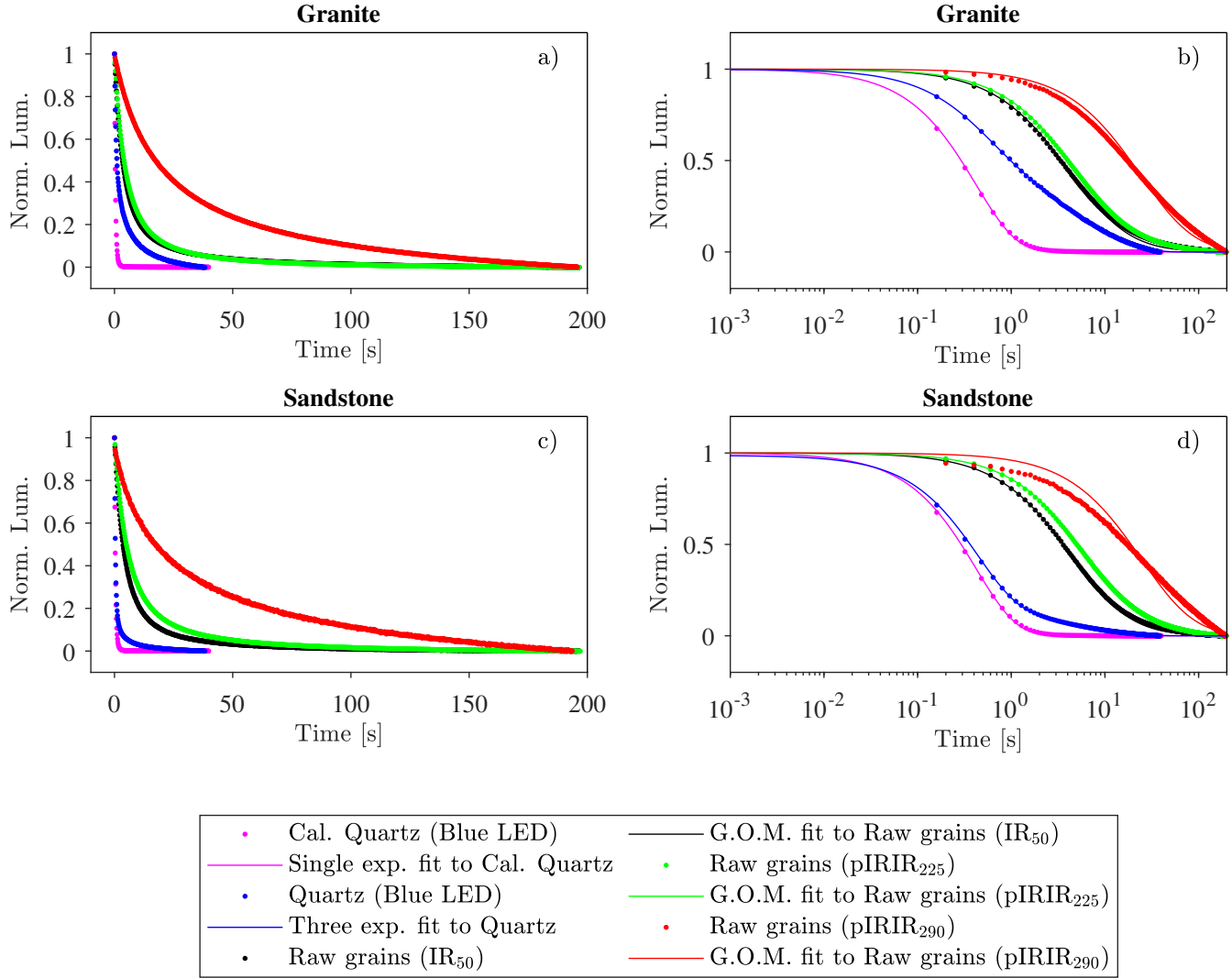
Figure 4.8: Representative stimulation curves for the granite sample (a and c) and the sandstone sample (b and d) for both quartz and raw grains. Quartz was stimulated with blue LEDs (blue data points), whereas the raw grains were stimulated with IR LEDs at consecutive stimulation temperatures of 50, 225, 290 (black, green and red data points, respectively). Also shown is a stimulation curve from calibration quartz (pink)[96] known to be fast component dominated. b) and d) show the same data sets as a) and c), respectively, on a logarithmic time scale. in b) and d) fitted curves are also shown using the G.O.M. for feldspar and the first order model for quartz. Calibration quartz has been fitted using a single exponential decaying function, whereas the quartz extracted from granite and sandstone has been fitted using a sum of three such exponentials.

4.5   Exposure experiments

Luminescence data from granite samples exposed to i) monochromatic light, ii) artificial light (from the halogen lamps), and iii) daylight are presented and analysed in this section. Here we also present the data obtained from the sandstone samples exposed to the halogen lamps. The data from samples that were light exposed and then irradiated are presented in section 4.6.

4.5.1   Granite exposure to monochromatic light

Three cylinders drilled from the same granite slab were each exposed, in a specially designed sample holder, to one of three calibrated monochromatic light sources, viz. infra red light (885 nm), green light (532 nm), and violet light (405 nm), with exposure times adjusted such that that they each received the same number of photons per unit area, independent of wavelength (photons/area: $1.3 \cdot 10^{22}$ cm^{-2} corresponding to exposure times of 0.5, 3.6, and 4 days, respectively), thus ensuring that φt is the same for all 3 samples.

Measured luminescence-depth profiles from quartz (blue stimulation), IR$_{50}$, pIRIR$_{225}$, and pIRIR$_{290}$ signals, respectively are shown in Figure 4.9. Qualitatively, we observe that for the IR$_{50}$ signal, the longest wavelength (infrared light source, red data points) gives luminescence profiles that penetrates most deeply. In contrast, for the post-IR signals, the shortest wavelength (violet light source, pink data points) give the deepest profiles. Also, the lower the stimulation temperature, the deeper the profile, for a given wavelength.

One of the objectives of this work is to determine the most appropriate method to use when modelling the profiles. Here we investigate four methods for fitting the G.O.M. with different constraints on the fitting parameters, g, and $\overline{\sigma\varphi_0}t$. (Note that quartz data have been fitted using a first order model (Eq.4.3), only feldspar data have been fitted using a G.O.M. (Eq.4.4)). Common to all four methods is that the order g was shared amongst profiles for the same signal, so that e.g. all the IR$_{50}$ profiles have been fitted simultaneously using the same shared g parameter.

Method 1	No additional constraints on the fitting parameters (see Figure 4.9b-d).
Method 2	The photoionisation cross-section, σ, for feldspar and quartz are given by the data of Spooner[58,111], i.e. $\overline{\sigma\varphi_0}t$ is fixed since values of $\varphi_0 t$ are known in this experiment (see Figure 4.9f-h).
Method 3	The kinetic order, g, is set equal to the order determined from the stimulation curves, g_{stim}, which for the four signals were 1, 2.2, 2.1 and 1.5 for quartz, IR$_{50}$, pIRIR$_{225}$, and pIRIR$_{290}$, respectively (see Figure 4.9f-h).
Method 4	Both $\overline{\sigma\varphi_0}t$ (as in Method 2) and g_{stim} (as in Method 3) are fixed. (see Figure 4.9n-p).

For quartz, Method 1 and 3 (Figure 4.9a and 4.9i) are identical, i.e. g=1, and all other parameters are free. Method 2 and 4 (Figure 4.9e and 4.9m) are identical fitting approx quartz, i.e. g=1, and

$\overline{\sigma\varphi_0}t$ is fixed, however fitting did not converge for these methods. In addition to the individual fits, the 95% confidence bands are also shown. The fitting of the pIRIR$_{290}$ profile using Method 2 also did not converge, probably because the constraints were too strict. Also note that the data by Spooner[58] for the photoionisation cross-section σ was measured at room temperature, so it is likely to apply to the IR$_{50}$ signal, but it is uncertain if it appropriate to the post-IR signals at 225°C and 290°C. Nevertheless, it was used in the absence of other information.

In general, the main effect of constraining parameters is that the fit becomes better known, i.e. the 95% confidence band decreases as seen when Method 1 (no constraints) is compared to the fits obtained with the other three models. However, when constraining $\overline{\sigma\varphi_0}t$ (Method 2 and 4), the model appears to fit the data more poorly. This is shown more clearly in Figure 4.10, which shows the regression standard error χ^2_ν for each method and each signal. Reduced chi-squared is defined as $\chi^2_\nu = \chi^2/\nu$, with degree of freedom $\nu = o - p$ (number of observations minus number of parameters) and $\chi^2_\nu = \sum \frac{n_{\mathrm{data}} - n_{\mathrm{fit}}}{\sigma^2}$ (n_{data} is measured luminescence at x and n_{fit} is fitted value x). However, it must be noted that the χ^2_ν values are calculated based on the fits to the entire profiles. Particularly for the two post-IR signals, the exposure duration was so short that most of the profiles are in saturation for most depths, and hence the absolute χ^2_ν should not be compared between the different signals[1]. Methods 1 and 3 appear to fit the data best. In subsequent analysis, Method 1, which does not constrain fitting parameters (other than by sharing g), is used.

4.5.1.1 Estimating photoionisation cross-sections

G.O.M. fitting of exposure profiles gives three parameters, i.e. g_{profile}, $\overline{\sigma\varphi_0}t$ and μ, whereas the first order model only gives two as the order g by definition is 1. Since $\varphi(\lambda)t$ was constant (and known) in this experiment, changes in $\overline{\sigma\varphi_0}t$ reflect changes in the cross-section, σ. Figure 4.11a shows $\overline{\sigma\varphi_0}t$ (derived using Method 1 with no fitting constraints) as a function of the wavelength of the exposure light. For quartz, $\overline{\sigma\varphi_0}t$ is seen to decrease with wavelength as expected from published measurements of the photoionisation cross-section dependence on wavelength [e.g. 58,112,127]. For the two post-IR signals the same trend is observed, even although the profiles were not fully bleached even at the very first slice, and thus the parameter estimation essentially rely on a single data point determining the shape of the profiles. As μ (and the order g) determines the slope of the profiles (see Eq.4.5 and Eq.4.6), an accurate estimate of μ presumably requires more data points on the rising edge of the profile than is present in these data sets. Nonetheless, for the pIRIR signals a decrease with wavelength is observed. On the other hand, for the IR$_{50}$ signal, an increase in $\overline{\sigma\varphi_0}t$ with increasing wavelength is observed.

Because of the experimental setup, the value of φ_t is known and thus it is possible to derive estimates of the photoionisation cross-section $\sigma(\lambda)$ at the three wavelengths investigated here. These estimates for feldspar are compared to the values measured by Spooner[58] for feldspar in Figure 4.12 (note the logarithmic y-axis). Note that the cross-sections in Spooner[58] were derived based on measurements made at room temperature, and thus we would expect these to be similar to those measured here at a temperature of 50°C, i.e. similar to those for the IR$_{50}$ signal. Photoionisation cross-sections for post-IR signals are yet to be published. However, the

---

[1]The absolute values of χ^2_ν are an order of magnitude smaller for the post-IR signals than for the blue (from quartz) and IR$_{50}$ signals, because more points are at the saturation level, which is well fitted by all the models, and thus does not represent how well the various methods fit the rising edge of the profiles.
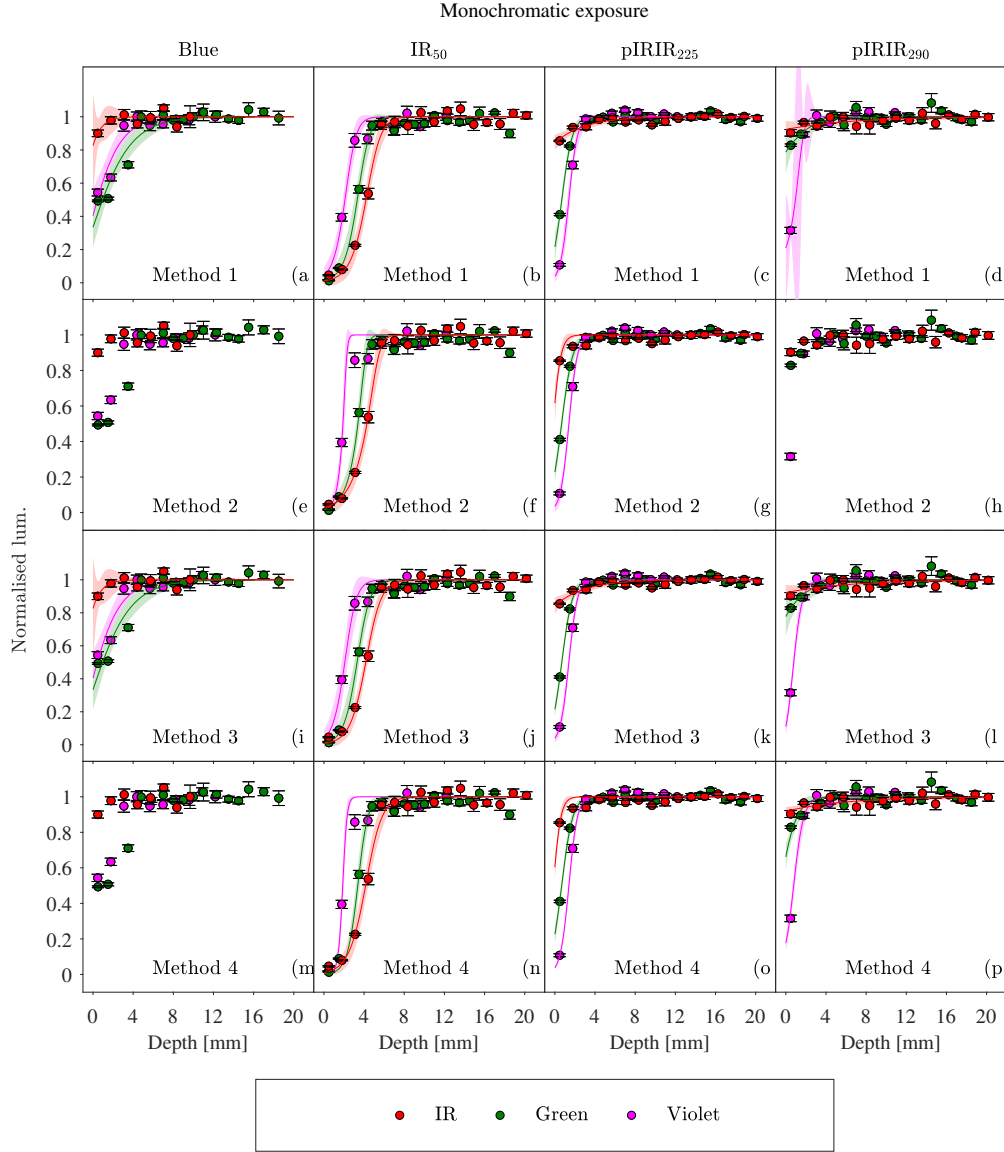
Figure 4.9: Normalised granite luminescence-depth profiles exposed to the same numbers of photons $(1.3 \cdot 10^{22})$ from IR (red data), green (green data), and violet lasers (pink data). The profiles were measured using four luminescence signals: Blue stimulation (quartz), IR_{50} (raw grains), $pIRIR_{225}$ (raw grains), and $pIRIR_{290}$ (raw grains). These are shown in columns 1, 2, 3, and 4, respectively. Quartz profiles were fitted using a first order model (i.e. Eq.4.3), whereas the feldspar profiles (raw grains, IRSL signals) were fitted using the G.O.M. (i.e. Eq.4.4). The data were fitted using four different methods which have different constraints on the fitting parameters: g, μ, and $\overline{\sigma \varphi_0} t$. In all methods, the order g was shared amongst profiles for same signal, e.g. all $pIRIR_{225}$ profiles were fitted simultaneously using the same, shared value of g. For quartz (1st column), the value of g is 1 for all fits. Method 1 (b-d): No constraints on the fitting parameters. Method 2 (f-h): Fixed $\overline{\sigma \varphi_0} t$ using experimental values for σ [58] and the known number of photons $\varphi_0 t$ impinging on the sample. Note that it was not possible to obtain a fit for the $pIRIR_{290}$ signal using this method (h). Method 3 (j-l): The kinetic order g is forced equal to the order determined from the stimulation curves, i.e. $g = g_{stim}$. Method 4 (n-p): Fixed $\overline{\sigma \varphi_0} t$ (known values) and order $g = g_{stim}$. For quartz, Method 1 and 3 (a, i) are identical, i.e. no constraints on the fitting parameters, and method 2 and 4 (e, m) are identical, i.e. fixed $\overline{\sigma \varphi_0} t$ and $g = g_{stim} \equiv 1$. confidence bands at 95% are given as shaded bands for each fit.
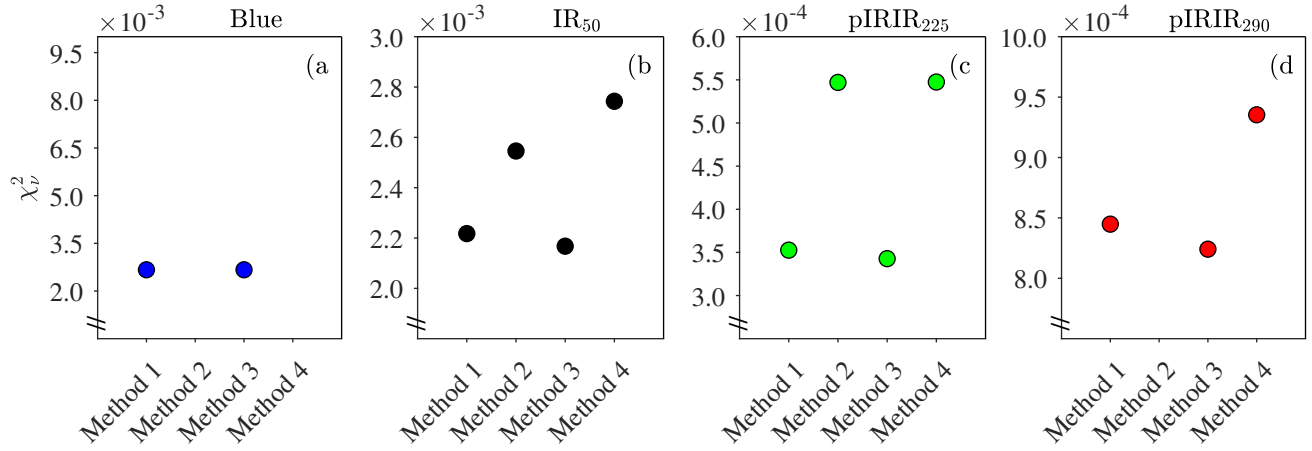
Figure 4.10: The regression standard error ($\chi_\nu^2 = \frac{\chi^2}{\nu}$, with ν being the degree of freedom) are plotted for each method using different constraints (see text for details). Note that the smaller absolute values of χ_ν^2 for the post-IR signals reflect that most of the profiles for these signals are in saturation and not necessarily that the rising edge of the profile is described better.

comparison between the cross-sections derived from the data of Spooner[58] and those derived here from luminescence-depth profiles is not very encouraging; our cross-sections are orders of magnitude smaller. Similar discrepancies have been reported before [e.g. 42]; clearly the IR$_{50}$ signal in rock bleaches much more slowly than when from loose grains, but the reason remains unknown. Similarly, for quartz the estimate of σ derived from profile fitting considerably underestimates previously published cross-sections for quartz[111–113] (see Figure 4.12).

4.5.1.2 Estimating the light attenuation coefficient

In Figure 4.11b estimates of the light attenuation coefficient, μ, are shown as a function of bleaching wavelength. The individual estimates of μ for quartz are relatively well-known ($\sim$10%). The violet and green exposures give attenuation values of $\sim$ 0.5 mm, whereas for the IR exposure it is significantly longer, i.e. 1.5 mm. However, it must be noted that the IR exposure affected the quartz luminescence signal by less than 10%, so this value of μ hinges on the slope between the luminescence measured for the first and second slice, where the latter is in saturation (see first column in Figure 4.11). For the three IR signals, the light attenuation coefficient decreases with wavelength, i.e. the longer wavelengths apparently pass more easily through the rock matrix than the shorter wavelengths.

In Figure 4.13a,b the μ_{profile} estimated from fitting luminescence-depth profiles is plotted against the values obtained from direct measurement using the spectrophotometer, μ_{absorb}. The ratios of μ_{profile} to μ_{absorb} averaged over all three wavelengths are on average 0.36$\pm$0.15, 0.75$\pm$0.03, 0.6$\pm$0.2, and 0.6$\pm$0.4 for blue (quartz), IR$_{50}$, pIRIR$_{225}$, and pIRIR$_{290}$ signals, respectively. These ratios are different from unity, and this may be because an inappropriate fitting method was used, or because attenuation was overestimated in direct measurements of absorbance (since scattered light is not measured). Ou et al.[74] made similar absorbance measurements to estimate μ and compared those to profile estimates of μ for IR$_{50}$ (assuming $\mu(\lambda = 860)$) and pIRIR$_{225}$ (assuming $\mu(\lambda = 500)$)
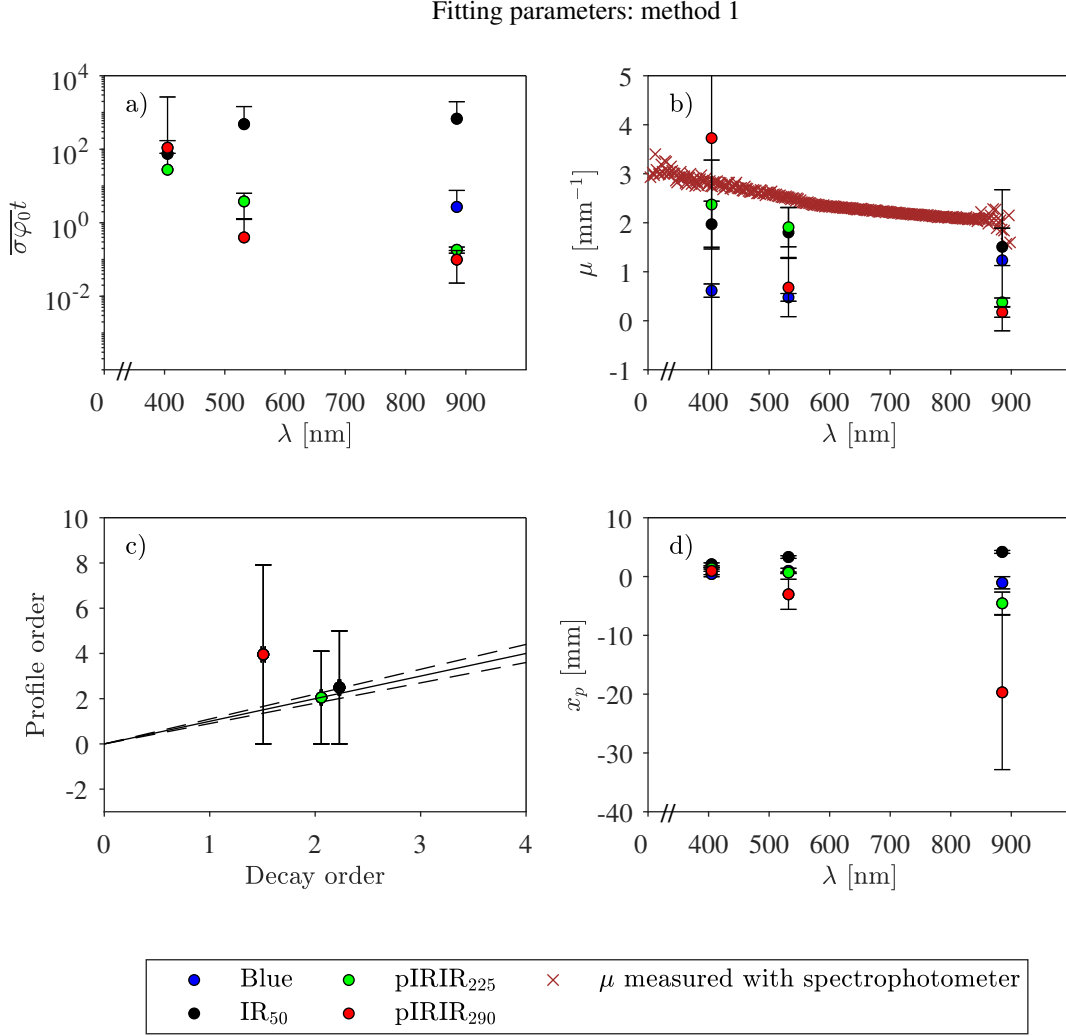
Figure 4.11: Parameters estimated using a first order model for quartz and the shared-order G.O.M. for feldspar, i.e. where the order g was shared between all profiles measured using the same signal. The luminescence-depth profiles were generated by exposure to laser light with wavelengths of 405, 532 and 885 nm (violet, green and IR). Four signals have been measured: blue stimulation (quartz), IR_{50}, $pIRIR_{225}$, and $pIRIR_{290}$ stimulation (feldspar). a) $\ln \overline{\sigma \varphi_0} t$. b) μ [mm^{-1}] estimated from profile fitting (circles), and μ estimated from direct absorbance measurements (crosses, see section 4.2.2) c) Kinetic order g_{profile} determined from fitting luminescence-depth profiles plotted against the decay order obtained from fitting IRSL stimulation curves (g_{stim}). Also shown is the 1:1 line; from first principles, the best fit line must pass through the origin. d) The inflection point x_p estimated from fitted profiles at a luminescence level of 0.5.
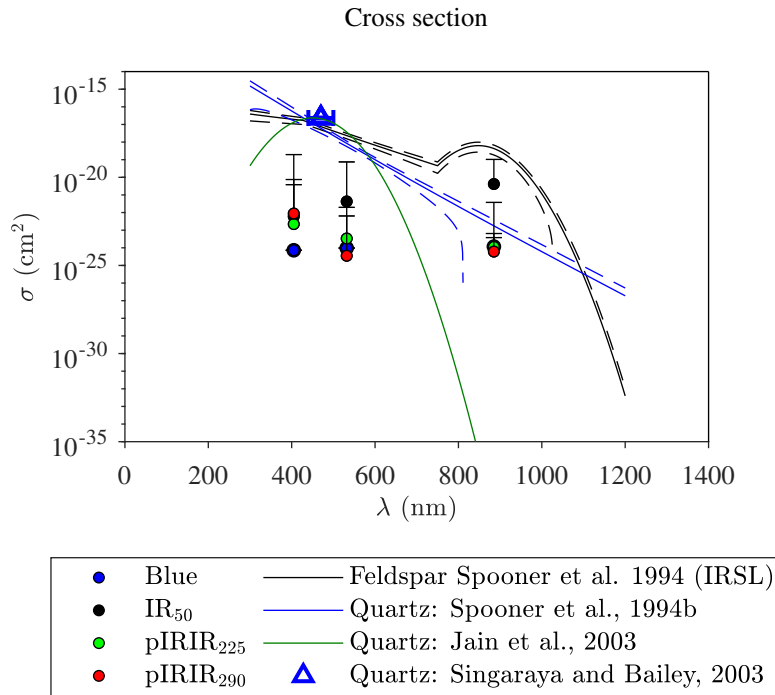
Figure 4.12: Photoionisation cross-sections $\sigma(\lambda)$ derived from fitting luminescence-depth profiles in granite samples exposed to monochromatic light with three different wavelengths (855, 532 and 405 nm). The fitting has been done using first order for quartz and the shared-order G.O.M. i.e. Method 1. The luminescence-depth profiles have been measured using IR_{50} (black data), $pIRIR_{225}$ (green data), and $pIRIR_{290}$ (red data), respectively. Also shown are photoionisation cross-sections $\sigma(\lambda)$ for feldspar and quartz as a function of wavelength. The data for feldspar (black lines) have been derived from Spooner,1994 [58] for the depletion of the IRSL signal measured at room temperature for microline by 10, 50 and 90%, respectively. Also shown are similar data from quartz (blue lines) obtained from Spooner,1994b [111] for the depletion of the OSL signal to 5, 50 and 95%, respectively. For quartz, we also show the data of Singarayer and Bailey,2003 [112] (green curve) and the single point (blue triangle) at 470 nm from Jain et al.,2003 [113].

signals. Their estimated ratios of μ_{profile} to μ_{absorb} were on average 0.23±0.06 and 0.79±0.14 for IR$_{50}$ and pIRIR$_{225}$, respectively. Our corresponding ratios, at wavelengths of 885 nm and 532 nm, respectively, are 0.8±0.2 and 0.76±0.16 for IR$_{50}$ and pIRIR$_{225}$, respectively. Thus, for the pIRIR$_{225}$ signal our measurements agree well with those of Ou et al.[74], but for the IR$_{50}$ signal our results are significantly different. Ou et al.[74] used the first order model when fitting their profiles and we use the general order model; this may explain the discrepancy, and is investigated further below.
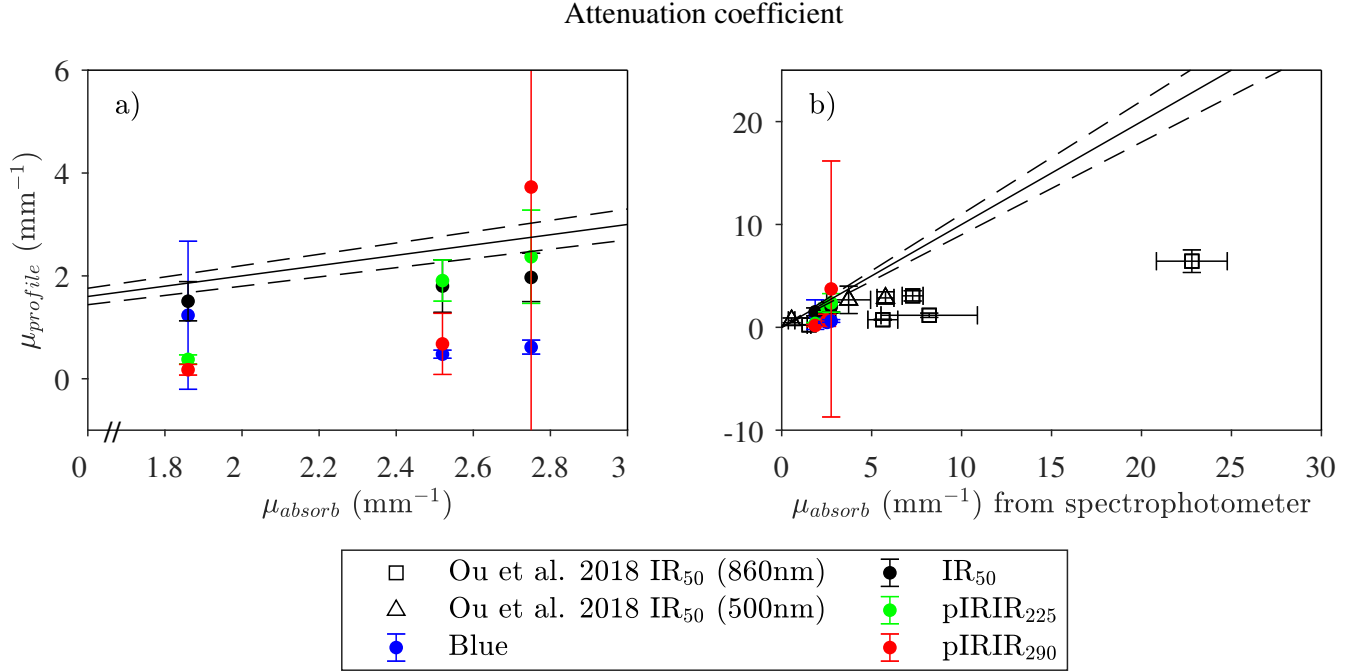
Figure 4.13: a) Estimates of μ_{profile} derived from fitting luminescence-depth profiles plotted against direct estimates of μ_{absorb} from absorbance measurements using a spectrophotometer at the same wavelength. The standard error on μ_{profile} for pIRIR$_{290}$ is 12 and thus very poorly known. b) the same data as in a) but also showing the data of Ou et al.[74] (open squares). The solid black line is the 1:1 line and the dashed lines are ±10%

4.5.1.3 Estimating the kinetic order

In Figure 4.11c, we compare the kinetic order obtained from fitting the individual IRSL stimulation curves ("Decay order"≡ g_{stim}) with those determined from fitting the profiles ("Profile order"≡ g_{profile}). The two estimates of the kinetic order (for the three signals) are consistent with each other, but it must be acknowledged that the uncertainties on g_{profile} are large (> 100%); especially for the pIRIR$_{290}$ signal.

4.5.1.4 Evaluating the ability to bleach the grains

In Figure 4.9, we observed that IR$_{50}$ profiles have a deeper penetration than that of all other signals. One way to quantify the profile depth is by using the inflection point x_p, i.e. the depth at which the luminescence signal is 50% of saturation, $L(x_p) = 0.5$. In Figure 4.11d, the inflection point x_p is shown as a function of exposure wavelength for each of the signals. The higher the value of x_p the deeper lies the profile. Note that for some of the points a physically unrealistic negative value of x_p is given. This simply implies that the exposure time was too short to deplete

the luminescence to 50% of saturation, and so a negative x_p value is given by the model fit. The x_p values for the IR_{50} signal increase with exposure wavelength, and the IR_{50} profile is lies deepest for IR exposure. On the other hand, the Violet exposure light affects the post-IR profile the most (largest x_p).For quartz the picture is not as clear. Comparing the ability to bleach at a particular depth for each wavelength may give a more clear picture of the bleachability.

To evaluate the ability of each signal to be bleached by a particular wavelength, the remaining luminescence levels at four given depths (i.e. 1 mm, 2 mm, 3 mm, and 4 mm) are estimated from the curve fits of Figure 4.9(a-d), and shown in Figure 4.14.

The IR_{50} signals are better bleached for all wavelengths at all depths compared to the three other signals. Furthermore, longer wavelengths are more effective at bleaching the IR_{50} signal than the shorter wavelengths. On the other hand, the $pIRIR_{225}$ and $pIRIR_{290}$ signals are better bleached by shorter wavelengths. Surprisingly, quartz is affected the most by the green (532 nm) laser, which is not consistent with the shape of the photoionisation cross-section shape published by Singarayer and Bailey[112], where the cross-section of violet stimulation is more than an order of magnitude larger than that for green stimulation. Again, this presumably means that the intensity of the shorter wavelengths is reduced more than the longer wavelengths.
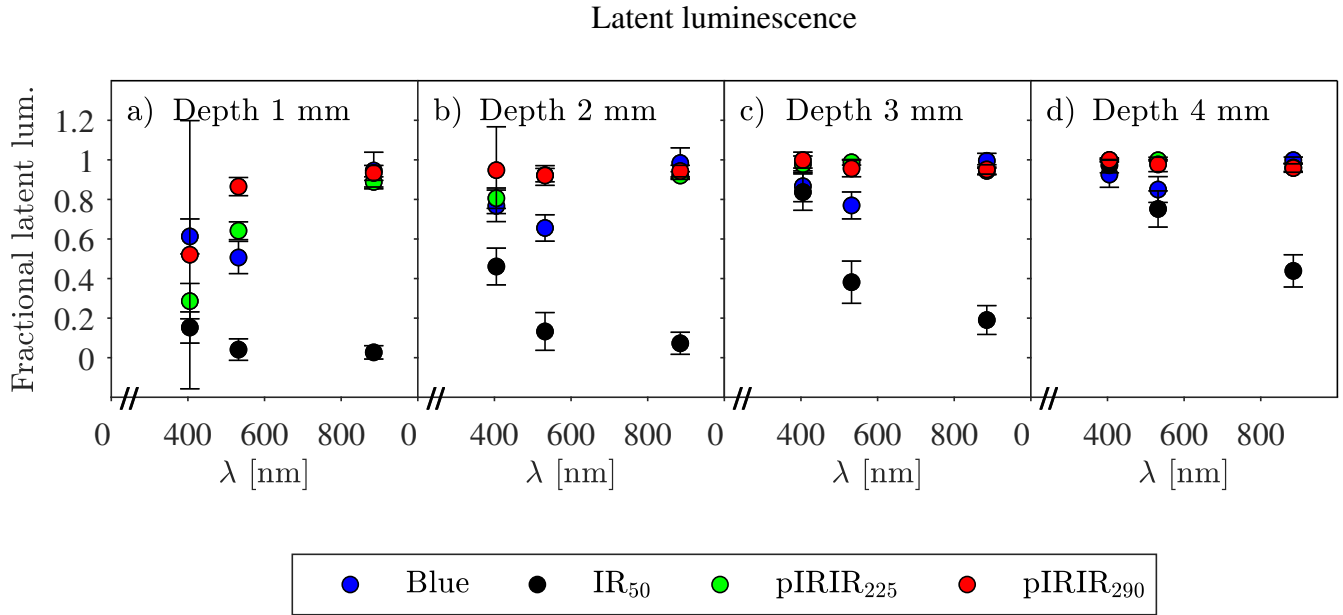
Figure 4.14: Residual luminescence signal estimated from fitting the profiles shown in Figure 4.9(a-d) at 1 mm, 2 mm, 3 mm, and 4 mm depths for the four signals i.e. quartz (blue LED), IR_{50}, $pIRIR_{225}$, and $pIRIR_{290}$, respectively, plotted as a function of light exposure wavelength.

4.5.1.5   Summary of monochromatic light exposure

From the monochromatic light exposure experiment, it can be concluded that IR_{50} signals are more bleachable for all wavelengths compared to quartz, $pIRIR_{225}$, and $pIRIR_{290}$ signals. This contradicts earlier observations[e.g. 50,55] that loose monolayers of quartz grains are more readily bleached than loose grains of feldspar. As expected, the $pIRIR_{290}$ signal is the least bleachable

signal followed by pIRIR$_{225}$ and quartz. The bleachablility increases with wavelength for IR$_{50}$ signals whereas it decreases with wavelength for pIRIR$_{225}$ and pIRIR$_{290}$ signals. However, quartz seems to be more sensitive to the middle part of the spectrum.

The excitation spectrum for quartz suggests that short wavelengths (i.e. violet light) should be most efficient in resetting the luminescence signal in quartz grains and that long wavelengths should be less effective; in particular IR light at room temperature does not reset the fast component in quartz[111,127]. We observe that the IR exposure only has a small effect on the first slice ($<10\%$) in quartz. However, exposure to green light is more efficient at resetting the luminescence to greater depths than the exposure to violet. This can be explained in terms of the measured light attenuation, which decreases strongly with increasing wavelength.

Excitation spectra from feldspar suggest strong absorption in the violet region and a decrease with wavelength with the exception of a resonance peak in the IR region around 850 nm[58]. From our data the resonance peak is apparently stronger in IR$_{50}$ signals than in post IR signals; the effect of IR light penetrates deeper into the rock than that of violet and is greater at a given depth.

As expected, a decrease in attenuation with wavelength was observed for feldspar signals. However this is not true for the quartz signals, perhaps because of the resolution of the data sets and the shallow profiles for all exposure wavelengths. Estimation of $\overline{\sigma\varphi_0}t$ gave large uncertainties, as observed in other studies [e.g. 6,44].

Estimating values for the cross-section σ from luminescence-depth profiles for the three given exposure wavelengths give significantly different results than those of Spooner[58], with the possible exception of IR$_{50}$ profiles exposed to IR light. This underestimation can be caused by underestimation of μ, but is more likely to be caused by the large uncertainty associated with the fitting parameter $\overline{\sigma\varphi_0}t$ as it is very sensitive to the profile depth. Roughly, if the profile depth is doubled, the corresponding estimate of $\overline{\sigma\varphi_0}t$ is squared.

4.5.2   Sandstone exposure to daylight

Eight sandstone samples were exposed to daylight for different durations ranging from 1 day to 730 days. Figure 4.15 shows luminescence-depth exposure profiles from the sandstone samples exposed to daylight for 30, 566, and 730 days. Quartz grains measured with blue LEDs are shown in (a) and raw grains measured with IR LEDs at three stimulation temperatures, i.e. IR$_{50}$, pIRIR$_{225}$, and pIRIR$_{290}$, respectively in b), c), and d). Also shown are model fits using Eq.(4.3) for quartz (first order, Blue stimulation) and Eq.(4.4) for the IR profiles. In the G.O.M. (IR profiles), the kinetic order g was fixed to the average order obtained when fitting 48 individual stimulation curves for each signal, i.e. g_{stim} was 2.097 ± 0.015, 1.995 ± 0.008 and 1.49 ± 0.03 for IR$_{50}$, pIRIR$_{225}$, and pIRIR$_{290}$ signals, respectively. Note that it was not possible to fit the two post-IR profiles for the 30 day exposure to Eq.(4.4) as the measured luminescence signal was in saturation for all depths, even the first mm.

It appears that a 30 day exposure to daylight was insufficient to detectably deplete the signal, even at the surface. In general, bleaching is poor in this sandstone, although profiles are detectable for exposures of 566 and 730 days for all signals. The maximum progression of the inflection point $x_{0.5}$, i.e. the depth at which the measured luminescence is at 50% of the saturation level
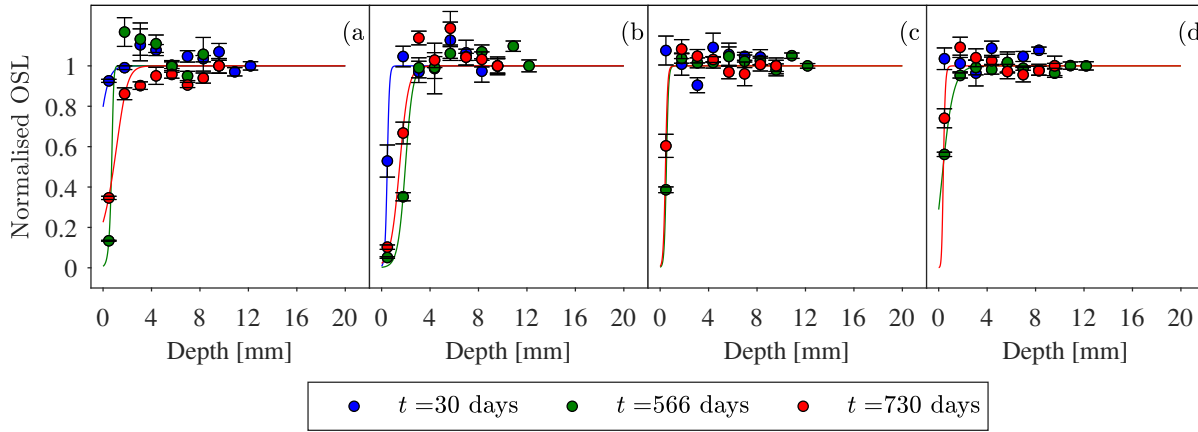
Figure 4.15: Luminescence-depth exposure profiles from sandstone samples exposed to daylight for 30, 566, and 730 days, measured with the quartz SAR protocol for quartz grains (a) and a pIRIR protocol generating three IR signals IR_{50}, $pIRIR_{225}$, and $pIRIR_{290}$, respectively, in b), c), and d). Quartz profiles were fitted with the first order model, whereas IR profiles were fitted with the G.O.M. using the order estimated from stimulation curves.

$((n(x_{0.5}))=0.5)$, is only ~ 2 mm, and with a slice thickness of ~ 1 mm, no more than two data points are on the rising edge of the exposure profiles. Thus, the measurement of other intermediate exposure durations profiles from this sandstone was not considered useful; additional values would not further constrain model fitting significantly. Nevertheless, and as was reported above, the IR_{50} signals appear to be bleached to greater depths than quartz, in contrast to what has been reported for loose grains exposed to daylight [e.g. 50,55]. Furthermore, the profile from the 566 day exposure has progressed further into the rock than the profile from the 730 day exposure, suggesting that the shorter exposure were able to bleach the luminescence signal more than the longer exposure. This seems unlikely and the apparent shift in profiles is rather assumed to be caused by uncertainties in the measurement of depth when slicing the individual cores.

Figure 4.16 shows luminescence levels (L_n/T_n) for the first slice normalised to the saturation level from these sandstone profiles plotted as a function of known exposure time. These data clearly show that the IR_{50} signals are bleached the most, then quartz, then $pIRIR_{225}$, and the $pIRIR_{290}$ signal is bleached the least. A parameter analysis is not necessarily very informative for these shallow profiles, but nonetheless the average values of μ are 7 ± 4 mm^{-1} ($n = 3$), 6 ± 3 mm^{-1} ($n = 3$), 11.345 ± 0.014 mm^{-1} ($n = 2$), and 7 ± 5 mm^{-1} ($n = 2$) for quartz, IR_{50}, $pIRIR_{225}$, and $pIRIR_{290}$ signals, respectively. These are more than double the values observed in other studies for of rock surface luminescence dating (e.g.[1,6,76,116]), however as they are mainly derived caused by a single to two points in the profiles these are considered unreliable.

Average values of $\overline{\sigma\varphi_0}$ estimated from $\overline{\sigma\varphi_0}t$ and known times t are 78 ± 77 days^{-1} ($n = 3$), 3 ± 2 days^{-1} ($n = 3$), 0.4 ± 0.2 days^{-1} ($n = 2$), and 0.05 ± 0.04 days^{-1} ($n = 2$) for blue, IR_{50}, $pIRIR_{225}$, and $pIRIR_{290}$ signals, respectively. The uncertainty on these estimates are $\sim 100\%$. The large uncertainties and the poor data resolution makes these sandstone samples unsuitable for further analysis.
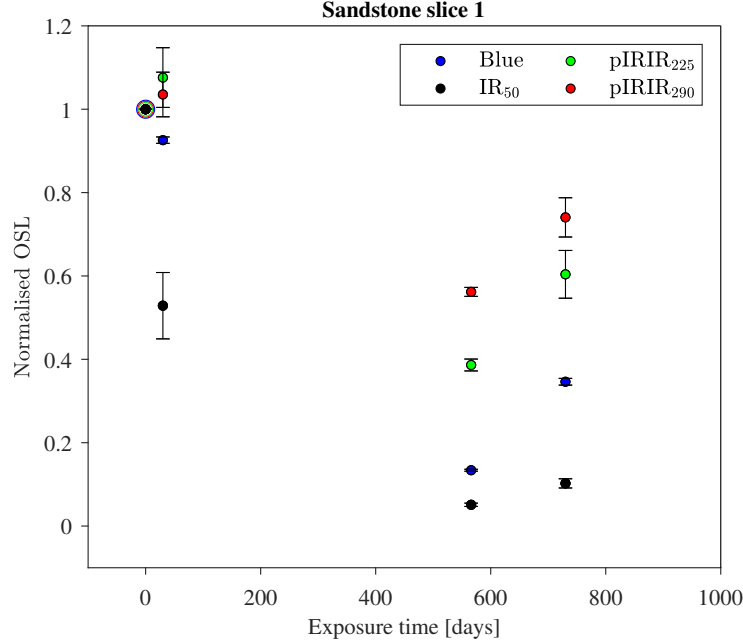
Figure 4.16: Luminescence levels (L_n/T_n) for the first slice normalised to the saturation level from the sandstone profiles plotted as a function of known exposure time. The four signals are coloured blue, black, green, and red for quartz, IR_{50}, $pIRIR_{225}$, and $pIRIR_{290}$, respectively).

4.5.3   Granite exposure to artificial broad-band light and daylight

Often in rock surface exposure dating, a calibration profile[(e.g. 1,44)] is used to calibrate an unknown profile, i.e. $\overline{\sigma\varphi_0}t_{cal}$ from the known age profile is used to estimate a value for $\overline{\sigma\varphi_0}$, which is then used to estimate the unknown time t from $(\overline{\sigma\varphi_0}t)_{unknown}$. Using both simulated and experimental laboratory data (see chapter 3), showed that the accuracy of this approach depends both on the appropriateness of the applied model (e.g. first order or general order) as well as the difference between the calibration age (t_{cal}) and the age of the unknown profile (t). In this study we have eight known profiles (see Table 4.2) with which to test the applicability of calibration profiles to obtain accurate exposure ages. We evaluate the calibration quality of the data sets in two ways: i) the conventional approach of using a single profile as a calibration profile. Here we use each profile as calibration for the remainder, and investigate whether a time dependency exists from one calibration profile to the next. ii) an Exposure Response Curve (ERC) is constructed from the profile depth and known exposure time of seven profiles and the age for the remaining profile is estimated from interpolation.

In Figure 4.17 luminescence-depth exposure profiles from granite samples exposed to a halogen lamp for times ranging between 2.5 hour to 320 days are shown. Four different signals were measured using: a) blue LED stimulation (quartz only) and IR LED stimulation at three stimulation temperatures: b) 50 °C, c) 225 °C, and d) 290 °C (see section 4.3.5 for details). Note that the data for IR_{50} has already been presented and discussed in Chapter 3. A first order fit is used for the quartz profiles shown in Figure 4.17a, and G.O.M fits for the IRSL profiles in Figure 4.17b,c,d. Fitted curves are shown as solid lines with 95% confidence intervals as pale areas. Two fitting methods were used with the G.O.M.: i) the order g was fixed to different values ranging from 1

to 4 (first order model has $g = 1$), and ii) the order was unconstrained, but shared amongst the profiles from the same signal (shared-order G.O.M.). Qualitatively, a progression in depth with time is observed for all signals. Furthermore, there is a change in slope with depth at any given luminescence value; this is most pronounced in the pIRIR$_{225}$ and pIRIR$_{290}$ data sets, where the slope decreases by approximately 35% and 55% at a luminescence level of 0.5 (see Figure 4.19).

Figure 4.17: Luminescence-depth exposure profiles from granite samples exposed to a halogen lamp for times ranging between 2.5 hour and 320 days, measured with blue and pIRIR protocols generating four signals (a: Blue b: IR$_{50}$, c: pIRIR$_{225}$, and d: pIRIR$_{290}$). Quartz profiles were fitted with first order model. IR profiles were fitted with the general order model with the order shared between profiles from same signal. 95% confidence intervals are shown as pale areas around the fitted lines.

Figure 4.18 shows luminescence-depth exposure profiles from granite samples exposed to daylight for times ranging from 1 day to 730 days. The data was fitted in the same way as that presented in Figure 4.17, and the fitted curves are again shown with 95% confidence bands. Again, we observe a change in slope with time. For the daylight exposure, the IR$_{50}$ data also seem to have a change in slope with depth. The slopes of the quartz profiles show a tendency to increase with depth, although the quartz data suffer from significant scatter, particularly the data from the short exposures. The observed change in slope at the inflection point x_p for both the halogen-lamp and the daylight exposed profiles are shown in Figure 4.19.

The G.O.M. used here does not include trap filling during exposure as the effect of trap filling during daylight exposure should be negligible on these time scales[73]. However, if trap filling was of significance, one would indeed expect to observe the slope decrease with depth (see Figure 1.1). Thus, to ensure that the observed change in slope with depth does not arise from trap filling, we also fitted the pIRIR$_{290}$ profiles including the trap filling term. We found the same decrease in μ, as when no trap filling was included in the model, i.e. a decrease of 31%, indicating that trap filling is indeed not responsible for the observed changes in slopes.

According to Eq.(4.5) and Eq.(4.6), the profile slope is determined by the light attenuation coeffi-
cient μ and the kinetic order g, so the observed change in slope with depth is most likely caused
by a change in μ as a function of depth as it is unlikely that the order would change with depth.
This is explored further below.

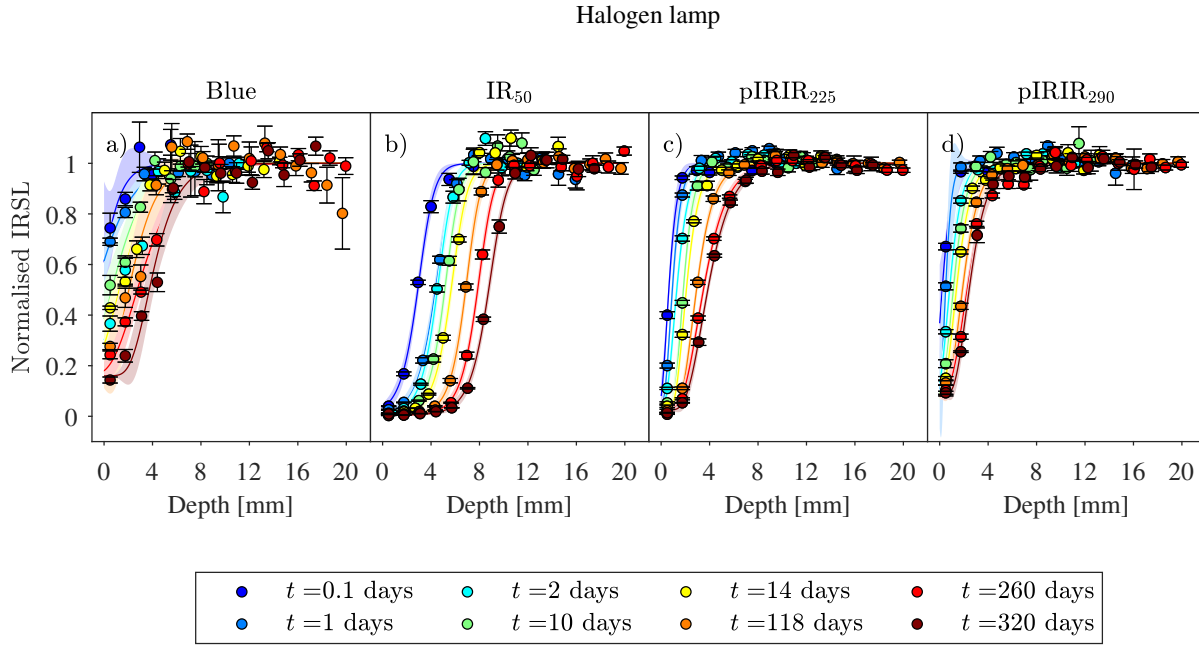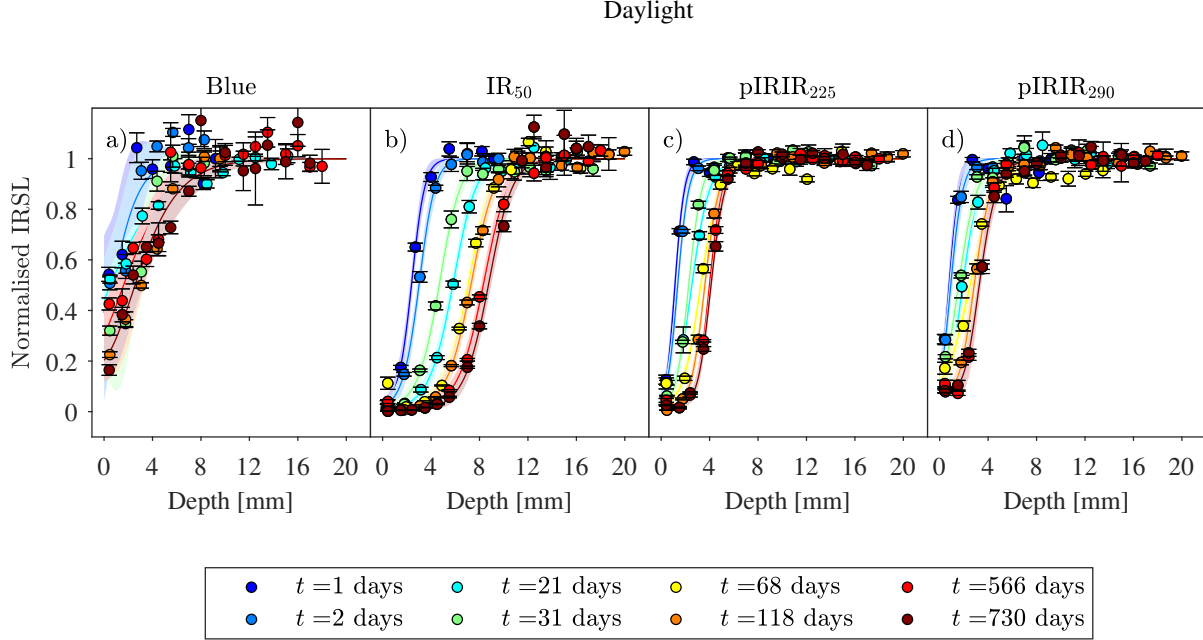**Figure 4.18:** Luminescence-depth exposure profiles from granite samples exposed to daylight for times ranging
between 1 to 730 days, measured with: a) Blue (quartz only), b),c),d) pIRIR protocol generating three signals
IR_{50}, $pIRIR_{225}$ and d: $pIRIR_{290}$, respectively. Quartz profiles were fitted with the first order model. IR profiles
were fitted with the general order model with the order shared between profiles from same signal. 95% confidence
intervals are shown as pale areas around the fitted lines.

Note that the sample exposed for 31 days in daylight (green data) was bleached to a shallower
depth than the samples exposed for 21 days (light blue data). This is likely to be real, and
caused by a smaller number of incident photons. The sample exposed for 31 days was exposed
in November, whereas the sample exposed for 21 days was exposed in July. The data presented
in Figure 4.20 supports this hypothesis. Here the number of photons ($\overline{\sigma\varphi}t$) received during each
individual exposure period are shown plotted against the sample exposure time. They do show a
linear trend as expected, but the sample exposed for 31 days (green data) in November, received
fewer photons than the sample exposed in 21 days in July (light blue data, see inset). This explains
the observation that the 21 day exposure (light blue data) resulted in the profile progressing deeper
into the rock than the sample exposed for 31 days (green data, see legend in Figure 4.20).

From the exposure profiles shown in Figures 4.17 and 4.18, it is apparent that the signal most
easily bleached as a function of depth is the IR_{50} signal. To further explore the bleachability
of the individual signals with respect to one another, Figures 4.21 and 4.22 show L_n/T_n values
normalised to the profile saturation level as a function of the known exposure time for the first
8 slices (corresponding to a depth of approximately 8 mm). The general pattern is that the
luminescence decreases monotonically with time although there is some scatter, particularly in the
quartz data. For the IR_{50} data, the decrease is small for the first two slices because all exposure
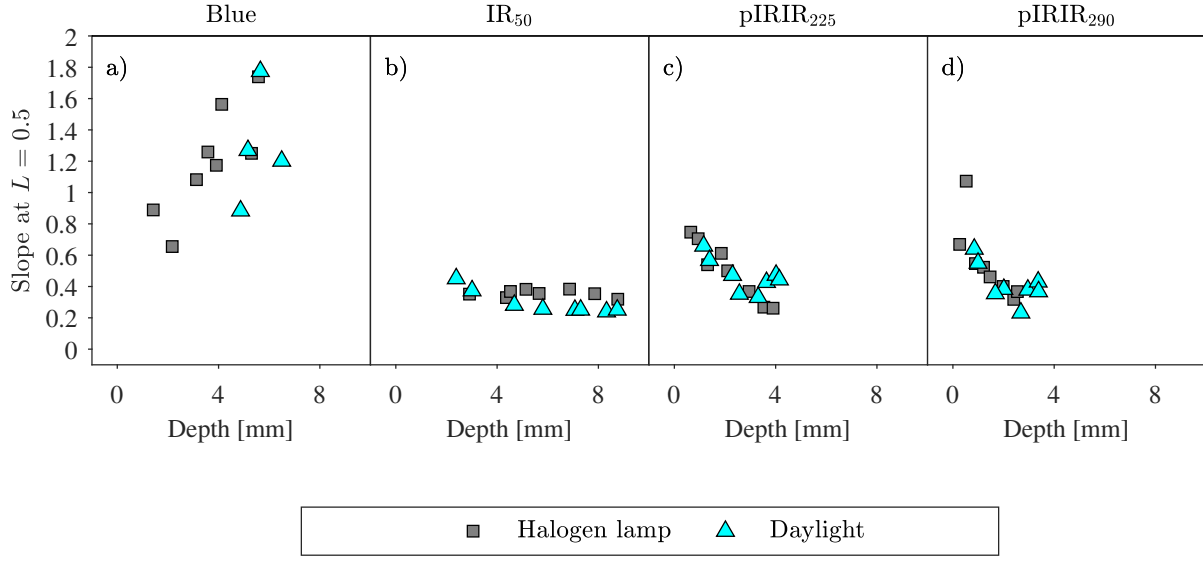
Figure 4.19: Slopes from fitted curves at luminescence level $L = 0.5$ for granite samples exposed to halogen lamps (grey squares) and samples exposed to daylight (blue triangles).
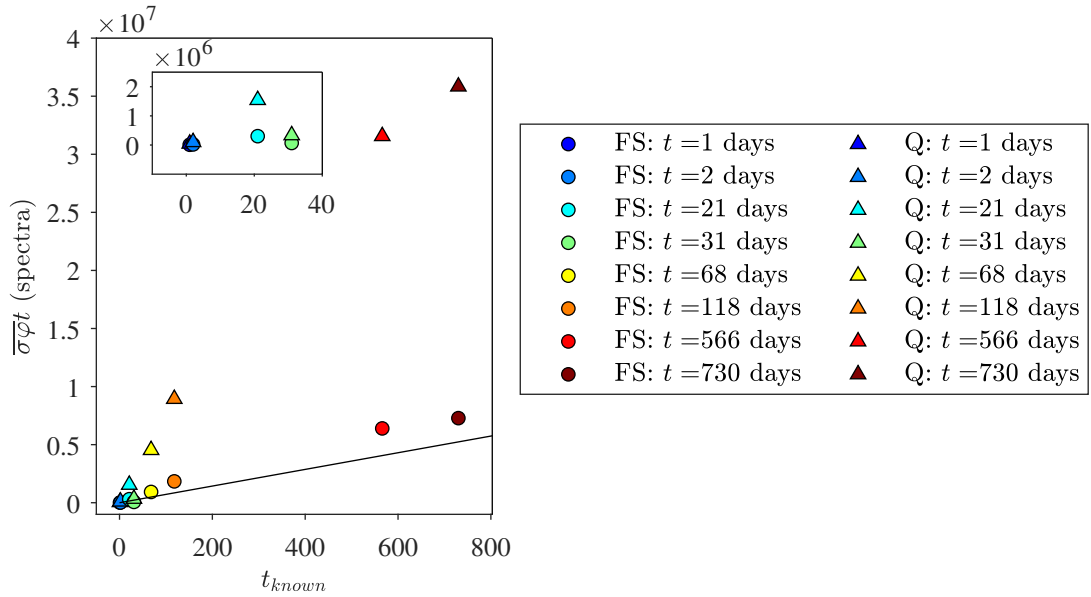
Figure 4.20: Effective photons estimated from photoionisation cross-sections for quartz (triangles) and feldspar (circles) Spooner[58,111] and the daylight spectrum for the specific exposure period, plotted with exposure time. Data points are coloured according to exposure time (as in the profile graphs Figure 4.18). Insert shows same data for exposure times less than 40 days.

times bleached the signal significantly, it then increases for the middle slices, where the shorter exposure times have not resulted in a large depletion of the signal, and for the final slices it is almost constant except for the largest exposure times, where it decreases again. Interestingly, the blue stimulated signal from quartz is, for the first slice, the signal that has bleached the least. Even the pIRIR$_{290}$ signal appear to have been better bleached. From slice 6 and deeper, both the blue signal from quartz and the post-IR signals are not significantly affected by any of the exposures.
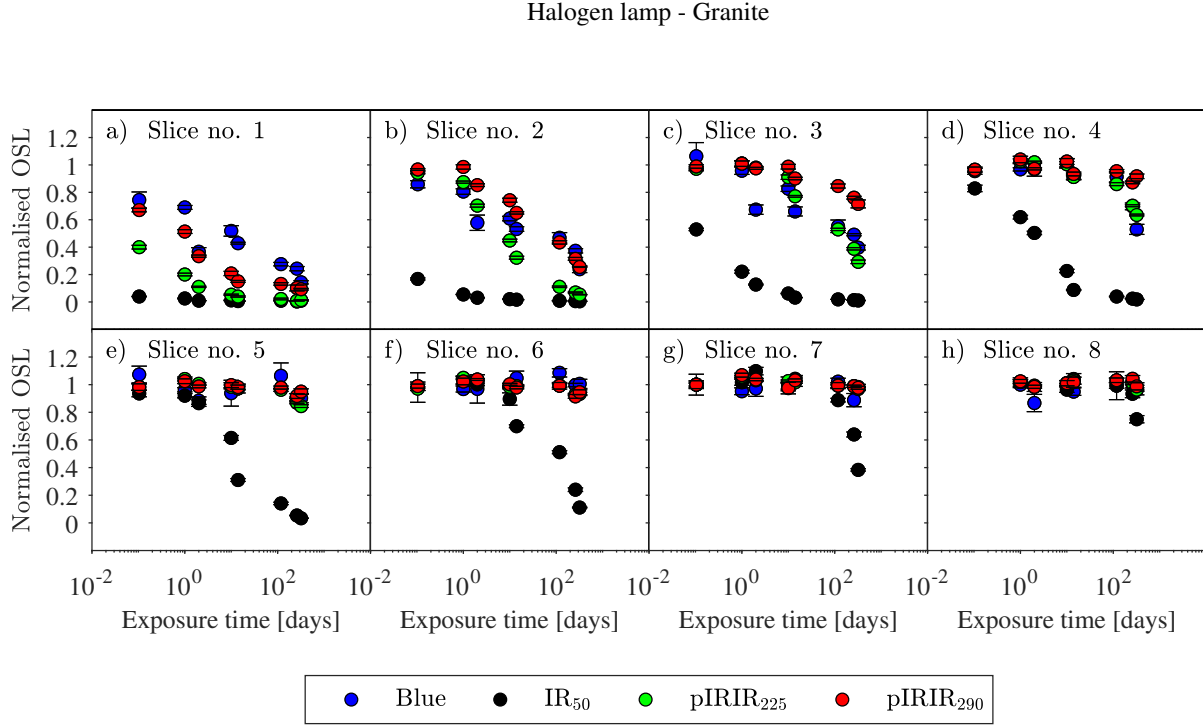
Figure 4.21: Luminescence values (L_n/T_n) normalised to the saturation level from halogen lamp-exposed granite samples slice number 1 to 8 (a to h) as a function of known exposure time. The four signals are shown in blue (quartz), black (IR$_{50}$), green (pIRIR$_{225}$), and red pIRIR$_{290}$.
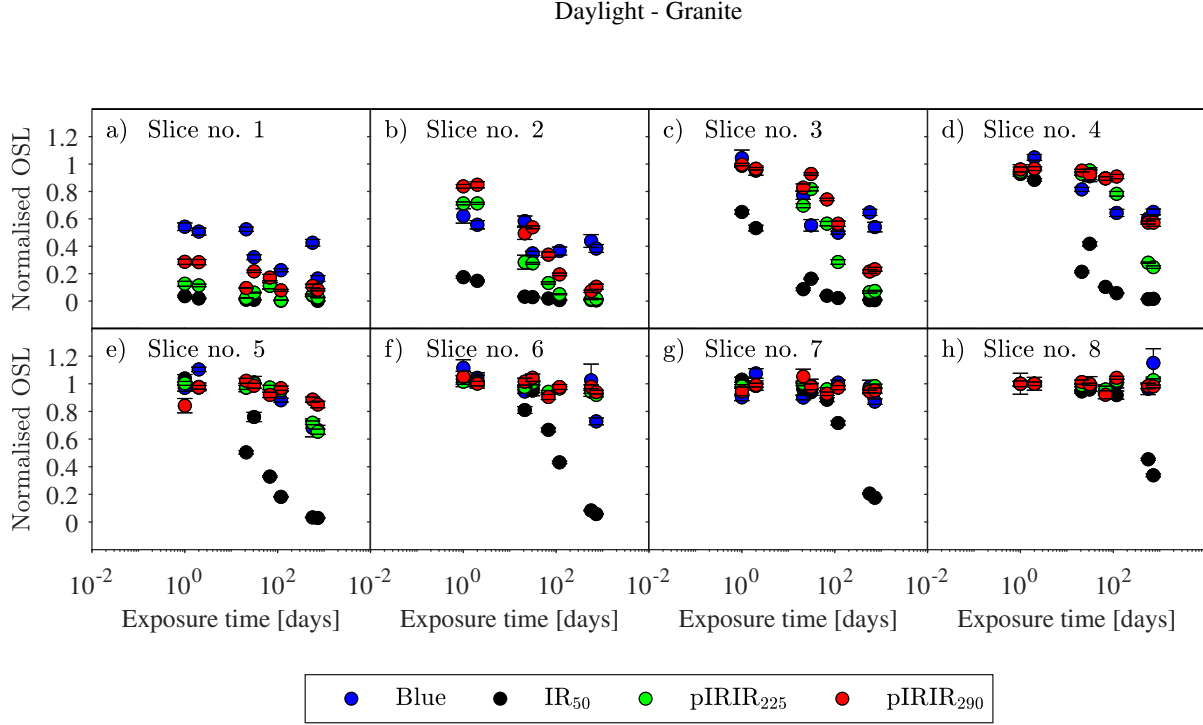
Daylight - Granite

Figure 4.22: Luminescence values (L_n/T_n) from daylight-exposed granite samples for slice numbers 1 to 8 (a to h) normalised to the saturation level and plotted as a function of known exposure time. The four signals are shown in blue (quartz), black (IR$_{50}$), green (pIRIR$_{225}$), and red pIRIR$_{290}$.

Fitting parameters

When using fitting parameters from a known exposure profile as calibration for an unknown profile it is implicitly assumed that the light attenuation coefficient μ and $\overline{\sigma\varphi_0}$ did not change with depth and wavelength[42]. This assumption gives an detrapping rate constant $E(x) = \overline{\sigma\varphi_0}e^{-\mu x}$ with μ and $\overline{\sigma\varphi_0}$ being constants. However both fitting parameters show a depth dependency as discussed below.

Figure 4.23 shows these depth dependencies for $(\overline{\sigma\varphi_0})_a$ (estimated from $(\overline{\sigma\varphi_0}t)_a/t_{\mathrm{known}}$) from halogen-lamp exposure and daylight exposure (a and b) and for the apparent light attenuation coefficients μ_a (c and d). The derived fitting values are plotted against their respective inflection points $x_{0.5}$ ($n(x_p) = 0.5$). The apparent value of $(\overline{\sigma\varphi_0})_a$ (photons per day) decreases with depth for all signals, except the IR$_{50}$ signal in the halogen-lamp-experiment (Figure 4.23a). A similar trend is observed in the daylight experiment, although there the values of $(\overline{\sigma\varphi_0})_a$ for the IR$_{50}$ data do appear to systematically decrease (Figure 4.23b; note the logarithmic scale on the y-axis). The effective photons per day from feldspar (full horizontal lines) and quartz (broken lines) are also shown, derived from the product of φ[114] and σ[58,111] (see red and blue curves in Figure 4.3 for the product $\varphi\sigma$ for the halogen exposure. A similar calculation was made for the daylight exposure using the data presented in Figure 4.1 and 4.2) summed over discrete wavelength intervals, coloured according to wavelength (see legend). The sum over all wavelengths are shown as a black lines. Profile fitting underestimates the $(\overline{\sigma\varphi_0})_a$ integrated over the full spectrum by orders of magnitude. However IR$_{50}$ only underestimates by one order of magnitude in the halogen exposure. Integrating
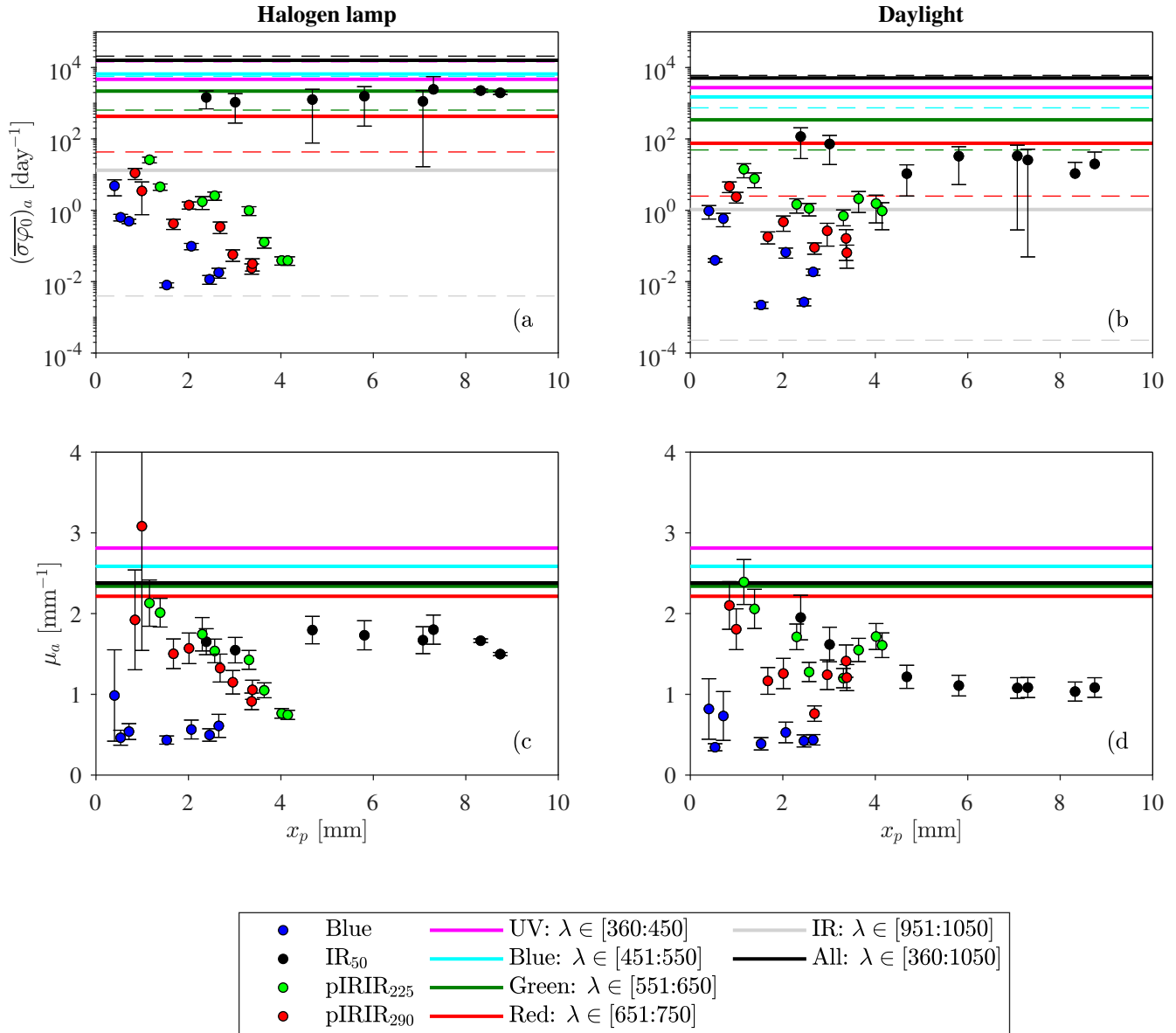
Figure 4.23: Estimated fitting parameters $\overline{\sigma\varphi_0}$ and μ from fitting with the general order model sharing the order amongst the profiles for same signal (IR_{50}, $pIRIR_{225}$, and $pIRIR_{290}$, shown as black, green, and red, respectively), and from fitting the quartz profiles (blue points) with the first order model. These parameters are plotted against estimated inflection points x_p satisfying $n(x_p)=0.5$. a), c) Halogen-lamp exposure experiment, and b), d) Daylight exposure experiment. Horizontal coloured lines in a) and b) represent spectrometer measurements of φ times σ for feldspar[58] summed over discrete wavelength intervals (indicated by colours). The sum over all wavelength are shown as a black line. Corresponding values using the cross section for quartz[111] are shown with broken lines. Similarly, horizontal lines in c) and d) represent measured values of attenuation coefficient by measuring absorbance with photo-spectrometer, averaged over discrete wavelength intervals.

only the longest wavelengths do make the two estimates closer for post IR signals and blue (see the grey line for IR wavelengths (951-1050)) and IR_{50} overestimates $\overline{\sigma\varphi_0}$ for this integration interval. The IR_{50} data in the halogen exposure are closest to the values from green light in the halogen exposed sample (a) and red light in the daylight (b) (although the uncertainties are large). This could reflect the effect of $\mu(\lambda)$ being larger for shorter wavelengths, thus changing the spectrum with depth so only longest wavelength penetrate to deeper depths.

All samples, daylight and halogen lamp exposed, did receive more effective photons of shorter wavelength. As these shorter wavelength photons suffer from higher attenuation (see Figure 4.4), it is likely that these do not penetrate very deeply into the surface. Thus, although more photons are received, in particular to quartz, not many are effective at resetting the quartz signal at depth. Furthermore the estimated light attenuation coefficient μ_a decreases with depth for the post-IR signals in the halogen lamp exposed samples, although no significant change with depth is observed for either IR_{50} or blue signals. In the daylight-exposed samples, a decrease with depth is seen for all feldspar signals, although again there is little or no change in the blue quartz signal. Similar observations of the depth dependency of μ_a have been reported before [e.g. 65,74,76]. This could reflects that the physical meaning of μ estimated from fitting, are others than attenuation.

Using the known number of incident photons $\overline{\sigma\varphi_0}t$ (from the spectra) resulting from the different exposure times, the fitting parameters can be re-evaluated. The fitting parameter $\overline{\sigma\varphi_0}t$ is expected to be proportional to the actual number of incident photons and follow a 1:1: line. However, this is not observed (see Figure 4.24a,b; 1:1 line shown as a solid black line with $\pm10\%$ lines) for neither the halogen lamp exposure nor the daylight exposure. μ would not be expected to change with number of incident photons and the observed decrease is presumably related to other light effects as discussed above.

Nevertheless higher numbers of incident photons results in a deeper penetration of the bleaching profile. This is shown in Figure 4.24c,d, where the inflection point x_p is plotted against the logarithm of $\overline{\sigma\varphi_0}t$ obtained from the spectra, the published cross-sections and the known exposure time. These two quantities are expected to be linearly correlated, which can be seen by isolating x in Eq.(4.3) and Eq.(4.4) for first and G.O.M, respectively, i.e.

$$x_{p,1} = \frac{\ln(\overline{\sigma\phi_0}t)}{\mu} - \frac{\ln(\ln(2))}{\mu} \tag{4.16}$$

$$x_{p,n} = \frac{\ln(\overline{\sigma\phi_0}t)}{\mu} + \frac{\ln\frac{(g-1)}{(0.5^{1-g}-1)}}{\mu} \tag{4.17}$$

where $n_1 = n_m = 0.5$. Indeed, the expected linear relationship is observed in Figure 4.24c,d, and estimated μ from Equation 4.16 and 4.17 are seen as broken lines in e) and f), showing significant different values from parameter estimates of μ. Thus, the profiles penetrate with time as expected, but the fitting parameters behave unexpectedly and possible in correlation.
Regardless of the light source (daylight or halogen light), a given number of photons has the same effect on the profile penetration depth. This could be of importance when generating experimental calibration profiles: illuminating samples with very high intensity light would presumable give a new approach to calibrating the time of exposure of field samples.
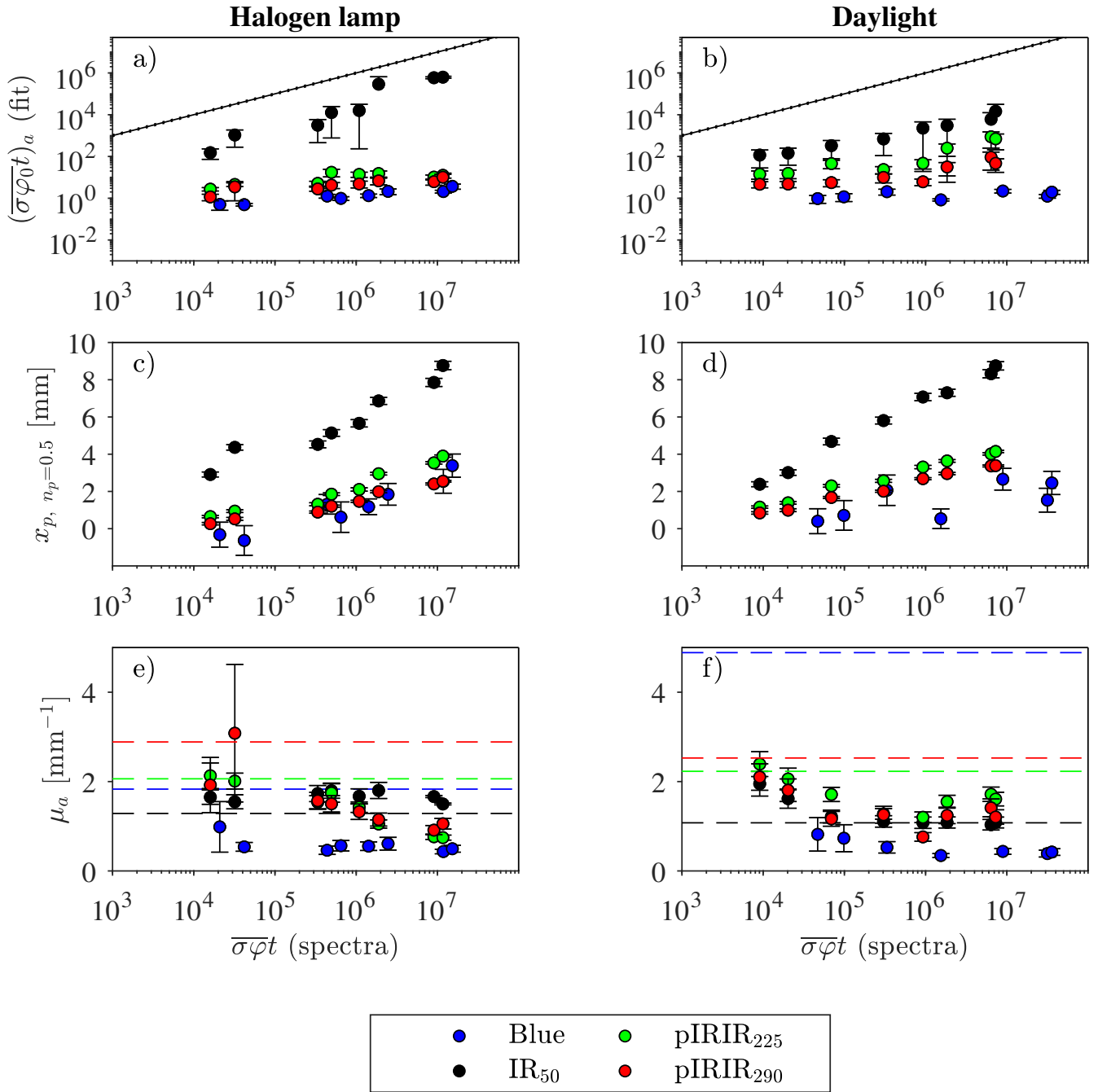
Figure 4.24: Various fitting parameters plotted as a function of $\overline{\sigma\varphi_0}t$ estimated from the halogen spectrum (a,c,e) and the daylight spectrum (b,d,f). Fitting used the first order model for quartz (blue) and the G.O.M. (with shared order for individual signals) for IR_{50} (black), $pIRIR_{225}$ (green), and $pIRIR_{290}$ (red). a),b) estimates of fitting parameter $\overline{\sigma\varphi_0}t$. c),d) Inflection depths x_p, where the luminescence level is 0.5, e), f) apparent light attenuation coefficient μ_a. Horizontal broken lines are the inverse on the slope of a plot like c) and d) but with the natural logarithm as base instead of log10 base, see Equation 4.16 and 4.17.

4.5.3.1 Exposure time estimation

Using each of the luminescence profiles from the granite samples in turn as a calibration profile for the other profiles, gives information on whether the model is able to estimate an unknown exposure time - apparent exposure time estimates are obtained from this method. Here we investigate whether ratios of apparent exposure time t_a to actual time t depend on the calibration time by comparing such ratios obtained using different profiles as "calibration" and different profiles as "unknown" profiles.

Often in rock surface exposure dating a calibration profile younger than an unknown profile is used. The effect on estimated apparent exposure times using such calibration profiles is seen on linear scales in Figures 4.25 and 4.26. It is observed that for these profiles using calibration profiles with known age of <20% of the age of the unknown profile, the age will be underestimated by more that 50% using the first order model when fitting. The improvement in using G.O.M. (second columns) when fitting compared to the first order model (first columns) is only particular significant for the IR_{50} profiles exposed to the halogen lamp. Here more estimates are close to the known age regardless of which profile is used as calibration. In this case, when the calibration profiles have a known age of <20% of the 'unknown', the calculated ages are over-estimated by up to $\sim 200\%$, rather than under-estimated as was seen above. In the daylight-exposed samples most ages are underestimated in both fitting methods. From the plots in these two figures it seems that there is a tendency to underestimate the age using first order, and sometimes using G.O.M..

To explore this further Figure 4.27 shows plots of $\ln \frac{t_a}{t}$ vs. $\ln \frac{t_{cal}}{t}$ using first order fitting (Eq.4.3) (a, c, e, and g) and using general order fitting (Eq.4.4) (b, d, f, and h) for Blue, IR_{50}, $pIRIR_{225}$, and $pIRIR_{290}$ signals from halogen lamp exposed samples. If the model predicts the profiles correctly, no dependency on calibration time should be observed, and thus the slope of these data should be zero. When fitting an inappropriate model to luminescence exposure depth data, we showed analytically (for assuming first order) and from simulated data (assuming first order or general order) in Chapter 3 that a linear relation as shown was expected. This is because the fitting parameter μ compensates for an inappropriate chosen model, and that μ determines the speed of progression (see Chaper 3 for details.)

Assuming first order (a, c, e, and g) a calibration time dependency is observed, i.e. the slope is positive for all signals. This implies that using a calibration time lower than the unknown time will underestimate the exposure time and visa versa using older calibration profiles. Using the general order model the situation improves, at least for the IR_{50} signal from the halogen-lamp exposed samples. However, for the $pIRIR_{225}$, and $pIRIR_{290}$ data sets we still observe a significant dependency on calibration time.

Corresponding plots from the daylight exposed samples are shown in Figure 4.28. Here the same trends are observed. Open black circles and squares represent the data arising from the sample exposed for 31 days in November, when it is used as a calibration profile (open circles) or as an unknown profile (open squares). This is done to show that, in particular in the IR_{50} data set this samples results in over or underestimation more than the other samples, presumably because the light intensity it did receive was significantly different than the others.

The results of the best linear fit to the data of Figure 4.27 and 4.28, and to the corresponding
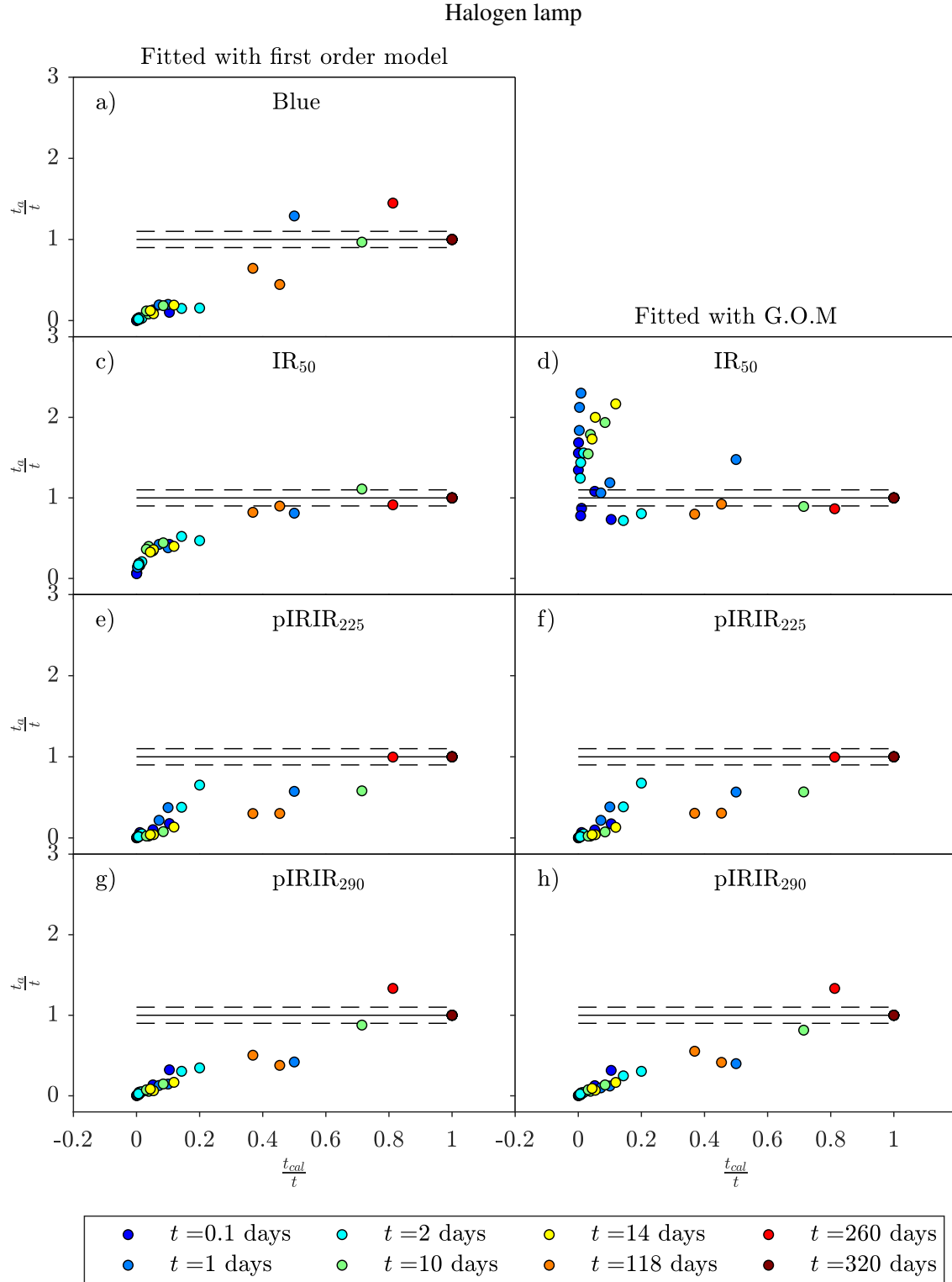
Figure 4.25: Apparent time to actual exposure time $(\frac{t_a}{t})$ for the halogen lamp data as a function of calibration time to actual time $(\frac{t_{cal}}{t})$ for first order fitting (a, c, e, and g) and general order fitting with shared order (b, d, f and h) to Blue (a, b), IR$_{50}$ (c, d), pIRIR$_{225}$ (e,f), and pIRIR$_{290}$ (g,h) signals. Data points are coloured according to the exposure time used for calibration.

Figure 4.26: Apparent time to actual exposure time $\left(\frac{t_a}{t}\right)$ for the daylight data as a function of the ratio of calibration time to actual time $\left(\frac{t_{cal}}{t}\right)$ for first order fitting (a, c, e, and g) and general order fitting with shared order (b, d, f and h) to Blue (a, b), IR_{50} (c, d), $pIRIR_{225}$ (e,f), and $pIRIR_{290}$ (g,h) signals. Data points are coloured according to the exposure time used for calibration.

Figure 4.27: Logarithm of the apparent time to actual exposure time in halogen lamp $(\ln \frac{t_a}{t})$ as a function of the logarithm of calibration time to actual time $(\ln \frac{t_{cal}}{t})$ for first order fitting (a, c, e, and g) and general order fitting with shared order (b, d, f and h) to Blue (a, b), IR$_{50}$ (c, d), pIRIR$_{225}$ (e,f), and pIRIR$_{290}$ (g,h) signals. Data points are coloured according to the exposure time used for calibration. Note the Blue y-axis is different from all IR y-axes

Figure 4.28: Logarithm of the apparent time to actual exposure time in halogen lamp ($\ln \frac{t_a}{t}$) as a function of the logarithm of calibration time to actual time ($\ln \frac{t_{cal}}{t}$) for first order fitting (a, c, e, and g) and general order fitting with shared order (b, d, f and h) to Blue (a, b), IR_{50} (c, d), $pIRIR_{225}$ (e,f), and $pIRIR_{290}$ (g,h) signals. Data points are coloured according to the exposure time used for calibration. Open black circles and squares surrounds the data points arising from the sample exposed in 31 days in November when used as a calibration profile (open circles) or as an unknown profile (open squares). Note the Blue y-axis is different from all IR y-axes

data, fixing orders g ranging from 1 to 4, tells how model-dependent this discrepancy is, and are summarised in Figure 4.29 for both the halogen lamp exposed samples (a) and the daylight exposed samples (b). For all signals the slope is positive at low order but decreases and becomes negative with increasing order. The order identified from stimulation curves is shown as coloured circles, and the most appropriate order resulting from free fitting by crosses (with shared order). Only when the lines cross the horizontal dotted line at $\frac{d\ln(t_a/t)}{d\ln(t_{\text{cal}})}) = 0$, are the results independent of the choice of calibration time. The IR_{50} data set from the halogen-lamp-exposed samples (black points in Figure 4.29) is almost independent of calibration time when the nonlinear fitting tool is allowed to find the optimal order without constraint (marked as a black cross). The estimated apparent times depend on the calibration time for the other signals, regardless of assumed orders in the range 1 to 4. For daylight exposure, none of the apparent exposure times are independent of calibration time, although it appears that the three IR data sets are independent of calibration time for orders of $\sim$ 3.8, 3.2, and 3.5. However, this is most likely to be a reflection of the poor fits to the data at high order - this observation is regarded as a result of the spread in the data, rather than a true linear relation.

We next evaluate the goodness of the fits. Figure 4.29c shows how the average fitting regression standard error (reduced chi-squared, $\chi_\nu^2 = \chi^2/\nu$, see Section 4.5.1) varies as a function of g. Notice that the lowest value (i.e. the best fit) is found for an order indistinguishable from the order estimated when letting the order be free, but shared among the profiles of the same signal. This indicates that only for the IR_{50} signal from the halogen-lamp-exposed samples does the best fit result in the expected time relationships between the profiles (see Figure 4.29a). For the daylight-exposed samples, neither of the signals gives the expected, known time relationship when one calibration profile is used to calibrate an unknown profile. It is concluded that the estimated exposure times are model dependent and furthermore that even choosing the correct model may result in an incorrect time estimate.

This is illustrated in Table 4.7, where the profile exposed to 260 days of the halogen lamp has been calibrated using the profile obtained after 10 days of exposure to the halogen lamp i.e. the ratio between the "unknown" exposure age and the "known" calibration profile age is 26. For the blue signal, we have fitted using the 1st order model and here we determine the apparent exposure age t_a to be less than 10% of the actual exposure age of 260 days (i.e. the exposure age was estimated to be 21 ± 7 d). The IR signals have all bee fitted using the G.O.M., and similar large underestimations are observed for the post-IR signal, although with very large estimates of uncertainty. For the IR_{50} signal, the absolute value of the apparent exposure age is twice that of the known exposure time, but again there is a very large estimate of uncertainty of $\sim$300 %.
For the daylight exposed sample, we have chosen the "unknown" profile, for this illustration, to be the one exposed outside for 566 days and the calibration profile to be the one exposed to 21 days, i.e. the ratio between the "unknown" exposure age and the "known" calibration profile age is 27. For the quartz (blue) signal (1st order model), the uncertainty is very large, but the uncertainty for three IR signals (G.O.M.) is a more reasonable 10-20%. However, all estimates of the exposure time t_a underestimates the actual time considerably, possibly with the exception of the $pIRIR_{225}$ signal which is just consistent at 95%. These are not very encouraging results and clearly a better method of exposure age determination is required.
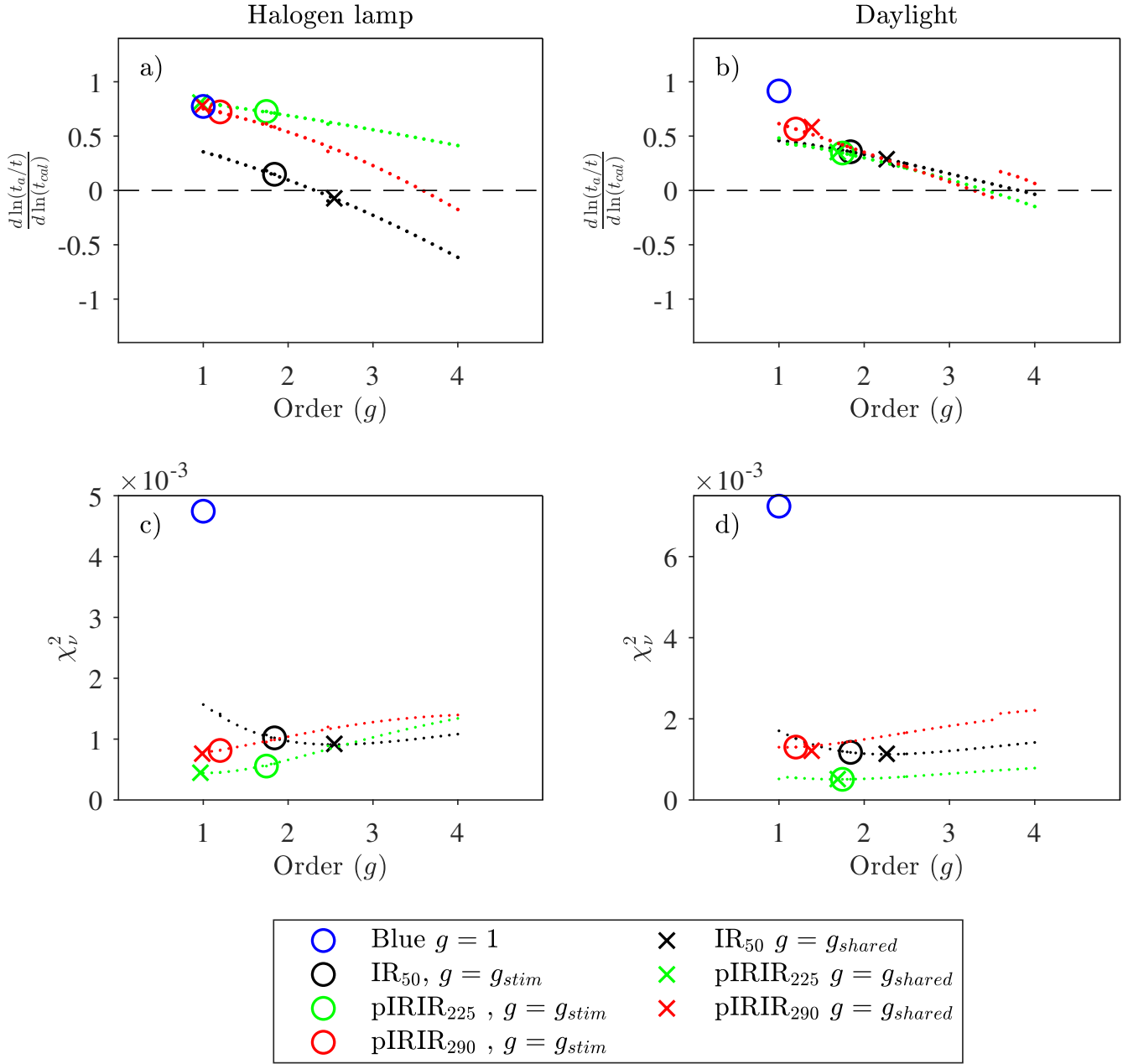
Figure 4.29: Change in the apparent to actual time with calibration time, i.e. $\frac{d\ln(t_a/t)}{d\ln(t_{\mathrm{cal}})}$) shown for different assumed orders for the three signals IR_{50}, $pIRIR_{225}$, and $pIRIR_{290}$, respectively in black, green, and red from samples exposed to a) halogen lamp and b) daylight. In c) and d) the average χ_ν^2 is shown for the 8 profiles, resulting from fitting with fixed order. χ_ν^2 from the shared order fit and decay order fit are shown as crosses and open circles, respectively in black, green, and red corresponding to the three signals.

Table 4.7: Exposure time recovery, i.e. the ratio of the apparent exposure time t_a to the known exposure time both for the Single profile calibration approach as well as the Exposure Response Curve (ERC) approach (see section 4.5.3.2). Results are shown for all four investigated signals in this work and for both halogen lamp and daylight exposure. The "unknown" profile for the halogen exposure was the sample exposed for 260 days, whereas the "unknown" profile for the daylight exposure was the sample exposed for 566 days. In the single profile calibration approach the calibration sample was exposed for 10 days ($Halogen_{10}$) or 21 days ($Daylight_{21}$). In the ERC approach all profiles (n=7, except the "unknown") was used for the calibration, i.e. $Halogen_{ERC}$ and $Daylight_{ERC}$, respectively.

Signal	Single profile calibration		ERC profile calibration	
	$Halogen_{10}$	$Daylight_{21}$	$Halogen_{ERC}$	$Daylight_{ERC}$
	t_a/t_{260}	t_a/t_{566}	t_a/t_{260}	t_a/t_{566}
Blue	0.08 ± 0.03	18 ± 53	0.91 ± 0.11	0.05 ± 0.10
IR_{50}	2 ± 3	0.2 ± 0.1	1.04 ± 0.05	0.73 ± 0.05
$pIRIR_{225}$	0 ± 2	0.6 ± 0.2	1.42 ± 0.05	0.79 ± 0.04
$pIRIR_{290}$	0 ± 2	0.3 ± 0.1	1.50 ± 0.04	1.04 ± 0.05

4.5.3.2   Depth of profile as calibration, ERC

In this section exposure ages are estimated from the progression of the depths of the profiles with exposure time. Profile depth is defined as that depth at which the latent luminescence signal has been reduced to 50% of the initial value, i.e. x_p. This depth is estimated either from the G.O.M. or from the first order model fits. Seven of the luminescence profiles are taken as known age and used to estimate the age of the remaining profile. In Figure 4.30 one such estimation is shown for all four signals. Profile depths x_p (luminescence level 0.5 of saturation level) are plotted against $\ln t_{known}$ for all profiles except that exposed to the halogen lamp for 260 days and that exposed to daylight for 566 days in a) to d) and (e) to h), respectively, as these two are used in this illustration as unknowns. The measured depth for these two "unknown" profiles (pink circles) are interpolated (dashed pink lines) onto the best linear fits through the data points from the "known age" profiles (i.e. full black lines). Similar interpolations based on first order model prediction of the 50% luminescence depth are also shown (blue dashed lines). The resulting exposure time recoveries are numerically given in Table 4.7. For all signals such Exposure Response Curves are model independent and with the exception of the quartz signal from the daylight exposure, all estimated values are within 50% of the known exposure times of 260 and 566 days, respectively. Although not perfect, this approach appear to obtain significantly more accurate and precise exposure estimates than the single profile approach, which has been used so far in rock surface dating.

Similar interpolations using each of the other profiles as "unknown" were undertaken, and the resulting estimated times are summarised in Figure 4.31. Here the two methods for estimating exposure times are compared. The resulting estimated exposure times are plotted against the known exposure time. Results using the profile depths for calibration are shown in a) to d) and using fitting parameters from one calibration profile in e) to h). The results from using the first order model and G.O.M. in fitting the profiles are shown with open circles and filled coloured circles, respectively. When the fitting parameter is used for calibration, estimates of exposure time are clearly model dependent, in contrast to when the profile depth is used. Then the exposure time estimates are essentially independent of the model. In Table 4.8 the average exposure time recoveries are shown for both F.O.M. and G.O.M fitting, i.e. here we average over all the exposure time recovery results obtained for the 8 profiles and compare them to the results obtained using
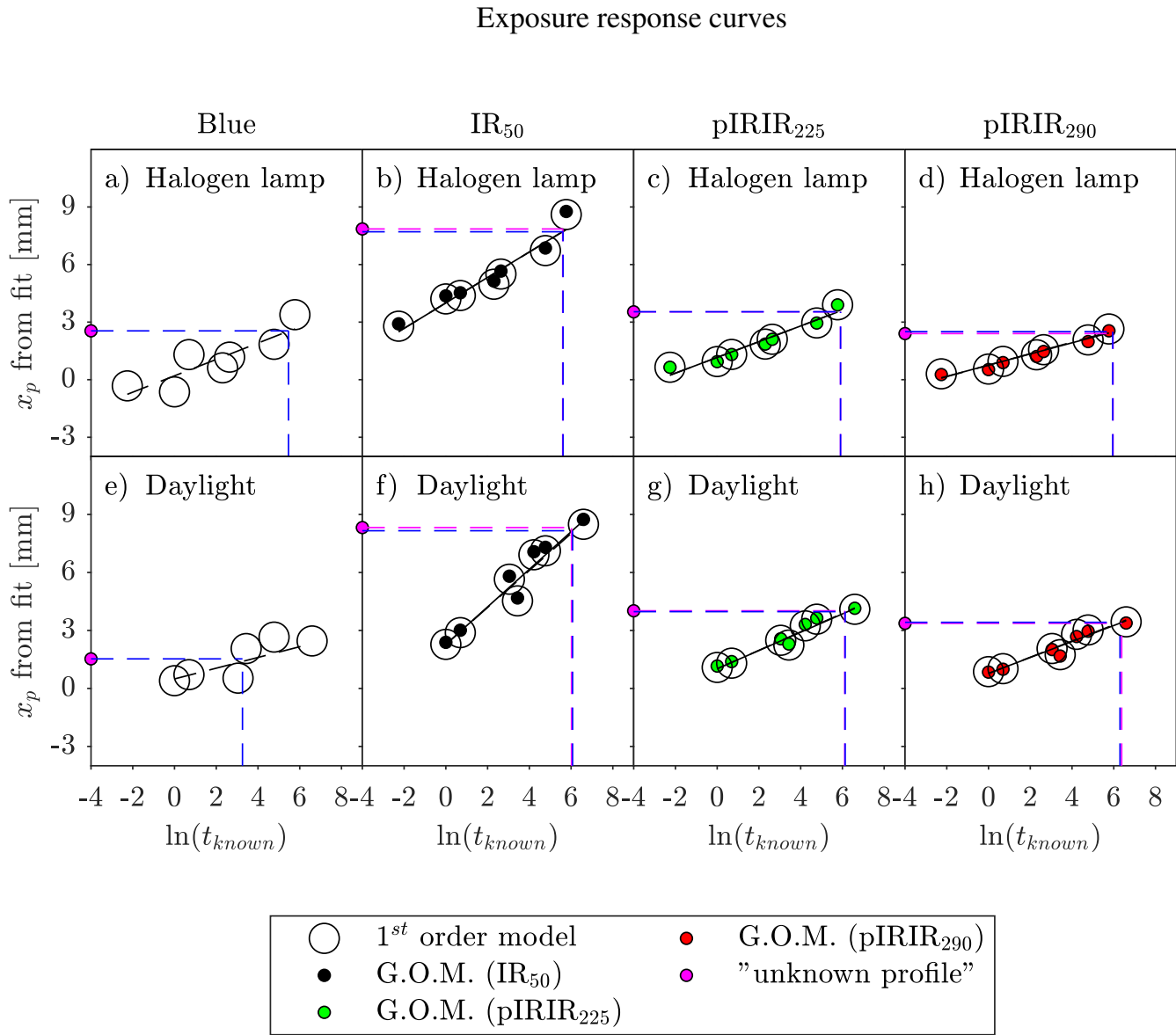
Figure 4.30: Exposure Response Curves from halogen lamp exposed samples (a-d) and daylight exposed samples (e-h) with x_p values (using $n_p = 0.5$) from fitting with first order (open circles) and from fitting with general order (closed circles) plotted against the logarithm of known time for Blue, IR_{50}, $pIRIR_{225}$, and $pIRIR_{290}$ signals. In this example, the 7th value (i.e. exposure times of 260 and 566 days for the halogen lamp and the daylight exposure, respectively) of x_p (taken as unknown, see pink circle) is interpolated onto the line defined by the known responses, full lines for G.O.M. and dashed lines from first order model.
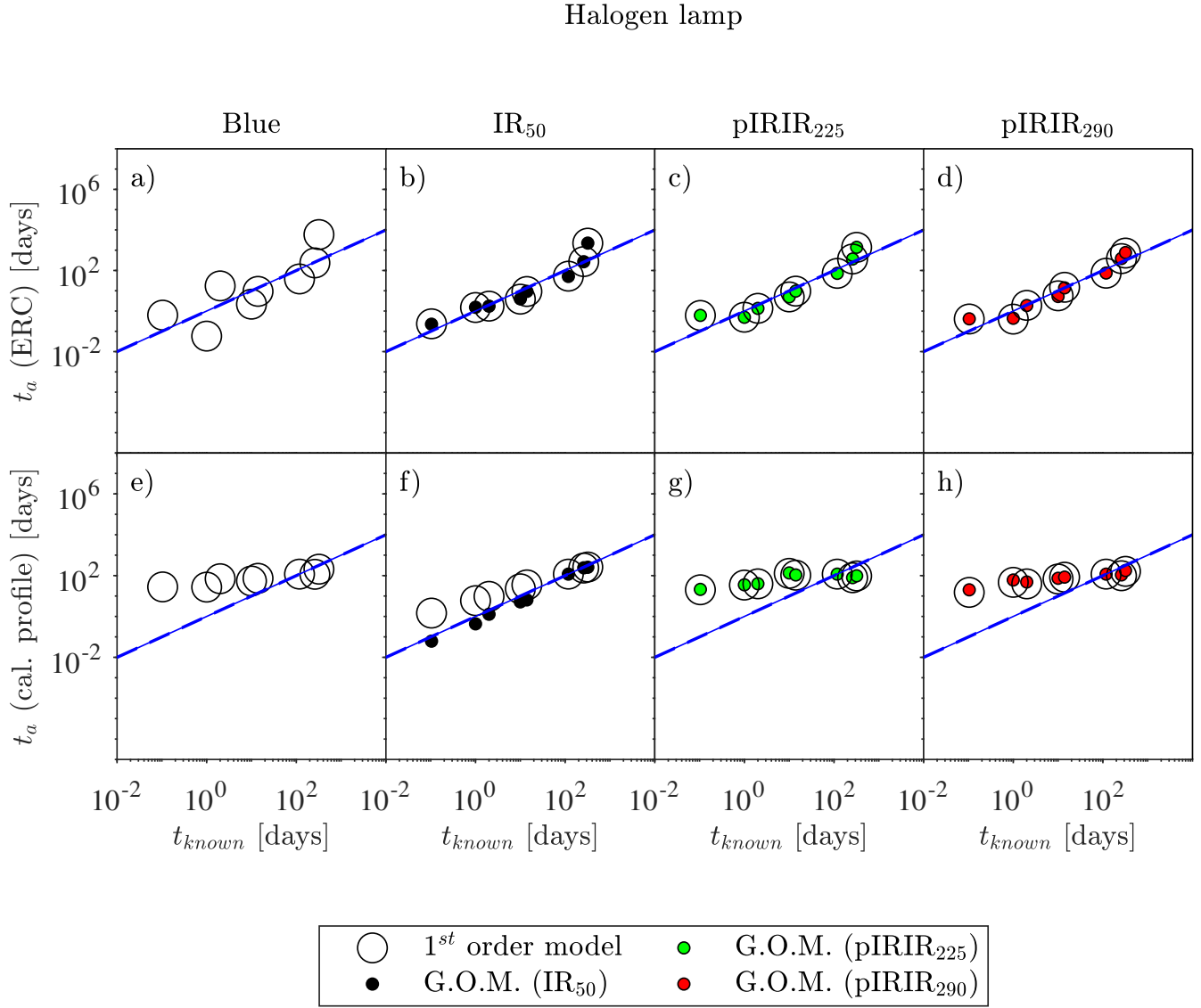
Figure 4.31: Halogen lamp exposures: a)-d) Estimated exposure days for each individual profile using all the other profiles to build an Exposure Response Curve. 1:1 lines are shown as dashed blue lines and ±10% with dotted blue lines. Linear fits to data points are indistinguishable from the 1:1 line both using first order fitting and general order fitting. e)-h) Estimated exposure days for each individual profile using the profile exposed for 118 days as calibration.
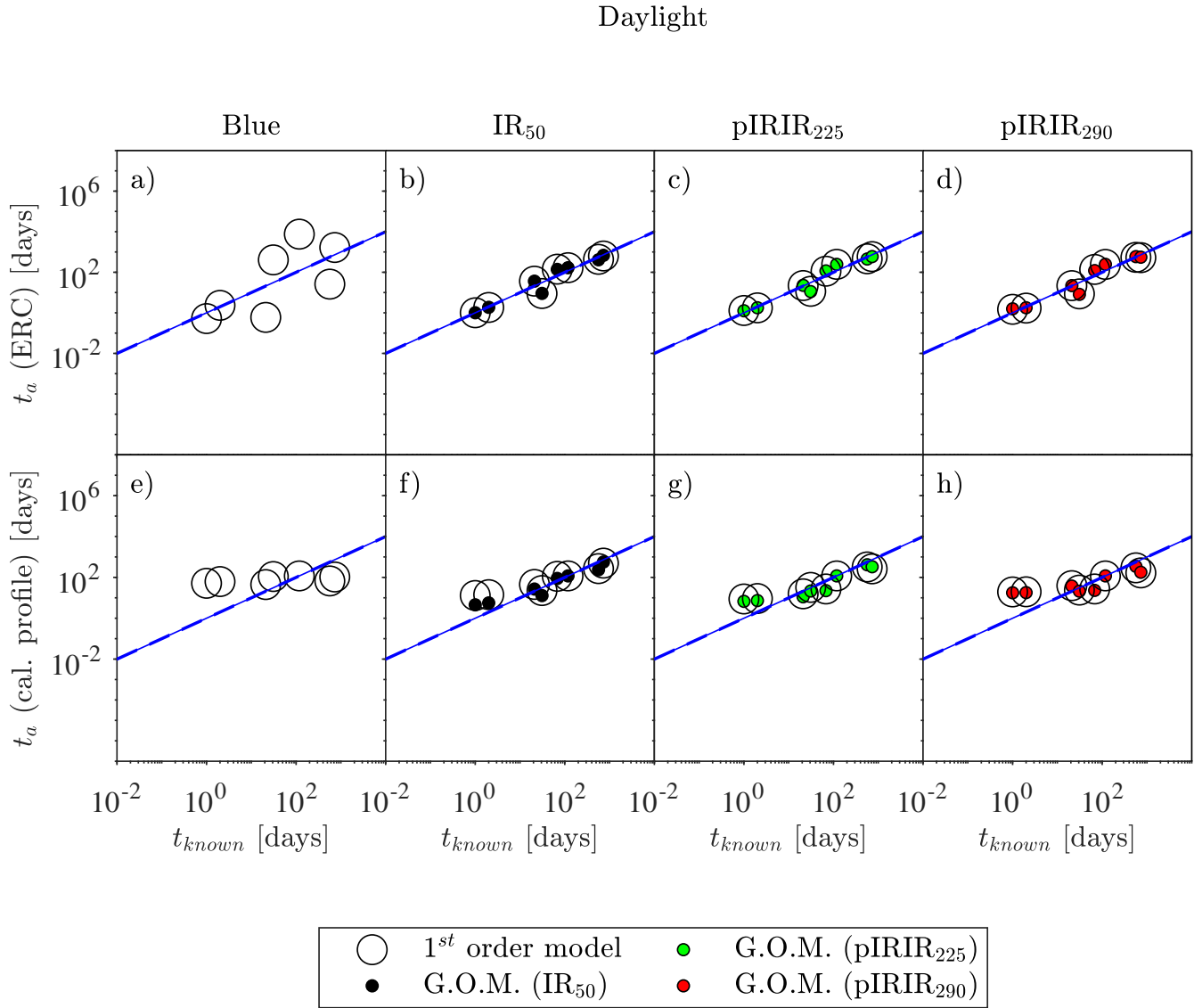
Daylight

Figure 4.32: Daylight exposure: a)-d) Estimated exposure days for each individual profile using all the other profiles to build an Exposure Response Curve. 1:1 lines are shown as dashed blue lines and ±10% with dotted blue lines. Linear fits to data points are indistinguishable from the 1:1 line both using first order fitting and general order fitting. e)-h) Estimated exposure days for each individual profile using the profile exposed for 118 days as calibration.

Table 4.8: Ratios of estimated exposure times to known exposure time using i) ERC curves for calibration and ii) a single profile as calibration. In both methods first order model (F.O.M.) and general order model (G.O.M. (IR signals)) was used to determine i) inflections points x_p ($n(x_p) = 0.5$) to be used in ERC calibration, and ii) to determine $\overline{\sigma\varphi_0}$ to be used in single profile calibration method. Here the results using the samples exposed for 118 days as the calibration profile are shown for illustration of the single calibration method.

	Halogen			
	ERC		Single cal.	
Signal	FOM	GOM	FOM	GOM
	t_a/t	t_a/t	t_a/t	t_a/t
Blue	2 ± 2	3 ± 2	43 ± 33	-
IR_{50}	1.8 ± 0.8	1.8 ± 0.8	4 ± 2	0.67
$pIRIR_{225}$	1.8 ± 0.7	1.8 ± 0.7	34 ± 23	35 ± 24
$pIRIR_{290}$	1.4 ± 0.4	1.4 ± 0.4	28 ± 18	37 ± 23

	Daylight			
	ERC		Single cal.	
Signal	FOM	GOM	FOM	GOM
	t_a/t	t_a/t	t_a/t	t_a/t
Blue	12 ± 8	17 ± 13	12 ± 7	-
IR_{50}	1.1 ± 0.2	1.1 ± 0.2	3.3 ± 1.6	1.6 ± 0.5
$pIRIR_{225}$	1.1 ± 0.2	1.1 ± 0.2	2.2 ± 1.1	1.8 ± 0.8
$pIRIR_{290}$	1.2 ± 0.2	1.2 ± 0.2	4 ± 2	4 ± 2

the single profile approach, where the calibrating profile is the profile exposed for 118 days (both halogen and daylight exposure). For the single profile calibration approach, the uncertainties are significantly greater than for the ERC approach (with the exception of the highly scattered quartz data) and also significantly more accurate regardless of the fitting model used.

4.5.3.3   Conclusions on controlled exposure experiments

The change in μ with depth is most likely caused by the different light attenuation processes in the samples - absorption (giving rise to luminescence), scattering and refraction. The latter two change the effective path-length compared to the apparent depth into the sample. As mentioned, the refraction index is lowest for the longer wavelength, thus letting for instance the red light pass in a more direct path. It is likely that shorter wavelength photons are more scattered and refracted at shallower near-surface depths compared to the longer wavelengths - effectively the shorter wavelengths have to travel further to reach a given depth, and so are more likely to be absorbed. This would explain first of all why IR_{50} profiles are bleached to greater depth than quartz profiles because IR_{50} signals are highly sensitive to the feldspar resonance peak at $\sim$860 nm. Furthermore it would explain the change in attenuation coefficient with depth: the shorter wavelengths are reduced in relative intensity compared to the longer wavelength because of, e.g. refraction. Then the effective μ is lower because μ decreases with wavelength.

In exposure dating, estimated exposure times are model dependent. Particular for IR_{50} profiles, using the G.O.M. improves the time estimation and the accuracy of a calibration for exposure

time estimation. However post-IR signals suffer from other processes that complicate exposure time estimation. The change in attenuation with depth, in particular, is more marked in post-IR signals. This is likely because post-IR signals are relatively more sensitive to high energy photons than IR_{50}. As discussed above, these high energy photons are most affected by scattering and refraction, and thus most likely to be absorbed. Then the photons still available deeper into the surface are of longer wavelength with lower attenuation. IR_{50} must suffer from the same effect, but as it is also sensitive to longer wavelength photons it is not as affected as the post-IR profiles.

An alternative approach to exposure dating is to avoid the difficulties caused by fitting parameter correlation, and instead plot inflection points as a function of the natural logarithm of known exposure times. The unknown exposure is then interpolated onto this exposure response curve (ERC). This method was suggested by Polikreti et al. [65] but has not been tested before, or used in practice. It has the limitation that it needs at least two known age samples, preferably bracketing the unknown age, and this is not commonly available in nature. However, it may be possible to prepare such profiles in the laboratory, using controlled exposure to intense simulated daylight. This approach has the considerable advantage that it is model independent.

4.6 Burial experiments

In this section, the multiple event model [3] including both exposure and burial events is tested. We ask whether i) a pre-burial profile can be accurately reconstructed from a profile that includes the effects of a burial dose, ii) after using some well-bleached criterion (see section 4.2.3) to identify that part of the profile that has been sufficiently bleached, the estimated burial dose is consistent with the expected dose, and iii) doses are estimated accurately, even if the profile is fitted with an inappropriate model (in this case, models of different order).

Three experiments are undertaken here, one with numerically simulated burial data and two experimentally simulated burial experiments: i) adding laboratory beta doses to aliquots from a pre-exposed profile, and ii) adding a gamma dose to a pre-exposed rock sample before sample preparation.

4.6.1 Simulated burial data

In this section, we use numerically simulated data to investigate if the use of an inappropriate model (i.e. using an incorrect value of g in the G.O.M. part of Equation 4.9) affects the estimate of the maximum depth for which the pre-burial profile was well-bleached and thus the burial dose estimate. The fitting models are

$$n_{1,1}(x,t) = n_{1,0}e^{-\overline{\sigma\varphi_0}te^{-\mu x}} \tag{4.18}$$

$$n_{m,1}(x,t) = [(g-1)\overline{\sigma\varphi_0}te^{-\mu x} + n_{m,0}^{1-g}]^{\frac{1}{1-g}}, \qquad (g>1) \tag{4.19}$$

$$n_{m,2}(x,D_e') = T + (1-T)\left([n_{m,1}(x,t)-1]e^{-D_e'}+1\right) \tag{4.20}$$

with T being thermal transfer expressed as a fraction of the saturation level. Using first order f´model $n_{m,1}$ becomes $n_{1,1}$. In use, all data are normalised to 'field' saturation (in these cases, the sensitivity-corrected luminescence from deep within the sample), so that $n_{1,0} = n_{m,0} = 1$.

A Monte-Carlo algorithm, using second order trap emptying kinetics, was used to generate simulated luminescence-depth data with a relative standard deviation of 1% and an absolute standard deviation for the saturated region of 5%. We simulated a slice depth of 0.5 (unit μ^{-1}), and 6 individual measurements per depth. The individual data points are the averages of the 6 simulated measurements and the assigned uncertainties are the associated standard errors. The exposure time $t' = \overline{\sigma\varphi_0}t$ ranged from e^4 to e^{20}, corresponding to exposure times of ~ 1 month to ~ 500 years with a value of $\overline{\sigma\varphi_0} = 1000$ ka^{-1} and $\mu = 1$. Thermal transfer is set to 5% of the saturated level, and burial fractions k range from 0.05 to 0.85. The burial fraction is the fraction of the light level at depth zero after burial, compared to the saturation level. The corresponding ratios of burial dose to D_c ($\frac{D_e}{D_c}$) range from 0 to 1.85 (see legend in Figure 4.33). All profiles were then fitted with the general order model (Eq. 4.20) sharing the order for all profiles for a given exposure time, and letting this order be fixed and vary to test the model dependency. Figure 4.33 shows the resulting profiles and 1$^{\mathrm{st}}$, 2$^{\mathrm{nd}}$ and 3$^{\mathrm{rd}}$ order model fits for an exposure time of $t' = e^{10}$. Not surprisingly, the 2$^{\mathrm{nd}}$ order model (coloured solid lines) visually fits the simulated data well for all depths, whereas the 1$^{\mathrm{st}}$ order model underestimates in the transition region between the visually apparent flat region near the surface and the steep part of the rising edge. On the other hand, the 3$^{\mathrm{rd}}$ order model (dashed black line) overestimates in the same region. This effect is more pronounced for smaller burial doses (i.e. small values of k).

The maximum depths for which the 2$^{\mathrm{nd}}$ order model indicates that the pre-burial profile was well-bleached using the bleaching criterion $B_{\mathrm{lum}} = 0.05$ (see section 4.2.3) are indicated by the pink vertical lines. As expected from the definition of the well-bleached depth, the depth identified as well-bleached increases with burial time (i.e. with increasing k). Visually, the well-bleached depths occur before the curve starts to rise from the burial plateau, i.e. the flat level near the surface.

Here, we want to investigate the effect on the estimated burial dose using the G.O.M. with g-values ranging between 1 and 2.6. In Figure 4.34a, the ratio of the maximum depth identified to be well-bleached (x'_{WB}) to the known well-bleached depth (actual x_{WB}) is shown as a function of the logarithm of the exposure time t' for the 1$^{\mathrm{st}}$ order model. For short exposure times (t') and small burial doses (i.e. small k), using the first order fit results in an overestimation of the well-bleached depth of 2.8 for the shortest exposure time ($\ln t' = 4$)) and the smallest burial dose (for $k = 0.25$). However, for long exposure times the ratio approaches unity regardless of the size of the burial dose.

In Figure 4.34b, this ratio is shown as a function of the order used in the modelling for a fixed exposure time $t' = e^{10}$. We observe that fitting with too low an order over-estimates the well-bleached depth by a factor of up to 1.33 for a burial fraction $k = 0.25$. This effect decreases with burial dose and exposure time. Assuming the correct order (i.e. 2$^{\mathrm{nd}}$ order: diamond symbols) gives a shallower well-bleached depth than the actual depth (ratio of ~ 0.9), presumably because of the uncertainty added to the individual data points. Assuming an order that is too high underestimates the well-bleached depth by up to 20% for the range investigated here. Again, the smallest burial dose causes the largest underestimation.
So in terms of depth, it is important to use the appropriate kinetic order when modelling the profile. However, the key question is how affected the estimated burial dose is when an inappropriate kinetic order is used in the modelling. This is investigated in Figure 4.34c and 4.34d, where the apparent well-bleached depths have been converted to burial doses ($D_{e,WB}$).
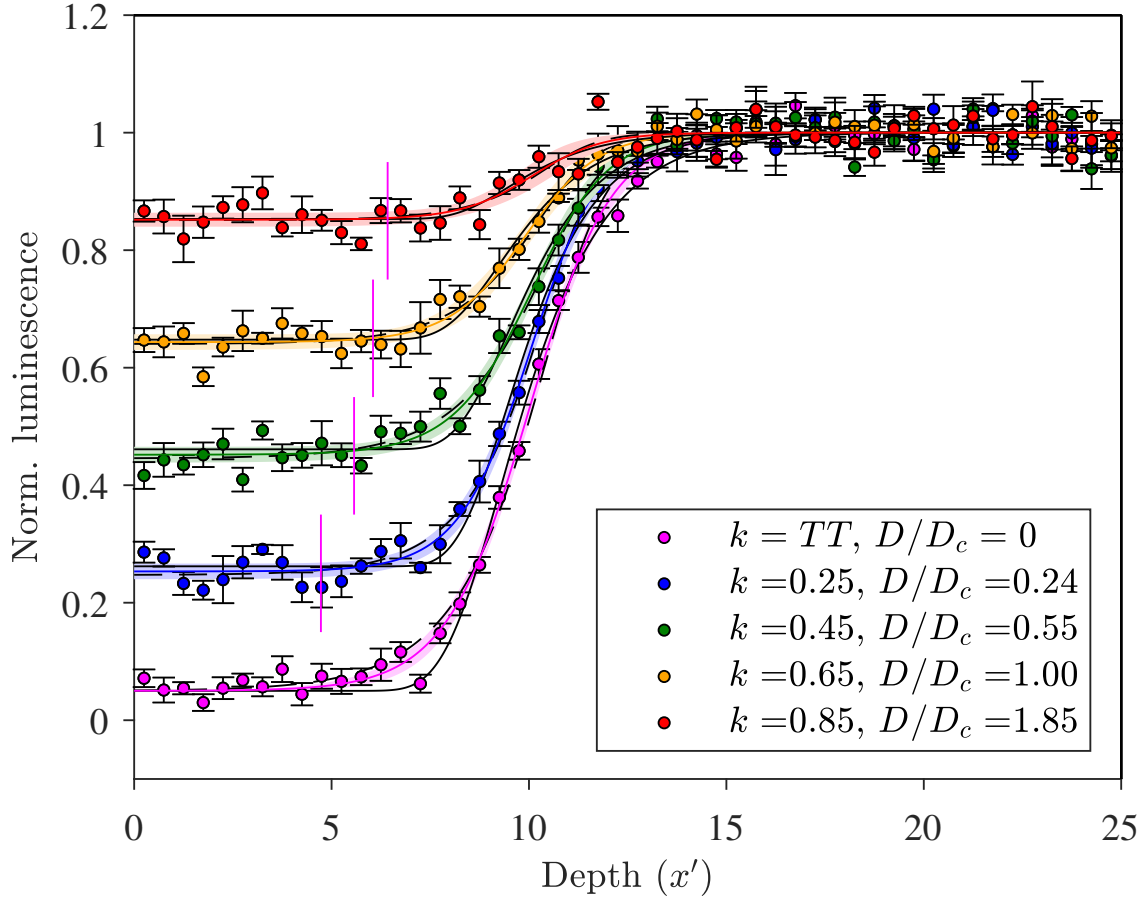
Figure 4.33: Simulated data assuming second order trap emptying kinetics. The individual data points are the average of 6 simulations using a relative standard deviation of 1% and an absolute standard deviation for the saturated region of 5%. The assigned uncertainty is the standard error of the 6 simulations. Data points are spaced by 0.5, the exposure time $t' = e^{10}$, thermal transfer is set to 5% of the saturation level, and burial fractions k range from 0.05 to 0.85. The corresponding ratios of burial dose to D_c range from 0 to 1.85 (see legend). All profiles are fitted using the general order model with shared parameters. Fitted curves are shown as coloured full lines, and the 95% confidence intervals are shown as shaded areas. The well-bleached depth from these fits, using $B = 0.05$, are shown as pink vertical lines. Also shown are the fits obtained using the first and $3^{\rm rd}$ order model (black solid and dashed lines, respectively).

For the first order fitting, the estimated burial doses are scattered and the majority overestimate the actual dose, but not by more than 12%, even although the maximum well-bleached burial depth was overestimated by a factor of 2.8. The data appears less scattered for large exposure times and the overestimation smaller. For the G.O.M. and a fixed exposure time of $t' = e^{10}$ (Figure 4.34d), an overestimation of the actual dose is observed for all orders used (1st order being the worst), but not by more than 6%. The overestimation becomes smaller the higher the order, but from a practical view point, the estimated well-bleached dose is largely insensitive to the kinetic order used.

In summary, assuming too low a kinetic order (e.g. first order) during model fitting will overestimate the well-bleached depth, but the overestimation decreases with increasing dose and exposure time. The resulting well-bleached burial doses estimated from the fitted curve overestimate the true burial dose, but only significantly for small doses and short exposure times.
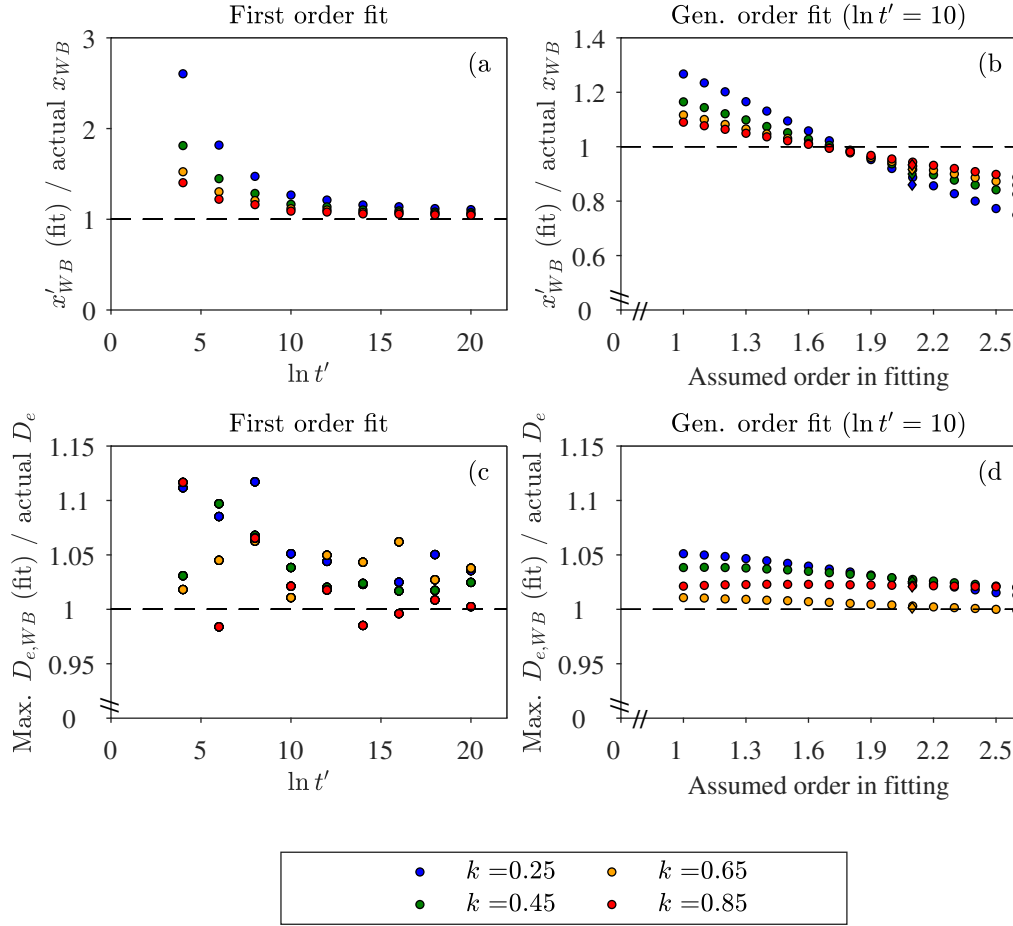
Figure 4.34: Effect on the estimated well-bleached depth and burial dose using the G.O.M. with kinetic order (g) ranging between 1 and 2.6 using 2nd order simulated data (see Figure 4.33 and text for details). a) The ratio of the depths determined to have been well-bleached at burial (x'_{WB}) using 1st order fitting to the known well-bleached depth (actual x_{WB}) as a function of previous exposure time. b) For a fixed exposure time of $\ln t' = 10$, the ratio of the depth determined to have been well-bleached at burial (x'_{WB}) to the known well-bleached depth (actual x_{WB}) as a function of the kinetic order used in G.O.M. c) The ratios of the well-bleached depths determined in a) converted to burial doses $D_{e,WB}$ to the known actual dose D_e as a function of the logarithm of the exposure time. d) The ratios of the well-bleached depths determined in b) converted to burial doses $D_{e,WB}$ to the known actual dose D_e as a function of the kinetic order used when fitting the G.O.M.

4.6.2   Experimental burial data

In this section, we experimentally investigate if we can accurately determine a laboratory dose added to an exposed granite profile and investigate whether the multiple event model predicts the burial profiles and the pre-burial profile sufficiently well. We use two approaches: i) adding different beta dose to individual aliquots extracted from different depths from a granite sample previously exposed for 730 days to the halogen lamp, and ii) adding 200 Gy and 500 Gy gamma doses to a granite sample previously exposed for 730 days to the halogen lamp.

4.6.2.1   Adding beta doses to aliqouts from halogen-lamp exposed samples

Here we experimentally investigate if we can accurately determine a beta dose added on top of an exposed profile, when the beta dose is given to individual aliquots in the OSL reader. For this purpose we make use of the granite sample that was exposed to daylight for 730 days (see Table 4.2). Sieved grains extracted from various depths between 0 and 17.5 mm were given beta doses ranging from 0 to 2266 Gy in the OSL Reader, before measuring the three signals, i.e. IR_{50}, $pIRIR_{225}$, and $pIRIR_{290}$. The residual doses prior to irradiation at the surface were 1.91 ± 0.14, 9.5 ± 0.9 and 25 ± 2 Gy. These data suggest the first mm is well bleached at least for IR_{50}. But as the definition of well-bleached depth also depend on given dose, these depths are estimated by modelling.

Figure 4.35 shows measured luminescence-depth profiles after irradiating grains extracted from the bleached profile with beta doses ranging from 35 to 2266 Gy in the Risø Reader. Also shown is measured luminescence-depth profiles from from the bleached profile with no irradiation, i.e. the true pre-burial profile (dark blue points). Three signals were measured, i.e. IR_{50}, $pIRIR_{225}$, and $pIRIR_{290}$ and these are shown in a), b) and c), respectively. Qualitatively, we observe an increase in the luminescence signals with given dose. As expected from the model distributions, this increase is largest for shallow depths, because the measured pre-burial profile was reset the most here. Given that the aliquots were measured immediately after irradiation, it is interesting to note that adding a dose of ~ 2.3 kGy does not bring any of the signals from depths less than ~ 5 mm in saturation, although the $pIRIR_{290}$ profiles are very close to saturation.

For 12 aliquots, full SAR dose response curves (DRCs) with regeneration doses ranging between 20 and 2000 Gy were measured. These DRCs were fitted with a single saturating exponential function, i.e. $L_x/T_x = A \times exp[-D/D_c]$, where D is dose and A is the saturation level. For the individual signals, these DRCs were very similar to each other and to save measurement time a common DRC was constructed by averaging the individual DRCs ($n = 12$). These common DRCs had the following parameters: i) IR_{50}: $A_{50} = 4.33 \pm 0.08$, $D_{c,50} = 566 \pm 16$, ii) $pIRIR_{225}$: $A_{225} = 2.98 \pm 0.04$, $D_{c,225} = 343 \pm 8$, and iii) $pIRIR_{290}$: $A_{290} = 2.4 \pm 0.04$, $D_{c,290} = 259 \pm 7$. The ratios of the natural saturation level of the profiles (average for 8 profiles) to that of the dose response curves (A) were 1.13 ± 0.04, 1.16 ± 0.03, and 1.18 ± 0.03, respectively for IR_{50}, $pIRIR_{225}$, and $pIRIR_{290}$ signals, indicating that the laboratory DRC had slightly lower saturation light levels than the profiles.

To extract quantitative information, we fit the data sets shown in Figure 4.35 using the general order model for burial (Equation 4.20 with assuming the luminescence L to be proportional with electron population n) while sharing the order for the profiles from each signal; the results of this fitting are shown with coloured solid lines and the 68% confidence bands are shown as shaded areas.

From the reconstructed pre-burial profiles ($L_1(x)$) the well-bleached depth x_{WB} was estimated using the criteria $0.05 < L_1(x_{WB})/L_2(x_{WB})$ (see section 4.2.3). These identified well-bleached depths are shown as vertical black lines in Figure 4.35. Note that not all pIRIR$_{290}$ profiles are sufficiently bleached to provide a well-bleached depth, only those with given doses of 283, 566 and 2266 Gy. In Figure 4.36, the same data sets are shown together with the modelled pre-burial profiles (black curves) and the actual (measured) pre-burial profiles (dark blue curves; also shown in Figure 4.35). The maximum depths identified as well-bleached from the modelled profile are indicated by vertical black lines. In general, the reconstructed pre-burial profiles are not significantly different from the actual pre-burial profiles for given doses less than 300 Gy, i.e. the grey and blue 68% confidence intervals overlap (exceptions are for the IR$_{50}$ signal at 71 and 142 Gy, but they overlap at 95% confidence). For given doses greater than 300 Gy, the observed and reconstructed curves begin to deviate significantly from each other.

To investigate how well the model is able to reconstruct the pre-burial profile, the difference in luminescence levels between the reconstructed pre-burial profile, $L_1(x)^{\text{Predicted}}$, and the measured pre-burial profile, $L_1(x)^{\text{Measured}}$, are plotted for every profile in Figure 4.37. If the reconstructed pre-burial luminescence level is smaller than the actual measured pre-burial profile luminescence, the well-bleached level and thus the dose will be overestimated, as doses from deeper depths are accepted with an actual residual greater than the criterion. Large residuals are observed for large given doses. The well-bleached depth is affected by this error in the reconstruction of several profiles (e.g. pIRIR$_{225}$ and pIRIR$_{290}$ with given doses of 566 Gy). However for the majority of the profiles, the residuals are only significantly different from zero at depths greater than the well-bleached depth, such that the prediction of the well-bleached depth is unaffected.

From the model fitting of the measured $L_2(x)$ profiles, we obtain estimates of the parameters $(\overline{\sigma\varphi_0}t)_{burial}$ and μ_{burial}. In the following we investigate how well these parameter estimates compare to those derived directly from the pre-burial profile, $L_1(x)$, i.e. $(\overline{\sigma\varphi_0}t)_{exp}$ and μ_{exp}. Parameter values are shown in Figure 4.38 and discussed below.

In Figure 4.38a, the ratio between $(\overline{\sigma\varphi_0}t)_{burial}$ and $(\overline{\sigma\varphi_0}t)_{exp}$ is plotted against the ratio of μ_{burial} and μ_{exp} and a linear correlation between the parameters is observed. A larger μ results in larger $\overline{\sigma\varphi_0}t$, as expected - a given profile depth depends on both the attenuation μ and the number of photons $\overline{\sigma\varphi_0}t$ at the surface. Thus, these two parameters are likely to correlate, i.e. errors in one "compensate" for errors in the other. The ratios for $(\overline{\sigma\varphi_0}t)$ and μ are also shown in c) and d) plotted against given dose. The ratio of $(\overline{\sigma\varphi_0}t)_{burial}$ to $(\overline{\sigma\varphi_0}t)_{exp}$ scatters significantly with an average ratio of 26 ± 25, 69 ± 61, and $(2 \pm 2) \cdot 10^3$ (n=7) for IR$_{50}$, pIRIR$_{225}$, and pIRIR$_{290}$, respectively (with medians of 0.5, 1.0, and 2.58). Particularly, the pIRIR$_{290}$ estimate for the sample given a dose of 566 Gy overestimates the value from the pre-burial profile by a factor of $\sim 6 \cdot 10^3$. In general, the difference between the two estimates increases with given dose. If we omit estimates derived from profiles given more than 300 Gy, the average ratios are 0.35 ± 0.04, 1.3 ± 0.3, and 0.6 ± 0.2 (n=4) for IR$_{50}$, pIRIR$_{225}$, and pIRIR$_{290}$, respectively.

The ratios of μ_{burial} to μ_{exp} are on average 1.04 ± 0.10, 1.03 ± 0.14, and 1.0 ± 0.2 (n=7) for IR$_{50}$, pIRIR$_{225}$, and pIRIR$_{290}$, respectively, when all profiles irrespective of given dose are included. Rejecting the high dosed samples does not make a significant difference; the average μ ratios become 0.87 ± 0.03, 1.00 ± 0.04, and 0.91 ± 0.07 (n=4) for IR$_{50}$, pIRIR$_{225}$, and pIRIR$_{290}$, respectively. The

Granite sample irradiated in reader
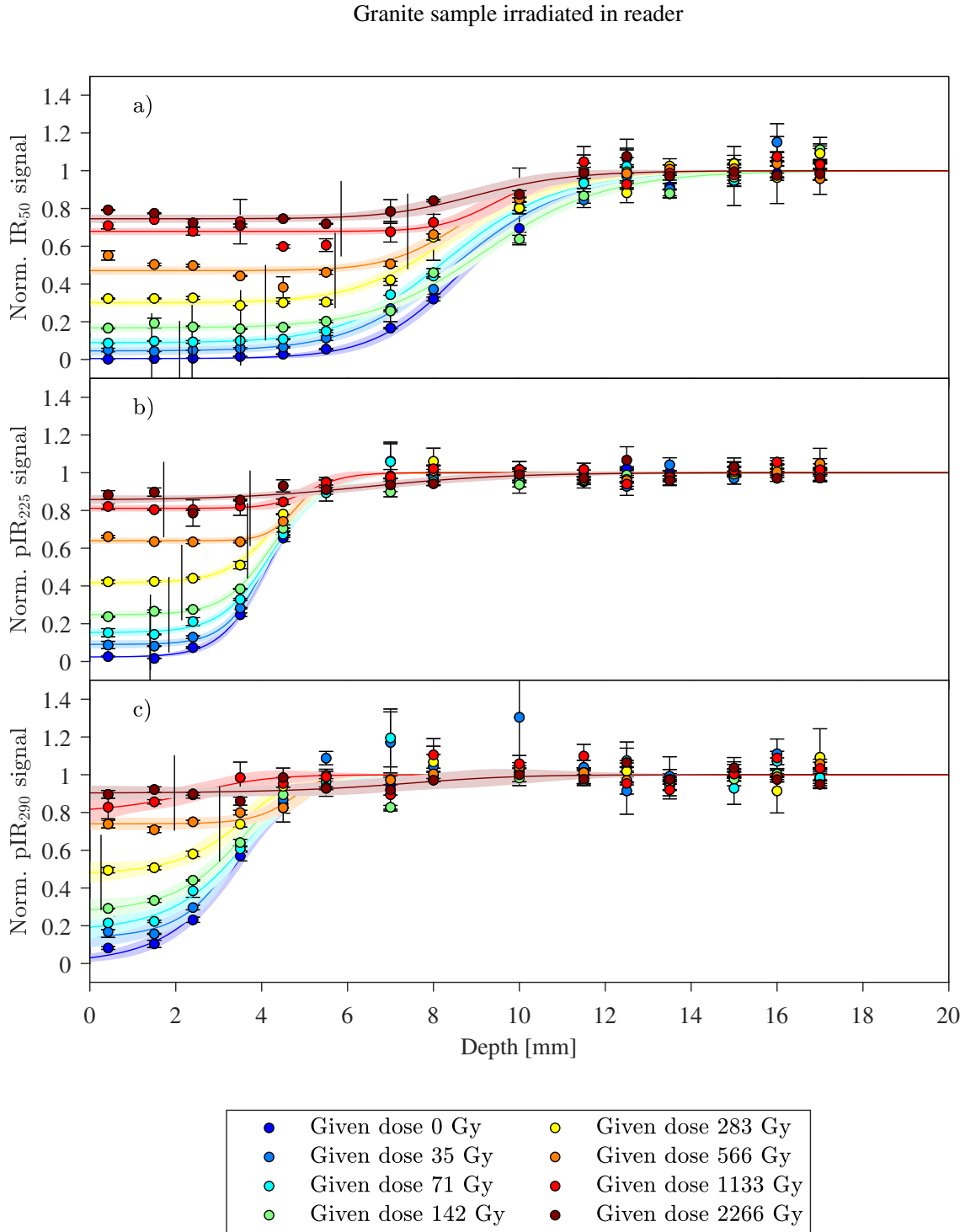
Figure 4.35: Luminescence-depth profiles after adding different beta doses to grains extracted from the daylight bleached profile (blue points). Three signal was measured: IR_{50}, $pIRIR_{225}$, and $pIRIR_{290}$, shown in a), b) and c), respectively. Results of fitting these data sets with the general shared-order model for burial, for each each individual signal are shown, together with 68% confidence bands (shaded areas). Vertical lines indicate well bleached depths determined using the criterion: $B_{lum} = 0.05$ and the reconstructed pre-burial profile.
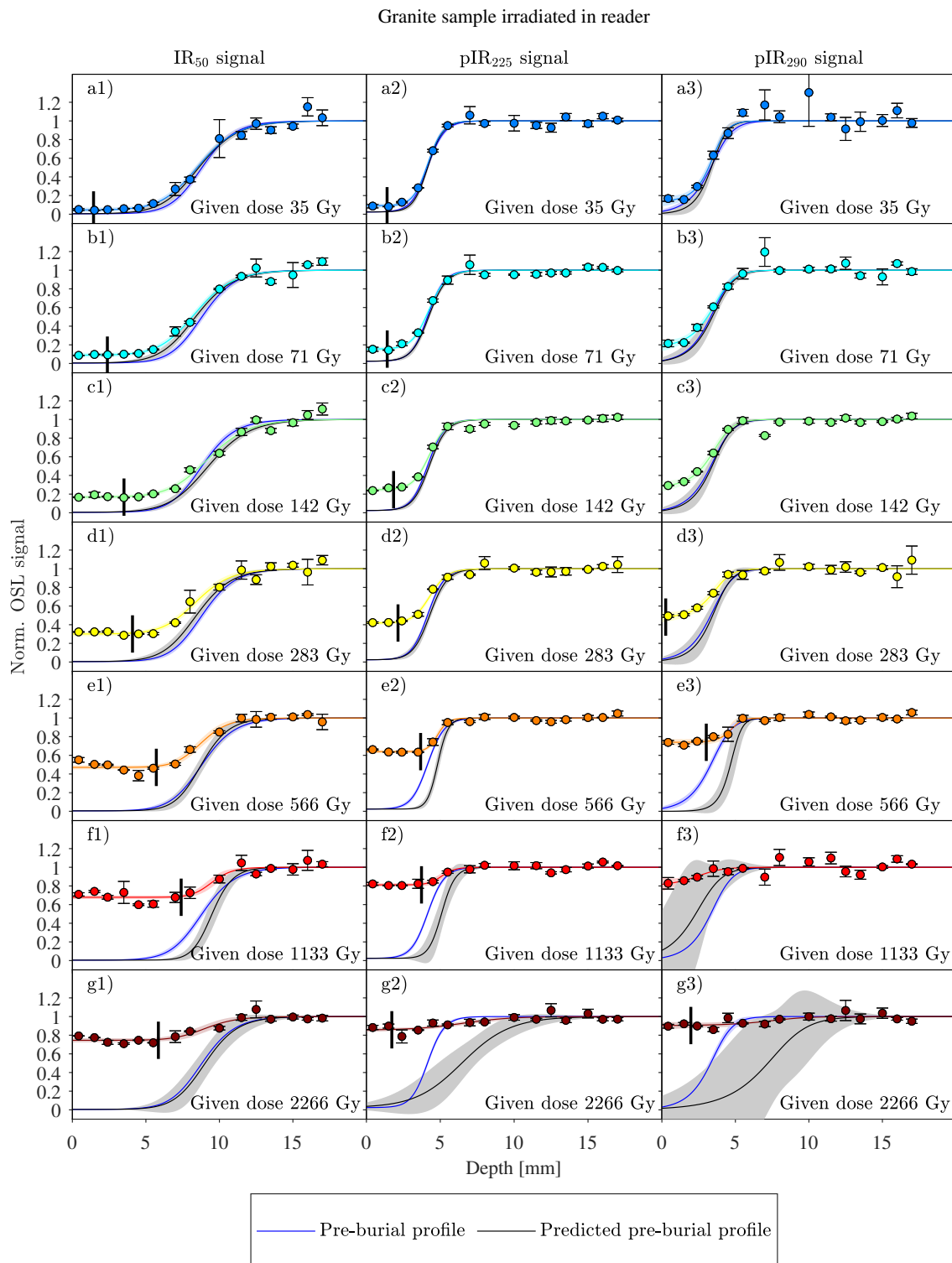
Figure 4.36: Same plots as in Figure 4.35 shown as individual profiles together with the reconstructed pre-burial profiles (black) and the actual pre-burial profile (dark blue - also shown in Figure 4.35). 68% confidence bands are shown as shaded areas. Vertical lines indicate well-bleached depths determined using the criterion: $B_{\mathrm{lum}} = 0.05$.
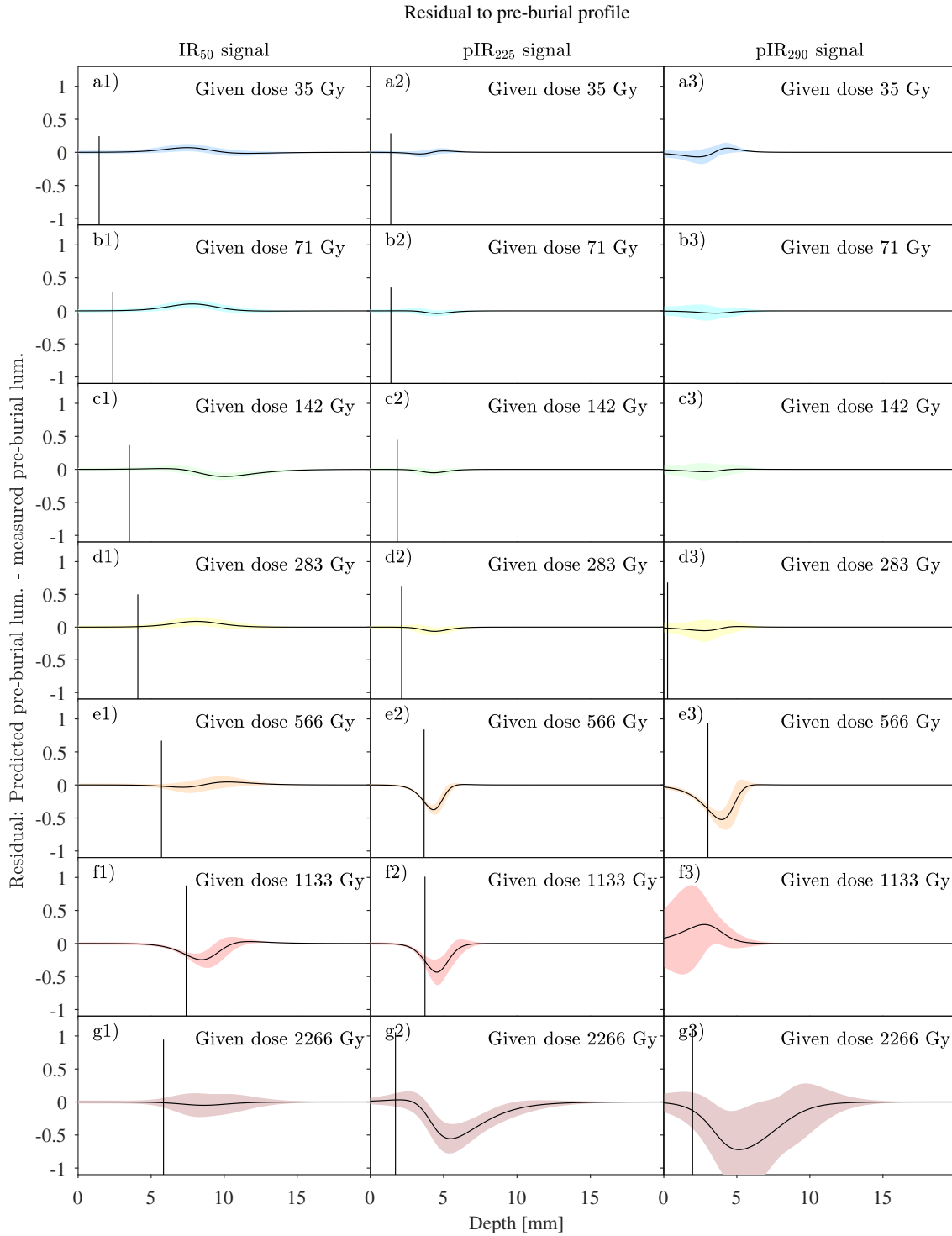
Figure 4.37: Residuals derived by subtracting reconstructed pre-burial luminescence levels (black curves in Figure 4.36) from measured pre-burial luminescence levels (dark blue curves in Figure 4.36). 68% confidence bands are shown as shaded areas. Vertical black lines indicate the well-bleached depths determined on the measures $L_2(x)$ profile by using the criterion: $B_{\mathrm{lum}} = 0.05$.

latter observation is consistent with the visual inspection of the profiles in Figure 4.36 as the slope of the profiles visually are similar for given doses<300 Gy.

Figure 4.38b shows the kinetic order estimated from fitting the profiles ($g_{profile}$) compared to the order estimated from fitting the IR stimulation curves (i.e. decay order, g_{stim}). Profiles from IR_{50} and $pIRIR_{225}$ signals. All estimated profile orders are consistent with the decay orders ($pIRIR_{290}$ within 2 standard errors though), although the uncertainties on the orders determined from the profile fitting have significant uncertainties, particularly for the $pIRIR_{290}$ signal.

Above, we observed that the reconstructed pre-burial profiles determined for $L_2(x)$ agree well with the actual pre-burial profile for given doses less than 300 Gy. Although, significant deviations do occur for given doses larger than 300 Gy, these are at depths which should not have a significant impact on the estimated well-bleached depths.
In the following we explore how well we are able to recover the known given doses. Using the SAR protocol the measured L_n/T_n values were converted to dose estimates making use of the common DRC. Figure 4.39a shows the ratio of the measured dose for the first slice ($D_{e(x=0)}$) to the known given dose (i.e. the dose recovery ratio) as a function of given dose. The dose recovery ratios systematically underestimate unity but becomes consistent with unity for larger doses. The average dose recovery ratios for the three signals are 0.81 ± 0.03 ($n = 6$), 0.80 ± 0.05 ($n = 6$), and 0.59 ± 0.07 ($n = 5$).
Figure 4.39b shows the dose recovery ratios obtained by using the doses from depths determined to have been well-bleached ($D_{e,WB}$) using the G.O.M. in fitting with the order being free, but shared. Again, all three signals underestimate the known given dose (not including the individual uncertainties) and the underestimation is constant with given dose, giving average dose recovery ratios of 0.77 ± 0.02 ($n = 7$), 0.78 ± 0.02 ($n = 6$), and $0.78 \pm 0.15$ ($n = 2$) for IR_{50}, $pIRIR_{225}$, and $pIRIR_{290}$), respectively. If we compare these dose recovery ratios to those determine from the very first slice (see Figure 4.39c), then we find that the estimated doses agree well with each other. Thus, the observed underestimation of the dose recovery ratio is more likely to indicate a problem in our measurement protocol rather than a problem with the identification of which depths can be considered to be well-bleached.
As the dose measurements were made immediately after adding the burial dose, we do not expect anomalous fading to be the cause of the underestimation. It is possibly not surprising that an underestimation is observed, as it was also observed in the initial dose recovery experiments used to examine the luminescence characteristics of our samples, described in section 4.4. Figure 4.39d shows the dose recovery ratios using $D_{e,WB}$, but with a fixed kinetic order g in the G.O.M. fitting. The dose recovery ratios for IR_{50} and $pIRIR_{225}$ are independent of the order used, but for $pIRIR_{290}$ the ratios increase as a function of order. Thus, the underestimation is not caused by assuming an inappropriate order.

In the simulated data (section 4.6.1) we found that assuming too low an order when fitting resulted in an overestimation of the well-bleached depths x_{WB}, but also that the effect of this on dose estimation was not significant. This is supported by our experimental observations described above. Nonetheless, it is interesting to explore by how much the well-bleached depths vary as a function of assumed order. This is done in Figure 4.40, which shows x_{WB} as a function of order between 1 and 3, for the three signals and the 7 given doses. The well-bleached depths decrease with order, as was seen in the simulated data. However, we do not observe a decrease in estimated
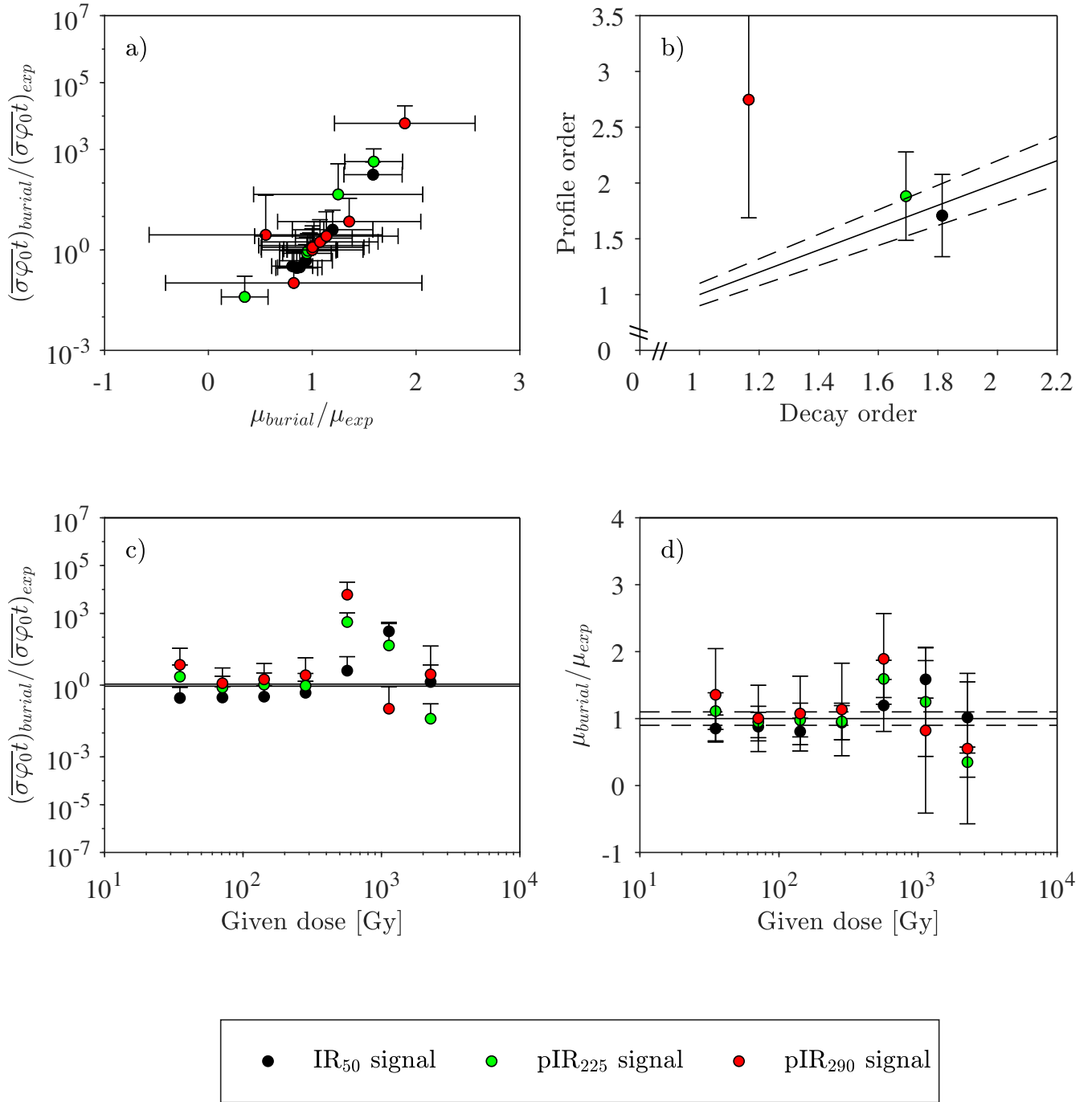
Figure 4.38: Fitting parameters obtained from fitting the general shared-order model among the profiles of the same signal (i.e. IR_{50}, $pIRIR_{225}$, and $pIRIR_{290}$). a) Correlation between fitting parameters $\overline{\sigma\varphi_0}t$ and μ, b) Estimated kinetic order obtained from fitting luminescence-depth profiles plotted against the order estimated from decay curves. The 1:1 line is shown with 10% uncertainty lines. c) Ratio of estimated value for $\overline{\sigma\varphi_0}t$ from profiles given a burial dose $((\overline{\sigma\varphi_0}t)_{burial})$ to the value estimated from the pre-burial profile before dosing $((\overline{\sigma\varphi_0}t)_{exp})$. d) Ratio of estimated value for μ from profiles given a dose (μ_{burial}) to estimated value of μ from the profiles before dosing (μ_{exp}).
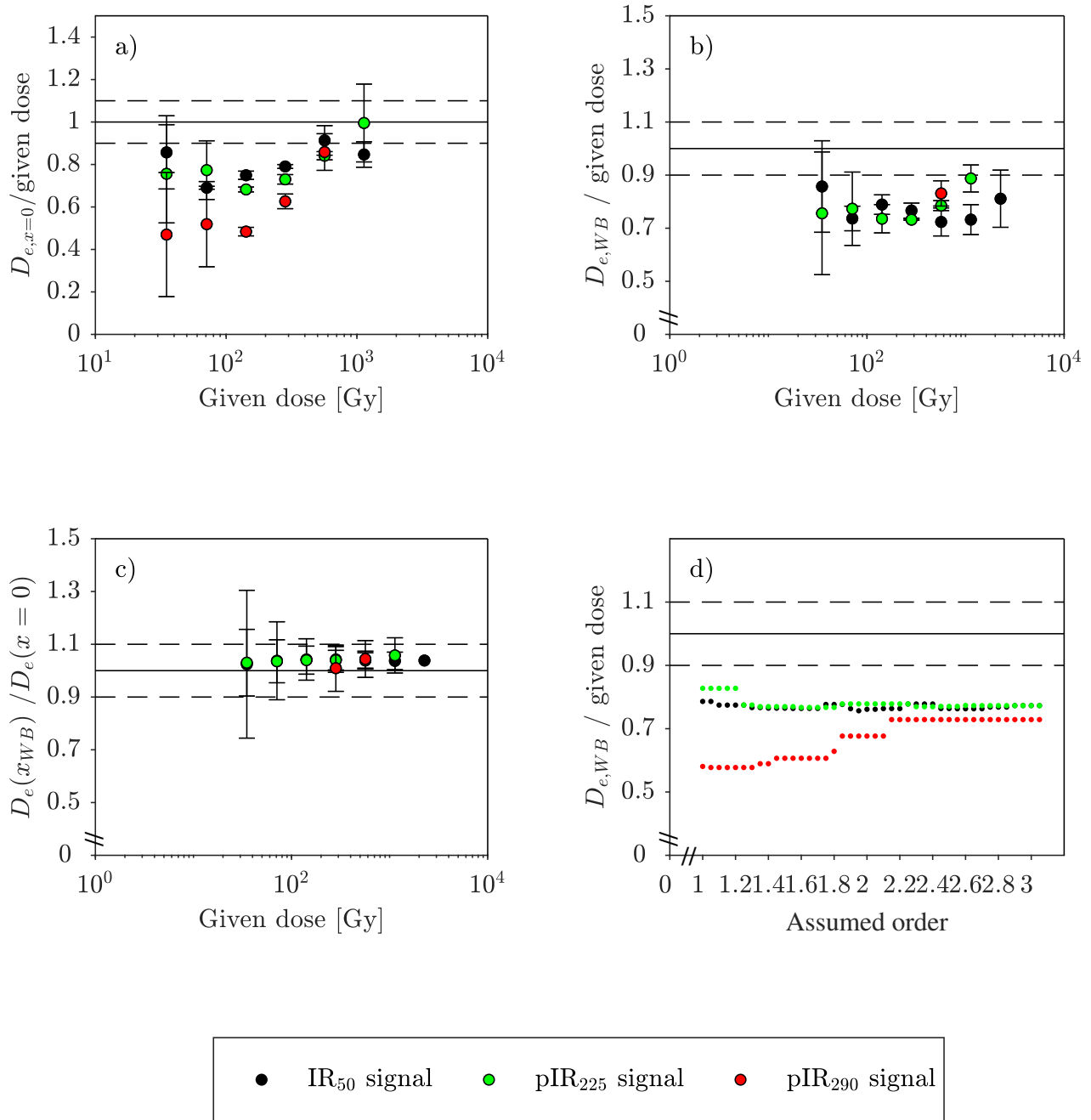
Figure 4.39: Granite beta dose recovery ratios (D_e/D_{given}) for three signals: IR$_{50}$ (black data), pIRIR$_{225}$ (green data), and pIRIR$_{290}$ (red data). The sensitivity corrected luminescence signals (L_n/T_n) shown in Figure 4.35 were converted to dose estimates using the common DRC (see text for details) and divided by the known given beta dose. Note that doses could not be estimated for all profile because of saturation effects, e.g. no dose could be estimated for pIRIR$_{290}$ for a given dose of 2.3 kGy a) Only doses from the first slice (x=0) are included in D_e. b) All dose estimates determined to be well-bleached (using the $B_{lum} = 0.05$ criterion) by shared free-order G.O.M fitting are included in the $D_{e,WB}$. The dose estimates have been corrected for thermal transfer as in a) (see section 4.4). Note that for pIRIR$_{290}$ only an estimate for a given dose of 566 Gy is given, because either no well-bleached depth could be determined (see Figure 4.37) or the L_n/T_n values could not be converted to doses because of saturation effects. c) Ratios of data presented in b) and a). d) Same as in b) but with a fixed assumed kinetic order g.
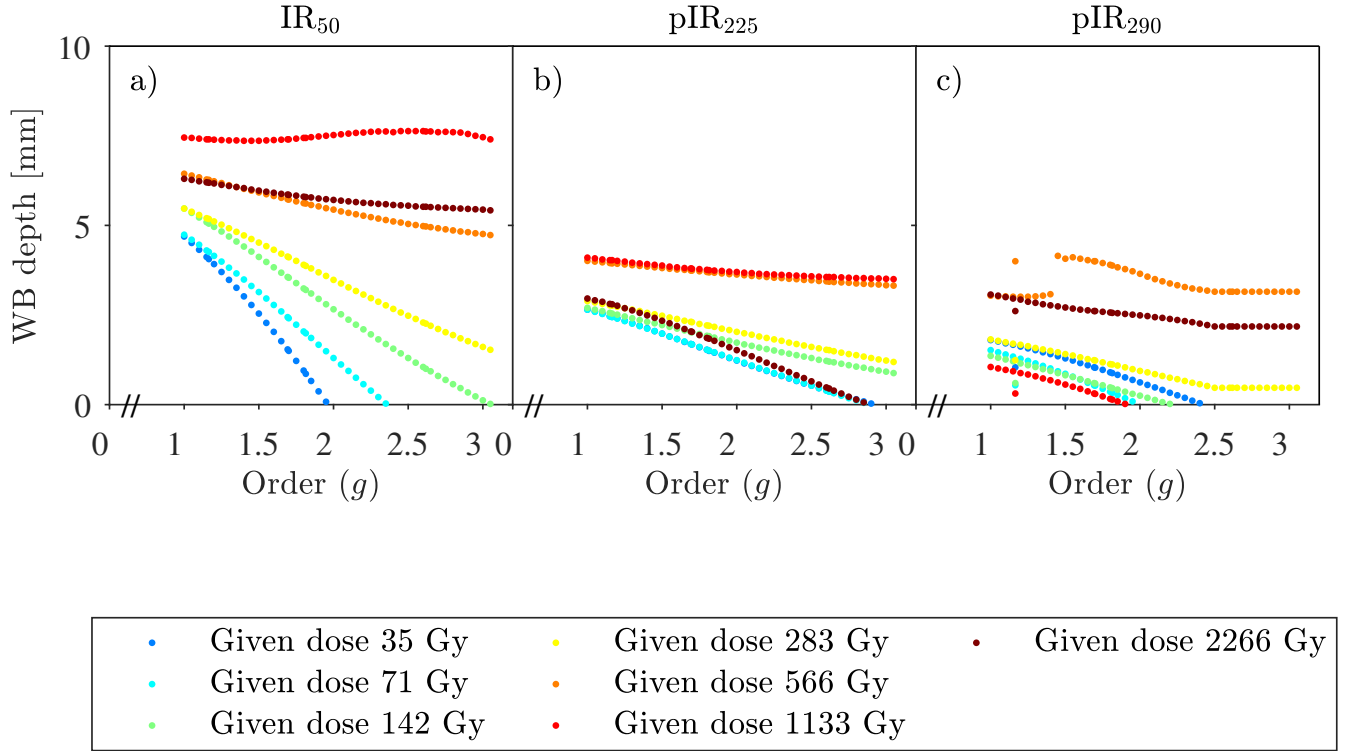
Figure 4.40: Well-bleached depths estimated from fitting with the general order model and a fixed order (from 1 to 3) for irradiated profiles, coloured according to irradiation.

dose with assumed order, and we conclude that even were we do use the first order model for feldspar profiles, this would not have a significant effect on the accuracy of the estimated burial dose. Whether the estimated dose is reliable in terms of e.g. fading is a separate question.

In the above, the multiple event model[(3)] has been modified to incorporate higher order kinetics and used to describe a luminescence-depth profile resulting from a single exposure and subsequent burial event. The individual fitting values obtained for $(\overline{\sigma\varphi_0}t)_{burial}$ and to a lesser degree μ_{burial} are scattered and poorly known. Nonetheless, it is possible to reconstruct the pre-burial profile accurately for given doses up to ~ 300 Gy. For doses greater than 300 Gy, the uncertainty on the prediction parameters becomes large ($>100\%$), and is presumably not useful for exposure time estimates. Nevertheless, the resulting accuracy and precision of the burial dose estimate is not different from that obtained at lower burial doses (see Figure 4.39).Assuming first order kinetics when fitting feldspar burial profiles does result in a significant overestimation of the the pre-burial well-bleached depth, but this does not significantly affect the burial dose estimate.

4.6.2.2   Gamma irradiation prior to sample preparation of granite sample

One granite sample was exposed to the halogen lamp for 320 days. Subsequently, part of the sample was i) measured directly (see section 4.5.3), ii) given a 200 Gy gamma dose before sample preparation (see section 4.3.3) and subsequent measurement, iii) given a 500 Gy gamma dose before sample preparation and subsequent measurement. Gamma irradiations were undertaken in a ^{60}Co gamma cell at DTU Health, and IR$_{50}$, pIRIR$_{225}$, and pIRIR$_{290}$ signals were measured from

all three profiles.

Figure 4.41 shows the measured luminescence-depth profiles after adding gamma doses of 0 Gy (blue points), 200 Gy (green points) and 500 Gy (red points). The IR_{50}, $pIRIR_{225}$, and $pIRIR_{290}$ profiles are shown in a), b) and c), respectively. As with the samples irradiated in the reader using a ^{90}Sr beta source, we qualitatively observe that the IR_{50} signal is reset furthest into the surface, and that the surface luminescence signal increases with given dose. To obtain a quantitative description, we fit these data with the general shared-order model for each individual signal (solid lines). The 68% confidence bands are shown as shaded areas. Using the resulting fitting parameters, the pre-burial profiles $L_1(x)$ were estimated. These are shown in Figure 4.42. From these profiles the well-bleached depth x_{WB} for each profile was estimated using the criterion $0.05 < L_1(x_{WB})/L_2(x_{WB})$. The resulting well-bleached depths are shown as vertical black lines in Figure 4.41. Note that no well-bleached depth could be determine for the $pIRIR_{290}$ signal for a given dose of 500 Gy, and for for a given dose of 200 Gy, the well-bleached depth only just includes the first slice.

In Figure 4.42, the same data sets are shown together with the reconstructed pre-burial profiles (G.O.M. black) and the observed pre-burial profiles (dark blue - also seen in Figure 4.41). For comparison, the pre-burial profiles reconstructed assuming 1st order kinetics are also shown, in pink. The reconstructed pre-burial profiles (G.O.M. black) differ to some degree from the actual pre-burial profiles (blue). The blue profile penetrates more than the reconstructed pre-burial profile for the sample given 200 Gy, but surprisingly is shallower for the sample given 500 Gy.
Employing the 1st order model results in deeper reconstructed pre-burial profiles. One can speculate that these observations may be due to problems with the reproducibility of the recorded depths, since the 3 cores were sliced independently of each other, or even the reproducibility of the rock itself, since the 3 cores were of necessity drilled at different locations in the same cylinder face. Vertical lines indicate the well-bleached depths predicted using the general shared-order model and the criterion $B_{lum} = 0.05$.

The differences between the reconstructed pre-burial profile and the actual pre-burial profiles(i.e. residual= $L_1(x)^{Predicted}$ - $L_1(x)^{Measured}$) against depth are shown in Figure 4.43. Again, we observe large residuals at depths deeper than the identified well-bleached depth. The well-bleached depth is significantly affected by this error in prediction, especially the $pIRIR_{225}$ well-bleached depth for the profile given 500 Gy. However in the IR_{50} signal and $pIRIR_{225}$ (200 Gy) the deviation from zero in the residuals happens at greater depths than the well-bleached depth, i.e. it does not affect the evaluation of the well-bleached depth from which reliable doses can be measured. At least part of these residuals may be caused by uncertainty in the depth assignment as the three profiles are sliced from three adjacent cores.

Dose estimates from the slices identified to be well-bleached are shown in Figure 4.44a. As the IR_{50} signal, in particular, is known to suffer from anomalous fading, fading correction was undertaken using two approaches:

i) NLS correction[47], where the measured doses are corrected with the ratio of the natural saturation level (the saturation level of the profiles) to the saturation level in laboratory dose response curves. These ratios are 1.05 ± 0.03, 1.10 ± 0.03, and 1.16 ± 0.04, respectively for IR_{50}, $pIRIR_{225}$, and $pIRIR_{290}$ signals and have been calculated using the average saturation level from three independent profiles and from 108 laboratory dose response curves. Note that
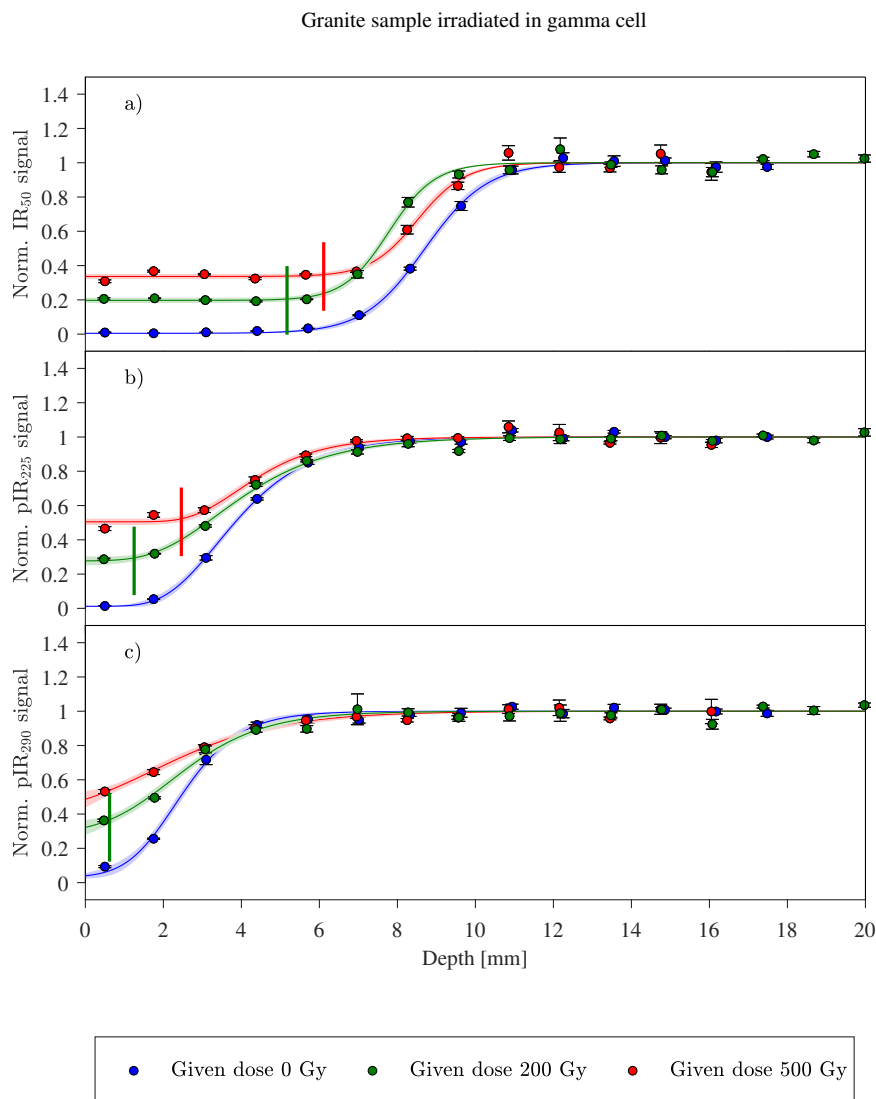
Figure 4.41: Luminescence-depth profiles from a granite sample exposed to 320 d of light from the halogen lamp (blue data). Subsequent to light exposure two unprepared parts of the rock sample were given gamma doses of 200 Gy (green data) or 500 Gy (red data). IR_{50}, $pIRIR_{225}$, and $pIRIR_{290}$ signals were measured and the resulting profiles are shown in a), b) and c), respectively. Fits to these data sets using the general shared-order model for each individual signal are shown as solid lines, with the 68% confidence bands as shaded areas. Vertical lines indicate the depths predicted to have been well-bleached prior to the addition of the gamma doses using the criterion $B_{\text{lum}} = 0.05$ and the predicted pre-burial profile shown in Figure 4.42.
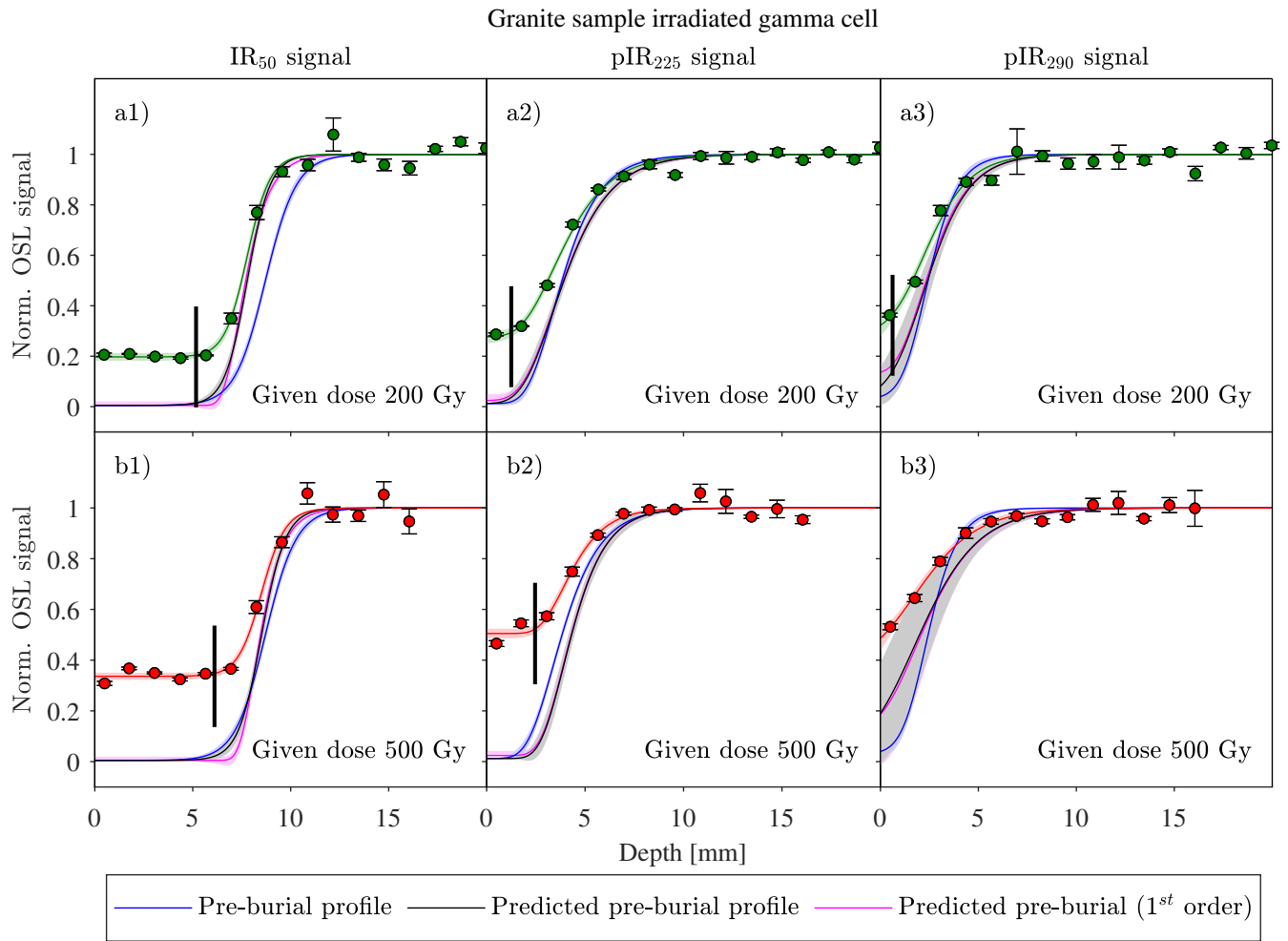
Figure 4.42: Same data as in Figure 4.41 but shown individually, and including the reconstructed pre-burial profiles (black) and the actual pre-burial profile (dark blue); the reconstructed pre-burial profile derived assuming the 1st order model is also shown (pink). 68% confidence bands are shown as shaded areas. Vertical black lines indicate well bleached depths derived using the general shared-order model and the criterion $B_{lum} = 0.05$.
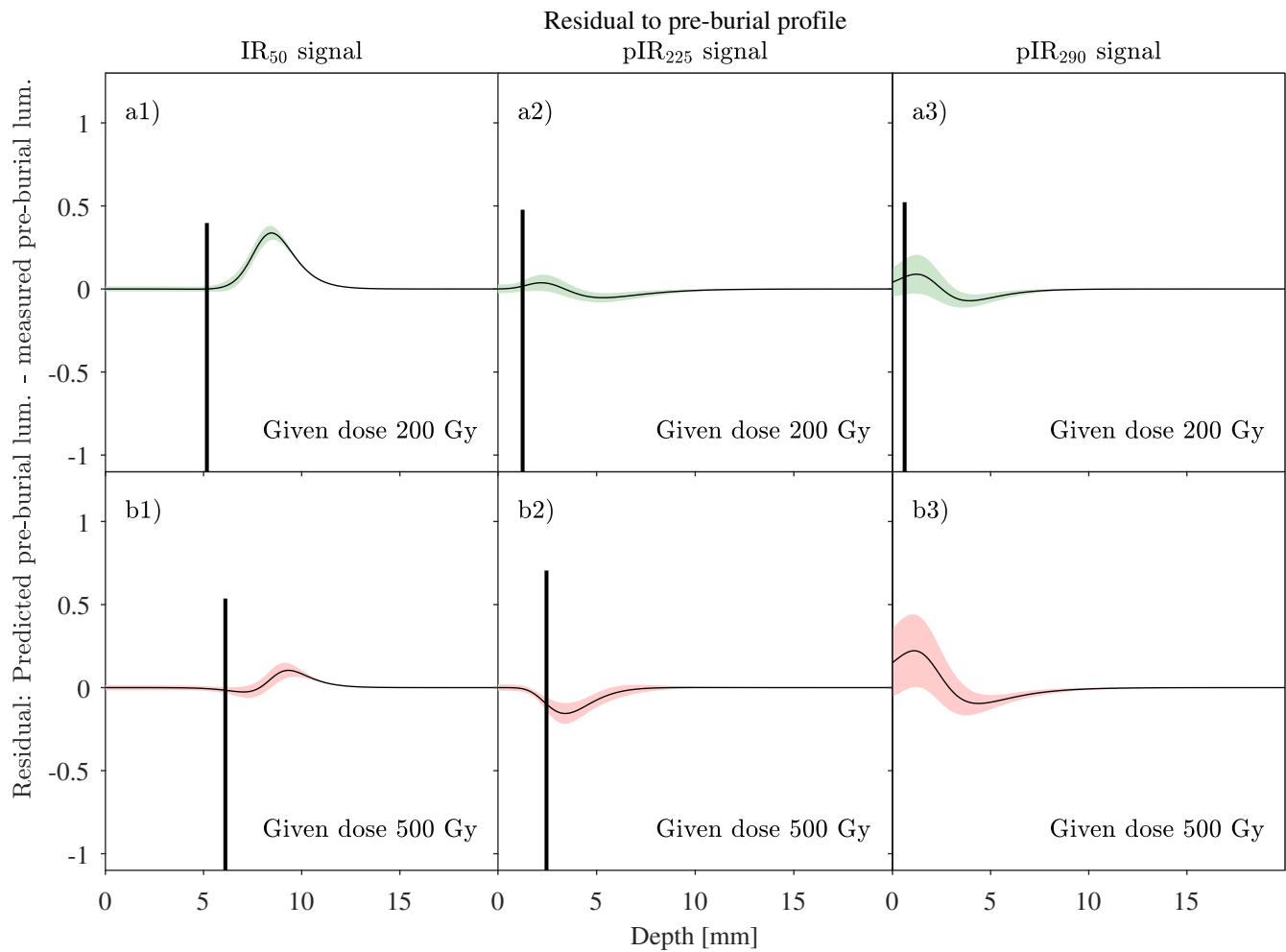
Figure 4.43: Residuals derived from the difference between the reconstructed pre-burial luminescence-depth profile (black lines in Figure 4.42) and measured pre-burial luminescence-depth profile (dark blue lines in Figure 4.42). 68% confidence bands are shown as shaded areas. Vertical black lines indicate the well-bleached depths identified using the criterion $B_{lum} = 0.05$.

Table 4.9: Ratios of dose estimates and given ^{60}Co doses of 200 or 500 Gy. Measured dose is the dose estimated from well-bleached depths. g-value correction are the doses fading corrected [59] using measured g-values (2.7±0.8 and 0.7±0.2 %/decade, $n = 5$) for IR$_{50}$ and pIRIR$_{225}$, respectively). Note that no g-value was measured for pIRIR$_{290}$. NLS is the fading correction of Rades et al. [47]. Fit correction is dose estimation directly from the fitting parameter D_e/D_c (see text for details).

Model	Signal	Measured dose		g-value correction		NLS correction		Fit correction	
		500 Gy	200 Gy	500 Gy	200 Gy	500 Gy	200 Gy	500 Gy	200 Gy
GOM	IR$_{50}$	0.59 ± 0.03	0.68 ± 0.01	0.79 ± 0.09	0.91 ± 0.11	0.56 ± 0.03	0.64 ± 0.02	0.52 ± 0.04	0.69 ± 0.07
GOM	pIRIR$_{225}$	0.77 ± 0.10	0.82 ± 0.02	0.83 ± 0.12	0.89 ± 0.03	0.70 ± 0.10	0.75 ± 0.03	0.64 ± 0.04	0.73 ± 0.09
GOM	pIRIR$_{290}$	-	0.86 ± 0.03	-	-	-	0.74 ± 0.04	0.3 ± 0.2	0.5 ± 0.2
FOM	IR$_{50}$	0.60 ± 0.02	0.68 ± 0.01	0.81 ± 0.10	0.90 ± 0.11	0.57 ± 0.02	0.64 ± 0.01	0.54 ± 0.04	0.71 ± 0.07
FOM	pIRIR$_{225}$	0.77 ± 0.10	0.82 ± 0.02	0.83 ± 0.11	0.89 ± 0.04	0.70 ± 0.09	0.75 ± 0.02	0.63 ± 0.04	0.70 ± 0.08
FOM	pIRIR$_{290}$	-	-	-	-	-	-	0.33 ± 0.14	0.46 ± 0.12

these ratios are greater than unity. The fading corrected dose estimates are shown in Figure 4.44b

ii) estimating the dose directly from the fitting parameter D_e/D_c, see Figure 4.44c

iii) using the measured fading g-values for IR$_{50}$ and pIRIR$_{225}$ of 2.7±0.8 and 0.7±0.2 ($n = 5$), see Figure 4.44d

The measured doses (Figure 4.44a) underestimate the given doses by ~30%, 20%, and 10%, for the three signals (see Table 4.9). If this underestimation is caused by anomalous fading, corrections for it ought to enable accurate dose estimation. However, using NLS (Figure 4.44b) decreases the dose estimates even more as the laboratory saturation limit was lower than the natural in these samples. Estimating the doses from the fitting parameter D_e/D_c and estimated D_c values from DRC, the doses are for the sample given 500 Gy: 262±18 Gy, 322±20 Gy, and 156±110 Gy for IR$_{50}$, pIRIR$_{225}$, and pIRIR$_{290}$, respectively), i.e. these doses underestimate the given doses similarly to the uncorrected doses and the NLS corrected doses (see Table 4.9). Using the g-values for fading correction, improves the ratio to ~ 0.9 and 0.8 for given doses of 200 Gy and 500 Gy respectively, in particular for the IR$_{50}$ doses with the highest g-value. The ratio between natural saturation limit and laboratory saturation limit imply no fading, actually it is above 1, implying higher growth in "nature" than in the dose response curve generated in the reader. However measured g-values do suggest fading. Of course, these dose estimates should be seen in the light of the dose recovery ratios with the chosen SAR-protocol (0.803±0.017, 0.812±0.015, and 1.088±0.044 for IR$_{50}$, pIRIR$_{225}$, and pIRIR$_{290}$, respectively). It seems most likely that the underestimation is caused primarily by poor dose recovery, and that fading, if any, cannot be detected in this experiment.

Dose estimates derived when the first order model was used to estimate the well-bleached depths (open squares) are also shown (Figure 4.44). It is clear that none of the signals generate significantly different doses from those derived using the G.O.M. Thus, burial dating is not as model dependent as exposure dating.

Dose estimation Rock surface dating
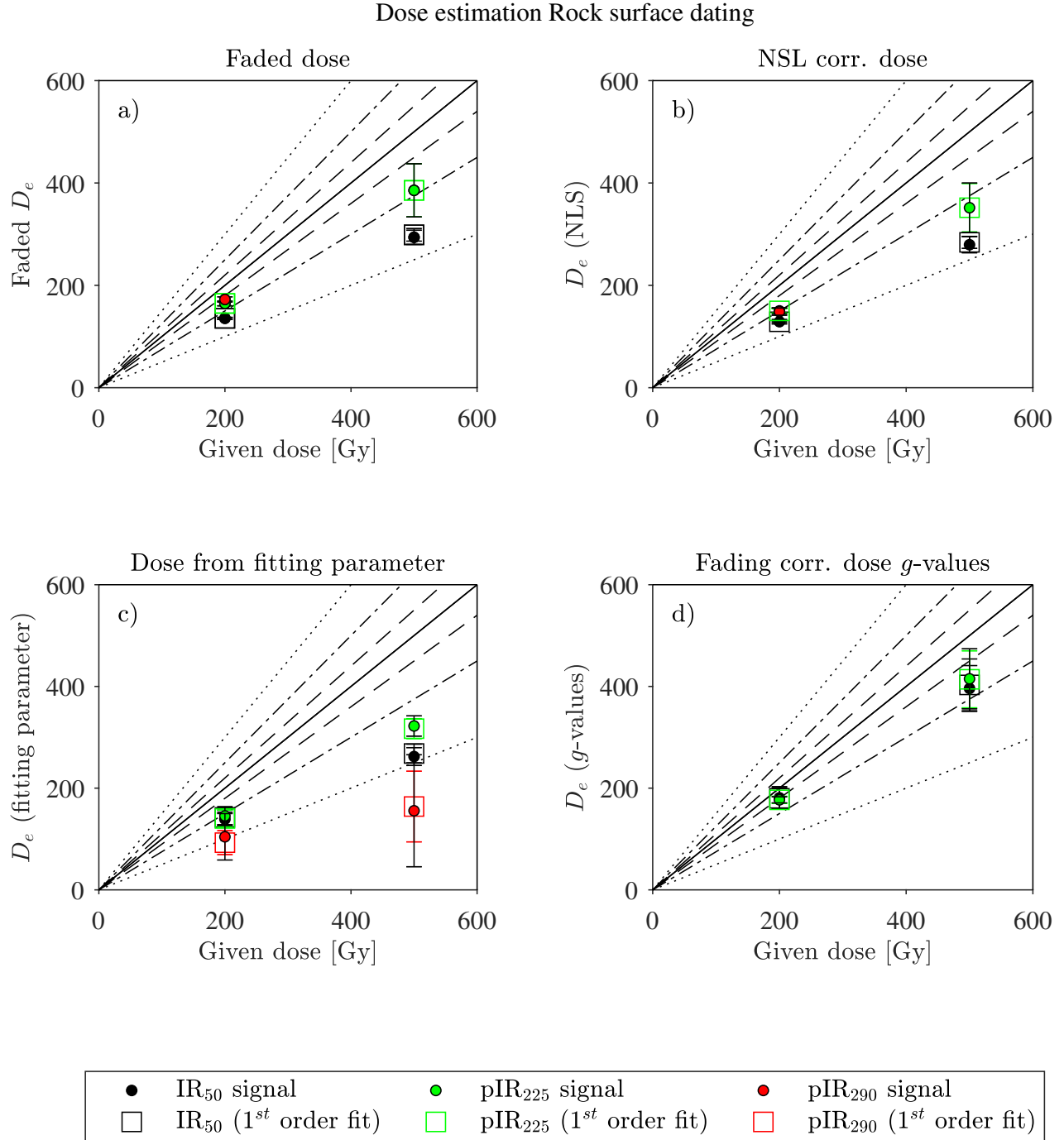
Figure 4.44: Dose estimates and given doses using a) aliquots from well-bleached depths measured with the SAR protocol chosen for these samples (see 4.3.5). b) Dose estimates from a) corrected for fading using NLS [47], i.e. correcting the dose with the ratio of the natural saturation level (from the profiles) to the saturation level from laboratory dose response curves (1.05 ± 0.03, 1.10 ± 0.03, and 1.16 ± 0.04, for IR$_{50}$, pIRIR$_{225}$, and pIRIR$_{290}$, respectively) c) Dose estimation directly from the fitting parameter D_e/D_c. d) doses from a) corrected for fading using the measured fading g-values for IR$_{50}$ and pIRIR$_{225}$ of 2.7 ± 0.8, 0.7 ± 0.2 ($n = 5$)). Closed circles show dose estimates obtained using the G.O.M., whereas open squares show the dose estimates obtained using the first order model. Also shown is the 1:1 line (solid line), the $\pm 10\%$ lines (dashed lines), the $\pm 25\%$ lines (dash-dotted lines), and the $\pm 50\%$ lines (dotted lines).

4.6.2.3   Conclusion on controlled burial experiments

From these controlled burial experiments, it can be concluded that the measured burial profile indeed shows the expected shape with the underlying exposure profile being altered the most near the surface, and that these burial profiles can be described and fitted by the multiple event model[3]. It was possible, at least for given doses <300 Gy to reconstruct the pre-burial profile with confidence, giving fitting parameters comparable to the values estimated from the known (measured) pre-burial profile. However these parameter estimates suffer from large uncertainties, as has been described elsewhere in the literature where orders of magnitude differences are reported (see e.g. Sohbati et al.[1]). Thus it is probably more appropriate to evaluate whether the predicted pre-burial profile is accurate by comparison with the "known" pre-burial profile, as we did in this particular test, than from the parameters.

Although the reconstructed pre-burial profiles (and so well-bleached depths) are model dependent, the estimated doses did not significantly depend on the choice of fitting model. Even first order models can be used when fitting feldspar burial profiles. Since the well-bleached depth depends on the chosen B_{lum} criterion, one can, if desired, make this criterion more restrictive, and so avoid any potential overestimation of the well-bleached depth.

Correcting for fading in rock surface dating using g-values, NLS correction or the estimated fitting parameter gives different age estimates. In the gamma irradiated samples no fading was expected from the ratio of saturation limits, in fact the laboratory saturation limit was lower than the natural saturation limit ($A_{\mathrm{lab}} < A_{\mathrm{nat}}$). However g-values did suggest the presence of fading. When using fitting parameter t_b/D_c, a fading correction is built into the analysis, because the profiles are normalised prior to fitting. If we assume that light levels fade by the same relative amount at any point in the growth curve (or the profile), then the ratio of the burial light level to the saturation light level is independent of fading. Then if this fraction is interpolated onto a laboratory (unfaded) growth curve and unfaded dose is read off. Unfortunately the dose recovery ratios were sufficiently different from unity to prevent any conclusions on whether one method is more accurate than another.

Chapter 5

Rock surface dating at La Roche Cotard

5.1 Introduction

La Roche Cotard (LRC) is an archaeological site located in the Loire Valley (France) near Tours and the river Loire (see Figure 5.1a and 5.1b). The site consists of a small cave (LRC I) and two nearby shelters (LRC III and IV). The cave itself is ~ 30 m long and contains four main chambers (see Figure 5.1c). At the site many Mousterian lithic artefacts[e.g. 128] attributed to Neanderthal occupation have been recovered. In addition, an ambiguous object referred to as the "Mask of La Roche-Cotard" (see Figure 5.1d) was recovered from a level just below the cave entrance (LRC II). This level also contains a typical Mousterian industry with Levallois debitage. Some argue that the object is a representation of a face and thus is a piece of prehistoric art [e.g. 129,130], whereas others argue that it has been formed by natural processes[e.g. 131,132]. Interestingly, no evidence for the presence of Anatomically Modern Humans (AMH) has been found at the site.

What is particularly interesting about LRC, is that the soft cave walls contain marks and engravings made both by animals (mainly claw marks attributable to Ursus sp.[133,134]) and humans. The engravings made by humans, using either fingertips or tools, can clearly be distinguished from those made by animals. They have distinct geometric forms (i.e. triangular, circular, or rectangular) and are often grouped together in panels[79]. An example of these engravings is given in Figure 5.1e. A total of 8 such engraved panels (13 m in total) have been identified in the cave (see Figure 5.1f) and they are all located in the "Pillar Chamber" (see red line in Figure 5.1c). The big question is: who made these engravings - Modern Humans or Neanderthals? Because of lack of a chronological method to date the marks directly this debate has been raging for decades.

At some time in the past, after human occupation, the cave was sealed by accumulation of cold-period colluvial and fluvial sediments which made entry into the cave impossible[129]. The site was then rediscovered in 1846, when large amounts sediments covering the cave entrance were removed for use in the construction of a nearby railway. The owner of the site, François d'Achon, then excavated the cave in 1912 and removed most of its sediments. Excavation of the site was resumed between 1975 and 1978 and then again from 2008 and until the present. Currently, five distinct lithological units (U5 to U1) have been identified based on their facies and sedimentary

composition. U5 is located in the karstic sediments, U4 is deposited fluvially, U3 is colluvium deposited during a colder climate[135], U2 is deposited from aeolian transport, also during a colder climate, and finally U1, the uppermost and thickest unit, is a mixture of primary and reworked colluvium[136]. The fact that , at some point in time, these sediments accumulated sufficiently to seal the cave and prevent further access by large animals (including humans) is important because if it can be determined when the cave was sealed, a lower limit to the age of the markings can be confidently deduced. The earliest presence of AMH in Europe is currently dated to be 40-45 ka ago[137,138], and in the region to about 37 ka ago[86], so if the cave was sealed more than 45,000 years ago, the engravings were almost certainly made by Neanderthals.

 Previous attempts to date the closing of the cave have made use of radiocarbon (^{14}C) analysis on bone fragments. The age limit of ^{14}C dating is 40-45 ka[139] in most circumstances, and 19 out of the 20 samples collected gave non-finite ^{14}C ages, implying that the closing of the cave occurred more than 40-45 ka ago[79].This is similar to the currently known first arrival of AMH in the region, and so it is not possible, from these data, to identify the origins of the engravings.

Optically stimulated luminescence (OSL) dating is a well-established method to determine the time since sedimentary grains were last exposed to daylight (i.e. the burial age) with an applicable range from 10 years to 500,000 years[32]. The method exploits the ability of two widespread minerals, quartz and feldspar, to store energy emitted by the naturally occurring radioactivity in the surroundings. Part of the stored energy is released when the minerals are exposed to daylight (or artificial light in the laboratory). The longer the mineral is buried, the more energy accumulates, until the system saturates. OSL dating has in recent years been applied to date rock surfaces [e.g. 60,91]. One of the potential advantages of luminescence dating of rock surfaces, compared to luminescence dating of buried sediments, is that rock surfaces record quantitative information about the light exposure history before the burial, and thus the bleaching history is recorded (see 4).

The age range of interest at La Roche Cotard is well within the applicable age range of optically stimulated luminescence (OSL). Prior to the current work, seven standard quartz multi-grain OSL ages had been published[130]. These ages were in broad stratigraphic order, but were too few to make firm conclusions about the closure age of the cave.

In this chapter, the main aim is to investigate if rock surface burial dating using OSL can be applied to determine the last time the entrance walls of the cave were last exposed to daylight, and so identify when the cave entrance was last buried. During the period of occupation, the entrance cave walls must have had sufficient sunlight exposure to completely reset the latent luminescence signal at the very surface of the entrance walls and thereby creating a luminescence-depth profile (see red curve in Figure 5.2a). To what depth the luminescence signal would have been reset depends on several factors, but particularly on the duration of exposure and the opacity of the rock to sunlight. When the cave entrance was buried by sediments, the latent luminescence signal increased where possible (it cannot increase where it is in saturation, see green curve in Figure 5.2b). The longer the entrance walls were shielded from light, the larger the luminescence signal at the surface. When the site was discovered (1846) and later first excavated (1912) the entrance cave walls were exposed to sunlight again, which restarts the bleaching process of the latent luminescence signal. If the entrance walls only saw light for a short duration (or if the opacity of the rock material is high), only the very surface layers would have had significant bleaching of the luminescence signal, but if
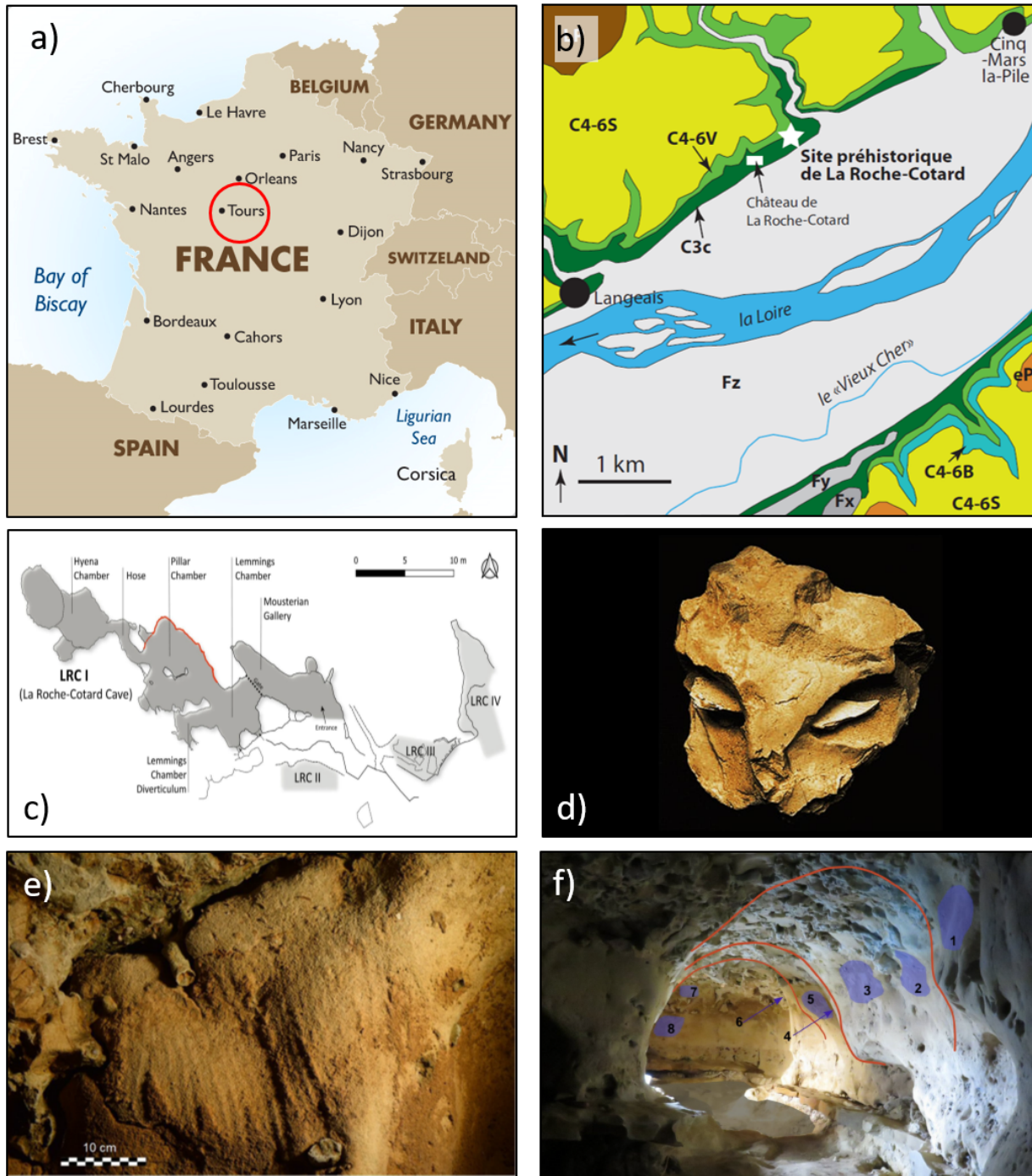
Figure 5.1: a) Location map of the site La Roche Cotard (indicated by a red cicle). b) Map of the area surrounding La Roche Cotard [136].c) Drawing of La Roche-Cotard showing the four individual loci (LRC I-IV). The location of the human marks/engravings are indicated by the red line [79]. d) Photograph of the "Mask of La Roche-Cotard" [130]. The object is 93 mm high, 105 mm wide, 40 mm thick. It weighs 299 g, and is argued to depict a face. If so, it represents an early example of prehistoric art [e.g. 129,130], although others argue that it has been formed by natural processes[e.g. 131,132]. e) Photograph of human engravings, so-called "Finger flutings" [79]. f) Picture of the "Pillar Chamber" indicating the location of markings. Red lines indicate ceiling sections and ridges, whereas marked panels are indicated by blue zones or arrows. Further details can be found in Marquet et al. [79] from where the figure is taken.

the exposure time was long (or the opacity low) then the luminescence-depth profile would move further into the rock surface (see pink lines in Figure 5.2c and 5.2d). Thus, if the exposure time was too long then there is a risk that the event of interest, i.e. the burial level, will be erased by the latest exposure and the measured profile may only indicate a single (recent) exposure event (e.g. see red line in Figure 5.2a). If the record of the burial is retained, despite the recent exposure, then mathematical modelling describing multiple sequential exposure and burial events is required to deconvolve the different events. Here we use a modified version of the model developed for this purpose by Freiesleben et al. [3]. The original model relied on the assumption that the detrapping process follows first order kinetics, but Freiesleben et al. [84] adapted the model to assume a general-order kinetic detrapping process for feldspar signals. The general-order model (G.O.M.) is more likely to describe the observed feldspar luminescence-depth profiles, (see Chapter 4). The model used can be summarised by the following three first-order equations for quartz signals:

$$L_{1,1}(x) = e^{-E(x)t_{e1}} \tag{5.1}$$

$$L_{1,2}(x) = [L_{1,1}(x) - 1]e^{-F(x)t_{b1}+1} \tag{5.2}$$

$$L_{1,3}(x) = L_2(x)e^{-E(x)t_{e2}} \tag{5.3}$$

$$\tag{5.4}$$

and following three general order equations for feldspar signals

$$L_{g,1}(x) = [(g-1)t_{e1}E(1) + 1]^{1/(1-g)} \tag{5.5}$$

$$L_{g,2}(x) = [L_{g,1}(x) - 1]e^{-F(x)t_{b1}+1} \tag{5.6}$$

$$L_{g,3}(x) = [(g-1)t_{e2}E(1) + 1]^{1/(1-g)} \tag{5.7}$$

$$\tag{5.8}$$

where $E(x) = \overline{\sigma\varphi_0}e^{-\mu x}$ and $F(x) = \dot{D}/D_c$. Correction for thermal transfer is implemented as $L_{i,g}^{\mathrm{TT}}(x) = TT + (1 - TT)L_{i,g}(x)$. This model does not take filling during exposure into account [73].

5.2 Sampling and sample preparation

14 rock samples were collected from La Roche Cotard in 2016. Figure 5.3 shows various sampling pictures, including the cave entrance (Figure 5.3a). The cave walls are made of soft marine limestone rich in fine quartz grains and glauconite, also known as "tuffeau jaune" [79] ("yellow tufa", n=12 samples). Part of the cave consist of chert (n=2 sample). Most rock samples were collected by drilling out cores from the cave walls (n=8), and others collected using a chisel and a hammer (n=4, samples 167801, 197334, 187313, 197325). Two samples (167824, 187319) were smaller cobbles (ø≈10 cm) embedded in the sediments at LRC IV and II. The drill used for sampling had a diameter of 8 cm and was mounted on an impact drill machine. The samples were placed in light tight black plastic bags immediately after sampling. Samples of the sediment likely to have covered (i.e. currently in close proximity to) the rock samples were collected for dose rate measurements.

In the laboratory, the sample bags were opened under subdued red-orange light. For sample 187313, 187319, 167824, 197325, 197334, 167801, cores of 4 cm in diameter were drilled in the
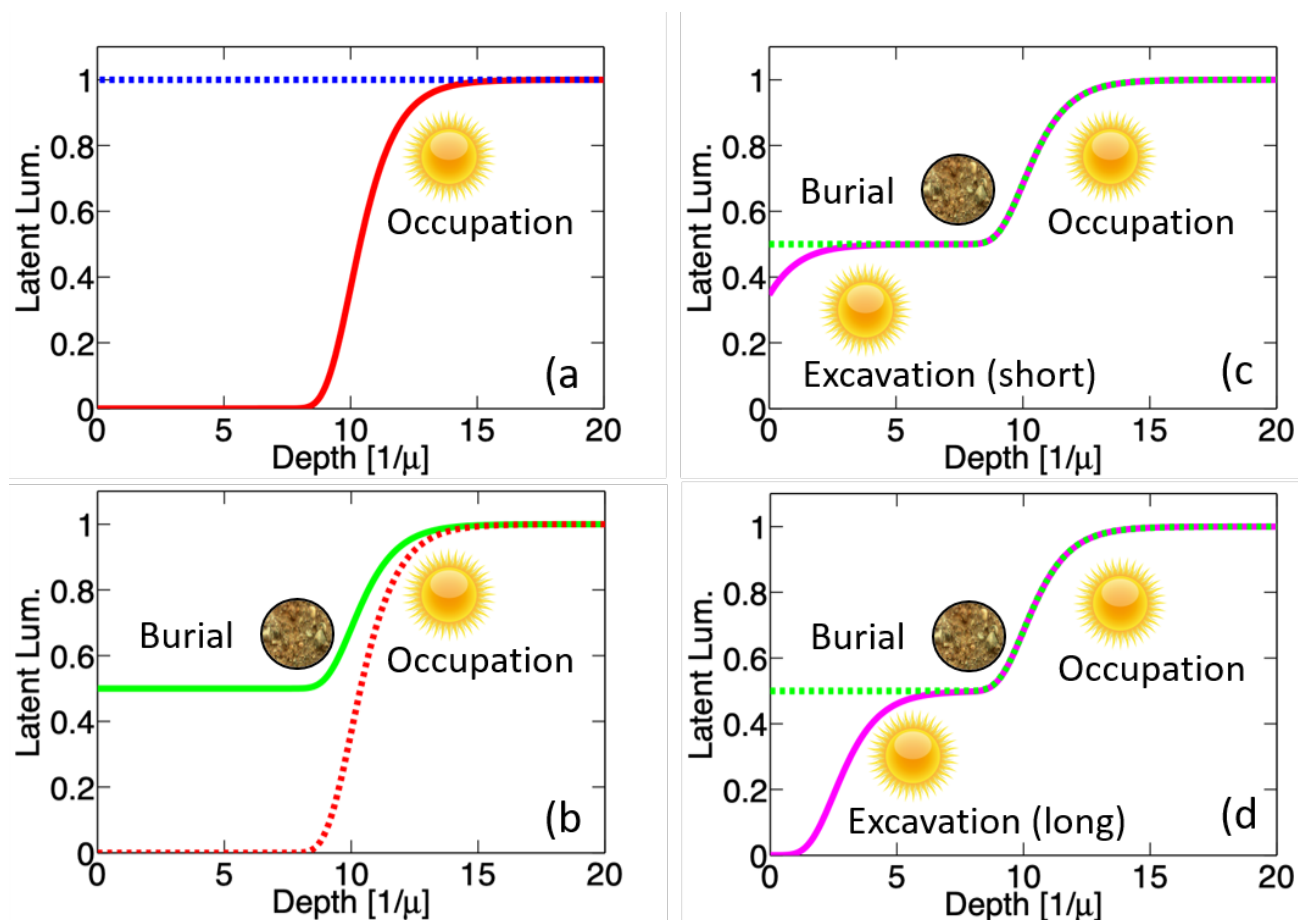
Figure 5.2: Schematic drawing of the expected effect of exposures and burial of the rock entrance walls on the latent luminescence signal. a) During occupation the luminescence-depth profile will migrate into the rock (red line). The longer the rock is exposed the further into the rock the luminescence signal will be bleached. b) when the cave entrance was sealed by sediments, the luminescence signal rebuilds again. The longer the entrance was shielded from light the larger the luminescence signal (and dose) at the surface (green line). c) and d) When the sediments covering the cave entrance was removed during excavation then luminescence signal was reset again. The level of resetting depends mainly on the exposure time (in this case ∼100-150 years).
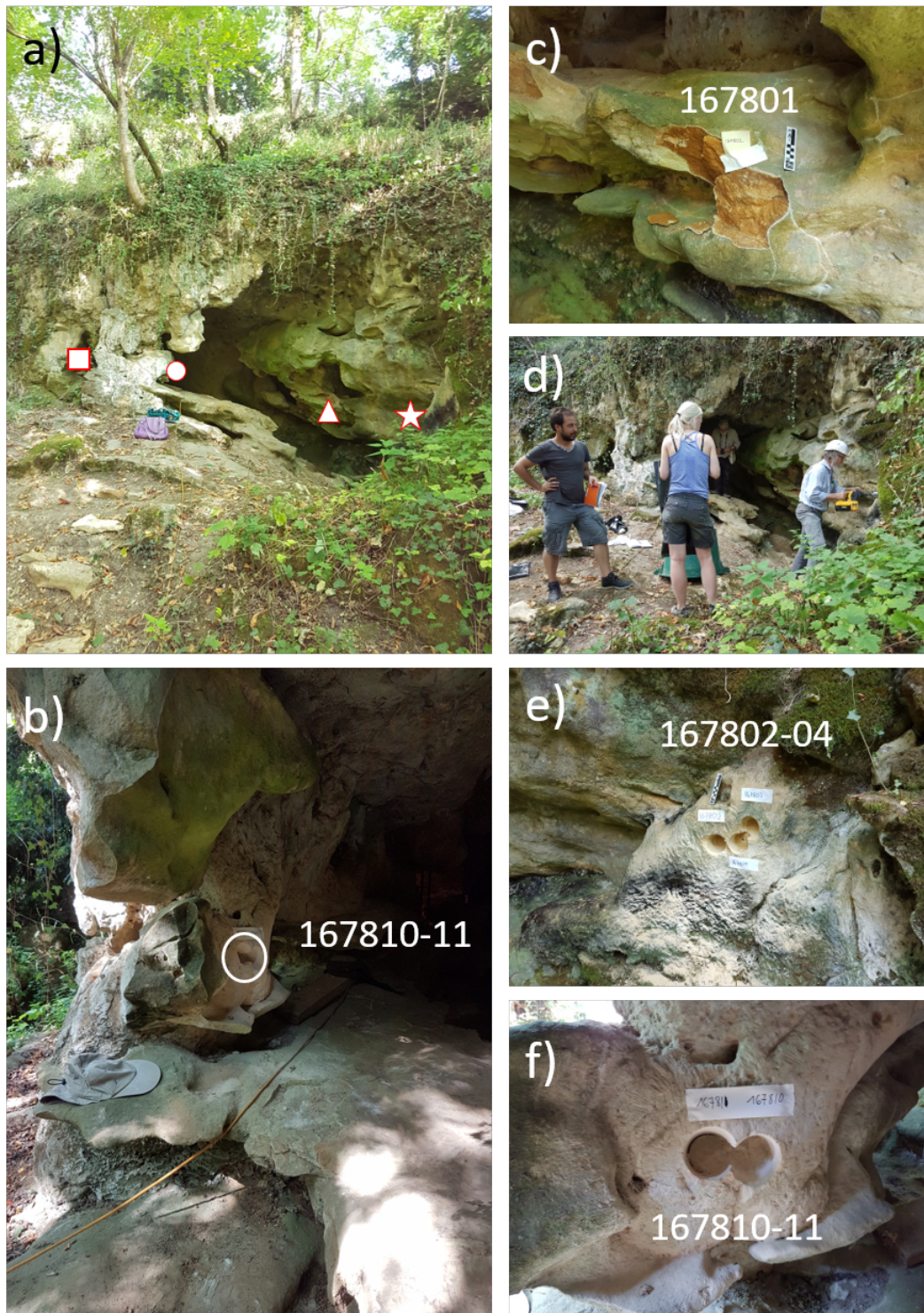
Figure 5.3: Photographs taken during the sampling campaign in 2016. a) The cave entrance to LRC I. The four white symbols show different sampling locations: 167801 (triangle), 167802-04 (star), 167810-11 (circle) and 167807 (square). b) Location of samples 167810 and -11 taken in the wall to the left of the entrance. c) Location of sample 167801. This chert sample was taken with a hammer and chisel. d) Sampling of samples 167802-04 using the impact drill machine. e) Close-up of sample locations 167802-04. f) Close-up of sample locations 167810-11.

Table 5.1: Overview of sampling locations, light exposure at sampling ("Type") and measured profile. "M.E" is main entrance (see Figure 5.3a), "SE" is a small entrance, where small animals might have been able to pass through (see square symbol in Figure 5.3a), "IC" is inside cave/shelter, where the light levels were significantly reduced. "Unit" refers to lithological unit. "Exp." is exposure (e.g. sample 167801 was exposed to light at the time of sampling and the measured profile indicates a single exposure event), "Bur." is buried and "In sat." means the measured profile was in saturation for all depths. Sample 197325 was only partly buried, i.e. it was covered by a thin layer of sediments and vegetation. All rock types were "tuffeau jaune" except sample 167801, which was chert.

No.	Loci	Location	Sample	Type	Profile
167801	LRC I	M.E., right	Wall	Exp.	Exp.
167802	LRC I	M.E., right	Wall	Exp.	Exp.
167803,04	LRC I	M.E., right	Wall	Exp.	Exp.+Bur.+Exp.
167807	LRC I	S.E (IC)	Wall	Exp.	In sat.
167810	LRC I	M.E., left	Wall	Exp.	Exp.+Bur.+Exp.
167811	LRC I	M.E., left	Wall	Exp.	Exp.
197325	LRC I	115 cm above M.E.	Wall	Exp./Bur.	Exp.+Bur.
197334	LRC I	1 m above M.E.	Wall	Bur.	Exp.
197326	LRC I	M.E., left	Wall	Exp.	Exp.
187313-01	LRC I	M.E., left	Cobble (top)	Exp.	Exp.
187313-02	LRC I	M.E., left	Cobble (bottom)	Bur.	In sat.
187319-01	LRC II	Unit 4	Cobble (top)	Exp.	Exp.
187319-02	LRC II	Unit 4	Cobble (bottom)	Bur.	In sat.
187319-03	LRC II	Unit 4	Cobble (bottom)	Bur.	In sat.
167824	LRC IV	Unit 4 (IC)	Cobble	Exp.+Bur.	In sat.
167832	LRC IV	Unit 1 (IC)	Wall	Exp.	Exp.

laboratory, as these were either loose cobbles or sampled using a chisel and a hammer. Samples taken directly from the wall were drilled at the site The individual samples were cast in plaster and set in a jig designed to allow the plaster and sample to advance in mm increments from a metal tube. Waterproof tungsten carbide abrasive paper[1], was then used to abrade the cast samples mm by mm. In this way loose sample material was collected for every mm of the length of the sample, with each rock sample giving 8-16 individual depth-samples. Each of these depth-samples was then taken through seven chemical steps to extract quartz and potassium feldspar grains. First 10% Hydrochloric acid (HCl) solution for one hour removed the carbonate matrix. After rinsing with water three times a 10% hydrofluoric acid (HF) solution was added for 20 min to clean the quartz grains, etch the feldspar grains (ideally this removes the external alpha irradiated volume), and to dissolve any attached clay grains. Any residual fluoride contamination was then removed using a 10% HCl solution for 40 min. Quartz and potassium-rich feldspar grains were separated by using an aqueous heavy liquid separation (FastFloat) with a density of 2.58 g/cm^3. The quartz fractions were subsequently treated with a 40% HF solution for 20 min to remove any remaining feldspar grains, and to remove the alpha irradiated outer layer. Finally any residual fluoride contamination was removed with 10% HCl for 40 min. The washed and dried grains were sieved to 90-180 μm and 8 mm aliquots were mounted on stainless steel discs with silicone oil and measured in a Risø Reader.

5.3   Experimental details

5.3.1   Instrumentation

Luminescence measurements made use of Risø TL/OSL Readers[95] equipped with blue (λ=470 nm, ~80 mW.cm^{-2}) and infrared (IR, λ=870 nm, ~150 mW.cm^{-2}) LEDs. Blue stimulation was used to measure quartz extracts whereas the IR LEDs were used to measure the potassium-rich feldspar extracts. Quartz and feldspar have strong emissions centered at 365 nm and 410 nm, respectively[140]. For quartz measurements, 7.5 mm of Hoya U-340 detection filters were used, whereas a combination of Schott BG39 and Corning 7-59 filters (2 and 4 mm, respectively) was used for feldspar measurements. The luminescence was detected using a blue/UV sensitive photomultiplication tube. In situ beta irradiation used a calibrated ^{90}Sr/^{90}Y source mounted on the reader[95].

Radionuclide concentrations were determined for both rock samples and sediments using high-resolution gamma spectrometry[97,98] and converted to infinite matrix dose rates using the conversion factors of Guérin et al.[99]. Cosmic ray dose rates were calculated following Prescott and Hutton[101] assuming a 5% uncertainty. After initial drying of the samples (at 50 °C for 24 h), they were pulverised and homogenised. Organic matter was then removed by ignition at 450 °C (for 24 h). The samples were then cast in wax, both to prevent radon loss and to provide a reproducible counting geometry, and stored for at least 21 days to ensure that ^{222}Rn had reached equilibrium with its parent ^{226}Ra[97]. An internal alpha dose rate of 0.020 ± 0.010 Gy.ka^{-1} to quartz[100] and 0.10±0.05 Gy.ka^{-1} to K-rich feldspar[141] were assumed. For K-rich feldspar extracts, an internal beta dose rate from ^{40}K and ^{87}Rb of 0.86±0.03 Gy.ka^{-1} was calculated assuming a mean grain diameter of 215 μm, a rubidium concentration of 400±100 ppm[142] and an effective potassium concentration of 12.5%[143]. The long term water content was taken to be 5% and 0% for the

sediments and rock samples, respectively.

5.3.2 Luminescence measurement protocols

Both quartz and feldspar doses were measured using the single aliquot regenerative (SAR) dose procedure[51] on large (8 mm) aliquots.

A pIRIR$_{180}$ SAR protocol was used to measure feldspar signals[55,144] with a preheat temperature of 200°C for 60 s, a first IR stimulation for 100 s at 50°C and a second IR stimulation also for 100 s at 180°C. A high temperature IR bleach at 215 °C for 100 s was used between individual SAR cycles. Signal sums based on the initial 1.80 s of the measured IR signals and the final 10 s were used in the analysis.

For quartz, a standard quartz SAR-protocol using a preheat of 240°C (for 10 s), a cutheat of 200°C and no high temperature bleach between SAR cycles was used. The initial 0.5 s of the measured blue signals (less the subsequent 0.5 s, i.e. early background subtraction) was used in subsequent analysis.

To identify and reject individual luminescence outliers, we use the InterQuartile Rejection (IQR) criterion[105], i.e. individual luminescence measurements more than 1.5 interquartile ranges above the upper quartile (75 percent), or below the lower quartile (25 percent) are rejected. Applying this rejection criterion has no significant effect on the estimated ages (see Table 5.3).

5.4 Dose rates

Table 5.2 summarises the radionuclide concentrations and dry infinite matrix dose rates, assuming a mean grain size of 135 μm and 215 μm for rock samples and sediments, respectively. The dose rate with depth into the rock samples were calculated following Marquet et al.[79] (see also section 2.4.2 for further details).

Table 5.2: Radionuclide concentrations and infinite matrix dose rates for a representative rock samples (167804) and a sediment sample (167812) taken in close proximity to the the rock sample. These data are also presented in Marquet et al.[79], where additional information about the sediment sample can be obtained.

Sample	Radionuclide concentration (Bq.kg^{-1})				Dry dose rates (Gy.ka^{-1})		Total dose rates (Gy.ka^{-1})	
	^{238}U	^{226}Ra	^{232}Th	^{40}K	Gamma	Beta	Q	KF
167804 (R)	4±6	11.6±0.9	12.3±0.8	88±10	0.30±0.02	0.42±0.03	0.74±0.04	1.68±0.12
167812 (S)	39±20	31.9±1.5	38.6±1.2	325±20	0.94±0.04	1.40±0.06	1.76±0.09	2.70±0.17

5.5 OSL characteristics

The quartz extracted from the rock samples is fast-component dominated and has satisfactory OSL characteristics, e.g. the quartz is not contaminated by feldspar (average IR depletion ratio[94] of 1.00 ± 0.03, $n = 6$) and the recuperation signal between SAR measurements cycles is low (average recuperation ratio of $0.39 \pm 0.02\%$, $n = 6$). Using the quartz protocol (see section 5.3.2), we are

able to recover a given dose of 19 Gy, the dose recovery ratio[145] is 1.06 ± 0.06 ($n = 6$; after correction for thermal transfer of 0.39 ± 0.04 Gy).

Feldspar was measured with a post-IRIR protocol using a preheat temperature of 250 °C (60 s) and an IR stimulation temperature of 50 °C and a post IR stimulation temperature of 180 °C (see section 5.3.2). Dose recovery ratios for a given dose of 40 Gy are 0.79 ± 0.02, and 1.01 ± 0.03 ($n = 6$) for IR_{50}, and $pIRIR_{180}$ signals, respectively, after correction for thermal transfer (IR_{50}: 2.7 ± 0.07 Gy and $pIRIR_{180}$: 9.65 ± 0.13 Gy). The average recuperation ratio between cycles is low, $0.080 \pm 0.017\%$ and $0.087 \pm 0.007\%$, for the IR_{50}, and $pIRIR_{180}$ signals, respectively.

Anomalous fading in feldspar[58] can be quantified by the g-value, which is the signal loss per decade of logarithmic normalised storage time[66], and can be determined by measuring a series of sensitivity corrected signals with varying delays between dosing and measurement[146]. The g-value measured for the IR_{50} signal is $4.6 \pm 0.7\%$/decade (n=6) and for post-IR $2.3 \pm 0.3\%$/decade. An alternative approach to assessing fading is to compare the (sensitivity corrected) light level from a saturated natural signal to that from a saturated laboratory signal (natural-to-laboratory saturation, NLS)[47,147,148]. Here, we used the inner part of rock sample 167810 (i.e. 50 mm from the surface, where the measured luminescence-depth profile appeared to be in saturation) as the naturally saturated signal and aliquots from the same sample given a laboratory dose of 2 kGy on top of the natural prior to measurement of this laboratory saturated signal. Taking the ratio between the naturally saturated signal and the laboratory saturated signal gives 0.342 ± 0.016 (n=6) and 0.55 ± 0.02 (n=6) for the IR_{50} and $pIRIR_{180}$ signals respectively, which could imply fading (although it could also simply reflect our inability to measure signals in saturation). Incidentally, the corresponding ratios for $pIRIR_{225}$ and $pIRIR_{290}$ signals (using preheats of 250°and 320°C, respectively) were 0.68 ± 0.02 (n=6) and 0.87 ± 0.03 (n=6), confirming that high temperature IR stimulated signals fade less[56]. The results from a similar experiment done on quartz extracted from a depth greater than 4 mm of sample 167810 gave a ratio of 0.94 ± 0.03 (n=30), with a given dose of 1.2 kGy.

5.6   Luminescence-depth profiles

The advantage of rock surface dating compared to standard OSL dating, is that the former, in principle at least, records the bleaching history of the sample and thus any uncertainty with respect to the presence of a residual signal at burial is significantly reduced, if not eliminated entirely. However, if the rock has suffered from significant erosion (i.e. the gradual or sudden removal of part of the surface), or if an exposure event subsequent to the burial event of interest has been long enough to remove the record of the burial event, then it may not be possible to recover an accurate age. In this section we measure and analyse luminescence-depth profiles into the rock samples from around the cave entrance. The resulting luminescence-depth profiles are fitted with the sequential multiple event model[3] assuming that detrapping follows general order kinetics[84].

Rock sample La Roche Cotard
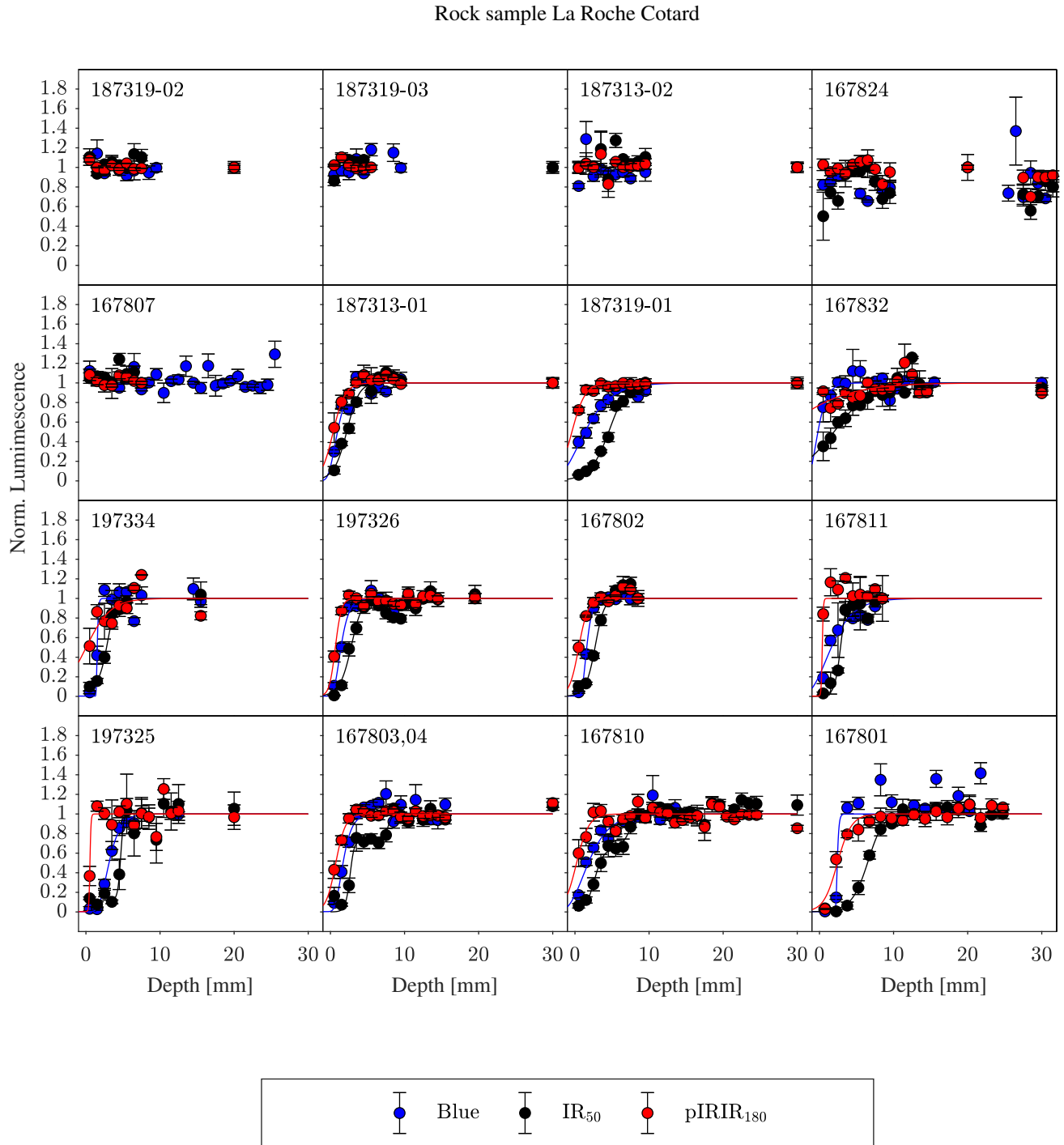
Figure 5.4: Normalised luminescence as a function of depth for i) quartz measured using blue light stimulation (blue), ii) K-rich feldspar measured using IR_{50} (black), and K-rich feldspar measured using $pIRIR_{180}$ (red). Also shown are the fits to the individual curves obtained using the sequential multiple event model[3] modified to assume that detrapping follows general order kinetics[84]. For samples 167803 and 167810, we model an exposure-burial-exposure sequence for the IR_{50} signal (see also Figure 5.5). For all other samples and/or signals, the model uses a single daylight exposure event.

Figure 5.4 shows the measured luminescence profiles (L/T) normalised to the saturation level of

each profile. Grains from the very inner part of each sample were measured to ensure that saturation was reached. Quartz profiles and shown in blue, IR_{50} profiles in black, and $pIRIR_{180}$ profiles in red. The individual data points are the averages of a minimum of 3 aliquots. Uncertainties on individual data points are the standard error. Also shown are the fits obtained using the sequential multiple event model by Freiesleben et al.[84] (see below). The samples that were buried at the time of sampling (i.e. samples 187319-02,-03, 187313-02, 167824) and 167807, all have profiles for which the luminescence level for all depths is indistinguishable from the level measured at depths of 20-30 mm, i.e. the profiles are in saturation. This indicates that either these samples were never exposed to sunlight or that the exposure was sufficiently long ago/short in duration that the record of it has been erased due to build-up of trapped charge during burial.

The remaining eleven samples show signs of daylight exposure, with inflection depths $x_{0.5}$ (i.e. $L(x_{0.5}) = 0.5$) up to ~ 8 mm. It is interesting to note that in all cases the best-bleached signal is the IR_{50} signal from feldspar, followed by the blue stimulated signal from quartz and then the least-bleached signal is the $pIRIR_{180}$ signal from feldspar. A similar observation was made by Freiesleben et al.[85] for their granite and sandstone samples. From measurements on grains extracted from sediment samples, it has repeatedly been shown that, when exposed to a full daylight spectrum, quartz bleaches about an order of magnitude faster then the IR_{50} signal from feldspar, which again bleaches faster than any post-IR signals from feldspar [e.g. 50,55,88]. Quartz OSL is only sensitive to shorter wavelengths, whereas the feldspar IR_{50} signal is sensitive to both shorter wavelengths and to wavelengths around 850 nm (see Chapter 4 for details). Thus, the fact that, in solid rocks, the IR_{50} signal from feldspar apparently bleaches faster than quartz at depth, indicates that shorter wavelengths are likely more rapidly attenuated in a rock matrix. The bleaching of sediment grains is presumably dominated by exposure to the full daylight spectrum, with little attenuation, because full daylight is very much more intense than an attenuated spectrum. As a result, the effects of shorter wavelengths dominate in transported unconsolidated material.

Initially, all eleven samples showing signs of daylight exposure were fitted with a sequential multiple event model describing three sequential events: i) exposure during occupation, $L_1(x)$ given in Eq.(5.1), ii) burial, $L_2(x)$ given in Eq.(5.2) and iii) exposure since excavation, $L_3(x)$ given in Eq.(5.1).

However, the model failed to fit the observed data for seven of the ten profiles (only for samples 167803, 167810 and 197325 for the IR_{50} signal was the model successful, see below). These seven profiles were, however, successfully fitted using a single exposure event (Eq.5.1). We interpret this as indicating that the exposure to daylight after excavation ($\sim$100 years) of these seven samples resulted in the bleaching and deletion of the record of the past burial event.

5.6.1 Burial ages

The IR_{50} profiles for two samples (167803 and 167810, see last row in Figure 5.4) were successfully fitted using the three-event model described above. The IR_{50} profile for sample 197325 was successfully fitted using a two event model, i.e. one exposure followed by a burial event. These profiles are

shown in more detail in Figure 5.5, where the black line is the model fit to the measured data and the grey band around it is the 95% confidence interval. The profiles for 167803 and 167810 (Figure Figure 5.5a and Figure 5.5b) show evidence of a past burial at a luminescence level of ~70% of the saturation level, i.e. the small luminescence plateaus occurring at depths of ~ 5 mm and 7 mm into the rock surfaces. After this burial, the sediments covering the cave walls were removed (presumably in 1912, when the cave was excavated), and the resulting daylight exposure reduced the luminescence signal to near zero at the surface. For this study, it is the burial period that is the event of interest. The model for sample 197325 indicates a presumably more recent burial giving rise to a luminescence signal at only ~10% of saturation, with a plateau region from the surface to a depth of 3.5 mm (Figure 5.5c). In order to determine if the rocks were well-bleached before these burial events, the pre-burial profile (red lines in Figure 5.5) resulting from the modelling must be examined. For all three samples, the pre-burial profiles indicate that the samples were indeed well-bleached until a depth of ~ 5 mm. Using the parameters determined from the modelling, it it is also possible to determine the depth at which the record of the burial event has not been affected by the most recent exposure event (samples 167803 and 167810). These depth limits are shown as pink horizontal lines. For sample 167810, only the measurements for a depth of 4.5 mm can be included, whereas for sample 167803 measurements for depths between 3.5 and 6.6 mm should be acceptable (see Table 5.3). For sample 197325 all measurements to a depth of 3.5 mm can be included.

To convert the luminescence signals identified as reflecting a burial period of interest into a burial age, the luminescence level must first be converted into a burial dose (using the SAR protocol) and then divided by the relevant dose rate (section 5.4), which varies as a function of depth into the rock. The dose rate, at a specific depth, is calculated from the measured infinite matrix dose rates for the rock and sediment. As the grains were sieved to 90-180 μm a grain size of 135 μm was used in the calculations. The variation of dose rate with depth into the rock takes the attenuation of beta and gamma radiation into account[66,106]. From the dose rate and burial doses, burial ages (not corrected for fading) of 83±15 ka ($n = 8$, sample 167810) and 124±8 ka ($n = 33$, sample 167803) are estimated for the cave wall. For the sample taken above the cave entrance (197325) a much younger uncorrected burial age of 18±3 ka ($n = 11$) is obtained. The IR$_{50}$ signal from feldspar is known to suffer from anomalous fading and thus these ages must be fading corrected. Using a g-value of 4.6 ± 0.7 the fading corrected ages are 138±31 ka, 201±21 ka, and 29±6 ka, respectively. However, if the ratio between the measured natural saturation level and the measured laboratory saturation level is used to correct fro fading (i.e. the NLS ratio[47]), ages of 243 ± 44, 351 ± 22 and 52 ± 7 ka, respectively, are obtained (see Table 5.3). However by making the NLS correction described above, we assume that the loss dose is linearly proportional to the loss in luminescenmce signal. A similar assumption is made when correcting using g-values. Although the physical basis for this method is unclear, it has shown to give ages not significantly different from age control[47]. Alternatively the fitting parameter t_b/D_c, from fitting with the multiple event model[3] can be used to estimate the burial time. The parameter t_b/D_c is derived from the normalised luminescence profile, where faded values of Ln/Tn are expressed as a fraction of the faded saturation value. If an estimate of D_c is derived from an (unfaded) dose response curves, this can be used to scales t_b, and so correct for the effect of fading. This method does not involve any assumption of a linear relationship between light levels and dose, but it does assume that the effect of fading is independent of trap filling. This is essentially the same as correcting luminescence
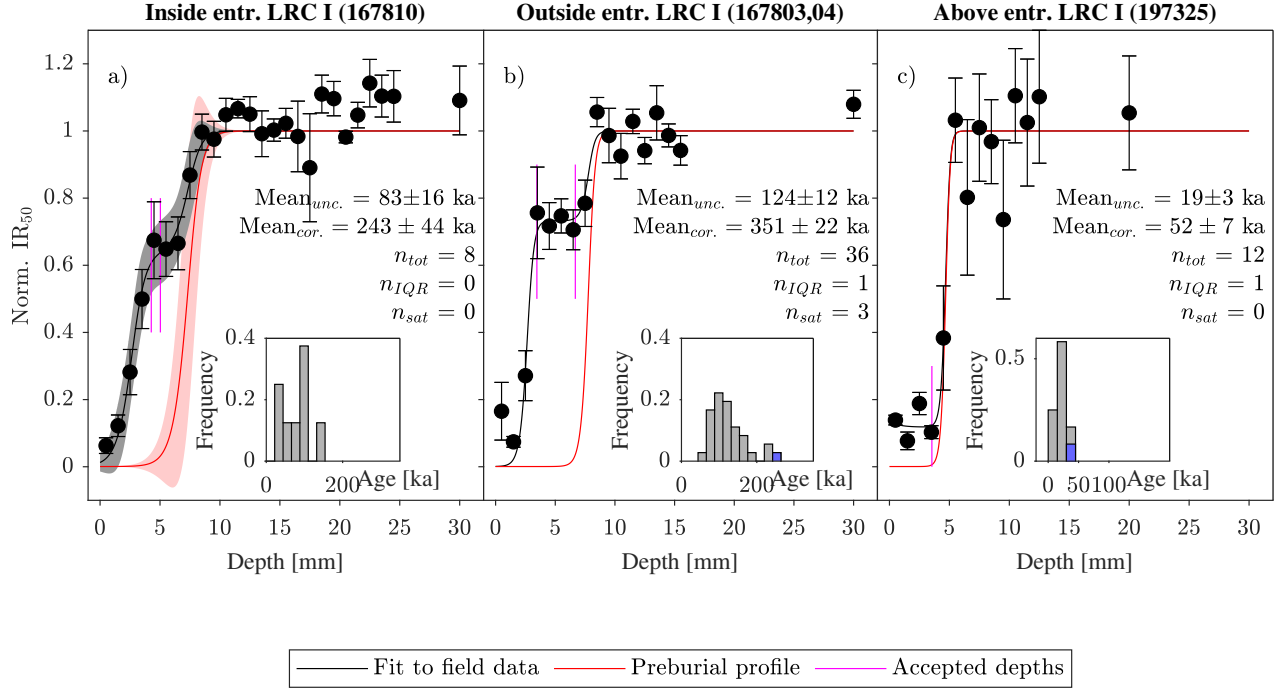
Figure 5.5: IR$_{50}$ luminescence-depth profiles for a) sample 167810 taken $\sim$1 m inside the entrance of LRC I (see Figure 5.3b and 5.3f). b) Sample 167803 taken from the cave wall outside the entrance of LRC I (see Figure 5.3a). c) Sample 197324 taken above the entrance of LRC I. The profiles have been fitted using the sequential multiple event model (black lines with 95 % confidence intervals shown as grey shaded areas) assuming general-order kinetics and for a) and b) three events: i) exposure (during occupation), ii) burial and iii) exposure (after excavation until sampling). For c) two events have been modelled: i) exposure (during occupation), ii) burial. The red lines show, the reconstructed pre-burial profiles. Vertical pink lines indicate the depth interval for which the IR$_5$0 signal is predicted to have been well-bleached prior to burial and also considered to be unaffected by a subsequent exposure event. Insets show the normalised IR$_{50}$ frequency age distributions (not corrected for anomalous fading) resulting from the depth interval predicted to be well-bleached. Mean$_{unc}$ is the burial age with no fading correction and Mean$_{cor}$ is with fading correction based on a measured g-value of $4.6 \pm 0.4\%$/decade. n_{tot} is the total number of individual age estimates, n_{IQR} is the number of age outliers identified and rejected by the objective IQR criterion (shown in blue in the histograms) and n_{sat} is the number of unbounded dose estimates, i.e. the number of aliquots for which no equivalent dose could be derived due to saturation effects.

light levels with the laboratory to natural saturation ratio. As seen in Table 5.3 the burial ages derived from light levels close to natural saturation level (i.e. sample 167810 and 167803,04 become significantly older using this correction.

Table 5.3: Summary of rock surface results from the individual slices identified as well-bleached by the pre-burial model and unaffected by the subsequent exposure event. Average equivalent doses (D_e), total dose rate ($\dot{D}_{tot}$), and OSL IR$_{50}$ age from the individual slices are given. n_{tot} is number of measured aliquots for each depth. Age is average IR$_{50}$ OSL age before application of the IQR rejection criteria. Age$_{IQR}$ is average IR$_{50}$ OSL age after application of the IQR rejection criteria. Age$_{g,corr}$ has been corrected for fading using a g-value of 4.6 ± 0.4 (n=6). Age$_{NLS}$ has been corrected for fading using the ratio of the field saturation level to the laboratory saturation level. Age$_{fit}$ is the age estimated from the fitting parameter t_b/D_c and the D_c values (1056 ± 16 Gy, 604 ± 9 Gy, 474 ± 37 Gy for samples 167810, 168703,04, and 197325) from the laboratory dose response curves. n_a is the number of accepted dose estimates after application of the IQR rejection criterion. Age uncertainties include both random and systematic uncertainties and are given at 68% confidence.

Sample	Depth [mm]	D_e [Gy]	n_{tot}	$\dot{D}_{tot}$ [Gy.ka^{-1}]	OSL age [ka]	Age [ka]	Age$_{IQR}$ [ka]	Age$_{g,corr}$ [ka]	Age$_{NLS}$ [ka]	n_a	Age$_{fit}$ [ka]
167810	4.5	162±30	8	1.95±0.06	83±16	83±16	83±16	138±30	243±44	8	546±81
167803,04	3.5	163±15	9	1.96±0.06	83±10						
	4.5	255±34	9	1.95±0.06	131±20	124±12	120±12	202±27	351±22	33	408±43
	5.5	268±28	9	1.95±0.06	137±18						
	6.5	254±31	9	1.95±0.06	131±19						
197325	0.5	44±5	3	2.15±0.06	20±3						
	1.5	23±8	3	2.00±0.06	11±4	19±3	18±3	29±6	52±7	11	30±3
	2.5	59±11	3	1.97±0.06	30±6						
	3.5	31±6	3	1.97±0.06	16±3						

Figure 5.6: Picture of the "calibration" sample, while being exposed to sunlight for 75 days in July-August 2019 at Risø, Denmark. The deepest part of sample 167810, where the luminescence signal was in saturation, is facing upwards.

5.6.2   Exposure ages

It has been possible to derive age estimates for a burial event for three samples (197325, 167810 and -03). However, as stated in the introduction rock surfaces record qualitative information not only about burial events but also the duration of past daylight exposure events. In this section use the results of fitting to indicate the lengths of time the rock surfaces were exposed to daylight. Previous attempts at obtaining credible exposure ages have been based on the use of calibration samples for which the exposure time is known a priori

5.6.2.1   Calibration sample

Here, we use a portion of sample 167810 as a calibration sample. All the measured luminescence profiles are in saturation a depths greater than 10 mm (see Figure 5.4) and thus by using the inner portion of a sample more than 30 mm thick, we can be confident that the luminescence signal is in saturation. We then exposed the sample to sunlight (with the saturated portion facing the sun, see Figure 5.6) for a period of 75 days in June-August 2019 in Denmark. The resulting profiles are shown in Figure 5.7. The pIRIR$_{180}$ profile (red points, Figure 5.7c) is in saturation for all depths implying that 75 days of exposure is insufficient to reset this signal even at the surface. However, both the IR$_{50}$ (black points, Figure 5.7b) and the quartz (blue points, Figure 5.7a) signals have been reset at the surface. The IR$_{50}$ signal from the second mm of the sample has been more affected by the sunlight than the quartz signal. The degree of resetting can be assessed by how far the luminescence curve has penetrated into the rock. Here we use the inflection point, x_p, to assess the degree of resetting. The inflection point $x_{0.5}$ (i.e. where the normalised luminescence signal is 0.5) for these two signals are 2.4 and 1.7 mm for IR$_{50}$ and quartz, respectively (it is not

defined for the pIRIR$_{180}$ signal as the measured luminescence never is 0.5). This again shows that the IR$_{50}$ signal bleaches faster in a rock matrix than does the blue stimulated quartz signals. In Figure 5.8a, $x_{0.5}$ is shown for all natural profiles. For the IR$_{50}$ signal, the inflection point of the calibration profile lies closest to the surface, as expected. Although the quartz OSL signal is much more scattered than the IR$_{50}$ signal, the inflection point for the calibration profile is similar to the inflection points for samples 197334.
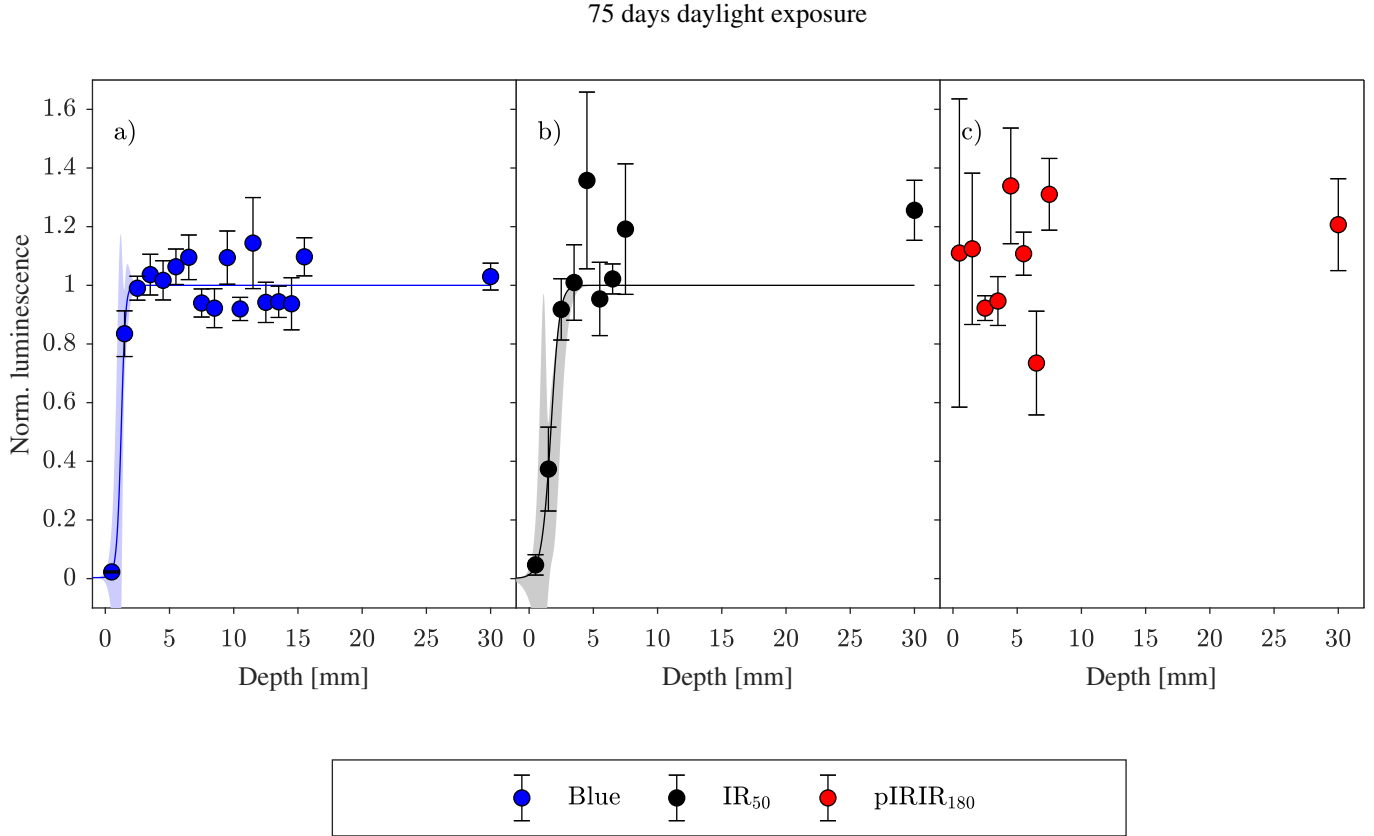
Figure 5.7: Luminescence-depth profiles from the deepest part of sample 167810 after exposure to 75 days of sunlight in July-August in Denmark. The natural profiles from this sample are shown in Figure 5.4. Subsequent to measuring these profiles, the remaining part of sample was turned inverted, such that the saturated part of the sample was facing upwards. The hole left in the sample from drilling out the cores at the sampling site, was filled with plaster and the sample placed outside for 1 month. The profiles have been fitted using a single exposure event.

The corresponding attenuation coefficient (μ) values are 3 ± 3 and 6 ± 4 for IR$_{50}$ and quartz, respectively. These estimates of μ are poorly known, because of the short exposure time of just 75 days (i.e. there is really only three data points in the rising edge of the profile). More precise estimates would presumably be obtained if the exposure time had been larger.

The experimentally exposed sample (Figure 5.5c) gives estimates of μ significantly different from those estimated from the rock profiles and with large uncertainties. Also the estimated $\overline{\sigma\varphi_0}t$ value for the exposed sample is an order of magnitude greater than those determined for the natural rock samples; for similar $\overline{\sigma\varphi_0}$, it was however expected to be a smaller value. This is presumable because of the larger μ, and thus $\overline{\sigma\varphi_0}t$ compensate. If this experimentally exposed sample is used

as calibration, the first of two exposure ages in sample 167803,04 and 167810 is $(3 \pm 10) \cdot 10^6$ ka
and (1 ± 4) ka (see triangles in Figure 5.9). If one were instead to use the most recent exposure in
the natural profiles obtained from samples close by (e.g. samples 167811, 197326, 167802) together
with the known exposure time from the excavation site (i.e. the time since excavation in 1912)
for calibration, the first of two exposure ages in sample 167803 and 167810 is $(2.9 \pm 0.7) \cdot 10^9$ ka
and $(5 \pm 19) \cdot 10^2$ ka (see circles in Figure 5.9). Both calibration samples give large uncertainties
and one would expect the two samples to reflect the same exposure event. Another approach to
using calibration samples, is to use the ERC approach presented in Chapter 4. In this approach
the inflection points of several calibration samples are used to determine the exposure age. The
profile position, i.e. the inflection point x_p ($n(x_p) = 0.5$)), in the experimentally exposed sample
from Denmark is, as expected, not as deep as all the natural profiles. Combining the profile depths
for the ERC approach of both the sample exposed in DK and the LRC exposed samples (samples
167811, 197326, 167802) to calibrate the two old exposure times, we get intervals for the exposure
time of $(30 \text{ to } 1000) \cdot 10^{10}$ ka and $(2 \text{ to } 50) \cdot 10^{10}$ ka for sample 167803,04 and 167810, respectively
(see dashed vertical lines in Figure 5.9). Both methods (single calibration and ERC) gave very
large relative uncertainties,i.e. $\sim 400\%$ for the single calibration method and $\sim 100\%$ for the ERC.
However, the exposure ages for 167803 are unrealistically old. They are in fact older than Earth.
One possible explanation for this vast overestimation is erosion[18]. This is discussed below.
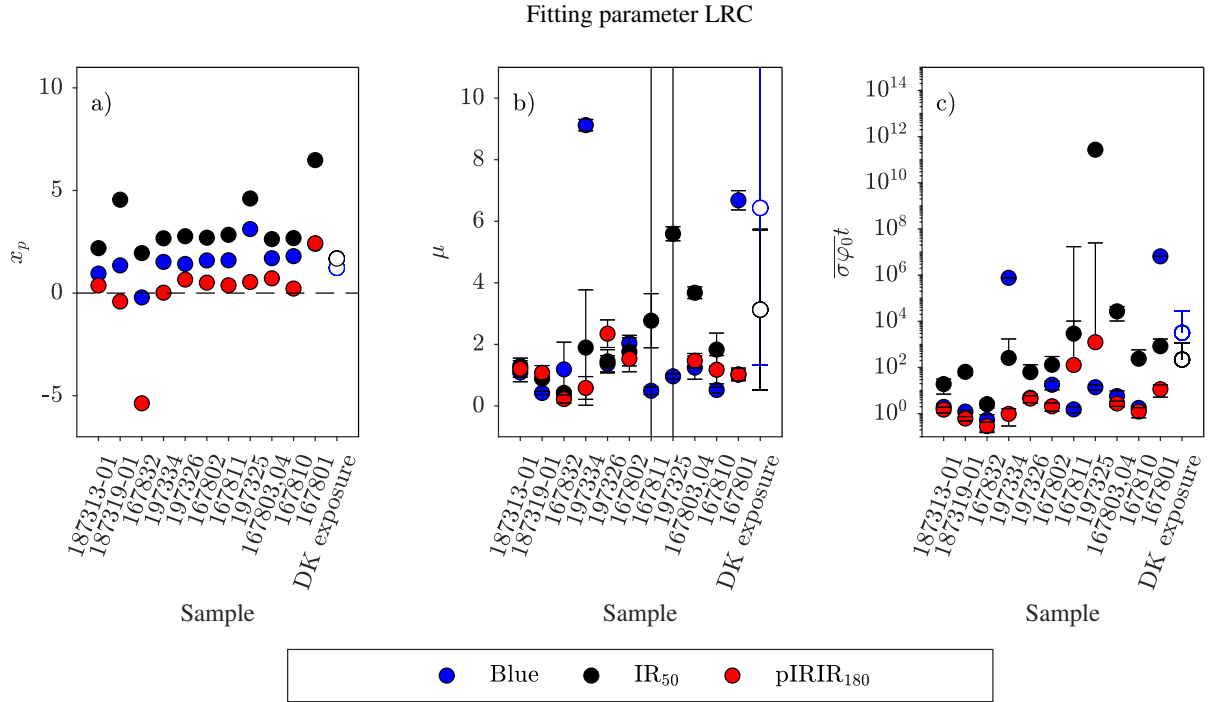
Figure 5.8: Fitting parameters and profile depths x_p that satisfy $n(x_p) = 0.9$ are shown in a, b, and c, for three
signals. Values from the sample exposed in Denmark are marked with open symbols.

Exposure age LRC
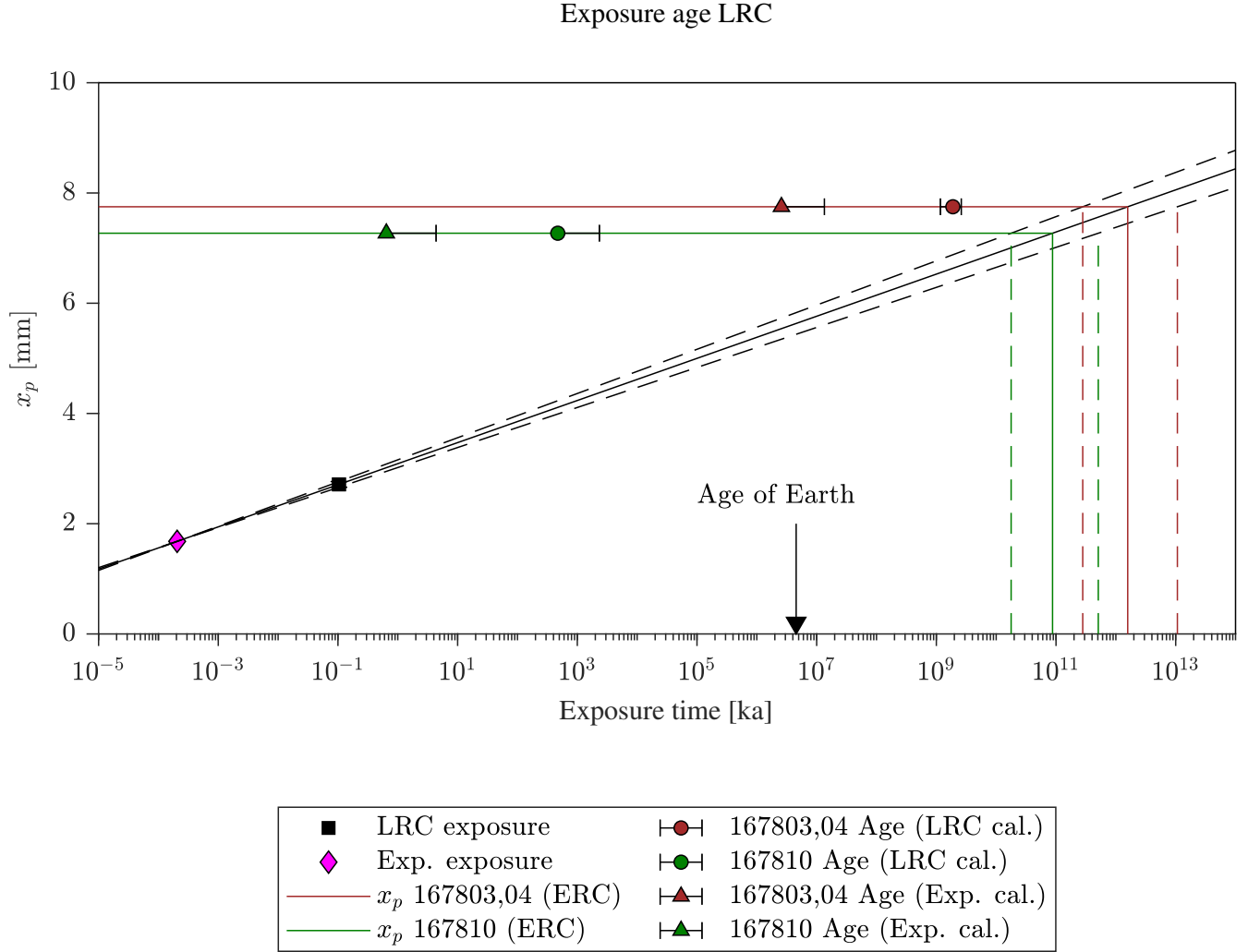
Figure 5.9: Mean of progression depths (black square) from samples near sample 167803,04 and 167810 and progression depths for the sample exposed for 75 days in Denmark (pink diamond). Extrapolating these progression depths to the depths of 167803,04 and 137810 gives estimate of exposure times (brown and green lines). The broken lines arises from the uncertainty in progression depths. Estimated exposure ages using fitting parameters from LRC samples (circles) and from the experimental exposed sample (triangles) as calibration profiles are shown with horizontal error bars in brown and green (167803,04 and 167810).

5.7 Discussion and Conclusions La Roche Cotard rock surface dating

All 4 samples that were buried at the time of sampling (187319-02 and -03, 187313-02, 167824) at La Roche Cotard do not show any detectable bleaching profile in any luminescence signal. Sample 167807 was not buried but was located deep inside the cave and also did not show any detectable bleaching profile. Although the dose rates to these samples were not formally evaluated, given typical dose rates at this site, this suggests that these surfaces were buried more or less continuously for more than 200 ka. Of the samples fully exposed to daylight at the time of sampling, all except one (197325) showed near-surface IR_{50} bleaching profiles that might be expected to result from

the known exposure up to the time of sampling, but only 3 recorded any previous exposure burial cycle. Since we know these surfaces were buried at least until 1846, this implies that either they had been buried for more than 200 ka until the most recent exposure (i.e. for the same minimum time as the buried samples discussed above) or that this last exposure has been sufficient to erase any profile that may have developed during previous cycles. The later would be perhaps surprising, as it suggest that any previous exposure time was similar to or less than 160 years, otherwise some part of the older profile would remain.

Alternatively, surface erosion may be playing a role. These are friable rock surfaces, and those that do not preserve any record of a previous burial event may now be eroding at such a rate that any such record has been removed by erosion, rather than by bleaching. In that case the migration (at the time of sampling) of the profiles into the rock would be at or close to equilibrium with the loss of surface to erosion[73].

Of the 3 surfaces that do seem to show an unambiguous record of multiple events (167810, 167803,04 and 197325), the first two recorded an early exposure, followed by burial, followed by what is presumably the post-1846 exposure. The third (197325) records a burial as the most recent event, suggesting that it had only very recently been exposed to daylight before sampling, perhaps only a few weeks to months before. These three samples also seem to record very different burial events, the first two suggest burial ages (uncorrected for fading) of 83 ± 16 and 120 ± 12 ka, respectively, while 197325 suggests burial only 18 ± 3 ka ago.

The youngest sample lies 115 cm above the cave entrance, and so a burial age of at least 30 ka (after a fading correction using either g-value or through fitting, see Table 5.3) places some constraint on the sealing of the cave. The two older samples were taken from either side of the cave entrance, and neither location can be used on its own to give an indication of the timing of cave closure. Nevertheless, they do suggest that sediment accumulation covered these parts of the entrance walls at least 140 ka ago (youngest of the fading corrected ages), and possibly much before this.

Figure 5.10 reproduces the sediment burial ages and the preferred quartz Bayesian age model from Chapter 6. The youngest rock burial age of 38 ± 7 ka (average of all 3 corrected ages using unlogged CAM with OD 29 ± 22) is completely consistent with the feldspar age model. However it underestimates the preferred quartz age model. Even the two older ages before fading correction are significantly older than the ages derived from the quartz age model for the appropriate depths. This should not necessarily indicate they are inaccurate; it is quite possible that, when most sediment was eroded allowing access to the cave, some was preserved in this sheltered position against the cave walls. Even if this older sediment was disturbed and removed during later deposition at this elevation, the light exposure could easily have been insufficient to reset the rock wall luminescence profile. Unfortunately the 1846 sediment mining and the later excavation in 1912 was sufficiently thorough that no trace of sediment at this elevation remains within the cave or cave entrance.

Unfortunately, it must be acknowledged that the application of rock surface dating to La Roche Cotard has not been particularly successful, mainly because most samples no longer preserved a record of prior burial. This was foreseen as a risk at the time of sampling because most of the samples of relevance were already exposed to daylight, although it is now realised that erosion may also have played a role. Nevertheless, some burial ages were recovered from these samples, and testing the reliability of these ages together with the importance of the archaeological question,

led to the work described in the next chapter, and summarised in Figure 5.10.
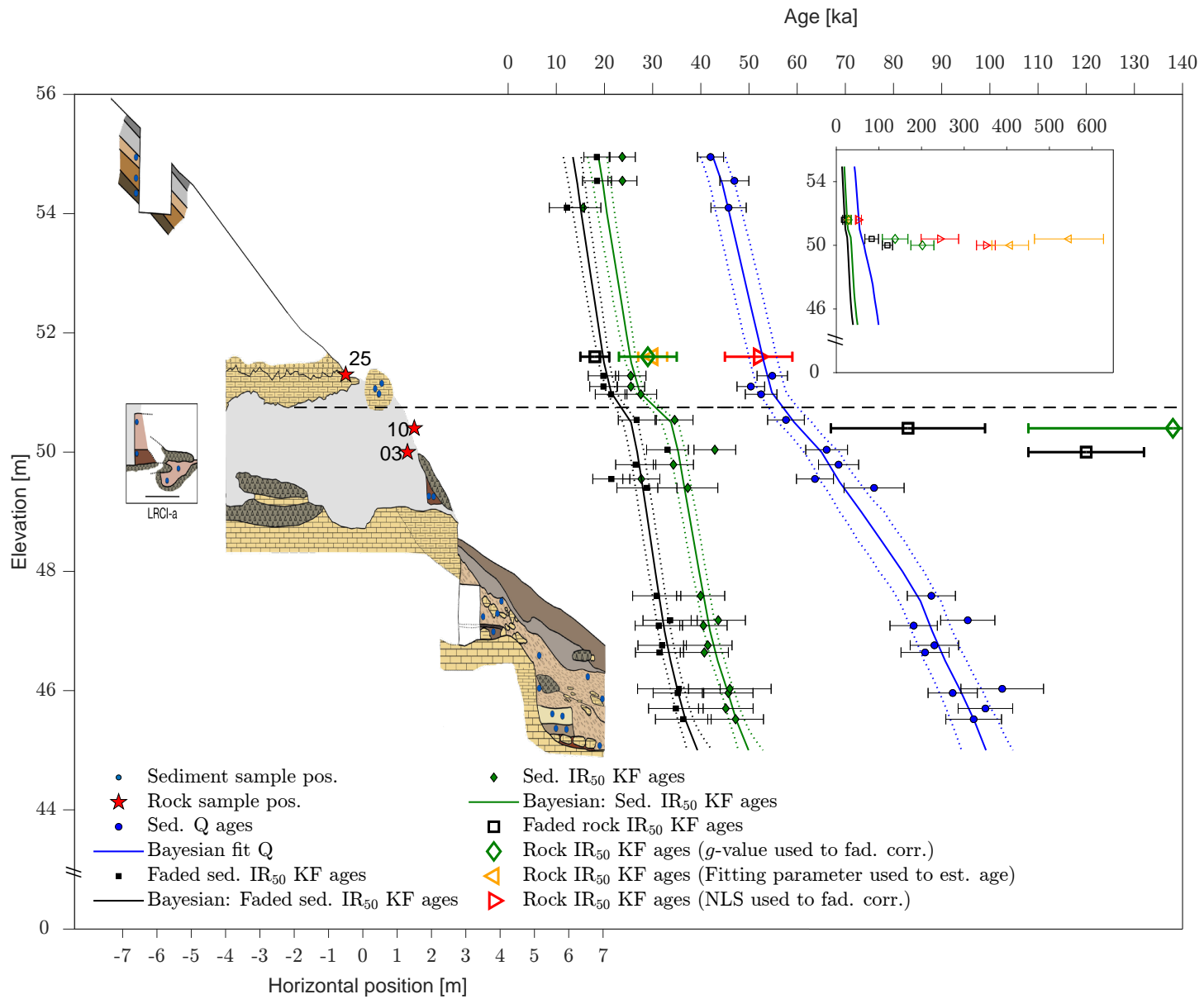
Figure 5.10: Sample positions for rock sample (red stars) and sediment samples (blue points) are shown to the left on the schematic drawing of LRC I and LRC II, with the inset showing two samples inside and two outside of LRC I. The right-hand side of the figure shows the 20 multi-grain quartz (blue circles) and faded IR_50 ages (black squares). IR_50 sediments ages are shown as black squares and green diamond symbols, respectively for faded ages and fading corrected ages. Bayesian models (Bacon script [108]) using the elevation as prior and only random uncertainties for the individual ages are shown in corresponding colours of the three sediment data sets. Dotted lines show the total uncertainty (including both random and systematic uncertainties) at the 68% confidence interval. IR_{50} ages estimated from three rock samples are shown as open symbols using no fading correction (open black squares), using g-value of 4.6±0.4 to fading correct the ages (green diamond symbol), age estimated from the fitting parameter t_b/D_c and known value of D_c from DRC (orange left pointing triangle), and using the ratio of natural saturation level to laboratory saturation level to correct for fading (red right pointing triangles). Horizontal black broken line indicates the level of the entrance roof in LRC I. Insert to the right shows the Bayesian models and rock ages on an extended x-axis.

Chapter 6

Sediment dating at La Roche Cotard

This chapter contain extracts of Marquet et al.[79] which is submitted for publication.

In this chapter, we use OSL dating to determine the time of deposition of the sediments in and around the cave entrance at La Roche Cotard (LRC) and so obtain information on when the cave entrance was last blocked by sediments, either partially or fully (see Chapter 5). To that end, we derive 48 optically stimulated luminescence (OSL) burial ages from the four loci at LRC, i.e. LRC I (n=18), II (n=14), III (n=1) and IV (n=15) using the the blue stimulated signals from multi-grain (8 mm) quartz aliquots. 12 of these quartz samples were also measured using the green OSL signal from single-grain quartz aliquots.

In OSL dating, quartz is usually the preferred mineral, mainly because of signal stability and the ubiquity of the mineral, but also because its OSL signal is readily reset ('bleached') by exposure to daylight. The bleaching rate of K-rich feldspar is at least an order of magnitude slower than that from quartz[50,55], so if quartz and feldspar ages are comparable, the sediment was most likely well-bleached at burial [e.g.,88]. Consequnetly, we also derive OSL ages using the infra-red stimulated luminescence (pIRIR) signal from multi-grain K-feldspar aliquots (2 mm).

The burial ages used for site interpretation are based on multi-grain quartz measurements; associated uncertainties (including all known random and systematic uncertainties on both dose and dose rate estimates) are given at the 68% confidence level. Bayesian modelling was applied to the multi-grain quartz ages as a function of elevation to determine when the cave entrance was last blocked and to give age estimates for individual deposition units and the Moustrian occupation level. The sediment layer in which the ambiguous object "Mask of La Roche-Cotard" is also dated.

Complete closure of the cave entrance is precisely defined by the elevation of the natural rock lintel (see green dashed horizontal line in Figure 6.1) ; by interpolation of this elevation onto our Bayesian age model we determine when sediment deposition closed the cave.

Here we test the hypothesis that the main cave and the shelters were accessible for some time after the arrival of *Homo sapiens* in the area, around 37,000 years ago[86].
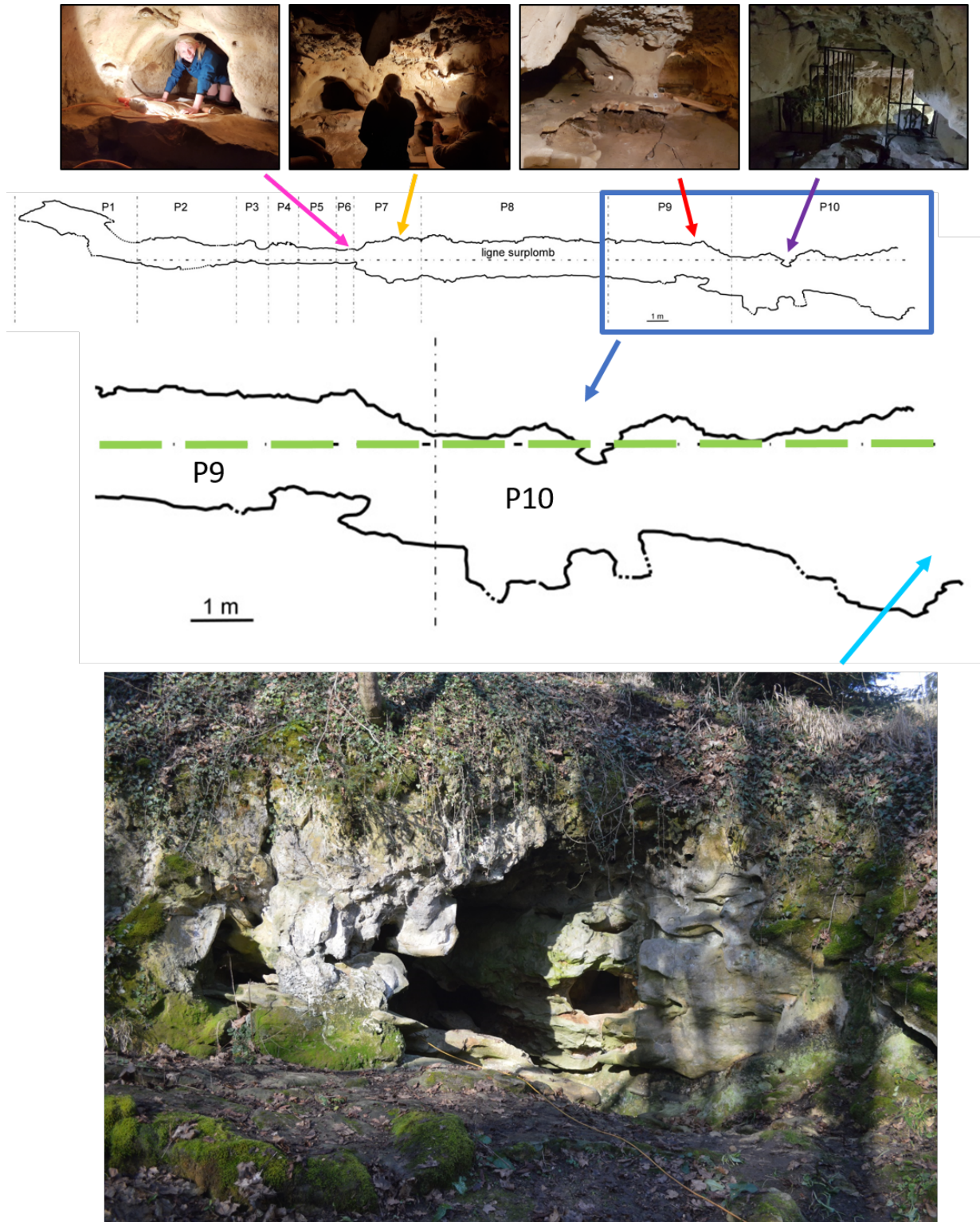
Figure 6.1: Schematic vertical cross-section of LRC I[149] and site photographs. The arrow from each picture points to the approximate location. The part of the cross-section contained in the blue square (P9 and P10) is enlarged immediately below. The green dashed horizontal line indicates the elevation of the natural rock lintel. When sediments covered the cave entrance up to this level, entrance into the cave was no longer possible.

6.1 Context and Sampling

La Roche Cotard is located in the Loire Valley in France and consist of a small cave and two nearby shelters. The cave itself is referred to as LRC I, the sediments in front of and below the cave entrance as LRC II and the two nearby shelters as LRC III and LRC IV. Samples were taken from five different deposition units (U1-5) and from within the inner cave of LRC I (I.C.) and from the entrance to the cave in LRC I (E.C). U5 is located in the karstic sediments. U4 is of fluvial origin (the Loire). U3 is colluvium deposited during a colder climate [135]. U2 is from aeolian transport, also during a colder climate, and U1, the uppermost and thickest unit, is a mixture of primary and reworked colluvium.

A total of 48 OSL samples were collected at La Roche Cotard (LRC), from 2016 to 2020. 41 samples were analysed in Denmark (DTU Physics) and the remaining seven samples in Hungary (Mining and Geological Survey of Hungary). Multi-grain quartz ages from 12 of the 41 samples (all from LRC IV, see below) analysed in Denmark, were published in Marquet et al. [136] and the seven multi-grain quartz samples analysed in Hungary (marked with asterisks in Table 6.5) were published in 2016 and 2019 [130,136]. In this study we date the 29 new samples and revise the previously published quartz ages using the new calculations described here (i.e. water content assumptions and dose rate modelling). On average, these recalculations increase the age of the samples measured in Hungary by 11±4 % (n=7) and 16±6 % (n=3) for publications in 2019 and 2016, respectively and those measured in Denmark by 11.0±1.6 % (n=12).

Three samples were taken from the inner part of the cave in LRC I (167809, -17 and -18). These samples are referred to as I.C. Within the entrance to LRC I, three samples were taken from holes in the entrance wall (197340, -38 and -39). These are referred to as E.C and have not been identified with a specific unit. This is in contrast to three important samples collected from holes in the rock wall outside and just above the cave entrance (samples 197332, -28 and -33). Based on elevation, these three samples should yield ages younger than the closure age. The two samples (167806 and -05) taken just below the closure elevation should yield ages older (or equal to) the closure age. The levels associated with human occupation (Mousterian levels) are all in unit 4.
Units 1-5 have different elevations at the four sites LRC I-IV. The elevation (NGF, General Levelling of France) for the individual units and the Mousterian occupation levels are given in Table 6.1.

Table 6.1: Elevation limits (NGF) for depositions units 1-5 and the Mousterian occupation levels in the four sites LRC I, LRC II, LRC III and LRC IV.

	Unit elevation limit [m]			
Unit/level	LRC I [m]	LRC II [m]	LRC III [m]	LRC IV [m]
Unit 1	50.90 - 55.35	-	-	47.00 - 50.10
Unit 2	49.00 - 50.70	-	45.80 - 46.00	44.90 - 47.00
Unit 3	-	45.13 - 48.00	-	-
Unit 4	49.20 - 50.29	45.30 - 45.80	44.85 - 45.80	44.10 - 44.90
Unit 5	-	44.80 - 45.13	-	42.40 - 43.90
Mousterian level	48.50 - 49.30	45.20 - 45.60	44.85 - 45.00	44.80 - 44.90

Sediment samples were taken by inserting steel tubes (ø=4 cm, length=20 or 15 cm) into cleaned sections. In the laboratory, the samples were prepared under subdued red-orange light conditions. The ends (outer 5 cm) of each sample, potentially light-exposed during sampling, were reserved for radionuclide concentration and water content measurements. The inner portions of the samples were used for OSL measurements.

For the latter, the material was first wet-sieved to 180-250 μm and then processed through several standard laboratory steps to extract clean quartz and potassium-rich feldspar grains. The samples were first treated in 10% HCl for one hour to remove carbonates. After rinsing, 10% hydrofluoric acid was added for 20 min to clean grain surfaces and remove any attached clay particles. Residual fluoride contamination from the hydrofluoric treatment was removed using 10% HCl for 40 min. Quartz and K-rich feldspar grains were separated using heavy liquid separation (sodium heteropolytungstate "LST Fastfloat'") with a density of 2.58 g/cm^3. Finally, the quartz-rich extract was treated with a 40% HF for 40 min to remove any remaining feldspar grains and the outer 10 µm affected by alpha radiation. Any residual fluoride contamination from the HF treatment was removed using 10% HCl for 40 min. The luminescence purity of the resulting quartz extract was examined by testing for IRSL sensitivity (a measure of feldspar contamination, see section 6.4.2).

6.2   Experimental details

6.2.1   Instrumentation

All luminescence signals were measured using automated TL/OSL Risø Readers[95] equipped with blue (470±30 nm) og IR (870±40 nm) stimulation LEDs, providing approximately 80 and 150 mW/cm^2 at the sample position, respectively. Single-grain quartz OSL signals were measured using a single grain attachment to the OSL reader[118], fitted with a steerable green 10 mW Nd:YVO$_4$ solid-state diode-pumped laser beam (532 nm) as the stimulation light source.

Quartz and feldspar have strong luminescence emissions centred at 365 nm and 410 nm, respectively[140]. These luminescence signals were detected using EMI 9635QA photomultipliers in combination with either 7.5 mm Hoya U-340 filters (quartz) or a filter pack consisting of 2 mm Schott

BG-39 in combination with 4 mm Corning 7-59 (feldspar).

In situ beta irradiations used calibrated ^{90}Sr/^{90}Y beta sources[96]. The beta dose uniformity across the sample area for all sources was better than 5% and thus no correction for spatial non-uniformity was applied[150].

Radionuclide concentrations were determined using high-resolution gamma spectrometry[97,98] and converted to infinite matrix dose rates using the conversion factors of Guérin et al.[151]. The sediment samples were crushed and homogenised before mixing with wax and cast in a fixed cup-shaped geometry to retain ^{222}Rn[98]. Equilibrium between ^{222}Rn and ^{226}Ra was ensured by storing the cups for more than 20 days (i.e., >5 half-lives of ^{222}Rn) before counting. Cosmic ray dose rates were calculated following Prescott and Hutton[101] assuming that the burial depths recorded in 1846[136] represents the life-time burial depths.

In situ gamma dose rates were measured for eight of the samples. These measurements were made because spatial heterogeneity in the gamma field was expected. These in situ gamma dose rates were measured in two different ways: 1) a 1.5" LaBr probe was inserted into the hole left after the OSL sample had been taken. The in situ spectrum was recorded for ∼20 minutes at each sample location. The acquired spectra were then converted into dose rates using the energy threshold technique[123] and the calibration curve established by Miallier et al.[152].
2) Al_2O_3:C pellets, inserted in aluminium tubes with a wall thickness of 3 mm, were placed in the OSL sample holes for for 215 days. The protocol of Kreutzer et al.[153] was used to measure the absorbed dose, which enabled the calculation of in situ gamma and cosmic dose rates.

An XRF attachment to the Risø reader was used to measure the K-contents, relative to the sum of K+Na+Ca, in seven samples[120,121].

6.2.2 OSL measurements

Equivalent dose determination used the single-aliquot regenerative-dose (SAR) procedure[51]. Laboratory dose response curves (DRCs) were determined using a minimum of three sensitivity-corrected regeneration dose points (L_x/T_x) bracketing the sensitivity corrected natural signal (L_n/T_n) as well as a recuperation point (zero dose point) and a recycling point. The sensitivity corrected IR depletion ratio[94] was measured at the end of each DRC.

The DRCs were fitted using a single saturating exponential function of the form $L_x/T_x = I_0[1 - \exp(-D/D_c)]$, where L_x/T_x is the sensitivity corrected OSL response, I_0 is the saturation value and D_c is a measure of the curvature (note that D_c is often termed "D_0" in the literature). Equivalent dose estimates were derived from individual aliquots by interpolation using "Analyst"[154] and uncertainties are based on counting statistics, fitting uncertainties and an instrument reproducibility of 0.5% per OSL measurement for multi-grain measurements and 2.5% per OSL measurement for single-grain measurements[155].

6.2.2.1 Multi-grain quartz OSL measurements

The OSL signals from multi-grain quartz aliquots were obtained using blue light stimulation at 125 °C for 100 s. A preheat temperature of 260 °C for 10 s, a cutheat temperature of 220 °C and a test dose of ∼30% of the natural dose was used for multi-grain quartz dose measurements, unless

otherwise specified. In addition, a high-temperature blue light stimulation at 280 °C for 40 s was inserted between SAR cycles to minimise potential recuperation effects[103].

The light sum over the initial 0.5 s of optical stimulation, less that from the subsequent 0.5 s of stimulation, was used for dose estimation, i.e., early background subtraction (EBG) to isolate the fast component[156]. Aliquots were prepared on stainless steel discs using an 8 mm spot of silicon oil, giving approximately 2,000 grains per aliquot[35].

In OSL dating it is common to reject results from individual aliquots according to certain rejection criteria, e.g., the recycling and IR depletion ratios are expected to be consistent with unity and the recuperation is usually only accepted if it is less than 5% of the sensitivity corrected natural signal. In this study, the application of these criteria did not result in significant changes to either equivalent doses or distribution width (see section 6.4.2). Here we also examine the effect of the InterQuartile Rejection (IQR) criterion, as described by Medialdea et al.[105]; this identifies and rejects individual dose values if they are more than 1.5 interquartile ranges above the upper quartile (75 percent), or below the lower quartile (25 percent).

6.2.2.2 Single-grain quartz OSL measurements

A similar single-aliquot regenerative-dose (SAR) protocol[51] was used for single-grain equivalent dose determination; it employed a preheat of 260 °C (for 15 s), a cutheat of 220 °C and a test dose of 50 Gy. An IR stimulation at 50 °C (for 100 s) was inserted prior to each OSL stimulation at 125 °C (0.9 s) to minimise any effects of potential feldspar contamination[102]. After each SAR cycle a high-temperature blue bleach[103] at 280 °C (for 100 s) was inserted to minimise potential recuperation effects. For single-grain measurements, the OSL signal was summed over the initial 60 ms and the background was summed over the final 150 ms.

Here, single-grain laboratory dose response curves (DRCs) consist of a minimum of six sensitivity-corrected regeneration dose points, a recuperation point (i.e., zero dose point), two recycling points and an IR depletion point[94]; i.e., a ratio between sensitivity corrected L_x/T_x values measured with and without the prior IR stimulation before the L_x measurement).

Several methods of data analysis are applied to the single-grain data: i) the central age model (CAM)[33], ii) the average dose model (ADM)[104] and iii) the Baysian central dose model (Bay-Lum)[157–160]. For the multi-grain quartz data, the DRCs are fitted using a single saturating exponential passing through the origin. In i) an ii) uncertainties are assigned to individual doses using "Analyst 4.52"[154] and consist, as a minimum, of contributions from Poisson counting statistics, instrument reproducibility and curve fitting errors. In iii) the OSL data is analysed in a Bayesian framework, where individual equivalent doses are not parameterised independently, but the selected grains are analysed simultaneously assuming they all belong to the same dose distribution.

Only grains with a relative uncertainty on the natural OSL test dose signal (T_n) of less than 20% ($s_{Tn} < 20\%$) were included in the analysis. Application of the following rejection criteria was tested: a) the recycling ratios must be consistent with unity within two standard deviations, b) the IR depletion ratio[94] with sensitivity correction must be consistent with unity within two standard deviations and (c) the recuperation dose must be consistent with zero Gy. On average, these criteria did not result in significant changes to either equivalent doses or distribution width (see section 6.5.2.1).

6.2.2.3 Multi-grain feldspar IRSL measurements

A preheat temperature of 320 °C for 100 s was used for all K-rich feldspar dose measurements unless otherwise specified (e.g., preheat plateau measurements in section 6.6.2). Multi-grain K-rich feldspar aliquots were stimulated with IR light at 50 °C for 200 s followed by IR stimulation at 290°C for 200 s, i.e., a pIRIR(50,290) protocol[56]. A test dose roughly equal to the size of the natural dose was used and a high-temperature IR bleach at 325 °C for 200 s inserted between SAR cycles to minimise potential recuperation effects. The light from the initial 2 s of stimulation less that from the last 10 s of stimulation was used for dose estimation, i.e., late background subtraction, LBG. Aliquots were prepared on stainless steel discs using a 2 mm spot of silicon oil, giving approximately 100 grains per aliquot[35].

6.3 Dose rate measurements

This section describes the dose rate measurements in the study and the corrections for heterogeneity due to the bedrock material at the site.

The radionuclide concentrations derived from the 48 OSL sediment samples and a single bedrock sample (167804R) are summarised in Table 6.2. The dry infinite matrix beta and gamma dose rates are also given, derived assuming a $20\pm10\%$ loss of ^{222}Rn compared to its parent ^{226}Ra. Note that the dose rate for sample 187307 is significantly lower than other sediment samples and gives the same dose rate as the bedrock material.

We assume an internal alpha dose rate due to ^{238}U and ^{232}Th to quartz of 0.02 ± 0.01 Gy.ka^{-1} [161] and to K-rich feldspar of 0.10 ± 0.05 Gy.ka^{-1} [141]. For K-rich feldspar extracts, an internal beta dose rate from ^{40}K and ^{87}Rb of 0.86 ± 0.03 Gy.ka^{-1} was calculated assuming a mean grain diameter of 215 μm, a rubidium concentration of 400 ± 100 ppm [142] and an effective potassium concentration of $12.60\pm0.15\%$. The latter was measured using a Risø XRF attachment[120,121] (see Figure 6.2) for seven of the samples. This is close to the 14.05% stoichiometric maximum for orthoclase, and consistent with the recommendation of Huntley and Baril[143].
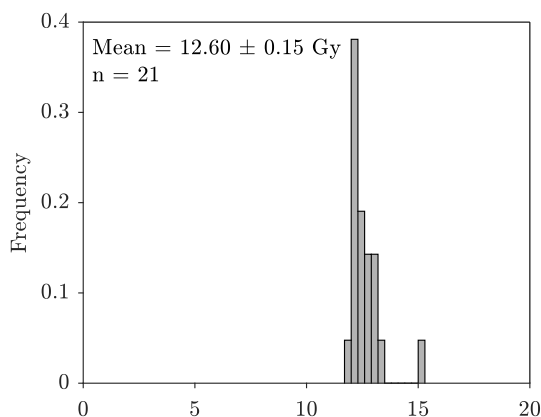

Figure 6.2: K concentration distribution measured with XRF on 7 KF extracts from samples 167805, -06, -12, -19, -20, -21, -22. Three multi-grain (2 mm) aliquots were measured for each sample.

Table 6.2: Dose rate summary for the 48 sediment samples and a single bedrock sample (167804R). Samples marked with * were prepared and measured in Hungary by Dr. Edit Thamóné Bozsó (Department of Geological Basic Research, Mining and Geological Survey of Hungary). "Fig. code" refers to the sample label used in ED 7 in Marquet et al. [79] and Figure 6.12. "Unit" is the deposition unit. "I.C." and "E.C." represents samples from the inner cave of LRC I and the entrance of LRC I, respectively (no specific deposition). Both current (field) and saturated "Water content" percentages are given. "Assumed" is the assumed water content (see section 6.7.4) used in the calculation of total dose rates. Dry infinite matrix dose rates are derived from radionuclide concentrations measured using high resolution gamma spectrometry. "R_{corr}" is the ratio of the modelled gamma dose rate to the infinite matrix dry dose rate (see section 6.3.3). Total dose rates include the contribution from cosmic rays, internal dose rates, and the effects of water content as well as the modelled correction for dose rate heterogeneity. "Q" and "KF" refer to dose rates to quartz and K-rich (12.60±0.15%) feldspar, respectively. "R_{tot}" is the ratio of the total dose rate (modelled) to the unmodelled total dose rate (see section 6.3.3).

Lab Code	Fig. code	Unit	Water content (percent)			Radionuclide concentration (Bq.kg⁻¹)				Infinite matrix dry dose rates (Gy.ka⁻¹)		R_{corr} dry dose rate	Total dose rates (Gy.ka⁻¹)		R_{tot} wet total DR	
			Current	Saturated	Assumed	^{238}U	^{226}Ra	^{232}Th	^{40}K	Gamma	Beta	Gamma	Q	KF	Q	KF
167804R			1	10	4	4±6	11.6±0.9	12.3±0.8	88±10	0.296±0.017	0.42±0.03	1	0.74±0.04	1.68±0.12	1	1
187301	1	1	1	34	17	24±6	25.9±0.6	28.6±0.5	387±11	0.82±0.02	1.43±0.03	1	1.87±0.08	2.82±0.17	1	1
187302	2	1	3	30	17	31±9	27.1±0.7	42.9±0.7	643±11	1.20±0.03	2.18±0.04	1	2.74±0.12	3.7±0.2	1	1
187303	3	1	7	51	17	-5±23	30.0±1.9	33.3±1.8	430±24	0.94±0.04	1.61±0.07	1	2.11±0.10	3.06±0.19	1	1
197332	4	1	15	63	17	19±5	29.4±1.1	58.3±0.9	429±12	1.23±0.03	1.77±0.04	0.52	1.92±0.09	2.86±0.18	0.80	0.85
197328	5	1	10	45	17	14±6	29.1±0.9	53.5±0.9	453±13	1.19±0.03	1.80±0.04	0.52	1.93±0.09	2.87±0.18	0.80	0.86
197333	6	1	12	50	17	27±16	31.1±1.2	54.7±1.3	443±20	1.21±0.04	1.80±0.06	0.52	1.93±0.09	2.88±0.18	0.80	0.86
197340	7	E.C.	23	77	25	32±13	30.3±1.0	48.1±1.0	242±12	0.97±0.03	1.24±0.04	0.65	1.42±0.08	2.36±0.18	0.84	0.90
197338	8	E.C.	23	77	25	32±13	30.3±1.0	48.1±1.0	242±12	0.97±0.03	1.24±0.04	0.58	1.37±0.08	2.31±0.17	0.81	0.88
197339	9	E.C.	27	70	25	43±15	29±3	46±2	222±30	0.92±0.05	1.16±0.09	0.59	1.30±0.09	2.24±0.18	0.82	0.88
167806	10	2	15	46	15	20±3	31.9±0.6	53.8±0.6	392±9	1.17±0.04	1.67±0.03	0.96	2.29±0.09	3.23±0.18	0.98	0.99
167809	11	I.C.	16	50	25	18±10	20.7±0.8	49.1±1.0	265±10	0.93±0.02	1.21±0.03	1	1.63±0.09	2.57±0.19	1	1
167817	12	I.C.	16	50	25	18±10	20.7±0.8	49.1±1.0	265±10	0.93±0.02	1.21±0.03	0.85	1.52±0.09	2.47±0.18	0.93	0.96
167818	13	I.C.	16	50	25	18±10	20.7±0.8	49.1±1.0	265±10	0.93±0.02	1.21±0.03	0.85	1.52±0.09	2.47±0.18	0.93	0.96
167805	14	4	11	44	17	40±16	30.3±1.2	47.6±1.1	388±18	1.08±0.03	1.61±0.05	0.89	2.07±0.10	3.01±0.19	0.96	0.97
187312	15	2	5	37	15	60±31	26±2	47.0±1.9	452±32	1.09±0.04	1.72±0.09	0.97	2.27±0.11	3.2±0.2	0.99	0.99
187311	16	2	3	45	15	32±10	25.9±0.8	47.2±0.9	389±15	1.04±0.03	1.56±0.04	0.98	2.12±0.09	3.06±0.18	0.99	0.99
161267*	17	4	29	37	17	31.7±0.5	31.7±0.5	41.3±0.4	424±5	1.04±0.03	1.67±0.03	0.82	2.07±0.09	-	0.93	-
167812	18	4	22	51	17	39±20	31.9±1.5	38.6±1.2	325±20	0.94±0.04	1.40±0.06	0.83	1.76±0.09	2.70±0.17	0.93	0.95
187321	19	3	10	39	15	21±7	17.5±1.5	13.0±1.1	305±16	0.52±0.03	1.03±0.05	0.95	1.28±0.06	2.22±0.15	0.98	0.99
187322	20	3	10	39	15	21±7	17.5±1.5	13.0±1.1	305±16	0.52±0.03	1.03±0.05	0.95	1.28±0.06	2.22±0.15	0.98	0.99
187320	21	3	13	41	15	26±7	16.5±1.5	29.2±1.1	447±18	0.81±0.03	1.49±0.05	0.99	1.89±0.08	2.83±0.17	1.00	1.00
187323	22	5	7	33	18	23±6	15.6±1.3	22.4±1.0	307±15	0.61±0.02	1.08±0.04	0.88	1.32±0.07	2.26±0.16	0.96	0.97
187310	23	3	2	36	15	19±14	16.4±1.1	20.5±1.1	343±16	0.63±0.02	1.17±0.04	1.00	1.49±0.07	2.44±0.16	1.00	1.00
187306	24	3	2	34	15	24±10	19.7±0.8	19.9±0.8	303±12	0.61±0.02	1.10±0.04	0.94	1.39±0.06	2.34±0.15	0.98	0.99
187309	25	3	1	46	15	66±35	32±2	11.6±1.8	171±29	0.50±0.04	0.83±0.08	0.95	1.10±0.08	2.05±0.15	0.98	0.99
187305	26	3	3	26	15	13±3	16.7±0.6	20.3±0.4	366±8	0.644±0.017	1.23±0.02	0.94	1.51±0.06	2.46±0.15	0.98	0.99
181362*	27	4	17	35	17	15.2±0.3	15.2±0.3	22.3±0.4	451±4	0.724±0.014	1.441±0.016	1.00	1.78±0.07	-	1.00	-
187308	28	4	1	64	17	28±13	26.2±1.0	22.8±0.8	269±13	0.66±0.03	1.09±0.04	1.00	1.43±0.07	2.38±0.16	1.00	1.00
207307	29	4	4	45	17	17±8	14.5±1.7	22.7±1.3	403±20	0.69±0.03	1.32±0.06	1.00	1.61±0.08	2.56±0.17	1.00	1.00
181361*	30	4	18	33	17	16.1±0.3	16.1±0.3	22.1±0.4	413±4	0.698±0.015	1.353±0.016	0.93	1.65±0.07	-	0.98	-
187307	31	4	0	64	17	11±10	8.6±0.8	9.9±0.8	165±13	0.307±0.017	0.57±0.03	0.97	0.74±0.04	1.69±0.13	0.99	1.00
187304	32	5	0	31	18	13±14	16.0±1.1	21.3±1.1	382±21	0.66±0.03	1.27±0.06	0.92	1.50±0.08	2.44±0.17	0.97	0.98
161263*	33	4	11	33	17	24.2±0.4	10.0±1.0	26.3±0.3	567±5	0.827±0.012	1.710±0.018	1	2.09±0.09	-	1	-
167831	34	1	2	35	17	28±17	30.6±1.2	40.6±1.2	574±21	1.14±0.03	2.03±0.06	1	2.52±0.12	3.5±0.2	1	1
167830	35	1	7	37	17	19±9	27.5±0.7	39.0±0.9	547±12	1.08±0.03	1.92±0.04	1	2.38±0.11	3.3±0.2	1	1
161264*	36	1	9	42	17	22.9±0.4	22.9±0.4	29.8±0.3	404±4	0.83±0.02	1.45±0.02	1	1.86±0.08	-	1	-
167829	37	1	7	43	17	23±26	22.5±1.8	31±2	384±23	0.83±0.04	1.41±0.06	1	1.78±0.09	2.73±0.18	1	1
167828	38	2	9	30	15	20±10	24.0±0.8	33.2±0.9	419±12	0.89±0.03	1.52±0.04	1	1.95±0.08	2.89±0.17	1	1
167827	39	2	8	40	15	30±10	23.4±1.7	27.9±1.5	439±22	0.84±0.03	1.53±0.06	1	1.91±0.09	2.85±0.18	1	1
167826	40	2	3	34	15	39±24	15.9±1.5	20.2±1.2	405±23	0.67±0.03	1.32±0.06	1	1.61±0.08	2.55±0.17	1	1
161266*	41	4	5	37	17	22.2±0.4	22.2±0.4	44.0±0.4	263±3	0.881±0.019	1.184±0.019	1	1.70±0.07	-	1	-
167823	42	4	7	32	17	17±6	21.2±1.1	30.4±0.8	480±13	0.89±0.02	1.63±0.04	1	1.99±0.09	2.93±0.18	1	1
167825	43	4	8	43	17	19±40	22±3	37±3	491±36	0.98±0.05	1.71±0.10	1	2.13±0.12	3.1±0.2	1	1
167822	44	4	8	42	17	26±7	29.1±1.0	45.5±1.1	426±13	1.08±0.03	1.67±0.04	1	2.18±0.10	3.13±0.19	1	1
167821	45	4	7	37	17	15±11	26.8±0.9	38.4±0.9	403±16	0.96±0.03	1.55±0.05	1	1.99±0.09	2.93±0.18	1	1
167820	46	5	17	54	18	-1±23	15.6±1.5	54.9±1.7	224±22	0.93±0.03	1.09±0.06	0.96	1.58±0.09	2.53±0.17	0.98	0.99
161265*	47	5	26	57	18	20.2±0.4	20.2±0.4	31.2±0.3	356±3	0.789±0.018	1.312±0.018	0.97	1.68±0.08	-	0.99	-
167819	48	5	27	53	18	17±25	30.9±1.7	59.7±1.6	213±21	1.09±0.04	1.25±0.06	0.97	1.83±0.10	2.77±0.18	0.99	0.99

The average saturated water content (w.c.) for each unit is summarised in Table 6.2. We assume a water content of $40\pm10\%$ of the saturated value averaged for each deposition unit. The w.c. values employed in dosimetric calculations for individual samples are given in Table 6.2 (Assumed). In section 6.7.4, we examine the significance of this assumption on the OSL ages.

Several of the sediment samples, particularly samples 197332, 197328, 197333, 197340, 197338 and 197339, were taken in close proximity to bedrock. As the gamma dose rate from bedrock at this site is about three times lower than that from sediment (see Table 6.2), the gamma radiation field in the vicinity of at least these samples must be heterogeneous. This is likely to affect the dose rate experienced by the sample significantly and thus the effect must be taken into account when calculating the sample-specific gamma dose rate based on radionuclide concentrations (before adding internal dose rates, cosmic dose rates and accounting for water content and grain size attenuation). This can for instance be done using Monte Carlo simulations [e.g., 106] or simple explicit models [e.g., 44].

In this study, the modifications for heterogeneity are based on modelling, and rely on the principle of superposition and the infinite matrix assumption[66]. Such model corrections are not as rigorous as those derived from Monte Carlo simulations, but they are more readily incorporated into age calculation software and spreadsheets.

6.3.1 Correction for heterogeneity in the gamma field

In general, the total gamma dose rate, $\dot{D}_{\text{total}}$, to a sample derives from the sample matrix itself, and from any material in the vicinity of the sample (in this case bedrock). Thus, the total gamma dose rate can be expressed as the sum of contributions from the external, $\dot{D}_{\text{ext,inf}}$, and internal $\dot{D}_{\text{int,inf}}$, infinite matrix dose rates, where the relative contributions are given by correction factors C_{int} and C_{ext}, i.e.,

$$\dot{D}_{\text{total}} = C_{\text{int}}\dot{D}_{\text{int,inf}} + C_{\text{ext}}\dot{D}_{\text{ext,inf}} \tag{6.1}$$

To determine the appropriate correction factors C_{int} and C_{ext} in Eq.(6.1), we first derive the general equations for the simple case where the sample material is surrounded by another material in all directions (see section 6.3.1.1). This model is then compared to the Monte Carlo simulation of Riedesel and Autzen[106]. Based on these general equations, we derive the correction factors relevant for this study, e.g., where a sample is surrounded by sediment on one side and bedrock on the other (section: 6.3.1.4). To further test the model, the derived dose rates are compared with in situ dose rate measurements (section 6.3.2). Finally, the significance of our dose rate modelling is evaluated by comparing it to the unmodelled dose rate data (see section: 6.3.3).
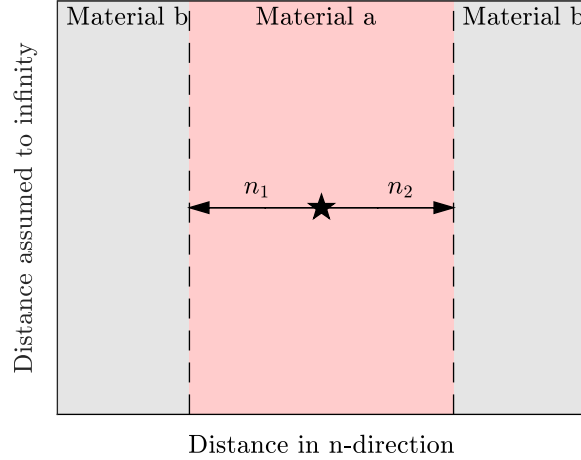
Figure 6.3: Schematic drawing of a simple 2D case, where material a (pale red) is surrounded by material b (grey) on both sides. Material b is assumed to be infinitely thick. The distances from the point of interest (the star) to the boundary between material a and b in direction n_i are shown as arrows.

To derive the correction factors C_{int} and C_{ext}, we use the principle of superposition as in Aitken[66]. For parallel infinite sheets illustrated in Figure 6.3, $N_{a,b}$ describes the dose rate attenuation in material a in the n direction due to the active material b[66]:

$$N_{a,b} = f_{b1}e^{-\mu_{a1}n_1} + f_{b2}e^{-\mu_{a2}n_2} \tag{6.2}$$

Where f_{b1} and f_{b2} are the fractional dose rate factors for the active material b, and μ_{a1} and μ_{a2} are the attenuation factors in material a. The numbers 1 and 2 relate to the distances n_1 and n_2. The factors f_{b1}, f_{b2}, μ_{a1} and μ_{a2} depend both on the type of material and on the distances in the n-direction from the point of interest to the boundary to the active material b, e.g., n_1 and n_2 in Figure 6.3. In the same way the attenuation of the internal dose rate from material a itself is described

$$1 - N_{a,a} = 1 - (f_{a1}e^{-\mu_{a1}n_1} + f_{a2}e^{-\mu_{a2}n_2}) \tag{6.3}$$

In real situations, it may be more complicated and material a may be surrounded by b on more than two parallel sides. The net attenuation in material a then becomes more complicated. Below we develop a model describing these situations by using Eq.(6.2) and Eq.(6.3) for x, y and z directions with N being X, Y or Z.

6.3.1.1   3D Correction factors for a simple case

In Figure 6.4 a material s (pale red) is surrounded by another material r (grey) in all directions. The grey material extends to infinity in all directions from the pale red material. The internal and external correction factors for this 3D geometry are derived below based on the principle of superposition.
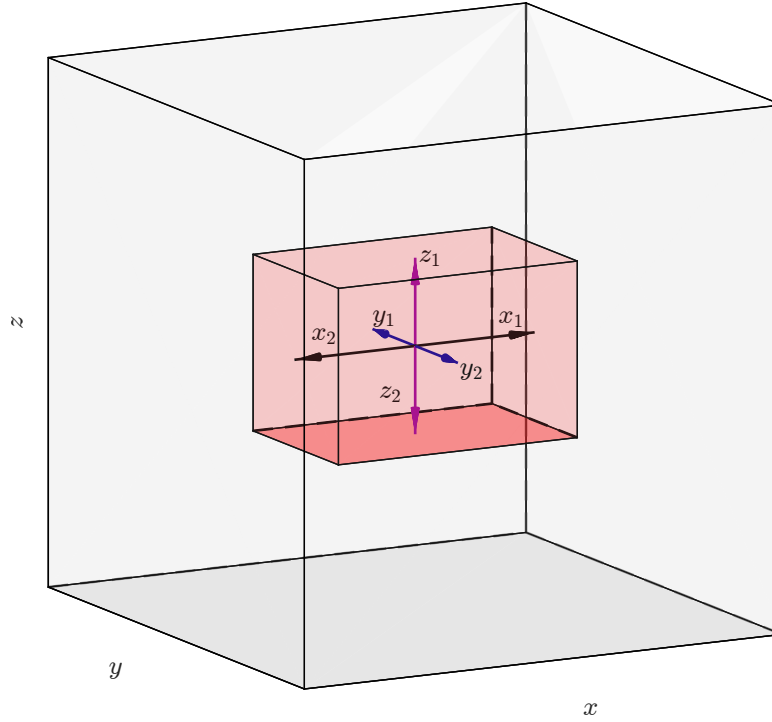
Figure 6.4: Material s (pale red) surrounded by material r (grey), on all sides. The grey material is assumed to continue to infinity. The distances from the point of interest (used as the origin of the coordinate system) to the boundary between material s and r in all directions are shown as arrows.

6.3.1.2 3D Internal correction factors

If material s is the active material, the correction factor, C_{int}, for the dose rate from material s to itself is

$$C_{\text{int}} = (1 - X_{s,s})(1 - Y_{s,s})(1 - Z_{s,s}) \qquad (6.4)$$

where $(1 - X_{s,s})$, $(1 - Y_{s,s})$ and $(1 - Z_{s,s})$ are defined in Eq.(6.3) with $a = s$ and n_1 and n_2 being the distances from the point of interest to the outer boundaries of material s in the x, y, and z-directions (i.e., x_1, x_2, y_1, y_2, z_1 and z_2 in Figure 6.4).

In Figure 6.5, we test the validity of our mathematical formulation for the internal correction factor, C_{int}, by comparing the results obtained using Eq.(6.4) to those obtained by Riedesel and Autzen[106] using Monte Carlo simulation for a granite cobble. Riedesel and Autzen[106] used a spherical geometry for their calculations, so we have calculated the internal fractional dose rate using Eq.(6.4) at the centre of a cube with the same volume as that of the sphere. We use the same μ and f values for granite for the Th series as Riedesel and Autzen[106] did.

In this study, the critical samples (from the point of view of dose rate heterogeneity) are located at distances ranging between ~6 cm and 30 cm to the nearest bedrock. Most of the samples are placed >100 cm away from bedrock.

For diameters of ~12 cm to ~24 cm our calculation of the internal fractional dose rate underestimates the Monte Carlo simulations by less than 25% (see inset in Figure 6.5). For diameters
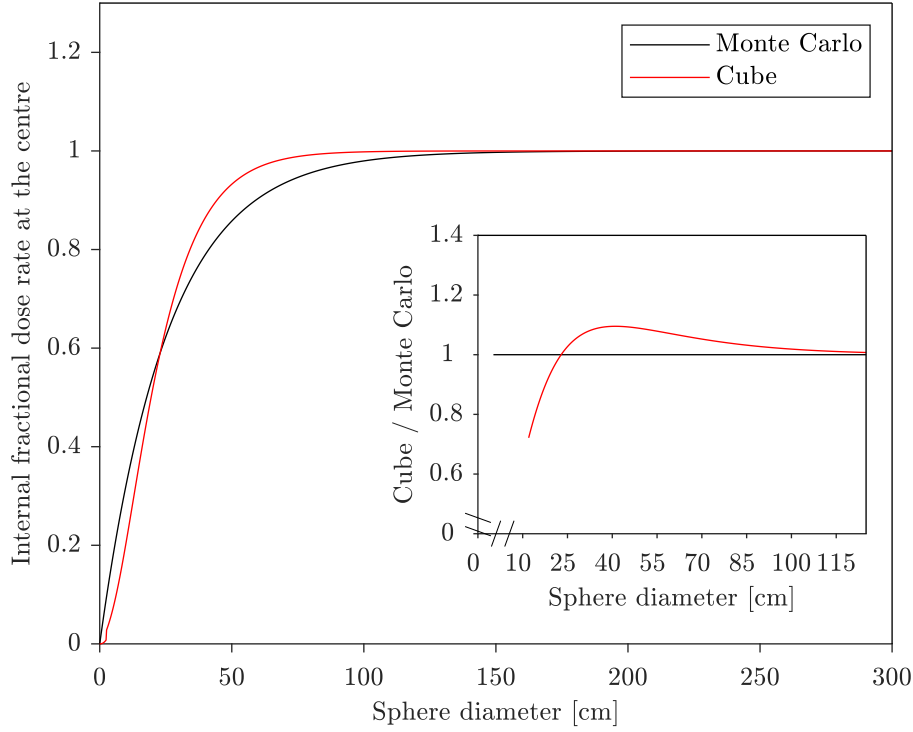
Figure 6.5: Internal fractional dose rate at the centre of a granite sphere simulated using Monte Carlo (data reproduced from Riedesel and Autzen[106], black line). Internal fractional dose rate calculated using Eq.(6.4) (red line) at the centre of a cube with the same volume as that of a sphere. Values for μ and f are taken from Riedesel and Autzen[106] for Th. The corresponding curves for U and K are similar to the ones shown here for Th. The inset shows the ratio of the red to black line for diameters ranging from 12 cm to 125 cm.

ranging between 24 and 120, cm our model overestimates less than 10%. For larger diameters (>120 cm), the internal fractional dose rate is unity (i.e., the internal dose rate corresponds to the infinite matrix dose rate).

In this study, although some samples are located inside 12 cm diameter holes in the wall, they are not surrounded by bedrock from all sides and the underestimation compared to Monte Carlo simulation of the sphere is not critical for these samples.

6.3.1.3   3D external correction factors

Now letting the surrounding material r being the active material, the correction factor for the external dose rate, C_{ext}, from material r to material s is given by Eq.(6.5) below.

$$C_{\text{ext}} = X_{s,r} + (1 - X_{r,r})Y_{s,r} + (1 - X_{r,r})(1 - Y_{r,r})Z_{s,r} \qquad (6.5)$$

where $X_{s,r}$, $Y_{s,r}$ and $Z_{s,r}$ given by Eq.(6.2) and $(1 - X_{r,r})$ and $(1 - Y_{r,r})$ by Eq.(6.3) with x_1, x_2, y_1, y_2, z_1 and z_2 defined as for the internal correction factor (see Figure 6.4).

The terms $(1 - X_{r,r})$ and $(1 - X_{r,r})(1 - Y_{r,r})$ in the second and third terms, respectively, have been included to avoid double counting. This is a consequence of the fact that some parts are geometrically included in the calculations in more than one direction if the sum of $X_{s,r}$, $Y_{s,r}$ and $Z_{s,r}$ were used instead of Eq.(6.5).
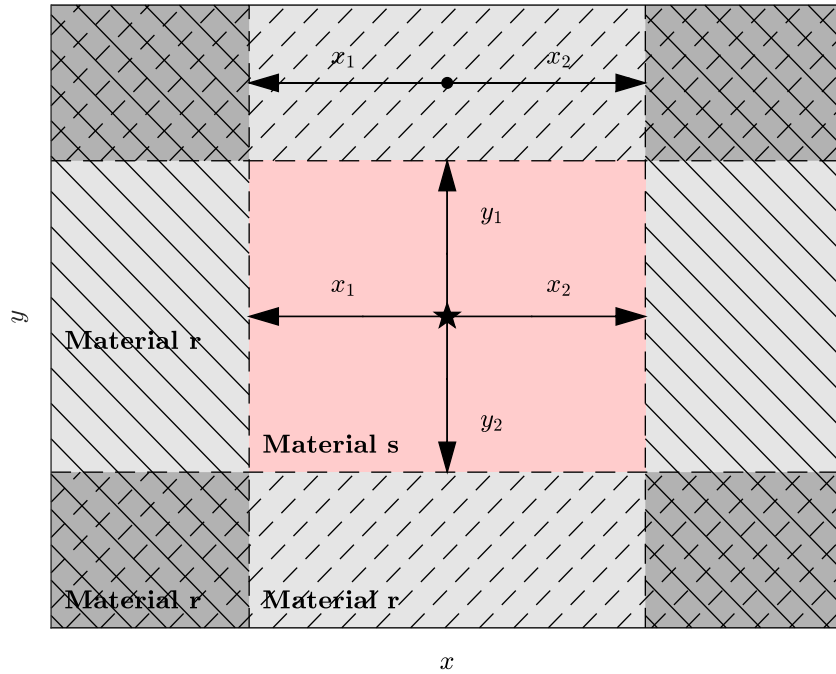
Figure 6.6: Illustration of material s (red) surrounded by active material r (grey) in all directions (assumed to continue to infinity) in two dimensions. The contributions from the external dose rate to material s from material r in the x-direction come from the two striped areas (including the corners). The contributions in the y-direction comes from the two broken striped areas, but the corners (striped and broken striped) must be omitted such that they are only counted once.

The issue of double counting is illustrated for a 2-dimensional case in Figure 6.6. Here material s (pale red) is surrounded by active material r (grey) in x- and y-directions. Material r is assumed to continue to infinity. The contributions from the external dose rate from material r in the x-direction comes from the two full line-striped areas (east/west of material s in Figure 6.6), including the corners, and are given from Eq.(6.2) as $X_{s,r} = f_{r1}e^{-\mu_{s1}x_1} + f_{r2}e^{-\mu_{s2}x_2}$.

The contributions in the y-directions come from the two broken line-striped areas (north/south of material s in Figure 6.6), but the corners (striped with both full and broken lines) were already accounted for in $X_{s,r}$. The contribution in the y-direction must therefore be corrected for this, by an "internal" correction for the material r in the x-direction, given as $(1 - X_{r,r})$ with μ and f defined for material r.

For the 3-dimensional case, this "internal" correction (in regard to material r itself) in the 3rd dimension is also necessary because two parts of the volume contributing in the z-direction have already been accounted for in the x- and y-directions, respectively. This results in the last term in Eq.(6.5) $(1 - X_{r,r})(1 - Y_{r,r})Z_{s,r}$.

This is illustrated in Figure 6.7, where the external contributions to the red volume in the x-, y- and z-directions come from the white, blue, and green volumes respectively, corresponding to the first, second, and third term in Eq.(6.5), respectively. Notice how the contribution in the x-direction (from the white volume) includes regions that would otherwise be counted as contributing in the y- and z-directions if the sum of $X_{s,r}$, $Y_{s,r}$ and $Z_{s,r}$ was used instead of Eq.(6.5). Similarly, the contribution in the y-direction (from the blue volume) includes regions that would otherwise be counted in the z-direction.
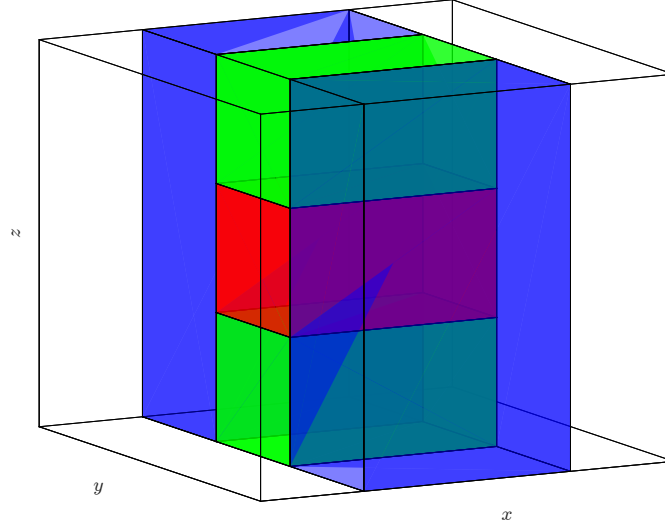
Figure 6.7: Illustration of the geometry relevant for external dose rate calculations to material s (red volume). The external material r (white, blue, and green volumes) all contribute to the total external dose rate. The white volume has already been included, and so is subtracted from the contribution in the y-direction (blue volume). Similarly, the white and blue volumes have already been included, and so must be subtracted from the contribution in the z-direction (green volume, see Eq.(6.5)).

The total dose rate to the sample in this simple symmetrical case is then given as the sum of external and internal infinite matrix dose rates, Eq.(6.1), both corrected for attenuation by the correction factors C_{int} and C_{ext} from Eq.(6.4) and Eq.(6.5), respectively

$$\dot{D}_{\text{total}} = C_{\text{int}}\dot{D}_{\text{int,inf}} + C_{\text{ext}}\dot{D}_{\text{ext,inf}} \tag{6.6}$$

6.3.1.4   Correction factors for life-time burial

In this study, the sediments samples were not surrounded by bedrock in all directions. During burial, sediments are assumed to fill the space on one side of the sample (see Figure 6.8). This gives an extra term in the correction factors C_{int} and C_{ext} compared to the simple case described above.

If x_1 is the distance from the middle of the sample volume to this main sediment body (see Figure 6.8), the correction factor for the internal dose rate, C_{int}, in the sediment volume due to the sediment s itself is

$$C_{\text{int}} = (1 - X_{s,s})(1 - Y_{s,s})(1 - Z_{s,s}) + f_{s1}e^{-\mu_{s1}x_{s1}} \tag{6.7}$$

where $(1 - X_{s,s})$, $(1 - Y_{s,s})$ and $(1 - Z_{s,s})$ are defined in Eq.(6.3) with μ_{s1} being the attenuation factor in sediment and x_1, x_2, y_1, y_2, z_1 and z_2 define the boundaries of the sediment volume from the point of interest (see Figure 6.8).
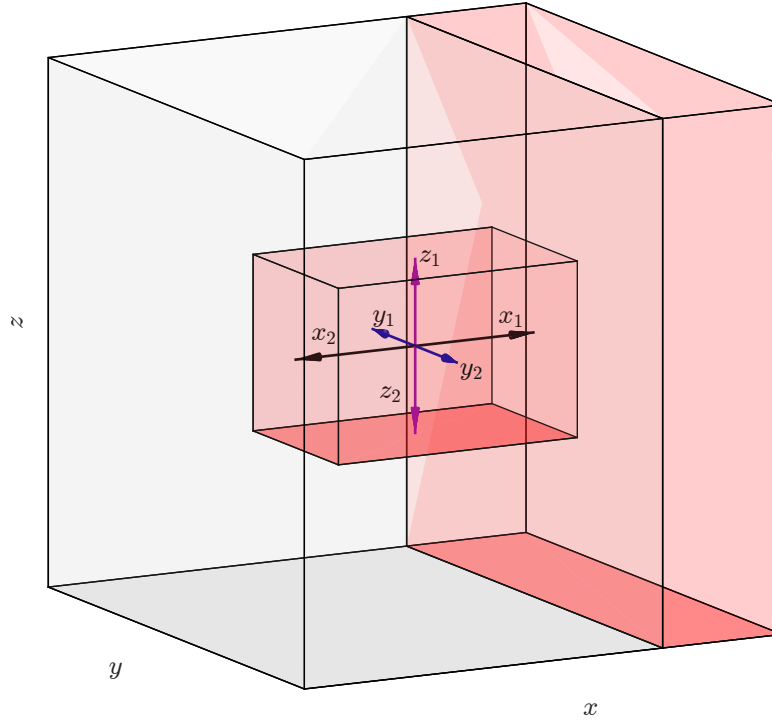
Figure 6.8: Illustration of the 3D geometry relevant for some samples dated in this study. Sediment is shown in pale red and bedrock in grey. During burial, sediments are assumed to fill the space in front of the sample hole to infinity. All outer boundaries in the figure are assumed to go to infinity.

The correction factor C_{ext}, for the external dose rate from bedrock material, r, to the sediment volume, is derived from Eq.(6.5). But that formulation assumed the bedrock to be on both sides of the sample; in this case it is only on one side, and so this extra contribution must be subtracted:

$$C_{\text{ext}} = X_{s,r} + (1 - X_{r,r})Y_{s,r} + (1 - X_{r,r})(1 - Y_{r,r})Z_{s,r} - f_{r1}e^{-\mu_{s1}x_{s1}} \qquad (6.8)$$

For sediment samples with no bedrock nearby (i.e., more than 30 cm away), C_{int} and C_{ext} effectively become 1 and 0 respectively, and the infinite matrix dose rate can be applied without correction.

In the derived corrections factors the parameters f_s, f_r, μ_s and μ_r are different for K-, Th- and U-series and thus each series must be corrected individually. By using Eq.(6.7) and Eq.(6.8) in Eq.(6.1), dry dose rates corrected for nearby rock material are obtained.

The bedrock material in this site is sandstone and the value for μ_r for the bedrock material and the value for μ_r for sediment material are calculated using the sediment values of Riedesel and Autzen[106], corrected for the density of the sandstone measured to 1.3 g.cm^{-3} and sediment measured to 1.8 g.cm^{-3}. The values used are summarised in Table 6.3 and 6.4, respectively.

Table 6.3: Beta and gamma attenuation factors (μ) and the fractional dose factor (f) for different distances (d) in sandstone with density 1.3 g.cm^{-3}, to the boundary of the active material. Adapted from Riedesel and Autzen[106] after density correction.

Bedrock

Decay chain	Beta			Gamma		
	μ [mm^{-1}]	f	d [mm]	μ [mm^{-1}]	f	d [mm]
^{40}K	1.83	0.50	all	0.014	0.50	<10
				0.009	0.45	>10
^{232}Th	3.03	0.50	<0.15	0.013	0.50	<10
	1.20	0.34	>0.15	0.009	0.42	>10
^{238}U	2.29	0.50	<0.15	0.018	0.50	<10
	0.98	0.37	>0.15	0.010	0.45	>10

Table 6.4: Beta and gamma attenuation factors (μ) and the fractional dose factor (f) for different distances (d) in sediment with density 1.8 g.cm^{-3}, to the boundary of the active material. Adapted from Riedesel and Autzen[106] after density correction.

Sediment

Decay chain	Beta			Gamma		
	μ [mm^{-1}]	f	d [mm]	μ [mm^{-1}]	f	d [mm]
^{40}K	2.53	0.50	all	0.019	0.50	<10
				0.013	0.45	>10
^{232}Th	4.19	0.50	<0.15	0.018	0.50	<10
	1.66	0.34	>0.15	0.013	0.42	>10
^{238}U	3.17	0.50	<0.15	0.024	0.50	<10
	1.35	0.37	>0.15	0.014	0.45	>10

In Figure 6.9, the two-dimensional life-time geometry is illustrated for a) a sample taken close to a cave wall and b) for a sample taken inside a hole in the cave wall. The distances from the centre of the sample hole (marked with a star) to the sediment boundary in the y directions are assumed to be infinite in a) and 20 cm in b). The latter is chosen to show the effect on samples taken inside holes in the cave wall.

Gamma correction factors vary as a function of distance in the x-direction corresponding to different positions in the sample hole (rectangle). Correction factors for both the internal dose rate (red) and the external dose rate (blue) are shown.

If the sample position is at the centre of the sample hole (at $x = $15 cm - location of the star) the gamma correction factors are 0.93 and 0.07 for sediment and rock, respectively for the geometry in Figure 6.9a and 0.88 and 0.12 for the geometry in Figure 6.9b where the sample is located in a hole in the bedrock material.

The correction factors for beta irradiation are essentially unity for the sediment contribution, and zero for the bedrock contribution for all distances from the boundary relevant to this study because of the short range of the beta particles.
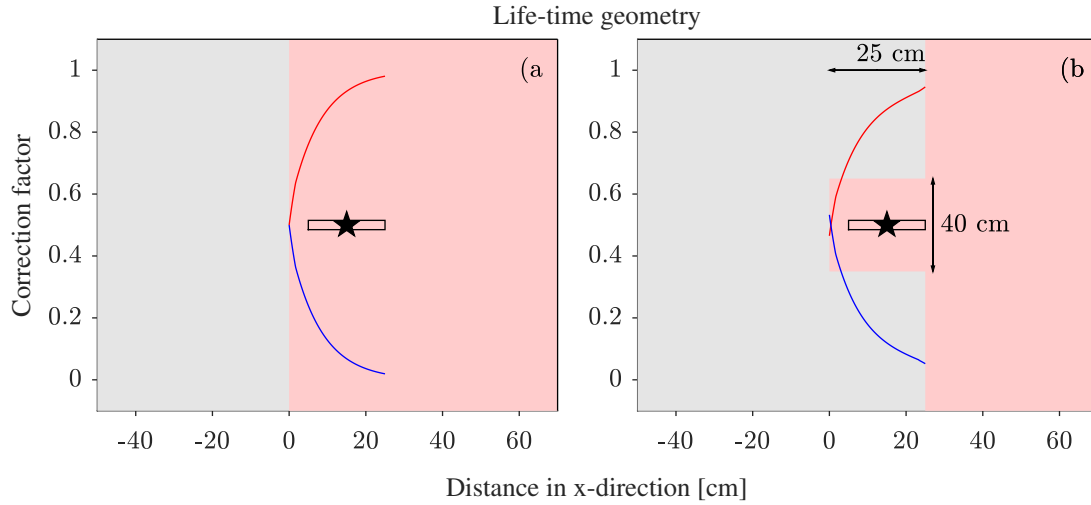
Figure 6.9: Gamma correction factors for two typical life-time geometries a) a sample taken close to a cave wall and b) for a sample taken inside a hole in the cave wall. Correction factors for the internal sediment gamma dose rate, C_{int} is shown in red, whereas that for the external bedrock dose rate, C_{ext} is shown in blue for x varying between 0 and 25 cm for a fixed y position. Pale red represents sediment whereas bedrock is represented in grey. Both materials are assumed to be infinite in the z-direction and assumed to be infinite outside the ranges shown on the axes. The rectangle in the centre illustrates the volume from which the sample is taken. The star illustrates the position from which the correction factors for age calculations are derived, i.e., in the middle of the sample hole.

The dose rates used for age calculation are given in Table 6.2 as "Total dose rates". These are based on beta and modelled gamma dose rates, both adjusted for water content and grain size attenuation, and include internal dose rates and a cosmic ray contribution. The latter has been calculated using the depths reported in the excavation report from 1846 [136]; these are likely to represent the life-time burial depth more accurately than the present-day burial depths, since a considerable amount of sediment has been removed from the slope during the last 150 years.

6.3.2 Comparison with in situ dose rate measurements

The gamma dose rates derived from radionuclide concentrations, corrected for heterogeneity in the gamma field (section: 6.3.1.4), current water content and cosmic dose rate are compared with the in situ dose rate measurements made with a LaBr probe and Al_2O_3:C pellets (see section: 6.2.1).

To enable comparison between the in situ dose rate measurements and the modelled gamma dose rates, the correction factors have to be modified slightly to take the different excavation geometry into account (see Figure 6.10). The excavation geometry, which applies to the in situ measurements, is different from the life-time geometry, because the in situ dose rate measurements were made by inserting the pellets or probe in the holes left after sampling, i.e., there is no sediment inside the sample hole, the in situ measurements were made at the end of the sample hole and most importantly there was no sediment in front of the sample hole.

The location at the end of the sample hole H (see star in Figure 6.10), receives radiation from the surrounding sediment in volume S and from the surrounding bedrock material. The two corrections factors due to these dose rates acting at the end point of the sample hole is given by Eq.(6.9) and
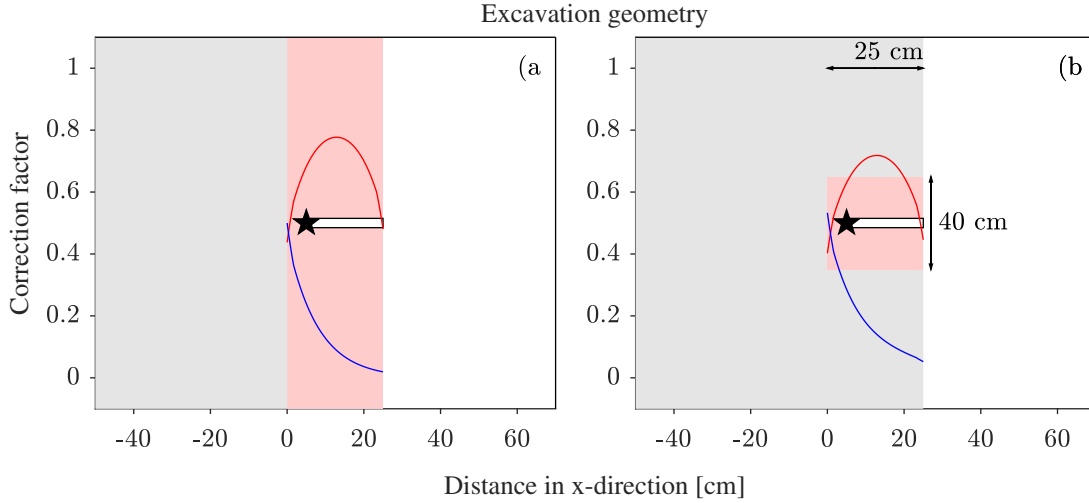
Figure 6.10: Gamma correction factors relevant to the present-day site (excavated geometry) for two different geometries: a) a sample taken close to a cave wall and b) for a sample taken inside a hole in the cave wall. Correction factors for the internal sediment gamma dose rate, C_{int} is shown in red, whereas that for the external bedrock dose rate, C_{ext} is shown in blue. The sample position is assumed to be at the end of the sample hole (where the star is shown) the depth of which varies between 0 and 25 cm. Pale red represents sediment, grey represents bedrock, white represents air. All materials are assumed to be infinite outside the axis ranges shown. The white rectangle illustrates a 20 cm long sample hole. The star illustrates the position from which the correction factors are derived, i.e., at the end of the sample hole.

Eq.(6.10)

$$C_{\text{int}} = I_s(S) - I_s(H) \tag{6.9}$$
$$C_{\text{ext}} = E_{s(r)}(H) - f_{r1}e^{-\mu_{s1}x_{1s,\text{hole}}} \tag{6.10}$$

with $I_s(S)$ and $I_s(H)$ defined as internal correction factors of the sediment geometry and the hole geometry respectively (Eq.6.11 and Eq.6.12 below). $E_{s(r)}(H)$ is defined as an external correction factor with respect to the hole geometry (Eq.6.13 below).

S refers to the distances to the outer sediment boundaries (i.e., the distances from the star to the outer boundary of the pale red area in Figure 6.10. H refers to the distances to the boundary of the hole (i.e., the distances from the star to the outer boundary of the sample hole in Figure 6.10).

$$I_s(S) \equiv (1 - X_{s,s}^{\text{sed}})(1 - Y_{s,s}^{\text{sed}})(1 - Z_{s,s}^{\text{sed}}) \tag{6.11}$$
$$I_s(H) \equiv (1 - X_{s,s}^{\text{hole}})(1 - Y_{s,s}^{\text{hole}})(1 - Z_{s,s}^{\text{hole}}) \tag{6.12}$$
$$E_{s(r)}(H) \equiv X_{s,r}^{\text{hole}} + (1 - X_{r,r}^{\text{hole}})Y_{s,r}^{\text{hole}} + (1 - X_{r,r}^{\text{hole}})(1 - Y_{r,r})Z_{s,r}^{\text{hole}} \tag{6.13}$$

The red and blue lines in Figure 6.10 (C_{int} and C_{ext}, respectively) show the corrections factors for different lengths of the sample hole (i.e., varying the length of the white rectangle). The white rectangles illustrate the sample hole and the star shows the position that was used in calculation of the correction factor. The in situ dose rate meter is assumed to have been positioned where indicated by the star (i.e., at the end of the sample hole).

By using Eq.(6.9) and Eq.(6.10) corrected laboratory calculated wet gamma dose rates are derived for comparison with in situ dose rate measurements.
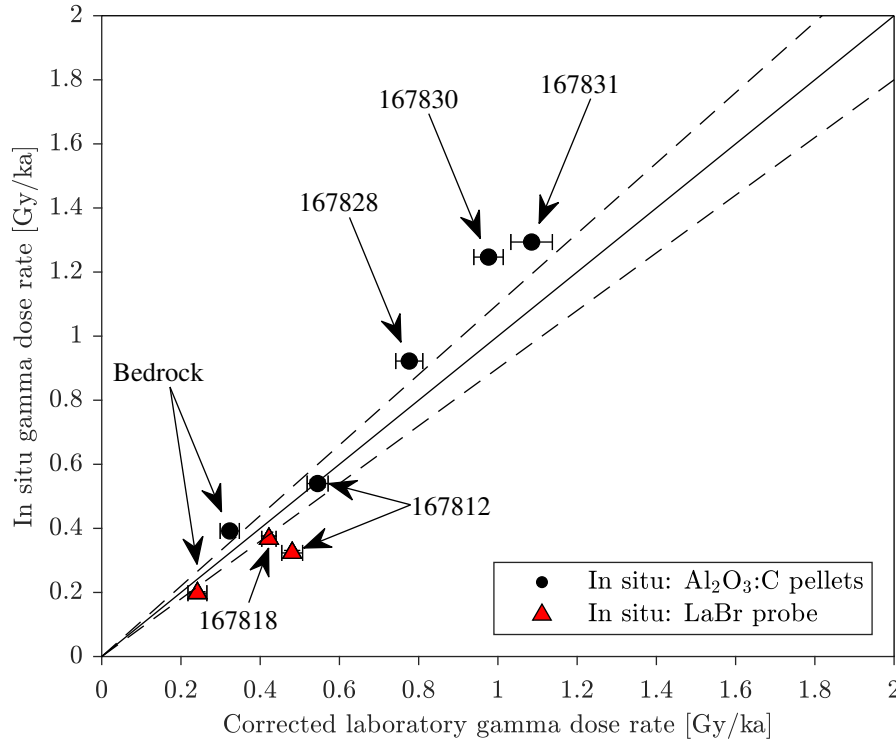
Figure 6.11: In situ measured gamma dose rates from a LaBr probe (red triangles) and Al_2O_3:C pellets (black circles) compared to wet (current w.c.) gamma dose rates derived from radionuclide concentrations and corrected for nearby rocks using Eq.(6.10) and Eq.(6.9). The cosmic dose rate is not included in the laboratory gamma dose rate (red points), since the LaBr probe does not measure cosmic dose rate. The numbers indicate the sample number. Also shown is the 1:1 line (solid) with a ± 10 % uncertainty (dashed lines).

In situ dose rate measurements were done using two different methods. i) Al_2O_3:C pellets were placed in four sediment sample positions and in one hole in the cave wall (black data points in Figure 6.11). ii) LaBr probe measurements were undertaken in two sediment samples positions and in one hole in the cave wall (red data points in Figure 6.11). Since the LaBr probe does not record the cosmic dose rate, this term has not been included in the laboratory dose rate for the purpose of this comparison (red points in Figure 6.11).

On average, the results from the Al_2O_3:C pellets tend to overestimate the calculated dose rates, whereas the LaBr probe results tend to underestimate. Note that both sample 167818 and the rock sample are measured using both in situ methods. The two in situ methods are not consistent with each other, and the corrected calculated dose rates lie between the two in situ methods. We conclude that there is no evidence that the in situ field dose rate measurements are more accurate than the dose rates from radionuclide concentrations (corrected for heterogeneity).

The mean ratio of corrected laboratory dose rate to in situ dose rate is 1.02 ± 0.09 (n=8) for the eight sample positions under consideration (Figure 6.11). This indicates that the laboratory corrected dose rate are, on average, indistinguishable from the measured values, and that the correction for heterogeneity is likely to give reliable dose rates when applied to the burial conditions assumed to apply before the beginning of excavation in 1846.
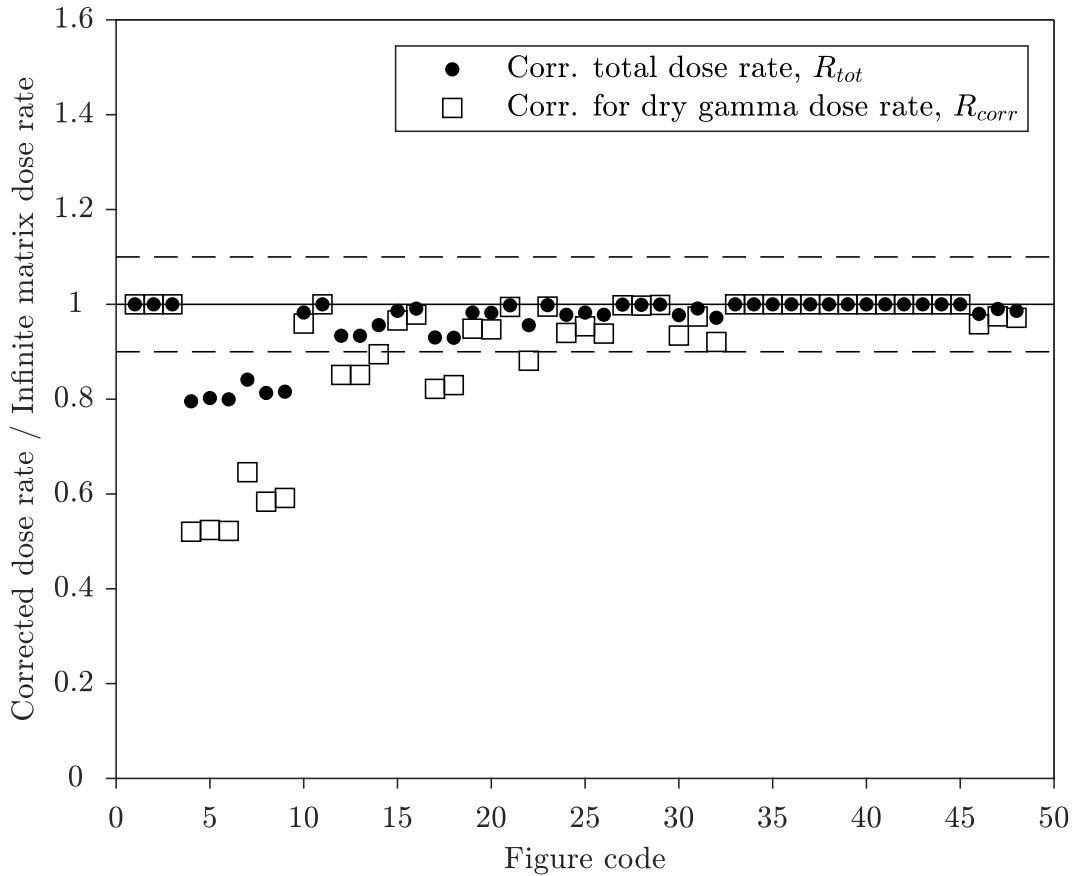
Figure 6.12: Ratio of corrected to infinite matrix dose rates for total dose rate to quartz (R_{tot}, black circles) and to dry gamma dose rate (R_{corr}, squares), plotted against figure codes (see Table 6.2). Six samples (197332, 197328, 197333, 197340, 197338 and 1973390 have R_{tot} values below 0.93 and below 0.7 for R_{corr}. These samples were all taken from holes (diameter of $\sim$12 cm and length of $\sim$15 cm) in the cave wall and clearly illustrate the necessity of correcting for heterogeneity in the gamma field in such cases.

6.3.3   Effect of dose rate modelling in LRC

The effect of the dose rate modelling is illustrated using the ratio of the corrected dose rate to the infinite matrix dose rate (see Table 6.2) for both the dry gamma dose rate (R_{corr}) and the total dose rate (R_{tot}). R_{corr} varies between 0.52 and 1, whereas R_{tot} varies between 0.80 and 1. R_{tot} for quartz is on average 0.964 ± 0.009 (n=48), i.e., close to unity because for most samples the sediment volume is effectively infinite and thus the dose rate for these samples do not require correction. In Figure 6.12 we plot R_{corr} (open squares) and R_{tot} (closed circles) for each sample. For 42 of the 48 samples, R_{tot} is >0.93, but for six samples (197328, -32, -33, -38, -39 and -40) the correction for total dose rate is $\sim$20% and significant. These samples are all taken from holes in the cave wall with a diameter of $\sim$12 cm and length of $\sim$15 cm, but assuming an infinite sediment body . Samples 197332, -28 and -33 are particularly important for determining the chronology for the closure of LRC I.

Our dose rate correction model has been tested against the Monte Carlo simulations of Riedesel and Autzen[106] (see Figure 6.5) and against in situ dose rate measurements. From the results, we conclude that we have confidence in our corrections for heterogeneity in the dose rate.

Our dose rate modelling is simple to implement, does not require Monte Carlo simulations, and can be readily incorporated into age calculation software and spreadsheets. It has considerable potential in sites such as LRC where the heterogeneity is significant and the position of the bedrock material can be most easily categorised by distances in the six directions from the sample position (front, back, left, right, top, bottom).

The dose rates used for age calculation are given in Table 6.2 as "Corrected total wet dose rates". These are based on infinite matrix beta dose rates and modelled gamma dose rates, both adjusted for water content and grain size attenuation, and include internal dose rates and a cosmic ray contribution calculated using reported (1846) burial depths[136] (i.e., life-time burial depths).

6.4 Multi-grain Quartz luminescence results

6.4.1 Multi-grain quartz dose response and stimulation curves

To investigate whether multi-grain quartz measurements are suitable for OSL analysis the OSL signal characteristics were first analysed. Figure 6.13 (data from sample 167828) serves as an illustration of the basic OSL characteristics displayed by the quartz multi-grain measurements. The main graph shows a typical DRC, while the inset shows the natural OSL stimulation curve from the same aliquot. Also shown is the OSL stimulation curve from Risø calibration quartz[96], which is known to be dominated by the fast component. These stimulation curves are very similar, implying that the OSL signals from these sedimentary samples are fast-component dominated. The main graph shows a typical quartz dose response curve with a recycling value of 0.96 ± 0.03, a recuperation value of 0.06 ± 0.01 Gy, and an IR depletion ratio of 0.96 ± 0.03. The DRC has a D_c value of 96 ± 4 Gy (average D_c for all aliquots is 114.4 ± 1.2, n=1251).

Thus, these multi-grain quartz measurements generally show that the dose response curve of this sedimentary quartz appears to be suitable for OSL analysis and that we can have confidence in our ability to measure multi-grain quartz doses up to approximately 225 Gy (i.e., $\sim 2D_c$).
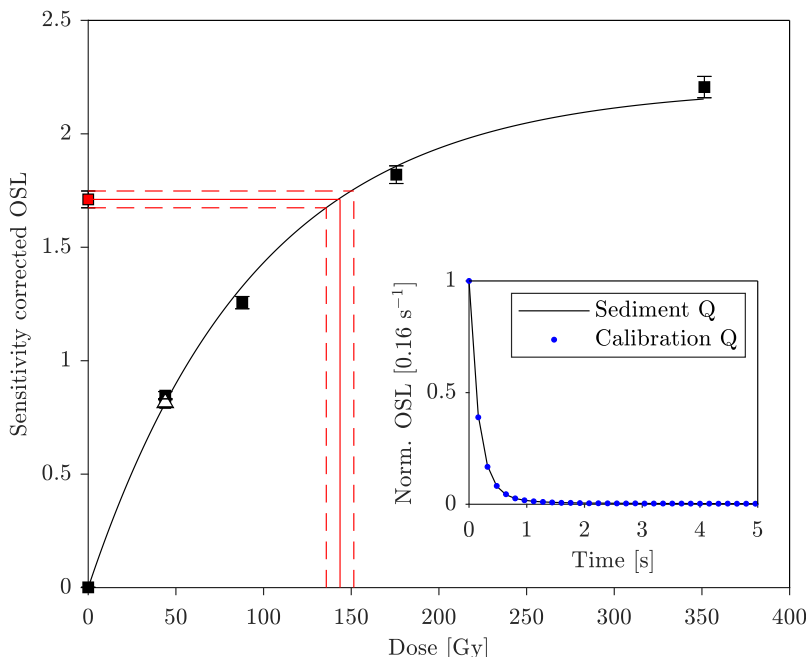
Figure 6.13: A typical quartz dose response curve (black squares) from sample 167828 fitted with a single saturating exponential function (black line). The sensitivity corrected natural signal (red square) is interpolated onto the dose response curve to obtain the estimate of equivalent dose. The recycling point is shown as an open triangle. The insert shows the initial 5 s of the natural OSL signal from the same aliqout (black line), as well as the OSL signal from calibration quartz (blue dots).

6.4.2   Multi-grain quartz rejection criteria

It is standard practice to test: 1) if the chosen measurement protocol accurately corrects for sensitivity change (i.e., the recycling ratio should be close to unity), 2) if the quartz signal is affected by presumed feldspar contamination (i.e., the IR depletion ratio should be close to unity), and 3) if there is significant carry-over between individual SAR measurement cycles (i.e., recuperation should be close to zero). For these samples, the average recycling ratio is 0.957 ± 0.002 (n=840), the average IR depletion ratio is 0.967 ± 0.002 (n=453) and the average recuperation is $0.132 \pm 0.012\%$ of the relevant natural signal (n=840). Based on this we conclude that the overall laboratory sample characteristics are satisfactory. However in the literature it has been argued that individual aliquots must be discarded if the individual recycling and/or IR depletion ratios are significantly different from unity, i.e., the dose estimate from aliquots where, at least, one of these ratios is more than two standard deviations away from unity, should be rejected.

In Figure 6.14 and 6.15, we show the individual dose estimates for 840 aliquots as a function of the corresponding recycling and IR depletion ratio, respectively. The individual doses have been normalised to the mean for each sample. There is no correlation between these quantities and the measured dose, and applying such rejection criteria does not significantly change the average dose or the relative standard error (RSE) at the 95% confidence level. Thus, there is no justification for applying such rejection criteria to these samples.

As stated in section 6.2.2.1, we have used the objective Inter quartile Range (IQR) criteria to reject outlying dose estimates. The natural quartz multi-grain dose distributions are shown as simple frequency histograms in Figure 6.17 with the rejected doses indicated. Applying the IQR

Figure 6.14: Individual doses normalised to the sample mean plotted against individual recycling ratios for every aliquot (n=840). Aliquots with recycling ratios consistent with unity at 68%, 95% and > 95% are shown in black, red, and blue, respectively.

rejects (to samples processed in Denmark) a total of 46 dose estimates for all samples out of the 1144 derived, i.e., ∼4% are rejected. The ratio of dose calculated with and without the IQR for individual samples range between 0.87±0.09 and 1.07±0.08 (see Table 6.5) with an average for all samples of 0.979±0.006 (n=41 samples), and the ratio for all individual samples is consistent with unity at 95% confidence. However, the average relative standard error (at 68 % level) is reduced by 17±3 % (n=41 samples). Thus, application of the IQR results mainly in a more precise dose estimate but does not significantly change the dose values.

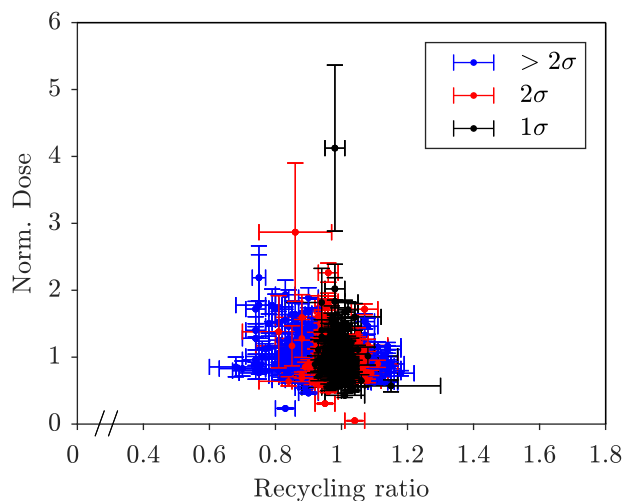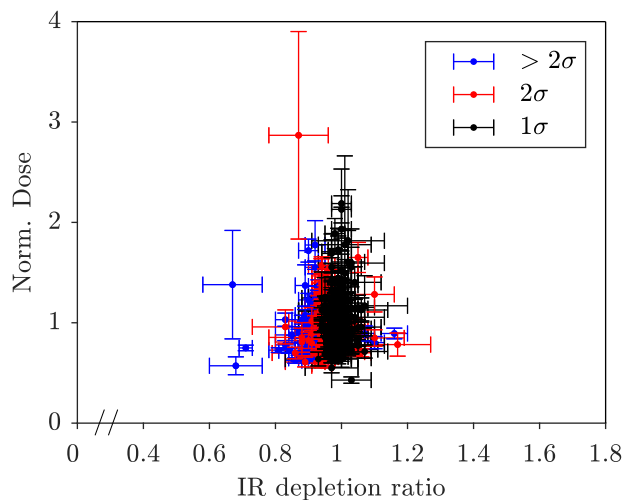**Figure 6.15:** Individual doses normalised to the sample mean plotted against individual IR depletion ratios (n=453). Aliquots with recycling ratios consistent with unity at 68%, 95% and > 95% are shown in black, red, and blue, respectively.

Table 6.5: Summary of multi-grain OSL results. Samples prepared and measured in Hungary [136] are marked with an asterisk (*). "Fig. code" refers to the sample codes given in ED 7 in Marquet et al. [79]. "a,b,c,d" refers to different locations ("Locus" in LRC I). "Unit" is the deposition unit. "I.C." and "E.C." represent samples from inner cave of LRC I and the entrance of LRC I, respectively (not identified with a specific unit). "Elevation" is the elevation [m] above sea level of the sample locations (NGF). "Q" and "KF" are quartz and K-rich feldspar, respectively. "Dose" is the arithmetic average equivalent dose after application of the IQR rejection criterion. All uncertainties are reported at the 68% confidence interval. "Age" is the equivalent dose divided by the total dose rate (see Table 6.2). "n" is the number of aliquots included in the equivalent dose estimation, i.e., the total number of measured aliquots less the aliquots which gave unbounded dose estimates and the number of dose estimates rejected by the IQR rejection. The latter can be seen in Figure 6.17. "In sat" is the relative number of aliquots giving unbounded dose estimates. The IR_{50} ages have been fading corrected using a g-value of $2.66 \pm 0.12\%$/decade. The $pIRIR_{290}$ ages have not been fading corrected. "IQR ratio" is the ratio between the average equivalent dose with and without the application of the IQR rejection criterion.

| | | | | | Multi-grain quartz | | | | Multi-grain K-feldspar | | | | | | | | Ratios | | | | |
| | | | | | | | | | IR_{50} | | | | $pIRIR_{290}$ | | | | Age | | IQR ratio | | |
Lab code	Fig. code	Locus	Unit	Elevation [m]	Dose [Gy]	Q age [ka]	n**	In sat (%)	Dose [Gy]	KF age [ka]	n**	In sat (%)	Dose [Gy]	KF age [ka]	n**	In sat (%)	IR_{50}/Q	$pIRIR_{290}$/Q	Q	IR_{50}	$pIRIR_{290}$
187301	1	LRC I-d	1	54.95	79±3	42±3	19	0	52±4	24±3	8	0	100±4	36±3	7	0	0.56±0.07	0.85±0.06	1.07	1	0.96
187302	2	LRC I-d	1	54.55	129±6	47±3	35	0	68±7	24±3	8	0	136±4	37±2	9	0	0.51±0.06	0.78±0.05	1	1	1
187303	3	LRC I-d	1	54.10	97±6	46±4	20	0	37±7	16±3	4	0	104±7	34±3	8	0	0.34±0.06	0.74±0.07	1	1	1.11
197332	4	LRC I-c	1	51.28	105±3	55±3	34	0	57±2	25±2	10	0	142±5	50±4	12	0	0.46±0.04	0.91±0.05	0.87	0.92	1
197328	5	LRC I-c	1	51.10	97±3	50±3	19	0	56.8±1.8	25.5±1.8	11	0	138±4	48±3	12	0	0.51±0.06	0.96±0.05	0.98	0.95	1
197333	6	LRC I-c	1	50.97	101±4	53±3	35	0	61.5±1.9	28±2	11	0	137±3	48±3	11	0	0.52±0.05	0.91±0.05	0.98	1.03	0.97
197340	7	LRC I	E.C.	50.78	449±69	317±53	4	69	346±57	195±38	11	8	1347±199	571±95	6	50	0.61±0.15	1.8±0.4	1	1	1
197338	8	LRC I	E.C.	50.66	228±14	167±18	40	17	404±20	233±22	10	0	1474±63	638±57	5	58	1.39±0.18	3.8±0.4	1	0.90	1
197339	9	LRC I	E.C.	50.57	320±11	247±20	33	25	405±19	241±24	12	0	1868±86	834±78	10	17	0.97±0.10	3.4±0.2	1.05	1	1
167806	10	LRC I-a	2	50.54	132±6	58±4	22	0	86±3	35±2	11	0	182±7	56±4	12	0	0.60±0.05	0.98±0.07	0.93	0.91	1
167809	11	LRC I	I.C.	50.20	321±26	197±20	14	32	317±22	163±18	12	0	1330±54	517±44	10	17	0.83±0.11	2.6±0.2	0.91	1	1
167817	12	LRC I	I.C.	50.20	311±49	204±34	14	42	263±39	141±24	11	0	802±82	325±41	8	25	0.69±0.16	1.6±0.3	1	0.90	0.86
167818	13	LRC I	I.C.	50.20	449±22	295±23	13	42	398±16	214±20	11	0	1786±59	725±60	9	25	0.73±0.08	2.46±0.16	1.04	0.96	1
167805	14	LRC I-a	4	50.04	137±6	66±4	21	8	100±6	43±4	12	0	214±10	71±6	12	0	0.65±0.07	1.07±0.07	0.97	1	1
167812	15	LRC I-a	2	49.79	155±4	69±4	34	3	85±11	34±5	5	0	141±4	44±3	8	0	0.50±0.08	0.64±0.03	0.98	1	0.97
187311	16	LRC I-a	2	49.55	135±5	64±4	38	5	66±18	28±8	4	0	130±10	43±4	9	0	0.43±0.13	0.67±0.06	0.96	1	1
161267*	17	LRC I-b	4	49.40	163±7	79±5	24	-	-	-	-	-	-	-	-	-	-	-	-	-	-
167812	18	LRC I-b	4	49.40	134±8	76±6	22	4	78±6	37±4	12	0	175±14	65±7	12	0	0.49±0.06	0.85±0.09	0.92	1	1
187321	19	LRC II	3	47.59	112±3	88±5	34	0	69±3	40±3	12	0	156±5	70±5	12	0	0.45±0.04	0.80±0.04	0.96	1	1
187322	20	LRC II	3	47.18	122±3	95±6	33	0	75±4	44±3	12	0	147±4	66±5	12	0	0.46±0.04	0.69±0.04	0.94	1	1
187320	21	LRC II	3	47.09	159±5	84±5	35	0	89±3	41±3	11	0	166±3	59±4	12	0	0.48±0.04	0.70±0.03	0.98	0.96	1
187323	22	LRC II	5	46.90	159±6	121±8	34	3	99±3	57±5	23	0	256±13	113±10	24	0	0.47±0.04	0.94±0.07	0.95	0.98	1
187310	23	LRC II	3	46.76	132±4	88±5	23	0	78±4	41±3	9	0	151±4	62±4	9	0	0.47±0.04	0.70±0.03	0.98	1	1
187306	24	LRC II	3	46.64	121±4	87±5	33	6	73±5	41±4	9	0	149±5	64±5	9	0	0.47±0.05	0.74±0.04	0.98	1	1
187309	25	LRC II	3	46.03	113±4	103±9	23	4	73±2	46±4	9	0	137±4	67±6	9	0	0.45±0.04	0.65±0.03	1	1	1
187305	26	LRC II	3	45.96	140±5	92±6	33	3	87±3	46±3	9	0	159±3	65±4	8	0	0.50±0.04	0.70±0.03	0.98	1	0.95
181362*	27	LRC II	4	45.70	138±4	78±4	33	-	-	-	-	-	-	-	-	-	-	-	-	-	-
187308	28	LRC II	4	45.70	142±3	99±6	47	0	83±6	45±5	9	0	179±8	75±6	9	0	0.46±0.05	0.76±0.05	0.96	1	-
207307	29	LRC II	4	45.52	156±4	97±6	66	6	93.0±1.9	47±3	12	0	182±4	71±5	12	0	0.49±0.04	0.74±0.03	0.97	1	1
181361*	30	LRC II	4	45.50	156±3	95±5	33	-	-	-	-	-	-	-	-	-	-	-	-	-	-
187307	31	LRC II	4	45.18	243±10	327±23	25	17	257±13	201±19	7	0	798±76	473±59	7	22	0.62±0.06	1.45±0.16	1	0.84	1
187304	32	LRC II	5	45.13	182±13	121±11	33	8	98±8	52±6	10	0	201±15	82±9	10	0	0.43±0.06	0.68±0.07	1	1	1
161263*	33	LRC III	4	45.20	135±4	65±3	24	-	-	-	-	-	-	-	-	-	-	-	-	-	-
167831	34	LRC IV	1	49.80	70±3	27.8±1.7	21	4	36±3	13.3±1.4	6	0	88±6	26±2	6	0	0.48±0.05	0.92±0.07	0.94	1	1
167830	35	LRC IV	1	48.20	121±4	51±3	23	0	69±5	27±3	6	0	151±6	45±3	6	0	0.53±0.06	0.90±0.05	0.97	1	1
161264*	36	LRC IV	1	47.20	104±4	56±3	27	-	-	-	-	-	-	-	-	-	-	-	-	-	-
167829	37	LRC IV	1	46.50	115±7	65±5	24	0	59.9±1.1	28.1±1.7	5	0	140.8±1.6	52±4	5	0	0.43±0.04	0.80±0.05	1	0.96	1.01
167828	38	LRC IV	2	46.20	134±7	69±5	24	0	71±3	32±3	12	0	156±2	54±3	12	0	0.46±0.05	0.78±0.05	1	1	1
167827	39	LRC IV	2	46.00	137±7	71±5	23	0	66±3	30±3	12	0	154±4	54±4	12	0	0.42±0.04	0.76±0.04	0.95	1	1
167826	40	LRC IV	2	44.90	127±6	79±6	21	8	62±5	32±3	12	0	143±6	56±4	12	0	0.40±0.04	0.71±0.05	0.96	1	1
161266*	41	LRC IV	4	44.60	156±2	92±5	22	-	-	-	-	-	-	-	-	-	-	-	-	-	-
167823	42	LRC IV	4	44.60	148±7	74±5	21	13	98±6	43±4	12	0	187±7	64±5	12	0	0.58±0.06	0.86±0.06	1	1	1
167825	43	LRC IV	4	44.60	157±11	73±7	21	13	89±3	38±3	10	0	180±3	59±4	11	0	0.51±0.05	0.80±0.06	1	1	0.97
167822	44	LRC IV	4	44.50	172±7	79±5	24	7	106±6	44±4	12	0	222±7	71±5	11	0	0.56±0.08	0.90±0.05	0.97	1	0.97
167821	45	LRC IV	4	44.10	192±11	96±7	24	8	130±4	58±4	12	0	260±6	89±6	11	0	0.60±0.05	0.92±0.06	1	1	0.97
167820	46	LRC IV	5	43.30	291±19	184±16	18	31	452±41	238±27	12	0	1486±18	588±42	6	33	1.29±0.17	3.2±0.2	1	1	0.99
161265*	47	LRC IV	5	42.50	295±9	176±10	19	-	-	-	-	-	-	-	-	-	-	-	-	-	-
167819	48	LRC IV	5	42.50	281±19	153±14	18	28	387±35	185±21	12	0	1397±78	504±45	9	25	1.21±0.16	3.3±0.3	1	1	1

**$n = n_{tot} - n_{sat} - n_{IQR}$
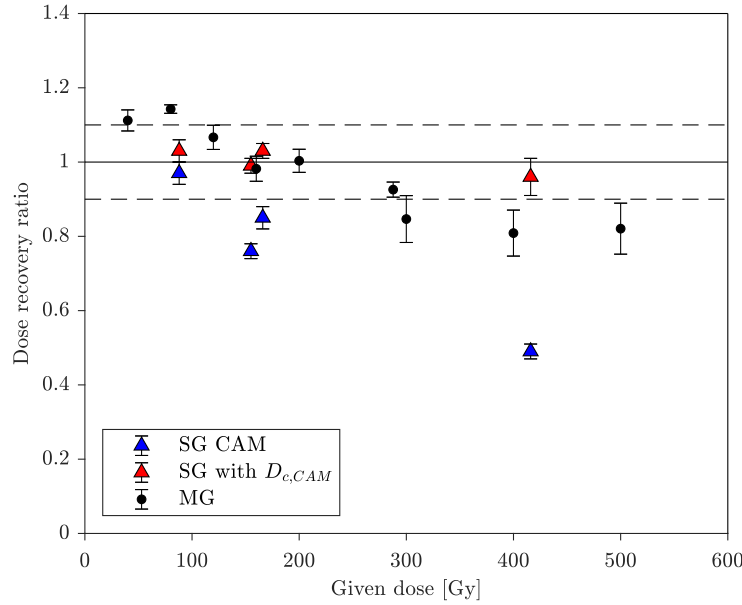
Figure 6.16: Average multi-grain (MG, black circles) and single-grain (SG, red and blue triangles) quartz dose recovery ratios for given doses ranging between 40 and 500 Gy. For MG (sample 167819), each point is an arithmetic average of 4-12 individual aliquots. For SG (samples 187302, 167806, 207307, 167319) each point is based on CAM and is shown both with (red triangles) and without (blue triangles) application of the D_c criterion (see section 6.5.1 for further details). The number of included dose estimates in each point range between 102 and 388 (CAM) and between 16 and 95 ($D_{c,CAM}$)

6.4.3 Multi-grain quartz dose recovery

Dose recovery experiments aim to assess whether a known laboratory dose, given prior to any thermal treatment of the sample, can be recovered accurately using the given measurement protocol. A dose recovery ratio within 10% of unity is generally considered to be satisfactory[107].

A SAR protocol with a preheat of 260 °C (220 °C for test dose) was used. In these experiments, aliquots were bleached twice for 100 s using blue light stimulation at room temperature, separated by a pause of 10 ks to allow charge transferred to the 110°C TL peak to decay to negligible levels. A known dose, ranging from 40 to 500 Gy, was given to batches of 6 to 48 aliquots from all samples from LRC IV and samples 187301-12, -20,-22,-23 and samples 167805,-06,-12 from LRC I and II. The given doses were chosen to be similar to the natural equivalent doses. The average dose recovery ratio of all experiments is 0.965 ± 0.012 (n=171) indicating that a laboratory dose given before the first thermal treatment can be measured using the chosen SAR protocol with sufficient accuracy. Note that this does not guarantee that natural doses can be measured with the same accuracy because we do not know whether the laboratory and natural dose response curves have the same shape[43,162].

In Figure 6.16 the average dose recovery ratios are shown as a function of given doses for sample 167819. Individual aliquots were given doses ranging between 40 and 500 Gy. It is worth noting that the three dose recoveries done at high doses, i.e., at 300, 400 and 500 Gy, all give low dose recovery ratios of 0.85 ± 0.06 (n=6, 0% of aliquots in saturation), 0.81 ± 0.06 (n=4, 33% of aliquots in saturation) and 0.82 ± 0.06 (n=12, 20% of aliquots in saturation), respectively.

6.4.4 Multi-grain quartz natural dose distributions

Between 12 and 72 multi-grain aliquots were measured for each sample and the estimated doses range between 70±3 Gy (167831) and 449±69 Gy (197340) (see Table 6.5). Figure 6.17 shows quartz multi-grain dose distributions processed in Denmark (ordered as in Table 6.5). The relative standard deviations of these range between 13% (sample 197328) and 59% (sample 167817) with an average value of ∼24%. There is a tendency for the relative standard deviations to increase with measured dose. We could not derive bounded dose estimates for a significant fraction of the aliquots (∼10% on average). Not surprisingly, the relative number of aliquots appearing to be in saturation increases with the measured dose.

When a significant number of aliquots appear to be in saturation, the accuracy of the resulting estimate of the burial dose must be questioned as it is likely that the estimate is significantly underestimated. There is no established method to determine when significant underestimation might be an issue due to saturation issues, but in line with Singh et al.[163] we regard samples with more than 15% of the individual multi-grain aliquots appearing to be in saturation as providing minimum burial dose estimates. This means that all samples from unit 5 in LRC IV, sample 187307 in LRC II and all samples from inside LRC I (I.C. and E.C.) are regarded as providing minimum burial ages. Note that these samples all give quartz multi-grain doses > 225 Gy (> $2D_c$).
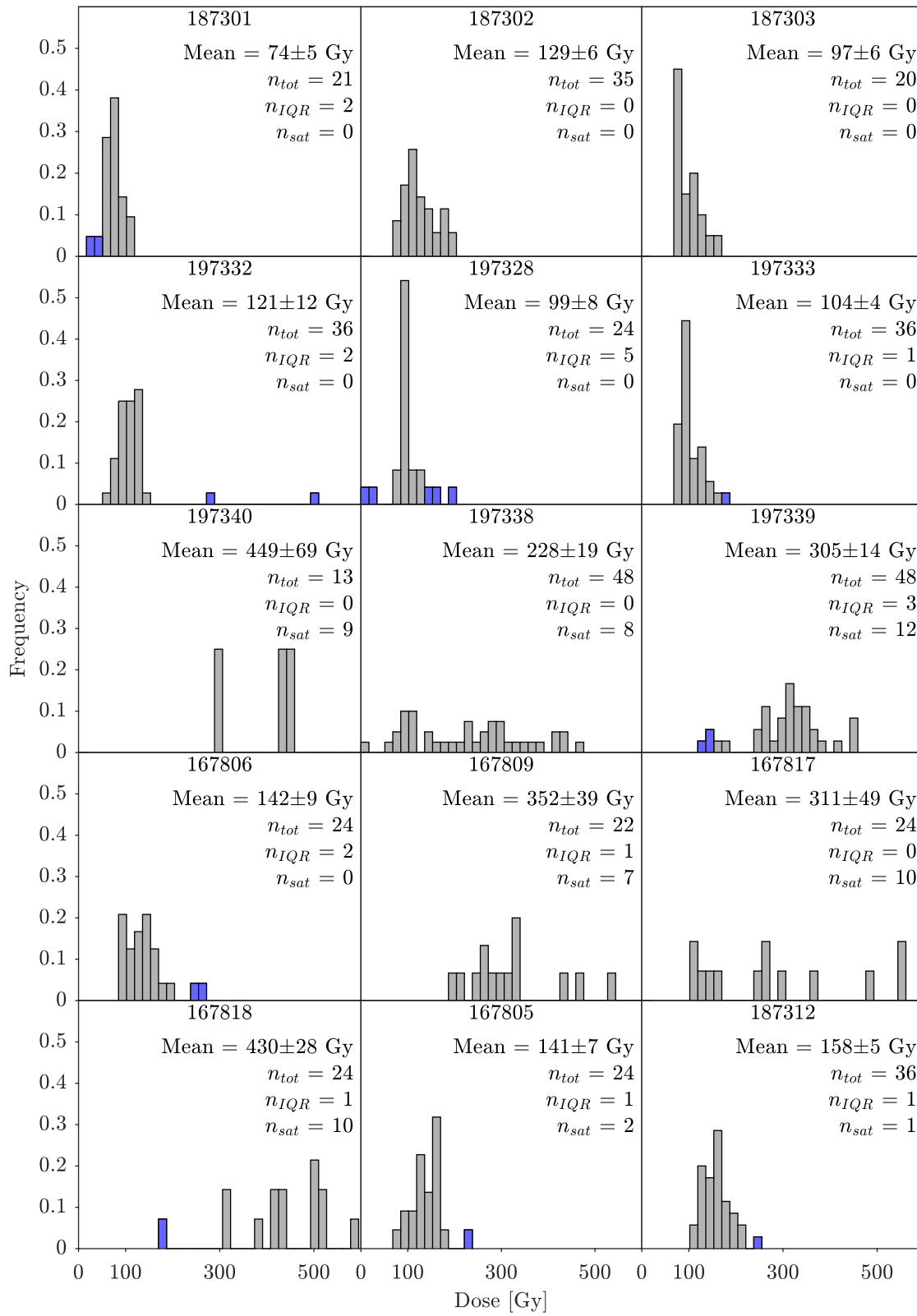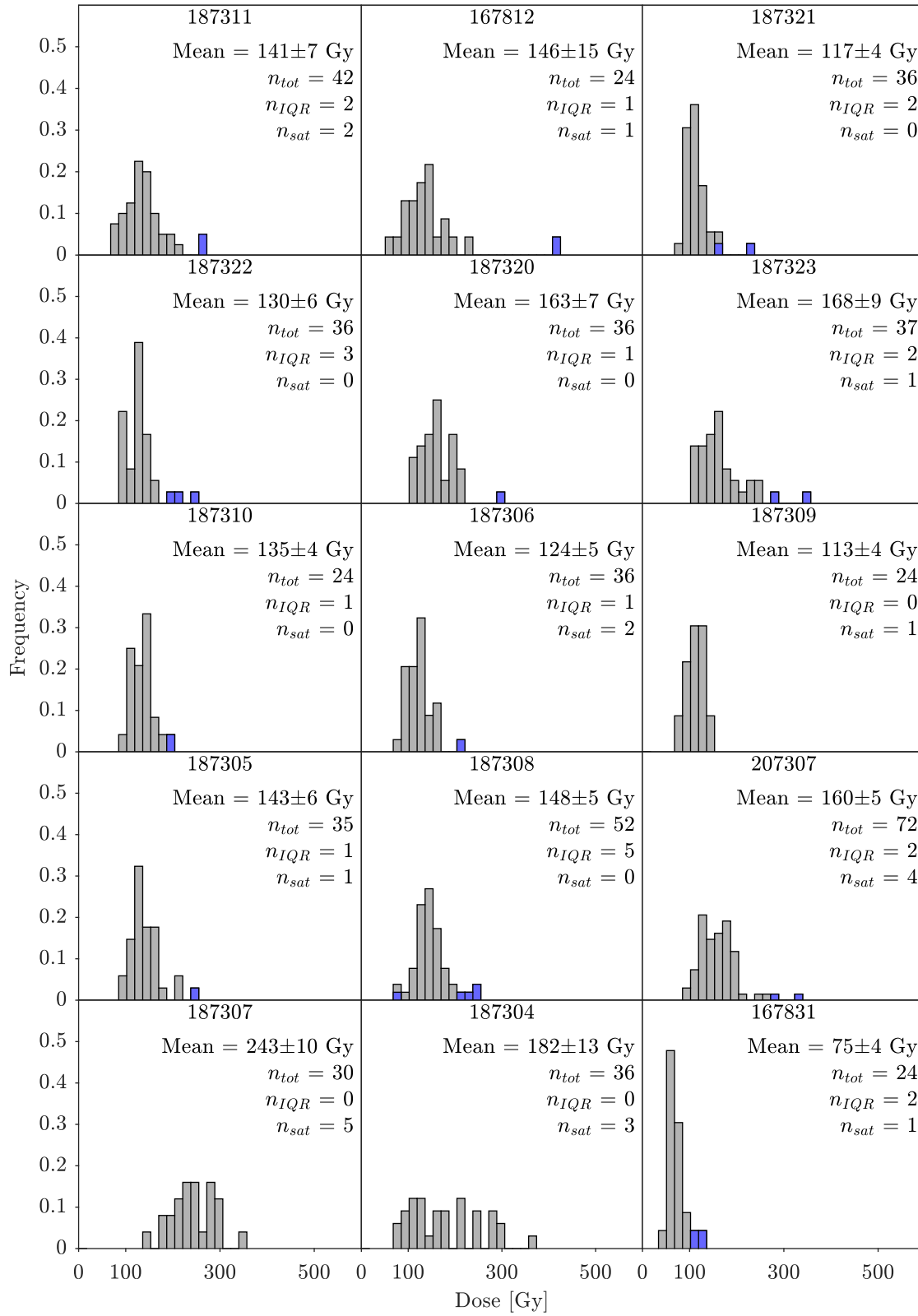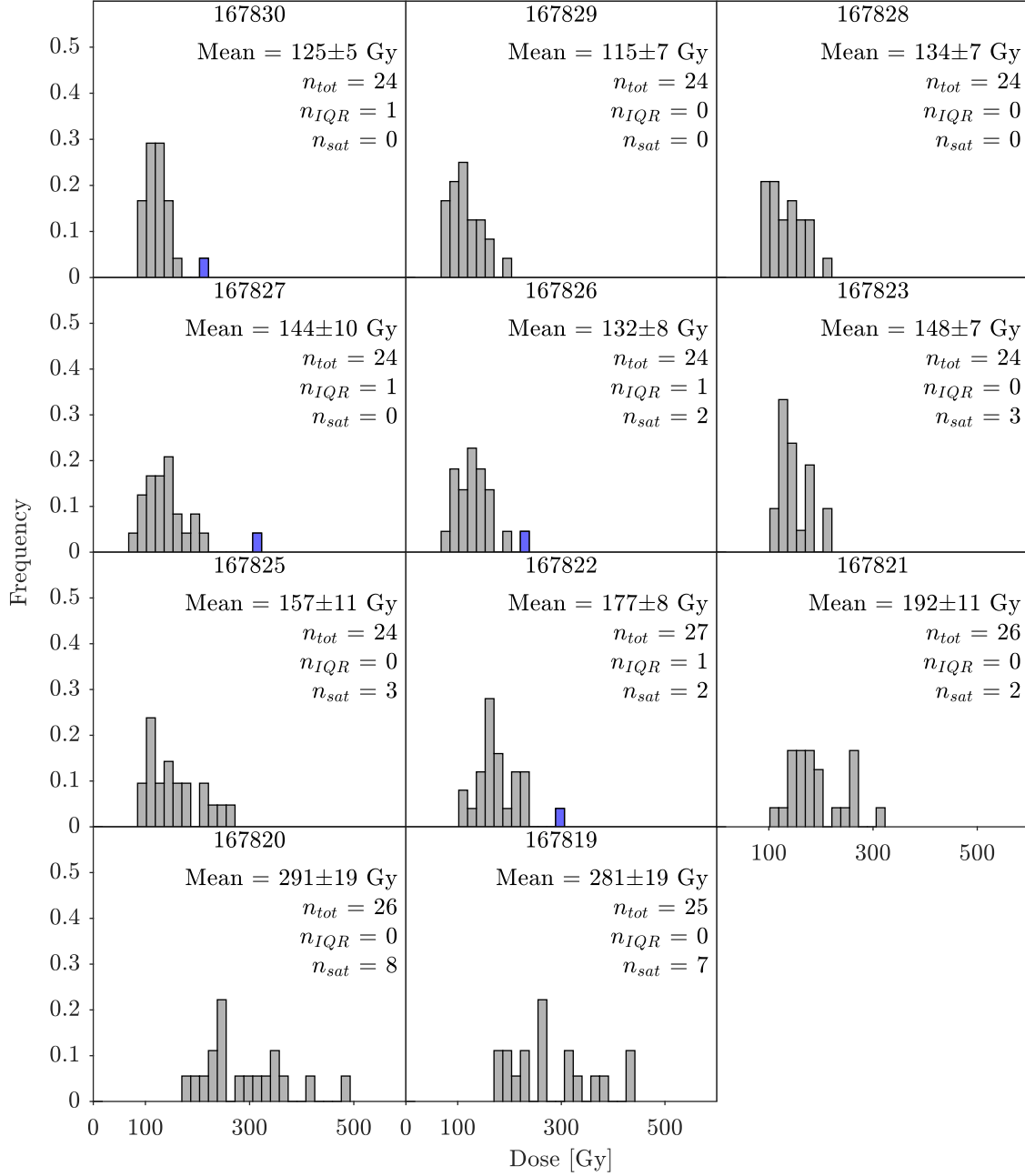
Figure 6.17: Multi-grain quartz dose distributions measured at Risø DTU. Grey bars: Doses after application of the IQR criterion. Blue bars: dose estimates rejected by the IQR criterion. The legend for each sample gives the arithmetic mean dose and its standard error of all measured aliquots giving a bounded dose estimate, the total number of measured aliquots (n_{tot}), the number of aliquots rejected by the IQR criterion (n_{IQR}), and the number of aliquots for which no bounded dose estimate could be derived (n_{sat}), i.e., the number of aliquots appearing to be in saturation on the laboratory dose response curve.

6.5   Single grain quartz results

Quartz single-grain analysis was undertaken for 12 samples to investigate whether the samples are likely to have been significantly incompletely bleached, mixed after deposition, and/or suffer from saturation effects. In the literature, it is also argued that single-grain OSL data are superior to multi-grain data, because it is possible to reject individual grains with poor luminescence characteristics [e.g.,38]. We assume that a good agreement between multi-grain and single-grain quartz dose estimates means that none of these concerns affect our multi-grain results significantly.

6.5.1   Single grain quartz dose recovery

Single grain dose recovery experiments, similar to those carried out for multi-grain aliquots (i.e., grains were bleached twice at room temperature with the blue LEDs for 100 s with an intervening pause of 10,000 s before giving a known laboratory dose), were undertaken for four samples (187302, 167806, 207307 and 167819). A total of 8,100 individual grains were measured and 17% of these were detectable, i.e., gave natural test dose responses with $s_{Tn} < 20\%$ (see Table 6.6). The given doses were 88, 166, 155 and 416 Gy for samples 187302, 167806, 207307 167819, respectively. The corresponding individual CAM dose recovery ratios (Figure 6.16) were 0.97±0.03 (n=102), 0.85 ± 0.03 (n=142), 0.76 ± 0.02 (n=388) and 0.49 ± 0.02 (n=259) with over-dispersion (OD) values of 17 ± 3, 29 ± 3, $36 \pm 2\%$ and $46 \pm 3\%$, respectively (see Tables 6.6 and 6.7)[1]. Only the dose recovery at a given dose of 88 Gy is acceptable (i.e., consistent with unity at two standard deviations). It is worth noting that for all experiments a significant number of grains (varying between 17 and 57%) with detectable T_n signals did not give bounded dose estimates. There is a strong linear correlation ($R^2 = 0.996$) between the given dose and the number of grains giving no bounded dose estimates due to saturation effects. However, applying the Bayesian approach the dose recovery ratios are 1.08 ± 0.04, 1.00 ± 0.02, 0.89 ± 0.02 and 0.90 ± 0.02, respectively, i.e., two of the four dose recovery ratios are acceptable. The average dose recovery ratios for all samples are 0.77 ± 0.10 and 0.97 ± 0.05 for CAM and BayLum, respectively. Thus we can, on average, recover the given dose when using BayLum analysis, whereas using CAM underestimates the given dose. This suggests that Bayesian modelling may be less biased by grains giving unbounded dose estimates (see below). Figure 6.18a shows the measured dose distribution for sample 207307 (black points). For this sample, 23% of the detectable grains gave unbounded dose estimates. As has previously been reported in the literature [e.g.,164] the average D_c value for grains with a natural OSL signal in saturation (i.e., no bounded dose estimate can be derived) is significantly lower than for those grains giving bounded dose estimates. The weighted average ratio of D_c values for grains in saturation to those giving bounded dose estimates is 2.0 ± 0.3 (n=4 samples) for the single-grain dose recovery data sets. Thomsen et al. [39] showed that, for their samples, individual grains should have D_c values approximately $\geq$ to the dose to be measured, before they are likely to act, on average, as accurate dosimeters. This condition is shown as the intersection of the solid line of unit slope with the measured data in Figure 6.18b, in this case measured to given dose ratio. Applying the approach of Thomsen et al. [39]; i.e., the "D_c criterion" in which grains, irrespective of equivalent dose, D_e, are filtered based on individual D_c values, changes the CAM dose recovery ratios to 1.03 ± 0.03 (n=81), 0.99 ± 0.02 (n=95), 1.03 ± 0.02 (n=71) and 0.96 ± 0.05 (n=16) and

---

[1]Note that the ADM should only be applied to dose distributions where extrinsic factors contribute to the observed variability
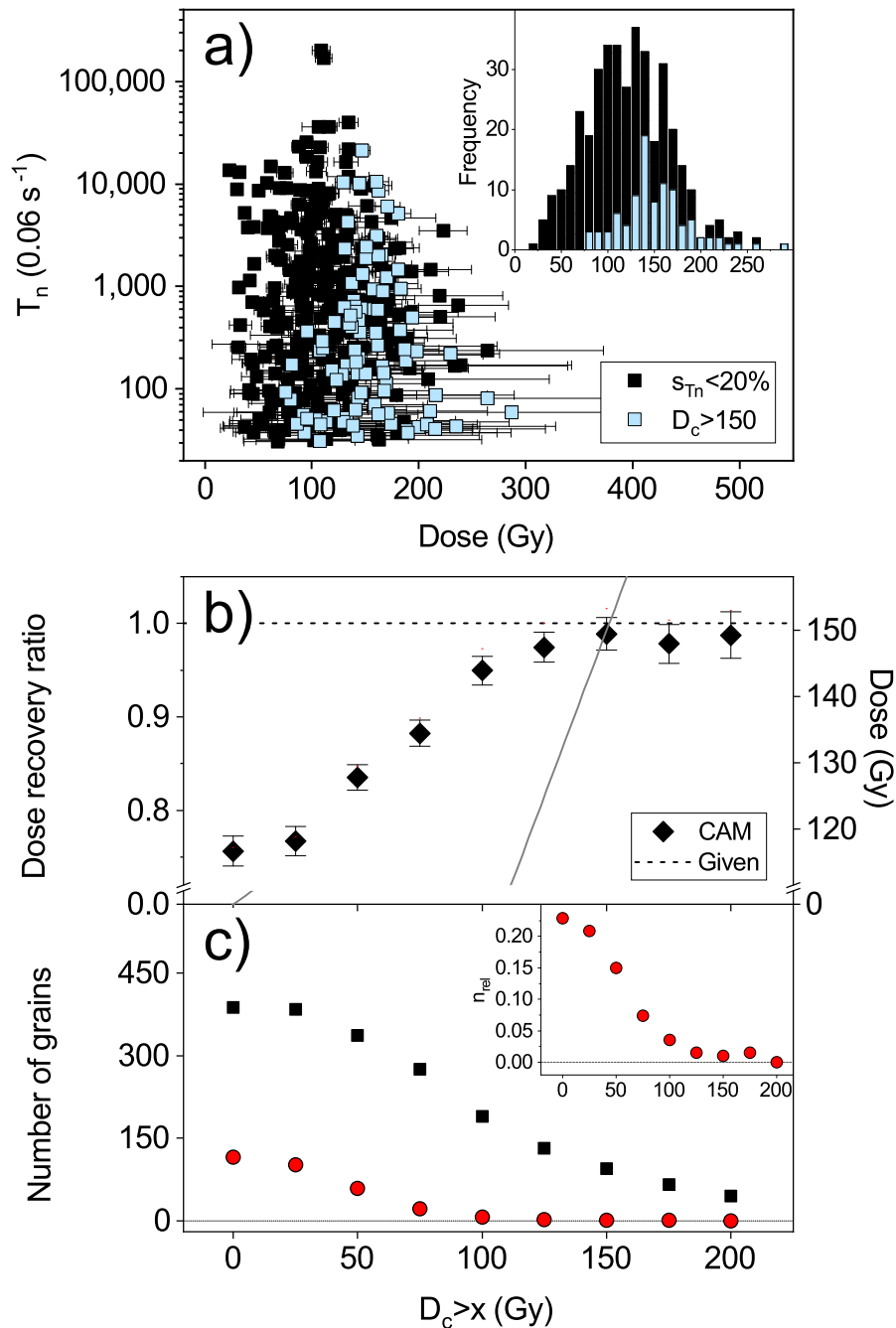
Figure 6.18: Single grain dose recovery data from sample 207307. a) The scatter plot shows intrinsic brightness (T_n, "natural" test dose response) against estimated dose, whereas the inset shows a simple frequency diagram of the dose values. The black data show all dose estimates (with $s_{Tn} < 20\%$), whereas the light blue data only show dose estimates which also have a D_c value greater than 150 Gy. b) Effect of rejecting grains according to their D_c values on the dose recovery ratio (left axis) and average dose (right axis) using CAM (black diamonds). The horizontal dashed line indicates a dose recovery ratio of unity. The 1:1 line (right axis) intersects the unit dose recovery ratio at a D_c of ~150 Gy indicating that, for this sample, the dose recovery is satisfactory if only grains with a D_c equal to greater than the given dose of 150 Gy are accepted. c) Effect of rejecting grains according to their D_c values on the number of grains with bounded estimates (black squares) and unbounded dose estimates (red circles). The inset shows the proportion of grains with unbounded dose estimates.

reduces the proportion of grains appearing in saturation to 2, 1, 5 and 0%, respectively. The resulting CAM OD values are 12 ± 4, 10 ± 2, $8 \pm 3\%$ and $7 \pm 9\%$, respectively.

Figure 6.18a also shows the remaining dose distribution from the dose recovery experiment on sample 207307 after all grains with a D_c value equal to or less than 150 Gy have been rejected (blue symbols). Figure 6.18b shows the effect on the dose recovery ratio and average dose as the D_c threshold is increased. The dose recovery ratio is consistent with unity when only grains with a D_c value larger than 125 Gy are included in the distribution. Following Thomsen et al.[39] and Singh et al.[163], the D_c threshold is determined as the value when the average dose of the remaining distribution is approximately equal to the minimum D_c value.

These results strongly suggest that D_c filtering is both appropriate and necessary.

The average dose recovery ratios for the four dose recovery samples after application of the D_c criterion are 1.00 ± 0.02 and 1.01 ± 0.03 for CAM and BayLum, respectively. It is interesting to note that the Bayesian approach to data analysis appears to be insensitive to including grains, which in conventional analysis (CAM) are incapable of recording the dose of interest accurately.

Figure 6.18c shows how the number of grains (with both bounded and unbounded dose estimates) decreases with the D_c threshold. Thus, applying the D_c criterion is expensive in terms of grain rejection, but does remove the apparent underestimation observed at given doses greater ~ 100 Gy caused by grains not able to record the dose of interest. The dose recovery ratios for the four samples are all acceptable using either of the two analytical approaches, when the D_c criterion is applied.

6.5.2 Single grain quartz dose estimation

The natural OSL signals from 18,900 individual quartz grains were measured. Of these grains, 18% gave test dose responses with $s_{Tn} < 20\%$, and $\sim 13\%$ had natural sensitivity-corrected signals which gave bounded dose estimates by interpolation on to the laboratory regenerated dose response curves.

6.5.2.1 Effect of single-grain rejection criteria

Figures 6.19a and 6.19b show the measured single-grain dose distribution for samples 207307 and 197339, respectively. The black bars/points represent all grains giving bounded dose estimates with $s_{Tn} < 20\%$, whereas the white bars/points represent the bounded dose estimates, which also fulfil the rejection criteria given in section: 6.2.2, i.e., recycling and IR depletion ratio within two standard deviations of unity and recuperation within 2 standard deviations of zero. Application of these rejection criteria for these two samples does not significantly change the average dose or the observed over-dispersion but does reduce the grain population by 55% and 41%, respectively. For all samples, the ratio of CAM doses, ODs and reduction in grain population with and without application of the rejection criteria is 0.97 ± 0.02, 0.95 ± 0.04 and 0.49 ± 0.03, respectively. Since the only significant effect of applying these rejection criteria is to reduce the accepted grain population, these rejection criteria are not considered further. Similar conclusions were reached by e.g., Thomsen et al.[164].

Table 6.6: Summary of single-grain quartz results. "Nat" is the natural signal and "DR" is dose recovery. The given doses were 88, 166, 155 and 416 Gy, respectively. "N_{tot}" is the total number of measured single grains. "s_{Tn}" is the uncertainty assigned to OSL response for the test dose for the natural SAR cycle. "n" is the number of accepted grains. "OD CAM" and "D_e CAM" is the over-dispersion and average equivalent dose, respectively, calculated using the Central Age Model (CAM, Galbraith, 1999). "D_e ADM" is the equivalent dose calculated using the average dose model[104] with an internal over-dispersion of 17% . Note that The ADM should only be applied to dose distributions where extrinsic factors contribute to the observed variability. "D_e BayLum" is the equivalent dose estimate calculated using the R-package BayLum[104]. Here, the dose is given as the midpoint of the 68% confidence interval. No doses are reported for the BayLum analysis after application of the D_c criterion to samples 197338 and 167819, since the analysis did not converge; presumably caused by the low number of accepted grains.

Sample	Signal	Site	Unit	N_{tot}	$s_{Tn}<20\%$						$s_{Tn}<20\%$ and $D_c>D_{e,av}$					
					n	n_{sat} (%)	OD CAM (%)	D_e CAM (Gy)	D_e ADM (Gy)	D_e BayLum (Gy)	n	n_{sat} (%)	OD CAM (%)	D_e CAM (Gy)	D_e ADM (Gy)	D_e BayLum (Gy)
197338	Nat	LRC I	E.C.	1,600	83	57%	71 ± 7	140 ± 13	178 ± 13	825 ± 154	20	41%	28 ± 9	278 ± 28	285 ± 24	-
197339	Nat	LRC I	E.C.	1,800	119	59%	52 ± 5	164 ± 10	186 ± 10	399 ± 24	15	21%	43 ± 11	264 ± 35	293 ± 46	410 ± 59
167812	Nat	LRC I	4	1,000	153	12%	42 ± 3	101 ± 4	109 ± 5	120 ± 5	101	5%	45 ± 4	110 ± 6	144 ± 10	125 ± 6
187311	Nat	LRC I	2	1,700	167	25%	36 ± 3	104 ± 3	110 ± 3	135 ± 5	65	10%	36 ± 4	126 ± 7	133 ± 7	157 ± 11
187312	Nat	LRC I	2	1,100	105	33%	33 ± 3	117 ± 5	121 ± 5	166 ± 10	50	12%	46 ± 5	127 ± 7	132 ± 8	164 ± 14
167805	Nat	LRC I	4	1,700	262	26%	37 ± 2	115 ± 3	122 ± 3	139 ± 3	108	7%	32 ± 3	134 ± 5	143 ± 6	
167806	Nat	LRC I	2	1,700	287	21%	29 ± 2	104 ± 2	107 ± 2	122 ± 3	147	6%	25 ± 2	115 ± 3	117 ± 4	127 ± 4
187302	Nat	LRC I	1	1,100	146	17%	36 ± 3	94 ± 3	99 ± 3	116 ± 4	92	3%	34 ± 3	97 ± 4	101 ± 5	110 ± 5
207307	Nat	LRC II	4	1,700	275	22%	32 ± 2	104 ± 2	108 ± 2	123 ± 3	114	5%	27 ± 3	119 ± 4	121 ± 4	132 ± 5
167819	Nat	LRC IV	5	1,800	126	64%	60 ± 5	198 ± 12	233 ± 16	3174 ± 827	12	0%	38 ± 11	384 ± 51	404 ± 66	-
167823	Nat	LRC IV	4	1,400	276	21%	32 ± 2	119 ± 3	123 ± 3	143 ± 3	122	3%	28 ± 2	125 ± 4	128 ± 4	137 ± 4
167831	Nat	LRC IV	1	2,300	409	5%	30 ± 1	72 ± 1	75 ± 1	79 ± 1	314	0%	28 ± 2	76 ± 1	78 ± 2	80 ± 2
187302	DR	LRC I	1	1,900	102	17%	17 ± 3	86 ± 2	-	96 ± 3	81	2%	12 ± 4	91 ± 3	-	93 ± 3
167806	DR	LRC I	3	1,100	142	25%	29 ± 3	141 ± 4	-	166 ± 4	71	5%	8 ± 3	171 ± 4	-	176 ± 5
207307	DR	LRC II	4	1,900	388	23%	36 ± 2	117 ± 2	-	138 ± 2	95	1%	10 ± 2	153 ± 3	-	151 ± 5
167819	DR	LRC IV	5	3,200	259	57%	46 ± 3	205 ± 7	-	374 ± 10	16	0%	7 ± 9	400 ± 22	-	396 ± 22

6.5.2.2 Application of the D_c criterion to single-grain dose distributions

The OD values from samples from unit 1-4 range between 29 ± 2 and $42 \pm 3\%$ with an average of $34.2 \pm 1.4\%$ (n=9, see Table 6.6). OD values of this magnitude is commonly reported for dose distributions obtained from samples expected to be well-bleached and not disturbed by post-depositional mixing[165]. The OD values of the three samples from unit 5 and E.C. are significantly higher, ranging between 52 ± 5 and $71 \pm 7\%$, which could indicate that these samples are suffering from significant incomplete bleaching, gross post-depositional mixing and/or saturation effects. Using the three methods of analysis (see section: 6.2.2) the average ratios of the single-grain dose estimates to that derived from multi-grain analysis for the samples from unit 1-4 are 0.79 ± 0.03 (CAM), 0.83 ± 0.04 (ADM) and 0.97 ± 0.03 (BayLum). Interestingly, the single-grain doses estimated by BayLum for samples 167819 and 197338 (unit 5 and E.C.), are > 800 Gy ($> 300\%$ higher than those estimated by multi-grain analysis) which may imply that these samples cannot be dated accurately using quartz OSL.

The dose recovery experiments indicate that single-grain measurements on these samples may underestimate the burial dose for doses larger than ~ 100 Gy unless saturation effects are appropriately dealt with. The number of single grains appearing to be in saturation (i.e., no bounded equivalent dose estimate could be derived) varies between 5% and 64% and correlates with sample dose. Of particular concern, are the samples from unit 5 and E.C. (167819, 197338 and 197339), which have 64%, 57% and 59%, respectively, of the light-giving grains giving unbounded dose estimates. This is cause for serious concern as it may lead to significant age underestimation for single-grain data sets [e.g., 39,163].

Figure 6.19c shows the D_c distribution for individual grains for sample 207337 (unit 4) and a clear overlap between bounded and unbounded estimates is observed. The grains with bounded (78%) and unbounded dose estimates (22%) have weighted average D_c values of 104 ± 3 Gy and 58 ± 3 Gy, respectively, i.e., the ratio between the D_cs is 1.80 ± 0.10. Figure 6.19d shows the same data for sample 197339 (E.C.), but for this sample the D_c distribution of the bounded dose estimates is very similar to the one for the unbounded dose estimates, i.e., weighted average D_c values of 114 ± 5 Gy and 102 ± 4 Gy, respectively, i.e., with a ratio of 1.12 ± 0.06. Figure 6.19e and 6.19f show the effect of increasing the D_c threshold for samples 207307 and 197339, respectively. As for the dose recovery data, the intersection of the dashed line with the equivalent dose data gives an estimate of the minimum acceptable D_c value. For sample 207307 the equivalent dose estimate increases by $\sim 15\%$ (at $D_c > 125$ Gy) but for sample 197339 by $\sim 60\%$ (at $D_c > 250$ Gy). Application of the D_c criterion decreases the number of grains included in the calculation by 59% (from n=275 to 114) and 87% (from n=119 to 15), for samples 207307 and 197339, respectively (see Table 6.6). For the two other samples from E.C. and unit 5 (samples 197338 and 167819), the accepted grain population is reduced by $\sim 90\%$ (from n=126 to 12) and 75% (from n=83 to 20), respectively. For unit 5 and E.C., the number of accepted dose estimates is small (i.e., 15, 12 and 20) and thus caution must be exercised when interpreting the resulting burial doses. However, it is worth noting that the dose recovery experiment for sample 167819 (given dose of 416 Gy) was satisfactory after application of the D_c criterion even all though only 16 grains remained. Before application of the D_c criterion, the average OD value for these three samples is 61 ± 6 %. However, after application of the D_c criterion, the average OD value decreases to 36 ± 5 %, which is entirely consistent with the average OD values observed for the samples from units 1-4 (average 34.1 ± 1.4 % or 34 ± 3 %
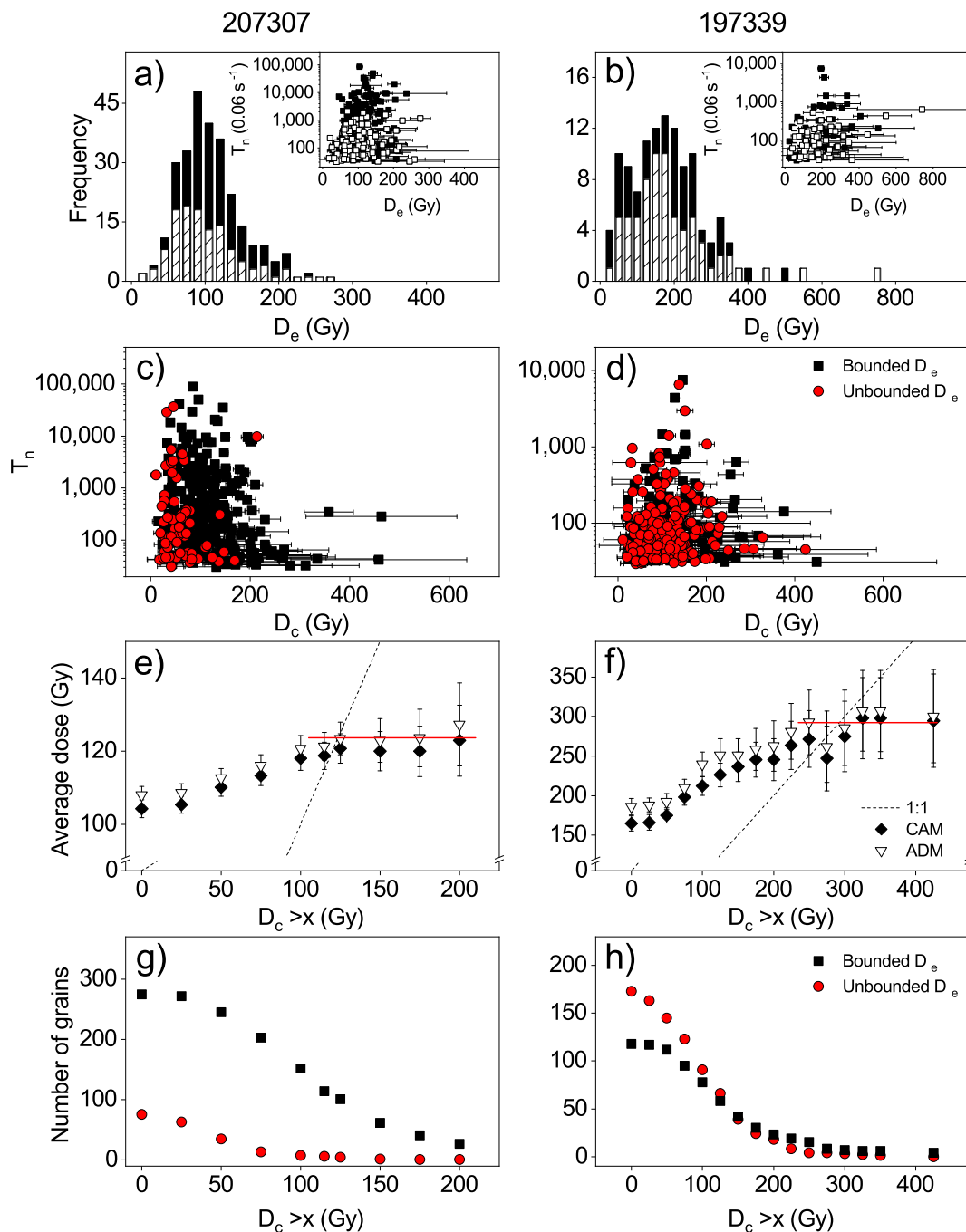
Figure 6.19: Natural single-grain quartz results for samples 207307 (a,c,e and g) and 197339 (b,d,f and h). a),b) Natural dose distributions for $s_{Tn} < 20\%$ (black data) and $s_{Tn} < 20\%$, recycling and IR depletion ratio consistent with unity at two standard deviations and recuperation consistent with zero at two standard deviations. c),d) D_c values plotted against natural OSL test dose response (T_n). Grains giving bounded dose estimates are shown as black squares, whereas grains giving unbounded dose estimates are shown as red circles. e),f) Effect on selecting grains based on their individual D_c values for CAM (closed symbols) and ADM (open symbols). Also shown is the 1:1 line (dashed). The average dose in the sample is determined as the point where the 1:1 line intersects the average dose curve. The red horizontal line indicates a plateau region in which the average dose is independent of tightening the D_c threshold further. g),h) The number of grains included for different D_c thresholds.

when the D_c criterion has been applied, see Table 6.6).

On average, the effect of using the D_c criterion is to increase the equivalent dose (CAM and ADM) by $\sim$11% (unit 1-4) and by $\sim$80% (unit 5 and E.C.). Using the Bayesian approach, there is no significant effect of applying the D_c criterion for samples from unit 1-4, i.e., the average dose ratio is 1.03 ± 0.02. For units 5 and E.C., the Bayesian analysis only converged for one out of three samples. For the sample that did converged (sample 197339) the ratio is 1.03 ± 0.16.

6.5.3   Comparison of single-grain and multi-grain quartz dose estimates

As mentioned above, single-grain analysis was undertaken to examine whether the quartz samples suffer from significant incomplete bleaching, post-depositional mixing and/or saturation effects. If the samples are significantly affected by any of these processes or contain a significant number of grains with unsuitable luminescence characteristics, it is possible that the multi-grain results are inaccurate. If, on the other hand, good agreement between multi-grain and single-grain quartz dose estimates is found, the multi-grain results are unlikely to be affected by the processes given above, and as a result, are more likely to be accurate.

In Table 6.7, we compare the individual single-grain dose estimates to those obtained from multi-grain measurements. For the samples from unit 1-4 (n=9), the ratio of the single-grain doses (selection criterion $s_{Tn} < 20\%$) to the corresponding multi-grain doses are 0.79 ± 0.03 (CAM), 0.83 ± 0.03 (ADM) and 0.97 ± 0.03 (BayLum). However, if the D_c criterion is applied to reduce the effect of grains not capable of recording the absorbed dose accurately, these ratios are 0.87 ± 0.04 ($D_{c,CAM}$), 0.93 ± 0.04 ($D_{c,ADM}$) and 0.99 ± 0.04 ($D_{c,BayLum}$). Thus, on average, both ADM and BayLum give doses consistent with those obtained using multi-grain aliquots, whereas the CAM doses appears to underestimate by $\sim$10%. For the three samples from units 5 and E.C., the multi-grain measurements are regarded as providing minimum burial ages due to likely saturation, but it is interesting to note that after application of the D_c criterion there is no significant difference between multi-grain and single-grain dose estimates, i.e., the single-grain to multi-grain ratios are 1.1 ± 0.2 ($D_{c,CAM}$) and 1.2 ± 0.2 ($D_{c,ADM}$). Note that for samples 197338 and 167819, no BayLum D_c dose estimate is given as the analysis did not converge. For sample 197339 the ratio is 1.3 ± 0.2.

CAM essentially calculates a weighted geometric mean of individual equivalent doses and it has been argued[104,158] that this increasingly causes CAM to underestimate the true dose as the OD increases. Using quartz OSL samples with independent chronological age control, these studies showed that the accuracy of single-grain CAM doses appeared to decrease with increasing dose/age. Using the same samples, Guérin et al.[104] showed that using the ADM on the other hand gave good agreement with the independent age control, but that the ADM also showed a small but increasing age underestimation with increasing age. By contrast, BayLum calculated doses that, on average, were in agreement with the expected value in laboratory-controlled experiments and did not appear to show a trend with increasing dose/age[166].
In this study, we have no independent age control available against which to test our OSL ages, but we do observe the same trends as Guérin et al.[104,158] and Heydari and Guérin[166], i.e., the CAM doses tend to underestimate, whereas ADM and BayLum doses agree with multi-grain doses. We conclude that the single-grain quartz measurements, on average, agree with those obtained using the multi-grain approach, when the D_c criterion is applied. Rejecting individual grains with poor

Table 6.7: Ratios of quartz single-grain (SG) and multi-grain (MG) equivalent doses. Multi-grain equivalent doses are calculated as an arithmetic mean (see Table 6.5), whereas the single-grain equivalent doses are calculated using various approaches (see Table 6.6).

Sample	Signal	Site	Unit	SG (s_{Tn}<20%) to MG or given			SG (s_{Tn}<20% and D_c>$D_{e,av}$) to MG or given		
				CAM	ADM	BayLum	CAM	ADM	BayLum
197338	Nat	LRC I	E.C.	0.62 ± 0.08	0.78 ± 0.09	3.6 ± 0.7	1.22 ± 0.16	1.25 ± 0.15	-
197339	Nat	LRC I	E.C.	0.51 ± 0.04	0.58 ± 0.04	1.25 ± 0.08	0.82 ± 0.11	0.91 ± 0.15	1.28 ± 0.19
167812	Nat	LRC I	4	0.76 ± 0.06	0.82 ± 0.06	0.90 ± 0.07	0.82 ± 0.07	1.07 ± 0.10	0.94 ± 0.08
187311	Nat	LRC I	2	0.77 ± 0.04	0.81 ± 0.04	1.00 ± 0.05	0.94 ± 0.06	0.98 ± 0.07	1.17 ± 0.09
187312	Nat	LRC I	2	0.75 ± 0.04	0.78 ± 0.04	1.07 ± 0.07	0.81 ± 0.05	0.85 ± 0.06	1.05 ± 0.10
167805	Nat	LRC I	4	0.84 ± 0.04	0.89 ± 0.04	1.01 ± 0.05	0.98 ± 0.05	1.01 ± 0.06	1.05 ± 0.06
167806	Nat	LRC I	2	0.79 ± 0.04	0.81 ± 0.04	0.92 ± 0.05	0.87 ± 0.05	0.89 ± 0.05	0.96 ± 0.05
187302	Nat	LRC I	1	0.73 ± 0.04	0.77 ± 0.04	0.90 ± 0.05	0.75 ± 0.05	0.79 ± 0.05	0.85 ± 0.05
207307	Nat	LRC II	4	0.67 ± 0.02	0.69 ± 0.02	0.79 ± 0.03	0.76 ± 0.03	0.78 ± 0.03	0.85 ± 0.04
167819	Nat	LRC IV	5	0.70 ± 0.07	0.83 ± 0.08	11 ± 3	1.4 ± 0.2	1.4 ± 0.3	-
167823	Nat	LRC IV	4	0.80 ± 0.04	0.83 ± 0.04	0.97 ± 0.05	0.84 ± 0.05	0.86 ± 0.05	0.93 ± 0.05
167831	Nat	LRC IV	1	1.03 ± 0.04	1.07 ± 0.04	1.13 ± 0.05	1.08 ± 0.04	1.11 ± 0.05	1.14 ± 0.05
187302	DR	LRC I	1	0.97 ± 0.03	-	1.08 ± 0.04	1.03 ± 0.03	-	1.06 ± 0.03
167806	DR	LRC I	3	0.85 ± 0.03	-	1.00 ± 0.02	1.03 ± 0.02	-	1.06 ± 0.03
207307	DR	LRC II	4	0.76 ± 0.02	-	0.89 ± 0.02	0.99 ± 0.02	-	0.97 ± 0.03
167819	DR	LRC IV	5	0.49 ± 0.02	-	0.90 ± 0.02	0.96 ± 0.05	-	0.95 ± 0.05

luminescence characteristics does not change the dose or observed variability in the single-grain dose distributions and it thus cannot be stated that single-grain quartz data is superior to multi-grain quartz data. Quartz ages (see section 6.7) are thus based on the multi-grain quartz dose measurements. The ultimate test for whether incomplete bleaching is an issue is to compare quartz ages with K-rich feldspar ages (see sections 6.6 and 6.7).

6.6 Multi-grain K-rich feldspar results

One of the main assumptions in OSL dating is that any latent OSL signal was reset at burial. If this was not the case then the OSL age is likely to overestimate the true burial age. The bleaching rate of the quartz OSL signal is at least an order of magnitude faster than that from K-rich feldspar [e.g., 55] and so a robust way to determine whether the quartz OSL signal was sufficiently reset at burial is to compare quartz and feldspar ages to each other [e.g., 88]. To facilitate such a comparison, multi-grain K-rich feldspar measurements using a pIRIR(50,290) protocol [125] were done on all samples measured at DTU, Denmark. All reported IR$_{50}$ doses/ages have been measured using the pIRIR(50,290) protocol unless otherwise specifically stated.

6.6.1 Multi-grain K-rich feldspar characteristics

Multi-grain K-rich feldspar measurements generally show that the sedimentary K-feldspar is suitable for OSL analysis, i.e., the dose response curves are reproducible (average recycling ratio of 1.040 ± 0.004, n=435 (IR$_{50}$) and 1.014 ± 0.002, n=450 (pIRIR$_{290}$) with a small recuperation (on average 3.5% of the natural dose).
Figure 6.20 shows a typical K-rich feldspar dose response curve. For this aliquot, the recycling ratios are 1.01 ± 0.03 for both (IR$_{50}$) and (pIRIR$_{290}$), the recuperations $2.33 \pm 0.11\%$ (IR$_{50}$) and
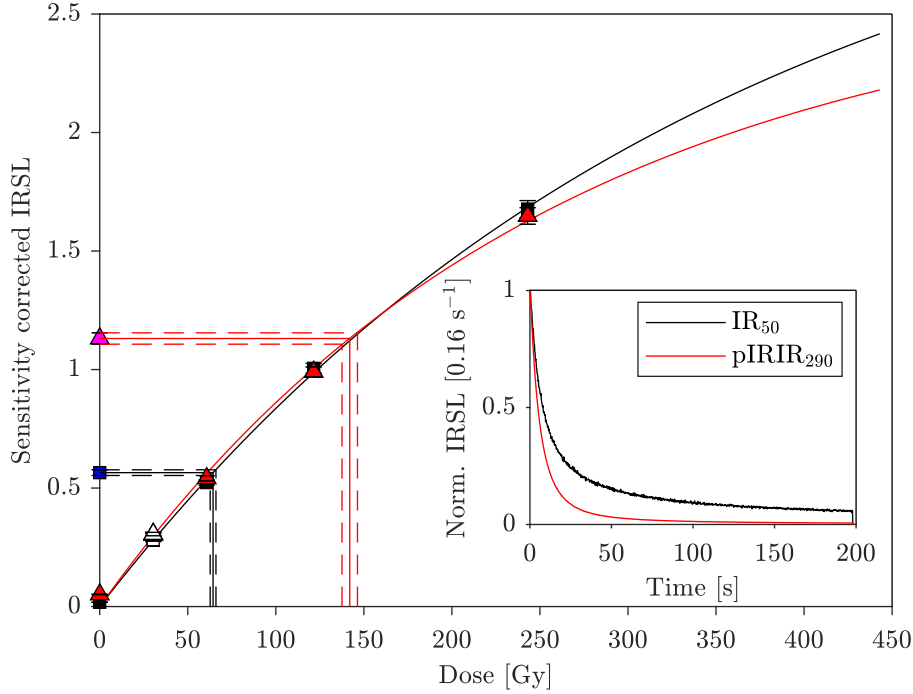
Figure 6.20: A typical dose response curve for a K-rich feldspar aliquot from sample 167830 for the IR_{50} signal (black squares) and the $pIRIR_{290}$ signal (red triangles). Recycling points are shown as corresponding open symbols. Natural signals are shown as blue and magenta symbols for the IR_{50} and $pIRIR_{290}$ signals, respectively. The data have been fitted using single saturating exponential functions. The insert shows the normalised natural OSL signals from this aliquot.

$4.50 \pm 0.14\%$ ($pIRIR_{290}$), and the D_c values 351 ± 31 Gy (IR_{50}) and 254 ± 19 Gy ($pIRIR_{290}$). The inset shows the natural OSL stimulation curve from the same aliquot. The $pIRIR_{290}$ signal was on average 13.6 ± 0.4 (n=435) times more intense than the IR_{50} signal. Average value D_c for all aliquots were 395 ± 4 Gy (n=435) and 390 ± 5 Gy (n=450) for IR_{50} and $pIRIR_{290}$, respectively. Based on the average dose response curve shapes, we would thus not expect to be able to accurately measure natural doses significantly greater than ~ 800 Gy.

6.6.2   Multi-grain K-rich feldspar preheat plateau and dose recovery

To investigate the dependence of the equivalent dose on our choice of thermal pre-treatment and pIRIR stimulation temperature in the SAR protocol, we measured a preheat plateau for sample 187323. In this experiment the first IR stimulation temperature was kept constant at 50°C, while the stimulation temperature for the second IR stimulation, i.e., the $pIRIR_T$ stimulation temperature, was increased in steps from 150°C to 290°C. The corresponding preheat temperature was increased from 170°C to 320°C. In Figure 6.21a, the measured average dose is shown as a function of the second stimulation temperature, T. Each point is the arithmetic mean of three aliquots corrected for thermal transfer. It appears that our equivalent doses are insensitive to the temperature T of the 2nd IR stimulation and the preheat temperature.

To investigate our ability to recover a known dose given in the laboratory a pIRIR(50,T) dose recovery experiment using three different 2nd stimulation temperatures (i.e., T=180, 225 or 290
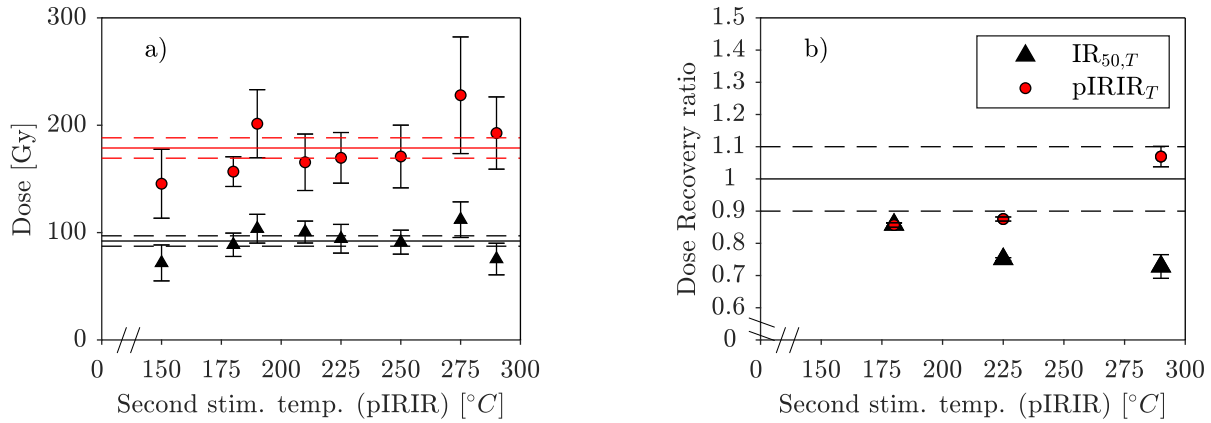
Figure 6.21: a) Equivalent doses (red circles, corrected for residual dose) for sample 187323 as a function of pIRIR stimulation temperature T (the first IR stimulation temperature was kept constant at 50 °C). The preheat temperature was 20 °C higher than the pIRIR stimulation temperature, except for pIRIR$_{290}$, where the preheat temperature was 320 °C. Also shown are the equivalent doses from the first IR stimulation at 50 °C (grey triangles). Each point is an average of three aliquots. The full horizontal lines show the average equivalent doses for pIRIR$_T$ (red) and IR$_{50}$ (black), respectively. The dashed lines show the standard error on the mean. b) Dose recovery ratios (corrected for thermal transfer) for different post IR stimulation temperatures for samples 187323, 16725, 167827, 167830: pIRIR$_{180}$ (n=12), pIRIR$_{225}$ (n=48), pIRIR$_{290}$ (n=12).

°C) was undertaken. The preheat temperatures were 200 °C, 250 °C and 320 °C, respectively. In these experiments, aliquots from samples 187323, 167825, 167827, 167830 were bleached for 48 hours in a solar simulator at room temperature. The residual dose in half of these aliquots were measured and these ranged between 2 and 24 Gy for the pIRIR$_T$ signals and between 0.8 and 2.9 Gy for the IR$_{50}$ signal. A known dose of 110 Gy (similar to the natural equivalent doses) were given to the remaining aliquots. The resulting dose recovery ratios (measured dose corrected for residual dose by subtraction and subsequently divided by given dose) are calculated using the arithmetic mean dose. The average dose recovery ratios are shown in Figure 6.21b. The dose recovery ratio for the pIRIR$_T$ signal appears to increase with stimulation temperature, whereas it for the IR$_{50}$ signal appears to decrease with temperature. Here we choose a standard preheat of 320°C for 60 s, an IR stimulation temperature of 50°C and a post IR stimulation temperature of 290°C.

In addition, a pIRIR$_{290}$ dose recovery with a given dose of 1150 Gy (n=6) was undertaken to investigate if we are able to recover doses in the high dose range as well. Dose recovery ratios of 0.60 ± 0.02 and 0.95 ± 0.03 were obtained for IR$_{50}$ and pIRIR$_{290}$, respectively. The corresponding light level ratios (i.e., the ratio between the sensitivity corrected "natural" signal to a sensitivity corrected signal from a regeneration dose equal to the "natural" dose) were 0.840 ± 0.012 and 1.009 ± 0.007, respectively. For these measurements, the D_c values were 524 ± 10 and 488 ± 9 (n=6) for IR$_{50}$ and pIRIR$_{290}$, respectively. So in the laboratory, we are for the pIRIR$_{290}$ signal able to recover doses up to at least $2.4 D_c$. However, it is worth noting that all aliquots gave bounded dose estimates.

6.6.3   Multi-grain K-rich feldspar dose estimation

Between 6 and 24 multi-grain K-rich feldspar aliquots were measured for all samples analysed at DTU, Denmark. The results are summarised in Table 6.5. As for the quartz multi-grain

measurements, we used the IQR criterion to objectively remove outliers. A total of 16 and 12 dose estimates (for IR_{50} and $pIRIR_{290}$, respectively) were removed in this way, from a total of 434 and 418 dose estimates, respectively. The average doses measured for the IR_{50} signal range between 36 ± 3 Gy (sample 167831, unit 1) and 452 ± 41 Gy (sample 167820, unit 5), whereas for the $pIRIR_{290}$ signal they range between 88 ± 6 Gy (sample 167831, unit 1) and 1868 ± 86 Gy (sample 197339, I.C.). The resulting dose distributions for the IR_{50} signal have relative standard deviations ranging between 4% (sample 167829) and 56% (sample 187311) with an average value of 20%. For this signal, we could not derive bounded dose estimates for a small fraction of the aliquots (~0.2% on average for IR_{50} signal). The resulting dose distributions for the $pIRIR_{290}$ signal have relative standard deviations ranging between 2% (sample 167829) and 36% (sample 197340) with an average value of 13%. For this signal, we could not derive bounded dose estimates for ~7 % (on average) of the measured aliquots. In fact, for the $pIRIR_{290}$ signal, nine samples (two samples from unit 5 in LRC IV, all six samples from inside LRC I (I.C. and E.C.) and sample 187307 from unit 4) give doses greater than 800 Gy. The fraction of saturated aliquots in these samples ranges between 17% and 58% and we regard the KF doses for these samples to be significantly affected by saturation effects, i.e., the ages from these samples are regarded as minimum ages (as are the corresponding quartz ages).

In Figure 6.22, we plot the IR_{50} doses against the $pIRIR_{290}$ doses. The dose recorded by the IR_{50} signal results from a competition between charge storage (from dose rate) and charge loss (from fading). The charge storage rate is constant, but the loss due to fading depends on the total stored charge, and so the loss rate increases with dose. This eventually results in a constant IR_{50} dose, at some level well below the laboratory saturation (for which fading is negligible). This is what is seen at higher doses in Figure SI.24 (compared with the typical laboratory dose response curve shown in Figure 6.20). In Figure 6.22, the data have been fitted using a saturated exponential function and show, as expected, a significant deviation from the 1:1 line even at low doses, because the IR_{50} signal is prone to significant anomalous fading. The bleaching rate of the $pIRIR_{290}$ signal is known to be approximately 1 order of magnitude slower than that of the IR_{50} signal [e.g., 56] and thus by comparing the IR_{50} and $pIRIR_{290}$ doses it may be possible to determine whether a given sample is suffering from incomplete bleaching. Buylaert et al. [167] also fitted a saturating single exponential to their data and rejected all data below 10% of their fitted line. This arbitrary but objective approach removed stratigraphic age outliers. In our data, the IR_{50} dose estimates all underestimate those from the $pIRIR_{290}$ data, but there are no significant outliers below the fitted line. The exponential fit suggests that at low doses the underestimate is about 40%, consistent with typical IR_{50} fading rates (see also next section). From these data we conclude that we have no evidence for significant differential bleaching between the two feldspar signals. Given that the IR_{50} signal bleaches approximately ten times faster than the $pIRIR_{290}$ signal, this observation is most likely explained by both signals being completely bleached before burial. This conclusion is supported by the observation that the feldspar ages are below or equal to the quartz ages, in the dose range over which quartz is considered reliable (see section 6.7.3).
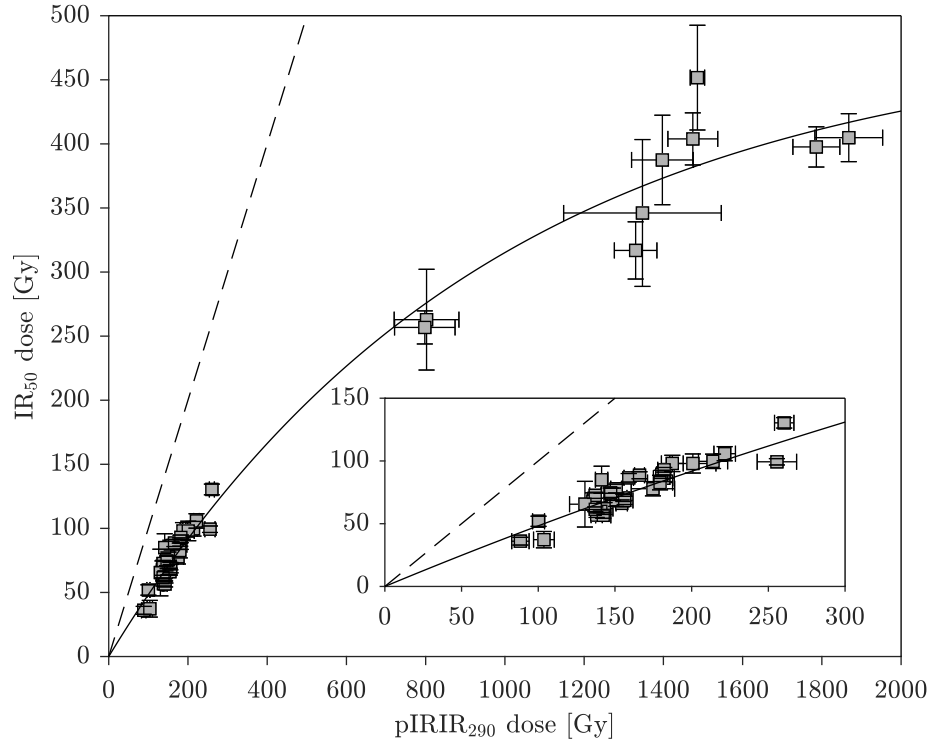
Figure 6.22: IR_{50} doses plotted as a function of $pIRIR_{290}$ doses. The solid line is a saturating exponential fitted to the data, whereas the dashed line represents the 1:1 line. The inset shows the same data for $pIRIR_{290}$ doses less than 300 Gy.

6.6.4 Multi-grain K-rich feldspar fading correction

K-rich feldspar luminescence signals are known to suffer from anomalous (athermal) fading [e.g., 57] and several models have been developed to correct for instability in the IRSL signal [e.g., 59]. Anomalous fading is usually quantified by the g-value (signal loss per decade of logarithmic normalised storage time) and we measured g-values for samples 207307 and 197328 following the approach of Auclair et al. [146] using given doses of 190 Gy. We determined average g-values of 2.66 ± 0.12, n=34 (IR_{50}) and 1.30 ± 0.05, n=34 ($pIRIR_{290}$). In accordance with Buylaert et al. [56] we fading correct the IR_{50} ages but not the $pIRIR_{290}$ ages. The IR_{50} ages are on averaged increased by 30% as a result of this fading correction. If we were to fading correct the $pIRIR_{290}$ ages, they would on average increase by 13%.

6.7   Luminescence ages

All burial ages derived from sediment samples are derived from the equivalent dose divided by the total dose rate for each sample. A summary of all multi-grain doses, dose rates and burial ages are found in Tables 6.2 and 6.5. The multi-grain OSL quartz ages processed in Hungary are included in these tables as well.

In the following sections, we first evaluate the quartz ages derived from LRC I, II and IV, compare KF and quartz multi-grain ages and then evaluate the effect of K-concentration on the KF to quartz

age ratio (section: 6.7.3). The effect of water content on burial ages is considered in section: 6.7.4. In section: 6.7.6, age-depth modelling is performed using Bayesian Statistics (Bacon script [108]), combining the multi-grain quartz ages for LRC I and II to find the best estimate of the closure of the cave (LRC I). Bayesian age-depth modelling is performed separately on the samples from LRC IV.

6.7.1   Multi-grain quartz ages

In LRC I, the multi-grain quartz ages measured in Denmark (n=11) range between 42±3 ka and 76±6 ka (excluding the samples taken inside the cave itself) and they are all in stratigraphic order (with respect to elevation and unit identification).
The multi-grain quartz ages measured from the samples from inside the cave range between 167±18 ka and 317±53 ka. For these samples bounded dose estimates could not be derived for between 17% and 69% of the measured aliquots and are all considered to be minimum ages. These samples are not in stratigraphic order and may be relics from previous cave filling events.

In LRC II, the multi-grain quartz ages measured in Denmark (n=12) range between 84±5 ka and 327±23 ka; they are in stratigraphic order except for two samples: 187323 (unit 5, 121±8 ka) and 187307 (unit 4, 327±23 ka).
With respect to sample 187323, then in LRC II, there is one other sample (187304) also collected from unit 5. This sample is located almost two meters below sample 187323 at the bottom of the section and gives an age of 121±11 ka, which is consistent with the age derived from sample 187323. Sample 187323 was taken in a pocket of relict unit 5 sediment, and thus one would expect this sample to yield an age significantly older than the ages derived from the unit 4 samples located immediately above and below, e.g., sample 187320 (Fig. code 21) just above has an age of 84±5 ka and sample 187310 (Fig. code 23) has an age of 88±5 ka.
The multi-grain quartz age of 327±23 ka derived for sample 187307 (Fig. code 31) is considered to be a minimum age, because bounded dose estimates could not be derived for 17% of the measured aliquots. This sample was collected close to bedrock but in the same layer as sample 207307 (Fig. code 29); the latter gives an age of only 97±6 ka. However, in the sample description notes, sample 187307 is described as being a mix of fluvial sand and with sand possibly derived from disaggregated bedrock, whereas sample 207307 is described as a pure fluvial sand. If bedrock is present in sample 187307, it is reasonable to assume that the estimated equivalent dose will overestimate the burial dose. Since the bedrock also has a lower radionuclide concentration, the infinite matrix dose rate would also be expected to be lower. Indeed, the infinite matrix dose rate derived for sample 187307 is only ∼40% of that derived for the pure sediment sample (see Table 6.2).
Thus, there are good reasons for discarding the two samples 187323 and 187307. Then the remaining multi-grain quartz ages for LRC II are in stratigraphic order.

In LRC IV, the multi-grain quartz ages measured in Denmark (n=12) range between 27.8±1.7 and 184±16 ka, with all samples appearing in stratigraphic order with the possible exception of sample 167819 (153±14 ka), which was collected 80 cm below sample 167820 (184±16 ka). However, both these sample are from unit 5 and are regarded as minimum ages as bounded dose estimates could not be derived from ∼30% of the measured aliquots.

Thus, in summary, the multi-grain quartz ages for the individual sites in LRC are in stratigraphic

order.

6.7.2 Multi-grain K-rich feldspar ages

In LRC I, the KF ages range between 16±3 ka and 43±4 ka, and between 34±3 ka and 71±6 ka, for IR_{50} and $pIRIR_{290}$, respectively (excluding the samples taken inside the cave itself). With respect to elevation, they are in stratigraphic order except for samples 187311 and -12. The ages derived from these samples are ~35% lower than would be expected based on the other ages in the section - particularly sample 167805 (71±6 ka) and sample 167812 (65±7 ka).
The KF ages measured from the samples from inside the cave (I.C. and E.C.) range between 141±24 ka and 241±24 ka and between 325±41 ka and 834±78 ka for IR_{50} and $pIRIR_{290}$, respectively. Only the three samples from the entrance (E.C.) are in stratigraphic order (with respect to elevation). For the $pIRIR_{290}$ measurements bounded dose estimates could not be derived for between 17% and 58% of the measured aliquots and thus they are all considered to be minimum ages. Between 0% and 8% of the measured IR_{50} doses gave bounded dose estimates.

In LRC II, the KF ages (n=12) range between 40±3 ka and 201±19 ka and between 59±4 ka and 473±59 ka for IR_{50} and $pIRIR_{290}$, respectively, and are in stratigraphic order except for two samples: 187323 and 187307. Based on the arguments given in section 6.7.1, it is expected that these sample will be out of stratigraphic order.

In LRC IV, IR_{50} and $pIRIR_{290}$ ages are in stratigraphic order, but the ages from the bottom samples (167820 and -19) are regarded as minimum ages because of saturation effects (i.e., $\sim 30\%$ of the aliquots did not give bounded dose estimates).

6.7.3 Multi-grain K-rich feldspar ages compared to multi-grain quartz ages

In this section, feldspar ages are compared to quartz ages to evaluate whether the sediments were well-bleached at the time of deposition.
In Figure 6.23, feldspar ages (using a measured average K-content of 12.6%) are plotted against quartz ages. The feldspar to quartz age (FQ) ratio is on average 0.59 ± 0.04 (n=41) for ages based on the IR_{50} signal (corrected for fading using a g-value of 2.66 ± 0.12) and 1.20 ± 0.13 (n=41) for ages based on the $pIRIR_{290}$ signal. However, all the samples from I.C. and E.C., from unit 5 in LRC IV and sample 187307, have quartz ages above 150 ka (and a > 15% of measured aliqouts in saturation and doses above 225 Gy) and are likely to be significantly affected by saturation effects (see section: 6.4.1). When these samples are removed from the average FQ ratios, they become 0.490 ± 0.011 (n=32) for IR_{50} and 0.806 ± 0.019 (n=32) for $pIRIR_{290}$. Thus, the feldspar ages underestimate the quartz ages significantly. Possible causes for this underestimation are considered below.
However, for the main question addressed here, concerning the closure of the cave entrance, five samples are of particular importance, i.e., samples 197332, -28, -33 and 167806 and -05. These are located 75 cm above and below the elevation at which the cave was closed. For these crucial samples, the FQ ratio for the $pIRIR_{290}$ signal is 0.96±0.03.
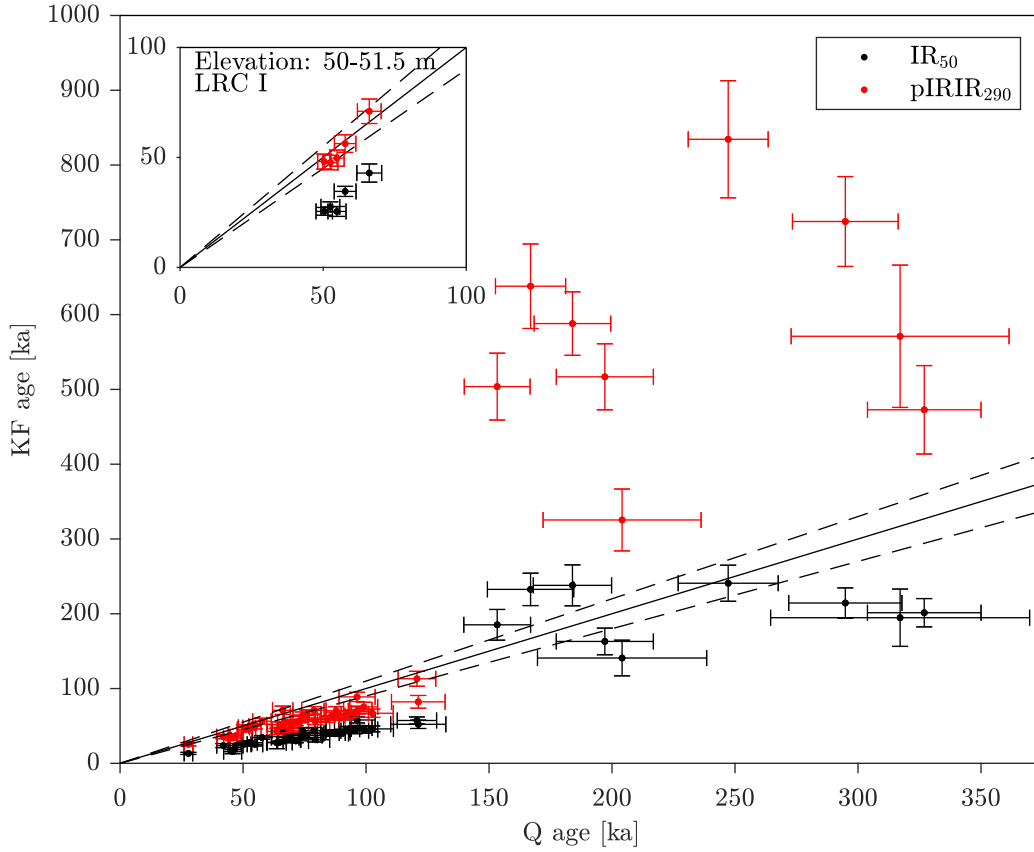
Figure 6.23: Feldspar (KF) ages plotted against quartz (Q) ages. IR_{50} ages (black symbols) are corrected for fading using a g-value of 2.66 ± 0.12. $pIRIR_{290}$ ages (red symbols) are not corrected for fading. Also shown is the 1:1 line (solid line) with a $\pm 10\%$ uncertainty interval (dashed lines). Inset shows same data for samples located 75 cm above and below the elevation of 50.75 m (i.e., the elevation at which the entrance in LRC I was sealed).

One possible explanation for this underestimation could be that the assumed K-content (used in the dose rate calculation) is incorrect. The effect of changing the K-concentration on the FQ ratios is shown in Figure 6.24a. Note that the ^{87}Rb concentration changes in proportion to the K-concentration[142] and that samples with quartz doses above 225 Gy (expected to be significantly affected by saturation effects) have been excluded in Figure 6.24. A FQ ratio of unity cannot be obtained for the IR_{50} signal by simply changing the assumed K-concentration, but is obtained if a K-concentration of 4.75% were to be used for the $pIRIR_{290}$ signal (see Figure 6.24a).

Given the variability in the external dose rates (Table 6.2) one would expect the variability in the FQ ratio to be at a minimum when the correct K concentrations are employed. Since we employ a single (average) K-concentration for all samples in our analysis this would only be true if all feldspar samples have, in fact, a similar effective K concentration. In Figure 6.24b, we show the relative standard deviation (RSD) of the FQ ratio as a function of K-concentration only using samples with Q doses < 225 Gy. A minimum RSD is found for a K-concentration of $\sim 1\%$ and $\sim 2\%$ for the $pIRIR_{290}$ and IR_{50} ratios, respectively. These K-concentrations correspond to internal dose rates from ^{40}K and ^{87}Rb of only 0.069 ± 0.002 Gy.ka^{-1} (1% ^{40}K, 32 ppm ^{87}Rb) and 0.137 ± 0.005 Gy.ka^{-1} (2% ^{40}K, 64 ppm ^{87}Rb), respectively , and is very different from the 0.86 ± 0.03 Gy.ka^{-1} derived from the measured concentration of 12.6% K and 400 ppm ^{87}Rb.
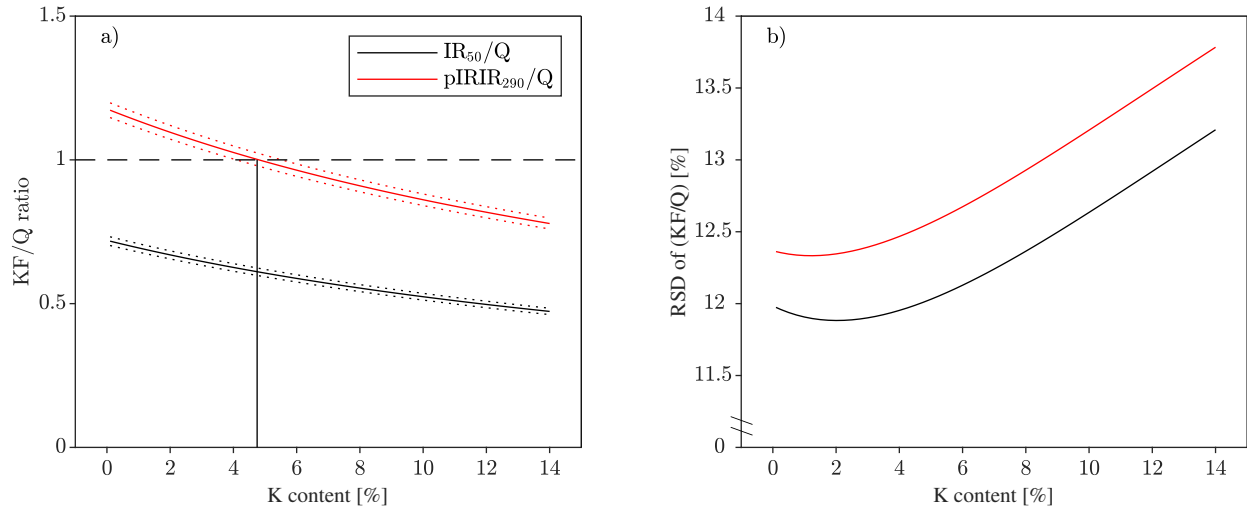
Figure 6.24: The average effect on the feldspar to quartz age (FQ) ratio when changing the assumed ^{40}K and ^{87}Rb concentrations. The ^{87}Rb concentrations are changed in proportion to the ^{40}K concentration. Only samples with quartz doses < 225 Gy have been included ($n = 32$). FQ ratios using the fading corrected IR$_{50}$ ages are shown as solid black lines, whereas those based on the pIRIR$_{290}$ ages are shown as solid red lines. a) Average FQ ratio. Standard errors are shown as dotted lines. Also shown is the K-concentration value for which the FQ ratio is unity b) Relative standard deviation of the average FQ ratio.

Another possible explanation for the underestimation of the KF ages is that the used grain size is incorrect, since reducing the grain size in the dose rate calculation would result in smaller internal dose rates from ^{40}K and ^{87}Rb in feldspar. In fact, an internal dose rate of 0.069 Gy.ka^{-1} is derived if a grain size of 10-20 µm is used (as opposed to the actual fraction of 180-250 µm) in combination with a K-concentration of 12.6% and 400 ppm of ^{87}Rb. In this case, the FQ ratio would be 1.14 ± 0.02 (pIRIR$_{290}$ signal).

Whichever K-concentration or K-rich feldspar grain size is appropriate, we can in any case conclude that, for samples with a quartz $D_e < 225$ Gy (i.e., those unlikely to be affected by saturation issues) the feldspar ages do not overestimate the quartz ages, and so it is very likely that the quartz (and the feldspar) was well-bleached at the time of deposition.

6.7.4 Water content correction

Current and saturated water contents (w.c.) were measured for all samples and the results are shown in Figure 6.25. The current water contents are likely to underestimate the average lifetime water content, mainly because of significant drying after excavation - both on site and in the laboratory. Therefore, the true water content is assumed to lie in between the current and saturated water content and it is assumed to be the same fraction of saturation for all samples. Two samples (167819 and 167820) from LRC IV were surrounded by bedrock underneath and on the sides (see Figure 6.29) and these samples are therefore more likely not to have dried significantly after excavation, i.e., the measured current water content is likely to better represent the present day w.c. These samples are marked by red (open and closed) squares in Figure 6.25. The ratios between the current and saturated water contents are 0.51 and 0.32 for samples 167819 and 167820, respectively, with an average of 0.41±0.10 (n=2). Thus, in the dose rate calculations we assume
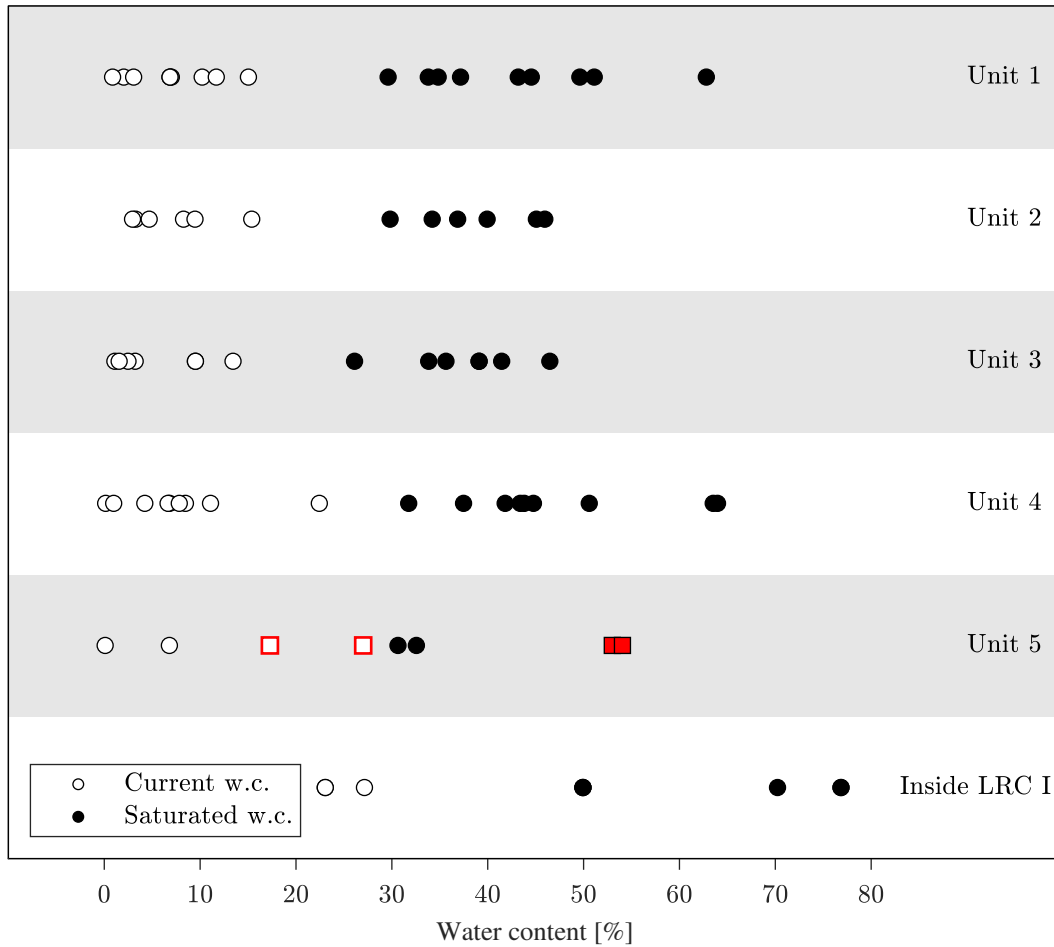
Figure 6.25: Measured current (open symbols) and saturated (closed symbols) water content. Squares indicate samples 167819 and 167820, which were taken from the bottom of LRC IV, where they were surrounded by bedrock on three sides. It is therefore less likely that these sample have experienced significant drying since excavation

that a fractional water content of 40% of the laboratory-measured saturated water content taken as a mean of each unit (1-5). Below, we examine the consequences of using different water content assumptions on the derived ages.

To investigate the effect of the choice of w.c. on the age calculation, the average ratio $(Q_{x,w.c.}/Q_{40,w.c.})$ of the quartz ages for different fractional saturation w.c. (x) to the quartz ages with a fractional saturation w.c. of $40 \pm 10\%$ have been calculated.

Figure 6.26a shows $Q_{x,w.c.}/Q_{40,w.c.}$ as a function of fractional saturation w.c. ranging between zero and unity, i.e., the w.c. ranges between 0 and 100% of the saturated water content. The ratio is shown both for fractional saturation w.c. using the measured saturated w.c. for individual samples (black line) as well as the average saturated w.c. for each of the five depositional units and the samples inside LRC I identified in the field (red line). Only samples with quartz doses less than 225 Gy are used in this analysis, to ensure that proximity to dose saturation does not influence the ratios. In the investigated range, the average relative quartz age changes between 0.84 and 1.23, but there is no significant difference between using the individual measured saturated w.c. or the average saturated w.c. for each depositional unit when calculating the fractional saturation w.c.
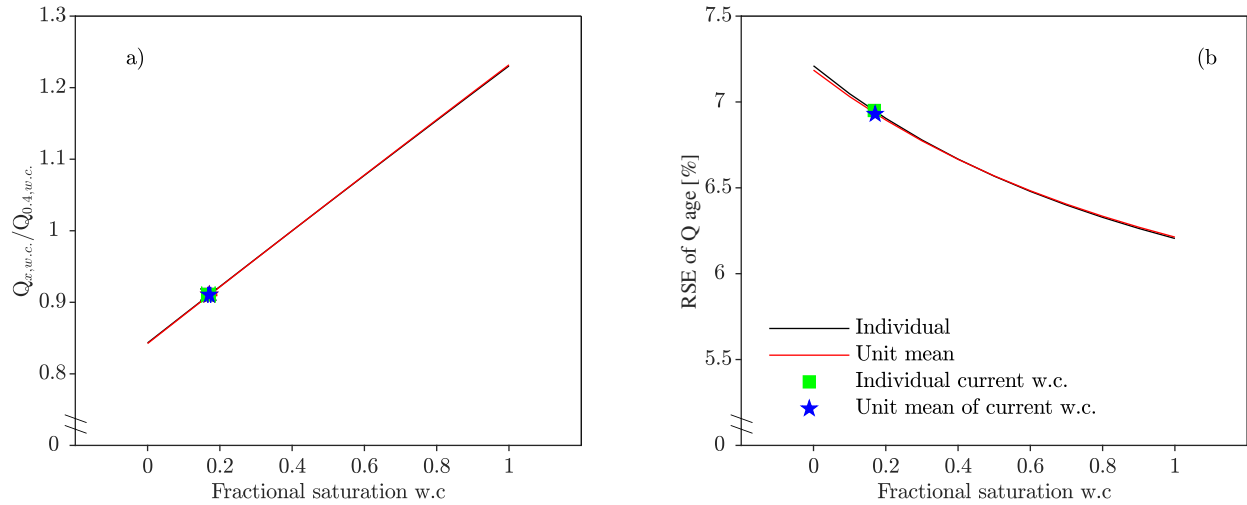
Figure 6.26: a) Effect of water content on a) the average ratio of quartz ages using fractional w.c. x to quartz ages for a fractional w.c. 0.4 ± 0.1, and on b) relative standard error (RSE) of quartz ages for different fractional w.c. x (i.e., fraction of saturated w.c.) Only samples with quartz dose < 225 Gy have been included in the analysis (n=32, i.e., samples where the quartz signal is suspected of being in saturation has been removed, see section: 6.2.2.1 for further details). Red line: using the average saturated water content for each unit. Black line: using individual saturated water contents. The result of using the current w.c. for individual samples or the average of current w.c. in each unit are shown as a green square and a blue star, respectively. Uncertainties on the mean i a) are small compared to the with of the lines.

Also in the relative standard errors (RSE) of the mean of quartz ages for different fractional saturation w.c. (Figure 6.26b) there is not a significant difference between using the unit mean saturated w.c. or the individual saturated w.c. for calculating the assumed fractional w.c.

As we see no minimum value, we can not from the analysis of the RSE justify whether the choice of w.c. plays a significant role in the observed variability of the ages, but it is clear that using the current w.c. would increase the variability between the ages, i.e., the RSE is higher when using the current w.c. compared to using the value chosen (40% of saturation).

We have chosen to use a fractional water content of 0.4±0.1. The uncertainty of 0.1 corresponds to $\pm$ 4% uncertainty in age. We are confident that the average life-time water content is higher than the measured current w.c. which, on average, is $7.0 \pm 0.9\%$ (n=32). If the measured current w.c. is used (instead of the fixed fractional w.c. of 0.4), the quartz ages will on average be reduced by 9%. In contrast, using a (very unlikely) fractional w.c. of 1 (i.e., saturated) increase the ages by 23%.

In any case, we assume it is more likely that each unit has had the same fractional w.c. during burial and we use a fractional w.c. of $40 \pm 10\%$ of the saturated value averaged over each unit in the age calculations.

Quartz OSL ages from samples from LRC IV and the seven samples processed by the Hungarian laboratory have been published in 2019[136] and 2016[130], respectively. In these publications current water contents were used. However, as argued previously, the current water content almost certainly underestimates the average water content during the burial life-time, and thus we recalculated these ages here using what we consider to be the more realistic water content assumption (see above and Figure 6.7). In addition, the ages presented in the previous publications were not

corrected for the dose rate heterogeneity - although it must be recognised that the samples from LRC IV are not significantly affected by this heterogeneity. Finally, in previous publications the internal dose rates to quartz were considered to be 0.06 Gy.ka^{-1} as opposed to the more current value of 0.02±0.01 Gy.ka^{-1}[161] used here.

The effect of using the higher w.c. (around 10% higher) and dose rate model corrections is an average increase in age of 12% (n=15) and 11% (n=7) compared to the ages published in 2019 and 2016, respectively.

6.7.5   OSL ages of La Roche Cotard

Both single-grain quartz and multi-grain pIRIR(50,290) measurements show that the multi-grain quartz ages are likely to have been well-bleached at burial and thus, in the following we only consider the quartz multi-grain ages.

In Figure 6.27 all multi-grain quartz ages from the four LRC sites, grouped into the five different deposition units (U1-5), are shown. For a given unit, the ages obtained from the different sites agree well with each other. Note that ages considered to be a minimum value due to quartz saturation are marked with open symbols in Figure 6.27). Ages from LRC IV agree with ages from LRC I and LRC II. Also the single age from LRC III agrees with the other ages in same unit (unit 4). This implies a connection in the deposition of the sites.

6.7.6   Bayesian modelling

To obtain a more precise estimate of the closure age, we model the age/depth relationship using Bayesian statistics (Bacon script[108]) with the elevation of the individual samples as priors. This is undertaken using only quartz ages, as these are considered the most reliable in this age range.

Because of the relative lateral and vertical positions of the four sites (LRC I, II, III and IV), data from LRC I and II are combined for modelling, whereas LRC IV is modelled separately. LRC III does not overlap the other sites and the single sample measured in Hungary for this site is not included. Modelling only makes use of the samples processed in Denmark, but those processed in Hungary are subsequently compared with the modelled results.

The results of the Bayesian modelling are shown in Figure 6.28 for LRC I and II, and Figure 6.29 for LRC IV. The full black lines in Figure 6.28 and Figure 6.29 represent the most likely age model based on a water content of 40±10% of the average saturated water content for each unit. All samples which gave average equivalent doses >225 Gy, i.e., all samples from unit 5, but two (see below), from inside the cave, and sample 187307, are considered to be significantly affected by saturation issues and are not included. Model fitting makes use of random uncertainties only - after fitting, the systematic uncertainties associated with beta calibration, internal dose rate, cosmic rays and water content are added to the fitting uncertainty. The resulting total uncertainty is plotted as dotted lines (one standard error). The uncertainties on individual data points are also total standard errors (at 68% confidence).
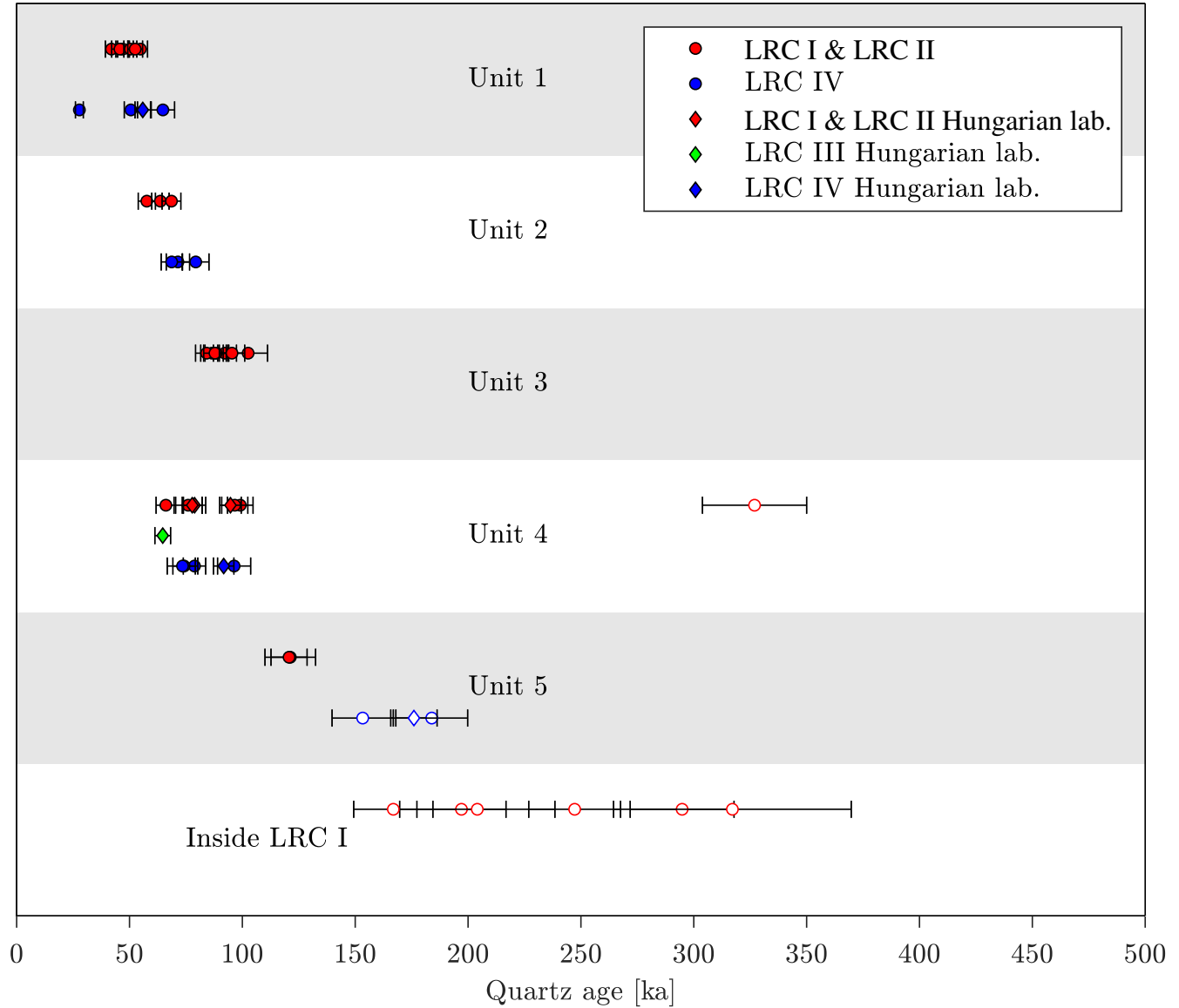
Figure 6.27: Multi-grain quartz ages grouped according to deposition unit (U1-5) and for samples from inside LRC I (I.C. and E.C.). For each unit, the individual ages have been grouped vertically according to site. LRC I & II (red symbols), LRC IV (blue symbols) and LRC III (green symbol). The samples processed in Denmark are shown as circles. The samples processed in Hungary are shown as diamonds. Open symbols indicate minimum ages due to dose saturation effects. Uncertainties on individual ages are given at 68% confidence.
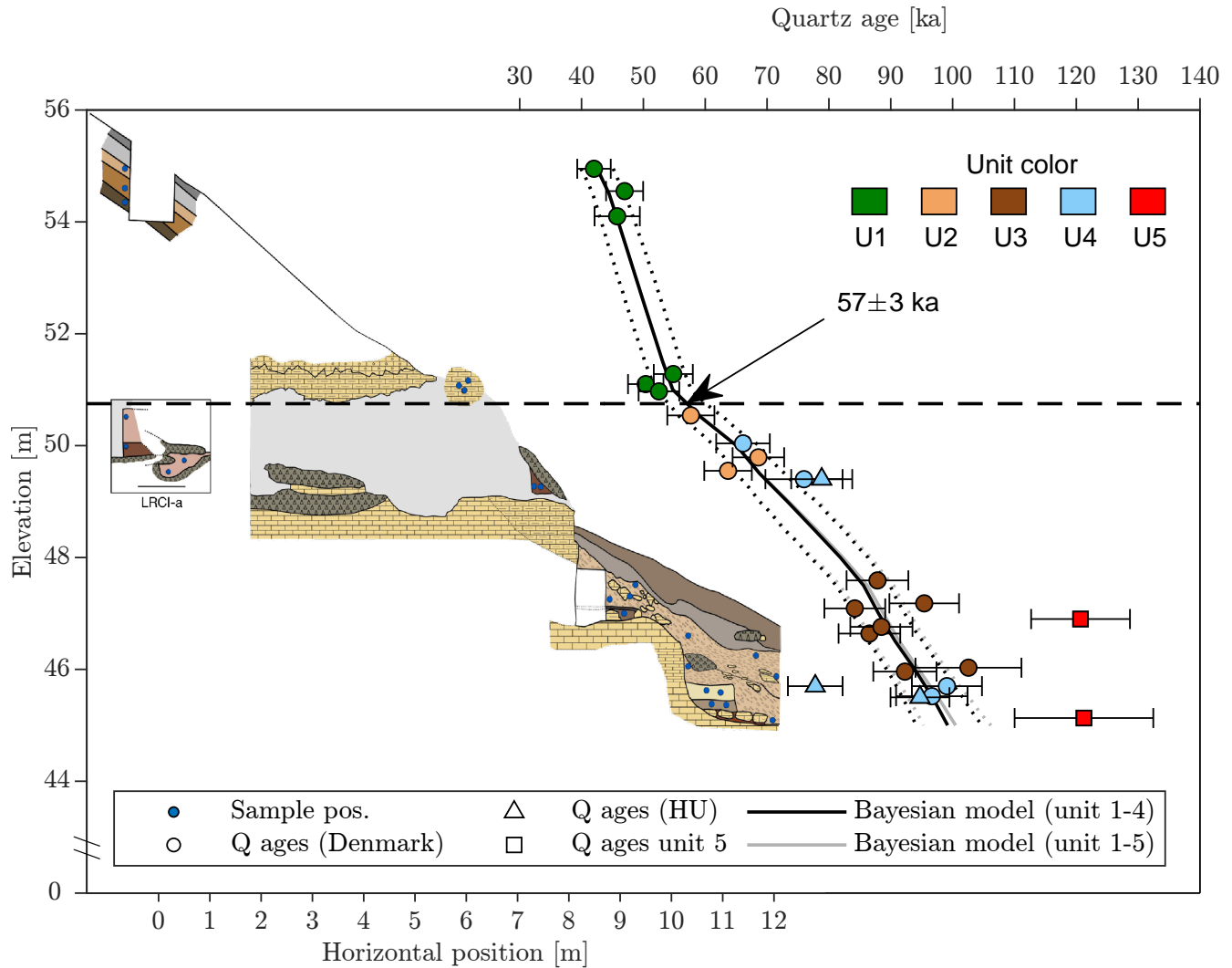
Figure 6.28: OSL sample positions (blue points) are shown to the left on the schematic drawing of LRC I and LRC II. The right-hand side of the figure shows the 20 multi-grain quartz ages from unit 1-4 (circles and triangles: measured in Denmark and Hungary, respectively) and squares show ages from unit 5. The individual units can be identified according to colour, i.e., unit 1-5 (green, light brown, dark brown, light blue and red, respectively). A Bayesian model (Bacon script[108]) using the elevation as prior and only random uncertainties for the individual ages is shown (grey and black line). The grey line shows the model for unit 1-5, whereas the black line shows the model for unit 1-4 only. Dotted lines (black and grey) show the total uncertainty (including both random and systematic uncertainties) at the 68% confidence interval. The OSL ages measured in Hungary are not included in the Bayesian model. Horizontal black broken line indicates the level of the entrance roof in LRC I. The insert shows LRC I-a, which includes two samples inside the cave (167805 and -06) and two outside the cave (187311 and -12). The adopted water content is 40±10 % of the average measured saturated water content for each deposition unit.

Table 6.8: Minimum and maximum ages for LRC. The "Age range" is derived from the minimum ("Min. age") and maximum ("Max. age") ages determined across sites at the 68% confidence level using the Bayesian models for LRC I & II and LRC IV, respectively. "Site" gives the site (LRC I, II, or IV) from which the minimum and maximum ages were determined for the given "elevation". The minimum age for unit 5 is derived from sample 187304. No maximum age can be given for this unit because of quartz saturation effects.

Unit/level	Age range [ka]	Min. ages			Max. ages		
		Elevation [m]	Site	Min. age [ka]	Elevation [m]	Site	Max. age [ka]
Unit 1	25- 66	50.10	LRC IV	28±3	47.00	LRC IV	62±4
Unit 2	54- 80	50.70	LRC I	58±3	44.90	LRC IV	76±4
Unit 3	77-104	48.00	LRC II	82±5	45.13	LRC II	99±5
Unit 4	58-103	50.29	LRC I	62±3	45.30	LRC II	98±5
Unit 5	>110	45.13	LRC II	121±11	-	-	-
Mousterian	67-103	49.30	LRC I	71±4	45.20	LRC II	98±5

OSL samples processed in Hungary (triangles in Figure 6.28) are in good agreement (95% confidence) with the Bayesian model except for one (181362, unit 4 in LRC II).

As mention above, only two samples from unit 5 (187323 and 187304, both LRC II) gave reliable quartz equivalent doses. The two corresponding ages are shown in Figure 6.28 as red squares. These samples have not been included in the Bayesian model (black line), because their elevation does not represent the deposition level with respect to vertical position. However, including them in the model does not change the overall model significantly (see grey line in Figure 6.28)

The limiting ages for deposition units 1-4 are estimated from the Bayesian models from i) LRC I and LRC II and ii) from LRC IV using the vertical positions (see Table 6.1) of the units in the respective sites. The minimum and maximum ages from each unit are given in Table 6.8.
The minimum age for unit 5 is given from the minimum quartz age of sample 187323 and 187304 (LRC II, see Table 6.8). Samples from unit 5 in LRC IV are regarded as minimum ages due to saturation effects. Since these minimum ages are larger that the maximum ages from samples 187323 and 187304 in LRC II, a maximum age cannot be given for unit 5.

The cave (LRC I) was completely closed when the sediment reached an elevation of 50.75 m NGF (see Figure 6.28)From the age model, this is most likely to have occurred 57 ± 3 ka ago (68% confidence level). This age is based on the assumption of a water content of 40% of saturation. Using the lowest possible water content (current water content, see Table 6.2) gives a burial age for the entrance of 52 ± 3ka (68% confidence level), but this fractional water content is considered highly unlikely.

In conclusion, based on the most likely values of water content, the minimum closure age for the cave entrance is >51 ka at 95% confidence.
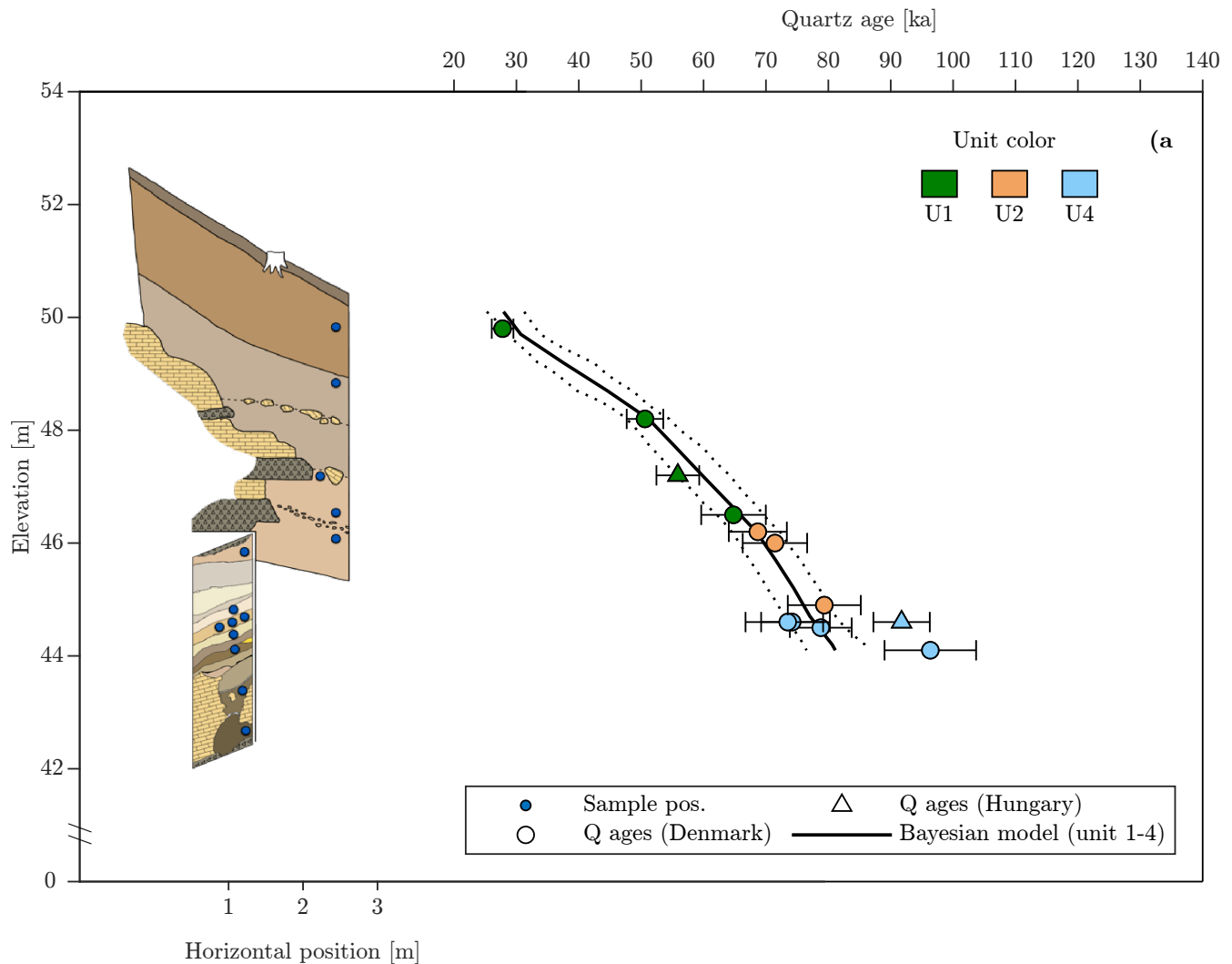
Figure 6.29: Schematic drawing of LRC IV to the left including OSL sample positions (blue points). The right-hand side of the figure shows the 12 multi-grain quartz ages from unit 1, 2 and 4 (circles and triangles: measured in Denmark and Hungary, respectively). The individual units can be identified according to colour, i.e. unit 1, 2, and 4 are green, light brown, light blue, respectively. (unit 3 is not present in LRC IV). A Bayesian model (Bacon script (19)) using the elevation as prior and only random uncertainties for the individual ages is shown (black line). Dotted lines show the total uncertainty (including both random and systematic uncertainties) at the 68% confidence interval. The OSL ages measured in Hungary are not included in the Bayesian model. Dotted black lines show the total uncertainty (including systematics) on the age model. A water content of 40±10 % of the average saturated water content for each deposition unit has been assumed. The bottom two samples (167819, 167820) are shown on the diagram to the left but not included in the Bayesian fit because of saturation effects.
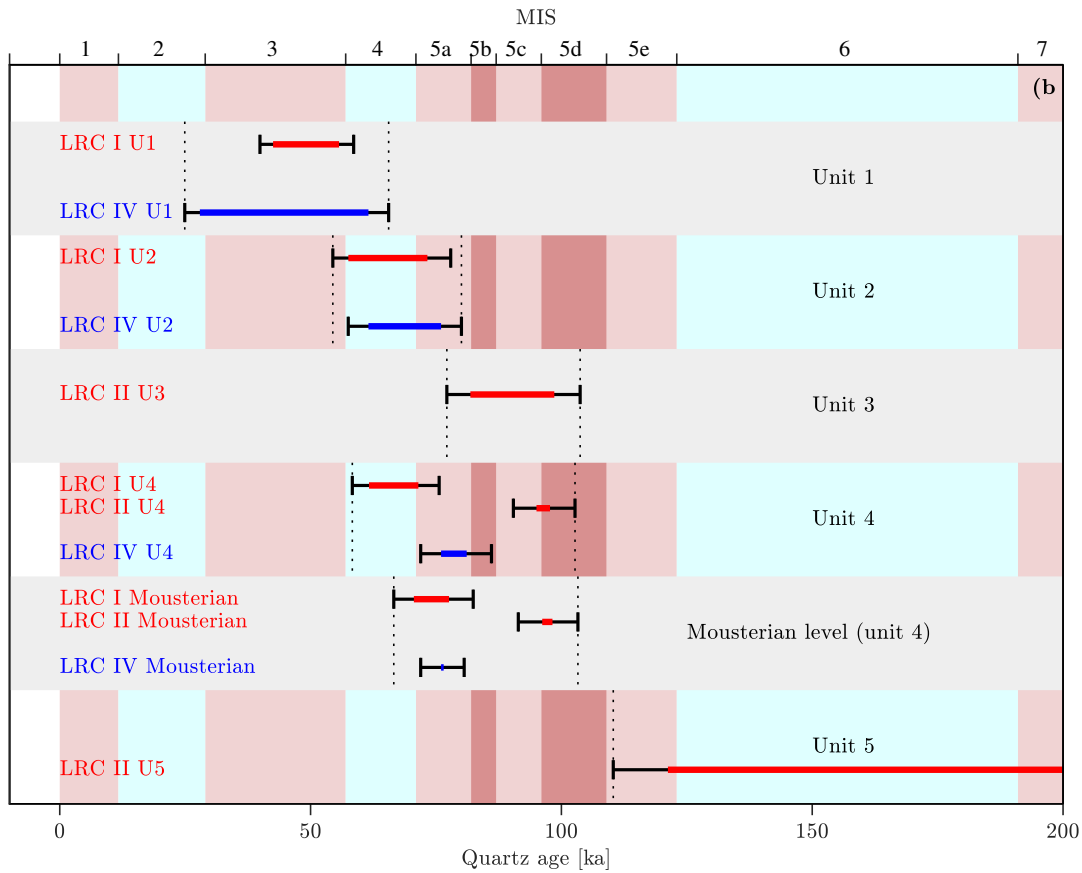
Figure 6.30: Limiting ages derived from Bayesian modelled ages using elevation limits for deposition units 1-4 from LRC I and II (red lines) and from LRC IV (blue lines). Uncertainty (68% confidence level) on these ages are shown with black error bars. The minimum and maximum ages in each unit and in the Mousterian level are indicated with vertical black dotted lines. For unit 5 (n = 5 samples), the lower age range is derived from sample 187304. No upper age limit is given for this unit because three of the samples were in saturation. Marine isotope stages 1-7 (MIS) are shown as red and blue vertical bands (top x-axis). Units are shown as horizontal grey and uncolored bands.

6.8   Summary La Roche Cotard sediments

This study uses the OSL signals from multi- and single-grain quartz aliquots, and the IR_{50} and $pIRIR_{290}$ signals from K-rich feldspar (KF). All equivalent doses are measured using standard SAR protocols. The dose rates are derived from radionuclide concentrations and corrected for heterogeneity in the gamma field (section 6.3.1). A water content of 40% of the measured saturated water content (averaged for each deposition units and inside LRC I, I.C.) has been adopted, based on the current values for two deepest samples least likely to have been affected since excavation of LRC IV in 2008 (see section: 6.7.4).

In the dose rate calculations, a grain size of 180-250 µm is used. We assume an internal dose rate to quartz of 0.02 ± 0.01 Gy.ka^{-1} and to KF of 0.10 ± 0.05 Gy.ka^{-1} from U and Th. The cosmic dose rate contribution is calculated for each individual sample (the average contribution for all samples is 0.064 ± 0.003 Gy.ka^{-1}). KF ages also include an internal dose rate component of 0.86 ± 0.06 Gy.ka^{-1} derived from the measured average K-content of $12.60 \pm 0.15\%$ (n=21) and a Rb-content of 400 ppm (see section 6.3).

For those sediment samples taken close to the rock walls or large clasts, the infinite matrix dose rates derived from radionuclide concentrations were modified to take heterogeneity in the gamma radiation field into account, using the principle of superposition. Modelled results were tested against Monte Carlo simulations and in situ dose rate measurements, both of which supported the use of the simpler analytically modelled dose rates.

Note, that in the section, 6.3.2, we discussed the reliability of our laboratory calculated dose rates when compared to the dose rates measured in situ. On average, we find a good agreement between the two dose rate estimates (1.02 ± 0.09, n=8), but for sample 167812, there was a significant and large difference between the in situ (LaBr probe) and the laboratory calculated gamma dose rates (with the cosmic contribution removed and current w.c. assumed), i.e., 0.323 ± 0.008 Gy.ka^{-1} and 0.48 ± 0.03 Gy.ka^{-1}, respectively (see Figure 6.11). If we were to use the in situ gamma dose rate in the total dose rate calculation, the burial age would increase by 21% (from 75±6 ka to 91±7 ka) and the age would no longer be in stratigraphic order (the elevation of sample 167812 is 49.4 m). This supports our conclusion in section 6.3.2 that the laboratory calculated dose rate is the more reliable, although it must be recognised that it is nevertheless important to correct for heterogeneity in the gamma field.

The quartz luminescence characteristics are satisfactory, although quartz multi-grain natural doses > 225 Gy are not considered to be accurate because of signal saturation issues. In practice, this implies that all samples from inside LRC I and from unit 5 in LRC IV are beyond the age range of multi-grain quartz dating. The main luminescence question remaining is whether the quartz was sufficiently bleached at the time of deposition to allow an accurate age estimate. This has been confirmed in two ways: (i) dose estimates based on quartz single-grain dose distributions are consistent with those from multi-grain aliquots, but only if those grains with a sufficiently large D_c are selected, and the average D_e is determined using the ADM or BayLum models and (ii) both IR_{50} and $pIRIR_{290}$ age estimates are consistently smaller than those based on multi-grain quartz OSL signals, with age ratios with respect to quartz of 0.491 ± 0.011 (n=32) for IR_{50} and 0.81 ± 0.02 (n=32) for $pIRIR_{290}$. The $pIRIR_{290}$ underestimate is surprising, and may be explained by either the use of an inappropriate internal dose rate or possibly by anomalous fading. But whichever explanation is correct, we in any case conclude that, for samples with a quartz D_e <225 Gy (i.e.,

those unlikely to be affected by saturation) the feldspar ages do not significantly overestimate the quartz ages. Taking these two results (single grain analyses and feldspar/quartz age ratios) together, we conclude that it is very likely that the quartz (and the feldspar) was well-bleached at the time of deposition.

Assuming that the quartz samples found inside the cave in LRC I and at the very bottom of LRC IV (unit 5) were also sufficiently bleached at deposition, quartz ages from these locations should be regarded as minimum ages, because these samples are at, or close to, saturation. Fortunately, the quartz ages from unit 5 in LRC IV and from inside LRC I (I.C. and E.C) are not important to the dating of the closure of the cave and can thus be safely omitted from the Baysian age depth model. This modelling gives a most likely closure age for the cave (LRC I) of 57 ± 3 ka (68% confidence level), and a minimum age for the closure of > 51 ka at the 95% confidence level. We thereby reject our hypothesis that the main cave and shelters were accessible for some time after the arrival of *Homo sapiens* in the region, around 37,000 years ago. The model also gives an age of 97 ± 5 ka (68% confidence level) for level 7 in LRC II, the location in unit 4, at which an artefact referred to as "The mask of La Roche-Cotard"[129] was found in 1979.

Chapter 7

Summary and conclusions

This thesis has addressed the question of whether existing rock surface dating models provide a sufficiently accurate description of luminescence depth profiles. The considerable discrepancies observed in the literature on fitting parameters in rock surface exposure dating are examined in the light of the kinetics of the detrapping process in the creation of a luminescence signal. In order to include the non-first order kinetics of feldspar, we tested two new models - a fading model and a general order model, (F.M., G.O.M,) and the existing first order model (F.O.M.) with no trap filling during exposure, using both modelled data and experimental data from rock surface luminescence depth profiles. It was concluded that it is necessary to incorporate the kinetics of the individual signal in the models to get accurate parameter estimates and thus exposure ages. Unfortunately the fading model proved not to be robust and requires further investigation, presumably including re-parameterisation, before it is likely to be of use in rock surface dating.

As established rock surface exposure dating makes use of a calibration profile to estimate $\overline{\sigma\varphi_0}$, the accuracy of this method was investigated using all three models (F.M., G.O.M, and F.O.M.). Use of the G.O.M. in fitting luminescence-depth profiles resulting from exposures of known times did improve the accuracy of age estimation when only a single known IR_{50} feldspar profile was used for calibration. . However profiles from post IR signals did not improve the accuracy of the calibration, and the only clearly accurate exposure age was estimated by interpolating the depth of an unknown profile onto a curve of profile depths of known age profiles (the ERC approach). This approach requires at least two known age samples preferably one older and one younger, than the unknown, and this is very unusual in the field. However this study has shown that artificial light from a broad band halogen light source appears to simulate daylight behaviour well and the effect on profile depth for a given number of photons is consistent with what is seen in daylight-exposed surfaces. Thus generating Exposure Response curves (ERC) by artificially illuminating surfaces at very high intensities may provide calibration profiles of arbitrary 'age', as determined by the total incident number of photons. Such an approach is very likely to give more accurate and precise light exposure ages than using parameters calculated from first principles, or even a single natural calibration profile. However other uncertainties still complicates rock surface exposure dating, as was seen at the archaeological site la Roche Cotard. An attempt was made to use both a calibration profile, and ERC curves from known age profile depths to calibrate unknown exposure profiles. The ERC method gave similar ages for the two samples and uncertainties 4

times smaller than using a single calibration profile, but, unfortunately, both methods gave ages older than planet earth indicating the sensitivity of rock surface exposure dating. Erosion was regarded having mayor influence in these samples.

Despite using the presumably correct model, discrepancies compared to measured values of $\varphi(\lambda)$ and estimates of $\sigma(\lambda)$ were still observed, particular for post IR signals. This emphasises the uncertainties in rock surface exposure dating especially. In particular a change in μ with depth was observed, which has also previously been reported in literature[e.g. 65,74,76]. These changes with depth could be due to light scattering and refraction phenomena not considered in the models. In addition to these discrepancies probably associated with the models themselves, large uncertainties in the $\overline{\sigma\varphi_0}t$ parameter were also observed.

The spectral dependency of these fitting parameters was investigated. In all three types of rocks in this study (granite, and two different sandstones) containing both sensitive quartz and feldspar grains, the IR_{50} signals were bleached to greater depths than the blue stimulated OSL from quartz grains, and than the post IR-stimulated signals $pIRIR_{225}$ and $pIRIR_{290}$. This is inconsistent with the repeated observation that quartz is much more readily bleached than than all feldspar signals in loose grains. Longer wavelengths appear to be more effective at bleaching the IR_{50} signal than the shorter wavelengths. On the other hand, the $pIRIR_{225}$ and $pIRIR_{290}$ signals are better bleached by shorter wavelengths. Surprisingly, quartz in solid rocks was more affected by green light than violet light. This is interpreted as happening because the intensity of the shorter wavelengths is reduced more than the longer wavelengths, as expected from the wavelength dependency of the light attenuation coefficient. This may be part of the reason why quartz is less bleachable than feldspars measured with an IR_{50} protocol in consolidated samples (rocks) despite quartz grains receiving more effective photons at the rock surface, compared to feldspar from a broad band spectrum such as a daylight spectrum or an artificial halogen lamp. However, a decrease in the slope of luminescence-depth profiles, and a resulting decrease in the estimated attenuation coefficient μ, indicates that the attenuation of light in rock samples does not follow a simple Lambert-Beers law. Other effects such as scattering, refraction, and molecular interaction complicate the picture further. Again, the IR_{50} profile was the least affected in terms of slope and μ, presumably because it is most sensitive to the longer wavelengths, which are in turn less affected by scattering and refraction. Estimation of the cross-section σ from luminescence-depth profiles give significantly lower values from those presented in literature[e.g. 58,112,113], again with the possible exception of IR_{50} profiles after exposure to IR light. Such discrepancies have been reported in other rock surface studies[1]. This underestimation may be contributed to by underestimation of μ, but may also be caused by the large uncertainty associated with fitting the parameter $\overline{\sigma\varphi_0}t$; this is very sensitive to the profile depth. Finally, in the present formulation, the attenuation coefficient μ is not included when integrating the number of effective photons over the daylight spectrum. If the wavelength dependency were to be incorporated, the detrapping rate constant would be $E(x) = \int \sigma(\lambda)\varphi(\lambda)e^{-\mu(\lambda)x}d\lambda$.

Although rock surface exposure dating has proved model-dependent, rock surface burial dating does not become significantly inaccurate when an inappropriate model is used to determine the exposure history of a buried surface. However rock surface burial dating does present other challenges. Dating rock surfaces demands dose rate modifications as the dose rate has a depth dependency. When dating smaller cobbles ($\lesssim$30 cm in diameter) the dose rate change is different than

from two parallel sheets. Although Monte Carlo simulation can be used to address this problem, a simple analytical model assuming rocks to be cubes was developed here to provide such a correction. This method is fast, and particularly applicable where size assumption is necessary. It can also be used to correct for inhomogeneity in the field dose rates in sediment dating and for the external dose rate to rock samples.

Estimating a dose, and thus an age from a buried luminescence profile is done in two ways in the literature; i) directly measured dose estimates from samples from known well-bleached depths. If these dose estimates are derived from feldspar then these are then corrected for fading either using measured g-values or using the difference in the laboratory saturation limit and the natural saturation limit (NLS). ii) from the fitting parameter t_b/D_c, and known values of D_c from laboratory generated dose response curves. Both methods assume that the light level fades to the same degree regardless of the degree of saturation (and thus the dose). When using NLS (and in many applications using g-values) one also assumes that the dose fades by the same fraction as the light level, whereas using the fitting parameter t_b/D_c essentially converts the fading-corrected light level to a dose using laboratory (unfaded) dose response curve parameters. In other studies [e.g. 47], it has been shown that correcting using NLS gives either similar or greater ages compared to correcting using g-values.

When used to derive a dose, the fitting parameter method incorporates uncertainties from the full profiles. Using the fitting parameters still have to be investigated further using known age samples that is likely to fade.

Using the fitting parameter method makes use of the non-linear relation between dose and light levels. It assumes that doses fade at different rates from light levels (because of the shape of the dose response curve) which is more physically meaningful, but it must be acknowledged that the process of fading is not yet fully understood for high doses.

Methods and models were tested on two archaeological sites both located in France, La Roche Cotard and Les Roche D'Abilly. Both were both successfully dated using OSL from sediments. Rock samples from Les Roche D'Abilly showed luminescence burial depth profiles from quartz grains from which burial ages were successfully estimated and shown to be consistent with quartz ages from sediments. Unfortunately, the application of rock surface dating to La Roche Cotard was not particularly successful. Most samples from this site no longer preserve a record of prior burial either because of erosion or long recent exposure times or a combination of these phenomena. Nevertheless some burial ages were recovered from these samples. Estimated burial ages from rock surfaces from La Roche Cotard (Chapter 5) using g-values on a burial age from an IR$_{50}$ luminescence-depth profile, gave ages similar to fading corrected IR$_{50}$ KF sediments. But only using the NLS correction gave ages similar to quartz multi-grain and single-grain ages. Using the fitting parameter gave ages similar to the g-value corrected estimates. The fitting parameter method relies on the measured dose response curve value D_c.

Using ERC curves for estimating exposure ages is a promising method well worth examining further in future work. Combing stronger methods for exposure dating with rock surface burial dating will help to strengthen these dating methods and provide more reliable ages.

Acknowledgements

Bibliography

[1] Sohbati, R., Murray, A. S., Chapot, M. S., Jain, M., and Pederson, J. Optically stimulated luminescence (OSL) as a chronometer for surface exposure dating. *J. Geophys.*, 117, 2012. doi: https://doi.org/10.1029/2012JB009383.

[2] Sohbati, R., Murray, A. S., Porat, N., Jain, M., and Avner, U. Age of a prehistoric "Rodedian" cult site constrained by sediment and rock surface luminescence dating techniques. *Quaternary Geochronology*, 30:90–99, 2015. ISSN 1871-1014. doi: https://doi.org/10.1016/j.quageo.2015.09.002. URL https://www.sciencedirect.com/science/article/pii/S1871101415300571.

[3] Freiesleben, T. H., Sohbati, R., Murray, A. S., Jain, M., Hvidt, S., and Jakobsen, B. Mathematical model quantifies multiple daylight exposure and burial events for rock surfaces using luminescence dating. *Radiation Measurements*, 81:16–22, 2015.

[4] Gliganic, L. A., Meyer, M. C., May, J.-H., Aldenderfer, M. S., and Tropper, P. Direct dating of lithic surface artifacts using luminescence. *Science Advances*, 7(23), 2021. doi: 10.1126/sciadv.abb3424. URL https://advances.sciencemag.org/content/7/23/eabb3424.

[5] Morgenstein, M. E., Luo, S., Ku, T. L., and Feathers, J. Uranium-series and luminescence dating of volcanic lithic artefacts. *Archaeometry*, 45:503–518, 2005.

[6] Gliganic, L. A., Meyer, M. C., Sohbati, R., Jain, M., and Barrett, S. OSL surface exposure dating of a lithic quarry in Tibet: Laboratory validation and application. *Quaternary Geochronology*, 49:199–204, 2019. ISSN 1871-1014. doi: https://doi.org/10.1016/j.quageo.2018.04.012. URL https://www.sciencedirect.com/science/article/pii/S187110141730225X. 15th International Conference on Luminescence and Electron Spin Resonance Dating, 11-15 September 2017, Cape Town, South Africa.

[7] al Khasawneh, S., Murray, A. S., and Abudanah, F. A first radiometric chronology for the Khatt Shebib megalithic structure in Jordan using the luminescence dating of rock surfaces. *Quaternary Geochronology*, 49:205–210, 2019. ISSN 1871-1014. doi: https://doi.org/10.1016/j.quageo.2018.02.007. URL https://www.sciencedirect.com/science/article/pii/S1871101417301899. 15th International Conference on Luminescence and Electron Spin Resonance Dating, 11-15 September 2017, Cape Town, South Africa.

[8] Galli, A., Panzeri, L., Rondini, P., Keller, R. P., and Martini, M. Luminescence Dating of

Rock Surface. The Case of Monoliths from the Megalithic Sanctuary of Ossimo-Pat (Valle Camonica, Italy). *Appl. Sci.*, 10:7403, 2020. doi: doi:10.3390/app10217403 w.

[9] Ageby, L., Angelucci, D. E., Brill, D., Carrer, F., Rades, E. F., Rethemeyer, J., Brückner, H., and Klasen, N. Rock surface IRSL dating of buried cobbles from an alpine dry-stone structure in Val di Sole, Italy. *Quaternary Geochronology*, 66: 101212, 2021. ISSN 1871-1014. doi: https://doi.org/10.1016/j.quageo.2021.101212. URL `https://www.sciencedirect.com/science/article/pii/S1871101421000625`.

[10] Feathers, J., More, G. M., Quinteros, P. S., and Burkholder, J. E. IRSL dating of rocks and sediments from desert geoglyphs in coastal Peru. *Quaternary Geochronology*, 49:177–183, 2019. ISSN 1871-1014. doi: https://doi.org/10.1016/j.quageo.2018.07.009. URL `https://www.sciencedirect.com/science/article/pii/S1871101417302169`. 15th International Conference on Luminescence and Electron Spin Resonance Dating, 11-15 September 2017, Cape Town, South Africa.

[11] Simms, A. R., DeWitt, R., Kouremenos, P., and Drewry, A. M. A new approach to reconstructing sea levels in Antarctica using optically stimulated luminescence of cobble surfaces. *Quaternary Geochronology*, 6(1):50–60, 2011. ISSN 1871-1014. doi: https://doi.org/10.1016/j.quageo.2010.06.004. URL `https://www.sciencedirect.com/science/article/pii/S1871101410000397`.

[12] Simkins, L. M., Simms, A. R., and DeWitt, R. Relative sea-level history of Marguerite Bay, Antarctic Peninsula derived from optically stimulated luminescence-dated beach cobbles, 2013. URL `https://doi.org/10.1594/PANGAEA.818537`. Supplement to: Simkins, LM et al. (2013): Relative sea-level history of Marguerite Bay, Antarctic Peninsula derived from optically stimulated luminescence-dated beach cobbles. Quaternary Science Reviews, 77, 141-155, https://doi.org/10.1016/j.quascirev.2013.07.027.

[13] Souza, P. E., Sohbati, R., Murray, A. S., Kroon, A., Clemmensen, L. B., Hede, M. U., and Nielsen, L. Luminescence dating of buried cobble surfaces from sandy beach ridges: a case study from Denmark. *Boreas*, 48(4):841–855, 2019. doi: https://doi.org/10.1111/bor.12402. URL `https://onlinelibrary.wiley.com/doi/abs/10.1111/bor.12402`.

[14] Souza, P. E., Sohbati, R., Murray, A. S., Clemmensen, L. B., Kroon, A., and Nielsen, L. Optical dating of cobble surfaces determines the chronology of Holocene beach ridges in Greenland. *Boreas*, 50(2):606–618, 2021. doi: https://doi.org/10.1111/bor.12507. URL `https://onlinelibrary.wiley.com/doi/abs/10.1111/bor.12507`.

[15] Jenkins, G. T. H., Duller, G. A. T., Roberts, H. M., Chiverrell, R. C., and Glasser, N. F. A new approach for luminescence dating glaciofluvial deposits - High precision optical dating of cobbles. *Quaternary Science Reviews*, 192:263–273, 2018. ISSN 0277-3791. doi: https://doi.org/10.1016/j.quascirev.2018.05.036. URL `https://www.sciencedirect.com/science/article/pii/S0277379118301008`.

[16] Lehmann, B., Valla, P. G., King, G. E., and Herman, F. Investigation of OSL surface exposure dating to reconstruct post-LIA glacier fluctuations in the French Alps (Mer de Glace, Mont Blanc massif). *Quaternary Geochronology*, 44:63–74,

2018. ISSN 1871-1014. doi: https://doi.org/10.1016/j.quageo.2017.12.002. URL https://www.sciencedirect.com/science/article/pii/S1871101417301127.

[17] Brill, D. and May, S. M. and Mhammdi, N. and King, G. and Lehmann, B. and Burow, C. and Wolf, D. and Zander, A. and Brückner, H. Evaluating optically stimulated luminescence rock surface exposure dating as a novel approach for reconstructing coastal boulder movement on decadal to centennial timescales. *Earth Surface Dynamics*, 9(2):205–234, 2021. doi: 10.5194/esurf-9-205-2021. URL https://esurf.copernicus.org/articles/9/205/2021/.

[18] Sohbati, R., Liu, J., Jain, M., Murray, A., Egholm, D., Paris, R., and Guralnik, B. Centennial- to millennial-scale hard rock erosion rates deduced from luminescence-depth profiles. *Earth and Planetary Science Letters*, 493:218–230, 2018. ISSN 0012-821X. doi: https://doi.org/10.1016/j.epsl.2018.04.017. URL https://www.sciencedirect.com/science/article/pii/S0012821X18302127.

[19] Lehmann, B., Herman, F., Valla, P. G., King, G. E., and Biswas, R. H. Evaluating postglacial bedrock erosion and surface exposure duration by coupling in situ optically stimulated luminescence and ^{10}Be dating. *Earth Surface Dynamics*, 7(3):633–662, 2019. doi: 10.5194/esurf-7-633-2019. URL https://esurf.copernicus.org/articles/7/633/2019/.

[20] Lehmann, B., Herman, F., Valla, P. G., King, G. E., Biswas, R. H., Ivy-Ochs, S., Steinemann, O., and Christl, M. Postglacial erosion of bedrock surfaces and deglaciation timing: New insights from the Mont Blanc massif (western Alps). *Geology*, 48(2):139–144, 2019. doi: https://doi.org/10.1130/G46585.1. URL https://esurf.copernicus.org/articles/7/633/2019/.

[21] Hansen, J. M., Aagaard, T., and Binderup, M. Absolute sea levels and isostatic changes of the eastern North Sea to central Baltic region during the last 900 years. *Boreas*, 41(2):180–208, 2012. doi: https://doi.org/10.1111/j.1502-3885.2011.00229.x. URL https://onlinelibrary.wiley.com/doi/abs/10.1111/j.1502-3885.2011.00229.x.

[22] Li, Y., Song, Y., and Lai, Z. Rapid and cyclic dust accumulation during MIS 2 in Central Asia inferred from loess OSL dating and grain-size analysis. *Scientific Reports*, 6:32365, 2016. doi: https://doi.org/10.1038/srep32365.

[23] Stevens, T., Buylaert, J.-P., Thiel, C., Újvári, G., Yi, S., Murray, A. S., Frechen, M., and Lu, H. Ice-volume-forced erosion of the Chinese Loess Plateau global Quaternary stratotype site. *Nature Communications*, 9:983, 2018. doi: https://doi.org/10.1038/s41467-018-03329-2.

[24] Willerslev, E., Cappellini, E., Boomsma, W., Nielsen, R., Hebsgaard, M. B., Brand, T. B., Hofreiter, M., Bunce, M., Poinar, H. N., Dahl-Jensen, D., Johnsen, S., Steffensen, J. P., Bennike, O., Schwenninger, J.-L., Nathan, R., Armitage, S., de Hoog, C.-J., Alfimov, V., Christl, M., Beer, J., Muscheler, R., Barker, J., Sharp, M., Penkman, K. E. H., Haile, J., Taberlet, P., Gilbert, M. T. P., Casoli, A., Campani, E., and Collins, M. J. Ancient Biomolecules from Deep Ice Cores Reveal a Forested Southern Greenland. *Science*, 317(5834):111–114, 2007. ISSN 0036-8075. doi: 10.1126/science.1141758. URL https://science.sciencemag.org/content/317/5834/111.

[25] Svendsen, J. I., Alexanderson, H., Astakhov, V. I., Demidov, I., Dowdeswell, J. A., Funder,

S., Gataullin, V., Henriksen, M., Hjort, C., Houmark-Nielsen, M., Hubberten, H. W., Óla-fur Ingólfsson, Jakobsson, M., Kjær, K. H., Larsen, E., Lokrantz, H., Lunkka, J. P., Lyså, A., Mangerud, J., Matiouchkov, A., Murray, A., Möller, P., Niessen, F., Nikolskaya, O., Polyak, L., Saarnisto, M., Siegert, C., Siegert, M. J., Spielhagen, R. F., and Stein, R. Late Quaternary ice sheet history of northern Eurasia. *Quaternary Science Reviews*, 23(11):1229–1271, 2004. ISSN 0277-3791. doi: https://doi.org/10.1016/j.quascirev.2003.12.008. URL `https://www.sciencedirect.com/science/article/pii/S0277379103003421`. Quaternary Environments of the Eurasian North (QUEEN).

[26] Ortuño, M., Masana, E., E. adn García-Meléndez, Martínez-Díaz, J., Štěpančíková, P., Cunha, P., Sohbati, R., Canora, C., Buylaert, J. P., and Murray, A. S. An exceptionally long paleoseismic record of a slow-moving fault: The Alhama de Murcia fault (Eastern Betic shear zone, Spain). *GSA Bulletin*, 124(9-10):1474–1494, 2012. doi: https://doi.org/10.1130/B30558.1.

[27] Kristensen, J. A., Thomsen, K. J., Murray, A. S., Buylaert, J.-P., Jain, M., and Breuning-Madsen, H. Quantification of termite bioturbation in a savannah ecosystem: Application of OSL dating. *Quaternary Geochronology*, 30:334–341, 2015. ISSN 1871-1014. doi: https://doi.org/10.1016/j.quageo.2015.02.026. URL `https://www.sciencedirect.com/science/article/pii/S1871101415000394`. LED14 Proceedings.

[28] Marean, C., Bar-Matthews, M., Bernatchez, J., Fisher, E., Goldberg, P., Herries, A. I. R., Jacobs, Z., Jerardino, A., Karkanas, P., Minichillo, T., Nilssen, P. J., Thompson, E., Watts, I., and Williams, H. M. Early human use of marine resources and pigment in South Africa during the Middle Pleistocene. *Nature*, 449:905–908, 2007. doi: https://doi.org/10.1038/nature06204.

[29] Jacobs, Z., Wintle, A. G., Duller, G. A. T., Roberts, R. G., and Wadley, L. New ages for the post-Howiesons Poort, late and final Middle Stone Age at Sibudu, South Africa. *Journal of Archaeological Science*, 35:1790–1807, 2008. doi: 10.1016/j.jas.2007.11.028.

[30] Jacobs, Z., Roberts, R. G., Galbraith, R. F., Deacon, H. J., Grün, R., Mackay, A., Mitchell, P., Vogelsang, R., and Wadley, L. Ages for the Middle Stone Age of Southern Africa: Implications for Human Behavior and Dispersal. *Science*, 322(5902):733–735, 2008. ISSN 0036-8075. doi: 10.1126/science.1162219. URL `https://science.sciencemag.org/content/322/5902/733`.

[31] Armitage, S. J., Jasim, S. A., Marks, A. E., Parker, A. G., Usik, V. I., and Uerpmann, H. P. The southern route "out of Africa": evidence for an early expansion of modern humans into Arabia. *Science*, 331:453–456, 2011. doi: 10.1126/science.1199113.

[32] Aitken, M. J. *An Introduction to Optical Dating*. Oxford University Press, Oxford, 1998.

[33] Galbraith, R. F., Roberts, R. G., Laslett, G. M., Yoshida, H., and Olley, J. M. Optical dating of single and multiple grains of quartz from Jinmium rock shelter, northern Australia: Part I, experimental design and statistical models. *Archaeometry*, 41:339–364, 1999.

[34] Thomsen, K. J., Murray, A. S., Bøtter-Jensen, L., and Kinahan, J. Determination of burial

dose in incompletely bleached fluvial samples using single grains of quartz. *Radiation Measurements*, 42:370–379, 2007.

[35] Duller, G. A. T. Single-grain optical dating of Quaternary sediments: why aliquot size matters in luminescence dating. *Boreas*, 37:589–612, 2008.

[36] Bateman, M. D., Boulter, C. H., Carr, A. S., Frederick, C. D., Peter, D., and Wilder, M. Detecting post-depositional sediment disturbance in sandy deposits using optical luminescence. *Quaternary Geochronology*, 2(1):57–64, 2007. ISSN 1871-1014. doi: https://doi.org/10.1016/j.quageo.2006.05.004. URL `https://www.sciencedirect.com/science/article/pii/S1871101406000367`. LED 2005.

[37] Galbraith, R. F. and Green, P. F. Estimating the component ages in a finite mixture. *Nuclear Tracks and Radiation Measurements*, 17:197–206, 1990. doi: 10.1126/science.1199113.

[38] Jacobs, Z., Duller, G. A. T., and Wintle, A. G. Optical dating of dune sand from Blombos Cave, South Africa: II - single grain data. *Journal of Human Evolution*, 44:613–625, 2003. doi: 10.1016/s0047-2484(03)00049-6.

[39] Thomsen, K. J., Murray, A. S., Buylaert, J.-P., Jain, M., Helt-Hansen, J., and Aubry, T. Testing single-grain quartz OSL methods using known age samples from the Bordes-Fitte rockshelter (Roches d'Abilly site, Central France). *Quaternary Geochronology*, 31:77–96, 2016.

[40] Guérin, G., Murray, A. S., Jain, M., Thomsen, K. J., and Mercier, N. How confident are we in the chronology of the transition between Howieson's Poort and Still Bay? *Journal of Human Evolution*, 64(4):314–317, 2013. ISSN 0047-2484. doi: https://doi.org/10.1016/j.jhevol.2013.01.006. URL `https://www.sciencedirect.com/science/article/pii/S0047248413000122`.

[41] Murray, A. S., Buylaert, J.-P., Guérin, G., Qin, J., Singhvi, A. K., Smedley, R. S., and Thomsen, K. J. Optically stimulated luminescence dating using quartz sand. *Nature Primer*, Accepted.

[42] Sohbati, R., Murray, A. S., Jain, M., Buylaert, J.-P., and Thomsen, K. J. Investigating the resetting of OSL signals in rock surfaces. *Geochronometria*, 38:249–258, 2011. doi: doi.org/10.2478/s13386-011-0029-2.

[43] Chapot, M. S., Roberts, H. M., Duller, G. A. T., and Lai, Z. P. A comparison of natural- and laboratory-generated dose response curves for quartz optically stimulated luminescence signals from Chinese Loess. *Radiation Measurements*, 47(11-12):1045–1052, 2012.

[44] Sohbati, R., Murray, A. S., Buylaert, J.-P., Almeida, N. A. C., and Cunha, P. P. Optically stimulated luminescence (OSL) dating of quartzite cobbles from the Tapada do Montinho archaeological site (east-central Portugal). *Boreas*, 41:452–462, 2012.

[45] Liu, J., Cui, F., Murray, A. S., Sohbati, R., Jain, M., Gao, H., Li, W., Li, C., Li, P., Zhou, T., and Chen, J. Resetting of the luminescence signal in modern riverbed cobbles along the course of the Shiyang River, China. *Quaternary Geochronology*, 49:184–

190, 2019. ISSN 1871-1014. doi: https://doi.org/10.1016/j.quageo.2018.04.004. URL `https://www.sciencedirect.com/science/article/pii/S1871101417302297`. 15th International Conference on Luminescence and Electron Spin Resonance Dating, 11-15 September 2017, Cape Town, South Africa.

[46] Stange, K. M., Midtkandal, I., Nystuen, J. P., Murray, A., Sohbati, R., Thompson, W., Spiegel, C., and Kuss, H.-J. Erosive Response of Non-Glaciated Pyrenean Headwater Catchments to the Last Major Climate Transition and Establishing Interglacial Conditions. *Quaternary*, 2(2), 2019. ISSN 2571-550X. doi: 10.3390/quat2020017. URL `https://www.mdpi.com/2571-550X/2/2/17`.

[47] Rades, E. F., Sohbati, R., Lüthgens, C., Jain, M., and Murray, A. S. First luminescence-depth profiles from boulders from moraine deposits: Insights into glaciation chronology and transport dynamics in Malta valley, Austria. *Radiation Measurements*, 120:281–289, 2018. ISSN 1350-4487. doi: https://doi.org/10.1016/j.radmeas.2018.08.011. URL `https://www.sciencedirect.com/science/article/pii/S1350448717308466`. 15th International Conference on Luminescence and Electron Spin Resonance Dating, 11-15 September 2017.

[48] Chapot, M. S., Sohbati, R., Murray, A. S., Pederson, J. L., and Rittenour, T. M. Constraining the age of rock art by dating a rockfall event using sediment androck-surface luminescence dating techniques. *Quaternary Geochronology*, 13:18–25, 2012.

[49] Rosato, A., Strandburg, K. J., Prinz, F., and Swendsen, R. H. Why the brazil nuts are on top: Size segregation of particulate matter by shaking. *Phys. Rev. Lett.*, 58:1038–1040, Mar 1987. doi: 10.1103/PhysRevLett.58.1038. URL `https://link.aps.org/doi/10.1103/PhysRevLett.58.1038`.

[50] Godfrey-Smith, D. L., Huntley, D. J., and Chen, W. H. Optically dating studies of quartz and feldspar sediment extracts. *Quaternary Science Reviews*, 7:373–380, 1988.

[51] Murray, A. S. and Wintle, A. G. Luminescence dating of quartz using an improved single-aliquot regenerative-dose protocol. *Radiation Measurements*, 32:57–73, 2000.

[52] Murray, A. S. and Wintle, A. G. Isothermal decay of optically stimulated luminescence in quartz. *Radiation Measurements*, 30(1):119–125, 1999. ISSN 1350-4487. doi: https://doi.org/10.1016/S1350-4487(98)00097-3. URL `https://www.sciencedirect.com/science/article/pii/S1350448798000973`.

[53] Tsukamoto, S., Nagashima, K., Murray, A. S., and Tada, R. Variations in OSL components from quartz from Japan sea sediments and the possibility of reconstructing provenance. *Quaternary International*, 234(1-2):182–189, 2011. doi: 10.1016/j.quaint.2010.09.003.

[54] Jain, M., Sohbati, R. B., Guralnik, Murray, A. S., Kook, M., Lapp, T., Prasad, A. K., Thomsen, K. J., and J.-P., B. Kinetics of infrared stimulated luminescence from feldspars. *Radiation Measurements*, 81:242–250, 2015.

[55] Thomsen, K. J., Murray, A. S., Jain, M., and Bøtter-Jensen, L. Laboratory fading rates of various luminescence signals from feldspar-rich sediment extracts. *Radiation Measurements*, 43:1474–1486, 2008.

[56] Buylaert, J.-P., Jain, M., Murray, A. S., Thomsen, K. J., Thiel, C., and Sohbati, R. A robust feldspar luminescence dating method for Middle and Late Pleistocene sediments. *Boreas*, 419: 435–451, 2012.

[57] Wintle, A. Anomalous Fading of Thermo-luminescence in Mineral Samples. *Nature*, 245: 143–144, 1973. doi: https://doi.org/10.1038/245143a0.

[58] Spooner, N. A. The anomalous fading of infrared-stimulated luminescence from feldspars. *Radiation Measurements*, 23(327):625–632, 1994.

[59] Huntley, D. J. and Lamothe, M. Ubiquity of anomalous fading in K-feldspars and the measurement and correction for it in optical dating. *Canadian Journal of Earth Sciences*, 38:1093–1106, 2001.

[60] Liritzis, I. A new dating method by thermoluminescence of carved megalithic stone building. *Comptes Rendus de l'Académie des Sciences-Série II*, 319:603–610, 1994.

[61] Liritzis, I., Guibert, P., Foti, F., and Schvoerer, M. The temple of Apollo (Delphi) strengthens novel thermoluminescence dating method. *Geoarchaeology*, 12:479–496, 1999.

[62] Theocaris, P. S., Liritzis, I., and Galloway, R. B. Dating of two Hellinic Pyramids by a novel application of thermoluminescence. *Journal of Archaeological Science*, 24:399–405, 1997.

[63] Polikreti, K., Michael, C. T., and Maniatis, Y. Thermoluminescence characteristics of marble and dating of freshly excavated marble objects. *Radiation Measurements*, 37(1):87–94, 2003.

[64] Liritzis, I. and Galloway, R. B. Dating implications from solar bleaching of thermoluminescence of ancient marble. *Journal of Radioanalytic and Nuclear Chemistry*, 241:361–368, 1999.

[65] Polikreti, K., Michael, C., and Maniatis, Y. Authenticating marble sculpture with thermoluminescence. *Ancient TL*, 20:11–18, 2002.

[66] Aitken, M. J. *Thermoluminescence Dating.* Academic Press, 1985. ISBN 0-12-046381-4.

[67] Huntley, D. J., Godfrey-Smith, D. I., and Thewalt, M. L. W. Optical dating of sediments. *Nature*, 313:105–108, 1985.

[68] Huntley, M., D. J.and Richards. The age of the Diring Quriakh archaeological site. *Ancient TL*, 15:48–51, 1997.

[69] Habermann, J., Schilles, T., Kalchgruber, R., and Wagner, G. A. Steps towards surface dating using luminescence. *Radiation Measurements*, 32(5-6):847–851, 2000. doi: 10.1016/S1350-4487(00)00109-8.

[70] Greilich, S., Glasmacher, U. A., and Wagner, G. A. Optical dating of granitic stone surfaces. *Archaeometry*, 47:645–665, 2005.

[71] Vafiadou, A., Murray, A., and Liritzis, I. Optically stimulated luminescence (OSL) dating investigations of rock and underlying soil from three case studies. *Journal of Archaeological Science*, 34(10):1659–1669, 2007. doi: 10.1016/j.jas.2006.12.004.

[72] Laskaris, N. and Liritzis, I. A new mathematical approximation of sunlight attenuation in rocks for surface luminescence dating. *Journal of Luminescence*, 131:1874–1884, 2011.

[73] Sohbati, R., Jain, M., and Murray, A. S. Surface exposure dating of non-terrestrial bodies using optically stimulated luminescence: a new method. *Icarus*, 221:160–166, 2012.

[74] Ou, X. J., Roberts, H. M., Duller, G. A. T., Gunn, M. D., and Perkins, W. T. Attenuation of light in different rock types and implications for rock surface luminescence dating. *Radiation Measurements*, 120:305–311, 2018.

[75] Sellwood, E. L., Guralnik, B., Kook, A. K., M. andPrasad, Sohbati, R., Hippe, K., Wallinga, J., and Jain, M. Optical bleaching front in bedrock revealed by spatially-resolved infrared photoluminescence. *Sci Rep*, 9:2611, 2019. doi: https://doi.org/10.1038/s41598-019-38815-0.

[76] Meyer, M. C., Gliganic, L. A., Jain, M., Sohbati, R., and Schmidmair, D. Lithological controls on light penetration into rock surfaces – Implications for OSL and IRSL surface exposure dating. *Radiation Measurements*, 120:298–304, 2018. ISSN 1350-4487. doi: https://doi.org/10.1016/j.radmeas.2018.03.004. URL `https://www.sciencedirect.com/science/article/pii/S1350448717308387`. 15th International Conference on Luminescence and Electron Spin Resonance Dating, 11-15 September 2017.

[77] Bailiff, I. K. and Poolton, N. R. J. Studies of charge transfer mechanisms in feldspars. *Nucl. Tracks Radiat. Meas.*, 18:111–118, 1991.

[78] Thomsen, K. J., Murray, A. S., and Jain, M. Stability of IRSL signals from sedimentary K-feldspar samples. *Geochronometria*, 38(1):1–13, 2011. doi: 10.2478/s13386-011-0003-z.

[79] Marquet, J. C., Freiesleben, T. H., Thomsen, K. J., Murray, A. S., Calligaro, M., Macaire, J.-J., Robert, E., Lorblanchet, M., Aubry, T., Bayle, G., Bréhéret, J.-G., Camus, H., Chareille, P., Egels, Y., Guillaud, E., Guérin, G., Gautret, P., Liard, M., O'Farrell, M., Peyrouse, J.-B., Thamó-Bozsó, E., Verdin, P., Wojtczak, D., Oberlin, C., and Jaubert, J. The earliest unambiguous Neanderthal engravings on cave walls: La Roche-Cotard, Loire Valley, France. *Nature*, submitted.

[80] Freiesleben, T. H. Developing a Method for Luminescence Dating of Rock surfaces - developing a mathematical model to describe multiple daylight exposure and burial events for rocks and developing a preparation method for rock samples for Optically Stimulated Luminescence Dating. Master's thesis, Roskilde University, 2014.

[81] Aubry, T., Dimuccio, L. A., Buylaert, J.-P., Liard, M., Murray, A. S., Thomsen, K. J., and Walter, B. Middle-to-upper Palaeolithic site formation processes at the Bordes-Fitte rockshelter (Central France). *Journal of Archaeological Science*, 52:436–457, 2014.

[82] Freiesleben, T. H., Thomsen, K. J., Murray, A. S., Sohbati, R., Jain, M., Hvidt, S., Jakobsen, B., and Aubry, T. Rock surface and sediment quartz dating using optically stimulated luminescence at the Bordes-Fitte rock shelter, Les Roches D'Abilly, France. *Quaternary Geochronology*, to be submitted.

[83] McKeever, S. and Chen, R. Luminescence models. *Radiation Measurements*, 27:625–661, 1997.

[84] Freiesleben, T. H., Thomsen, K. J., and Jain, M. Do luminescence exposure chronologies depend on the chosen kinetic model of electron detrapping? *to be decided*, to be submitted.

[85] Freiesleben, T. H., Thomsen, K. J., Sellwood, E., and Murray, A. S. Testing luminescence-depth models for exposure and burial dating using controlled experiments. *to be decided*, to be submitted.

[86] Slimak, L. Le Néronien et la structure historique du basculement du Paléolithique moyen au Paléolithiqie supérieur en France méditerranéenne. *C.R. Palevol*, 6:301–309, 2007.

[87] Aubry, T., Dimuccio, L. A., Almeida, M., Buylaert, J.-P., Fontana, L., Higham, T., Liard, M., Murray, A. S., Neves, M. J., Peyrouse, J.-B., and Walter, B. Stratigraphic and technological evidence from the Middle Palaeolithic-Châtelperronian-Aurignacian record at the Bordes-Fitte rockshelter (Roches d'Abilly site, Central France). *Journal of Human Evolution*, 62 (1):116–137, 2012.

[88] Murray, A. S., Thomsen, K. J., Masuda, N., Buylaert, J.-P., and Jain, M. Identifying well-bleached quartz using the different bleaching rates of quartz and feldspar luminescence signals. *Radiation Measurements*, 47:688–695, 2012.

[89] Olley, J. M., Caitcheon, G., and Roberts, R. G. The origin of dose distributions in fluvial sediments, and the prospect of dating single grains from fluvial deposits using optically stimulated luminescence. *Radiation Measurements*, 30:207–217, 1999.

[90] Liritzis, I. Surface dating by luminescence: an overview. *Geochronometria*, 38:292–302, 2011.

[91] Sohbati, R. Luminescence, Rock surfaces. *Encyclopedia of Scientific Dating Methods.*, 221, 2013. doi: 10.1007/978-94-007-6326-5-83-4.

[92] Reimer, P. J., Bard, E., Bayliss, A., Beck, J. W., Blackwell, P. G., Ramsey, C. B., Buck, C. E., Cheng, H., Edwards, R. L., Friedrich, M., and et al. IntCal13 and Marine13 Radiocarbon Age Calibration Curves 0–50,000 Years cal BP. *Radiocarbon*, 55(4):1869–1887, 2013. doi: 10.2458/azu-js-rc.55.16947.

[93] Reimer, P. J., Austin, W. E. N., Bard, E., Bayliss, A., Blackwell, P. G., Bronk Ramsey, C., Butzin, M., Cheng, H., Edwards, R. L., Friedrich, M., Grootes, P., Guilderson, T., Hajdas, I., Heaton, T., Hogg, A., Hughen, K., Kromer, B., Manning, S., Muscheler, R., Palmer, J., Pearson, C., van der Plicht, J., Reimer, R., Richards, D., Scott, E., Southon, J., Turney, C., Wacker, L., Adolphi, F., Büntgen, U., Capano, M., Fahrni, S., Fogtmann-Schulz, A., Friedrich, R., Köhler, P., Kudsk, S., Miyake, F., Olsen, J., Reinig, F., Sakamoto, M., Sookdeo, A., and Talamo, S. The IntCal20 Northern Hemisphere Radiocarbon Age Calibration Curve (0–55 cal kBP). *Radiocarbon*, 62(4):725–757, 2020. doi: 10.1017/RDC.2020.41.

[94] Duller, G. A. T. Distinguishing quartz and feldspar in single grain luminescence measurements. *Radiation Measurements*, 37:161–165, 2003.

[95] Bøtter-Jensen, L., Thomsen, K. J., and Jain, M. Review of optically stimulated luminescence

(OSL) instrumental developments for retrospective dosimetry. *Radiation Measurements*, 45: 253–257, 2010.

[96] Hansen, V., Murray, A. S., Buylaert, J.-P., Yeo, E. Y., and Thomsen, K. J. A new irradiated quartz for beta source calibration. *Radiation Measurements*, 81:123–127, 2015.

[97] Murray, A. S., Marten, R., Johnston, A., and Martin, P. Analysis for naturally occurring radionuclides at environmental concentrations by gamma spectrometry. *J. Radioanalytical Nucl. Chem.*, 115:263–288, 1987.

[98] Murray, A. S., Helsted, L. M., Autzen, M., Jain, M., and Buylaert, J.-P. Measurement of natural radioactivity: Calibration and performance of a high-resolution gamma spectrometry facility. *Radiation Measurements*, 120:215–220, 2018. doi: 10.1016/j.radmeas.2018.04.006.

[99] Guérin, G., Mercier, N., Nathan, R., Adamiec, G., and Lefrais, Y. On the use of the infinite matrix assumption and associated concepts: A critical review. *Radiation Measurements*, 47 (9):778–785, 2012.

[100] Vanderbenghe, D., De Corte, F., Buylaert, J.-P., Kučerac, J., and Vanden Haute, P. On the internal radioactivity in quartz. *Radiation Measurements*, 43:771–775, 2008.

[101] Prescott, J. R. and Hutton, J. T. Cosmic ray contributions to dose rates for luminescence and ESR dating: large depths and long-term variations. *Radiation Measurements*, 23:497–500, 1994.

[102] Banerjee, D., Murray, A. S., Bøtter-Jensen, L., and Lang, A. Equivalent dose estimation using a single aliquot of polymineral fine grains. *Radiation Measurements*, 33:73–94, 2001.

[103] Murray, A. S. and Wintle, A. G. The single aliquot regenerative dose protocol: potential for improvements in reliability. *Radiation Measurements*, 37:377–381, 2003.

[104] Guérin, G., Christophe, C., Philippe, A., Murray, A. S., Thomsen, K. J., Tribolo, C., Urbanova, P., Jain, M., Guibert, P., Mercier, N., Kreutzer, S., and Lahaye, C. Absorbed dose, equivalent dose, measured dose rates, and implications for OSL age estimates: Introducing the Average Dose Model. *Quaternary Geochronology*, 41:163–173, 2017.

[105] Medialdea, A., Thomsen, K. J., Murray, A. S., and Benito, G. Reliability of equivalent-dose determination and age-models in the OSL dating of historical and modern palaeoflood sediments. *Quaternary Geochronology*, 22:11–24, 2014.

[106] Riedesel, S. and Autzen, M. Beta and gamma dose rate attenuation in rocks and sediment. *Radiation Measurements*, 133(106295), 2020.

[107] Wintle, A. G. and Murray, A. S. A review of quartz optically stimulated luminescence characteristics and their relevance in single-aliquot regeneration dating protocols. *Radiation Measurements*, 41:369–391, 2006.

[108] Blaauw, M. and Christen, J. A. Flexible paleoclimate age-depth models using an autoregressive gamma process. *Bayesian Anal.*, 6:457–474, 2011.

[109] Pagonis, V., Kitis, G., and Furetta, C. *Numerical and practical exercises in thermoluminescence.* Springer Science & Business Media, 2006.

[110] Chen, R. and McKeever, S. W. *Theory of thermoluminescence and related phenomena*. World Scientific, 1997.

[111] Spooner, N. On the optical dating signal from quartz. *Radiation Measurements*, 23(2): 593–600, 1994b. ISSN 1350-4487. doi: https://doi.org/10.1016/1350-4487(94)90105-8. URL `https://www.sciencedirect.com/science/article/pii/135044879490105-8`.

[112] Singarayer, J. S. and Bailey, R. M. Further investigations of the quartz optically stimulated luminescence components using linear modulation. *Radiation Measurements*, 37(4): 451–458, 2003. ISSN 1350-4487. doi: https://doi.org/10.1016/S1350-4487(03)00062-3. URL `https://www.sciencedirect.com/science/article/pii/S1350448703000623`. Proceedings of the 10th international Conference on Luminescence and Electron-Spin Resonance Dating (LED 2002).

[113] Jain, M., Murray, A., and Bøtter-Jensen, L. Characterisation of blue-light stimulated luminescence components in different quartz samples: implications for dose measurement. *Radiation Measurements*, 37(4):441–449, 2003. ISSN 1350-4487. doi: https://doi.org/10.1016/S1350-4487(03)00052-0. URL `https://www.sciencedirect.com/science/article/pii/S1350448703000520`. Proceedings of the 10th international Conference on Luminescence and Electron-Spin Resonance Dating (LED 2002).

[114] Riedel-Lyngskær, N., Ribaconka, M., Pó, M., Thorsteinsson, S., Thorseth, A., Dam-Hansen, C., and Jakobsen, M. L. Spectral Albedo in Bifacial PV Modeling: What can be Learned from Field Measurements? In *48th IEEE Photovoltaic Specialists Conference, Miami, FL*, 2021.

[115] Toon, O. B., Pollack, J. B., and Sagan, C. Physical properties of the particles composing the martian dust storm of 1971-1972. *Icarus*, 30:663–696, 1977. doi: 10.1016/0019-1035(77)90088-4.

[116] al Khasawneh, S., Murray, A., Thomsen, K., AbuAzizeh, W., and Tarawneh, M. Dating a near eastern desert hunting trap (kite) using rock surface luminescence dating. *Archaeological and Anthropological Sciences*, 11(5), 2018. ISSN 2571-550X. URL `https://www.mdpi.com/2571-550X/2/2/17`.

[117] Thompson, W. personal communication, 2021.

[118] Bøtter-Jensen, L., Andersen, C. E., Duller, G. A. T., and Murray, A. S. Developments in radiation, stimulation and observation facilities in luminescence measurements. *Radiation Measurements*, 37:535–541, 2003.

[119] Thomsen, K., Kook, M., Murray, A., and Jain, M. Resolving luminescence in spatial and compositional domains. *Radiation Measurements*, 120:260–266, 2018. ISSN 1350-4487. doi: https://doi.org/10.1016/j.radmeas.2018.06.002. URL `https://www.sciencedirect.com/science/article/pii/S1350448717308703`. 15th International Conference on Luminescence and Electron Spin Resonance Dating, 11-15 September 2017.

[120] Kook, M. H., Lapp, T., Murray, A. S., and Thiel, C. Risø XRF attachment for major element

analysis of aliquots of quartz and feldspar separates. In *UK Luminescence and ESR Meeting, Aberystwyth, September 2012*, page 37, 2012.

[121] Porat, N., Faerstein, G., Medialdea, A., and Murray, A. S. Re-examination of common extraction and purification methods of quartz and feldspar for luminescence dating. *Ancient TL*, 33:22–30, 2015.

[122] Bu, M., Murray, A. S., Kook, M., Helsted, L. M., Buylaert, J.-P., and Thomsen, K. J. Characterisation of scintillator-based gamma spectrometers for determination of sample dose rate in OSL dating applications. *Radiation Measurements*, 120:253–259, 2018. ISSN 1350-4487. doi: https://doi.org/10.1016/j.radmeas.2018.07.003. URL https://www.sciencedirect.com/science/article/pii/S1350448717308454. 15th International Conference on Luminescence and Electron Spin Resonance Dating, 11-15 September 2017.

[123] Guérin, G. and Mercier, N. Determining gamma dose rates by field gamma spectroscopy in sedimentary media: results of Monte Carlo simulations. *Radiation Measurements*, 46(2): 190–195, 2011.

[124] Jain, M. Extending the dose range: Probing deep traps in quartz with 3.06eV photons. *Radiation Measurements*, 44(5):445–452, 2009. ISSN 1350-4487. doi: https://doi.org/10.1016/j.radmeas.2009.03.011. URL https://www.sciencedirect.com/science/article/pii/S1350448709000444. Proceedings of the 12th International Conference on Luminescence and Electron Spin Resonance Dating (LED 2008).

[125] Thiel, C., Buylaert, J.-P., Murray, A. S., Terhorst, B., Hofer, I., Tsukamoto, S., and Frechen, M. Luminescence dating of the Stratzing loess profile (Austria)–Testing the potential of an elevated temperature post-IR IRSL protocol. *Quaternary International*, 234:23–31, 2011.

[126] Li, B. and Li, S.-H. Luminescence dating of K-feldspar from sediments: A protocol without anomalous fading correction. *Quaternary Geochronology*, 6(5):468–479, 2011. ISSN 1871-1014. doi: https://doi.org/10.1016/j.quageo.2011.05.001. URL https://www.sciencedirect.com/science/article/pii/S1871101411000343.

[127] Bøtter-Jensen, L., Duller, G. A. T., and Poolton, N. Excitation and emission spectrometry of stimulated luminescence from quartz and feldspars. *Radiation Measurements*, 23(2): 613–616, 1994. ISSN 1350-4487. doi: https://doi.org/10.1016/1350-4487(94)90108-2. URL https://www.sciencedirect.com/science/article/pii/1350448794901082.

[128] d'Achon, F. Au pays des châteaux. La Roche-Cotard. Sa grotte préhistorique. *La Touraine*, 4(1ère année):125–131, 1913.

[129] Marquet, J. C. and Lorblanchet, M. A Neanderthal face? The proto-figurine from La Roche-Cotard, Langeais (Indre-et-Loire, France). *Antiquity*, 77(298), 2003.

[130] Marquet, J.-C., Lorblanchet, M., Oberlin, C., Thamo-Bozso, E., and Aubry, T. Nouvelle datation du « masque » de La Roche-Cotard (Langeais, Indre-et-Loire, France). *Paleo*, 27: 253–263, 2016. doi: https://doi.org/10.4000/paleo.3144.

[131] Pettitt, P. Is this the infancy of art? Or the art of an infant? - A possible Neanderthal face from La Roche-Cotard, France. *Before Farming (Western Academic & Specialist Press)*, 11 (3), 2003.

[132] Nicoud, L. L'art néandertalien : réalité et énigme. *Archéologia*, 407, 2004.

[133] Ladier, E. Traces expérimentales de griffades. *Prehistoire du Sud-Ouest*, 10:153–156, 2003.

[134] Delluc, B. and Delluc, G. Griffades d'ours et pseudo-griffades paléolithiques en Dordogne. *Prehistoire du Sud-Ouest*, 10:131–137, 2003.

[135] Magaire, J.-J., Gay-Overero, I., Bacchi, M., Cocirta, C., Patryl, L., and Rodrigues, S. Petrography of alluvial sands as a past and present environmental indicator: Case of the Loire River (France). *International Journal of Sediment Research*, 28(3):285–303, 2013.

[136] Marquet, J. C., Macaire, J., Bayle, G., Peyouse, J., Guillaud, E., Aubry, T., Liard, M., Bréhéret, J., Thomsen, K. J., Freiesleben, T., Thamóné-Bozsó, E., Guérin, G., and Murray, A. S. Le site Prehistorique de la Roche-Cotard IV (Indre-et-loire, France): Une séquence du Pléistocene moyen et supérieur, référence pour le val de Loire Tourangeau. *Quaternaire*, 30 (2):185–209, 2019.

[137] Higham, T., Douka, K., Wood, R., Ramsey, C. B., Brock, F., Basell, L., Camps, M., Arrizabalaga, A., Baena, J., Barroso-Ruíz, C., Bergman, C., Boitard, C., Boscato, P., Caparrós, M., Conard, N., Draily, C., Froment, A., Galván, B., Gambassini, P., Garcia-Moreno, A., Grimaldi, S., Haesaerts, P., Holt, B., Iriarte-Chiapusso, M.-J., Jelinek, A., Pardo, J. F. J., Maíllo-Fernández, J.-M., Marom, A., Maroto, J., Menéndez, M., Metz, L., Morin, E., Moroni, A., Negrino, F., Panagopoulou, E., Peresani, M., Pirson, S., de la Rasilla, K., Riel-Salvatore, J., Ronchitelli, A., Santamaria, D., Semal, D., Slimak, L., Soler, J., Soler, N., Villaluenga, A., Pinhasi, R., and Jacobi, R. The timing and spatiotemporal patterning of Neanderthal disappearance. *Nature*, 512:306–309, 2014. doi: https://doi.org/10.1038/nature13621.

[138] Hublin, J.-J. The modern human colonization of western Eurasia: when and where? *Quaternary Science Reviews*, 118:194–210, June 2015. doi: 10.1016/j.quascirev.2014.08.011.

[139] Higham, T. European Middle and Upper Palaeolithic radiocarbon dates are often older than they look: problems with previous dates and some remedies. *Antiquity*, 85(327):235–249, 2011. doi: 10.1017/S0003598X00067570.

[140] Huntley, D. J., Godfrey-Smith, D. I., and Haskell, E. H. Light induced emission spectra from some quartz and feldspars. *Nuclear Tracks and Radiation Measurements*, 18:127–131, 1991.

[141] Zhao, H. and Li, S. Internal dose rate to K-feldspar grains from radioactive elements other than potassium. *Radiation Measurements*, 40(1):84–93, 2004.

[142] Huntley, D. J., Hancock, R. G. V., and Haskell, E. H. The Rb contents of the K-feldspar grains being measured in optical dating. *Ancient TL*, 19:43–46, 2001.

[143] Huntley, D. J. and Baril, M. R. The K content of the K-feldspars being measured in optical dating or in thermoluminescence dating. *Ancient TL*, 15:11–13, 1997.

[144] Reimann, T., Thomsen, K. J., Jain, M., Murray, A. S., and Frechen, M. Single-grain dating

of young sediments using the pIRIR signal from feldspar. *Quaternary Geochronology*, 11: 28–41, 2012. ISSN 1871-1014. doi: https://doi.org/10.1016/j.quageo.2012.04.016. URL `https://www.sciencedirect.com/science/article/pii/S187110141200091X`.

[145] Murray, A. Developments in optically stimulated luminescence and photo-transferred thermoluminescence dating of young sediments: Application to a 2000-year sequence of flood deposits. *Geochimica et Cosmochimica Acta*, 60(4):565–576, 1996. ISSN 0016-7037. doi: https://doi.org/10.1016/0016-7037(95)00418-1. URL `https://www.sciencedirect.com/science/article/pii/0016703795004181`.

[146] Auclair, M., Lamothe, M., and Huot, S. Measurement of anomalous fading for feldspar IRSL using SAR. *Radiation Measurements*, 37:487–492, 2003.

[147] Sohbati, R., Murray, A. S., Jain, M., and Egholm, D. Burial and exposure dating of glaciated rock surfaces using luminescence: a case study from Norway. In *Book of abstracts: 14th International Conference on Luminescence and Electron Spin Resonance Dating*, page 190, 2014.

[148] Rhodes, E. J. Dating sediments using potassium feldspar single-grain IRSL: Initial methodological considerations. *Quaternary International*, 362:14–22, 2015. ISSN 1040-6182. doi: https://doi.org/10.1016/j.quaint.2014.12.012. URL `https://www.sciencedirect.com/science/article/pii/S1040618214009471`. 9th New World Luminescence Dating Workshop.

[149] Marquet, J.-C. personal communication, 2019.

[150] Lapp, T., Jain, M., Thomsen, K. J., Murray, A. S., and Buylaert, J. P. New luminescence measurement facilities in retrospective dosimetry. *Radiation Measurements*, 47:803–808, 2012.

[151] Guérin, G., Mercier, N., and Adamiec, G. Dose-rate conversion factors: update. *Ancient TL*, 29:5–8, 2011b.

[152] Miallier, D., Guérin, G., Mercier, N., Pilleyre, T., and Sanzelle, S. The Clermont radiometric reference rocks: a convenient tool for dosimetric purposes. *Ancient TL*, 27(2):37–42, 2009.

[153] Kreutzer, S., Martin, L., Guérin, G., Tribolo, C., Selva, P., and Mercier, N. Environmental dose rate determination using a passive dosimeter: techniques and workflow for $\alpha - Al_2O_3$:C chips. *Geochronometria*, 45(1):56–67, 2018.

[154] Duller, G. A. T. The Analyst software package for luminescence data: overview and recent improvements. *Ancient TL*, 33:35–42, 2015.

[155] Thomsen, K. J., Murray, A. S., and Bøtter-Jensen, L. Sources of variability in OSL dose measurements using single grains of quartz. *Radiation Measurements*, 39(1):47–61, 2005.

[156] Ballarini, M., Wallinga, J., Wintle, A. G., and Bos, A. J. J. A modified SAR protocol for optical dating of individual grains from young quartz samples. *Radiation Measurements*, 42: 360–369, 2007.

[157] Combès, B., Lanos, P., Philippe, A., Mercier, N., Tribolo, C., Guérin, G., Guibert, P., and

Lahaye, C. A Bayesian central equivalent dose model for optically stimulated luminescence dating. *Quaternary Geochronology*, 28:62–70, 2015.

[158] Guérin, G., Combès, B., Tribolo, C., Lahaye, C., Mercier, N., Guibert, P., and Thomsen, K. J. Testing the accuracy of a single grain OSL Bayesian central dose model with known-age samples. *Radiation Measurements*, 81:62–70, 2015.

[159] Christophe, C., Philippe, A., Kreutzer, S., and Guerin, G. BayLum: Chronological Bayesian Models Integrating Optically Stimulated Luminescence and Radiocarbon Age Dating. R package version 0.1.3. https://CRAN.R-project.org/package=BayLum, 2018.

[160] Philippe, A., Guérin, G., and Kreutzer, S. BayLum - An R package for Bayesian analysis of OSL ages: An introduction. *Quaternary Geochronology*, 49:16–24, 2019. doi: 10.1016/j.quageo.2018.05.009.

[161] Vandenberghe, D., De Corte, F., Buylaert, J.-P., and Kučera, J. On the internal radioactivity in quartz. *Radiation Measurements*, 43(2-6):771–775, 2008.

[162] Timar-Gabor, A. and Wintle, A. G. On natural and laboratory generated dose response curves for quartz of different grain sizes from Romanian loess. *Quaternary Geochronology*, 18:34–40, 2013.

[163] Singh, A., Thomsen, K. J., Sinha, R., Buylaert, J.-P., Carter, A., Mark, D. F., Mason, P. J., Densmore, A. L., Murray, A. S., Jain, M., Paul, D., and Gupta, S. Counter-intuitive influence of Himalayan river morphodynamics on Indus Civilisation urban settlements. *Nature Communications*, 8:1–14, 2017.

[164] Thomsen, K. J., Murray, A. S., and Jain, M. The dose dependency of the overdispersion of quartz OSL single grain dose distributions. *Radiation Measurements*, 47:732–739, 2012.

[165] Arnold, L. J. and Roberts, R. G. Stochastic modelling of multi-grain equivalent dose (De) distributions: implications for OSL dating of sediment mixtures. *Quaternary Geochronology*, 4:204–230, 2009.

[166] Heydari, M. and Guérin, G. OSL signal saturation and dose rate variability: investigating the behaviour of different statistical models. *Radiation Measurements*, 120:96–103, 2018.

[167] Buylaert, J.-P., Murray, A. S., Gebhardt, A. C., Sohbati, R., Ohlendorf, C., Thiel, C., Wastegård, S., Zolitschka, B., and The PASADO Science Team. Luminescence dating of the PASADO core 5022-1D from Laguna Potrok Aike (Argentina) using IRSL signals from feldspar. *Quaternary Science Reviews*, 71:70–80, 2013.

Appendix

Derivations of luminescence exposure models

We define the dimensionless time as $t' = \overline{\sigma\varphi_0}t$ for first order and general order model, and as $t'' = \overline{\sigma\varphi_0}bzs^{-1}t$ for the fading model. Working with these dimensionless time give more simple derivations. We use

$$\frac{\partial n}{\partial t'} = \frac{\partial n}{\partial t}\frac{\partial t}{\partial t'} \tag{A1}$$

and likewise with t''. We use a dimensionless depth $x' = \mu x$ as well.

General order model

The derivation of the analytical solution for general order luminescence profiles with order a (Eq. 3.7) is given below with initial condition $n_m(t' = 0) = 1$.

$$\frac{\partial n_m}{\partial t'} = -e^{-x'}n_m^a \tag{A2}$$

$$\Rightarrow \int_{n_{m,0}}^{n_m} n_m^{-a}dn_m = \int_0^{t'} -e^{-x'}dt' \tag{A3}$$

$$\Rightarrow \frac{1}{(1-a)}\left(n_m^{1-a} - n_{m,0}^{1-a}\right) = -t'e^{-x'}, \qquad (a > 1) \tag{A4}$$

$$\Rightarrow n_m(x', t') = [(a-1)t'e^{-x'} + n_{m,0}^{1-a}]^{\frac{1}{1-a}}, \qquad (a > 1) \tag{A5}$$

$$= [(a-1)t'e^{-x'} + 1]^{\frac{1}{1-a}}, \qquad (a > 1, n_{m,0} = 1) \tag{A6}$$

With real depth and times we get an expression for the general order model (using $E(x) = \overline{\sigma\varphi_0}e^{-\mu x}$)

$$n_m(x, t) = [(a-1)tE(x) + 1]^{\frac{1}{1-a}}, \qquad (a > 1, n_{m,0} = 1) \tag{A7}$$

Fading model

To get a fading model for luminescence depth profiles we combine the two relations described by Jain et al.[54] (their Equations 8 and 9):

$$\frac{dn_f}{dt} = -3n_f z\rho'^{1/3}\left(\ln\frac{n_{f,0}}{n_f}\right)^{2/3}\tau_c^{-1} \tag{A8}$$

$$\tau_c = b^{-1}e^{\xi + \left(\frac{1}{\rho'}\ln\frac{n_{f,0}}{n_f}\right)^{1/3}} \tag{A9}$$

b [s^{-1}] is the attempt-to-tunnel frequency, $n_{f,0}$ [m^{-3}] is the trapped electron concentration at time t_0 prior to start of stimulation and corresponding to a full nearest neighbour distribution. ρ' is the dimensionless number density of hole sites; $\rho = 4/3\pi\rho\alpha^{-1}$ (ρ [m^{-3}] is the number density of the randomly distributed acceptors). z is the rate of change of lifetime $d\tau_c/dt = z$. ξ is the relative activation threshold $\xi = \ln\left(s/\overline{\sigma\phi_0}\right)$. τ_c [s] is the instantaneous lifetime at the critical tunnelling distance. In order to investigate this model with respect to luminescence-depth profiles we introduce a depth dependency on the excitation probability $\xi(x)$ as $e^{-\xi(x)} = s^{-1}\overline{\sigma\varphi_0}e^{-\mu x}$. We now combine these two expressions and integrate. (We assume no truncating and thereby $n_{f,i} = n_{f,0}$).

$$\frac{\partial n_f}{\partial t''} = -3n_f\rho'^{1/3}\left(\ln\frac{n_{f,0}}{n_f}\right)^{2/3}e^{-\left(\frac{1}{\rho'}\ln\frac{n_{f,0}}{n_f}\right)^{1/3}}e^{-x'} \tag{A10}$$

$$\Rightarrow \int_{n_{f,i}}^{n_f} -\rho'^{-1/3}\frac{1}{3}n_f^{-1}\left(\ln\frac{n_{f,0}}{n_f}\right)^{-2/3}e^{\left(\frac{1}{\rho'}\ln\frac{n_{f,0}}{n_f}\right)^{1/3}}du = e^{-x'}\int_0^{t''}dt' \tag{A11}$$

$$\Rightarrow e^{\left(\frac{1}{\rho'}\ln\frac{n_{f,0}}{n_f}\right)^{1/3}} - 1 = e^{-x'}t'' \tag{A12}$$

$$\Rightarrow n_f(x',t'') = n_{f,0}e^{-\rho'\left(\ln(t''e^{-x'}+1)\right)^3} \tag{A13}$$

With real depth and time, we get an expression for the fading model (using $E(x) = \overline{\sigma\varphi_0}e^{-\mu x}$ and $\beta = bzs^{-1}$)

$$n_f(x,t) = n_{f,0}e^{-\rho'(\ln(\beta E(x)t+1))^3} \tag{A14}$$

Truncated fading model

For each depth, the change in trapped charge results in a luminescence signal $L_{n_f}(t'') = -\frac{dn_f}{dt''}$. With $k \equiv \ln(\beta E(x)t+1) = \ln(t''e^{-x'}+1)$ and then $n_f = n_{f,0}e^{-\rho'k^3}$, the change in trapped charges is derived from differentiating Eq. A14 with t'' ($t'' = \beta E(x)$)

$$L_{n_f}(t'') = -\frac{\partial n_f}{\partial t''} = 3\rho'n_{f,0}k^2e^{-(\rho'k^3+k)}e^{-x'} \tag{A15}$$

L_{n_f} has a maximum at time t''_{max} due to loss before stimulation. t''_{max} is found by differentiating L_{n_f} with time and using $t''_{max}e^{-x'} = e^{k_{max}} - 1$.

$$\frac{\partial L_{n_f}}{\partial t''} = 0 \Rightarrow \frac{\partial L_{n_f}}{\partial k}\frac{\partial k}{\partial t''} = 0 \Rightarrow \frac{\partial L_{n_f}}{\partial k} = 0 \Rightarrow 3\rho'k_{max}^3 + k_{max} - 2 = 0 \tag{A16}$$

$$\Rightarrow k_{max} = q^{\frac{1}{3}} - \frac{1}{9\rho'}q^{-\frac{1}{3}} \tag{A17}$$

$$q(\rho') = \left(\frac{1}{(3\rho')^2} + \frac{1}{(9\rho')^3}\right)^{\frac{1}{2}} + \frac{1}{3\rho'} \tag{A18}$$

To let the decay curve have maximum at time $t'' = 0$, we introduce a truncated function $\hat{L}_u$ with $\hat{k} \equiv \ln[e^{-x'}(t'' + t''_{\max}) + 1]$. Inserting this in Eq. (A15) we get

$$\hat{L}_{n_f}(t'') = 3n_{f,0}\rho'\hat{k}^2 e^{-(\rho'\hat{k}^3+\hat{k})}e^{-x'} \tag{A19}$$

Although the time $t_{\max}$ is negligible small compared to exposure times often seen in rock surface dating, the corresponding truncated luminescence-depth profile is given as $\hat{n}_f(x,t)$

$$\int_{\hat{n}_{f,0}}^{\hat{n}_f} d\hat{n}_f = \int_0^t \hat{L}_{n_f}(t'')dt''$$

$$\hat{n}_f(x',t'') = n_{f,0}e^{-\rho'\left(\ln[(t+t_{\max})e^{-x'}+1]\right)^3}$$

$$= \hat{n}_{f,0}e^{\rho'k^3_{\max}}e^{-\rho'\left(\ln[t''e^{-x'}+e^{k_{\max}}]\right)^3}$$

with the initial value for $\hat{n}_f$ given by the integral

$$\hat{n}_{f,0} = -\int_0^\infty \hat{L}dt'' = n_{f,0}e^{-\rho'k^3_{\max}}$$

With real depth and time, the expression for the truncated fading model is (using $E(x) = \overline{\sigma\varphi_0}e^{-\mu x}$ and $\beta = bzs^{-1}$)

$$\hat{L}_{n_f}(t) = 3n_{f,0}\rho'\hat{k}^2 e^{-(\rho'\hat{k}^3+\hat{k})}\beta E(x) \tag{A20}$$

$$\hat{n}_f(x,t) = \hat{n}_{f,0}e^{\rho'k^3_{\max}}e^{-\rho'\left(\ln[\beta tE(x)+e^{k_{\max}}]\right)^3} \tag{A21}$$

Derivations of erosion for all three models

First-order model including erosion

The derivation for the first-order model including erosion (Eq. 3.38) is given below with $\epsilon' = \mu\epsilon$.

$$\frac{\partial n_{1,\epsilon'}}{\partial t'} = -e^{-(x'_i-\epsilon't)}n_{1,\epsilon'} \tag{A22}$$

$$\Rightarrow \int_1^{n_{1,\epsilon'}} n_1^{-1}dn_{1,\epsilon'} = -e^{-x'_i}\int_0^{t'} e^{\epsilon't}dt' \tag{A23}$$

$$\Rightarrow \ln n_{1,\epsilon'} = -\overline{\sigma\varphi_0}e^{-x'_i}\frac{1}{\epsilon'}\left(e^{\epsilon't}-1\right) \tag{A24}$$

$$= -\overline{\sigma\varphi_0}e^{-(x'_i-\epsilon't)}\frac{1}{\epsilon'}\left(1-e^{-\epsilon't}\right) \tag{A25}$$

$$\Rightarrow n_{1,\epsilon'}(x',t'_{\epsilon'}) = e^{-t'_{\epsilon'}e^{-x'}} \tag{A26}$$

With real times, depth and erosion rate we get

$$n_{1,\epsilon}(x,t_\epsilon) = e^{-t_\epsilon E(x)} \tag{A27}$$

$$t_\epsilon = \frac{1}{\mu\epsilon}\left(1-e^{-\mu\epsilon t}\right) \tag{A28}$$

with t_ϵ being an apparent exposure time, i.e. the exposure time one would obtain when fitting an eroded luminescence profile but not taking erosion into account.

General-order model including erosion

The derivation for the general-order model including erosion (Eq. 3.39) is given below.

$$\frac{\partial n_{m,\epsilon}}{\partial t'} = -e^{-\mu(x_i - \epsilon t)} n_{m,\epsilon}^a \tag{A29}$$

$$\Rightarrow \int_{n_{m,0}}^{n_{m,\epsilon}} n_{m,\epsilon}^{-a} dn_{m,\epsilon} = -e^{-x_i'} \int_0^{t'} e^{\epsilon' t} dt' \tag{A30}$$

$$\Rightarrow \frac{1}{(1-a)} \left(n_{m,\epsilon}^{1-a} - n_{m,0}^{1-a} \right) = -\overline{\sigma \varphi_0} e^{-x_i'} \frac{1}{\epsilon'} \left(e^{\epsilon' t} - 1 \right) \tag{A31}$$

$$\Rightarrow n_{m,\epsilon}(x', t) = [(a-1)\overline{\sigma \varphi_0} e^{-(x_i' - \epsilon' t)} \frac{1}{\epsilon'} \left(1 - e^{-\epsilon' t} \right) + n_{m,0}^{1-a}]^{\frac{1}{1-a}} \tag{A32}$$

$$\Rightarrow n_{m,\epsilon}(x, t_\epsilon) = [(a-1)t_\epsilon E(x) + n_{m,0}^{1-a}]^{\frac{1}{1-a}} \tag{A33}$$

Again with t_ϵ defined in Eq. A28.

Fading model including erosion

The derivation of the fading order model including erosion (Eq. 3.40) is given below.

$$\frac{\partial n_{f,\epsilon}}{\partial t''} = -3 n_{f,\epsilon} \rho'^{1/3} \left(\ln \frac{n_{f,0}}{n_{f,\epsilon}} \right)^{2/3} e^{-\left(\frac{1}{\rho'} \ln \frac{n_{f,0}}{n_{f,\epsilon}} \right)^{1/3}} e^{-(x_i' - \epsilon' t)} \tag{A34}$$

$$\Rightarrow \int_{n_{f,0}}^{n_{f,\epsilon}} -\rho'^{-1/3} \frac{1}{3} n_{f,\epsilon}^{-1} \left(\ln \frac{n_{f,0}}{n_{f,\epsilon}} \right)^{-2/3} e^{\left(\frac{1}{\rho'} \ln \frac{n_{f,0}}{n_{f,\epsilon}} \right)^{1/3}} dn_{f,\epsilon} = \int_0^{t'} e^{-(x_i' - \epsilon' t)} dt' \tag{A35}$$

$$\Rightarrow e^{\left(\frac{1}{\rho'} \ln \frac{n_{f,0}}{n_{f,\epsilon}} \right)^{1/3}} - 1 = e^{-x_i'} \int_0^{t'} e^{\epsilon' t} dt' \tag{A36}$$

$$= \beta \overline{\sigma \varphi_0} e^{-(x_i' - \epsilon' t)} \frac{1}{\epsilon'} \left(1 - e^{-\epsilon' t} \right) \tag{A37}$$

$$\Rightarrow n_{f,\epsilon}(x, t_\epsilon) = n_{f,0} e^{-\rho'(\ln(t_\epsilon \beta E(x) + 1))^3} \tag{A38}$$

Again with t_ϵ defined in Eq.(A28).

Derivation of apparent fitting parameters using 1st. order

$$\ln(t')_a = -\frac{y_1^m x_{p,2}^m - y_2^m x_{p,1}^m}{x_{p,2}^m - x_{p,1}^m} = f(t', a, p, \Delta p)$$

$$= \frac{\ln(-\ln p_1))\ln\frac{t'(a-1)}{p_2^{1-a}-1} - \ln(-\ln p_2))\ln\frac{t'(a-1)}{p_1^{1-a}-1}}{\ln(p_1^{1-a}-1) - \ln(p_2^{1-a}-1)}$$

$$= \ln t'\frac{\ln\frac{\ln p1}{\ln p2}}{\ln\frac{p_1^{1-a}-1}{p_2^{1-a}-1}} + \frac{\ln(-\ln p_1))\ln\frac{(a-1)}{p_2^{1-a}-1} - \ln(-\ln p_2))\ln\frac{(a-1)}{p_1^{1-a}-1}}{\ln(p_1^{1-a}-1) - \ln(p_2^{1-a}-1)}$$

$$= \ln t'\frac{\ln\frac{\ln p1}{\ln p2}}{\ln\frac{A_2}{A_1}} + \frac{\ln(-\ln p_1))\ln A_2 - \ln(-\ln p_2))\ln A_1}{\ln(p_1^{1-a}-1) - \ln(p_2^{1-a}-1)}$$

$$\ln(t')_\rho = -\frac{y_1^u x_{p,2}^u - y_2^u x_{p,1}^u}{x_{p,2}^u - x_{p,1}^u} = f(t'', \rho, p, \Delta p)$$

$$= \frac{\ln(-\ln p_1))\ln\frac{t''}{e^{\left(\frac{\ln p2}{-\rho}\right)^{1/3}}-1} - \ln(-\ln p_2))\ln\frac{t''}{e^{\left(\frac{\ln p1}{-\rho}\right)^{1/3}}-1}}{\ln(e^{\left(\frac{\ln p1}{-\rho}\right)^{1/3}}-1) - \ln(e^{\left(\frac{\ln p2}{-\rho}\right)^{1/3}}-1)}$$

$$= \ln t'\frac{\ln\frac{\ln p1}{\ln p2}}{\ln\frac{B_2}{B_1}} + \frac{\ln(-\ln p_1))\ln B_2 - \ln(-\ln p_2))\ln B_1}{\ln(p_1^{1-a}-1) - \ln(p_2^{1-a}-1)}$$

$$\mu_a = \frac{y_1^m + \ln(t')_a}{x_{p,1}^m} = \mu f(t', a, p, \Delta p)$$

$$= \mu\frac{\ln t'\frac{\ln\frac{p_1}{p_2}}{\ln\frac{A_2}{A_1}} - \ln(-\ln(p_1)) + \frac{\ln(-\ln p_1))\ln A_2 - \ln(-\ln p_2))\ln A_1}{\ln(p_1^{1-a}-1) - \ln(p_2^{1-a}-1)}}{\ln t' + \ln A_1}$$

$$\mu_\rho = \frac{y_1^u + \ln(t')_\rho}{x_{p,1}^u} = \mu f(t'', \rho, p, \Delta p)$$

$$= \mu\frac{\ln t'\frac{\ln\frac{\ln p1}{\ln p2}}{\ln\frac{B_2}{B_1}} - \ln(-\ln(p_1)) + \frac{\ln(-\ln p_1))\ln B_2 - \ln(-\ln p_2))\ln B_1}{\ln(p_1^{1-a}-1) - \ln(p_2^{1-a}-1)}}{\ln t' + \ln B_1}$$